Physics of the Solid State, Vol. 47, No. 2, 2005, pp. 199–201. Translated from Fizika Tverdogo Tela, Vol. 47, No. 2, 2005, pp. 193–195.

METALS AND SUPERCONDUCTORS

Influence of External Conditions on Crystallization Mechanisms in Eutectic Sn–Pb Melts

A. P. Belyaev and V. P. Rubets

St. Petersburg Technological Institute (Technical University), Moskovskiĭ pr. 26, St. Petersburg, 198013 Russia

e-mail: Belyaev@tu.spb.ru

Received February 27, 2004; in final form, April 26, 2004

Abstract—Crystallization of a eutectic Sn–Pb melt was studied under strongly nonequilibrium and equilibrium conditions with an ac electric field applied to the sample from a rectangular-pulse generator having a frequency of above 150 kHz. Cooling curves and surface micrographs of various sections through the sample volume were obtained. It was shown that the crystallization time decreases and the eutectic grain scale changes under a field.

1. INTRODUCTION

In [1], the influence of inhomogeneous conditions on the crystallization mechanisms of a eutectic Sn–Pb melt was reported on. The possibility of consistently describing detected features on the basis of recent theoretical advances [2] was also shown. However, crystallization features under strongly nonequilibrium conditions and in an electric field were not considered in [1]. Meanwhile, the implementation of these conditions is currently considered a promising technique for producing materials with new properties. For this reason, we studied the crystallization of a eutectic Sn–Pb melt under strongly nonequilibrium conditions and in an energetically weak (in terms of the determination of basic thermodynamic parameters) ac unipolar electric field.

2. EXPERIMENTAL

Crystallization of a eutectic Sn–Pb melt was studied in vacuum at a pressure of ~10^{-3} Pa using the setup shown schematically in Fig. 1. A eutectic was placed into a quartz cell with platinum electrodes and heated in a special cylindrical furnace to a homogeneous melt. Then, the cell was removed from the furnace and the cooling curve was measured. After that, the cell with the eutectic was again placed into the furnace, a generator of positive rectangular pulses was turned on, and then the cell was removed from the furnace and the cooling curve was measured again. The generator terminals were connected to the sample so that the electric field was directed from the cold to the hot part of the sample. The experiment was repeated several times to monitor the reproducibility of the measurement result. The current pulse amplitude was monitored using a measuring resistance R and an oscilloscope. The main results were obtained at a current amplitude of 5 A and a pulse repetition rate of 170 kHz with a duty ratio of 10. The electric field strength inside the sample did not exceed a few tenths of a volt per centimeter.

Crystallization under strongly nonequilibrium conditions was modeled by placing a eutectic melt into liquid nitrogen.

Eutectic samples were shaped like cylinders 1.0 cm in diameter and 5.0 cm long. Morphological studies were carried on sections through the points designated by letters in Fig. 1. Samples were prepared using the technique described in [1]. Morphological studies were performed using a JSM-35 scanning electron microscope. All micrographs were made in z contrast.

3. RESULTS

We studied the morphology of sections of eutectics synthesized during eutectic-melt crystallization under conditions close to equilibrium and under strongly nonequilibrium conditions. Eutectics obtained by crystalli-

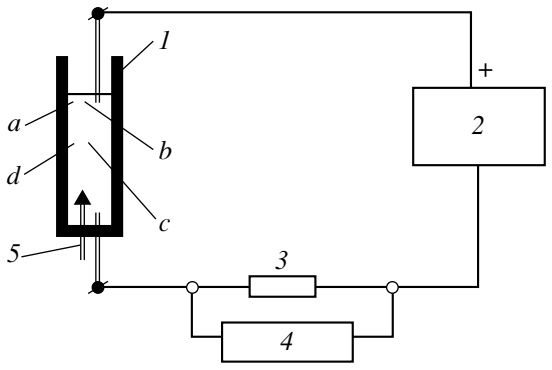

Fig. 1. Schematic representation of the setup for melt crystallization: (*1*) quartz cell, (*2*) rectangular pulse generator, (*3*) measuring resistance, (*4*) oscilloscope, and (*5*) thermocouple. Letters designate the regions corresponding to micrographs in Fig. 2.

1063-7834/05/4702-0199$26.00 © 2005 Pleiades Publishing, Inc.

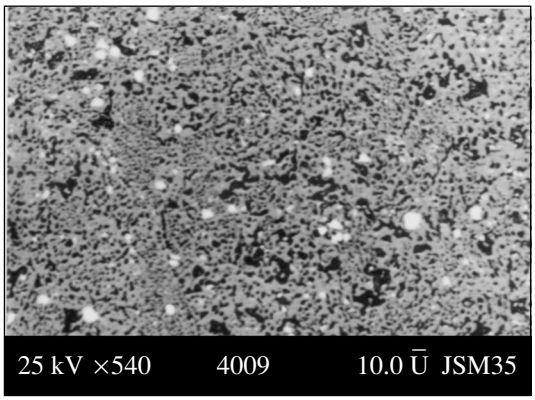

Fig. 2. Micrograph of a cross section of a eutectic produced by melt crystallization under strongly nonequilibrium conditions.

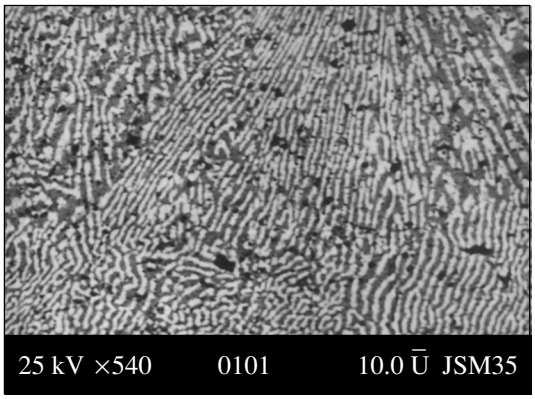

Fig. 3. Micrograph of a cross section of a eutectic produced by melt crystallization under equilibrium conditions in a zero external field.

zation in a nonzero and zero electric field were studied. In the case of melt crystallization under conditions close to equilibrium, cooling curves were additionally measured. Their shape was characteristic of eutectic-melt crystallization [1]. The duration of melt crystallization (the region where the temperature ceases to change) depended on whether the crystallization was carried out in an external field or without a field. In the former case, this region decreased in size by ~14% (186 s in comparison with 216 s).

The main results of the study of the eutectics section morphology are shown in Figs. 2–4. The section morphology of samples synthesized under strongly nonequilibrium conditions was characteristic of anomalous eutectics, in which it was difficult to separate regions enriched with lead or tin (Fig. 2; white inclusions correspond to traces of paste used when preparing the sample).

The morphology of all sections of all the samples obtained by crystallization under equilibrium conditions was close to that of normal eutectics. The eutectics produced by crystallization in a zero field were characterized by uniform sizes of eutectic grains over the sample volume (~2.5 μm). The typical morphology of such a sample is shown in Fig. 3. The samples synthesized in an electric field were characterized by nonuniform sizes of eutectic grains in various eutectic regions. Near the surface (regions *a*, *b* in Fig. 1), the eutectic grain size decreased (Figs. 4a, 4b) by factors of ~2 and ~1.5 in the periphery (region *a*) and in the central region, respectively, in comparison with the sample synthesized in a zero field. In the sample volume

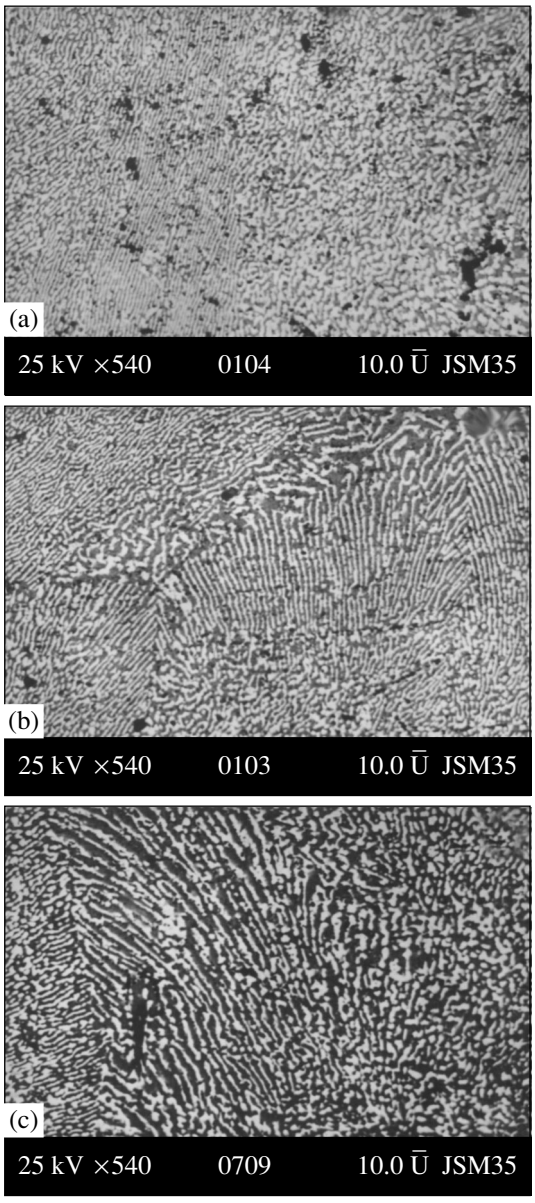

Fig. 4. Micrographs of cross sections of eutectics produced by melt crystallization under equilibrium conditions in an external electric field; the eutectic section surface (a, b) in regions *a* and *b*, respectively, and (c) in regions *c* and *d* in Fig. 1.

(regions *c*, *d*), the grain size remained almost unchanged (Fig. 4c).

The above-described influence of the field on the crystallization took place only under an ac external field having a frequency of above 150 kHz and directed from the cold part of the sample to the hot part. In the case where the field was in the opposite direction, no influence of the field on crystallization was detected.

However, we were unable to propose a fully argued, consistent explanation of the entire set of observed phenomena.

4. CONCLUSIONS

(i) An ac unipolar electric field directed from the cold part of a sample to the hot part reduces the crystallization time of a eutectic Sn–Pb melt and decreases the eutectic grain size.

(ii) The efficiency of the influence of the electric field on the crystallization depends on its frequency. The effect of an electric field becomes appreciable at frequencies of above 150 kHz.

ACKNOWLEDGMENTS

The authors thank S.A. Kukushkin for helpful discussions of the results.

This study was supported by the Russian Foundation for Basic Research, project no. 02-03-40432.

REFERENCES

1. A. P. Belyaev, S. A. Kukushkin, and V. P. Rubets, Fiz. Tverd. Tela (St. Petersburg) **43** (4), 577 (2001) [Phys. Solid State **43**, 597 (2001)].
2. S. A. Kukushkin and A. V. Osipov, Fiz. Tverd. Tela (St. Petersburg) **39** (8), 1464 (1997) [Phys. Solid State **39**, 1299 (1997)].

Translated by A. Kazantsev

Physics of the Solid State, Vol. 47, No. 2, 2005, pp. 202–213. Translated from Fizika Tverdogo Tela, Vol. 47, No. 2, 2005, pp. 196–207.

METALS AND SUPERCONDUCTORS

The Nernst–Ettingshausen Coefficient in the Normal Phase of Doped HTSCs of the $YBa_2Cu_3O_y$ System

V. E. Gasumyants, N. V. Ageev, and M. V. Elizarova

St. Petersburg State Polytechnic University, Politekhnicheskaya ul. 25, St. Petersburg, 195251 Russia

e-mail: VGAS@rphf.spbstu.ru

Received March 9, 2004; in final form, May 17, 2004

Abstract—The temperature dependence of the Nernst–Ettingshausen coefficient $Q(T)$ in the normal phase of doped HTSCs of the yttrium system was studied. The main features characterizing the behavior of this coefficient were revealed, and the character and mechanism of the effect that various nonisovalent substituents exert on the $Q(T)$ dependence were analyzed. It is shown that the narrow-band model permits one not only to describe all the specific features observed in the $Q(T)$ curves but also to perform a simultaneous quantitative analysis of the temperature dependences of four kinetic coefficients (the electrical resistivity and the Seebeck, Hall, and Nernst–Ettingshausen coefficients) with the use of a common set of model parameters characterizing the band structure and carrier system in the normal phase of an HTSC. This approach was employed to determine the carrier mobilities and the asymmetry of the dispersion curve in the systems studied ($YBa_2Cu_3O_y$, y = 6.37–6.91; $YBa_2Cu_{3-x}Co_xO_y$, x = 0–0.3; $Y_{1-x}Ca_xBa_2Cu_3O_y$, x = 0–0.25; $Y_{1-x}Ca_xBa_{2-x}La_xCu_3O_y$, x = 0–0.5) and to analyze the effect of the substitutions involved on the variation of these parameters. © *2005 Pleiades Publishing, Inc.*

1. INTRODUCTION

Systematic experimental studies of electronic transport phenomena in HTSCs of various families are widely used to probe various features of the band structure and properties of the carrier system in these materials. A wealth of information has been accumulated on the temperature dependence of three major kinetic coefficients (the electrical resistivity and the Seebeck and Hall coefficients) in samples of various families. The extent to which these dependences (and the value of the critical temperature) are influenced by various deviations in the sample composition from its optimum level from the standpoint of its superconducting properties has been studied in detail (see, e.g., reviews [1–3]). While a variety of models have been proposed for the normal state (see, e.g., review [4]), none of them has been universally accepted.

A substantially smaller number of studies have dealt with the behavior exhibited in the normal phase by another kinetic parameter, the Nernst–Ettingshausen coefficient Q, which has not received as much research attention. Unlike the thermopower and the Hall effect, the Nernst–Ettingshausen thermomagnetic effect is insensitive to the sign of the carriers and is determined, according to the classical theory of kinetic phenomena, by the band structure and the character of the energy dependence of the carrier relaxation time [5]. As a result, even qualitative analysis of the $Q(T)$ behavior would require detailed knowledge of the band structure of the material under study. It is the lack of this information for the HTSC materials that apparently accounts for the extremely limited number of experimental studies of the $Q(T)$ behavior in the normal phase and of attempts to analyze them (experimental results can be found in [6–9]; for a qualitative analysis of the available data, see [7–10]).

In recent years, interest in the Nernst–Ettingshausen coefficient (NEC) has substantially increased starting with [11]. A study of the $Q(T)$ dependences was reported in [11]. That study was performed on a series of $La_{2-x}Sr_xCuO_4$ samples, in which the NEC was observed to remain anomalously large at temperatures 50–100 K above T_c. It was concluded that there are superconducting fluctuations in HTSCs at these temperatures and that the NEC is influenced by vortex-type interactions. The results reported in [11] stimulated both experimental and theoretical investigations of the NEC in HTSCs. The $Q(T)$ dependences have been studied experimentally in various magnetic fields on samples of the systems $La_{2-x}Sr_xCuO_4$ [12–14], $Bi_2Sr_{2-y}La_yCuO_6$ [12], and $Pr_{2-x}Ce_xCuO_4$ [15]. The above studies attempted to separate the contributions from free carriers and superconducting fluctuations to the NEC measured at $T > T_c$. Those studies, in turn, stirred interest in a theoretical investigation of the NEC behavior in the region of existence of fluctuating superconducting pairs [16–18].

While the papers referred to are certainly of interest, the methods they propose to analyze the $Q(T)$ behavior are not free of shortcomings. This relates primarily to the NEC having been discussed with no connection at all to the behavior of other kinetic coefficients of HTSC materials. We believe that only an approach that provides a common explanation of the anomalous behavior

for all four main kinetic coefficients (electrical resistivity and the Seebeck, Hall, and Nernst–Ettingshausen coefficients) from the same standpoint could be considered meaningful. It is the development of such an approach that is the subject of the present study. Our analysis of the experimental $Q(T)$ relations is based on the narrow conduction band model [19]. As has been shown by us more than once, this model can be used to interpret and quantitatively analyze the temperature dependence of resistivity and of the Hall and Seebeck coefficients obtained for samples of different HTSC systems with various deviations from the stoichiometric composition (for the most complete exposition of the results, see review [4]). It turns out possible not only to explain and describe the specific features of the behavior of the three kinetic coefficients but also to derive (by analyzing their temperature dependences) valuable information on the parameters of the carrier system in the normal phase. We also performed a comprehensive theoretical analysis of the behavior of the Nernst–Ettingshausen effect in conductors with a narrow conduction band and demonstrated that it is possible to employ the proposed approach to describe the $Q(T)$ relations observed in HTSC materials [20]. The present paper reports on a correlated analysis of the temperature dependences of the kinetic coefficients in the normal phase based on experimental data obtained on samples of four doped HTSC systems of the $YBa_2Cu_3O_y$ family.

2. SAMPLES

We studied four series of ceramic samples of the following compositions: $YBa_2Cu_3O_y$ (y = 6.37–6.91), $YBa_2Cu_{3-x}Co_xO_y$ (x = 0–0.3), $Y_{1-x}Ca_xBa_2Cu_3O_y$ (x = 0–0.25), and $Y_{1-x}Ca_xBa_{2-x}La_xCu_3O_y$ (x = 0–0.5). All samples were prepared by the standard solid-phase method using the same procedure. The annealing was done in air at a temperature T = 920–950°C, with two or three intermediate grindings. Next, to saturate the samples with oxygen to the maximum extent possible, they were cooled slowly and annealed in an oxygen flow at T = 450°C for 4 h with subsequent slow cooling to room temperature.

All samples were highly homogeneous, which was revealed by thermoprobe measurements of the Seebeck coefficient at T = 300 K. X-ray analysis showed them to be single phase to within 1–2%. Furthermore, in all samples, the oxygen content was checked by iodometric titration (the accuracy of determination of the values of y was ±0.01 per formula unit).

The $YBa_2Cu_3O_y$ series with variable oxygen content consisted of seven samples with a gradually decreasing oxygen index y (6.91, 6.82, 6.72, 6.65, 6.61, 6.48, 6.37), which was achieved by annealing in an oxygen-deficient atmosphere at different temperatures. The $YBa_2Cu_{3-x}Co_xO_y$ series was made up of ten samples with x = 0.01, 0.02, 0.03, 0.05, 0.07, 0.10, 0.15, 0.20, 0.25, and 0.30. In this case, the oxygen content increases with x successively from y = 6.89 for x = 0 to y = 7.06 for x = 0.3.

The last two series of samples were chosen for studying the effect of the $Ca^{2+} \longrightarrow Y^{3+}$ substitution, which is known to give rise to a number of unusual sample properties in both the normal and the superconducting state [4, 21]. We studied the effect of both single doping with calcium (the $Y_{1-x}Ca_xBa_2Cu_3O_y$ system) and codoping (the $Y_{1-x}Ca_xBa_{2-x}La_xCu_3O_y$ system) with equal concentrations of the two dopant impurities. The oxygen content in these series was originally reduced by joint annealing of the samples of each series at T = 450°C in an oxygen-deficient atmosphere for two hours to increase the kinetic coefficients, thereby making quantitative analysis of their behavior in terms of the narrow conduction band model more reliable. A specific feature of the samples in these series is that they are charge-compensated. In the case of $Y_{1-x}Ca_xBa_2Cu_3O_y$, the smaller charge of calcium as compared with that of yttrium is compensated for by the successive decrease in the oxygen content (from y = 6.73 at x = 0 to y = 6.33 for x = 0.2). In the $Y_{1-x}Ca_xBa_{2-x}La_xCu_3O_y$ system, the impurity cations differing in the valence state from the elements they substitute for ($Ca^{2+} \longrightarrow Y^{3+}$ and $La^{3+} \longrightarrow Ba^{2+}$) compensate for each other in their effect on the total-charge balance in the lattice. As a result, the oxygen content varies only insignificantly with increasing doping level (from y = 6.83 at x = 0 to y = 6.89 for x = 0.5). For a detailed description of the properties of all our samples, the reader may refer to our previous publications [4, 19, 22, 23]. Some of the data obtained are listed in the table.

3. MEASUREMENT TECHNIQUES

We first measured the temperature dependences of the resistivity ρ and of the Seebeck (S) and Hall (R_H) coefficients, which were subsequently used together with the NEC data in an analysis within the narrow conduction band model. These relations demonstrate well-known features, and their behavior is described and analyzed in considerable detail in [4, 19, 22, 23].

The $Q(T)$ dependences were studied in the cell shown schematically in Fig. 1. It consists of two massive copper blocks sandwiching the sample. One of the blocks can be displaced to clamp the sample. To produce a temperature gradient, an electrical heater is mounted in one of the copper blocks. The temperature difference is measured with a differential Cu–constantan thermocouple, with its junctions fixed in the blocks. The cell temperature is monitored with a diode, which is also mounted in a copper block. The sample is insulated by thin mica spacers to preclude electrical contact between the sample and the copper blocks. The measuring circuit contains a compensation loop (which reduces the induction currents generated when the magnetic field is turned on and off) and a special com-

Compositions, critical temperatures, kinetic coefficients for $T = 300$ K, and band structure parameters as derived from the temperature dependences of the Seebeck coefficient using the narrow-band model for the samples studied

x	y	T_c, K	S, μV/K ($T = 300$ K)	$R_H \times 10^3$, cm^3/C ($T = 300$ K)	F	W_D, meV	$C = W_\sigma/W_D$	b
				$YBa_2Cu_3O_y$				
–	6.91	89.5	2.5	0.48	0.508	85	0.35	0
–	6.82	87.2	12.5	1.75	0.533	135	0.34	0
–	6.72	66.5	16.4	2.74	0.547	185	0.33	0
–	6.65	60.0	29.0	3.41	0.552	225	0.32	0
–	6.61	57.1	35.8	4.36	0.586	270	0.30	0
	6.48	34.7	64.1	8.98	0.615	420	0.28	0
–	6.37	<4.2	176.0	13.96	0.625	530	0.24	0
				$YBa_2Cu_{3-x}Co_xO_y$				
0.02	6.98	93.1	1.7	1.10	0.504	70	0.41	0
0.03	6.99	92.6	3.1	1.63	0.508	80	0.40	0
0.05	7.00	92.2	5.0	2.50	0.514	80	0.43	0
0.07	7.01	91.8	7.8	3.31	0.517	125	0.25	0
0.1	7.02	87.9	11.0	4.16	0.523	150	0.25	0
0.15	7.04	76.9	19.6	6.00	0.533	190	0.23	0
0.2	7.04	67.9	30.6	6.72	0.544	230	0.21	0
0.25	7.05	60.6	37.1	7.32	0.544	360	0.17	0
0.3	7.06	49.7	57.8	8.26	0.554	440	0.16	0
				$Y_{1-x}Ca_xBa_2Cu_3O_y$				
0	6.73	63.7	17.8	2.23	0.528	175	0.31	0
0.025	6.72	70.8	14.0	2.17	0.524	170	0.26	–0.003
0.05	6.70	72.0	12.4	2.15	0.517	180	0.23	–0.005
0.075	6.68	75.1	13.3	2.13	0.511	200	0.21	–0.010
0.1	6.66	80.0	9.4	2.10	0.503	205	0.20	–0.012
0.15	6.58	80.6	9.3	2.09	0.494	220	0.19	–0.020
0.2	6.53	80.9	8.0	2.06	0.485	235	0.19	–0.027
				$Y_{1-x}Ca_xBa_{2-x}La_xCu_3O_y$				
0	6.83	85.6	8.3	1.81	0.514	170	0.27	0
0.05	6.84	81.4	8.3	1.76	0.508	190	0.22	–0.005
0.1	6.85	76.9	9.1	1.89	0.502	200	0.19	–0.011
0.2	6.86	75.1	9.2	1.96	0.492	235	0.16	–0.021
0.3	6.85	67.9	10.0	2.02	0.480	265	0.15	–0.033
0.4	6.87	66.9	9.4	1.98	0.470	275	0.14	–0.042
0.5	6.89	65.3	11.8	2.16	0.461	295	0.14	–0.052

pensating circuit permitting suppression or a substantial reduction of the originally present (for zero magnetic field) parasitic thermopower signal induced by the longitudinal temperature drop and nonuniform thermal contact of the sample with the heater. To isolate the Nernst–Ettingshausen voltage from the background of voltages produced by the even effects in a magnetic field, the measurements are performed in two opposite orientations of the magnetic field. The measurements are conducted under heating of the cell after preliminary cooling with liquid nitrogen. A measurement cycle extending from $T = 77$ to 300 K lasts about two hours, which provides a sufficiently slow sample temperature variation. The magnetic fields used in the experiments were typically 1.8 T, and the temperature gradient was on the order of 100 K/cm.

The sides of a sample are ground, with particular emphasis placed on adjusting its planes perpendicular to the gradient ∇T so as to make them parallel to each

other. On one of them, longitudinal grooves are cut and filled by molten indium to prepare a contact pad, to which thin copper wires are attached with a paste based on finely dispersed silver; from these wires, the signal of the Nernst–Ettingshausen effect is obtained. The total contact resistance does not exceed 1 Ω, thus providing a substantially reduced noise level in the measuring circuit. The sample dimensions are typically 3–4 mm in the magnetic field direction, 1 mm along the temperature gradient, and 8–10 mm in the signal base direction.

The measurements are conducted at T = 80–350 K; the error with which the NEC values are determined in $Q(T)$ measurements does not exceed 10%, and the minimum reliably determined NEC value in mobility units, $Q/(k_B/e)$, is 5×10^{-3} cm^2/V s at T = 300 K.

Check experiments showed that the signal voltage depends linearly on the temperature gradient, magnetic field, and the distance between the measuring probes. It was also experimentally established that the real temperature gradient across the sample is 10% smaller than that calculated from readings of the thermocouple inserted into the copper blocks, which should be assigned to part of the gradient dropping across the thermal resistance between these blocks and the sample. This figure is almost temperature-independent, which allows one to introduce corrections for the true value of the temperature gradient across the sample in calculating Q.

4. EXPERIMENTAL $Q(T)$ RELATIONS

The experimental temperature dependences of the NEC are shown in Figs. 2–5 for all four sample series. Note that the $Q(T)$ relations for the samples of the first three lightly doped series could be measured only for $T > 150$ K and that no temperature measurements could be performed for $YBa_2Cu_{3-x}Co_xO_y$ with $x < 0.07$. It can be seen from Figs. 2–5 that, in the region T = 100–300 K, the NEC exhibits the same temperature dependence for all the types of off-stoichiometry studied. The values of the NEC of the $YBa_2Cu_3O_y$ HTSC system in the normal phase are very small; indeed, for close-to-stoichiometric compositions, $Q(300\text{ K})/(k_B/e) \le 0.1$ cm^2/V s, which is two to three orders of magnitude smaller than the values of Q in the region of mixed states [24–26]. As the temperature is raised from 100 K, the NEC grows to reach a broad maximum at T = 200–270 K, depending on the actual sample composition, and subsequently falls off slightly up to T = 300 K. Note that, although the NEC at T = 300 K is always positive, $Y_{1-x}Ca_xBa_{2-x}La_xCu_3O_y$ samples exhibit a transition to values $Q < 0$ at low temperatures (T < 130–160 K). However, the existence of a temperature interval within which $Q < 0$ is apparently not connected in any way with $YBa_2Cu_3O_y$ being codoped with calcium and lanthanum. This suggestion is corroborated by the presence of this temperature interval in the $Q(T)$ graph measured on the original (undoped) sample of the $Y_{1-x}Ca_xBa_{2-x}La_xCu_3O_y$

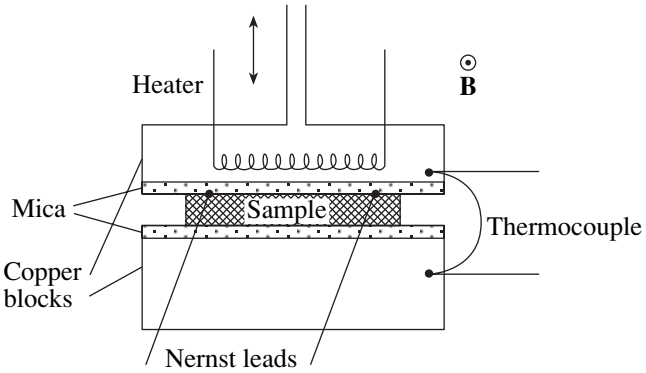

Fig. 1. Cell employed in measurements of the $Q(T)$ relations (schematic).

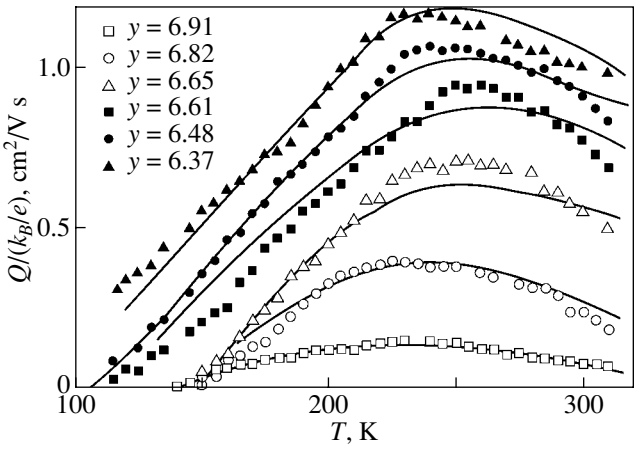

Fig. 2. Temperature dependence of the Nernst–Ettingshausen coefficient in $YBa_2Cu_3O_y$ samples. Symbols refer to experimental data, and the curves are model calculations.

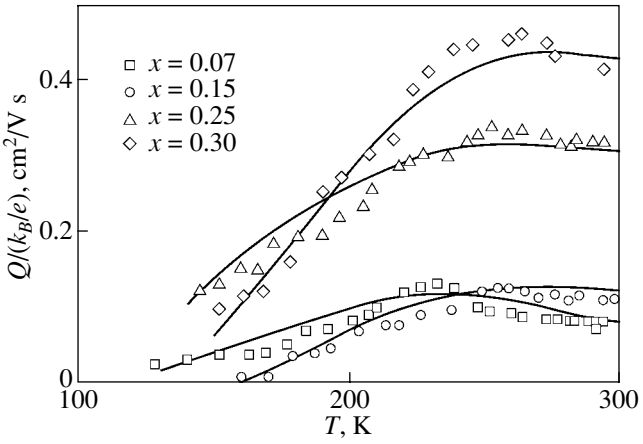

Fig. 3. Temperature dependence of the NEC in $YBa_2Cu_{3-x}Co_xO_y$ samples. Symbols refer to experimental data, and the curves are model calculations.

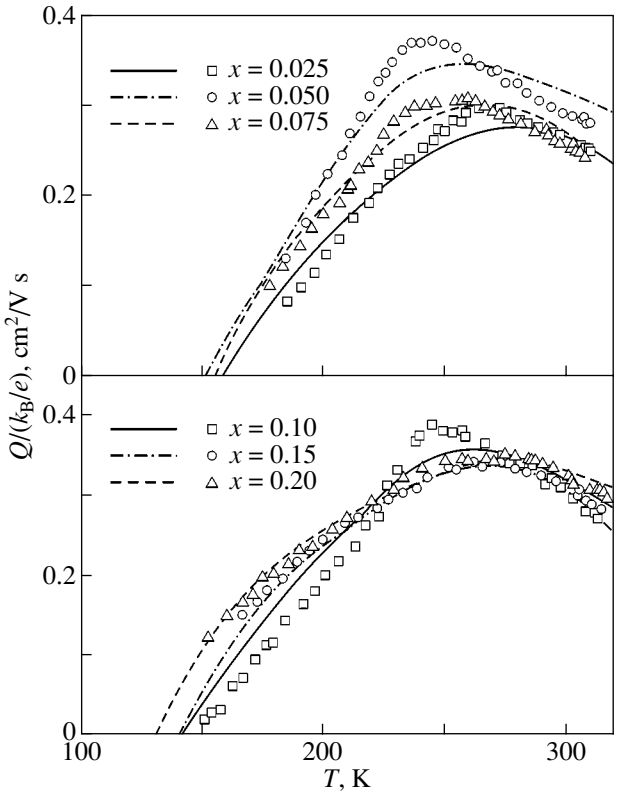

Fig. 4. Temperature dependence of the NEC in $Y_{1-x}Ca_xBa_2Cu_3O_y$ samples. Symbols refer to experimental data, and the curves are model calculations.

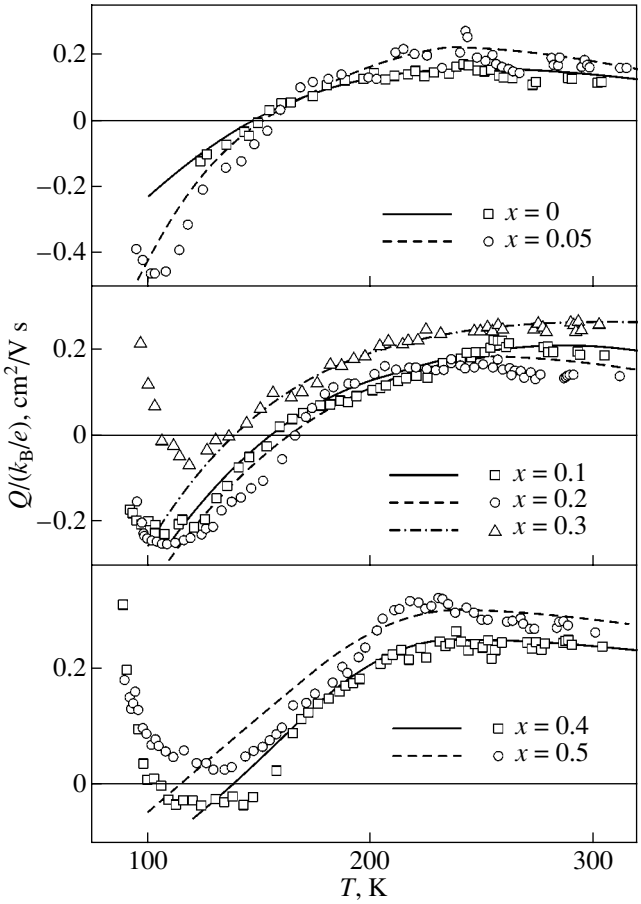

Fig. 5. Temperature dependence of the NEC in $Y_{1-x}Ca_xBa_{2-x}La_xCu_3O_y$ samples. Symbols refer to experimental data, and the curves are model calculations.

series (Fig. 5). Note that for $T > 150$ K this relation is almost identical to that obtained for $YBa_2Cu_3O_{6.82}$ (Fig. 2). In the samples of the first three series, no crossover to negative values of the NEC was observed to occur, because in these cases there was successful measurement of the $Q(T)$ relation at low temperatures only on samples with a sufficiently large deviation from stoichiometry, for which the absolute values of Q are relatively large. In $Y_{1-x}Ca_xBa_{2-x}La_xCu_3O_y$ samples, the charge effects of the two impurities cancel each other, so the critical temperature and the kinetic coefficients (electrical resistivity and the Hall and Seebeck coefficients) in these samples vary only weakly with increasing doping level [23]. Similarly, for all the values of x studied, the quantity Q(300 K) remains very low, which makes it possible to reliably observe the crossover to negative values of the NEC in the low-temperature domain. Thus, we believe that the crossover to negative values of NEC is a common feature in the behavior of the NEC in $YBa_2Cu_3O_y$ that becomes manifest in cases where the NEC is very small in magnitude.

Figure 6 displays the concentration dependences of the NEC for all four systems measured at T = 300 K. Note that these values were obtained for all the samples under study due to the higher sensitivity of the technique employed in measurements at a fixed tempera-

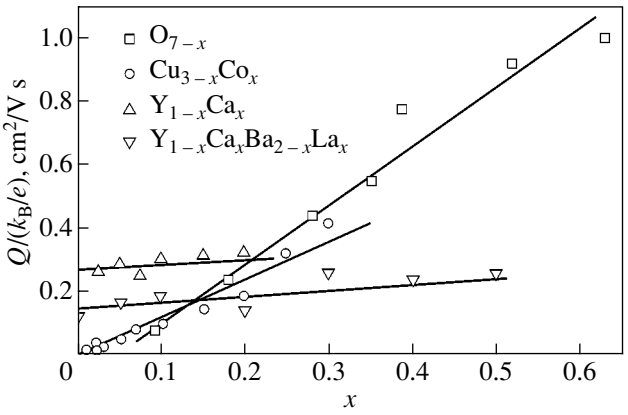

Fig. 6. Concentration dependences of the NEC at T = 300 K in the systems studied.

ture. This allowed us to establish that the value of $Q/(k_B/e)$ obtained at $T = 300$ K on samples as close to stoichiometric composition as possible becomes extremely small (down to 0.016 cm^2/V s for the $YBa_2Cu_{3-x}Co_xO_y$ sample with $x = 0.01$). Obviously enough, the absolute values of Q obtained for two different kinds of deviation from stoichiometry vary in ways that differ qualitatively. For $YBa_2Cu_3O_{7-x}$ with variable oxygen content, just as for $YBa_2Cu_{3-x}Co_xO_y$, the NEC at $T = 300$ K grows markedly with an increase in the doping level following a close-to-linear law. As a result, $Q(T = 300\ \text{K})$ in a sample with the maximum deviation from oxygen stoichiometry ($YBa_2Cu_3O_{6.36}$) reaches a value of 1 cm^2/V s. In the $Y_{1-x}Ca_xBa_2Cu_3O_y$ and $Y_{1-x}Ca_xBa_{2-x}La_xCu_3O_y$ systems, the NEC varies only slightly with increasing x (note that the absolute values of the other kinetic coefficients, as well as the critical temperature, vary in a qualitatively similar manner in the series studied; see table). This difference in the behavior of the NEC stems from the difference in the charge balance variation in the lattice initiated by the dopants studied. Indeed, in the first two series of samples, the deviation from stoichiometry brings about a strong change in the charge balance, whereas in the third and fourth systems the charge state of the samples remains almost unchanged due to compensation of the charge introduced by calcium, by a decrease in oxygen content ($Y_{1-x}Ca_xBa_2Cu_3O_y$), or by the charge of the second dopant ($Y_{1-x}Ca_xBa_{2-x}La_xCu_3O_y$) [4]. However, all the features present in the temperature dependences of $Q(T)$ remain unchanged in all four sample series.

The data obtained permit identification of the following general features of the NEC behavior in the normal phase, which are characteristic of doped HTSCs of the $YBa_2Cu_3O_y$ system as a whole:

(1) At $T = 300$ K, the NEC is positive and extremely small for compositions close to stoichiometry. At very small absolute values of Q, a crossover to negative values is observed at $T < 150$ K.

(2) As the temperature decreases, the NEC increases slightly and $Q(T)$ reaches a broad maximum and then falls off rapidly. Qualitatively, the pattern of the $Q(T)$ relation remains unchanged for different types of deviation from stoichiometry.

(3) The effect of deviations from stoichiometry on the magnitude of the NEC is governed by the change in the charge balance in the lattice. Under the conditions of oxygen deficiency or nonisovalent substitution of cobalt for the chain copper, the $Q(300\ \text{K})$ increase strongly in magnitude, while in samples doped with calcium (singly or with a codopant substitution Co $\longrightarrow$ Cu(1)), the variation in the NEC is insignificant.

(4) For all kinds of deviation from stoichiometry, the NEC varies in magnitude in the same way as the other kinetic coefficients and correlates with the variation in the superconducting properties of $YBa_2Cu_3O_y$.

5. DISCUSSION OF THE RESULTS

As mentioned in Section 1, no systematic analysis of the NEC behavior in HTSC materials has been performed thus far. Fairly rare attempts at such an analysis have been limited in most cases to a discussion of the $Q(T)$ relation obtained for a specific sample and did not consider the behavior of the NEC jointly with data available on other kinetic coefficients. In what follows, we perform a correlated analysis of the above experimental data on the $Q(T)$ relations combined with the results obtained earlier on the same samples for the temperature dependences of the Seebeck and Hall coefficients [4, 19, 22, 23].

We chose as a basis of this integrated approach the narrow-band model, which, as demonstrated more than once in our earlier publications, allows quantitative description of the temperature dependences of three kinetic coefficients (the electrical resistivity and the Seebeck and Hall coefficients) obtained for various samples of different HTSC systems [4, 19, 21–23]. Our earlier detailed theoretical analysis of the specific features of the Nernst–Ettingshausen effect in semiconductors with a narrow conduction band demonstrated that this model can provide an interpretation of experimental $Q(T)$ data [20]. It was shown that, in the case where the conduction band width is comparable to the Fermi broadening, the energy dependence of the relaxation time $\tau(\varepsilon)$ does not exert, in contrast to the predictions from the classical theory of electronic transport phenomena, any substantial influence on the NEC behavior. The calculations performed in [20] showed that the sign, magnitude, and character of the NEC temperature dependence are determined primarily by the extent to which the dispersion relation $\varepsilon(k)$ deviates from the quadratic law, whereas other details of the band structure turn out to be less significant and can be disregarded in calculations in a first approximation. This allowed us to propose and substantiate model approximations of the density-of-states function $D(\varepsilon)$, the differential conductivity $\sigma(\varepsilon)$, and the Hall conductivity $\sigma_H(\varepsilon)$. These approximations take into account the asymmetry in the $\varepsilon(k)$ relation and make it possible to obtain theoretical $Q(T)$ curves that are in overall qualitative agreement with the available experimental data on doped $YBa_2Cu_3O_y$. These approximations, retaining the rectangular shape accepted for the narrow-band model, are shown in Fig. 7. Within these approximations, the $Q(T)$ relation can be calculated as [20]

$$Q = -\frac{1}{eT}u\left(\frac{I_{H_1}}{I_0} - \frac{I_{H_0}I_1}{I_0^2}\right), \tag{1}$$

where

$$I_0 = \int_{-W_\sigma/2 + bW_D}^{W_\sigma/2 + bW_D} \left(-\frac{\partial f_0}{\partial \varepsilon}\right) d\varepsilon,$$

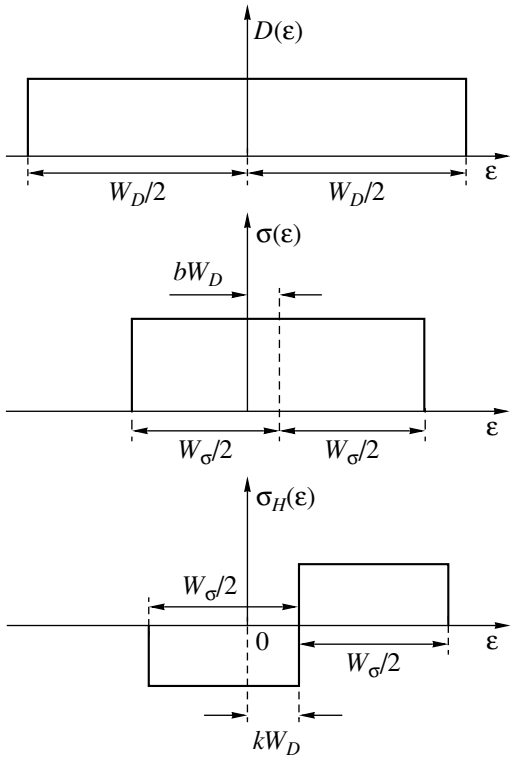

Fig. 7. Model approximations of the density-of-states functions, differential conductivity, and Hall conductivity employed in analyzing the $Q(T)$ relations.

$$I_{H_0} = \int_{-W_\sigma/2 + kW_D}^{W_\sigma/2 + kW_D} \left(-\frac{\partial f_0}{\partial \varepsilon}\right) \mathrm{sgn}(\varepsilon - kW_D)\, d\varepsilon,$$

$$I_1 = \int_{-W_\sigma/2 + bW_D}^{W_\sigma/2 + bW_D} \left(-\frac{\partial f_0}{\partial \varepsilon}\right) \varepsilon\, d\varepsilon,$$

$$I_{H_1} = \int_{-W_\sigma/2 + kW_D}^{W_\sigma/2 + kW_D} \left(-\frac{\partial f_0}{\partial \varepsilon}\right) \mathrm{sgn}(\varepsilon - kW_D)\, \varepsilon\, d\varepsilon,$$

$$f_0 = \frac{1}{1 - \exp[(\varepsilon - \mu)/k_\mathrm{B}T]}$$

is the Fermi–Dirac distribution function,

$$\mu = k_\mathrm{B}T\left(\ln\frac{FW_D/2k_\mathrm{B}T}{(1-F)W_D/2k_\mathrm{B}T} - bW_D\right)$$

is the electrochemical potential, k_B is the Boltzmann constant, $F = n/N$ is the filling of the conduction band by electrons (n and N are the total numbers of electrons and states in the band, respectively), W_D is the total effective band width, W_σ is the effective width of the interval of delocalized (conducting) states, b is the conduction band asymmetry, k is the asymmetry of the dispersion curve, and u is the band-averaged electron mobility.

Thus, in general, the $Q(T)$ relation for a sample of a given composition is described by six model parameters, namely, F, W_D, W_σ, b, k, and u. One should, however, stress the following point. When carrying out a correlated analysis of experimental data on the temperature dependence of the kinetic coefficients, the first four parameters (F, W_D, W_σ, b) can be unambiguously derived from the temperature dependences of the Seebeck coefficient and should be subsequently used to analyze the $Q(T)$ relations obtained for the same samples. As a result, the behavior of the NEC will now be determined by two additional parameters only, k and u. The mobility is involved in Eq. (1) as a factor and, hence, is significant only in calculations of the absolute values of the NEC but does not affect its temperature dependence. Thus, if the values of the parameters F, W_D, W_σ, and b are known, then the character of the $Q(T)$ dependence is fully determined by the value of the parameter k and the absolute values of Q are dictated by the parameter u. Therefore, these parameters can be determined unambiguously by analyzing experimental data on $Q(T)$. Thus, a study of the Nernst–Ettingshausen effect in narrow-band conductors (just as in the classical case) can be used to find the carrier mobility. Experimental investigation and analysis of the NEC is in this case a very efficient and informative tool. First, intercrystallite layers in polycrystalline samples have a marked effect on the measured electrical resistivity, which gives rise to errors in the determination of the absolute values of σ. Second, in the narrow-band case, the Hall concentration cannot be identified with the true carrier concentration [4]. Both these factors turn out to be very significant when analyzing experimental data for HTSC materials in the sense that determination of the carrier mobility from resistive and Hall measurements as $u = \sigma R_H$ is incorrect.

It seems worthwhile to note that the above modification of the approximation of the $\sigma_H(\varepsilon)$ relation does not affect the calculated $S(T)$ relations but is capable of markedly changing the pattern of the theoretical $R_H(T)$ curve. For this reason, the agreement between the $R_H(T)$ curves calculated using the values of the model parameters derived from $S(T)$ and $Q(T)$ and the experimental data should be considered an additional verification of the validity of the proposed approach to analyzing electronic transport in HTSC materials. In particular, as shown in [20], this implies the need to choose negative values of the parameter k when analyzing the $Q(T)$ relations. In this connection, we calculated the temperature dependence of the Hall coefficient for each sample of the series under study using values of the model parameters derived from an analysis of both the Seebeck coefficient (F, W_D, W_σ, and, in the case of an asymmetric band, b) and the Nernst–Ettingshausen coefficient (k). We achieved good qualitative agreement between the experimental and calculated $R_H(T)$ relations in all cases. For illustration, Fig. 8 presents the experimental and

calculated (using our approach) temperature dependences of the Hall coefficient for the $YBa_2Cu_3O_y$ series with variable oxygen content. We can see that the values of the model parameters extracted from an analysis of the $S(T)$ and $Q(T)$ relations also permit a satisfactory description of the $R_H(T)$ relation. Thus, by using the narrow-band model with a common set of parameters characterizing the band structure and properties of the carrier system, we can describe the temperature dependences of the Seebeck and Nernst–Ettingshausen coefficients quantitatively and explain the temperature dependences of the resistivity and the Hall coefficient qualitatively. Note that an arbitrarily chosen set of model parameters capable of describing the $Q(T)$ relation cannot produce a pattern that represents $R_H(T)$ qualitatively. Even a slight deviation of the model parameters from their values derived from an analysis of the Seebeck coefficient and NEC gives rise to a pronounced change in the pattern of the calculated $R_H(T)$ curve (for instance, to a growth in R_H with an increase in temperature and to a reversal of the sign of the Hall coefficient or even to negative values of the Hall coefficient throughout the temperature range covered, which is at odds with experiment). The fact that the set of model parameters calculated theoretically from the $S(T)$ and $Q(T)$ relations fits the $R_H(T)$ relation qualitatively also argues for the correctness of the parameter determination and for the validity of our approach on the whole.

This approach was employed to analyze the temperature dependences of the kinetic coefficients obtained for the four sample series studied. As already pointed out, in the first stage, an analysis of the $S(T)$ relations yielded the values of the main band-structure parameters (F, W_D, W_σ, b). This analysis is treated in considerable detail in our previous publications [4, 19, 22, 23], and the values thus obtained are listed in the table. Next, these values were used in interpreting the experimental NEC relations. The $Q(T)$ relations calculated for all the sample series are presented in Figs. 2–5, together with the experimental data. We see that the theoretical curves can be fitted well to the experimental data in all cases. This enabled us to determine the mobility u and the asymmetry of the dispersion curve k for all the samples studied (Figs. 9, 10).

In considering the data on the carrier mobility (Fig. 9), one immediately notices its extremely low values, which are characteristic of all the sample series investigated. In our opinion, this should be attributed to the large effective mass of carriers, a feature typical of narrow-band systems. We note in this connection that, in the literature, the estimates of the mass m^* in $YBa_2Cu_3O_y$ yield $m^* = (10–40)m_0$ [27, 28]. The dynamics of mobility variation is different in sample series with different kinds of deviation from stoichiometry; more specifically, in $YBa_2Cu_3O_{7-x}$ with variable oxygen content and $YBa_2Cu_{3-x}Co_xO_y$, one observes a close-to-linear growth in mobility with an increase in x (the only exception is the last sample

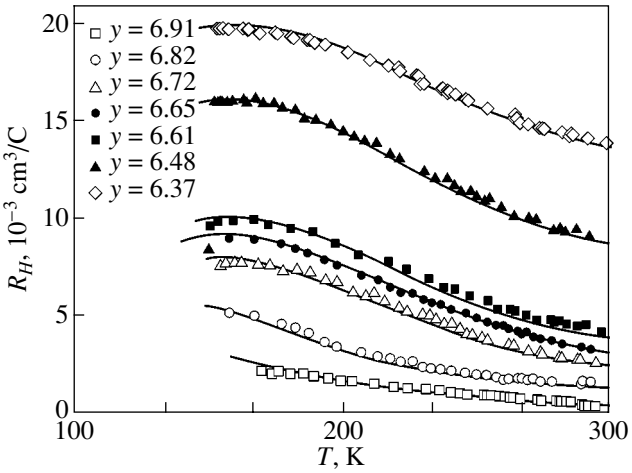

Fig. 8. Temperature dependence of the Hall coefficient in $YBa_2Cu_3O_y$ samples. Symbols refer to experimental data, and the curves are model calculations.

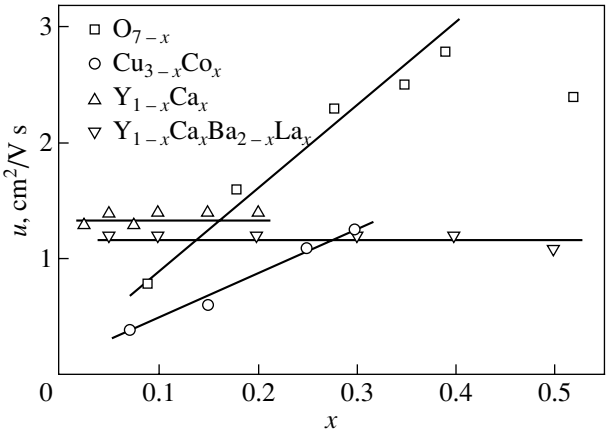

Fig. 9. Concentration dependences of the carrier mobility in the systems under study.

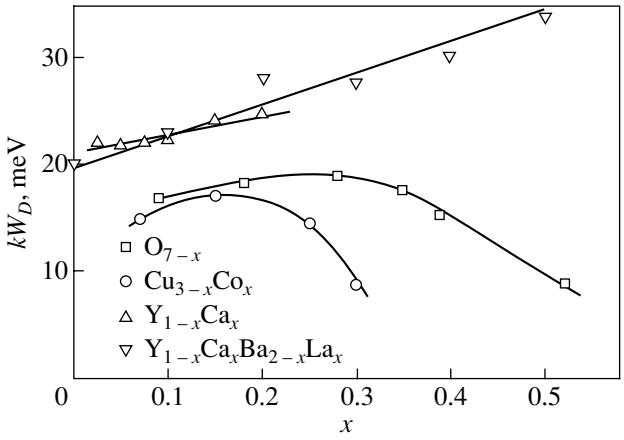

Fig. 10. Concentration dependence of the asymmetry of the dispersion curve for the systems studied.

of the $YBa_2Cu_3O_{7-x}$ system with the maximum oxygen deficiency), while in $Y_{1-x}Ca_xBa_2Cu_3O_y$ and $Y_{1-x}Ca_xBa_{2-x}La_xCu_3O_y$ samples the mobility remains practically unchanged as the doping level is varied. To understand this behavior of the mobility, the following considerations should be taken into account. On the one hand, as shown by the analysis of the $S(T)$ relations, an increase in the doping level in all the series studied entails an intensification of disorder on the oxygen subsystem (see the results of the analysis in [4, 19, 22, 23], as well as the values of the parameter $C = W_\sigma/W_D$ characterizing the extent of disorder in the system, which are listed in the table). This disordering should give rise to an increase in the scattering probability and a decrease in the carrier relaxation time. As a result, because $u \propto \tau$, the carrier mobility should decrease. On the other hand, broadening of the narrow band should bring about a decrease in the effective mass, thus increasing the carrier mobility, because $u \propto (m^*)^{-1}$. Both these processes set in with increasing doping level and affect the mobility in opposite ways. Depending on which of them will dominate, the mobility will either grow or decrease. As seen from the table, $YBa_2Cu_3O_y$ and $YBa_2Cu_{3-x}Co_xO_y$ samples reveal a considerably larger band broadening than do the calcium-doped or codoped samples. Hence, in this case, the stronger decrease in the effective mass dominates over the decrease in the relaxation time, as a result of which the mobility increases. In both calcium-containing series, as already mentioned, the dopants act in the direction of charge compensation [4, 21]. Nevertheless, an increase in the doping level in both series naturally entails an enhancement of disorder and increases the concentration of structural defects, although this process is not so strongly manifest as in the $YBa_2Cu_3O_y$ and $YBa_2Cu_{3-x}Co_xO_y$ series. As a result, the observed band broadening in the calcium-doped series is not as pronounced (see table) and the effects of the two above-mentioned processes of a decrease in effective mass and relaxation time on the mobility cancel each other, as a result of which the mobility remains practically the same as the doping level is increased.

It is significant that the mobility analyzed by us is a parameter of the narrow-band model. Although this mobility is derived from NEC data, it is not a Nernst mobility in the classical sense and is not equal (as in the case of a wide band) to the ratio $Q/(k_B/e)$. As pointed out earlier in a theoretical analysis of the NEC in narrow-band conductors [20], this should be assigned primarily to carriers with a positive and a negative effective mass being simultaneously present in the transport flow. Thus, our analysis deals with the carrier mobility in the systems under study under the assumption that they have a narrow-band electronic structure. Therefore, it would make no sense to directly compare the "Nernst" mobility obtained by us with the classical Hall mobility u_H defined by the product $R_H\sigma$. One may, however, compare the value of the mobility derived by us from the $Q(T)$ relations with the mobility extracted from an analysis of the Hall coefficient and electrical resistivity within the narrow-band model. Using the expressions for these two kinetic coefficients obtained within the narrow-band model in [4, 19] and taking into account the approximation of the $\sigma_H(\varepsilon)$ function we have accepted, we can derive the following relation for the "Hall" mobility in terms of the narrow-band model:

$$u_H = R_H\sigma\frac{(1+e^{(-W_\sigma/2-\mu)/k_BT})^{-1}-(1+e^{(W_\sigma/2-\mu)/k_BT})^{-1}}{2(1+e^{(kW_D-\mu)/k_BT})^{-1}-(1+e^{(W_\sigma/2+kW_D-\mu)/k_BT})^{-1}-(1+e^{(-W_\sigma/2-kW_D-\mu)/k_BT})^{-1}}, \quad (2)$$

where R_H and σ are experimentally measurable values of the Hall coefficient and conductivity, respectively.

Reliable determination of the resistivity of polycrystalline samples is complicated by the presence of various defects in them. Nevertheless, in view of the theoretical significance of comparing the "Hall" and "Nernst" mobilities, we calculated them from our experimental data on the resistivity and the Hall coefficient. For this purpose, we chose a sample of the $YBa_2Cu_3O_y$ series with $y = 6.91$, which revealed a very low resistivity ($\rho(T = 300\ \text{K}) = 0.54\ \text{m}\Omega\ \text{cm}$) close to the figures obtained on single crystals. The mobility calculated using Eq. (2) with due allowance for our experimental data was found to be $u_H = 1.3\ \text{cm}^2/\text{V s}$, which is close to its value derived from the NEC ($u_H = 0.8\ \text{cm}^2/\text{V s}$). This difference between the values of u and u_H may be due to a weak effect of defects, as well as to our disregarding the anisotropy in transport properties in the theoretical calculations, which may have resulted in overestimation of the mobility derived from data on the resistivity and the Hall coefficient. Considered within our model, the agreement between u and u_H can be accepted as quite satisfactory.

Let us discuss now the dynamics of the variation in the degree of asymmetry in the dispersion relation $\varepsilon(k)$ observed in the sample series under study. Recall that, in the case of a simple rectangular approximation, the parameter k characterizing this asymmetry is defined as the displacement of the point of sign reversal of the Hall conductivity function with respect to the center of the narrow band (Fig. 7) [20]. This parameter should not be directly related to the asymmetry parameter b derived from the Seebeck coefficient, which is connected with the asymmetry of the density-of-states function. In contrast to the parameter b, which is zero in the sample series without calcium, the asymmetry of the Hall con-

ductivity function $\sigma_H(\varepsilon)$ is observed, as follows from our calculations, in all the series studied. Moreover, as shown in [20], only by taking this asymmetry into account can one derive theoretical $Q(T)$ relations that are qualitatively consistent with experimental data. The asymmetry in the density-of-states function for the $YBa_2Cu_3O_y$ system arises only when calcium is doped into the lattice and originates, in our opinion, from calcium creating additional states in the conduction band. By contrast, the asymmetry in the dispersion relation $\varepsilon(k)$ is in no way connected with the specific influence of any impurity but is rather a fundamental property of the $YBa_2Cu_3O_y$ system. Note that this conclusion is corroborated in studies dealing with the existence of a Van Hove singularity in HTSC materials. This singularity brings about not only the appearance of a narrow peak in the density of states near the Fermi level but also an $\varepsilon(k)$ relation that has different patterns in different directions in k space (see, e.g., review [29]).

When analyzing the character of the dispersion relation, one may conveniently use the absolute values of the energy displacement kW_D of the Hall conductivity function rather than the values of the parameter k. The concentration dependences of kW_D are displayed graphically in Fig. 10 for all the sample series studied. Just as in the case where the carrier mobility is varied, two different trends are clearly seen in the variation of the energy displacement with an increase in the doping level both of samples containing calcium and of samples not containing any calcium. As the oxygen deficiency in the $YBa_2Cu_3O_{7-x}$ series and the cobalt content in the $YBa_2Cu_{3-x}Co_xO_y$ system increase, the energy displacement of the point of sign reversal in the $\sigma_H(\varepsilon)$ relation increases insignificantly at low doping levels and then falls off rapidly. By contrast, in the calcium-doped series and in the series with codoping, the energy displacement grows monotonically. In our opinion, this difference in the dynamics of variation in the asymmetry originates from the specific effect of the substitutions studied on the modified conduction band.

Let us consider first the results obtained for the $YBa_2Cu_3O_y$ and $YBa_2Cu_{3-x}Co_xO_y$ systems. Oxygen deficiency gives rise to a strong band broadening and suppression of the superconducting properties (see table). The Co $\longrightarrow$ Cu substitution acts similarly on the properties of $YBa_2Cu_3O_y$; this effect should also be attributed to the properties of the oxygen subsystem being influenced by nonisovalent doping [19]. According to [30], oxygen deficiency brings about a change in both the number of carriers and the number of states in the conduction band. Obviously enough, the number of states also varies in the $YBa_2Cu_{3-x}Co_xO_y$ system, and this variation is likewise connected with the oxygen deficiency in cells that do not contain cobalt. It appears logical to assume that the decrease in the number of states in these series brings about the transformation of the dispersion curve $\varepsilon(k)$. As follows from our studies, this transformation occurs in such a way that the asymmetry in the $\varepsilon(k)$ relation decreases gradually and apparently vanishes at a sufficiently heavy doping level. The value of the parameter k falls off gradually with increasing doping level from $k = -0.28$ for the $YBa_2Cu_3O_{6.91}$ sample to –0.03 and –0.02 in the strongest doped samples of the $YBa_2Cu_3O_y$ and $YBa_2Cu_{3-x}Co_xO_y$ series, respectively. The slight growth in the energy displacement kW_D at light doping levels should apparently be assigned to the fact that, in this region, the doping-induced variation in the number of states in the band is still very small, while the effective width of the conduction band has already increased noticeably (see table). Thus, the increase in the oxygen deficiency, as well as the increase in the cobalt content, causes a weakening of the asymmetry of the dispersion curve $\varepsilon(k)$ through a decrease in the number of band states.

The $Y_{1-x}Ca_xBa_2Cu_3O_y$ and $Y_{1-x}Ca_xBa_{2-x}La_xCu_3O_y$ samples are remarkable in the specific effect the calcium exerts on the conduction band structure. Introducing additional states into the band with calcium changes the shape of the density-of-states function and causes it to be asymmetric [21, 22]. In the rectangular approximation, this asymmetry manifests itself in the center of the $\sigma(\varepsilon)$ rectangle becoming displaced with respect to the $D(\varepsilon)$ rectangle toward lower energies [4, 19]. This change in the energy dependence of the density of states should also enhance the asymmetry of the dispersion relation $\varepsilon(k)$. Interestingly, the asymmetry parameter k of the dispersion relation and the parameter b characterizing the asymmetry of the function $D(\varepsilon)$ have the same (negative) sign. As a result, both the $\sigma(\varepsilon)$ and $\sigma_H(\varepsilon)$ rectangles shift downwards in terms of energy relative to the band center. This result suggests that, unlike the effect of a decrease in the number of states in the $YBa_2Cu_3O_y$ and $YBa_2Cu_{3-x}Co_xO_y$ series, the generation of additional states in the conduction band by calcium that occurs in the $Y_{1-x}Ca_xBa_2Cu_3O_y$ and $Y_{1-x}Ca_xBa_{2-x}La_xCu_3O_y$ systems gives rise to a growth in asymmetry in the dispersion relation $\varepsilon(k)$.

In this connection, it appears of interest to compare the energy displacements for series with single calcium doping and codoping. In the former case, the energy displacement increases fairly weakly with a variation in calcium content, while in the latter case the growth is more pronounced (Fig. 10). This difference in the dynamics of varying the asymmetry in the dispersion relation is associated with the fact that the effect of calcium on charge balance in $Y_{1-x}Ca_xBa_2Cu_3O_y$ and $Y_{1-x}Ca_xBa_{2-x}La_xCu_3O_y$ samples is compensated for differently. In the case of single doping with calcium, an increase in its content causes a simultaneous decrease in the oxygen content, which gives rise to increased disorder on the oxygen subsystem and a decreased number of band states. This should bring about, in turn, a decrease in the asymmetry of the dispersion relation similar to that observed in the oxygen-deficient series. Thus, we witness here two oppositely

directed processes, namely, an increase in the calcium doping level and a growth in oxygen deficiency, which act in opposite ways on kW_D. As a result of this compensating action, the energy displacement in the $Y_{1-x}Ca_xBa_2Cu_3O_y$ series increases only insignificantly. In the $Y_{1-x}Ca_xBa_{2-x}La_xCu_3O_y$ system, the charge effect of calcium is counteracted by the simultaneous nonisovalent $La^{3+} \longrightarrow Ba^{2+}$ substitution, which tends to maintain a constant oxygen index with increasing doping level [23]. Hence, the oxygen subsystem does not suffer any change, thus making it possible to observe the effect of calcium, as it were, in pure form. As a result, the introduction of calcium into the codoped system is the only factor that influences the magnitude of the energy displacement, and this is what causes its substantially stronger growth than in the case of the $Y_{1-x}Ca_xBa_2Cu_3O_y$ series.

Thus, a correlated analysis of the temperature dependences of the kinetic coefficients makes it possible to consistently interpret the experimental concentration dependences of the parameters u and kW_D for the sample series under study. This should be considered a convincing argument for the validity of our approach to analyzing electronic transport phenomena in doped HTSCs of the $YBa_2Cu_3O_y$ system and, hence, for the conclusion that their band spectrum has a narrow conduction band, which exerts a major effect on the properties of these materials in both the normal and superconducting states.

6. CONCLUSIONS

In summary, we have carried out a systematic experimental investigation of the temperature dependences of the NEC in doped HTSCs of the $YBa_2Cu_3O_y$ system in the normal phase and a coordinated analysis of the data thus obtained, together with data on other kinetic coefficients, in terms of the narrow-band model. The main results and conclusions are as follows.

(1) The Nernst–Ettingshausen coefficient in HTSCs of the $YBa_2Cu_3O_y$ system in the normal phase is extremely small. At $T = 300$ K, Q is always positive and grows weakly with decreasing temperature until it reaches a broad maximum, after which the value of Q falls off rapidly. At small absolute values of the NEC in the temperature region $T < 150$ K, a transition to negative values of Q occurs.

(2) An increase in oxygen deficiency and the $Co \longrightarrow Cu$ substitution give rise to a fast growth of Q without any qualitative change in the pattern of $Q(T)$, whereas a single $Ca \longrightarrow Y$ substitution, as well as codoping, in the $Y_{1-x}Ca_xBa_{2-x}La_xCu_3O_y$ system affects the value of the NEC and the character of its temperature dependence only weakly. Note that, for all kinds of deviations from stoichiometry, the NEC varies in magnitude in the same way as the other kinetic coefficients and correlates with the variation of the superconducting properties of $YBa_2Cu_3O_y$.

(3) It has been demonstrated that, using a common set of parameters that characterize the band structure and the properties of the carrier system in terms of the narrow-band model, it is possible to simultaneously describe the temperature dependences of the Seebeck and Nernst–Ettingshausen coefficients qualitatively and the temperature dependences of the resistivity and of the Hall coefficient quantitatively in all the systems studied.

(4) The carrier mobility has been determined in the samples studied. In order of magnitude, the mobility is a few centimeters squared per volt per second. In the $YBa_2Cu_3O_{7-x}$ and $YBa_2Cu_{3-x}Co_xO_y$ series, an increase in x gives rise to an increase in carrier mobility, which may be due to a decrease in the effective mass associated with the strong broadening of the conduction band. In the $Y_{1-x}Ca_xBa_2Cu_3O_y$ and $Y_{1-x}Ca_xBa_{2-x}La_xCu_3O_y$ series, the mobility remains almost the same as the doping level is varied, which should be assigned to the fact that the effects of decreasing effective mass and of a decrease in the relaxation time cancel each other.

(5) HTSCs in the $YBa_2Cu_3O_y$ system are characterized by an asymmetric dispersion relation $\varepsilon(k)$. This property is a common feature of this system, which manifests itself in both undoped samples and samples with various kinds of substitution. Analysis of the dynamics of the asymmetry in $Y_{1-x}Ca_xBa_2Cu_3O_y$ and $Y_{1-x}Ca_xBa_{2-x}La_xCu_3O_y$ systems has provided supportive evidence for our earlier conclusion that the calcium introduces additional states into the conduction band of $YBa_2Cu_3O_y$.

ACKNOWLEDGMENTS

This study was supported by the Russian Foundation for Basic Research (project nos. 02-02-16841a, 03-02-06404), the Ministry of Education of the Russian Federation (project no. E02-3.4-120), and the St. Petersburg Administration (project no. PD03-1.2-184).

REFERENCES

1. Y. Iye, in *Physical Properties of High Temperature Superconductors III*, Ed. by D. M. Ginsberg (World Sci., Singapore, 1992).
2. N. P. Ong, in *Physical Properties of High Temperature Superconductors II*, Ed. by D. M. Ginsberg (World Sci., Singapore, 1990).
3. A. B. Kaiser and C. Ucher, in *Studies of High Temperature Superconductors*, Ed. by A. V. Narlikar (Nova Sci., New York, 1991), Vol. 7.
4. V. E. Gasumyants, in *Advances in Condensed Matter and Materials Research*, Ed. by F. Gerard (Nova Sci., New York, 2001), Vol. 1, p. 135.
5. F. J. Blatt, Solid State Phys. **4**, 200 (1957).
6. J. A. Clayhold, A. W. Linnen, F. Chen, and C. W. Chu, Phys. Rev. B **50** (6), 4252 (1994).
7. J. A. Clayhold, Phys. Rev. B **54** (9), 6103 (1996).

8. M. Pekala, H. Bougrine, and M. Ausloos, J. Phys.: Condens. Matter **7** (28), 5607 (1995).
9. P. Fournier, X. Jiang, W. Jiang, S. N. Mao, T. Venkatesan, C. J. Lobb, and R. L. Greene, Phys. Rev. B **56** (21), 14149 (1997).
10. S. Lambrecht and M. Ausloos, Phys. Rev. B **53** (21), 14047 (1996).
11. Z. A. Xu, N. P. Ong, Y. Wang, T. Kakeshita, and S. Ushida, Nature **406** (6795), 486 (2000).
12. Y. Wang, Z. A. Xu, T. Kakeshita, S. Ushida, S. Ono, Y. Ando, and N. P. Ong, Phys. Rev. B **64** (22), 224519 (2001).
13. Y. Wang, N. P. Ong, T. Kakeshita, S. Ushida, D. A. Bonn, R. Liang, and W. N. Hardy, Phys. Rev. Lett. **88** (25), 257003 (2002).
14. C. Capan, K. Behnia, J. Hinderer, A. G. M. Jansen, W. Lang, C. Marcenat, C. Marin, and J. Flouquet, Phys. Rev. Lett. **88** (5), 056601 (2002).
15. H. Balci, C. P. Hill, M. M. Qazilbash, and R. L. Greene, cond-mat/0303469 (2003).
16. H. Kontani, Phys. Rev. Lett. **89** (23), 237003 (2002).
17. I. Ussishkin, S. L. Sondhi, and D. A. Huse, Phys. Rev. Lett. **89** (28), 287001 (2002).
18. S. Tan and K. Levin, cond-mat/0302248 (2003).
19. V. E. Gasumyants, V. I. Kiadanov, and E. V. Vladimirskaya, Physica C (Amsterdam) **248** (3–4), 255 (1995).
20. N. V. Ageev and V. É. Gasumyants, Fiz. Tverd. Tela (St. Petersburg) **43** (10), 1761 (2001) [Phys. Solid State **43**, 1834 (2001)].
21. V. E. Gasumyants, M. V. Elizarova, E. V. Vladimirskaya, and I. B. Patrina, Physica C (Amsterdam) **341–348**, 585 (2000).
22. V. É. Gasumyants, E. V. Vladimirskaya, M. V. Elizarova, and I. B. Patrina, Fiz. Tverd. Tela (St. Petersburg) **40** (12), 2145 (1998) [Phys. Solid State **40**, 1943 (1998)].
23. V. E. Gasumyants, M. V. Elizarova, and I. B. Patrina, Supercond. Sci. Technol. **13** (12), 1600 (2000).
24. M. Zeh, H. C. Ri, F. Kober, R. P. Huebener, A. V. Ustinov, J. Mannhart, R. Gross, and A. Gupta, Phys. Rev. Lett. **64** (26), 3195 (1990).
25. R. P. Huebener, F. Kober, H. C. Ri, K. Knorr, C. C. Tsuei, C. C. Chi, and M. R. Scheuermann, Physica C (Amsterdam) **181** (4–6), 345 (1991).
26. T. Sasaki, K. Yamada, K. Watanabe, S. Watauchi, K. Kishio, and N. Kobayashi, Physica C (Amsterdam) **282–287**, 2009 (1997).
27. Z. Schlesinger, R. T. Collins, D. Kaisor, F. Holtzberg, G. V. Chandrashekhar, M. W. Shafer, and T. M. Plaskett, Physica C (Amsterdam) **153–155**, 1734 (1988).
28. J. Molenda, T. Bak, and A. Stoklosa, Physica C (Amsterdam) **207** (1–2), 147 (1993).
29. R. S. Markiewicz, J. Phys. Chem. Solids **58** (8), 1179 (1997).
30. Yu. M. Baĭkov, V. É. Gasumyants, S. A. Kaz'min, V. I. Kaĭdanov, V. I. Smirnov, and V. A. Tselishchev, Sverkhprovodimost: Fiz. Khim. Tekh. **3** (2), 254 (1990).

Translated by G. Skrebtsov

Physics of the Solid State, Vol. 47, No. 2, 2005, pp. 214–216. Translated from Fizika Tverdogo Tela, Vol. 47, No. 2, 2005, pp. 208–209.

SEMICONDUCTORS AND DIELECTRICS

Conduction through Localized States in a Single Crystal of the $TlGa_{0.5}Fe_{0.5}Se_2$ Alloy

S. N. Mustafaeva, É. M. Kerimova, and A. I. Dzhabbarly

Institute of Physics, National Academy of Sciences of Azerbaijan, pr. Dzhavida 33, Baku, 1143 Azerbaijan

Received May 5, 2004

Abstract—Layered single crystals of the $TlGa_{0.5}Fe_{0.5}Se_2$ alloy in a dc electric field at temperatures ranging from 128 to 178 K are found to possess variable-range-hopping conduction along natural crystal layers through states localized in the vicinity of the Fermi level. The parameters characterizing the electrical conduction in the $TlGa_{0.5}Fe_{0.5}Se_2$ crystals are estimated as follows: the density of states near the Fermi level $N_F = 2.8 \times 10^{17}$ eV^{-1} cm^{-3}, the spread in energy of these states $\Delta E = 0.13$ eV, the average hopping length $R_{av} = 233$ Å, and the concentration of deep-lying traps $N_t = 3.6 \times 10^{16}$ cm^{-3}. © *2005 Pleiades Publishing, Inc.*

1. INTRODUCTION

Layered compounds of the $TlMeX_2^6$ type (*Me* = In, Ga; *X* = S, Se) and alloys based on them are of scientific and practical interest. With knowledge of the composition dependences of the electrical, photoelectrical, and optical properties of $TlMeX_2^6$ layered compounds, it is possible to control these properties. Upon partial substitution of iron for gallium, the $TlGaSe_2$ crystals acquire magnetic properties. This can be useful in designing materials with characteristics that can be controlled by a magnetic field.

Earlier [1, 2], we investigated the transport properties of the $TlGaSe_2$ single crystal and $TlFeSe_2$ polycrystals. Moreover, we revealed that these crystals possess hopping conduction at low temperatures.

The purpose of this work was to investigate the conduction through localized states in a single crystal of the $TlGa_{0.5}Fe_{0.5}Se_2$ alloy in a dc electric field and to compare the results obtained with available data for $TlGaSe_2$ and $TlFeSe_2$.

2. SAMPLE PREPARATION AND EXPERIMENTAL TECHNIQUE

Polycrystals of composition $TlGa_{0.5}Fe_{0.5}Se_2$ were synthesized by alloying initial components (Tl, Ga, Fe, Se) of high-purity grade (no less than 99.99) in silica glass ampules evacuated to a residual pressure of 10^{-3} Pa. Single crystals were grown using the Bridgman–Stockbarger method.

The $TlGa_{0.5}Fe_{0.5}Se_2$ samples used in electrical measurements had a thickness $d = 0.14$ cm, and the distance between the contacts was $l = 0.4$ cm. Ohmic contacts to the samples were fabricated through electrolytic deposition of copper. The electrical conductivity σ of the samples prepared was measured in the temperature range 128–303 K. The strength of the dc electric field applied along the natural layers of the crystal corresponded to an ohmic portion of the current–voltage characteristic.

3. RESULTS AND DISCUSSION

Figure 1 shows the temperature dependences of the electrical conductivity for a single crystal of the $TlGa_{0.5}Fe_{0.5}Se_2$ alloy. The dependence of $\log\sigma$ on $10^3/T$ is characterized by an exponential portion in the temperature range 178–303 K. As the temperature decreases below 178 K, the activation energy for electrical conduction decreases in a gradual manner. The temperature dependence of the electrical conductivity with a monotonically decreasing activation energy is

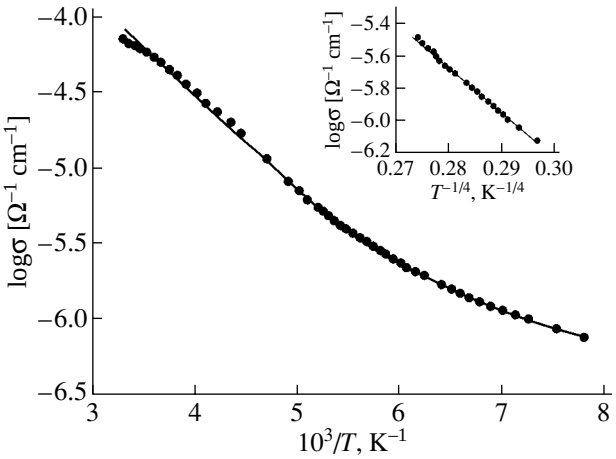

Fig. 1. Temperature dependences of the electrical conductivity in a single crystal of the $TlGa_{0.5}Fe_{0.5}Se_2$ alloy.

1063-7834/05/4702-0214$26.00

Parameters of the $TlGa_{1-x}Fe_xSe_2$ crystals (x = 0, 0.5, 1.0)

Crystal	Electrical resistivity ρ, Ω cm at 298 K	T_0, K	N_F, eV^{-1} cm^{-3}	R_{av}, Å	ΔE, eV	N_t, cm^{-3}
$TlGaSe_2$	10^4	5.4×10^5	1.3×10^{19}	150	0.011	1.4×10^{17}
$TlGa_{0.5}Fe_{0.5}Se_2$	1.5×10^4	1.7×10^7	2.8×10^{17}	233	0.13	3.6×10^{16}
$TlFeSe_2$	25	1.4×10^6	3.3×10^{18}	104	0.13	4.3×10^{17}

plotted in the $T^{-1/4}$–logσ coordinates in the inset to Fig. 1. It can be seen that virtually all the experimental points fall on a straight line in these coordinates. This suggests that, in the aforementioned temperature range (128–178 K), the charge transfer occurs along natural layers of the $TlGa_{0.5}Fe_{0.5}Se_2$ single crystal through the mechanism of hopping conduction over the states lying in a narrow energy band near the Fermi level [3]:

$$\sigma \sim \exp[-(T_0/T)^{1/4}]. \quad (1)$$

The slope of the straight line $\log\sigma(T^{-1/4})$ was determined to be $T_0 = 1.7 \times 10^7$ K. The density of localized states near the Fermi level in $TlGa_{0.5}Fe_{0.5}Se_2$ crystals ($N_F = 2.8 \times 10^{17}$ eV^{-1} cm^{-3}) was obtained according to the formula [3]

$$N_F = \frac{16}{T_0 k a^3}, \quad (2)$$

where k is the Boltzmann constant and a is the localization length. In this case, the localization length was taken to be a = 34 Å. This value was determined for a GaSe single crystal in the experiments performed earlier in [4].

The hopping length R of charge carriers at different temperatures was estimated from the formula [3]

$$R(T) = \frac{3}{8} a T_0^{1/4} T^{-1/4}. \quad (3)$$

As a result, we obtained the hopping length R = 243 Å at a temperature T = 128 K and R = 224 Å at T = 178 K. The average hopping length R_{av} in the temperature range studied was equal to 233 Å, which exceeds the average distance between the localization centers of charge carriers by a factor of ~7. The energy positions of the localization centers are separated by an energy ΔE, which can be estimated from the expression [3]

$$\Delta E = \frac{3}{2\pi R^3 N_F}. \quad (4)$$

According to expression (4), the spread in energy of trapping states near the Fermi level was found to be ΔE = 0.13 eV. The concentration of deep-lying traps in $TlGa_{0.5}Fe_{0.5}Se_2$ was estimated at 3.6×10^{16} cm^{-3} from the following formula:

$$N_t = N_F \Delta E. \quad (5)$$

The results of investigations into the hopping conduction along layers in $TlGaSe_2$ [1], $TlGa_{0.5}Fe_{0.5}Se_2$, and $TlFeSe_2$ [2] are compared in the table. It can be seen from the table that, unlike the $TlGaSe_2$ single crystals, crystals of compositions $TlGa_{0.5}Fe_{0.5}Se_2$ and $TlFeSe_2$

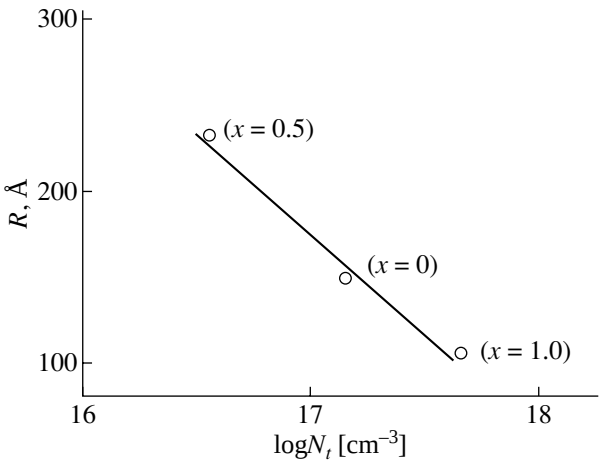

Fig. 2. Dependence of the average hopping length in $TlGa_{1-x}Fe_xSe_2$ crystals (x = 0, 0.5, 1.0) on the concentration of deep-lying traps.

are characterized by a broad energy band (ΔE) in the vicinity of the Fermi level. This indicates that the latter crystals are similar in energy band structure to amorphous semiconductors. The concentration of deep-lying traps N_t is maximum in the $TlFeSe_2$ polycrystals and is one order of magnitude lower in the $TlGa_{0.5}Fe_{0.5}Se_2$ alloy. Therefore, it is quite reasonable that the average hopping length R_{av} in $TlGa_{0.5}Fe_{0.5}Se_2$ exceeds the average hopping length in the $TlGaSe_2$ and $TlFeSe_2$ single crystals by a factor of ~ 1.5 and ~ 2, respectively. Figure 2 shows the dependence of the average hopping length in $TlGa_{1-x}Fe_xSe_2$ (x = 0, 0.5, 1.0) on the concentration of deep-lying traps. It can be seen that the average hopping length R_{av} decreases linearly as $\log N_t$ increases.

REFERENCES

1. S. N. Mustafaeva, V. A. Aliev, and M. M. Asadov, Fiz. Tverd. Tela (St. Petersburg) **40** (1), 48 (1998) [Phys. Solid State **40**, 41 (1998)].
2. S. N. Mustafaeva, É. M. Kerimova, and A. I. Dzhabbarly, Fiz. Tverd. Tela (St. Petersburg) **42** (12), 2132 (2000) [Phys. Solid State **42**, 2197 (2000)].
3. N. F. Mott and E. A. Davis, *Electronic Processes in Non-Crystalline Materials* (Clarendon, Oxford, 1971; Mir, Moscow, 1974).
4. S. N. Mustafaeva, Neorg. Mater. **30** (5), 619 (1994).

Translated by N. Korovin

Physics of the Solid State, Vol. 47, No. 2, 2005, pp. 217–224. Translated from Fizika Tverdogo Tela, Vol. 47, No. 2, 2005, pp. 210–216.

SEMICONDUCTORS AND DIELECTRICS

Kinetic Theory of Ionization and Electron Capture by a Charged Impurity in a Semiconductor

V. D. Kagan

Ioffe Physicotechnical Institute, Russian Academy of Sciences, Politekhnicheskaya ul. 26, St. Petersburg, 194021 Russia
e-mail: victor.kagan@mail.ioffe.ru

Received May 28, 2004

Abstract—Inelastic electron–phonon scattering in which the electron is captured or escapes from the Coulomb field of an impurity is taken into account in the kinetic equation for conduction electrons. This scattering is shown to become strong in a certain energy range. In this range, the distribution functions of free and bound electrons are correlated in such a way that there is a balance between the trapping and ionization processes. The existence of a region of strong scattering is the decisive factor in calculating the experimentally measurable trapping and ionization coefficients, which enter into the electron balance equation. © *2005 Pleiades Publishing, Inc.*

1. STATEMENT OF THE PROBLEM

An electron in the conduction band of a semiconductor is subjected to the Coulomb field of a charged impurity. If the kinetic energy of the electron exceeds the potential energy of interaction with the impurity, the impurity cannot capture the electron and the electron is in an extended state. If the potential energy exceeds the kinetic energy, the electron is trapped by the impurity and moves near it.

The densities of free electrons in the conduction band and of electrons bound to impurities can vary due to inelastic processes; an impurity state can be ionized if the electron gains energy by absorbing phonons, and a free electron can be trapped by an impurity if the electron loses energy by emitting phonons. Both processes make a contribution to the balance equation that describes the evolution of the nonequilibrium density of free electrons n_e in a semiconductor containing impurities with a concentration n_{im}. The electron balance equation is linear, because variations in the electron density are assumed to be small in comparison with the average density, and has the form

$$\frac{dn_e}{dt} = k_i n_{\text{im}} - k_r n_{\text{im}} n_e + G, \qquad (1)$$

where G describes the generation of nonequilibrium electrons (the generation is assumed to occur suddenly and not to involve the impurities), and k_i and k_r are the ionization and trapping coefficients, respectively, which are assumed to be independent of the impurity and electron concentrations. In the right-hand side of Eq. (1), the first term is the increase in the free-electron density due to ionization of impurities and the second term is the increase in this density due to electron capture by impurities. Each of these terms is proportional to the impurity concentration. At equilibrium, there is no generation of electrons; the electron density does not vary with time; and, hence, the right-hand side of Eq. (1) is zero, from which it follows that

$$k_i = k_r n_{e0}, \qquad (2)$$

where n_{e0} is the equilibrium density of free electrons. The coefficients k_r and k_i can be measured experimentally. In order to calculate these coefficients, one must derive Eq. (1) using microscopic theory. This derivation has not been performed; the coefficients k_r and k_i have been found microscopically by using a cascade method [1]. In this method, Eq. (1) is not derived; therefore, it has not been proved that the coefficients calculated using this method are those that enter into Eq. (1) and are measured experimentally.

The objective of this study is to derive microscopic kinetic equations for the distribution functions of free and trapped electrons. The motion of electrons is described classically and then, in the last section, quantum-mechanically. By integrating the kinetic equation for free electrons over the microscopic variables, we obtain Eq. (1) for the electron density. Therefore, the coefficients k_r and k_i in this equation are the coefficients that are measured experimentally.

If the motion of electrons is described in terms of classical mechanics, the distribution function of electrons depends on their coordinates **r** and momenta **p**. However, in describing the trapping and ionization processes, it suffices to consider the distribution functions to be dependent on the total energy alone rather than on the coordinates and momenta separately. For free electrons, this energy is positive:

$$E = \varepsilon_{\mathbf{p}} - \frac{e_1^2}{r}, \quad \varepsilon_{\mathbf{p}} = \frac{p^2}{2m}, \quad e_1^2 = \frac{ze^2}{\kappa}, \qquad (3)$$

1063-7834/05/4702-0217$26.00

where m is the effective electronic mass, z is the impurity charge, and κ is the static dielectric constant of the crystal. For trapped electrons, the total energy is negative. In this case, it is convenient to assume that the distribution function depends on the modulus of the total energy (which we will also denote by E). By averaging the kinetic equations over a constant-energy surface in phase space, we obtain kinetic equations for the distribution functions of free and trapped electrons $f^{(1,2)}(E)$:

$$\partial f^{(1)}(E)/\partial t + \hat{J}_{1,1}(f^{(1)}(E)) = \hat{J}_{1,2}(f^{(1)}(E), f^{(2)}(E)), \quad (4)$$

$$\partial f^{(2)}(E)/\partial t + \hat{J}_{2,2}(f^{(2)}(E)) = \hat{J}_{2,1}(f^{(2)}(E), f^{(1)}(E)). \quad (5)$$

We assume that the time variation in the distribution functions is dictated by the time variation in the electronic density. The term responsible for the instant electron generation is assumed to determine the nonequilibrium density of free electrons (this term is omitted from the above equations). The collision integrals $\hat{J}_{i,i}$ describe electron–electron collisions during which the free electrons are not trapped and the trapped electrons are not released, and the collision integrals $\hat{J}_{i,k}$ describe collisions during which impurity states are ionized or the free electrons are trapped by impurities.

Free electrons move through the entire sample. Therefore, after averaging over phase space, the motion of the electrons that remain free is determined by regions comparable to the sample in size. For these regions, we can neglect the interaction energy between an electron and an impurity, so the distribution function depends only on momenta. In other words, the term $\hat{J}_{1,1}$ is averaged only over momentum space. In the term $\hat{J}_{1,2}$, both free and trapped electrons are of importance. A trapped electron moves near an impurity. Let us determine the changes in the number of free electrons near each impurity and sum them over all impurities. The spacing between impurities is sufficiently large, so the changes calculated for individual impurities can be summed independently. Since the impurities are macroscopic in number, their contribution is finite after averaging and is proportional to the impurity concentration:

$$\hat{J}_{1,2}(f^{(1)}(E), f^{2}(E)) = \frac{n_{\mathrm{im}}}{16\pi^5\hbar^4\rho_1(E)}$$
$$\times \int d\mathbf{p}\,d\mathbf{r}\,d\mathbf{q}\,\delta\left(E - \varepsilon_{\mathbf{p}} + \frac{e_1^2}{r}\right)\delta(\varepsilon_{\mathbf{p}} - \varepsilon_{\mathbf{p}-\hbar\mathbf{q}} - \hbar\omega_{\mathbf{q}})|c_{\mathbf{q}}|^2 \quad (6)$$
$$\times [f^{(2)}(\mathbf{p}-\hbar\mathbf{q}, \mathbf{r})n_{\mathbf{q}} - f^{(1)}(\mathbf{p}, \mathbf{r})(n_{\mathbf{q}}+1)]$$
$$\times \Theta\left(\varepsilon_{\mathbf{p}} - \frac{e_1^2}{r}\right)\Theta\left(\frac{e_1^2}{r} - \varepsilon_{\mathbf{p}-\hbar\mathbf{q}}\right).$$

Here, $\rho_1(E) = 2\int d\mathbf{r}\,\delta(E - \varepsilon_{\mathbf{p}})/(2\pi\hbar)^3 = m\sqrt{2mE}/\pi^2\hbar^3$ is the density of states of free electrons; $\mathbf{q}$ and $\omega_{\mathbf{q}} = sq$ are the wave vector and frequency of a phonon, respectively; s is the velocity of sound; $c_{\mathbf{q}}$ is the electron–phonon coupling constant; $n_{\mathbf{q}} = (e^{\hbar\omega_{\mathbf{q}}}/T - 1)^{-1}$ is the Planck distribution function for phonons; and T is the temperature (in energy units). The functions $\Theta(x)$ (equal to unity for $x > 0$ and zero for $x < 0$) in Eq. (6) correspond to the conditions that an electron with momentum p be free and its energy be positive or that an electron with momentum $\mathbf{p} - \hbar\mathbf{q}$ be trapped and its energy be negative. These conditions determine the region of phase space involved in the trapping of a free electron or the release of a trapped electron from an impurity. The collision integral that accounts for the change in the distribution function of trapped electrons due to ionization and electron capture is analogous to that in Eq. (5). This integral is related to an individual impurity and is averaged over the region of motion of the trapped electrons:

$$\hat{J}_{2,1}(f^{(2)}(E), f^{(1)}(E)) = \frac{1}{16\pi^5\hbar^4\rho_2(E)}$$
$$\times \int d\mathbf{p}\,d\mathbf{r}\,d\mathbf{q}\,\delta\left(\frac{e_1^2}{r} - \varepsilon_{\mathbf{p}} - E\right)\delta(\varepsilon_{\mathbf{p}} - \varepsilon_{\mathbf{p}+\hbar\mathbf{q}} + \hbar\omega_{\mathbf{q}})|c_{\mathbf{q}}|^2 \quad (7)$$
$$\times [f^{(2)}(\mathbf{p}, \mathbf{r})n_{\mathbf{q}} - f^{(1)}(\mathbf{p}+\hbar\mathbf{q}, \mathbf{r})(n_{\mathbf{q}}+1)]$$
$$\times \Theta\left(\frac{e_1^2}{r} - \varepsilon_{\mathbf{p}}\right)\Theta\left(\varepsilon_{\mathbf{p}+\hbar\mathbf{q}} - \frac{e_1^2}{r}\right).$$

Here, $\rho_2(E) = \int d\mathbf{r}\,d\mathbf{p}\,\delta(e_1^2/r - \varepsilon_{\mathbf{p}} - E)2/(2p\hbar)^3 = m\sqrt{2m}e_1^6/4\hbar^3E^{5/2}$ is the density of states of trapped electrons.

We use a simple model of the interaction of electrons with longitudinal phonons in which $|c_{\mathbf{q}}|^2 = \pi\Lambda^2\hbar q/\rho s$, where Λ is the deformation-potential constant and ρ is the density of the material. After integrating over all angular variables, the expressions for $\hat{J}_{1,2}$ and $\hat{J}_{2,1}$ are simplified to

$$\hat{J}_{1,2}(f^{(1)}(E), f^{(2)}(E))$$
$$= \int_E^\infty dE_1 W_1(E, E_1) f^{(2)}(E_1 - E) e^{-E_1/T} - \frac{1}{\tau_r(E)} f^{(1)}(E),$$
$$W_1(E, E_1) = \frac{32\sqrt{2} n_{\text{im}} e_1^6 m^{1/2} s^2}{3l} \times \frac{E_1^2}{\sqrt{E}(1 - e^{-E_1/T})[(E_1 + 2ms^2)^2 - 8ms^2 E]^3}, \quad (8)$$
$$\frac{1}{\tau_r(E)} = \int_E^\infty dE_1 W_1(E, E_1),$$

$$\hat{J}_{2,1}(f^{(2)}(E), f^{(1)}(E))$$
$$= \int_E^\infty dE_1 W_2(E, E_1) f^{(1)}(E_1 - E) e^{E_1/T} - \frac{1}{\tau_i(E)} f^{(2)}(E),$$
$$W_2(E, E_1) = \frac{512\sqrt{2ms^2}}{3\pi l} \times \frac{E^{5/2} E_1^2}{(e^{E_1/T} - 1)[(E_1 - 2ms^2)^2 + 8ms^2 E]^3}, \quad (9)$$
$$\frac{1}{\tau_i(E)} = \int_E^\infty dE_1 W_2(E, E_1),$$

where $l = \rho\hbar^4/4\Lambda^2 m^3$ is the energy mean free path.

By integrating the distribution functions (with allowance for the density of states) over all energies, we obtain the electronic density. At equilibrium, we have Boltzmann distribution functions

$$f^{(1)}(E) = \exp\left(\frac{\mu - E}{T}\right), \quad f^{(2)}(E) = \exp\left(\frac{\mu + E}{T}\right), \quad (10)$$

where $\mu = T\ln[n_{e0}\hbar^3\sqrt{2\pi^3}/(mT)^{3/2}]$ is the chemical potential of electrons, which is conventionally related to the density of free electrons. In the case of the equilibrium distribution functions of free and trapped electrons, the collision integrals (6) and (7) vanish. The generation of electrons changes the distribution function of free electrons, and the relaxation processes rapidly transform it into a Boltzmann distribution with a nonequilibrium total electronic density, $f^{(1)}(E) = [n_e\hbar^3\sqrt{2\pi^3}/(mT)^{3/2}]\exp(-E/T)$.

The electron balance equation (1) is obtained by multiplying Eq. (4) by the density of states and integrating over energy. The integral of $\hat{J}_{1,1}$ vanishes due to the conservation of the total number of electrons in electron–electron collisions. The right-hand side of Eq. (1) is determined by the integral of $\hat{J}_{1,2}$. The coefficients k_i and k_r are thus obtained to be

$$k_r = \frac{2}{n_{\text{im}}\sqrt{\pi T^3}} \int_0^\infty \frac{\sqrt{E}}{\tau_r(E)} \exp\left(-\frac{E}{T}\right) dE, \quad (11)$$
$$k_i = k_r n_{e0}.$$

Let us consider the expression for $\tau_r(E)$ at $E \sim 2ms^2$. It turns out that $\tau_r(E) \sim (E - 2ms^2)^4$. Substituting this expression into Eq. (11), we find that the integral for k_r diverges in a cubic power–law fashion. The expression for k_i exhibits the same divergence. This divergence has been pointed out by Wannier [2]. Physically, this divergence is due to the long-range character of Coulomb forces. By calculating the phase volume that determines the probability of an electron being trapped, we can find the relation between the distance at which an electron becomes trapped by an impurity and the energy of the electron. When the energy is $2ms^2$, the phase volume covers all coordinate space; the cubic divergence is due to the fact that space is three-dimensional. The divergence originates from the assumption that the distribution functions near the energy $2ms^2$ correspond to a Boltzmann distribution and, hence, that the trapping process influences these functions only slightly. The basic idea behind the theory developed below is that this assumption is wrong and that a region of strong interaction exists for free electrons near the energy $2ms^2$; in this region, the ionization and trapping processes cannot be separated and both terms in the collision integral $\hat{J}_{1,2}$ must be considered as a whole. Expression (9) describes the same processes for the trapped electrons; therefore, a region of strong interaction also exists for these electrons. In this energy region, the distribution functions correspond to Boltzmann distributions with an equal preexponential factor, with the consequence that the collision integrals responsible for the trapping and release of electrons vanish. In integrating over energy, the divergences of both terms cancel each other. This energy region also does not contribute to the integral that determines the electron balance, i.e., to the coefficients k_i and k_r. As the electron energy deviates from this "dangerous" value, the intraband relaxation will become dominant; hence, the role of the operator $\hat{J}_{1,2}$ will become less significant and the matching of the distribution functions will be destroyed. At energies far from the value $2ms^2$, the energy distributions for free and trapped electrons are Boltzmann distributions corresponding to different electron densities. The region where the relationship between the energy distributions of free and trapped electrons changes can be determined using kinetic theory. In deriving Eq. (1), this region is important for determining the numerical values of the coefficients k_i and k_r.

The divergence of integrals, which makes calculations of the trapping and ionization coefficients difficult, is likely the reason why these coefficients are calculated using the cascade method [1, 3]. In this method, the kinetic equation is used only for trapped electrons at thermal energies and the collision integral $\hat{J}_{2,1}$ is not included in this equation. In energy space, there is a diffusion flux into the low-energy region. The diffusion rate is assumed to be constant. The diffusion flux is related to the ionization process, and a new definition of the trapping coefficient is introduced; this coefficient is calculated using the changed normalization of the distribution function of trapped electrons. Since the electron balance equation (1) has not been derived, it seems questionable whether this coefficient can be identified with the experimentally measured coefficient k_r.

2. IONIZATION PROCESSES AT LOW TEMPERATURES

Let us consider the range of very low temperatures $T \ll 2ms^2$. Over this range, the region where the equilibrium distribution functions change corresponds to high energies. At thermal energies, we can simplify Eq. (8) for the relaxation time $\tau_r(E)$ by neglecting the low energy E in comparison with energies of the order of ms^2. In this case, under the assumption that the main contribution to Eq. (11) comes from thermal energies, we obtain the following expression for k_r:

$$k_r = \frac{4\sqrt{2}e_1^6}{45l\sqrt{\pi T}m^{5/2}s^4} = \frac{0.09\sqrt{2}e_1^6}{l\sqrt{\pi T}m^{5/2}s^4}. \quad (12)$$

This expression coincides with that from [1]. In the cascade method, an electron is assumed to lose its energy a little at a time. At low temperatures, however, electrons are involved in essentially inelastic processes. For this reason, in [1], the coefficient k_r was calculated directly, with the capture rate being described by an expression identical to that obtained by us by modifying Eq. (8).

Equation (12) is erroneous, even if attractive. Indeed, let us consider the set of equations (4) and (5) without approximations. In deriving Eq. (12), we assumed that the distribution function of free electrons rapidly reaches equilibrium due to collisions between free electrons and then a slow trapping process occurs. The collision integral $\hat{J}_{1,1}$ is given by

$$\hat{J}_{1,1}(f^{(1)}(E)) = \frac{1}{4\pi^2\hbar}\int d\mathbf{q}|c_\mathbf{q}|^2[\delta(\varepsilon_\mathbf{p} - \varepsilon_{\mathbf{p}-\hbar\mathbf{q}} - \hbar\omega_\mathbf{q}) \times (f^{(1)}(\mathbf{p},\mathbf{r})(n_\mathbf{q}+1) - f^{(1)}(\mathbf{p}-\hbar\mathbf{q},\mathbf{r})n_\mathbf{q}) + \delta(\varepsilon_\mathbf{p} - \varepsilon_{\mathbf{p}+\hbar\mathbf{q}} + \hbar\omega_\mathbf{q}) \times (f^{(1)}(\mathbf{p},\mathbf{r})n_\mathbf{q} - f^{(1)}(\mathbf{p}+\hbar\mathbf{q},\mathbf{r})(n_\mathbf{q}+1))]. \quad (13)$$

Due to the conservation of energy and momentum, an electron can emit a phonon only if the momentum of the electron exceeds ms. Therefore, this process is forbidden for thermal electrons. Due to the same conservation laws, a thermal electron can absorb a phonon only if the latter has a momentum of the order of ms. Since the absorption probability is proportional to the number of phonons, this probability can be as small as $\exp(-ms^2/T)$. Therefore, at thermal energies, the integral $\hat{J}_{1,1}$ is exponentially small in comparison with $\hat{J}_{1,2}$ and there is no reason to assume that the distribution function of free electrons corresponds to the Boltzmann distribution, but with a nonequilibrium electron density; quite the contrary. The distribution function must be determined from kinetic equation (4) under the assumption that ionization and trapping are the dominant processes in the relaxation of free electrons. Collisions with trapped electrons are not less probable than the ionization and trapping processes. It follows from Eq. (5) that the distribution of trapped electrons is described by equilibrium distribution function (10).

For free electrons, Eq. (4) is solved iteratively, with a zero approximation being chosen such that $\hat{J}_{1,2}(f^{(1)}(E), f^{(2)}(E)) = 0$ for $E \ll ms^2/2$. In this approximation, the solution is the Boltzmann distribution with an equilibrium electron density, which is dictated by the distribution function of trapped electrons. This simple solution also makes the integral $\hat{J}_{1,1}$ equal to zero at thermal energies. Therefore, this energy region makes no contribution to electron balance equation (1) in both the zero and first approximations with respect to the operator $\hat{J}_{1,1}$. The contribution is nonzero only at energies of the order of ms^2, where the operators acting on $f^{(1)}(E)$ are of the same order of magnitude. In this energy range, however, the distribution function of free electrons is exponentially small. If we are interested in quantities of this order of magnitude, then it should be taken into account that the modification of the relaxation time $\tau_r(E)$ is inapplicable in this energy range. Although the distribution function of free electrons will accommodate itself to the distribution function of trapped electrons in the region of $E = 2ms^2$ and at thermal energies and will reach complete equilibrium, the high-energy region will make a nonzero contribution to the coefficients k_i and k_r. The dominant contribution will come from energies of the order of $ms^2/2$, which correspond to the lower limit of the high-energy region where free-electron relaxation becomes important. We estimate the trapping coefficient (to within a numerical factor) by substituting this energy for the lower limit of the integral in Eq. (11). The result is

$$k_r = \frac{0.08\sqrt{2}e_1^6}{l\sqrt{\pi T}m^{5/2}s^4}\exp(-ms^2/2T). \quad (14)$$

The most essential feature of Eq. (14) is that it depends exponentially on temperature, in contrast to Eq. (12).

The theory considered above is valid if the processes that involve different impurities can be treated independently, which is the case if the average spacing between impurities is sufficiently large:

$$n_{\text{im}}^{-1/3} \gg \frac{e_1^2}{E_a}. \tag{15}$$

Here, the energy E_a is the characteristic energy of the process under study. For Eq. (14), this energy is $ms^2/2$ and for Eq. (13), a lower energy, T. Estimates of the impurity concentration from condition (15) show that our theory is valid only for low impurity concentrations.

3. IONIZATION PROCESSES AT HIGH TEMPERATURES

At high temperatures $T \gg 2ms^2$, the region of strong interactions is far below the average thermal electron energy. We find the solutions to the set of equations (4) and (5) that coincide asymptotically with the Boltzmann distribution at high energies. This distribution reaches complete equilibrium for trapped electrons and is characterized by a nonequilibrium electron density for free electrons. For energies in excess of $4ms^2$ in the case where an electron emits or absorbs a phonon, the change in the electron energy is small in comparison to the energy of the electron. In this case, the collision operators $\hat{J}_{i,i}$ can be reduced to the differential form [1]

$$\begin{aligned}
&\hat{J}_{1,1}(f^{(1)}(E)) \\
&= -\frac{1}{\sqrt{E}}\frac{d}{dE}\left[\frac{\sqrt{2}E^2}{l\sqrt{m}}\left(T\frac{df^{(1)}(E)}{dE} + f^{(1)}(E)\right)\right], \\
&\hat{J}_{2,2}(f^{(1)}(E)) \\
&= E^{5/2}\frac{d}{dE}\left[\frac{1}{El\sqrt{2m}}\left(-T\frac{df^{(2)}(E)}{dE} + f^{(2)}(E)\right)\right].
\end{aligned} \tag{16}$$

Qualitatively, the behavior of the solutions to the set of equations (4) and (5) is clear. At low energies, their behavior is determined by the accommodation between the distributions of free and trapped electrons in the region of strong scattering. At thermal energies, the distribution functions correspond to the Boltzmann distributions but are different. There is a region where these two asymptotic behaviors are matched together. Let us contract the transition region into a point corresponding to an energy E_0. In Eq. (11), the behavior of the integrand depends on the energy region. At high thermal energies, the integrand increases with a decrease in energy; therefore, the main contribution comes from the lower limit of this region. In the region of low energies (of the order of ms^2), the distribution functions are accommodated at the lower limit of this region and, therefore, are concurrently subtracted from the integral in Eq. (11) and the integral that defines the coefficient k_i. Near the upper limit of the low-energy region, this accommodation is destroyed and the contribution to the integral is maximum. Thus, in both energy regions, the main contribution to the integral in Eq. (11) comes from the vicinity of the point E_0. The contributions from high and low energies to the integral differ only numerically. Let us estimate the coefficients k_i and k_r qualitatively by evaluating the integral in Eq. (11) for high energies and setting the low limit equal to E_0.

Using Eq. (16) and simplifying Eq. (8), we write the set of equations (4) and (5) for energies in excess of ms^2 in the form

$$\begin{aligned}
&\frac{d}{dE}\left[E^2\left(\frac{df^{(1)}E}{dE} + \frac{1}{T}f^{(1)}(E)\right)\right] = \frac{32}{3}n_{im}e_1^6ms^2 \\
&\times\int_E^\infty dE_1\frac{1}{E_1^5}[f^{(1)}(E) - f^{(2)}(E_1 - E)e^{-E_1/T}], \\
&\frac{d}{dE}\left[\frac{1}{E}\left(\frac{df^{(2)}(E)}{dE} - \frac{1}{T}f^2(E)\right)\right] = \frac{1024}{3\pi}ms^2 \\
&\times\int_E^\infty dE_1\frac{1}{E_1^5}[f^{(2)}(E) - f^{(1)}(E_1 - E)e^{E_1/T}].
\end{aligned} \tag{17}$$

By considering Eqs. (17) at the energy E_0, we can determine this energy using dimensional analysis. Indeed, for trapped electrons, it follows from the second of Eqs. (17) that $|\hat{J}_{2,2}| \gg |\hat{J}_{2,1}|$ for $E \gg 4ms^2$. Therefore, the trapped electrons are described by the equilibrium distribution function. For free electrons, we find from the first of Eqs. (17) that the ratio $|\hat{J}_{1,2}|/|\hat{J}_{1,1}|$ is equal to $n_{\text{im}}e_1^6 4ms^2/E_0^4$. We seek E_0 in the form $T^{1-\nu}(4ms^2)^\nu$; this energy lies between T and $4ms^2$ if ν is not equal to zero or unity. The choice of the value of ν depends on the impurity concentration. For low concentrations ($n_{\text{im}}^{-1/3} \gg e_1^2/4ms^2$), we have $|\hat{J}_{1,2}| \ll |\hat{J}_{1,1}|$ even at $E_0 = 4ms^2$ and put $\nu = 1$. In this case, the trapping coefficient is estimated to be

$$k_r = \frac{e_1^6}{18l\sqrt{2\pi T}m^{5/2}s^4}. \tag{18}$$

In the case of a low impurity concentration, ionization of impurities can be observed in a semiconductor with a very high static dielectric constant, where the Coulomb interaction between an electron and an impurity is weak. For most semiconductors, however, it is more natural to assume that

$$\frac{e_1^2}{4ms^2} \gg n_{\text{im}}^{-1/3} \gg \frac{e_1^2}{T}. \tag{19}$$

A condition that involves temperature must be imposed. However, there is another argument in favor of condition (19), which has not been discussed in the literature. The presence of trapped electrons increases the number of possible electronic states that must be included in the condition from which the chemical potential is determined [1, 4]. Using the density of states $\rho_2(E)$, we can calculate the partition function by summing over all impurities independently. It turns out that, in the presence of impurities, the density of free electrons increases, with the fractional increase being equal to $\sqrt{n_{\text{im}}e_1^6/T^3}$. Only if condition (19) is satisfied is this increase small and can the standard expression for the chemical potential of electrons be applied [4]. Condition (19) also makes it possible to consider trapping processes for different impurities to be independent.

With the solution to the set of equations (17), we can choose the energy E_0 such that its value is as close to the region of strong interaction as possible and such that the intraband scattering becomes dominant at this energy. These conditions are satisfied in the case of $\nu = 1/4$. However, we must verify that condition (15) is satisfied for $E_a = E_0 = T^{3/4}(4ms^2)^{1/4}$. If

$$\frac{n_{\text{im}}e_1^6}{T^3} \ll \left(\frac{4ms^2}{T}\right)^{3/4}, \tag{20}$$

our consideration is self-consistent. In this case, the coefficient k_r is estimated to be

$$k_r = \frac{8e_1^6\sqrt{s}}{9\sqrt{\pi}lT^{11/4}m^{1/4}}. \tag{21}$$

Condition (20) is imposed on two small quantities and is independent of condition (19). If the inequality opposite to condition (20) is satisfied, then the parameter ν must be zero; otherwise, the characteristic distance is longer than the average spacing between impurities and our equation (3) ceases to be true. Thus, we choose $E_0 = T$. In this case, the expression for k_r coincides with that derived by Lax [5]:

$$k_r = \frac{16e_1^6\sqrt{2m}s^2}{9\sqrt{\pi}lT^{7/2}}. \tag{22}$$

Let us indicate the conditions under which the motion of electrons can be described in terms of classical (nonquantum) mechanics. We characterize an electron by a coordinate e_1^2/E_0 and a momentum $\sqrt{2mE_0}$; therefore, these quantities must satisfy the uncertainty relation, which can be written in the form

$$\frac{e_1^2\sqrt{m}}{\hbar\sqrt{2E_0}} \gg 1. \tag{23}$$

Various values of E_0 ($E_0 = 4ms^2$, $T^{3/4}(4ms^2)^{1/4}$, T) in the cases of low, medium, and high impurity concentrations lead to different criteria for the applicability of classical mechanics to ionization and electron capture by an impurity.

The results from kinetic theory differ from those obtained using the cascade method [1]. We indicated above that there is a difference in the definition of the trapping coefficient and that electron balance equation (1) is not derived in the cascade method. Another difference is that our theory relates the energy of a trapped electron to the distance at which the electron is trapped. This relation determines all properties of the solutions to the relevant equations. The cascade method does not involve this relation and, hence, ignores the basic feature of the physics of ionization and electron capture by an impurity.

4. QUANTUM THEORY OF THE TRAPPING AND IONIZATION PROCESSES

In the case where the sense of inequality (23) is reversed, the kinetic equations should be derived in terms of the quantum-mechanical model of the motion of an electron in the field of a Coulomb center (the model of quantum states of the hydrogen atom [6]). The spectrum of free-electron states is continuous, and the momentum $\mathbf{p}$ is a quantum number characterizing a Coulomb wave function and the energy $\varepsilon_{\mathbf{p}} = \mathbf{p}^2/2m$ in the continuum. The states of trapped electrons belong to a discrete spectrum of negative energies $\varepsilon_n = me_1^4/2\hbar^2n^2$, where n is the principal quantum number. In Eqs. (4) and (5), the collision operators must include the probabilities of transitions between quantum-mechanical states caused by the interaction between electrons and phonons.

The quasi-classical description of the states of the continuum in the Coulomb problem corresponds to small momenta, as seen from criterion (23), whereas the quantum conditions correspond to large momenta. In the latter case, the Coulomb wave functions reduce to plane waves and our description of free electrons reduces to the approximation (used by us) in which free electrons have only kinetic energy $\varepsilon_{\mathbf{p}} = \mathbf{p}^2/2m$ and have no potential energy. The distribution function depends on this energy, and the collision operator $\hat{J}_{1,1}$ takes the form of Eq. (13) [or of Eq. (16) in the case of $\varepsilon_{\mathbf{p}} \gg 4ms^2$]. However, the operator $\hat{J}_{1,2}$ takes a form different from that of Eq. (8),

$$\hat{J}_{1,2}(f^{(1)}\varepsilon_{\mathbf{p}}, f^{(2)}(\varepsilon_n)) = \frac{1}{(2\pi)^2\hbar}\int d\mathbf{q}\sum_{\alpha,(n)}\delta(\hbar\omega_{\mathbf{q}}-\varepsilon_{\mathbf{p}}-\varepsilon_n) \times |M_{\mathbf{p},\alpha}(\mathbf{q})|^2|c_{\mathbf{q}}|^2[f^{(2)}(\varepsilon_n)n_{\mathbf{q}} - f^{(1)}(\varepsilon_{\mathbf{p}})(n_{\mathbf{q}}+1)], \quad (24)$$

$$M_{\mathbf{p},\alpha}(\mathbf{q}) = \int d\mathbf{r}\psi^*_{\mathbf{p}}(\mathbf{r})e^{i\mathbf{qr}}\psi_\alpha(\mathbf{r}).$$

Here, α denotes a complete set of quantum numbers characterizing a state of the continuum and summation is performed over all quantum numbers at the given principal quantum number n on which the energy depends.

Due to orthogonality of the eigenfunctions of the Coulomb problem, we have $M_{\mathbf{p},\alpha}(\mathbf{q}=0)=0$. Since this condition may be violated in approximate calculations of the matrix element (which would lead to an erroneous result), we use the following exact equality that allows for this property of the matrix element:

$$M_{\mathbf{p},\alpha}(\mathbf{q}) = \hbar^2 i\mathbf{q}\mathbf{M}^{(1)}_{\mathbf{p},\alpha}(\mathbf{q})/m\left(\varepsilon_p+\varepsilon_n+\frac{\hbar^2q^2}{2m}\right), \quad (25)$$

$$\mathbf{M}^{(1)}_{p,\alpha}(\mathbf{q}) = \int d\mathbf{r}\psi_\alpha(\mathbf{r})e^{i\mathbf{qr}}\nabla\psi^*_{\mathbf{p}}(\mathbf{r}).$$

The matrix element $\mathbf{M}^{(1)}_{\mathbf{p},\alpha}(\mathbf{q})$ can be calculated approximately. At high energies, we replace the Coulomb function by the exponent $\psi^*_{\mathbf{p}}(\mathbf{r}) \sim \exp(-i\mathbf{pr}/\hbar)$, which considerably simplifies the expression for the matrix element. In order to calculate the sum in Eq. (24), one should use the eigenfunctions of the Coulomb problem in the coordinates in which the problem is solved [6]. In [1], the sum was calculated using spherical coordinates, but, for greater convenience, we used parabolic coordinates to obtain

$$\sum_{\alpha,(n)}|M_{\mathbf{p},\alpha}(\mathbf{q})|^2 = \frac{\hbar^2(\mathbf{qp})^2 64\pi n^5 a_{\mathrm{B}}^3}{m^2\left(\varepsilon_{\mathbf{p}}+\varepsilon_n+\frac{\hbar^2q^2}{2m}\right)^2\left[1+\left(\frac{\mathbf{p}}{\hbar}-\mathbf{q}\right)^2 n^2 a_{\mathrm{B}}^2\right]^4}. \quad (26)$$

Here, $a_{\mathrm{B}} = \hbar^2/me_1^2$ is the Bohr radius for wave functions in the field of the impurity. First, we integrate over the angular variable and then, using the denseness of the discrete spectrum, integrate over the variable n. As a result, we obtain $\hat{J}_{1,2}$ in a form analogous to that of Eq. (8). Designating $E = \varepsilon_{\mathbf{p}}$ for free electrons and $E = \varepsilon_n$ for trapped electrons, the result can be written as

$$\hat{J}_{1,2}(f^{(1)}(E), f^{(2)}(E)) = \int_E^\infty dE_1 W_1(E,E_1)f^2(E_1-E)e^{-E_1/T} - \frac{1}{\tau_r(E)}f^{(1)}(E),$$

$$W_1(E,E_1) = \frac{128\pi n_{\mathrm{im}}e_1^6m^2s^5}{3l} \times \frac{E[(E_1+2ms^2)^2+24ms^2E]}{E_1(1-e^{-E_1/T})(E_1+2ms^2)^2[(E_1+2ms^2)^2-8ms^2E]^3}, \quad (27)$$

$$\frac{1}{\tau_r(E)} = \int_E^\infty dE_1 W_1(E,E_1).$$

The term $\hat{J}_{2,1}$ can be transformed in the same way.

Thus, the probability of transitions between free and bound states in the quantum and classical cases is different. However, the dominant features of the energy dependence are the same. Therefore, the main feature of the trapping process, namely, the existence of a region of strong interaction, manifests itself in the same way in the quantum and classical cases. Let us estimate the coefficient k_r at high temperatures for the case where the impurity concentration satisfies condition (19). The equation for $f^{(1)}(E)$ can be written in a form analogous to that of Eq. (17):

$$\frac{d}{dE}\left[E^2\left(\frac{df^{(1)}(E)}{dE}+\frac{1}{T}f^{(1)}(E)\right)\right] = \frac{64\pi\sqrt{2}n_{\mathrm{im}}e_1^6(ms^2)^{5/2}}{3} \times\int_E^\infty\frac{E^{3/2}}{E_1^8}[f^{(1)}(E)-f^{(2)}(E_1-E)e^{-E_1/T}]dE_1. \quad (28)$$

The modulus of the ratio of the right-hand to left-hand side at the energy E_0 is $n_{\mathrm{im}}e_1^6(ms^2)^{5/2}/E_0^{11/2}$. By choosing $E_0 = T^{1-\nu}(4ms^2)^\nu$, we find that $\nu = 5/11$. This energy satisfies criterion (15) if the following equality analogous to condition (20) is satisfied:

$$\frac{n_{\mathrm{im}}e_1^6}{T^3} \ll \left(\frac{4ms^2}{T}\right)^{15/11}. \quad (29)$$

The trapping coefficient under these conditions can be found to be

$$k_r = \frac{32e_1^6s}{189lT^{65/22}(4ms^2)^{1/22}}. \quad (30)$$

If the impurity concentration satisfies the inequality opposite to inequality (29), then $E_0 = T$ and the trapping coefficient is estimated to be

$$k_r = \frac{512 e_1^6 m^2 s^2}{189 l T^5}. \quad (31)$$

Note that Eq. (2) is always true. The temperature dependence of the trapping coefficient in the classical and quantum cases is different, which is no surprise, because the relations between the semiconductor parameters and temperature in these cases are different. In the classical case, inequality (23) is satisfied, whereas in the quantum case the opposite inequality holds.

In closing, it should be noted that we considered the simplest case of the kinetics of transitions between free and bound states of electrons in a semiconductor. The kinetic theory developed here can be generalized to consider more complicated cases and the effect of external fields on the ionization and trapping processes.

ACKNOWLEDGMENTS

The author is grateful to S.V. Gantsevich and M.I. Muradov for discussions of the work.

This work was supported by grant NSh-2242.2003.2.

REFERENCES

1. V. N. Abakumov, V. I. Perel', and I. N. Yassievich, *Nonradiative Recombination in Semiconductors* (S.-Peterb. Inst. Yad. Fiz. Ross. Akad. Nauk, St. Petersburg, 1997) [in Russian].
2. G. H. Wannier, Phys. Rev. **91** (2), 207 (1953).
3. E. M. Lifshitz and L. P. Pitaevskiĭ, *Physical Kinetics* (Nauka, Moscow, 1979; Pergamon, Oxford, 1981).
4. A. I. Ansel'm, *Introduction to Semiconductor Theory* (Fizmatgiz, Moscow, 1962; Prentice Hall, Englewood Cliffs, 1981).
5. M. Lax, Phys. Rev. **119** (3), 1502 (1960).
6. L. D. Landau and E. M. Lifshitz, *Course of Theoretical Physics*, Vol. 3: *Quantum Mechanics: Non-Relativistic Theory*, 3rd ed. (Nauka, Moscow, 1974; Pergamon, New York, 1977).

Translated by Yu. Epifanov

Physics of the Solid State, Vol. 47, No. 2, 2005, pp. 225–228. Translated from Fizika Tverdogo Tela, Vol. 47, No. 2, 2005, pp. 217–219.

SEMICONDUCTORS AND DIELECTRICS

Temperature Dependence of the SmS Lattice Parameter

V. V. Kaminskiĭ, N. V. Sharenkova, L. N. Vasil'ev, and S. M. Solov'ev

Ioffe Physicotechnical Institute, Russian Academy of Sciences, Politekhnicheskaya ul. 26, St. Petersburg, 194021 Russia
e-mail: Vladimir.Kaminski@mail.ioffe.ru

Received June 1, 2004

Abstract—The behavior of the lattice parameter of single-crystal SmS with temperature was studied by x-ray diffractometry in the range 100–700 K. The observed features are assigned to a temperature-induced variation in the filling of the Sm^{2+} f-shell ground-state multiplet levels. The temperature dependence of the thermal expansion coefficient of SmS was measured. It is shown that the lattice constant behavior in samples that exhibit a pronounced emf generation effect under heating is influenced by the transition of defect samarium ions from the divalent to trivalent state and that the effect itself derives from phase transitions in SmS. © *2005 Pleiades Publishing, Inc.*

Samarium monosulfide (SmS) is an *n*-type rare-earth semiconductor compound that crystallizes in a NaCl-type structure with a lattice constant $a = 5.97$ Å. The most remarkable properties of SmS derive from the capacity of the samarium ion to change its valence state comparatively easily under varying external conditions. When in a metal state or bound in a compound, most of the rare-earth metals are trivalent (Ln^{3+}). Certain of them, however, can reside in an anomalous valence state (Ln^{2+} or Ln^{4+}). This property should be assigned to the particular stability of completely filled, empty, or half-filled atomic 4*f* shells. On account of this, the elements that exhibit anomalous valence under normal conditions are located in the beginning (Ce), in the middle (Eu, Sm), or at the end (Tm, Yb) of the 4*f* period. The divalent state is the most stable in Eu (in Eu^{2+} with the $4f^7$ configuration, the *f* shell is filled exactly to one-half) and in Yb (Yb^{2+} has a completely filled *f* shell, $4f^{14}$). In Sm, the divalent state is much less stable than in Eu or Yb, because Sm^{2+} has a $4f^6$ configuration [1]. This instability manifests itself in SmS undergoing an isostructural (NaCl–NaCl, $a = 5.97$ and 5.70 Å, respectively) first-order semiconductor–metal phase transition at a hydrostatic pressure of ~6.5 kbar [2] and exhibiting generation of an electromotive force (emf) under heating at $T \geq 400$ K in the absence of external temperature gradients [3]. Both these phenomena originate from a change in the valence state, $Sm^{2+} \longrightarrow Sm^{3+}$. The Sm^{2+} and Sm^{3+} ions differ substantially in size and have ionic radii of 1.14 and 0.96 Å, respectively, which becomes manifest in the SmS unit cell parameters. While the lattice-constant behavior at the pressure-induced phase transition in SmS is fairly well known [4], no such studies have thus far been performed for the emf generation effect. Experimentally, the valence state is usually derived from the lattice parameter by linear interpolation; therefore, investigating $a(T)$ dependences that reflect the behavior of the valence state of samarium ions with temperature may contribute considerably to our understanding of the physical mechanism responsible for the emf generation in SmS. Furthermore, knowledge of the $a(T)$ behavior makes it possible to determine the thermal expansion coefficient (α) of SmS and its temperature dependence. The quantity α is an important parameter of technological interest for the development of various SmS-based structures. Earlier, α of SmS was measured only in the range 80–300 K. Those observations revealed good agreement between the x-ray diffraction data and galvanomagnetic dilatometric measurements [5]. The present communication reports on an extension of the study of the $a(T)$ and $\alpha(T)$ dependences to temperatures up to $T \sim 700$ K.

Samarium monosulfide was synthesized from elemental substances Sm and S and melted in an induction furnace in airtight welded molybdenum crucibles. X-ray phase analysis showed the SmS single crystals to be single-phase and well formed.

In the temperature interval 100–300 K, x-ray patterns needed for determination of the lattice constant were obtained on an URNT-180 low-temperature attachment to a DRON-2 x-ray diffractometer. In the interval 300–700 K, diffractograms were recorded on the same diffractometer equipped with an URVT-2000 high-temperature attachment. The measurement accuracy was ±0.0005 Å.

Figure 1 presents the SmS unit cell parameter measured on a single-crystal sample with a conduction electron concentration $n = 9 \times 10^{18}$ cm^{-3} (experimental points).

1063-7834/05/4702-0225$26.00 © 2005 Pleiades Publishing, Inc.

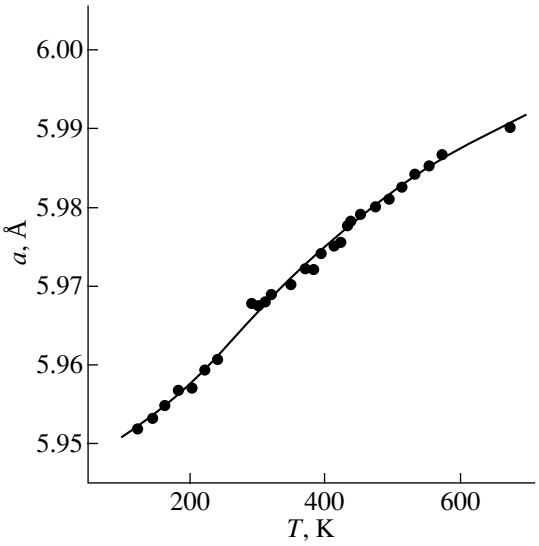

Fig. 1. Temperature dependence of the lattice constant of single-crystal SmS. Points are experiment, and the solid line is a plot of Eq. (1).

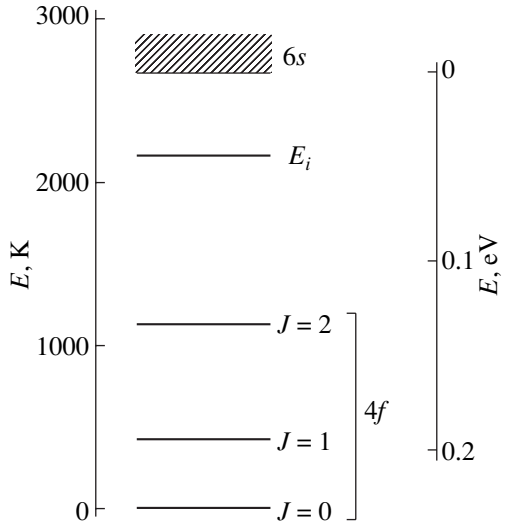

Fig. 2. Energy level diagram of SmS near the conduction band bottom (6s states). E_i are defect levels. The 4*f* levels are represented by the ground state ($J = 0$) and the first two excited states ($J = 1, 2$).

The $a(T)$ relation was analyzed in terms of a model proposed in [5] to account for the behavior of the temperature dependence of the coefficient of thermal expansion of SmS. The model is based on the variation in the filling of the Sm^{2+} *f*-shell ground-state multiplet levels with temperature. The Sm^{2+} ion contains six *f* electrons having a total orbital angular momentum $L = 3$ and a total spin $S = 3$. The total angular momentum of the lowest multiplet level is $J = 0$ (singlet). The level next in energy with $J = 1$ (triplet) is separated by 415 K from the lowest one; the third level with $J = 2$ (quintet), by 1115 K; and so on. The diagram of the lowest levels is presented in Fig. 2 (the higher levels will not be taken into account). At low temperatures, all Sm^{2+} ions have $J = 0$. As the temperature increases, part of the ions are excited to the $J = 1$ state and, subsequently, to the state with $J = 2$. Excited ions have a larger radius than nonexcited ones and, therefore, increase the average lattice constant. The curve in Fig. 1 was calculated using the standard statistics relation

$$a = (a_0W_0 + a_1W_1 + a_2W_2)/Z, \qquad (1)$$

where $W_i = (2J_i + 1)\exp(-E_i/T)$ is the probability of filling of states with energy E_i, $Z = W_0 + W_1 + W_2$ is the partition function, and a_i are the SmS lattice constants calculated under the assumption that all Sm^{2+} ions are in the $J = 0$, 1, and 2 states, respectively. The calculated curve was obtained by least squares fitting to experimental data, with a_i being used as a fitting parameter. The best fit to the experimental points was attained for $a_0 = 5.9500$ Å, $a_1 = 5.9727$ Å, and $a_2 = 6.0624$ Å. Assuming that these values are adequate, one can estimate the ionic radii (r) of Sm^{2+} ions in the ground and excited states: $r = (a - 2r_S)/2$, where $r_S = 1.84$ Å is the sulfur ionic radius. The values $r_0 = 1.13$ Å, $r_1 = 1.141$ Å, and $r_2 = 1.186$ Å appear reasonable.

Figure 3 plots the $\alpha(T)$ relation derived from the data in Fig. 1 using the expression

$$\alpha = \frac{1}{a}\frac{\partial a}{\partial T} = \frac{\partial \ln a}{\partial T}. \qquad (2)$$

Also presented are dilatometric data [5] (dashed line). The discrepancies range from 0 to 15%, depending on

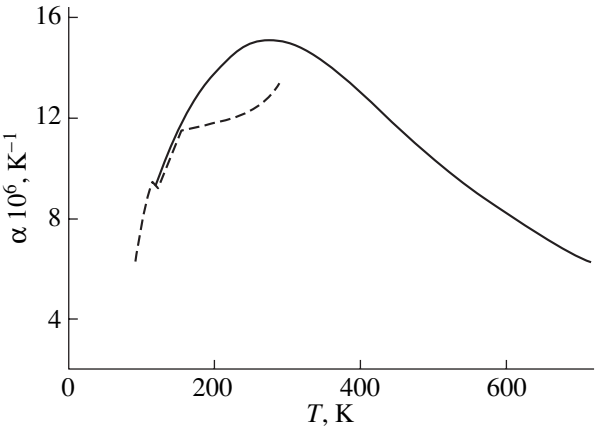

Fig. 3. Linear thermal expansion coefficient of single-crystal SmS plotted vs. temperature (solid curve). The dashed line shows experimental data [5].

the temperature, which should be assigned to differences in the parameters of the samples, in particular, their defect concentration, rather than to the different methods used and the errors in them.

It is of interest to consider the behavior of the lattice constant of SmS samples that exhibit a clearly pronounced effect of emf generation under heating in the absence of external temperature gradients [3]. Because the effect originates from the defect samarium ions that occupy vacancies on the sulfur sublattice [6], experiments should be conducted on nominally stoichiometric samples with a high concentration of such defects and a large gradient of their distribution over the sample. The number of defect samarium ions was estimated as was done in [6], from the conduction electron concentration n, which was extracted from Hall effect measurements. As a result, we chose a single-crystal sample $2 \times 2 \times 0.5$ mm in size, which was cleaved along the [100] cleavage planes from a larger single crystal with $n = (1–2) \times 10^{19}$ cm^{-3}. The large scatter of n in the original sample provided a gradient of n in the SmS single crystal under study. Figure 4a presents the temperature dependence of the emf generated in the sample under heating. The temperature of the onset of generation, 450 to 500 K, is consistent with the calculated values [6] of 440 to 640 K. Figure 4b plots the temperature dependence of the lattice parameter measured on the same sample. This graph exhibits a discontinuous decrease in slope at the temperatures corresponding to the onset of generation. Thus, the emf generation is accompanied by a decrease in the lattice constant. This can be interpreted in terms of the model of the generation effect proposed in [3], according to which the defect samarium ions change their valence state during generation, $Sm^{2+} \longrightarrow Sm^{3+} + e^-$. The Sm^{3+} ionic radius is smaller than that of Sm^{2+} (0.96 and 1.14 Å, respectively). In the course of generation, the number of Sm^{3+} ions grows gradually with increasing temperature as a result of new crystal regions becoming involved in the process as the local defect concentration decreases. However, this effect does not give rise to a decrease in the parameter a but rather decreases the rate of its growth with temperature (due to Sm^{2+} ions being excited to higher states), because the number of defect ions in our sample is only ~1% of the total number of samarium ions (calculation made according to [6]). Thus, the behavior of the $a(T)$ relation supports the model of the emf generation effect in SmS.

Figure 4c plots the temperature dependence of α for the SmS single crystal calculated from the $a(T)$ dependence shown in Fig. 4b. Because the change in crystal volume, ΔV, is proportional to $3\Delta a$, the graphs in Figs. 4b and 4c suggest that the SmS single crystal undergoes, on the whole, a second-order phase transition (a varies continuously with increasing temperature), whereas

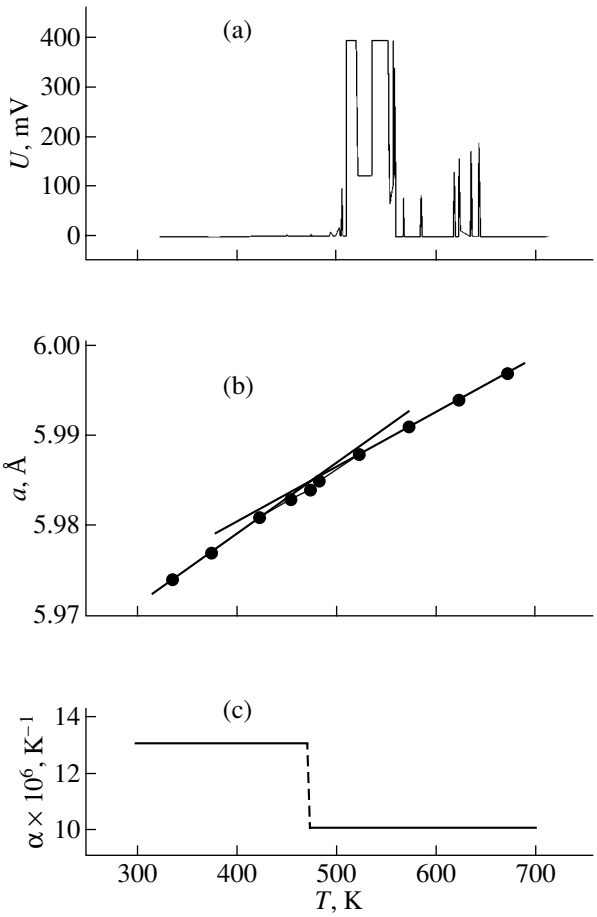

Fig. 4. Behavior of the SmS parameters under the conditions of emf generation: (a) emf generated in the sample under heating, (b) temperature dependence of the lattice parameter, and (c) temperature dependence of the linear thermal expansion coefficient of the same SmS sample.

$\alpha = \frac{1}{a}\frac{\partial a}{\partial T}$ changes abruptly; i.e., the derivative $\frac{1}{V}\frac{\partial V}{\partial T}$ and the thermodynamic expansion coefficient change in a jumplike manner. In the defect samarium ion subsystem, however, the phase transition is first-order, because the samarium ionic radii vary in a jumplike manner in the subsystem (the phase transition energy is 46 J/cm^3 [3]). This conclusion may be of significance for practical applications of the generation effect. First, thermal effects and the emf generation effect should have a reversible (pulsed) character, because the basic matrix of samarium ions in SmS remains stable at the phase transition in the defect system. Second, the inverse population of the conduction band may give rise, as a result of the Mott transition in the defect system, to the generation of radiation with an energy of 0.03–0.06 eV as electrons return to the defect levels $E_i = 0.045 \pm 0.015$ eV (Fig. 2).

ACKNOWLEDGMENTS

The authors are indebted to A.V. Golubkov for providing the SmS single crystals for the study.

REFERENCES

1. D. I. Khomskiĭ, Usp. Fiz. Nauk **129** (3), 443 (1979) [Sov. Phys. Usp. **22**, 879 (1979)].
2. A. Jayaraman, V. Narayanamurti, E. Bucher, and R. G. Maines, Phys. Rev. Lett. **25** (20), 1430 (1970).
3. V. V. Kaminskiĭ and S. M. Solov'ev, Fiz. Tverd. Tela (St. Petersburg) **43**, 423 (2001) [Phys. Solid State **43**, 439 (2001)].
4. I. A. Smirnov and V. S. Oskotskiĭ, Usp. Fiz. Nauk **124** (2), 241 (1978) [Sov. Phys. Usp. **21**, 117 (1978)].
5. T. B. Zhukova, V. V. Zhdanova, V. M. Sergeeva, L. S. Parfen'eva, V. P. Sergeev, V. S. Oskotskiĭ, E. V. Shadrichev, and I. A. Smirnov, in *Refractory Compounds of Rare-Earth Metals*, Ed. by K. E. Mironova (Nauka, Novosibirsk, 1979), p. 220 [in Russian].
6. V. V. Kaminskiĭ, A. V. Golubkov, and L. N. Vasil'ev, Fiz. Tverd. Tela (St. Petersburg) **44** (8), 1501 (2002) [Phys. Solid State **44**, 1574 (2002)].

Translated by G. Skrebtsov

Physics of the Solid State, Vol. 47, No. 2, 2005, pp. 229–232. From Fizika Tverdogo Tela, Vol. 47, No. 2, 2005, pp. 220–223.

SEMICONDUCTORS AND DIELECTRICS

Anisotropy of Electric Resistivity of Sapele-Based Biomorphic SiC/Si Composites[1]

T. S. Orlova[1], B. I. Smirnov[1], A. R. de Arellano-Lopez[2], J. Martínez Fernández[2], and R. Sepúlveda[2]

[1] *Ioffe Physicotechnical Institute, Russian Academy of Sciences, Politekhnicheskaya ul. 26, St. Petersburg, 194021 Russia*
e-mail: orlova.t@mail.ioffe.ru

[2] *Departamento de Fisica de la Materia Condensada, Universidad de Sevilla, Sevilla, 41080 Spain*

Received June 23, 2004

Abstract—The electrical resistivity of Sapele-based biomorphic SiC/Si materials was measured in a wide temperature range from 10 K to room temperature. The samples were fabricated by the reactive infiltration of molten silicon into a carbonized Sapele (African Entandrophragma Cylindricum) wood preform. All the samples studied contained residual Si (10–35 wt %). It was found that the resistivity-temperature ($\rho(T)$) dependences have semimetallic behavior which becomes very close to linear metallic behavior at $100 < T < 300$ K. The obtained values of resistivity were quite low ($\rho \approx 0.002$–$0.02\ \Omega$ cm) and showed strong anisotropy: the resistivity along the wood growth axis was several times lower than that in the perpendicular direction. The extent of this anisotropy was in correlation with the amount of residual Si (and, hence, with the amount of residual porosity) in a sample. The resistivity perpendicular to the wood growth axis drastically increased with the Si content, whereas the resistivity parallel to it was practically independent of the Si content. It is suggested that the presence of residual carbon in the samples and carrier scattering at SiC/Si interphases could determine the observed character of $\rho(T)$ dependences. © *2005 Pleiades Publishing, Inc.*

Wood-based biomorphic SiC (bioSiC) materials have been a subject of interest over the last decade [1–7]. This biomorphic SiC is fabricated by the reactive infiltration of molten silicon into a porous preform of carbonized wood [1–3, 5, 7]. The final product has a cellular structure of SiC with elongated silicon "channels." Some residual carbon and empty pores are also present in varying amounts [4, 6]. Moreover, the fine structure of the obtained SiC phase is not uniform throughout a sample: it could exist in micron sized grains and also in colonies of nanosized grains nearby the interfaces with carbon [8, 9]. A wide variety of SiC/Si composites can be fabricated by melt Si-infiltration of wood depending on the type of wood and technological conditions.

The bioSiC fabrication technique has several important advantages, such as low cost (not requiring high-purity starting powders or very high processing temperatures) and fast fabrication (by using an open-cell porous carbon template) [8].

BioSiC ceramics have already demonstrated outstanding mechanical properties as compared to other porous or siliconized SiC [10], which have found application in different areas. For example, bioSiC ceramics have been successfully developed as reinforcements for refractory concrete [9]. They are also considered to be promising materials for dental and orthopaedic implants [11]. However, the physical properties of these materials have not been studied in detail.

At present, there are several different kinds of performance SiC materials, such as chemically deposited (CDV) SiC and Black SiC ceramics, which are specially important for their application at high temperature in corrosive environments [12]. Such materials are available with various resistances, from conducting to insulating. The conducting type is used as heating elements because of its excellent thermal characteristics. The insulating type can be used as high-frequency plasma components.

The bioSiC ceramics have a complex structure, hence their electric properties can also differ from the standard performance SiC. We studied the resistivity temperature behavior of bioSiC ceramics fabricated from Sapele precursors. The resistivities in the directions parallel and perpendicular to the wood axis are compared.

1. EXPERIMENTAL

Biomorphic SiC was fabricated by the reactive infiltration of molten silicon into a porous preform of carbonized Sapele wood (African Entandrophragma Cylindricum). The infiltration was performed in vacuum following the conventional procedure for reaction formed SiC described in [4, 13, 14]. The fabricated SiC ceramics had a cellular structure of SiC with elongated silicon channels (residual Si remained in the pores) in

[1] This article was submitted by the authors in English.

Table 1. Microstructural characterization of bioSiC Sapele-based ceramics

Sample	Si content, wt %	Si content, vol % (from SE image in SEM)	Si content, vol % (from BSE image in SEM)	Mean diameter of Si-filled pores, μm	Residual porosity, vol %	*A*–Si/SiC interface specific area, μm^{-1}
Bio-I	32 (>40% from XRD)	26–39	29	12	4.7–5.5	0.1
Bio-II	23	24	21	10.5	12–13.8	0.07–0.08
Bio-III	23.2	11	10	9	18–21	0.04

the axial direction of the original wood. Depending on the weight ratio between the carbonized wood and infiltrating Si piece, it is possible to obtain final SiC/Si samples with different amounts of residual Si. Three different pieces of bioSiC/Si with different weight ratios between the carbonized wood and infiltrating Si piece were prepared. In a first approximation, the weight percentage of the residual Si content in each of the pieces was obtained based on the weights of the initial carbon perform, initial infiltrating Si, and the obtained product of Si + SiC. The obtained data are shown in Table 1, where the studied compositions are denoted as Bio-I, Bio-II, and Bio-III.

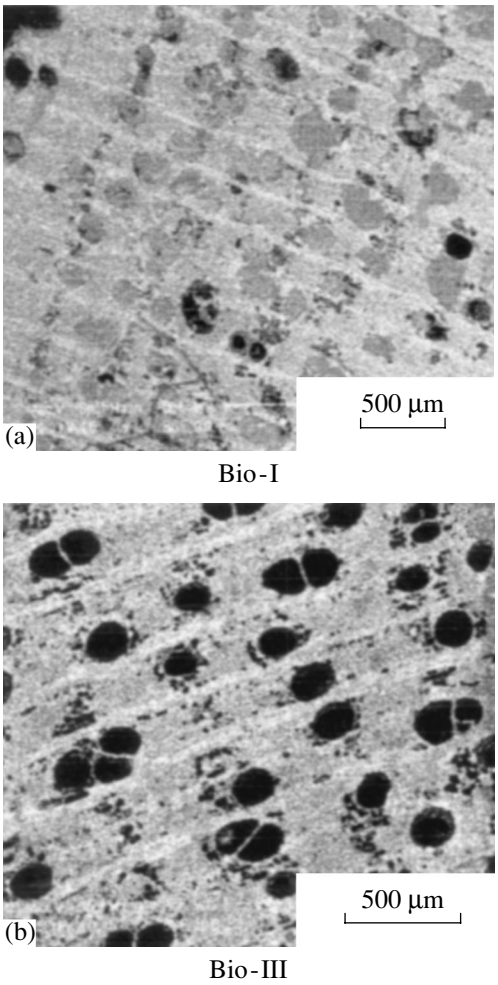

Fig. 1. SEM (in back scattered electrons) micrographs of the as-fabricated materials, (a) Bio-I and (b) Bio-III, perpendicular to the wood fibres (Si is given by round grey phases, empty pores are black).

Samples were cut into parallelepipeds with the approximate dimensions $1.5 \times 2.5 \times 15$ mm. The electrical resistance–temperature (*R–T*) dependences were measured using the four-probe technique in a wide temperature range from about 10 K to room temperature. Electric resistivity ρ was calculated without regard for sample residual porosity.

Microstructural observations were performed by optical microscopy and by scanning electron microscopy (SEM) using a Philips XL-30 electron microscopy operating at 30 kV. The volume fraction of the remaining Si in a sample was calculated from topological measurements of SEM images. Topological studies based on the image contrast were completed by analyzing the phases in the back scattering electron (BSE), allowing a clear distinction between phases.

2. RESULTS AND DISCUSSION

In Table 1, the amount of residual silicon and porosity are presented for all three studied SiC/Si compositions. The weight percentage of Si content estimated base on the weight of the carbon preform, initial infiltrating Si, and the obtained product of Si + SiC is only approximate because the product of such Si infiltration also contains a residual amount of **C**. In addition, the structure of the fabricated piece of ceramics is not homogeneous due to the nature of wood and, additionally, the nonhomogenous distribution of silicon inside the carbon piece during the fabrication process. Surface fraction analysis of SEM images in secondary electrons (SE) and in back scattered electrons (BSE) allowed better estimation of the residual silicon and porosity in each sample. We identified the presence of a Si distribution in SE and BSE images in SEM and estimated the volume fraction of silicon and the mean diameter of the silicon filled pores and volume portion of the unfilled ones. These data are presented in Table 1. From composition Bio-I to composition Bio-III, the amount of residual silicon decreases. This is even evident visually from the SEM micrographs shown in Fig. 1, where the

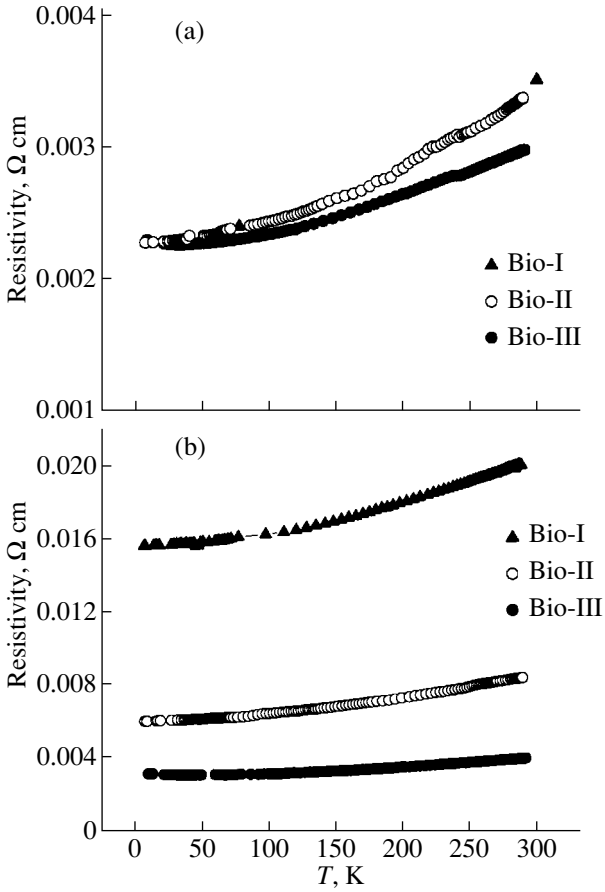

Fig. 2. Resistivity vs. temperature dependence for the orientation (a) parallel and (b) perpendicular to the growth wood axis.

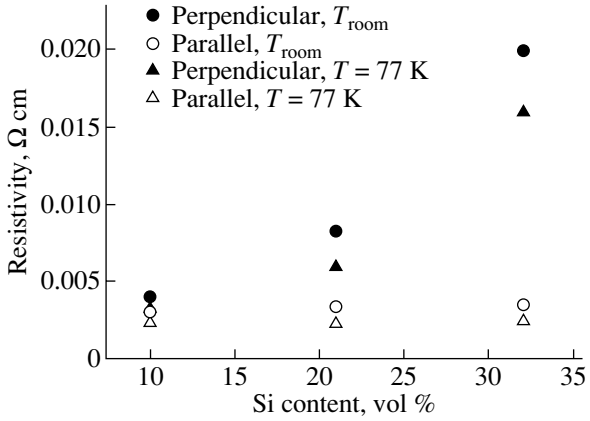

Fig. 3. Dependence of resistivity on residual silicon content at 77 K and room temperature for sample orientations parallel and perpendicular to the pore channels in the initial wood.

structure perpendicular to the wood axis is shown (SiC is the round grey phase, residual pores are black).

Figure 2 shows the ρ–*T* behavior of the studied compositions in a wide temperature range from about 10 to 300 K. The resistivity was measured in the directions parallel ($\rho_\parallel$) (Fig. 2a) and perpendicular ($\rho_\perp$) (Fig. 2b) to the growth wood axis. As seen, there is pronounced anisotropy of the resistivity for these two directions. This anisotropy is the largest for composition Bio-I, which contains the largest amount of residual Si and, hence, the lowest content of unfilled pores. Figure 3 presents the resistivity versus the Si content. The resistivity in the direction parallel to the wood axis does not depend on the Si content, whereas the resistivity in the perpendicular direction dramatically increases with it.

The dependence of the resistivity on the temperature for these ceramics shows a semimetallic behavior; the dependences are not completely linear. The resistivity at room temperature (Table 2) is quite low and about one order of magnitude lower (in the case of the highest $\rho_\perp$ value for Bio-I) than the average data for β-SiC single crystals in the literature [15]. However, some special SiC materials with comparable low electrical resistivity are known in the literature. These are Black SiC ceramics [12] and a siliconized SiC based on carbon fibres in a textile preform [16].

The observed anisotropy in the electric conductivity can be associated with the scattering of carriers on the SiC/Si interfaces when the current passes through them, i.e., in the direction perpendicular to the wood axis. We estimated the summary interface area *A* between Si and SiC per unit volume for the studied sample. Then parameter *A* is calculated as follows:

$$A = 2\frac{k}{R}, \quad (1)$$

where *k* is the volume fraction (vol %) of pores occupied by the residual Si and *R* is the mean radius of such pores. The obtained values of the *A* parameter are presented in Table 1. The Bio-I composition has the highest value of *A*. There is an apparent correlation between the extent of anisotropy and the value of the *A*-parame-

Table 2. Electrical resistivity of bioSiC Sapele-based ceramics

Ceramics	ρ at T_{room}, Ω cm	$\rho_\perp/\rho_\parallel$ at T_{room}	ρ at 10 K, Ω cm	$\rho_\perp/\rho_\parallel$ at 10 K
Bio-I	$\rho_\perp$, 0.02	5.7	$\rho_\perp$, 0.016	6.7
	$\rho_\parallel$, 0.0035		$\rho_\parallel$, 0.0024	
Bio-II	$\rho_\perp$, 0.0083	2.5	$\rho_\perp$, 0.0059	2.6
	$\rho_\parallel$, 0.0034		$\rho_\parallel$, 0.0023	
Bio-III	$\rho_\perp$, 0.00395	1.33	$\rho_\perp$, 0.0031	1.35
	$\rho_\parallel$, 0.003		$\rho_\parallel$, 0.0023	

Note: $\rho_\perp$ is the resistivity in the direction perpendicular to the growth wood axis, and $\rho_\parallel$ is the resistivity in the direction parallel to it.

ter: the higher the *A*-parameter value, the higher the anisotropy.

In biomorphic SiC materials, there is always some amount of residual carbon [6]. The amount of residual carbon also seems to be in correlation with the residual amount of Si and, hence, of empty pores after the infiltration. There will most probably be a lesser amount of residual porosity in the samples with more a completed reaction between Si and C during the infiltration. Carbon most likely participates in electric transport in bio-SiC ceramics providing metallic behavior. However, the question regarding which type of carriers is responsible for the conductivity in these ceramics remains open and requires additional investigation.

Thus, it was found that the electric transport properties of BioSiC/Si (Sapele-based) are anisotropic in a wide temperature range from 10 K to room temperature. The value of this anisotropy depends on the Si content in the sample and, hence, on the residual porosity. The resistivity perpendicular to the wood axis drastically increased with Si content (and with a decrease in the residual porosity), whereas the resistivity parallel to the wood axis did not show a strong dependence on the unreacted Si content; it remained about the same for a variation in Si content from 10 to 35 vol %. The $\rho(T)$ dependences showed a semimetallic behavior.

ACKNOWLEDGMENTS

This work was supported at the Universidad de Sevilla by MCYT (grant MAT2003-05202-C02-01) and at the Ioffe Institute by the Russian Foundation for Basic Research (no. 04-03-33183).

REFERENCES

1. T. Ota, M. Iakahashi, T. Hibi, M. Ozawa, and H. Suzuki, J. Am. Ceram. Soc. **78**, 3409 (1995).
2. C. E. Byrne and D. E. Nagle, Mater. Res. Innovations **1**, 137 (1997).
3. P. Greil, T. Lifka, and A. Kaindl, J. Eur. Ceram. Soc. **18**, 1961 (1998).
4. J. Martínez-Fernández, F. M. Varela-Feria, and M. Singh, Scr. Mater. **43**, 813 (2000).
5. M. Singh, Ceram. Eng. Sci. Proc. **21**, 39 (2000).
6. F. M. Varela-Feria, J. Martínez-Fernández, A. R. de Arellano-Lopez, and M. Singh, J. Eur. Ceram. Soc. **22**, 2719 (2002).
7. F. M. Varela-Feria, S. Lopez Pombero, J. Martínez-Fernández, A. R. de Arellano-Lopez, and M. Singh, Ceram. Eng. Sci. Proc. **23**, 681 (2002).
8. J. Martínez-Fernández, A. Munoz, A. R. de Arellano-Lopez, F. M. Varela-Feria, A. Dominguez-Rodriguez, and M. Singh, Acta Mater. **51**, 3259 (2003).
9. A. R. de Arellano-Lopez, J. Martínez-Fernández, P. Gonzalez, C. Dominguez, V. Fernandez-Quero, and M. Singh, Int. J. Appl. Ceram. Tech. **1**, 95 (2004).
10. P. Greil, Mater. Chem. Phys. **61**, 64 (1999).
11. P. Greil, J. Eur. Ceram. Soc. **21**, 105 (2001).
12. Black Ceramics, in *Technical Report 2000. News of Technology and Materials* (2000), p. 49.
13. M. Singh and D. R. Behrendt, J. Mater. Res. **9**, 1701 (1994).
14. M. Singh and D. R. Behrendt, Mater. Sci. Eng. A **194**, 193 (1995).
15. *Physicochemical Properties of Semiconducting Materials*, Ed. by A. V. Novoselova and V. B. Lazarev (Nauka, Moscow, 1978) [in Russian].
16. S. K. Brantov and A. V. Efremov, Materialovedenie **2**, 48 (1999).

Physics of the Solid State, Vol. 47, No. 2, 2005, pp. 233–237. Translated from Fizika Tverdogo Tela, Vol. 47, No. 2, 2005, pp. 224–228.

SEMICONDUCTORS AND DIELECTRICS

Effective Mass and Mobility of Carriers in p-$Bi_{2-x}Sb_xTe_{3-y}Se_y$ Solid Solutions at Temperatures below 300 K

L. N. Luk'yanova, V. A. Kutasov, and P. P. Konstantinov

Ioffe Physicotechnical Institute, Russian Academy of Sciences, Politekhnicheskaya ul. 26, St. Petersburg, 194021 Russia
e-mail: lidia.lukyanova@mail.ioffe.ru

Received June 3, 2004

Abstract—The temperature dependences of the Seebeck coefficient α and of the electrical conductivity σ of p-$Bi_{2-x}Sb_xTe_{3-y}Se_y$ solid solutions were studied under atomic substitution on the cation ($1 \le x \le 1.5$) and anion ($0.04 \le y \le 0.09$) bismuth and antimony telluride sublattices within the temperature interval 80–340 K. The effect of variation in the solid-solution composition on the average effective density-of-states mass (m/m_0) and carrier mobility (μ_0, calculated with due account of degeneracy) was studied under the assumption that carrier scattering is isotropic and that the relaxation time can be approximated by a power-law function $\tau = aE^{r_{\text{eff}}}$, where r_{eff} is an effective scattering parameter. It is shown that variations in the pattern of the m/m_0 and μ_0 temperature dependences produced in the temperature region under study by properly varying the number of substituted atoms in the solid solutions may favor an increase in thermoelectric efficiency. © *2005 Pleiades Publishing, Inc.*

1. INTRODUCTION

p-$Bi_{2-x}Sb_xTe_{3-y}Se_y$ solid solutions with atomic substitution on both sublattices, as well as p-$Bi_{2-x}Sb_xTe_3$ ($x \le 1$), have application potential in the low-temperature region ($T < 220$ K) [1–4]. The transition to operating temperatures $T < 220$ K is motivated by the use of these solid solutions in applications associated with deep cooling and requires the development of materials whose maximum thermoelectric efficiency (Z_m) is shifted to low temperatures. Such a shift of Z_m can be attained by reducing the carrier concentration below the level which is optimum near room temperature, as well as by properly varying the solid solution composition.

The materials under study have a complex band structure described by a six-ellipsoid energy spectrum model both for the main and the additional valence band [5–7]. The additional valence band affects the thermoelectric properties through a change in the parameters of the ellipsoidal constant-energy surfaces and interband scattering. Nevertheless, the properties determining the thermoelectric efficiency are customarily analyzed in terms of a model with a single parabolic energy band in which the effective density-of-states mass (m/m_0) is isotropic.

The main mechanisms of scattering in Bi_2Te_3-based solid solutions are known to be scattering from acoustic phonons, the cores of ionized impurities, and atoms of the second component in a solid solution [8]. If a model with a single parabolic energy band is used in which carrier scattering is isotropic, the concentration dependence of the effective mass is neglected, and the relaxation time is assumed to be a power-law function of energy, $\tau = aE^r$ (where a is a constant), then these mechanisms are characterized by a scattering parameter close to $r = -0.5$. However, combined studies of galvanomagnetic effects in weak magnetic fields and of the Seebeck coefficient have shown that the scattering parameter r differs from –0.5 [9–11].

The changes in r in the materials under consideration can be accounted for by introducing the effective scattering parameter r_{eff} calculated in [9]. Therefore, in accordance with [9–11], we determine the effective mass m/m_0 and mobility of carriers μ_0, with due allowance for degeneracy, from experimental data on the temperature dependences of the Seebeck coefficient α and the electrical conductivity σ.

2. EFFECTIVE SCATTERING PARAMETER

Numerical calculations of r_{eff} and of the reduced Fermi level η [9] based on data on the degeneracy parameter $\beta_d(r, \eta)$ and the Seebeck coefficient $\alpha(r, \eta)$ revealed that r_{eff} varies from –0.45 to –0.78 at $T = 80$ K with increasing carrier concentration in p-$Bi_{2-x}Sb_xTe_{3-y}Se_y$ solid solutions. Thus, the results obtained in [9] permit determination of the dependence of the r_{eff} parameter on the Seebeck coefficient α, which is shown graphically in Fig. 1.

A similar behavior of the parameter r_{eff} with concentration and temperature was derived by us earlier for n-$Bi_{2-x}Sb_xTe_{3-y}Se_y$ solid solutions of various composition [10, 11] (Fig. 1). The temperature dependence of r_{eff} is consistent with the values of r_{eff} quoted in [12] for p-$Bi_2Te_{3-y}Se_y$.

1063-7834/05/4702-0233$26.00

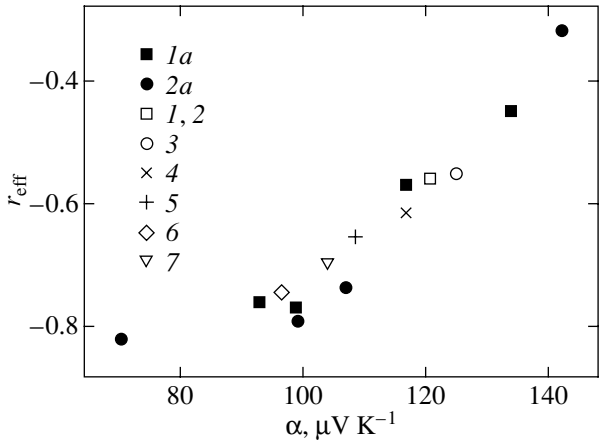

Fig. 1. Effective scattering parameter r_{eff} plotted vs. the Seebeck coefficient α at 80 K in solid solutions (*1a*) p-$Bi_{2-x}Sb_xTe_{3-y}Se_y$ ($1 \le x \le 1.2$, $0.06 \le y \le 0.09$) [9], (*2a*) n-$Bi_{2-x}Sb_xTe_{3-y}Se_y$ ($x = 0.4$, $y = 0.6$) [10, 11], and (*1–7*) p-$Bi_{2-x}Sb_xTe_{3-y}Se_y$ ($1 \le x \le 1.5$, $0.06 \le y \le 0.09$). The samples are numbered *1* through *7* as in the table.

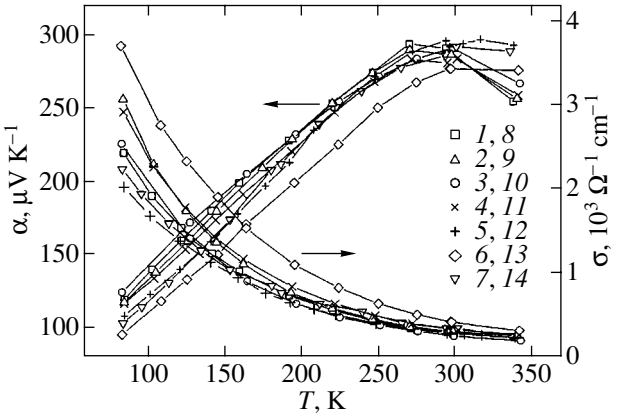

Fig. 2. Temperature dependences of (*1–7*) the Seebeck coefficient α and (*8–14*) electrical conductivity σ of the p-$Bi_{2-x}Sb_xTe_{3-y}Se_y$ solid solutions. (*1, 8*) $x = 1$, $y = 0.06$; (*2, 9*) $x = 1.1$, $y = 0.06$; (*3, 10*) $x = 1.2$, $y = 0.06$; (*4, 11*) $x = 1.2$, $y = 0.09$; (*5, 12*) $x = 1.3$, $y = 0.09$; (*6, 13*) $x = 1.3$, $y = 0.07$; and (*7, 14*) $x = 1.5$, $y = 0.09$.

The scattering parameter was also found to be temperature-dependent in a study of the Nernst–Ettingshausen effect in n-Bi_2Te_3 [13]. The parameter r increased with temperature to reach a value $|r| = 0.55$ near room temperature. However, in calculating the mobility μ (which is needed to determine r), Champness and Kipling [13] did not take into account the anisotropy parameter when deriving the carrier concentration from Hall effect measurements in weak magnetic fields, which led to an overestimated mobility. Our estimates, made with due account of the anisotropy parameter, showed that the scattering parameters calculated for the mobilities corrected in this way are close to the values of r_{eff} extracted from data on the degeneracy parameter β_d and the Seebeck coefficient α.

As follows from Fig. 1, r_{eff} varies over the carrier concentration region $(4–8) \times 10^{18}$ cm^{-3}. It is known that, at carrier concentrations of about $(3–4) \times 10^{18}$ cm^{-3}, the additional band in the valence band of Bi_2Te_3 and related solid solutions starts to fill [5–7]. At higher carrier concentrations in p-$Bi_{2-x}Sb_xTe_{3-y}Se_y$ and with the temperature increasing to room level, the parameter r_{eff} stabilizes at a level of –(0.75–0.78). In other words, the concentration dependence of r_{eff} shows that it is in this region of carrier concentrations, $(4–8) \times 10^{18}$ cm^{-3}, that the additional band in the p-$Bi_{2-x}Sb_xTe_{3-y}Se_y$ solid solutions starts to fill.

3. SAMPLES FOR THE STUDY

The samples chosen for studies of the thermoelectric properties (the Seebeck coefficient α, electrical conductivity σ) of p-$Bi_{2-x}Sb_xTe_{3-y}Se_y$ solid solutions ($x \le 1.5$, $y \le 0.09$) were grown by vertical zone leveling with high-precision temperature control during crystallization. The control was effected by means of a microprocessor-based TP 403 heat controller to within ±1°C, which permitted growth of homogeneous ingots of multicomponent solid solutions [14].

The samples were single-crystal blocks extended along the growth axis, which was perpendicular to C_3. The carrier concentration could be reduced by Bi ⟶ Sb and Te ⟶ Se substitutions and addition of Te in excess of the stoichiometric composition of the solid solution. Such changes in the composition bring about a decrease in the number of antisites, which favors a decrease in the concentration of native acceptor-type charged point defects [15].

4. THE SEEBECK COEFFICIENT AND ELECTRICAL CONDUCTIVITY

Figure 2 displays the temperature dependences of the Seebeck coefficient α and of the electrical conductivity σ of p-$Bi_{2-x}Sb_xTe_{3-y}Se_y$ solid solutions. The $\alpha(T)$ dependences typically exhibit a certain weakening as the solid-solution composition is varied. Compositional variations caused by a decrease in the Sb concentration in the solid solution ($x = 1.5–1$) reduce the slope $s_1 = d\ln\alpha/d\ln T$ for samples with similar carrier concentrations by no more than 7–8% (see table). This weakening of the temperature dependences of the Seebeck coefficient α suggests that it is possible to increase the thermoelectric efficiency Z in the low-temperature domain by reducing the Sb concentration to $x = 1–1.2$. p-$Bi_{2-x}Sb_xTe_{3-y}Se_y$ compositions with $x = 1$ and 1.1 and $y = 0.06$ (curves *1, 2* in Fig. 2) exhibit a shift of the maximum in the $\alpha(T)$ dependence toward lower temperatures, which, together with a weakening of this dependence, also gives rise to an increase in Z.

Because the carrier concentration is only very weakly temperature-dependent in the range 80–300 K

Slopes of the temperature dependences of the Seebeck coefficient α (s_1), effective density-of-states mass m/m_0 (s_2, s_3), and mobility μ_0 (s_4, s_5) in p-$Bi_{2-x}Sb_xTe_{3-y}Se_y$ solid solutions

Sample no. in the figures	x	y	s_1 (T < 150 K)	s_2 (T < 150 K)	s_3 (T > 150 K)	$\lvert s_4\rvert$ (T < 150 K)	$\lvert s_5\rvert$ (T > 150 K)	$p \times 10^{-19}$, cm^{-3}
1	1	0.06	0.80	0.25	0.35	1.45	2.15	0.4
2	1.1	0.06	0.76	0.05	0.65	1.85	2.2	0.5
3	1.2	0.06	0.76	0.15	0.5	1.85	2.2	0.4
4	1.2	0.09	0.74	0.1	0.5	1.7	2.15	0.7
	1.2	0.09	0.76	0.05	0.5	1.7	2.1	0.8
	1.2	0.09	0.79	0.15	0.45	1.15	2.3	2
5	1.3	0.09	0.72	0.15	0.8	1.6	2.15	0.3
	1.3	0.06	0.81	0.1	0.75	1.7	2.4	0.5
	1.3	0.07	0.78	0.05	0.8	1.8	2.45	0.7
6	1.3	0.07	0.80	0.1	0.65	1.7	2.3	0.9
	1.3	0.09	0.81	0.05	0.5	1.7	2.4	1.8
7	1.5	0.09	0.81	0.2	0.8	1.6	1.7	0.5

[9], the temperature dependence of electrical resistivity σ determines the variation in the mobility with temperature. The dependences of α and σ on T can be used to determine the product $(m/m_0)^{3/2}\mu_0$ [9] needed to calculate the carrier effective mass m/m_0 and mobility μ_0 with due account of degeneracy.

5. EFFECTIVE DENSITY-OF-STATES MASS

The effective density-of-states mass m/m_0 and mobility μ_0 of carriers, entering the expression for the performance coefficient

$$ZT \sim \beta = \frac{2(2\pi)^{3/2}}{h^3 e} k_0^{7/2} \left(\frac{m}{m_0}\right)^{3/2} \mu_0 T^{5/2} \kappa_L^{-1}, \qquad (1)$$

were derived for the p-$Bi_{2-x}Sb_xTe_{3-y}Se_y$ solid solutions from the temperature dependences of the Seebeck coefficient α and electrical conductivity σ using the technique described in [16], with due account of r_{eff}, in accordance with the relations for the carrier concentration and mobility applicable to semiconductors in the extrinsic-conductivity region.

The carrier concentration in the p-$Bi_{2-x}Sb_xTe_{3-y}Se_y$ solid solutions was derived from the $\alpha(p)$ relation, which, in turn, was extracted from studies of galvanomagnetic effects in weak magnetic fields [9] (Fig. 3).

Figure 4 gives the dependence of the effective mass m/m_0 on temperature and carrier concentration in the form of a three-dimensional surface. We see that the effective mass m/m_0 increases with temperature and

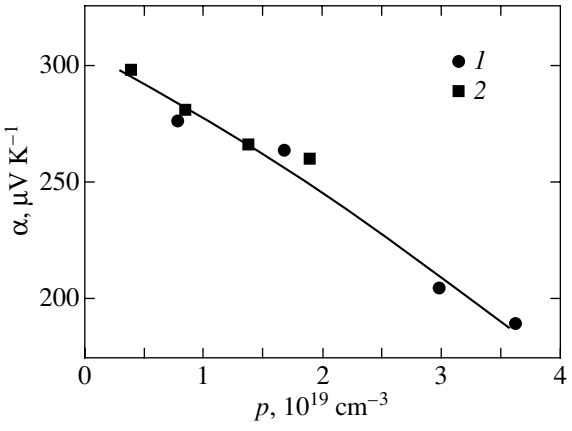

Fig. 3. Concentration dependences of the Seebeck coefficient α in solid solutions (*1*) p-$Bi_{2-x}Sb_xTe_{3-y}Se_y$ ($x \le 1.2$, $y \le 0.09$) [9] and (*2*) n-$Bi_{2-x}Sb_xTe_{3-y}Se_y$ ($x = 0.4$, $y = 0.6$) [10, 11] obtained at 300 K.

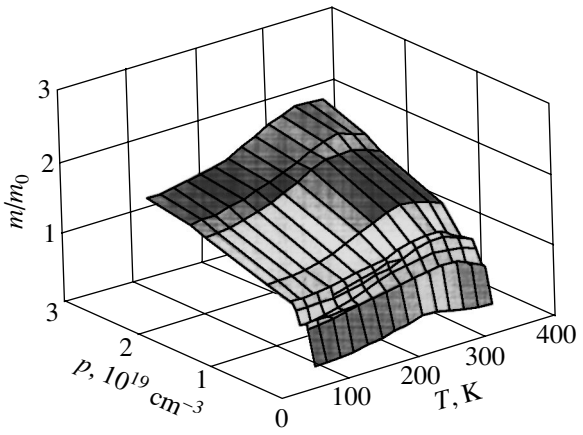

Fig. 4. Effective density-of-states mass m/m_0 plotted vs. temperature and carrier concentration in p-$Bi_{2-x}Sb_xTe_{3-y}Se_y$ solid solutions for x = 1–1.5 and y = 0.06–0.09.

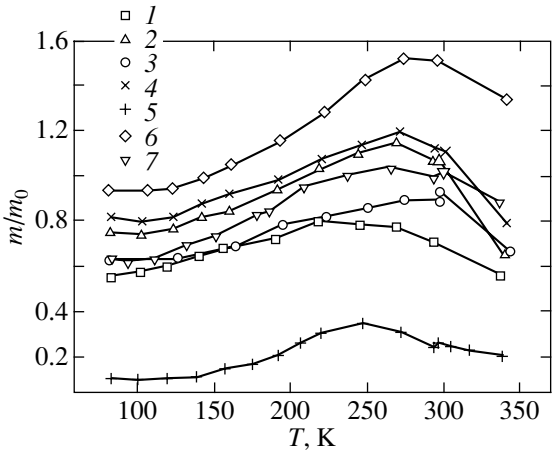

Fig. 5. Temperature dependences of the effective density-of-states mass m/m_0 in p-$Bi_{2-x}Sb_xTe_{3-y}Se_y$ solid solutions. (*1*) $x = 1$, $y = 0.06$; (*2*) $x = 1.1$, $y = 0.06$; (*3*) $x = 1.2$, $y = 0.06$; (*4*) $x = 1.2$, $y = 0.09$; (*5*) $x = 1.3$, $y = 0.09$; (*6*) $x = 1.3$, $y = 0.07$; and (*7*) $x = 1.5$, $y = 0.09$.

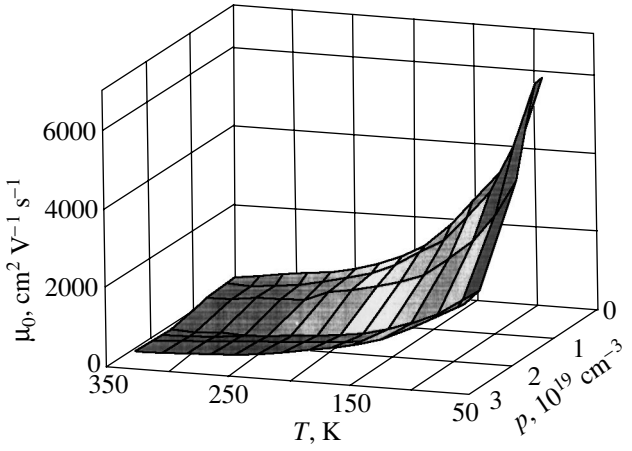

Fig. 6. Mobility μ_0 plotted vs. temperature and carrier concentration in p-$Bi_{2-x}Sb_xTe_{3-y}Se_y$ solid solutions for $x = 1.3$ and $y = 0.06$–0.09.

carrier concentration for all compositions, thus demonstrating the valence band nonparabolicity of the p-$Bi_{2-x}Sb_xTe_{3-y}Se_y$ solid solutions. As in n-$Bi_2Te_{3-y}Se_y$ [16], the dependence of m/m_0 on T in p-$Bi_{2-x}Sb_xTe_{3-y}Se_y$ cannot be described by a power-law function m^s [8] within a broad temperature interval, because the value of s varies with temperature (see table).

Within the interval 80–150 K, the effective mass m/m_0 depends only weakly on temperature. After that, the dependence of m/m_0 on T becomes steeper up to the temperatures at which intrinsic conduction sets in, as a result of which the effective mass decreases. The temperature at which m/m_0 starts to decrease is 200–220 K in samples with low carrier concentrations. This pattern of the m/m_0 dependence on T persists for all solid-solution compositions. As the carrier concentration in the solid solution increases, the maximum in this dependence shifts toward higher temperatures (Fig. 4).

Figure 5 displays temperature dependences of m/m_0 measured for carrier concentrations less than 1×10^{19} cm^{-3} on p-$Bi_{2-x}Sb_xTe_{3-y}Se_y$ samples of different composition. In the range 150–220 K, the slope $s_3 = d\ln(m/m_0)/d\ln T$ increases with increasing Sb content in the solid solution (see table). The growth of the coefficient s_3 was the largest for the compositions with $x = 1.3$ and 1.5 (see table and Fig. 5).

Note that the increase in the effective mass m/m_0 with the concentration increasing from 0.3×10^{19} to $(4–5) \times 10^{19}$ cm^{-3} can be attributed to the onset of filling of the additional valence band in the p-$Bi_{2-x}Sb_xTe_{3-y}Se_y$ solid solution (Figs. 4, 5). This growth of m/m_0 with carrier concentration is paralleled in Fig. 4 by a change in the slope of the $m/m_0(T, p)$ surface to the (T, p) plane.

The dependences of m/m_0 on temperature, composition, and carrier concentration in p-$Bi_{2-x}Sb_xTe_{3-y}Se_y$ can be explained as being due to changes in the shape parameters (u, v, w) of the constant-energy surface, which govern the ratios of the effective-mass tensor components (m_i/m_j). The variations in m/m_0 with T, p, and solid-solution composition also depend on the degeneracy parameter $\beta_d(r_{\text{eff}}, \eta)$, which determines scattering processes in the model assuming isotropic carrier scattering [17].

6. CARRIER MOBILITY

Figure 6 displays the behavior of the mobility μ_0 with temperature and concentration for a composition with $x = 1.3$ and $y = 0.06$–0.09. As the carrier concentration increases, the mobility decreases as the number of scattering centers increases. Analogous dependences of μ_0 on carrier concentration are observed for all the solid-solution compositions studied.

As is the case with the temperature dependence of the effective mass m/m_0, the dependences of μ_0 on T follow a power law $T^{s(T)}$ over various temperature intervals. The values of the slope of the μ_0 temperature dependence over the range 80–150 K ($|s_4| = d\ln\mu_0/d\ln T$) are less than those over the range 150–220 K, $|s_5|$, due to impurity scattering (see table).

A comparison of samples with different compositions and similar carrier concentrations reveals a decrease in the mobility and slope $|s_5| = d\ln\mu_0/d\ln T$ of the temperature dependence for $T > 150$ K with increasing Sb content in the solid solution as x varies from 1 to 1.5 (curves *1*, *3*, *7* in Fig. 7).

Variation in the Se content in the solid solution in the interval $y = 0.06$–0.09 does not affect the carrier mobility in samples with similar carrier concentrations. However, adding excess Se in amounts no greater than 0.5 wt % together with excess Te brings about a

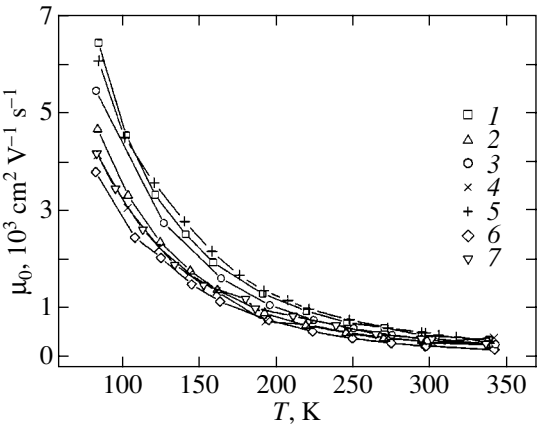

Fig. 7. Temperature dependences of the mobility μ_0 in p-$Bi_{2-x}Sb_xTe_{3-y}Se_y$ solid solutions. Curve notation is the same as in Fig. 5.

decrease in mobility μ_0 due to the additional scattering on Se atoms (see curve *5* in Fig. 7, table).

The coefficient $|s_5| = d\ln\mu_0/d\ln T$, as well as $s_3 = d\ln(m/m_0)/d\ln T$, increases with Sb content in the solid solution in the range 150–220 K (see table). The growth of the coefficient $|s_5|$ was the largest in the $x = 1.3$ composition. Such changes in the slopes of the temperature dependences of m/m_0 and μ_0 favor growth of the effective mass and mobility of carriers in the $x = 1.3$ composition as compared to those for $x < 1.3$.

Studies of the thermal conductivity of the solid solution compositions under consideration [4] showed that the total thermal conductivity κ and, hence, the lattice thermal conductivity κ_L decrease as compared with those in p-$Bi_{2-x}Sb_xTe_3$ (for $x = 1.5$), where there is no substitution on the Te sublattice. Therefore, if we take into account the weak changes in the lattice thermal conductivity κ_L with solid solution composition, the observed increase in the effective mass and mobility in the $x = 1.3$ composition brings about an increase in thermoelectric efficiency Z in the temperature interval 150–220 K.

At low temperatures ($T < 150$ K), one may expect an increase in Z in solid solutions with a lower Sb content ($x = 1.2$), because for this composition the effective mass and mobility for $T < 150$ K are higher in samples with low carrier concentrations, at which the additional valence band starts to fill (curves *3* in Figs. 5, 7).

Thus, our studies have identified the specific features of the temperature dependences of the effective mass m/m_0 and mobility μ_0 that favor an increase in thermoelectric efficiency in p-$Bi_{2-x}Sb_xTe_{3-y}Se_y$ solid solutions under substitution on both sublattices of Bi_2Te_3.

ACKNOWLEDGMENTS

This study was supported by the Russian Foundation for Basic Research, project no. 03-02-17605a.

REFERENCES

1. E. Müller and H. Süßmann, in *Proceedings of the XVII International Conference on Thermoelectrics* (Nagoya, Japan, 1998), p. 85.
2. A. I. Anukhin, S. Ya. Skipidarov, and O. B. Sokolov, in *Proceedings of the XII International Conference on Thermoelectrics* (Yokogama, Japan, 1993), p. 97.
3. M. N. Ettenberg, W. A. Jesser, and F. D. Rosi, in *Proceedings of the XV International Conference on Thermoelectrics* (Passadena, CA, 1996), p. 52.
4. V. A. Kutasov, P. P. Konstantinov, and L. N. Luk'yanova, in *Proceedings of V International Seminar on Thermoelectrics and Their Applications* (St. Petersburg, 1997), p. 14.
5. H. Kohler and A. Freudenberger, Phys. Status Solidi B **84**, 195 (1977); V. A. Kulbachinskii, M. Inoue, M. Sasaki, H. Negishi, W. X. Gao, K. Takase, J. Giman, P. Lostak, and J. Horak, Phys. Rev. B **50** (23), 16921 (1994).
6. V. A. Kulbachinskii, Z. M. Dashevskii, M. Inoue, M. Sasaki, H. Negishi, W. X. Gao, P. Lostak, and J. Horak, Phys. Rev. B **52** (15), 10915 (1995).
7. G. Simon and W. Eichler, Phys. Status Solidi B **107**, 201 (1981).
8. B. M. Gol'tsman, V. A. Kudinov, and I. A. Smirnov, *Semiconducting Thermoelectric Materials Based on Bi_2Te_3* (Nauka, Moscow, 1972) [in Russian].
9. L. N. Luk'yanova, V. A. Kutasov, V. V. Popov, and P. P. Konstantinov, Fiz. Tverd. Tela (St. Petersburg) **46** (8), 1366 (2004) [Phys. Solid State **46**, 1404 (2004)].
10. V. A. Kutasov and L. N. Luk'yanova, Fiz. Tverd. Tela (Leningrad) **26** (8), 2501 (1984) [Sov. Phys. Solid State **26**, 1515 (1984)].
11. V. A. Kutasov and L. N. Luk'yanova, Fiz. Tverd. Tela (Leningrad) **28** (3), 899 (1986) [Sov. Phys. Solid State **28**, 502 (1986)].
12. H. Kaibe, M. Sakata, I. J. Ohsugi, and I. Nishida, in *Proceedings of the VIII International Conference on Thermoelectrics* (Nancy, France, 1989), p. 195.
13. C. H. Champness and A. L. Kipling, J. Phys. Chem. Solids **27**, 1409 (1966).
14. K. S. Luzgin, V. A. Kutasov, and L. N. Luk'yanova, in *Proceedings of VIII International Seminar on Thermoelectrics and Their Applications* (St. Petersburg, 2002), p. 275.
15. R. R. Shvangiradze and E. P. Sabo, Neorg. Mater. **36** (11), 1316 (2000).
16. V. A. Kutasov, L. N. Luk'yanova, and P. P. Konstantinov, Fiz. Tverd. Tela (St. Petersburg) **42** (11), 1985 (2000) [Phys. Solid State **42**, 2039 (2000)].
17. V. A. Kutasov, L. N. Luk'yanova, and P. P. Konstantinov, Fiz. Tverd. Tela (St. Petersburg) **41** (2), 187 (1999) [Phys. Solid State **41**, 164 (1999)].

Translated by G. Skrebtsov

Physics of the Solid State, Vol. 47, No. 2, 2005, pp. 238–242. Translated from Fizika Tverdogo Tela, Vol. 47, No. 2, 2005, pp. 229–232.

SEMICONDUCTORS AND DIELECTRICS

Mechanoelectric Effect in Solid Electrolytes

V. I. Barbashov and Yu. A. Komysa

Donetsk Physicotechnical Institute, National Academy of Sciences of Ukraine, Donetsk, 83114 Ukraine

e-mail: yurkom@inbox.ru

Received March 5, 2004; in final form, May 27, 2004

Abstract—The mechanoelectric effect in solid electrolytes of the compositions ZrO_2 + 8 mol % Sc_2O_3 and ZrO_2 + 8 mol % Y_2O_3 is investigated experimentally. The mechanical properties of polycrystalline specimens are studied using four-point bending in air. It is shown that a negative charge is induced on the extended side of the bent specimen and that the magnitude of this charge depends on the external mechanical load and the temperature of measurement. The assumption is made that the observed phenomena are associated with the uphill diffusion of vacancies in response to a nonuniform field of mechanical stresses. The theoretical model is compared with the experimental results. © *2005 Pleiades Publishing, Inc.*

1. INTRODUCTION

The prospects for wide use of solid electrolytes in thermoelectric energy converters have given a powerful impetus to investigations into the physical properties of these materials over the two past decades [1–4]. There have appeared a large number of works concerned with the design of functional ceramic materials intended for use in fuel cells characterized by a high electrical conductivity and based on zirconia and ceria doped with different oxides [5]. The particular emphasis placed on the materials-science aspects of research into solid electrolytes has left aside the problem regarding the interrelation between the mechanical and electrical properties of these materials. Among the earlier studies devoted to the mechanoelectric effect in metal oxides, special mention should be made of the work performed by Obrosov and Koksharov [6], who noted, however, that their own results obtained for these materials are rather contradictory.

The effect of mechanical loading on the electrical properties of nonoxide solid electrolytes, so-called superionics (such as RbI, Na_4RbI_5, β-Al_2O_3, etc.), has been investigated in a number of works [7–11]. In particular, it has been found that Na_4RbI_5 polycrystals subjected to concentrated or distributed loading exhibit direct and inverse baroelectric effects [7–11]. It should be noted that the materials used in those experiments differed in the mechanism of electrical conduction from the zirconia-based polycrystals studied in the present work; moreover, mechanical testing of these materials was performed using nonstandard methods. Still earlier, Hull [12] carried out bending tests of RbI specimens and observed induced electric charges on the bent surfaces of the specimens.

Apart from the aforementioned baroelectric effect, the best known mechanoelectric phenomenon exhibited by solids is the piezoelectric effect. The piezoelectric effect is associated with the appearance of a charge anisotropy in unit cells under mechanical loading of the specimen due to collective displacements of atoms in the crystal lattice. The high electrical resistivity of piezoelectric materials, which, as a rule, are dielectrics, limits the range of their applications in electric current generators.

In this work, we analyzed the possibility of inducing an electric charge in solid electrolytes due to variations in the diffusion motion of positively charged vacancies under inhomogeneous mechanical stresses. The experiments were based on a well-known physical phenomenon, namely, the uphill diffusion of point defects in a nonuniform field of external stresses.

2. UPHILL DIFFUSION IN SOLIDS

The uphill diffusion or the Gorsky effect [13] was predicted in 1935. In essence, this phenomenon is as follows. In a nonuniform field of mechanical stresses, for example, upon bending of a crystal that is a substitutional solid solution, the impurity ions involved in the crystal structure experience a force proportional to the difference between the volume of an impurity atom and the volume of a lattice atom. In this situation, atoms with a larger ionic radius move into an extended region of the crystal, whereas atoms with a smaller ionic radius migrate into a compressed region of the crystal. This effect is reversible; i.e., the concentrations of point defects level off over the specimen after removal of the external load. Subsequently, Kosevich [14] showed that, in a nonuniform field of external stresses, intrinsic defects (such as vacancies and interstitial atoms) of the crystal can also come into effect and the forces acting on these defects can be written in the form

$$\mathbf{f}_v = \Omega_0 \nabla P, \quad \mathbf{f}_i = -\Omega_0 \nabla P. \tag{1}$$

Here, Ω_0 is the volume of the point defect and ∇P is the pressure gradient.

For four-point bending, the pressure gradient in the region of the specimen between the interior load applicators is given by the formula $\nabla P = 2\sigma/h$ (where σ is the normal stress on the surface of the specimen and h is the thickness of the specimen). Under an external load, the increment of the vacancy concentration on a compressed surface of the specimen with respect to the equilibrium concentration c_v can be represented in the form

$$\delta c_v = \frac{\Omega_0 \sigma}{kT} c_v. \tag{2}$$

Likewise, the decrement of the vacancy concentration on an extended surface of the specimen is described by the same expression. The interstitial atoms are characterized by an inverse effect as compared to the vacancies.

It is reasonable to assume that, under conditions where the aforementioned point defects are electrically charged and there is no compensation for electric charge (for example, by conduction electrons in metals) in the system, electric charges can be induced on the solid surfaces subjected to opposite deformations. In this case, the electric charge induced in the system can be represented in the form

$$\delta q = ze \frac{\Omega_0 \sigma}{kT} c_v, \tag{3}$$

where z is the valence of point defects.

It follows from this relationship that the magnitude of the effect is directly proportional to the mechanical stress and the total vacancy concentration and is inversely proportional to the temperature of the experiments. Among the oxide ceramic materials known to date, the solid electrolytes based on stabilized zirconia satisfy the above conditions best of all. The specific features of the electrical properties of these materials most clearly manifest themselves in stabilized cubic zirconia [15–17]. The cubic phase of zirconia, which is unstable under normal conditions, can be stabilized by doping with bivalent or trivalent metal impurities that substitute for zirconium in the unit cell. Numerous investigations have established that stabilized zirconia in the form of a single crystal or a ceramic material possesses virtually ionic conduction (with respect to oxygen) even at a temperature of 600°C and that, at 1000°C, the electrical conductivity of stabilized zirconia becomes comparable to the conductivity of semiconductors, η = (0.1–0.01) Ω^{-1} m^{-1}. It should be emphasized that, at these temperatures, zirconia retains its high-strength properties. This makes it possible to use zirconia as a constructional or functional ceramic material over a wide range of practical applications (fuel cells, electrolyzers, analyzers, etc.).

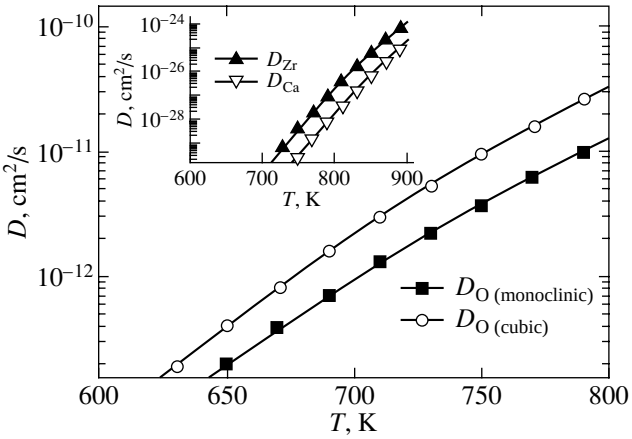

Fig. 1. Temperature dependences of the diffusion coefficients of oxygen, calcium, and zirconium ions in the CaO–ZrO_2 solid solution. The inset shows the temperature dependences of the self-diffusion coefficients of calcium and zirconium cations according to the data taken from [17].

The conducting properties of zirconia are determined by an anomalously high diffusion mobility of oxygen ions. As an illustration, Fig. 1 shows the temperature dependences of the diffusion coefficients of oxygen ions in monoclinic and cubic CaO–ZrO_2 solid solutions. The temperature dependences of the self-diffusion coefficients of calcium and zirconium cations, which were constructed according to the data taken from [17], are depicted in the inset to Fig. 1.

It can be seen from Fig. 1 that, in the temperature range under investigation, the diffusion coefficient of oxygen ions is more than ten orders of magnitude larger than the diffusion coefficients of zirconium ions and dopant cations. The same is also true for the ZrO_2–Y_2O_3 and ZrO_2–Sc_2O_3 systems.

3. OBJECTS OF INVESTIGATION AND EXPERIMENTAL TECHNIQUE

Polycrystals of zirconia ZrO_2 doped with 8 mol % Y_2O_3 (stabilized zirconia) or with 8 mol % Sc_2O_3 (partially stabilized zirconia, which predominantly exists in the cubic phase) were chosen as the objects of our investigation. The choice of the ZrO_2–Sc_2O_3 compound was motivated by the fact that this partially stabilized zirconia exhibits an extremely high conductivity as compared to the other zirconia-based compounds. Specimens 2 × 15 × 40 mm in size were prepared by sintering a powder (grain size, 10–30 nm). The characteristic size of grains in the specimen fell in the range 0.2–0.5 μm. The density of the material was no lower than 5.7×10^3 kg/m^3, and the flexural strength of the

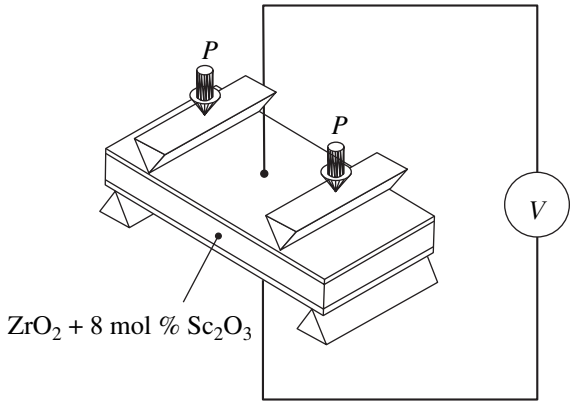

Fig. 2. Schematic diagram of the setup for testing of the mechanoelectric properties of specimens.

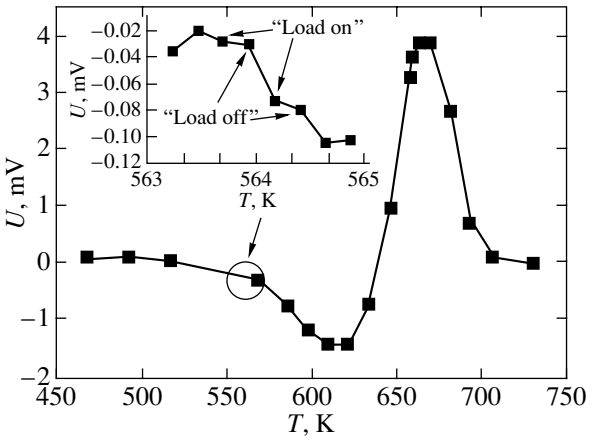

Fig. 3. Polarization curve of an unloaded specimen. The inset shows the electric response of the system to mechanical loading ("load on") and unloading ("load off").

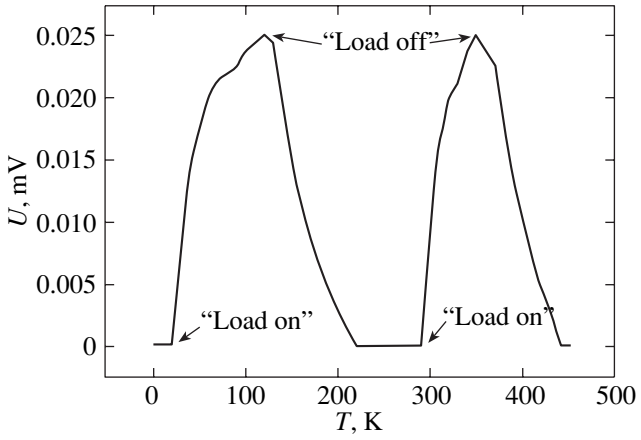

Fig. 4. Variation in the polarization potential across the specimen after mechanical loading ("load on") and unloading ("load off") at a temperature of 400°C.

specimen was no less than 300 MPa. After mechanical polishing, silver electrodes were fired into the largest opposite faces. The electrolytic cell thus fabricated was placed in a four-point bending apparatus positioned in a compact electric furnace. In the high-temperature zone of the furnace, a mechanical force was applied to the specimen with the use of a special rod from which a necessary weight was suspended. The temperature was controlled by a thermocouple located in the immediate vicinity of the specimen. The schematic diagram of the setup used for loading specimens is shown in Fig. 2. The potential across the specimen was written with a recorder operating in a time-base sweep mode.

4. RESULTS

The characteristic polarization curve of an unloaded specimen is depicted in Fig. 3. This curve shows the change in the potential across the electrodes of the electrolytic cell upon heating of the specimen at a rate of approximately 10 K/min in the absence of flexural stress. The application of flexural stress to the specimen (see inset to Fig. 3) at different temperatures (corresponding to different portions of the polarization curve) leads to an increase in the rate of change in the charge at the electrodes of the electrolytic cell. After removal of the flexural stress, the kinetic parameters of the specimen regain their initial values observed in the unloaded state. At temperatures of approximately 600°C and above, the time of change in the potential across the electrodes under mechanical loading is smaller than the RC time constant, which results in a considerable damping of the signal. This effect is most likely associated with the high diffusion mobility of oxygen ions and oxygen vacancies. Moreover, since the experiments were performed in air, the high mobility of oxygen ions "shunted" the mechanoelectric effect.

In addition to the qualitative experiments, which demonstrated the electric response of the solid electrolyte to inhomogeneous mechanical stresses, we carried out quantitative measurements at a constant temperature. The variation in the potential across the electrodes of the electrolytic cell after loading of the specimen at $\sigma = 50$ MPa and after its unloading at a temperature of 400°C is shown in Fig. 4. The change in the potential ΔU across the electrodes of the specimen lies in the range 0.025–0.030 mV. The sign of the effect (i.e., "minus" on the extended surface of the specimen and "plus" on the compressed surface) indicates that negative (oxygen) ions move toward the extended surface of the specimen, whereas positively charged vacancies move toward the compressed surface of the specimen. Since plastic deformation can occur through different diffusion mechanisms, it should be particularly emphasized that the observed effect is reversible and inconsistent with the plastic deformation of the specimen. The

above circumstances give grounds to believe that this effect is caused by the uphill diffusion of vacancies toward the compressed surface of the specimen, which, in turn, is accompanied by a reverse flow of oxygen ions carrying a negative charge.

5. DISCUSSION

As was noted above, the high conductivity (with respect to oxygen) observed in stabilized zirconia ceramic materials in the temperature range 600–1200°C (Fig. 1) is caused by the presence of oxygen vacancies in the crystal lattice at a concentration that is substantially higher than their equilibrium concentration in the undoped material (the equilibrium concentration at a temperature of 1200°C and at atmospheric pressure is equal to 10^{-8} [17]). The high concentration of nonequilibrium vacancies is observed under the electroneutrality condition upon doping of zirconia with bivalent or trivalent cations. In the majority of cases, charge transfer in stabilized zirconia has been simulated in the framework of the cluster model proposed by Solier *et al.* [18] and the model of a "vacancy–impurity atom" complex put forward by Bogicevic *et al.* [19]. In both models, the mechanism of electrical conduction is described by a two-step process: the formation of an active vacancy (decomposition of a complex) and its subsequent migration over the crystal bulk in a gradient field of mechanical stresses or voltages (in this case, oxygen ions move in the opposite direction). According to the results obtained by Zavodinsky [20], the activation energies for zirconia containing 12.5 mol % Y_2O_3 are estimated as $E_a \sim 0.6$ eV and $E_m \sim 0.7$ eV.

One of the purposes of this work was to determine the possible difference in the magnitudes of the mechanoelectric effect observed in polycrystals of the ZrO_2–Y_2O_3 (8 mol %) and ZrO_2–Sc_2O_3 (8 mol %) solid solutions. This assumption is based on the mechanism of stabilization of the high-temperature cubic zirconia phase, according to which the stabilization occurs through the replacement of zirconium atoms by impurity atoms with a larger ionic radius ($r_{Zr^{4+}} = 0.82$ Å, $r_{Y^{3+}} = 0.97$ Å, $r_{Sc^{3+}} = 0.83$ Å [21]). This process can be considered to be similar to that proceeding in the material at high pressures or temperatures. Consequently, the energy of the crystal lattice in the vicinity of impurity ions should increase under induced local stresses. The stabilization of the cubic phase requires a smaller amount of doping impurities with a larger ionic radius (Y^{3+}), all other factors being equal. Another important property of these materials is that the cubic zirconia stabilized by doping impurities with a smaller ionic radius (Sc^{3+}) should exhibit a higher sensitivity to external actions. This circumstance allowed us to assume that the magnitude of the mechanoelectric effect in polycrystals of the ZrO_2–Sc_2O_3 (8 mol %) compound should be larger than that of the mechanoelectric effect in polycrystals of the ZrO_2–Y_2O_3 (8 mol %) compound. However, the measured magnitudes of the mechanoelectric effect in both compounds turned out to be virtually identical to within the experimental error of the measurement. Most likely, this can be associated with the fact that the observed mechanoelectric effect is very small in magnitude.

The uphill diffusion effect can be quantitatively estimated from relationship (1) under the assumption that the elastic and electric forces acting on a vacancy at equilibrium are equal to each other ($2eU/h = 2\Omega_0\sigma/h$). The calculated elastic force is greater than the Coulomb force by a factor of approximately 5. This discrepancy can be caused by the "shunting" effect of oxygen ions (penetrating into the specimen from the atmosphere) and the passage of leakage currents in measuring circuits. It can be expected that the performance of similar experiments under vacuum or in an oxygen-free atmosphere will lead to better agreement between the theoretical and experimental data. In conclusion, we note that the uphill diffusion effect can be used to investigate the kinetic properties of ions in a gradient field of mechanical stresses.

ACKNOWLEDGMENTS

We would like to thank G.Ya. Akimov, V.M. Timchenko, and É.V. Chaĭka for supplying the specimens used in our experiments and for their participation in discussions of the results and helpful remarks.

REFERENCES

1. M. Feng and J. B. Goodenout, J. Solid State Inorg. Chem. **31**, 663 (1994).
2. T. Ishihara, Solid State Ionics **86–88**, 197 (1996).
3. J. A. Kilner, Solid State Ionics **129** (1–4), 13 (2000).
4. W. G. Coors and D. W. Ready, J. Am. Ceram. Soc. **85**, 2637 (2002).
5. S. M. Haile, Mater. Today **6** (3), 24 (2003).
6. V. P. Obrosov and V. D. Koksharov, Élektrokhimiya **12** (5), 673 (1976).
7. Yu. M. Gerbshteĭn, E. I. Nikulin, and F. A. Chudnovskiĭ, Fiz. Tverd. Tela (Leningrad) **25** (4), 1148 (1983) [Sov. Phys. Solid State **25**, 659 (1983)].
8. Yu. M. Gerbshteĭn and S. E. Nikitin, Fiz. Tverd. Tela (Leningrad) **30** (1), 210 (1988) [Sov. Phys. Solid State **30**, 117 (1988)].
9. M. P. Brennan, Electrochim. Acta **25** (4), 621 (1980).
10. A. V. Virkar, G. R. Miller, and R. S. Gardon, Electrochim. Acta **26** (6), 1023 (1981).

11. M. E. Kompan, V. P. Kuznetsov, V. V. Rozanov, and A. V. Yakubovich, Fiz. Tverd. Tela (St. Petersburg) **46** (2), 1078 (2004) [Phys. Solid State **46**, 1110 (2004)].

12. M. N. Hull, Energy Convers. **10** (2), 215 (1970).

13. W. S. Gorsky, Phys. Z. Sowjetunion **8**, 443 (1935).

14. A. M. Kosevich, Usp. Fiz. Nauk **114** (3), 509 (1974) [Sov. Phys. Usp. **17**, 920 (1975)].

15. V. N. Chebotin and M. V. Perfil'ev, *Electrochemistry of Solid Electrolytes* (Khimiya, Moscow, 1978) [in Russian].

16. D. S. Rutman, Yu. S. Toropov, S. Yu. Pliner, and Yu. M. Neĭumin, *Highly Refractory Materials from Zirconium Dioxide* (Metallurgiya, Moscow, 1985) [in Russian].

17. P. Kofstad, *Nonstoichiometry, Diffusion, and Electrical Conductivity in Binary Metal Oxides* (Wiley, New York, 1972; Mir, Moscow, 1975).

18. J. D. Solier, I. Cachadina, and A. Dominquez-Rodriguez, Phys. Rev. B **48**, 3704 (1993).

19. A. Bogicevic, C. Wolverton, G. M. Crosbie, and F. B. Stechel, Phys. Rev. B **64**, 14106 (2001).

20. V. G. Zavodinsky, Fiz. Tverd. Tela (St. Petersburg) **46** (3), 441 (2004) [Phys. Solid State **46**, 453 (2004)].

21. *Modern Crystallography*, Vol. 2: *Structure of Crystals*, Ed. by B. K. Vaĭnshteĭn, V. M. Fridkin, and V. L. Indenbom (Nauka, Moscow, 1979; Springer, Berlin, 1982).

Translated by O. Borovik-Romanova

Physics of the Solid State, Vol. 47, No. 2, 2005, pp. 243–245. Translated from Fizika Tverdogo Tela, Vol. 47, No. 2, 2005, pp. 233–235.

DEFECTS, DISLOCATIONS, AND PHYSICS OF STRENGTH

Photoionization Spectrum of 1.2–2.2-eV Electronic States Created by Plastic Deformation in γ-Irradiated NaCl Crystals

E. V. Korovkin

Institute of Solid State Physics, Russian Academy of Sciences, Chernogolovka, Moscow oblast, 142432 Russia
e-mail: Korovkin@issp.ac.ru

Received February 2, 2004; in final form, June 22, 2004

Abstract—The kinetics of light-induced depletion of electronic states created by plastic deformation in γ-irradiated NaCl crystals was studied experimentally, which permitted reconstruction of the photoionization spectrum of these states in the range 1.2–2.2 eV. Additional arguments are presented in support of this spectrum deriving from photoexcitation of electrons from the dislocation band. It is shown that, in this case, the spectrum thus obtained is not admixed with the photoionization spectrum of dislocation-related point defects. © *2005 Pleiades Publishing, Inc.*

1. It was found in [1, 2] that plastic deformation of γ-irradiated NaCl crystals brings about the formation of a broad band starting at a photon energy $E = 0.64$ eV and extending up to at least 2.1 eV in the IR photoionization spectrum stimulated by a preliminary *F*-light pulse. We succeeded in isolating this band from a sum of spectra by means of a special, fairly sophisticated procedure [2] and measured the spectrum of this band in the range 0.64–1.2 eV. Extending similar measurements to higher energies was impossible at that time because of the fast drop in equipment sensitivity in this region. However, since the photoionization signal at $E = 0.74$ eV belongs almost entirely to this band, we attempted to establish its short-wavelength edge [2]. To do this, following the standard procedure [1, 2] intended to fill the electronic states producing this broad spectrum and developed for $T = 110$–120 K, the sample was subjected to additional monochromatic treatment (AMT) with a light pulse of variable duration and photon energy E (1.2 to 2.1 eV). The photoconductivity generated by 0.74-eV photons was then measured, and its intensity was used to judge the efficiency of depletion of the states under study by the AMT. It was found that the depletion was efficient irrespective of the wavelength in this range. Thus, this band was established to extend at least up to 2.1 eV. The dependence of the photoconductivity signal (and, hence, of the density of these states) on the AMT duration was an exponential function, with its asymptotic value depending on the wavelength (larger asymptotic values usually correspond to longer wavelengths). This feature can be due to the two ways in which the AMT light acts. On the one hand, being in the region of sensitivity of the states of interest to us, it depletes them, while on the other hand, by exciting the *F* and other color centers donating electrons to the conduction band, it fills them again, and this accounts for the establishment of a constant level depending on the AMT wavelength. It immediately follows that, by studying the time dependence of the characteristics measured at different AMT wavelengths, one can reconstruct the photoionization spectrum of these states, and this is what motivated the present investigation.

2. The electronic density of states n can be written as

$$dn/dt = -nAf(E)I(E) + BF(E)I(E), \qquad (1)$$

where t is the time, $f(E)$ is the photoionization spectrum of these states, $I(E)$ is the AMT light intensity, $F(E)$ is the spectrum of the color centers acting as electron sources, and A and B are constants including all coefficients independent of E and n. In other words, we can get by with only one variable, because the variation in the *F*-center concentration over such short times (no longer than 30 s) can be safely neglected. Equation (1) can be solved to yield

$$n = (C - D)\exp(-t/\tau) + D, \qquad (2)$$

where $C = n(t = 0)$ and $D = n(t \longrightarrow \infty)$. Thus, we have

$$f(E) \sim 1/\tau(E)I(E) \qquad (3)$$

and $D(E) \longrightarrow F(E)/f(E)$. We see that, if $f(E)$ is a fairly smooth function in the region of interest, then $D \sim F(E)$ and will grow with E by reflecting the growth of $F(E)$ as one approaches the maximum in the *F* band, in full agreement with experiment (see table, column 4).

The experiment was conducted at 113 K on NaCl single crystals that were γ-irradiated to a dose of 10^7 rad and subsequently compressed at a strain rate of 1.8×10^{-5} s^{-1} to a strain of 12–13%. The experimental technique employed is described in detail in [2]. The AMT light was produced by an SI-8 tungsten lamp equipped with a set of color filters. The same lamp, but with different color filters, served to excite the *F* centers. Due to frequent filter replacement, special measures were required to preclude the scattering of light intensity.

1063-7834/05/4702-0243$26.00

Dependences of the following quantities on AMT photon energy E: coefficient k related to AMT light intensity; ratio Δ of the rms deviation of experimental points from the fitting curve to the initial amplitude of this curve; D/C; $\tau(E)$; and the reconstructed photoionization spectrum $f(E)$

E, eV	$k = 1/I(E)$, arb. units	Δ, %	D/C	$\tau(E)$, s	$f(E) \sim k/\tau$, arb. units
2.206	0.57	0.43	0.23	7.8	731
2.067	1.00	0.31	0.28	14.1	709
1.870	0.76	0.64	0.19	12.0	633
1.761	0.72	0.58	0.16	11.5	626
1.636	0.83	0.47	0.18	12.7	654
1.550	0.96	1.08	0.17	13.4	716
1.375	0.44	1.01	0.11	7.6	572
1.240	0.42	1.30	0.13	6.8	621

Figure 1 shows six of the eight measured photoconductivity signals initiated by 0.74-eV photons plotted versus AMT duration. By properly choosing the parameters C, D, and τ in Eq. (2) so as to obtain the best fit to experimental data (Fig. 1), $\tau(E)$ could be determined and, using the measured $I(E)$ dependence and Eq. (3), the $f(E)$ spectrum could be derived (see table). Figure 2 displays the photoionization spectrum of the states under study in the range 0.6–2.2 eV representing the data from [2] (0.6–1.2 eV) and the present results (1.24–2.2 eV). We see that the photoionization spectrum exhibits a steep rise (threshold) at $E \approx 0.65$ eV, which transforms rapidly into a smooth course (if we disregard oscillations related to the spectral structure) up to 2.2 eV, i.e., up to the edge of the range covered.

3. As follows from [1, 2], the states of interest to us here form under plastic deformation of a sample. It is known that deformation gives rise to the formation of dislocations, as well as intrinsic defects and their complexes. The intrinsic defects forming in NaCl crystals are known to be primarily vacancies. Chlorine vacancies and their complexes are capable of capturing electrons from the conduction band to form various color centers. The simplest of them, *F*, *F*', *M*, and *R* centers, are well known and can be identified with fairly deep states (2.7–1.2 eV below the conduction band bottom). More intricate complexes are shallower. Thus, if the states under study here derive from complexes of intrinsic defects, these complexes should be more intricate (in our case, the depth is less than 0.65 eV). The Coulomb interaction that binds a trapped electron to this complex, as well as the large size of the complex and its low energy depth (0.65 eV for a band gap of about 8 eV), should make the width of its photoionization spectrum finite, and the position of its maximum should not be more than two times the photoionization threshold [3]). In our case, the photoionization threshold is ≈0.65 eV and no maximum is observed even at 2 eV. This makes the formation of our states of complexes of intrinsic defects very improbable and leaves dislocations as a viable alternative (a dislocation electronic band). In these conditions, long vacancy chains, which may also form under plastic deformation, may be considered a specific case of dislocations (narrow dislocation loops).

It is common knowledge that dislocations can also produce defects capable of trapping electrons from both the conduction and the dislocation band. Photostoppers are an example of such defects [4]. In this case, photoexcitation of electrons from these defects into the conduction band will give rise to their capturing of

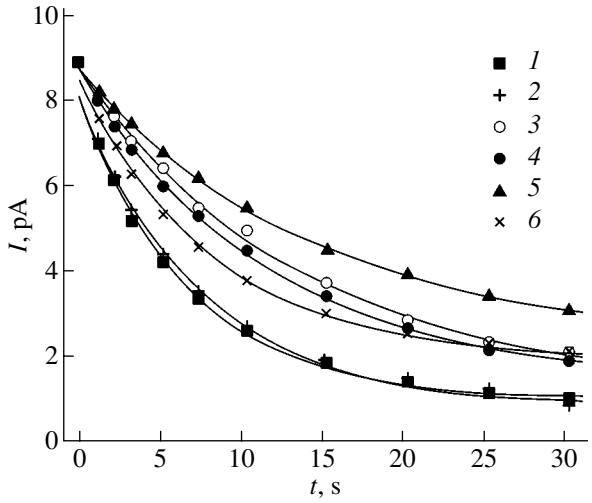

Fig. 1. Photoconductivity signal plotted vs. AMT duration for different AMT photon energies: (*1*) 1.240, (*2*) 1.375, (*3*) 1.550, (*4*) 1.761, (*5*) 2.067, and (*6*) 2.206 eV. Solid curves are best-fit exponential functions in Eq. (2).

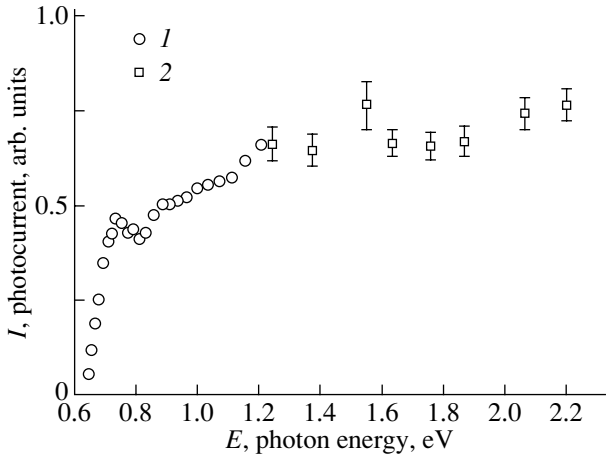

Fig. 2. Photoionization spectrum of the electronic states studied. (*1*) Data from [2] and (*2*) this study.

electrons from the dislocation band, thus reducing the dislocation electron concentration and the subsequent decrease in the photoionization signal produced by photons with $E = 0.74$ eV. A question naturally arises as to whether the photoionization spectrum of these defects may become admixed to the spectrum obtained by us (curve *2* in Fig. 2).

We assume that the capture of a dislocation electron by a depleted defect occurs instantaneously (in our case, the characteristic times of the exponential relation are of the order of 10 s, so any times from the pico- to millisecond scale can be considered instantaneous). Therefore, Eq. (1) should be complemented by the term $-z(E)I(E)G$, where $z(E)$ is the photoionization spectrum of these defects and G is a constant. No new variables are added, and Eq. (3) remains valid, because adding this term will not change $\tau(E)$ but rather reduce the limiting level D and, hence, increase the amplitude of the exponential function. If electron capture by defects is a slower process, the time dependences will be more complex than the ones described by Eq. (3). Because this relation is satisfied with a high accuracy in our case (see table, column 3), this process either produces a negligible contribution or is entirely absent. Hence, if photoionization of electrons from the dislocation band does occur, the spectrum obtained is not admixed with the spectrum due to dislocation-related point defects.

ACKNOWLEDGMENTS

This study was supported by the Russian Foundation for Basic Research, project no. 04-02-17140.

REFERENCES

1. E. V. Korovkin and T. A. Lebedkina, Fiz. Tverd. Tela (St. Petersburg) **44** (12), 2155 (2002) [Phys. Solid State **44**, 2257 (2002)].
2. E. V. Korovkin, Fiz. Tverd. Tela (St. Petersburg) **46** (6), 1013 (2004) [Phys. Solid State **46**, 1043 (2004)].
3. P. S. Kireev, *Physics of Semiconductors* (Vysshaya Shkola, Moscow, 1975), p. 528 [in Russian].
4. G. A. Ermakov, E. V. Korovkin, and Ya. M. Soĭfer, Fiz. Tverd. Tela (Leningrad) **16** (6), 1756 (1974) [Sov. Phys. Solid State **16**, 1139 (1974)].

Translated by G. Skrebtsov

Physics of the Solid State, Vol. 47, No. 2, 2005, pp. 246–251. Translated from Fizika Tverdogo Tela, Vol. 47, No. 2, 2005, pp. 236–241.

DEFECTS, DISLOCATIONS, AND PHYSICS OF STRENGTH

Analysis of Structural Factors That Control Necking during Tension of FCC Metals and Alloys

G. A. Malygin

Ioffe Physicotechnical Institute, Russian Academy of Sciences, Politekhnicheskaya ul. 26, St. Petersburg, 194021 Russia
e-mail: malygin.ga@mail.ioffe.ru

Received April 27, 2004

Abstract—The relation between the strength and ductility of structural materials is theoretically analyzed using stress–strain curves for a number of fcc metals and alloys. The theoretical analysis is based on the criterion of necking in a tensile specimen and on a stress–strain curve, which reflects the evolution of the dislocation density in a material with increasing strain and the effect of structural factors on this evolution. Theoretical relationships are obtained for the uniform strain and the ultimate tensile strength. The effects of the stacking-fault energy, the solid-solution hardening, and the grain size on these quantities are considered. © *2005 Pleiades Publishing, Inc.*

1. INTRODUCTION

An increase in the strength of structural materials is known to be accompanied by a decrease in their ductility. This rule is very important for practice but has not yet been explained with regard for all the factors (including structural factors) that affect the relation between the strength and ductility of a material. Usually, the strength and ductility characteristics of structural materials at low and moderate temperatures are considered to be the yield strength σ_y, the stress σ_u, and the strain ε_u of the onset of necking (necking strain) in a tensile specimen.

Numerous experiments show that, irrespective of the method of increasing the yield strength (solid-solution hardening [1, 2], precipitation hardening [3], grain refinement [4], or neutron irradiation [5]), the uniform strain ε_u decreases with increasing yield strength. Apart from these factors, the necking strain depends on temperature and (in fcc metals and alloys) on the stacking-fault energy [6], which determines the splitting of dislocations and their cross slip ability. Depending on these factors, the uniform strain can vary over wide limits, namely, from 50–100% to virtually zero, i.e., to the complete disappearance of material ductility or to its embrittlement (more specifically, to its quasi-embrittlement, since necking implies that fracture results from a strong localization of plastic deformation).

Although the effect of plastic instability and strain localization in the form of a neck has a macroscopic character and is controlled by the well-known criterion $d\sigma/d\varepsilon < \sigma$ (where σ is the stress and ε is the strain), the fulfillment of this criterion and the character of the relation between the strength and ductility depend on microscopic processes that determine the strain (dislocation) hardening of a material and the increase in dislocation density with strain. The rate of dislocation accumulation in a deformed material has been found to depend substantially on its structure, dislocation properties, and dislocation interaction. These factors specify the shape and character of stress–strain curves.

The effect of structural factors on stress–strain curves has been studied both experimentally and theoretically, which allows one to analyze the effect of the structure on the relation between the strength and ductility of a material from physical microscopic positions. In this work, we perform this analysis for fcc metals and alloys.

In Section 2, we use the criterion $d\sigma/d\varepsilon < \sigma$ and the dislocation-kinetics equations that include the effect of the structure on the character of stress–strain curves to obtain relationships for the uniform strain ε_u and the ultimate tensile strength σ_u. In the following sections, these relationships are used to analyze the effects of the stacking-fault energy (Section 3), solid-solution hardening (Section 4), and the grain size (Section 5) on the ultimate tensile strength and the necking strain for a number of fcc metals and alloys whose properties are available in the literature [1, 2, 4, 6]. The effect of radiation hardening and precipitation hardening on these parameters will be analyzed in a later paper.

2. STRESS–STRAIN CURVES AND THE PLASTIC-INSTABILITY CRITERION

As noted above, the criterion of the appearance of a plastic instability in the form of necking in a specimen subjected to uniaxial tension is

$$\frac{d\sigma}{d\varepsilon} \le \sigma. \qquad (1)$$

This criterion has a simple physical meaning: deformation becomes unstable when, due to a decrease in the

cross-sectional area of a tensile specimen, the strain hardening ceases to compensate for an increase in the stress. Since the stress σ and the strain-hardening coefficient $d\sigma/d\varepsilon$ depend on strain, there is a critical value of ε_u at which condition (1) begins to be satisfied. Stress–strain curves are often fitted by relations of the type $\sigma = \sigma_y + \chi\varepsilon^n$, where σ_y is the yield strength and χ is a parameter. In certain cases, these $\sigma(\varepsilon)$ dependences with $n = 0.5$–1.0 indeed describe the initial stage of the stress–strain curves of real materials; however, they cannot describe the third stage of these curves, namely, the stage of dynamic recovery. Since these dependences are phenomenological in character, one cannot estimate the effect of a certain structural factor on the critical strain ε_u and the ultimate tensile strength σ_u of a material. To this end, it is necessary to know the effect of the structural factor on the $\sigma(\varepsilon)$ curve of this material.

The strain (dislocation) hardening of a material is described by the well-known formula

$$\tau(\gamma) = \tau_c + \alpha\mu b\rho(\gamma)^{1/2}, \tag{2}$$

where α is the effective dislocation interaction constant, which depends on the dislocation distribution; μ is the shear modulus; b is the Burgers vector; and τ_c is the critical shear stress in the case where dislocations interact with structural defects. To find the $\tau(\gamma)$ and, hence, $\sigma(\varepsilon)$ dependences (where $\sigma = m\tau$ and $\varepsilon = \gamma/m$, with m being the Taylor factor for a polycrystal), we have to establish how the dislocation density ρ evolves with the shear strain γ. In the case of fcc metals and alloys at low and moderate temperatures, this evolution obeys the equation

$$\frac{d\rho}{d\gamma} = k_m + k_f\rho^{1/2} - k_a\rho \tag{3}$$

as has been demonstrated experimentally and theoretically many times [7–13]. The first term in the right-hand side of Eq. (3) is the rate of dislocation multiplication and accumulation when dislocations interact with obstacles of other than deformation origin ($k_m = 1/b\lambda_m$, where λ_m is the effective free path length of dislocations between these obstacles). The second term describes dislocation multiplication by forest dislocations ($bk_f \approx 10^{-2}$ is the coefficient determining the multiplication of dislocations that interact with forest dislocations). The third term is the annihilation rate of the screw sections of dislocation loops ($h_a = bk_a$ is the effective annihilation length for screw dislocations). The annihilation of screw dislocations is related to the appearance of the third stage (dynamic recovery) in the stress–strain curves of fcc metals. The structure-sensitive parameters in Eq. (3) that can affect the dislocation density in a material are the free path length of dislocations λ_m and the effective dislocation annihilation length h_a. Structural defects in a material (impurity atoms, dispersed particles, grain boundaries, radiation defects) decrease the free path length of dislocations and, thus, increase the rate of their accumulation in the material. In fcc metals, the effective length h_a and the annihilation coefficient k_a of screw dislocations depend on the stacking-fault energy [11].

Equation (3) can be integrated to find the $\rho(\gamma)$ dependence in an implicit form, which hinders analysis of the $\tau(\gamma)$ and $\sigma(\varepsilon)$ dependences for real materials in terms of criterion (1). Therefore, we consider two limiting cases, where the concentration of structural defects is low [in Eq. (3), the coefficient $k_m \ll k_f^2/4k_a$] or high. In the first case, we integrate Eq. (3) at $k_m = 0$ and substitute the result into Eq. (2). As a result, we have

$$\sigma(\varepsilon) = \sigma_y + \sigma_3\left[1 - \exp\left(-\frac{1}{2}mk_a\varepsilon\right)\right],$$
$$\sigma_3 = m\alpha\mu\left(\frac{bk_f}{k_a}\right). \tag{4}$$

In the second case, dislocation multiplication by obstacles of other than deformation origin dominates over dislocation multiplication by forest dislocations. Therefore, we obtain

$$\sigma(\varepsilon) = \sigma_y + \sigma_m[1 - \exp(-mk_a\varepsilon)]^{1/2},$$
$$\sigma_m = m\alpha\mu\left(\frac{b^2k_m}{k_a}\right)^{1/2}. \tag{5}$$

By substituting Eq. (4) into condition (1), we can find the dependences of the necking strain and the ultimate tensile strength on the yield strength σ_y and on the coefficients of Eq. (3):

$$\varepsilon_u = \frac{2}{mk_a}\ln\frac{1 + \frac{1}{2}mk_a}{1 + \frac{\sigma_y}{\sigma_3}}, \tag{6a}$$

$$\sigma_u = \frac{\frac{1}{2}mk_a}{1 + \frac{1}{2}mk_a}(\sigma_y + \sigma_3). \tag{6b}$$

Similarly, we can find the strain ε_u and the stress σ_u by substituting stress (5) into condition (1). For further analysis, we will mainly use Eqs. (6); therefore, for the sake of brevity, expressions for ε_u and σ_u in the case of stresses (5) are not given.

Figure 1 shows the stress–strain curves calculated from Eq. (4) at $mk_a = 10$ and various values of the yield strength (its relative magnitude σ_y/σ_3) in the σ/σ_3–ε coordinates. The dropping segments of the curves conventionally indicate the uniform strain ε_u calculated from Eq. (6a). It is seen that an increase in the yield strength causes the ultimate tensile strength σ_u to increase, according to Eq. (6b); however, the uniform strain is strongly decreased in this case. The cause of this behavior is clear: as the yield strength increases,

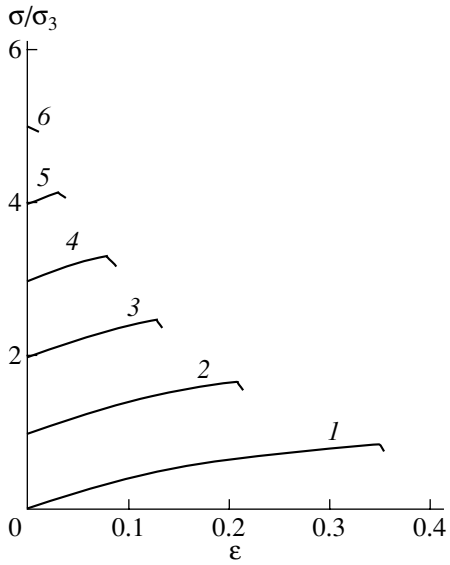

Fig. 1. Stress–strain curves calculated using Eq. (4) at mk_a = 10 and various values of the yield strength σ_y/σ_3:(*1*) 0, (*2*) 1, (*3*) 2, (*4*) 3, (*5*) 4, and (*6*) 5.

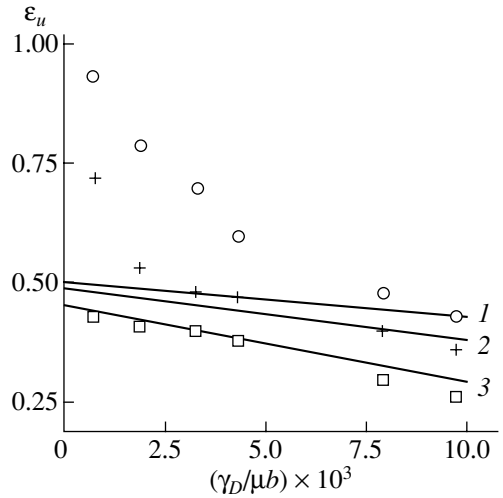

Fig. 2. Dependence of the uniform strain ε_u on the stacking-fault energy γ_D in Cu–Zn, Cu–Al, and Ni–Al alloys at (*1*) 77, (*2*) 150, and (*3*) 293 K [6]. Theoretical curves are calculated using Eqs. (7)–(10).

the right-hand side of condition (1) increases, whereas its left-hand side remains unchanged; therefore, as σ_y increases, condition (1) is satisfied at lower strains.

3. EFFECT OF DISLOCATION SPLITTING

As is seen from Eqs. (6), the uniform strain depends not only on the yield strength σ_y but also on the dislocation annihilation coefficient k_a. In the case of $\sigma_y \ll \sigma_3$, it follows from Eq. (6a) that the uniform strain is only determined by the annihilation coefficient:

$$\varepsilon_u = \frac{2}{mk_a}\ln\left(1 + \frac{1}{2}mk_a\right). \quad (7)$$

It follows from Eq. (7) that, as k_a increases, the strain ε_u decreases and, at $k_a \longrightarrow 0$ (i.e., in the absence of dynamic recovery), tends to the limiting value (unity), according to the law of strain hardening $\sigma \sim \varepsilon$ (4) without dislocation annihilation.

According to [14], the annihilation coefficient for screw dislocations is

$$k_a = \frac{\omega_s^{5/2}}{2\pi^2 p\alpha}\left(\frac{\mu}{\tau_a}\right), \quad (8)$$

where ω_s is the fraction of screw sections in growing dislocation loops, p is the number of operating slip systems, and τ_a is the friction stress that determines the critical distance of spontaneous annihilation of unlike screw dislocations. In the case of fcc metals and alloys, we have $\tau_a = \tau_{III} + \tau_f$, where $\tau_{III}(T, \gamma_D)$ is the stress corresponding to the onset of the third stage in the stress–strain curves of these materials, which depends on the temperature T and the stacking-fault energy γ_D [15], and $\tau_f(T, c)$ is the friction stress due to the interaction of dislocations with impurity atoms in a solid solution with concentration c. By substituting τ_{III} and τ_f into Eq. (8), we obtain the dependence of the annihilation coefficient on the temperature, strain rate $\dot{\gamma}$, dislocation splitting, and impurity concentration c:

$$k_a(T, \gamma_D, c) = \frac{\omega_s^{5/2}}{2\pi^2 p\alpha}\left(\frac{\mu}{\tau_{III}(T, \gamma_D) + \tau_f(T, c)}\right). \quad (9)$$

Here, according to [15],

$$\tau_{III} = \tau_{III}(0)\exp\left[-\left(1 + 180\frac{\gamma_D}{\mu b}\right)\frac{kT}{0.35\mu b^3}\ln\left(\frac{\dot{\gamma}_0}{\dot{\gamma}}\right)\right], \quad (10)$$

where $\tau_{III}(0)$ is the stress τ_{III} at $T = 0$, k is the Boltzmann constant, and $\dot{\gamma}_0$ is a preexponential factor.

In Fig. 2, experimental points show the dependence of the uniform tensile strain ε_u on the stacking-fault energy for alloys Cu–Zn (c_{Zn} = 0.03–0.25), Cu–Al (c_{Al} = 0.01–0.14), and Ni–Al (c_{Al} = 0.02–0.08) at three temperatures [6]; this energy varied from 3 to 180 mJ m^{-2} in these alloys [6, 16]. The experimental points below $\gamma_D/\mu b = 4 \times 10^{-3}$ belong to the Cu–Zn and Cu–Al alloys, and those above this value belong to the Ni–Al alloys. As can be seen, an increase in γ_D is accompanied by a decrease in the uniform strain. This result is consistent with Eqs. (7)–(10). Indeed, as follows from Eqs. (9) and (10), a decrease in the dislocation splitting causes an increase in the dislocation annihilation coefficient, which in turn decreases the strain ε_u [according to Eq. (7)].

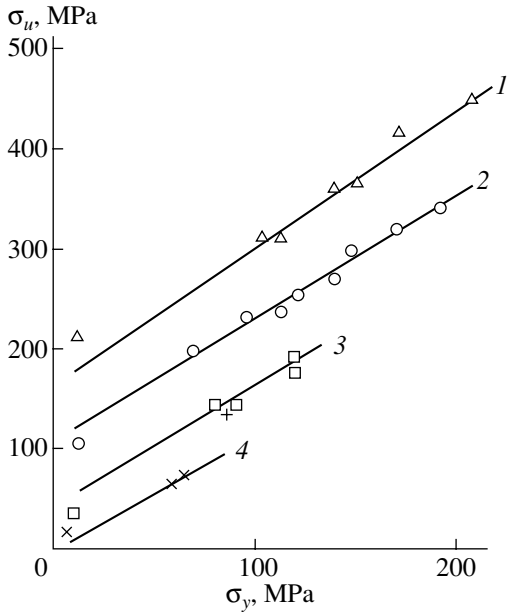

Fig. 3. Dependence of the ultimate tensile strength σ_u on the yield strength σ_y in Al–Mg alloys at (*1*) 77, (*2*) 195–373, (*3*) 473, and (*4*) 573 K [1, 2].

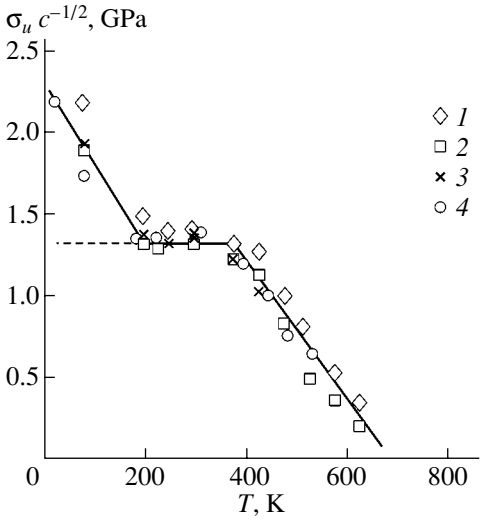

Fig. 4. Temperature dependence of the ultimate strengths of aluminum–magnesium alloys [1, 2] reduced to the same concentration of Mg atoms: (*1*) AMg2, (*2*) AMg3, (*3*) AMg5, and (*4*) AMg6.

The straight lines in Fig. 2 are plotted using Eqs. (7)–(10) with $\tau_f = 0$, $\omega_s = 0.5$, $\alpha = 0.5$, $p = 12$, $\ln(\dot{\gamma}/\dot{\gamma}_0) = 35$, $m = 3$, and the Ni parameters $\tau_{III}(0)/\mu = 10^{-3}$ [15] and $\mu b^3 = 10$ eV. As is seen, the calculated curves are in satisfactory agreement with the experimental data for the Ni–Al alloys at all temperatures and stacking-fault-energies. In the case of the Cu–Zn and Cu–Al alloys at temperatures below 293 K, there is a strong deviation from the calculated curves. Alloying in these alloys results not only in a decrease in energy γ_D but also in an increase in the yield strength ($\sigma_y \sim \tau_f \sim c^{1/2}$ [17]); therefore, the deviation from theory can be caused by an additional decrease in the annihilation coefficient due to dislocation hindering by impurity atoms [see Eqs. (7), (9)]. The friction stress τ_f increases strongly at temperatures below 293 K [17]. This circumstance can explain the fact that the deviation from theory occurs specifically at these temperatures (Fig. 2, curves *1*, *2*).

4. EFFECT OF ALLOYING

In the case where alloying does not affect the dislocation splitting, solid-solution hardening leads to a decrease in the uniform strain. This behavior is analyzed below using Al–Mg commercial alloys with a magnesium concentration of 2–6% (AMg2–AMg6 alloys [1, 2]). Figures 3–5 show the results of processing the experimental data obtained in [1, 2] for these alloys in order to find the dependences of their ultimate tensile strengths and uniform strains on the yield strength at various temperatures.

As is seen from Fig. 3, the dependences of σ_u on the yield strength σ_y at various temperatures in these alloys can be fitted by the straight lines

$$\sigma_u = \sigma_0(T) + A\sigma_y, \tag{11}$$

where $A \approx 1.25$ and $\sigma_0(T)$ is the ultimate strength at $\sigma_y = 0$ (i.e., the ultimate strength of pure aluminum). The left-hand extreme points in Fig. 2 show an ultimate strength of 99.995% Al (our data). We substitute k_a from Eq. (9) into Eq. (6b) by making allowance for the second relation in Eqs. (5) and for the fact that $\sigma_y = m\tau_y$

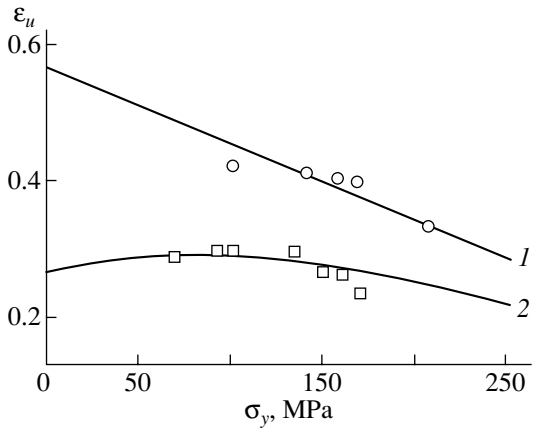

Fig. 5. Dependence of the uniform strain ε_u on yield strength σ_y in AMg2–AMg6 alloys at (*1*) 77 and (*2*) 293 K [1, 2]. Theoretical curves are calculated using Eq. (13).

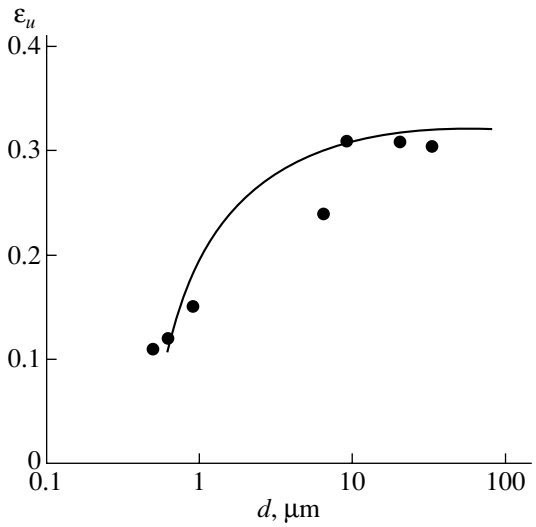

Fig. 6. Dependence of the uniform strain on the grain size in austenitic steel at 293 K [4]. The theoretical curve is calculated using Eq. (16).

(where $\tau_y \approx 3.5\tau_f$ [17]) and obtain the theoretical dependence of the ultimate strength on the yield strength:

$$\sigma_u = \frac{\frac{1}{2}mk_a}{1+\frac{1}{2}mk_a}\left[B\sigma_{\text{III}}(T) + \left(1+\frac{B}{3.5}\right)\sigma_y\right], \quad (12a)$$

where

$$B = 2\pi^2\alpha^2(bk_f)p/\omega_s^{5/2}, \quad \sigma_{\text{III}}(T) = m\tau_{\text{III}}(T). \quad (12b)$$

This dependence has the form of empirical relation (11). When the parameter mk_a varies from 6 to 30 [10], the expression outside the square brackets in Eq. (12a) varies over narrow limits (from 0.75 to 1); therefore, as a first approximation, it can be considered a constant. In this case, for the coefficient A and the stress $\sigma_0(T)$ in Eq. (11), we have the relations $A = 1 + B/3.5$ and $\sigma_0(T) = B\sigma_{\text{III}}(T)$. According to Eq. (12b), at $\omega_s = 0.5$, $\alpha = 0.5$, $p = 5$, and $bk_f = 10^{-2}$, we have $B = 1.4$; therefore, $A = 1.4$, which is close to the experimental value of this coefficient, 1.25.

It should be noted that the experimental points in Fig. 3 are concentrated near straight line *2* over a rather wide temperature range (200–400 K). As is shown by the data processed for the AMg2–AMg6 alloys (Fig. 4), the temperature dependences of the ultimate strength in this temperature range exhibit an athermal plateau. To the left of this plateau, the temperature dependence of σ_u is controlled by thermally activated dislocation motion through a system of fixed point obstacles—Mg atoms in a solid solution with an effective mean distance between solute atoms $l_{\text{Mg}} \sim c^{-1/2}$. This circumstance explains the fact that the experimental points for the Al–Mg alloys with different magnesium concentrations fall on one curve in the $\sigma_u c^{-1/2}$–T coordinates. In the range of the plateau, dynamic strain aging (the Portevin–Le Chatelier effect) takes place in the aluminum–magnesium alloys, which indicates a high mobility of magnesium atoms in the aluminum matrix in this temperature range. This high mobility is stimulated by deformation-induced nonequilibrium vacancies [18]. Above 400 K (which is $0.43T_m$, where T_m is the melting temperature), the concentration of equilibrium thermal vacancies becomes sufficient for magnesium atoms to exert progressively weaker resistance to dislocation motion in the Al–Mg solid solution due to their high diffusion mobility. As a result, the flow stress decreases strongly with increasing temperature. In this case, Eq. (12a) still holds true, as seen from Fig. 3 (curves *3*, *4*).

Figure 5 shows the dependence of the uniform strain on the yield strength in the alloys at 77 and 293 K. These curves are calculated from Eq. (6a) with σ_3 given by Eq. (4) and k_a given by Eq. (9) with allowance made for Eq. (10), the notation in Eq. (12b), and the corresponding numerical parameters. As a result, for ε_u we have

$$\varepsilon_u = \frac{2}{mk_a}\ln\frac{1+\frac{1}{2}mk_a}{1+\frac{3.5}{B}\left(\frac{\sigma_y}{\sigma_y+3.5\sigma_{\text{III}}(T)}\right)}. \quad (13)$$

As is seen from Fig. 5, the uniform necking strain increases with decreasing temperature and decreases with increasing yield strength. The decrease in this strain is not as strong and unambiguous as in the case shown in Fig. 1, since magnesium atoms in the solid solution hinder dislocation annihilation.

5. EFFECT OF GRAIN REFINEMENT

The authors of [4] found that, during tension of polycrystalline specimens with a grain size of less than 10 μm, the uniform strain decreases with decreasing grain size. Figure 6 shows the corresponding data for austenitic Fe–30% Ni–0.045% C steel having an fcc lattice [4]. For fine-grained specimens, the flow stress is seen to be described well by a quadratic rather than a linear [given by Eq. (2)] law of stress addition:

$$\sigma(\varepsilon) = \left[\sigma_y^2 + \sigma_3^2\left(1-\exp\left(-\frac{1}{2}mk_a\varepsilon\right)\right)^2\right]^{1/2}, \quad (14)$$

where $\sigma_y = K_y d^{-1/2}$ (according to the Hall–Petch relation), d is the grain size, and K_y is the Hall–Petch constant. Using criterion (1) and hardening law (14), the uniform strain can be expressed as

$$\varepsilon_u = \frac{2}{mk_a}\ln\frac{1+\frac{1}{2}mk_a}{1+\frac{1}{4}mk_a-\left[\left(\frac{1}{4}mk_a\right)^2-\left(1+\frac{1}{2}mk_a\right)\frac{\sigma_y^2}{\sigma_3^2}\right]^{1/2}}. \quad (15)$$

By substituting $\sigma_y = K_y d^{-1/2}$ into this expression, we find the dependence of the uniform strain on the grain size:

$$\varepsilon_u = \frac{2}{mk_a} \times \ln \frac{1 + \frac{1}{2}mk_a}{1 + \frac{1}{4}mk_a - \left[\left(\frac{1}{4}mk_a\right)^2 - \left(1 + \frac{1}{2}mk_a\right)k_a^2 \frac{d_3}{d}\right]^{1/2}}, \quad (16)$$

where

$$d_3 = \left(\frac{K_y}{m\alpha\mu(bk_f)}\right)^2.$$

In Fig. 6, the theoretical curve demonstrates the dependence of ε_u on d calculated from Eq. (16) at $k_a = 4$ and $d_3 = 0.056$ μm. This value of the parameter d_3 corresponds to reasonable values of the relevant parameters, namely, $K_y = 0.3$ m$^{1/2}$ MPa, $\alpha = 0.5$, $\mu = 83$ GPa, $bk_f = 10^{-2}$, and $m = 3$.

Thus, the stress–strain curves obtained using physical microscopic equations that describe the evolution of the dislocation density during deformation allow one to quantitatively analyze the effect of various structural factors on the relation between the strength and ductility of a material.

REFERENCES

1. S. I. Gudkov, *Mechanical Properties of Industrial Non-Ferrous Metals at Low Temperatures* (Metallurgiya, Moscow, 1971) [in Russian].
2. A. P. Smiryagin, N. A. Smiryagin, and A. V. Belova, *Industrial Non-Ferrous Metals and Alloys* (Metallurgiya, Moscow, 1974) [in Russian].
3. *Strengthening Methods in Crystals*, Ed. by R. B. Nicholson and A. Kelly (Wiley, New York, 1971).
4. B. Morrison and R. L. Miller, in *Ultra-Fine Grained Metals*, Ed. by J. Burke and V. Weiss (Syracuse Univ., Syracuse, New York, 1970; Metallurgiya, Moscow, 1973).
5. A. I. Ivanov and Yu. M. Platov, *Radiation Physics of Metals* (Nauka–Interperiodika, Moscow, 2002) [in Russian].
6. E. F. Dudarev, L. A. Kornienko, and G. P. Bakach, Izv. Vyssh. Uchebn. Zaved., Fiz. **34** (3), 35 (1991).
7. H. Mecking and U. F. Kocks, Acta Metall. **29** (11), 1865 (1981).
8. Yu. Estrin and H. Mecking, Acta Metall. **32** (1), 57 (1984).
9. G. A. Malygin, Fiz. Tverd. Tela (Leningrad) **29** (7), 2067 (1987) [Sov. Phys. Solid State **29**, 1189 (1987)].
10. G. A. Malygin, Phys. Status Solidi A **119** (2), 423 (1990).
11. G. A. Malygin, Usp. Fiz. Nauk **169** (9), 979 (1999) [Phys. Usp. **42**, 887 (1999)].
12. G. A. Malygin, Fiz. Tverd. Tela (St. Petersburg) **43**, 1832 (2001) [Phys. Solid State **43**, 1909 (2001)].
13. U. F. Kocks and H. Mecking, Prog. Mater. Sci. **48** (3), 171 (2003).
14. G. A. Malygin, Fiz. Tverd. Tela (St. Petersburg) **34** (9), 2882 (1992) [Sov. Phys. Solid State **34**, 1543 (1992)].
15. R. Berner and H. Kronmüller, *Plastische Verformung von Einkristallen* (Springer, Berlin, 1965; Mir, Moscow, 1969).
16. T. Steffens, C. Schwink, A. Korner, and H. Karnthaler, Philos. Mag. A **56** (2), 161 (1987).
17. E. F. Dudarev and L. A. Kornienko, Izv. Vyssh. Uchebn. Zaved., Fiz. **25** (8), 69 (1982).
18. G. A. Malygin, Fiz. Tverd. Tela (St. Petersburg) **34** (8), 2356 (1992) [Sov. Phys. Solid State **34**, 1262 (1992)].

Translated by K. Shakhlevich

Physics of the Solid State, Vol. 47, No. 2, 2005, pp. 252–262. Translated from Fizika Tverdogo Tela, Vol. 47, No. 2, 2005, pp. 242–251.

DEFECTS, DISLOCATIONS, AND PHYSICS OF STRENGTH

Structure and Properties of Ti–B–N, Ti–Cr–B–(N), and Cr–B–(N) Coatings Deposited by Magnetron Sputtering of Targets Prepared by Self-Propagating High-Temperature Synthesis

D. V. Shtansky*, F. V. Kiryukhantsev-Korneev*, A. N. Sheveiko*, I. A. Bashkova*, O. V. Malochkin*, E. A. Levashov*, N. B. D'yakonova, and I. V. Lyasotsky****

** Moscow State Institute of Steel and Alloys, Leninskiĭ pr. 4, Moscow, 119049 Russia*

e-mail: shtansky@shs.misis.ru

*** Bardin Central Research Institute for the Iron and Steel Industry, Vtoraya Baumanskaya ul. 9/23, Moscow, 107005 Russia*

Received June 24, 2004

Abstract—Transmission and scanning electron microscopy, x-ray phase analysis, x-ray photoelectron spectroscopy, and atomic-force microscopy were used to study the structure and surface topography of Ti–B–N, Ti–Cr–B–(N), and Cr–B–(N) thin films. Physical, mechanical, and tribological characteristics of coatings were comparatively analyzed, including determination of the hardness, elastic modulus, elastic recovery, critical load, friction coefficient, and wear rate. It was shown that Ti–B–N and Ti–Cr–B–N coatings are superior to conventional TiN- and Ti–C–N-based coatings in terms of their physicomechanical and tribological properties. Ti–B–N and Ti–Cr–B–N coatings deposited under optimum conditions were characterized, accordingly, by a hardness of 31–34 and 40–47 GPa, an average elastic modulus of 378 and 506 GPa, a friction coefficient of 0.49–0.60 and 0.45–0.52, a dry-wear rate of $(3.4–4.6) \times 10^{-7}$ and $(6.0–6.8) \times 10^{-7}$ $mm^3\ N^{-1}\ m^{-1}$, and a largest critical load of 50 and 22 N. Features in the determination of the physicomechanical properties of films during nanoindentation and their wear properties are discussed. © *2005 Pleiades Publishing, Inc.*

1. INTRODUCTION

Nanostructured coatings based on the Ti–B–N system attract considerable interest due to their high hardness [1–3]; thermal stability [4–6]; oxidation resistance at high temperatures [7]; wear [8–11], corrosion [12], and impact [13] resistance; and high resistivity [14]. It is known that chromium has a positive effect on the oxidation resistance of titanium carbides, borides, and nitrides [15] and improves their wear resistance, especially at elevated temperatures [16]. Chromium boride coatings, in comparison with other borides of transition metals, are characterized by a good resistance to high-temperature oxidation and, hence, are promising heat-resistive materials [17].

In this paper, we report on a comprehensive study of the structural, physical, mechanical, and tribological properties of coatings in Ti–B–N, Ti–Cr–B–(N), and Cr–B–(N) systems. Coatings were deposited by magnetron sputtering of targets of TiB_2 + 2TiN, TiB + Ti_9Cr_4B + Cr_2Ti, and CrB_2 composition in an argon or argon–nitrogen atmosphere. The targets were prepared using self-propagating high-temperature synthesis (SHS). SHS compaction was carried out using exothermic mixtures of titanium (brand name, PTS), chromium (PKh-1S), boron nitride (99.0% pure, SVS-M), and amorphous brown boron powders. The influence of the technological parameters of SHS compaction on the composition, structure, and properties of functionally gradient targets based on TiB_2 and TiN was studied in detail in [18]. The target porosity did not exceed 5%.

The diameter of planar targets was 125 mm, and the substrate–target distance was 100 mm. Sputtering was carried out at a pressure of 0.2 Pa in a vacuum chamber. Single-crystal silicon (100) wafers, 65Kh13 stainless chromium steel, and TT8K6 hard alloy were used as substrates. The substrate surface was prepared by mechanical polishing (stainless steel, hard alloy) and ultrasonic cleaning in ethanol. Hard-alloy substrates were additionally cleaned by Ar^+ ions using a slit ion source (ion energy, 1.5–2.0 keV; current density on the substrate, 2–10 mA/cm^2). Deposition of Ti–B–N and Ti–Cr–B–(N) films onto hard alloy was preceded by the deposition of thin Ti and TiN underlayers. For the first 1–2 min of deposition, a high negative bias U_{bias} = –500 V was applied to substrates. The coating deposition time was 15 to 90 min for various substrates. The bias applied to substrates during deposition was –400 to 0 V, and the substrate temperature was maintained constant in the range 100–400°C.

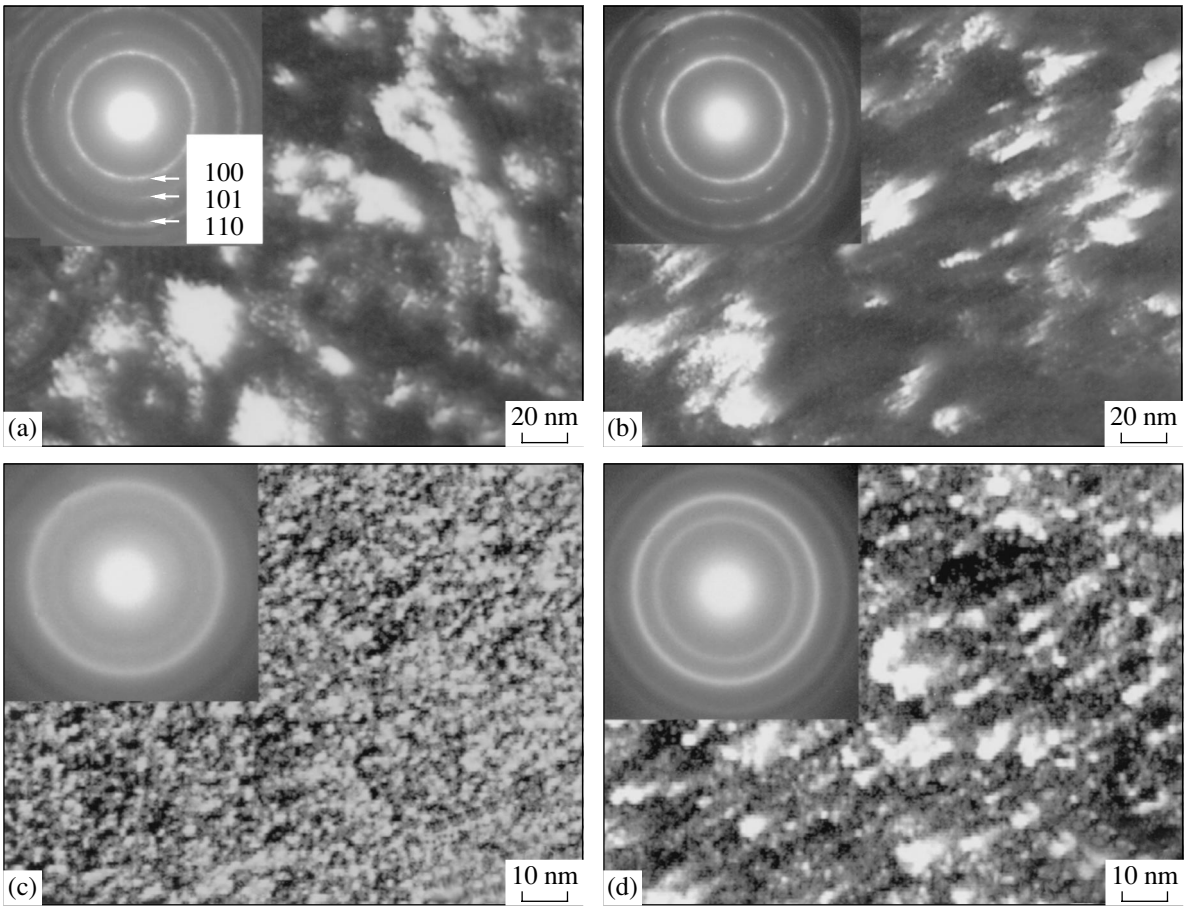

Fig. 1. Dark-field images of the structure and corresponding electron-diffraction patterns of (a, b) Cr–B and (c, d) Cr–B–N coatings measured at bias voltages U_{bias} equal to (a, c) 0 and (b, d) 250 V.

Foils for transmission electron microscopy (TEM) were prepared using one-side electrolytic polishing followed by finishing using an ionic gun. The coating structure was studied using a JEM-200CX transmission electron microscope at an accelerating voltage of 200 kV. The size distribution of crystallites was determined from dark-field images of the structure using the VideoTest-4.Struktura software. X-ray phase analysis (XPA) was carried out using a Geigerflex diffractometer with monochromatized CoK_α radiation. X-ray photoelectron spectra were measured using a Perkin-Elmer PHI 5500 ESCA spectrometer. High-resolution spectra were measured before and after ion etching. The energy scale was calibrated using the nitrogen binding energy in titanium nitride. The film surface topography was determined using a Seiko SPI3800N atomic-force microscope. The hardness, elastic modulus, and elastic recovery were determined with a Nano Hardness Tester (CSM Instruments, Switzerland) using the Oliver and Pharr method [19, 20] and a Berkovich indenter. The friction coefficient and wear rate of coatings was measured with a ball-on-disk tribometer (CSM Instruments, Switzerland) at loads of 2 and 5 N and a linear velocity of 10 cm/s. As a counterpart material, a WC-6 wt % Co ball 3 mm in diameter was used. The critical load at which coatings are destroyed and flake off when scratched by a diamond pyramid was determined using a scratch tester (CSM Instruments, Switzerland). The critical load L_c was determined using two methods: visually, i.e., by observing cracks and cleavages in coatings using an optical microscope with a magnification of ×200, and by observing a change in the acoustic emission current.

The deposition parameters, i.e., the substrate temperature T, bias voltage U_{bias}, and partial nitrogen content $[N_2/(N_2 + Ar)]$ in the gas mixture, are listed in the table.

2. CrB_2 COATINGS

Magnetron sputtering of a CrB_2 target in an Ar atmosphere results in the formation of one-phase coatings based on the CrB_2 phase [AlB_2 ($C32$) structure] with a crystallite size not exceeding 50 nm (Figs. 1a, 1b). In contrast to previous results indicating selective magnetron sputtering of a CrB_2 target [17], the lattice

Main deposition parameters and coating characteristics

Coating no.	Target	Coating composition	T, °C	U_{bias}, V	$N_2/(N_2 + Ar)$	Lattice parameter, nm	Si substrate			TT8K6 substrate			μ	$V_W^{film} \times 10^7$, $mm^3\ N^{-1}\ m^{-1}$	Air humidity, %	L_{cr}, N
							H, GPa	E, GPa	W_e, %	H, GPa	E, GPa	W_e, %				
1	TiB_2 + 2TiN	–	100	0	0	–	25	219	60	–	–	–	–	–	–	–
2		–	250	0	0	0.435	20	196	55	–	–	–	–	–	–	–
3		–	400	0	0	0.435	17	182	50	–	–	–	–	–	–	–
4		–	250	–125	0	0.437	15	181	48	–	–	–	–	–	–	–
5		$TiB_{0.8}N_{0.4}$	250	–250	0	0.434	32	260	67	34	380	60	0.6	3.4	54	30
6		–	250	–400	0	–	–	–	–	33	378	63	0.57	3.6	51	–
7		$TiBN_{0.6}$	250	–250	0.14	0.434	24	221	61	31	376	59	0.49	4.6	57	50
8	TiB + Ti_9Cr_4B + Cr_2Ti	–	200	0	0	–	21	216	49	–	–	–	–	–	–	–
9		$TiB_{1.3}Cr_{0.6}$	200	–125	0	–	25	226	57	–	–	–	–	–	–	–
10		–	200	–250	0	–	20	217	53	–	–	–	–	–	–	–
11		–	200	0	0.14	0.430	21	214	52	–	–	–	–	–	–	–
12		$TiBN_{0.6}Cr_{0.5}$	200	–125	0.14	–	29	257	61	40	496	62	0.52	6	59	22
13		–	200	–250	0.14	0.430	34	268	63	47	517	70	0.45	6.8	59	–
14	CrB_2	–	250	0	0	*	27	300	58	–	–	–	–	–	–	–
15		–	250	–125	0	//–//	28	310	53	–	–	–	–	–	–	–
16		–	250	–250	0	//–//	27	300	54	36	475	57	0.4	10.0	46	–
17		–	250	0	0.14	//–//	18	190	52	–	–	–	–	–	–	–
18		–	250	–125	0.14	//–//	18	190	52	–	–	–	–	–	–	–
19		–	250	–250	0.14	//–//	21	230	52	19	245	50	–	–	–	–

* For coatings 14–19 with an AlB_2-type structure, the lattice parameters were a = 0.306 nm and c = 0.297 nm.

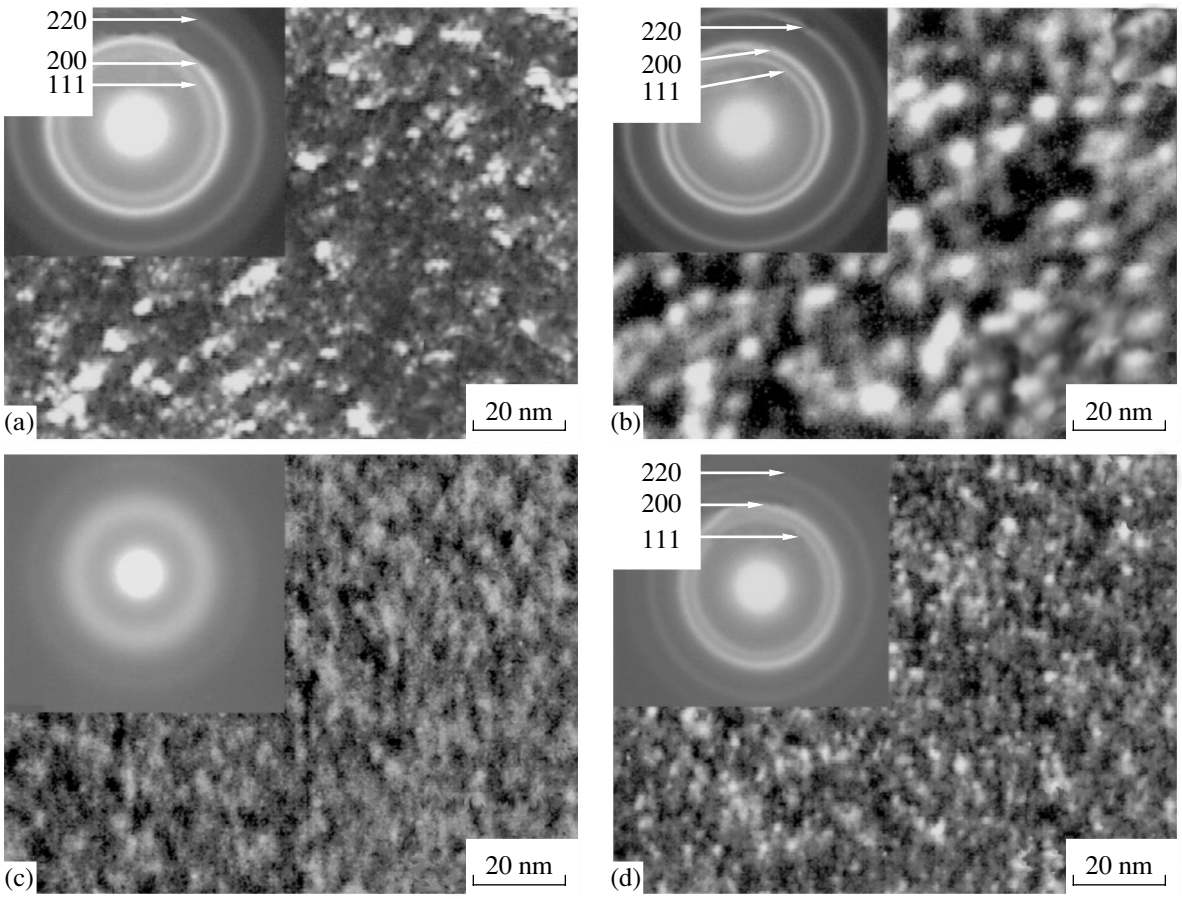

Fig. 2. Dark-field images of the structure and the corresponding electron-diffraction patterns of (a, b) Ti–B–N and (c, d) Ti–Cr–B–N coatings deposited at U_{bias} = –250 V in (a, c) argon and (b, d) gas mixture $N_2/(N_2 + Ar) = 0.14$.

parameters a = 0.297 and c = 0.307 nm (according to TEM data) did not differ from the known values for the CrB_2 phase (card no. 34-269, Joint Committee on Powder Diffraction Standards (JCPDS), International Centre for Diffraction Data), which indicates a composition that is close to stoichiometric. An axial texture is observed in coatings in which the c axis coincides with the direction of coating growth. The crystallite size and coating texture are independent of the bias voltage.

3. Cr–B–N COATINGS

When a CrB_2 target is sputtered in a $N_2/(N_2 + Ar) = 0.14$ gas mixture, the coating phase composition does not change significantly, at least with respect to the crystalline component. Although the position of the ring diffraction maxima in the electron-diffraction patterns remains unchanged to within experimental error, the lines are significantly broadened, which is mainly caused by the decrease in the crystallite size of the CrB_2 phase. When the substrate bias voltage is zero, the contrast scale in dark-field images is only 1–5 nm; as U_{bias} becomes equal to –250 V, the contrast scale reaches 2–10 nm (Figs. 1c, 1d). Texture is almost completely absent in the coating. Taking into account the published data indicating that nitrogen is insoluble in MeB_2-type structures (Me = Ti, Mo, V, Cr) and that the lattice parameters of the CrB_2 phase are unchanged, it can be assumed that nitrogen is mainly arranged in intergrain amorphous interlayers in the BN form [21]. These facts are confirmed, in particular, by a significantly lower hardness of Cr–B–N coatings in comparison with CrB_2. We note that Cr–B–N coatings were previously grown by magnetron sputtering of CrB_2 [17] and CrB [22] targets, as well as by Cr and B evaporation using an electron gun [23]; however, the CrB_2 phase was not observed in the films synthesized.

4. Ti–B–N COATINGS

These coatings consist of nanocrystalline particles with the fcc structure (Figs. 2a, 2b). Electron-diffraction patterns of coatings show spread ring reflections from the fcc lattice up to the (422) line. Texture was absent in all the Ti–B–N coating samples except in coating 1, which contained a weak (100)-type texture.

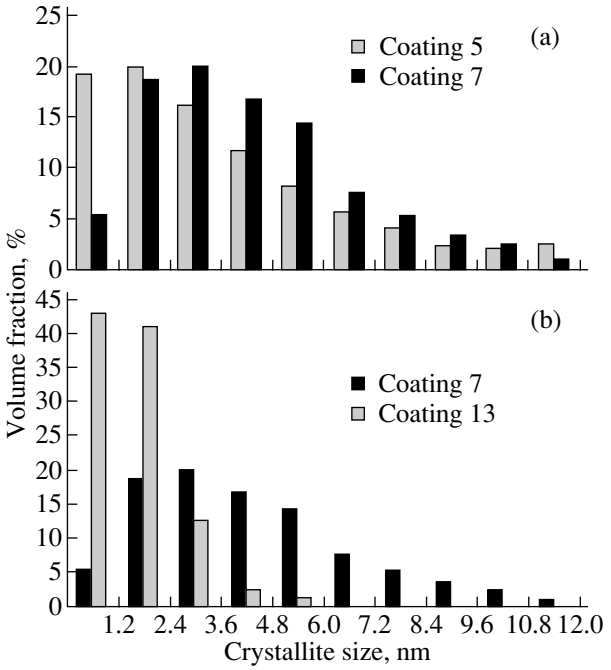

Fig. 3. Size distribution of crystallites as a function of (a) nitrogen and (b) chromium content.

Figure 3a shows the size distribution of particles as a function of working-gas composition. According to TEM data, the average size of crystallites was 2 nm for coating deposition in an argon medium and 3–4 nm with a nitrogen admixture.

Characteristic x-ray spectra of Ti–B–N coatings are shown in Fig. 4. The x-ray patterns of coatings contain two broad peaks near the (111) and (200) reflections from the fcc structure with a lattice parameter of 0.433 nm, which is significantly larger than 0.424 nm for TiN (JCPDS card no. 38-1420).

Additional information on the phase composition of coating can be obtained by analyzing the corresponding x-ray photoelectron (XPE) spectra. Peaks in the XPE spectra are caused by the electron–nucleus binding energy, which carries information on the nearest neighbor atomic neighborhood. The XPE spectra of the nitrogen 1*s* level (N1*s*) for coatings 5 and 7 have a characteristic peak at 396.9 eV, which is caused by the nitrogen–titanium bond in TiN. There is insignificant broadening of the spectra to higher binding energies, which indicates a superposition of lines corresponding to various chemical states. In coating 5, the second-peak fraction is negligible. Fitting of the spectrum of coating 7 showed that the position of the next peak (398.1 eV) is caused by the boron–nitrogen bond.

The XPE spectra of the boron 1*s* level (B1*s*) of coatings 5 and 7 taken after their etching are shown in Fig. 5. Coating 5 is characterized by a single peak at 187.5 eV, which corresponds to the boron–titanium

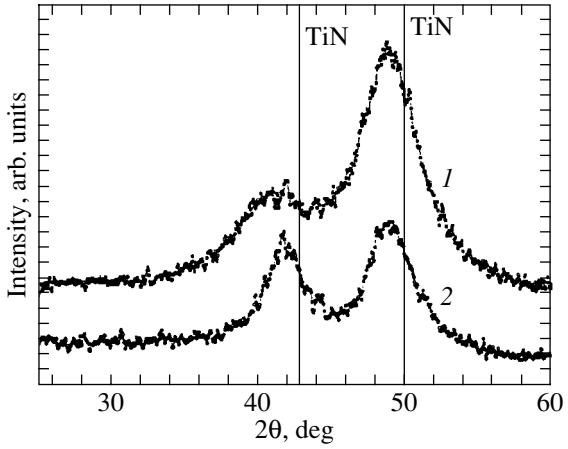

Fig. 4. X-ray spectra of Ti–B–N coatings (*1*) 5 and (*2*) 7.

bond in titanium diboride. The B1*s* spectrum of coating 7 contains two characteristic peaks at 187.5 and 190.5 eV caused by the boron bond to titanium and nitrogen. Since the TiB_2 and BN phases are not detected by x-ray and electron diffraction, it can be assumed that boron is in the nitrogen and titanium neighborhood in the amorphous phase of these compositions. This conclusion is consistent with the previous assumption that boron in Ti–B–N films can be in a TiB_2-type [24] or BN-type [25] quasi-amorphous phase.

Summarizing the XPA, TEM, and XPE spectroscopy data, it is worth noting the following. The structure of Ti–B–N coatings deposited in argon consists of nanocrystalline fcc particles of TiN and an amorphous phase with a composition close to TiB_2. In coatings grown in an argon–nitrogen mixture, the structure is mainly a TiN-type fcc phase. The high intensity of the B1*s* peak at 190.5 eV indicates a preferential boron–nitrogen bond in the amorphous phase; the TiB_2 phase amount here is much less than that in samples deposited

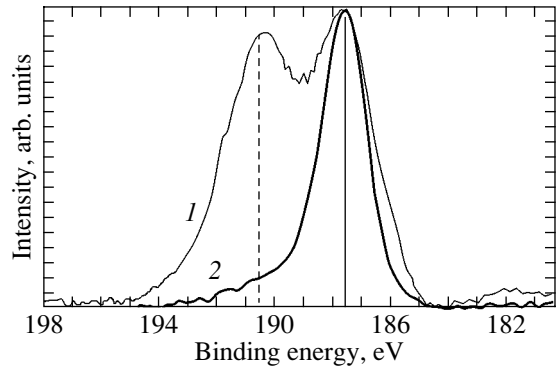

Fig. 5. X-ray photoelectron spectra of Ti–B–N coatings (*1*) 7 and (*2*) 5. Vertical solid and dashed lines indicate the binding energies corresponding to the TiB_2 (187.5 eV) and BN (190.5 eV) phases.

in argon. We note that the compositions of coatings 5 and 7 lie in the two-phase TiN_x–TiB_2 and three-phase TiN–TiB_2–BN regions, respectively, in the equilibrium phase diagram, which is qualitatively consistent with the results of the phase analysis.

5. Ti–Cr–B–(N) COATINGS

According to the XPA and TEM data, Ti–Cr–B coatings deposited in an argon medium had an amorphous structure (Fig. 2c). In the case with a nitrogen admixture to the working gas, the coatings consist mainly of the fcc phase with a lattice parameter of 0.430 nm. When the coatings were deposited with a zero bias voltage, the diffraction peaks were strongly broadened. In this case, the contrast scale in dark-field images of the structure was almost identical to that of coatings deposited in an Ar medium and was 1–2 nm (Figs. 2c, 2d). Figure 3d shows the size distribution of particles for Ti–Cr–B–(N) coatings. We can see that the introduction of chromium into the Ti–B–N coating composition results in a significant decrease in the crystallite size and a narrower size distribution of particles. The reason for this is that chromium in the coating composition prevents grain growth and stimulates the nucleation of new crystallites.

According to the XPE spectroscopy data, coating 12 consists of a TiN_{1-x} + CrB_2 phase mixture, as indicated by the peaks in the Ti2*p*, Cr2*p*, B1*s*, and N1*s* spectra at 454.8 (TiN), 574.3 (CrB_2), 188.0 (CrB_2), and 397.3 eV, respectively. The small shift of the N1*s* line to higher binding energies with respect to that in TiN (396.9–397.2 eV) indicates that there is a nitrogen deficiency in comparison with the stoichiometric composition.

The fcc lattice parameter in all the coatings studied exceeds that for TiN (0.424 nm) significantly, which can be caused by macroscopic stresses. It should be noted that the lattice parameters are independent of bias voltage and do not differ for coating deposition on silicon and stainless steel, i.e., on materials with different thermal expansion coefficients. This fact suggests that there is no contribution from thermal macroscopic stresses to the total compressive stresses. The smaller lattice parameter of Ti–Cr–B–N coatings in comparison with that of Ti–B–N can be caused by chromium replacing titanium in the metal sublattice.

An electron microscopy study of Ti–B–N and Ti–Cr–B–N coatings in cross cuts showed the absence of a columnar structure (Fig. 6a). The film surface is very smooth; the values of the root-mean-square roughness (measured over an area of 0.5×0.5 μm) of the Ti–B–N and Ti–Cr–B–N film surface on the silicon substrate are 0.08 and 0.19 nm, respectively (Figs. 6b, 6c).

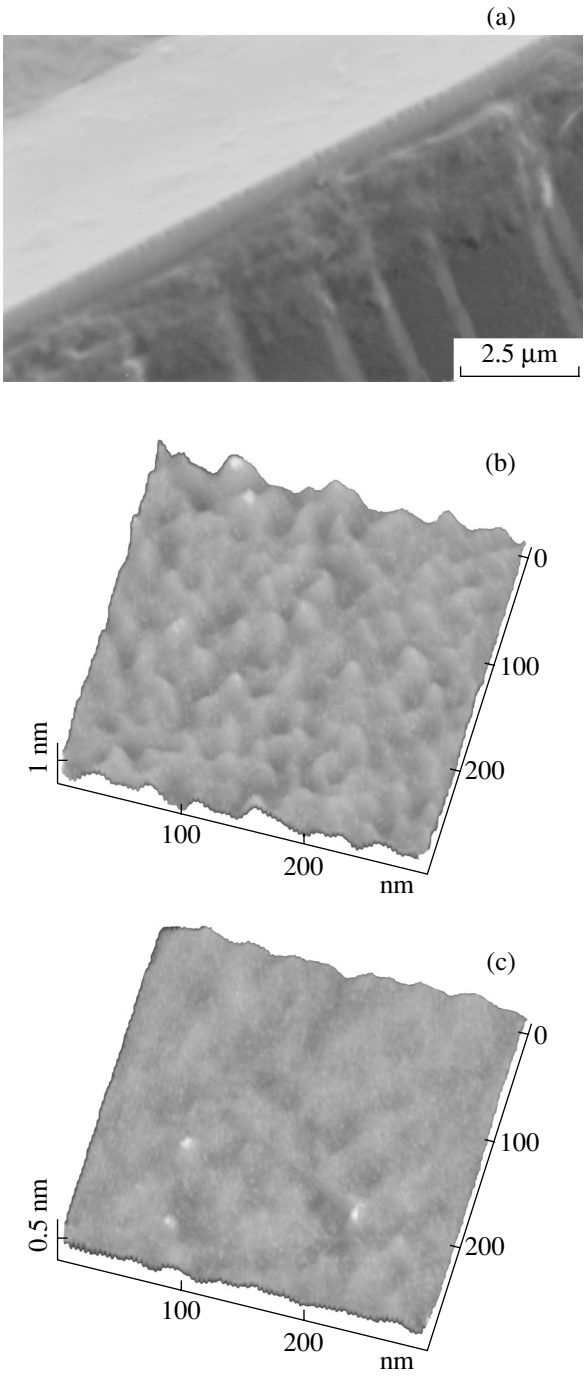

Fig. 6. Structure and surface topography of (a, b) Ti–Cr–B–N and (c) Ti–B–N films.

6. PHYSICAL AND MECHANICAL PROPERTIES

The hardness (*H*), elastic modulus (*E*), and elastic recovery (W_e) of films were determined using a nanohardness tester and a Berkovich indenter at loads of 1.5–7.5 mN. The coating nanoindentation technique at weak loads and the insignificant influence of external factors on the measured values are described in detail, e.g., in [26]. In this method, the initial portion of the

unloading curve is fitted by the power function $P_{max} = B(h - h_f)^m$, where P_{max} is the maximum load, h is the indenter penetration depth, h_f is the indenter penetration depth after unloading, and B and m are empirical parameters. The slope of the initial stage of the unloading curve defines the material hardness:

$$S = \left(\frac{dP}{dh}\right)_{h = h_{max}} = mB(h_{max} - h_f)^{m-1}.$$

The indenter penetration depth h_c at which the indent reproduces the diamond pyramid shape is also determined from the loading–unloading curve using the formula $h_c = h_{max} - \varepsilon P_{max}/S$, where h_{max} is the maximum indenter penetration depth and $\varepsilon = 0.75$ for the Berkovich pyramid. The values of H and E are calculated using the formulas $H = P_{max}/A$, $E_{eff} = \frac{1}{\beta}\frac{\sqrt{\pi}}{2}\frac{S}{\sqrt{A}}$, and $\frac{1}{E_{eff}} = \frac{1-\nu^2}{E} + \frac{1-\nu_i^2}{E_i}$, where ν is the Poisson ratio of a coating, $\beta = 1.034$ for the Berkovich pyramid, and A is the indent projection area determined from the maximum indenter penetration depth h_{max}. For the diamond indenter, the Poisson ratio ν_i and the elastic modulus E_i are 0.07 and 1141 GPa, respectively. Before measurements, the device was thoroughly calibrated to determine the point of the indenter contact with the sample surface and the correction for imperfection of the indenter tip shape. The value of the elastic recovery of coatings was determined using the formula

$$W_e = (h_{max} - h_f)/h_{max}.$$

The values of H and E for coatings deposited on silicon were calculated using at least five points for each load. When determining these values for coatings on hard alloy, the number of measurements was increased to 15–20, since the TT8K6 alloy structure is inhomogeneous and consists of grains of the hard carbide phase and soft Co binder. Measurements with identical loading–unloading curves that correspond to the response of the coating/carbide system (Ti, W, Ta)C were selected for further analysis. The measured results are listed in the table. The highest hardnesses of Ti–B–N coatings, equal to 33–34 GPa, agree well with previous results [11, 27]. The Young moduli of the coatings deposited on hard-alloy substrates were 370–380 GPa. The literature demonstrates a wide variance in the Young modulus of Ti–B–N films, from 325 GPa [25] to 430–480 GPa [14]. These values are smaller than those of bulk TiN (618 GPa) and TiB_2 (550–580 GPa) compounds [14]. It is known that insignificant porosity of a material can cause a significant decrease in the elastic modulus [28]. Therefore, lower values of E can result from a large volume fraction of defects and incoherent interfaces in nanostructured thin films, which decrease the density of the material.

The values of H, E, and W_e for Ti–Cr–B–(N) and Cr–B–(N) coatings deposited on silicon and TT8K6 hard-alloy substrates are listed in the table. In the Ti–Cr–B–N system, coatings with record high hardness (47 GPa) were grown. These coatings also showed high elastic recovery during unloading, reaching 70%. For Cr–B–(N) coatings on hard-alloy substrates, two groups of values of the hardness and elastic modulus can be distinguished depending on the deposition medium: H = 36 GPa, E = 475 GPa (Ar) and H = 19 GPa, E = 245 GPa (Ar + 14N_2). Hence, the physicomechanical properties of Cr–B–(N) coatings are mainly controlled by the coating composition and, to a lesser extent, by the bias voltage. It is worth noting that the hardness of CrB_2 films grown in this study is much higher than that of Cr–B films (17–21 GPa) obtained previously [17, 22].

The fact that, as a rule, the hardness and elastic modulus of coatings deposited on hard alloy exceed those of coatings deposited on silicon under the same conditions is also worth noting. For the elastic modulus, this difference is larger than for the hardness. This difference seems to be caused by the fact that long-range fields of elastic stresses induced by the indenter penetration into the coating depth extend over not only the coating thickness but also reach the substrate material [29]. Indeed, the elastic moduli of hard alloy and silicon (used in this study) are 450 and 172 GPa, respectively. The thickness of films on silicon and hard alloy did not exceed 0.7–0.8 and 1.5–2.0 nm, respectively, and the largest depth of indenter penetration reached 100 and 120 nm. We also note that the elastic moduli of coatings on Si are lower than those of bulk materials by a factor of 2–2.5. This difference can be explained by assuming that the elastic moduli measured during nanoindentation of hard coatings on rather soft substrates are close to the shear moduli rather than to the Young moduli [30, 31]. For example, according to [32], the Young modulus and shear modulus are 541 and 237 GPa for TiB_2 and 440 and 170 GPa for TiN, respectively.

7. TRIBOLOGICAL PROPERTIES

To carry out tribological tests, Ti–B–N, Ti–Cr–B–(N), and Cr–B–(N) coatings were deposited on TT8K6 hard-alloy substrates with preliminary deposition of Ti and TiN underlayers to improve adhesion. Figure 7 shows the dependence of the friction coefficient μ on the number of test cycles. The friction coefficient of Ti–B–N coatings deposited in an Ar medium was 0.57–0.6, which is comparable to that of TiN (0.55) [33] but is significantly lower than that of Ti–B–N (0.85–0.95) [11, 13, 34]. As the boron and nitrogen contents in coatings were decreased and increased, respectively, the friction coefficient lowered to 0.49. The smaller friction coefficient in coating 7, in comparison with coatings 5

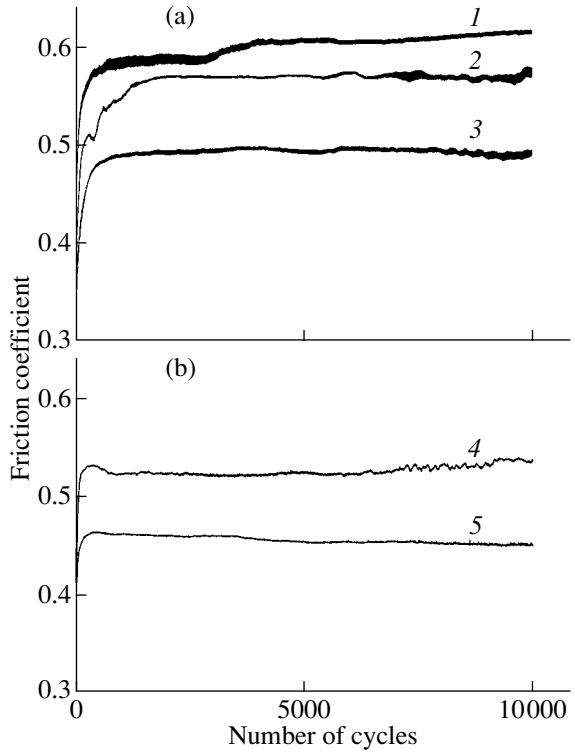

Fig. 7. Dependence of the friction coefficient of (a) Ti–B–N and (b) Ti–Cr–B–N coatings on the number of test cycles; curves *1–5* correspond to coatings 5–7, 12, and 13, respectively.

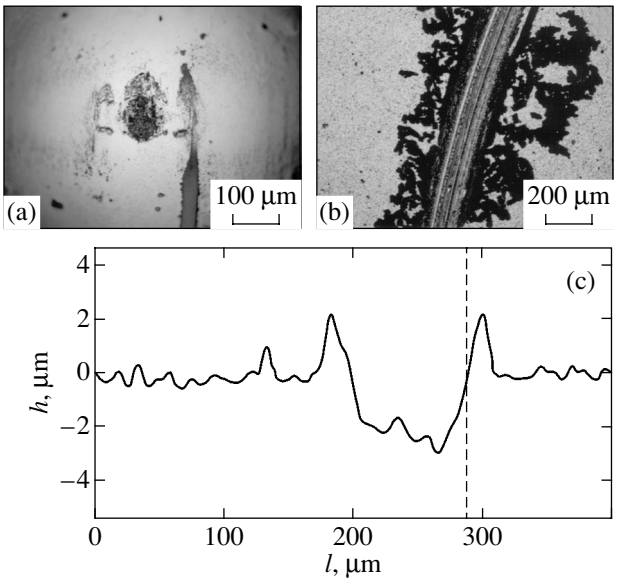

Fig. 8. Micrographs of the wear region of (a) a rider (WC + 6 wt % Co ball 3 mm in diameter) and (b) Ti–B–N coating 5 after 10 000 test cycles at a load of 5 N and a sliding velocity of 10 cm/s; (c) a wear groove profilogram.

and 6, can also be associated with the BN phase. As shown previously, the friction coefficient of Ti–B–N coatings depends on air humidity, decreasing from 0.9 to 0.4 as the humidity increases from 15% to 85% [35]. In this study, the friction coefficient was measured to be 0.49 at an air humidity of 57%.

The dependence of the friction coefficient on the number of test cycles remained unchanged as chromium was introduced into the film composition. The coatings exhibited a steady, low friction coefficient of 0.45 (coating 13) and 0.52 (coating 12) throughout the tests. The general tendency inherent in Ti–B–N and Ti–Cr–B–N coatings is a decrease in the friction coefficient observed as the nitrogen content increases in coatings, as nitrogen is introduced into the working gas composition, or as a negative bias voltage is applied to the substrate.

It should be noted that the wear dynamics of Ti–B–N and Ti–Cr–B–N coatings are different. In the former case, uniform abrasive wear of a friction pair is observed, which is accompanied by an intense removal of wear debris particles from a groove (Fig. 8). Analysis of the profile of the vertical cross section of a wear groove shows that wear debris bulks are formed along the groove edges, whose height approximately corresponds to the wear groove depth (Fig. 8c). The sharpened shape of the bulk tops indicates the absence of adhesion contact with the ball surface. The ball wear region is a characteristic circle with traces of wear debris at opposite edges (Fig. 8a). In the case of Ti–Cr–B–N coatings, a transition layer is formed from wear debris particles, which changes the ball wear dynamics. Figures 9b and 9c show that wear debris particles adhere densely over groove boundaries and bulks (indi-

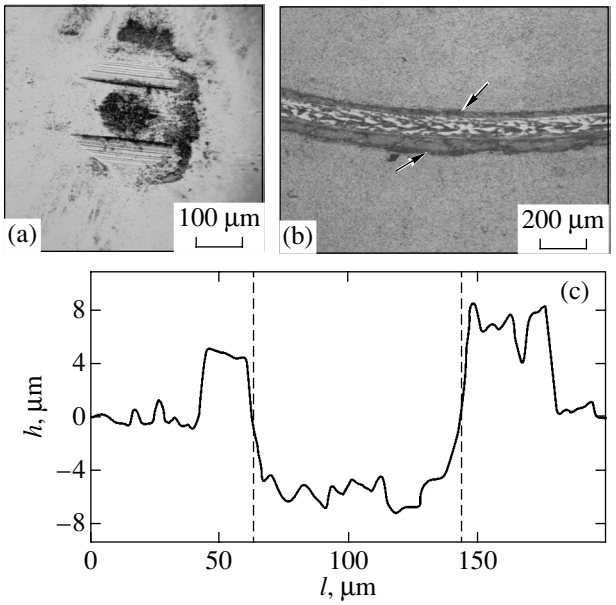

Fig. 9. The same as in Fig. 8, but for Ti–Cr–B–N coating 12. Arrows indicate wear debris bulks.

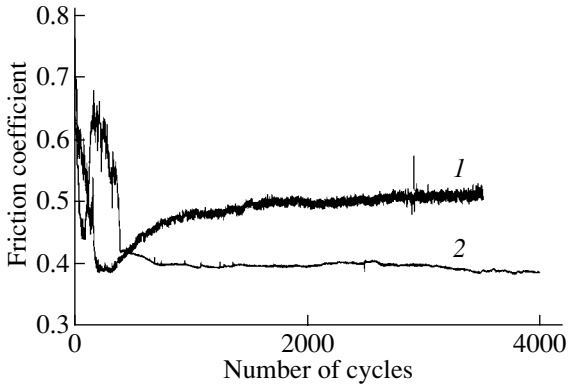

Fig. 10. Dependences of the friction coefficients of Cr–B–N coatings (*1*) 19 (at 5 N) and (*2*) 16 (at 2 N) on the number of test cycles.

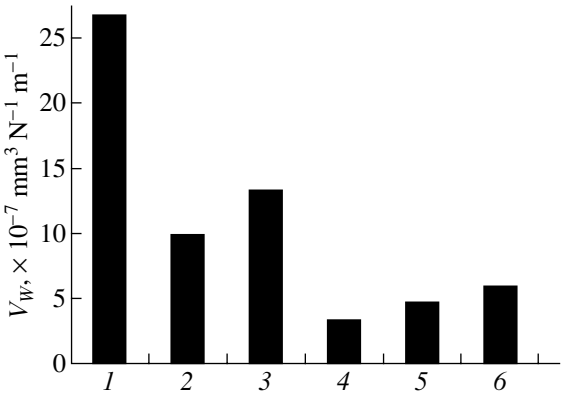

Fig. 11. Comparison of the wear rates of various coatings: (*1*) TiN, (*2*) Ti–C–N, (*3*) Ti–Si–N [36], (*4*) Ti–B–N (coating 5), (*5*) Ti–B–N (coating 7), and (*6*) Ti–Cr–B–N (coating 12).

cated by arrows) are formed during tests. The profilogram of the vertical cross section of the wear groove clearly shows flat tops of bulks, caused by the abrasive interaction between wear debris particles and the counterpart material. As a result, the region of the most intense ball wear shifts gradually during tests to the edges of the path where bulks are arranged. Accordingly, the regions of the most intense ball wear are arranged symmetrically and are shaped like segments (Fig. 9a).

The friction coefficient of Cr–B and Cr–B–N coatings tested at a load of 5 N had a characteristic peak in the initial wear stage reaching 0.7–0.8 (Fig. 10). The counterpart material wear rate was much higher than in the case of Ti–B–N and Ti–Cr–B–(N) coatings. This indicates strong adhesion interaction at the contact point of the friction pair, as well as an intense formation of wear debris particles, which causes a change in the friction coefficient. In approximately 200 cycles, the friction coefficient decreased to 0.4, remaining unchanged during the first 120 cycles (curve *1* in Fig. 10). The subsequent increase in the friction coefficient to 0.5 is caused by total failure of the coating. The CrB_2 coating without underlayers stood 10 000 test cycles with a load of 2 N (curve *2* in Fig. 10).

Figure 11 shows the comparative diagrams of wear rates of Ti–B–N and Ti–Cr–B–N coatings in comparison with TiN, Ti–C–N, and Ti–Si–N coatings [36] deposited by magnetron sputtering of Ti, $TiC_{0.5}$, and Ti_5Si_3 + Ti targets. The wear rates for Ti–B–N and Ti–Cr–B–N coatings are (3.4–4.6) × 10^{-7} and (6.0–6.8) × 10^{-7} mm^3 N^{-1} m^{-1}, respectively. As can be seen in the diagram, the wear rate of Ti–B–N and Ti–Cr–B–N coatings is significantly lower than that of TiN, Ti–C–N, and Ti–Si–N. The wear resistance of Ti–B–N and Ti–Cr–B–N coatings also exceeds that of Ti–B–N coatings grown previously, which are characterized by a wear rate of 10^{-4}–10^{-6} mm^3 N^{-1} m^{-1} [9] and (3.0–4.5) × 10^{-5} mm^3 N^{-1} m^{-1} [13]. According to the classical wear theory, the low abrasion is generally associated with a high hardness. Materials with high fracture toughness should be highly resistant to plastic deformation, which is estimated using the parameter H^3/E^2 [37]. Therefore,

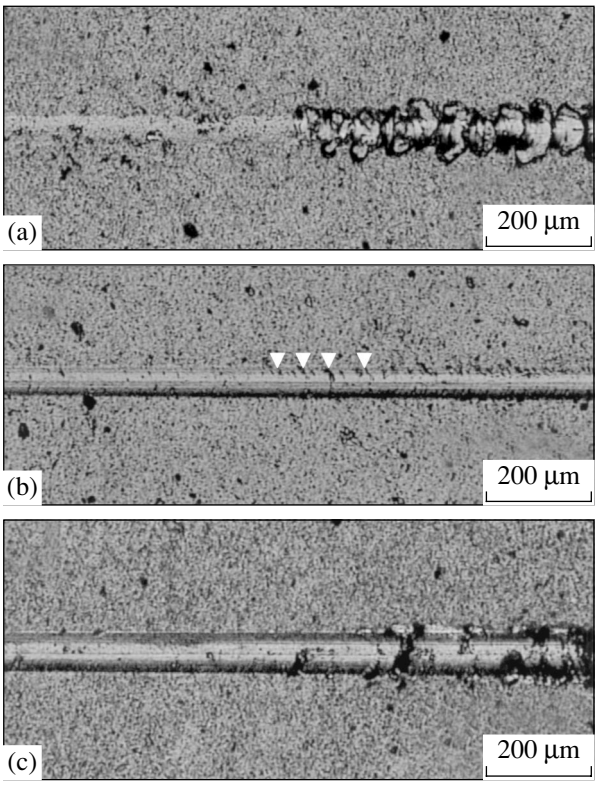

Fig. 12. Coating failure structure during scratching by a diamond pyramid with an increasing load: (a) Ti–Cr–B–N (coating 12), critical load for failure L_{cr} = 22 N; (b) Ti–B–N (coating 5), L_{cr} = 30 N; and (c) Ti–B–N (coating 7), L_{cr} = 50 N.

materials with high values of H^3/E^2 should be characterized by increased crack resistance. However, in this study, we did not detect any dependence between the hardness, H^3/E^2, and the wear resistance of coatings. Instead, other factors, such as the composition and the properties of wear debris particles, as well as the adhesion of coatings, can control the behavior of coatings during friction and wear.

To determine the adhesion strength of coatings, sclerometry tests were carried out. The values of the critical load L_{cr}, at which cracking or flaking of coating regions takes place, are listed in the table. Micrographs of the region of initiation of film destruction during scratching by a diamond pyramid with increasing load are shown in Fig. 12. We note that coatings 5 and 7 at similar values of H, E, and W_e are characterized by different destruction features on reaching critical loads of 30 and 50 N, respectively. A decrease in the coating–substrate cohesion strength with an increase in the boron content in Ti–B–N coatings was indicated previously [38]. This circumstance can be associated with microstresses increasing due to the increased fineness of the structure and to an increase in the volume fraction of defects and incoherent interfaces.

8. CONCLUSIONS

A combination of various methods has made it possible to determine the structure and the phase composition of Ti–B–N, Ti–Cr–B–(N), and Cr–B–(N) coatings. From the viewpoint of their mechanical and tribological properties, TiN + TiB_2, TiN + TiB_2 + BN, and TiN_{1-x} + CrB_2 nanostructured mixtures are optimum (one or several structural components in them can be in an amorphous state). Coatings deposited under optimum conditions were characterized by a high hardness, wear resistance, and adhesion with the substrate, as well as by a low friction coefficient.

ACKNOWLEDGMENTS

The authors would like to thank M.I. Petrzhik for his assistance in the nanoindentation and sclerometry experiments.

This study was supported by the International Science and Technology Center, grant no. 1852.

REFERENCES

1. P. Losbichler, C. Mitterer, P. N. Gibson, W. Gissler, F. Hofer, and P. Warbichler, Surf. Coat. Technol. **94–95**, 297 (1997).
2. S. Veprek, P. Nesladek, A. Niederhofer, F. Glatz, M. Jilek, and M. Šima, Surf. Coat. Technol. **108–109**, 138 (1998).
3. R. A. Andrievski and G. V. Kalinnikov, Surf. Coat. Technol. **142–144**, 573 (2001).
4. R. A. Andrievskiĭ, G. V. Kalinnikov, A. E. Oblezov, and D. V. Shtanskiĭ, Dokl. Akad. Nauk **384** (1), 36 (2002) [Dokl. Phys. **47**, 353 (2002)].
5. P. Karvankova, M. G. J. Veprek-Heijman, O. Zindulka, A. Bergmaier, and S. Vepzek, Surf. Coat. Technol. **163–164**, 149 (2003).
6. C. Mitterer, P. H. Mayrhofer, and J. Musil, Vacuum **71**, 279 (2003).
7. S. Veprek, J. Vac. Sci. Technol. **17** (5), 2401 (1999).
8. D. V. Shtanskiĭ, E. A. Levashov, N. N. Khavskiĭ, and J. J. Moore, Izv. Vyssh. Uchebn. Zaved., Tsvetn. Metall. **1**, 59 (1996).
9. J. L. He, S. Miyake, Y. Setsuhara, I. Shimizu, M. Suzuki, K. Numata, and H. Saito, Wear **249**, 498 (2001).
10. C. Heau and J. P. Terrat, Surf. Coat. Technol. **108–109**, 332 (1998).
11. M. Stoiber, C. Mitterer, T. Schoeberi, E. Badisch, G. Fontaivo, and R. Kullmer, J. Vac. Sci. Technol. B **21** (3), 1084 (2003).
12. M. Tamura and H. Kubo, Surf. Coat. Technol. **54–55**, 255 (1992).
13. C. Rebholz, H. Ziegele, A. Leyland, and A. Matthews, J. Vac. Sci. Technol. **5**, 2851 (1998).
14. R. A. Andrievskiĭ, G. V. Kalinnikov, N. P. Kobelev, Ya. M. Soĭfer, and D. V. Shtanskiĭ, Fiz. Tverd. Tela (St. Petersburg) **39** (10), 1859 (1997) [Phys. Solid State **39**, 1661 (1997)].
15. L. Donohue, I. J. Smith, W.-D. Münz, I. Petrov, and J. E. Greene, Surf. Coat. Technol. **94–95**, 226 (1997).
16. E. Pflüger, A. Schröer, P. Voumard, L. Donohue, and W.-D. Münz, Surf. Coat. Technol. **115**, 17 (1999).
17. M. Zhou, M. Nose, Y. Makino, and K. Nogi, Thin Solid Films **343–344**, 234 (1999).
18. E. A. Levashov, D. V. Larikhin, D. V. Shtanskiĭ, A. S. Rogachev, and A. É. Grigoryan, Tsvetn. Met. **5**, 49 (2002).
19. G. M. Pharr, Mater. Sci. Eng. **253**, 151 (1998).
20. G. M. Pharr, W. C. Oliver, and F. R. Brotzen, J. Mater. Res. **3**, 613 (1992).
21. M. A. Baker, T. P. Mollart, P. N. Gibson, and W. Gissler, J. Vac. Sci. Technol. **15** (2), 284 (1997).
22. Y. Sakamaoto, M. Nose, T. Mae, E. Honbo, M. Zhou, and K. Nogi, Surf. Coat. Technol. **174**, 444 (2003).
23. S. M. Aouadi, F. Namavar, E. Tobin, N. Finnegan, R. T. Haasch, R. Nilchiani, J. A. Turner, and S. L. Rohde, J. Appl. Phys. **91** (3), 1040 (2002).
24. A. Gupper, A. Fernández, C. Fernández-Ramos, F. Hofer, C. Mitterer, and P. Warbichler, Monatsch. Chem. **133**, 837 (2002).
25. S. M. Aouadi, F. Namavar, T. Z. Goroshnyy, and S. L. Rohde, Surf. Coat. Technol. **160**, 145 (2002).

26. R. A. Andrievskiĭ, G. V. Kalinnikov, N. Hellgren, P. Sandstrom, and D. V. Shtanskiĭ, Fiz. Tverd. Tela (St. Petersburg) **42** (9), 1624 (2000) [Phys. Solid State **42**, 1671 (2000)].
27. R. Wiedemann, V. Weihnacht, and H. Oettel, Surf. Coat. Technol. **116–119**, 302 (1999).
28. D. Schneider, Th. Schwarz, H.-P. Buchkremer, and D. Stöver, Thin Solid Films **224**, 177 (1993).
29. R. Saha and W. D. Nix, Acta Mater. **50**, 23 (2002).
30. S. Veprek, S. Mukherjee, P. Karvankova, H.-D. Männling, J. L. He, J. Xu, J. Prochazka, A. S. Argon, A. S. Li, Q. F. Fang, S. Z. Li, M. H. Manghnani, and S. Tkachev, Mater. Res. Soc. Symp. Proc. **750**, Y1.3 (2002).
31. D. V. Shtansky, E. A. Levashov, N. A. Glushankova, N. B. D'yakonova, S. A. Kulinich, M. I. Petrzhik, F. V. Kiryukhantsev-Korneev, and F. Rossi, Surf. Coat. Technol. **182**, 101 (2004).
32. R. A. Andrievskiĭ and I. I. Spivak, *Handbook on Strength of Refractory Compounds and Materials Based on Them* (Metallurgiya, Chelyabinsk, 1989) [in Russian].
33. K. N. Jallad and D. Ben-Amotz, Wear **252**, 956 (2002).
34. H. Holleck and V. Schier, Surf. Coat. Technol. **76–77**, 328 (1995).
35. R. Kullmer, C. Lugmair, A. Figueras, J. Bassas, M. Stoiber, and C. Mitterer, Surf. Coat. Technol. **174–175**, 1229 (2003).
36. D. V. Shtansky, I. V. Lyasotsky, N. B. D'yakonova, F. V. Kiryukhantsev-Korneev, S. A. Kulinich, E. A. Levashov, and J. J. Moore, Surf. Coat. Technol. **182**, 204 (2004).
37. A. Leyland and A. Matthews, Wear **246**, 1 (2000).
38. W. Gissler, Surf. Coat. Technol. **68/69**, 556 (1994).

Translated by A. Kazantsev

Physics of the Solid State, Vol. 47, No. 2, 2005, pp. 263–266. Translated from Fizika Tverdogo Tela, Vol. 47, No. 2, 2005, pp. 252–254.

MAGNETISM AND FERROELECTRICITY

Structure of the Inhomogeneous Magnetic State of an $FeBO_3$: Mg Easy-Plane Weak Ferromagnet

B. Yu. Sokolov

National University of Uzbekistan, Tashkent, 700174 Uzbekistan

e-mail: optic@nuuz.uzsci.net

Received March 30, 2004

Abstract—The magnetic linear birefringence of an $FeBO_3$: Mg ferromagnetic crystal is investigated as a function of the magnetic field strength, the magnetic field orientation, and the coordinates. The structure of the inhomogeneous magnetic phase of this weak ferromagnet is determined by analyzing the experimental results obtained. It is shown that, in an inhomogeneous magnetic state, the ferromagnetic moment does not deviate from the basal plane of the crystal and the angle of its deviation from the direction of the applied magnetic field is described by a one-dimensional harmonic function of the spatial coordinate along the axis of magnetization.

1. INTRODUCTION

Previous investigations [1] have demonstrated that, upon magnetization in the basal plane, iron borate doped with diamagnetic ions of magnesium ($FeBO_3$: Mg) undergoes a phase transition from the homogeneous magnetic state to the inhomogeneous magnetic state. The inhomogeneous magnetic state of this weak ferromagnet is observed at temperatures $T < 130$ K under the condition where the external magnetic field H is aligned parallel to the hard magnetization axes of the in-plane hexagonal crystalline anisotropy (in a direction perpendicular to any of the three C_2 axes). In our previous work [1], we performed a magneto-optical investigation of the inhomogeneous magnetic state in $FeBO_3$: Mg ferromagnetic crystals with the use of a light-polarizing microscope and visually observed the appearance of magnetic inhomogeneities of the crystal in the form of a quasi-periodic system of alternating bright and dark fringes with diffuse boundaries directed perpendicularly to the applied magnetic field.

When interpreting the results obtained in [1], it was assumed that, in an inhomogeneous magnetic state, the vector of the weak ferromagnetic moment **m** oscillates about the direction of the magnetic field **H** aligned parallel to the axis of magnetization but remains in the basal plane of the crystal. However, another situation can also occur. In observations of the crystal in polarized light (in the experiment, the light waves propagate along the normal to the basal plane), the appearance of a system of bright and dark fringes on the image of the crystal surface can be caused by a spatial modulation of the azimuth of the vector **m** when the magnetization vector deviates from the basal plane. This leads to a periodic variation in the magnitude of the Faraday effect along the direction of the magnetic field **H** due to the change in the projection of the ferromagnetic moment **m** onto the direction of the propagation of light waves.

In this work, the structure of the inhomogeneous magnetic state of an $FeBO_3$: Mg ferromagnetic crystal was determined by analyzing the spatial distribution of the vector **m** in this crystal as a function of the applied magnetic field.

2. EXPERIMENTAL TECHNIQUE

It is known that the magnetic linear birefringence substantially depends on the orientation of the magnetization in the crystal (see, for example, [2]). Therefore, in order to determine the structure of the inhomogeneous magnetic state of an $FeBO_3$: Mg crystal, it is expedient to investigate the dependence of this even magneto-optical effect on the spatial coordinates in the basal plane of the crystal. Let us elucidate how the orientation of the ferromagnetic moment in an $FeBO_3$: Mg crystal affects the magnetic linear birefringence of this crystal. A similar problem was solved earlier by Fedorov *et al.* [3], who considered the structure of the photoinduced modulated magnetic state in $FeBO_3$: Ni crystals.[1]

According to Fedorov *et al*. [3], when a light wave propagates in iron borate along the optic axis (i.e., along the C_3 axis of the crystal), the magnetic linear

[1] Since the crystal in our experiments was always exposed to light, we specially investigated the influence of the illumination on the magnetic state of the crystal. However, no noticeable variation in the domain structure, parameters, or conditions of existence of the inhomogeneous magnetic state in the $FeBO_3$: Mg crystal was revealed with a change in the intensity or in the spectral composition of the radiation from the optical sources used.

1063-7834/05/4702-0263$26.00 © 2005 Pleiades Publishing, Inc.

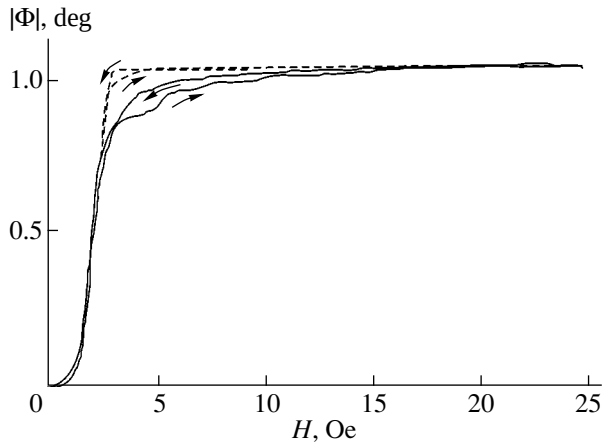

Fig. 1. Field dependences of the magnetic linear birefringence of the $FeBO_3$: Mg ferromagnetic crystal at temperature T = 80 K for two orientations of the magnetic field: $\mathbf{H} \perp C_2$ (solid line) and $\mathbf{H} \parallel C_2$ (dashed line). Arrows indicate the direction of variation in the magnetic linear birefringence during magnetization reversal of the crystal. The scanning time of the magnetic field is approximately equal to 1 min.

birefringence at a point on the basal plane with the coordinates (x, y) can be represented in the form

$$\Phi = A(x, y)\sin 2[\theta - \varphi(x, y)],$$
$$A(x, y) = A_0(a^2 + b^2)^{1/2},$$
$$A_0 = 2\pi(n_\parallel - n_\perp)l/\lambda, \quad (1)$$
$$a = l^{-1}\int_0^l \cos 2\varphi(x, y, z)dz,$$
$$b = l^{-1}\int_0^l \sin 2\varphi(x, y, z)dz.$$

Here, φ is the angle between the direction of projection of the vector **m** onto the basal plane and the X axis of the laboratory system of coordinates (for definiteness, it is assumed that $X \perp C_2$); θ is the azimuthal angle between the plane of polarization of the light incident on the crystal and the X axis; $n_\parallel$ and $n_\perp$ are the refractive indices for the light linearly polarized parallel and perpendicular to the direction of the two-dimensional component of the vector **m**, respectively; λ is the emission wavelength; and l is the thickness of the crystal along the Z axis ($Z \parallel C_3$).

It follows from relationships (1) that, in the case when the coordinates x and y are taken to be fixed, the dependence $\Phi(\theta)$ can be described by a harmonic function with an initial phase φ and an amplitude A that specify the direction and magnitude of the ferromagnetic moment at a given point on the basal plane of the crystal, respectively. Therefore, the spatial orientation of the vector **m** in the crystal can be judged from the results of analyzing the coordinate dependence of the magnetic linear birefringence in terms of relationships (1).

Our experiments were performed with the same ferromagnetic crystal of magnesium-doped iron borate $FeBO_3$: Mg (~0.1 wt % Mg) that was studied earlier in [1]. The sample had the form of a plane-parallel plate ~3-mm wide and ≈60 μm thick. The developed surface of the plate coincided with the basal plane. The magnetic linear birefringence was measured using emission from a He–Ne laser at a wavelength λ = 0.63 μm in a constant magnetic field $H \le 30$ Oe at temperature T = 80 K. The vector **H** was oriented in the plane of the sample, whereas the direction of light propagation was perpendicular to the plane of the sample. The magnetic linear birefringence was measured with the use of a phase compensator (plates $\lambda/4$) according to the traditional technique with modulation of the azimuth of the plane of light polarization [4]. The instrument sensitivity to variations in the angle Φ was ~0.001°, and the relative measurement error was ~5%.

In order to investigate the coordinate dependence of the magnetic linear birefringence, laser radiation was focused onto a spot ~15 μm in diameter on the surface of the sample with the use of a microscope. Taking into account that the spatial period of the magnetic inhomogeneity in the $FeBO_3$: Mg ferromagnetic crystal is approximately equal to 100 μm [1] and assuming that, within the light spot, $\varphi(x, y) \approx$ const, the surface under examination can be considered a point. In our experiments, the cryostat with a sample could be displaced along two coordinates in the focal plane of the microscope. This made it possible to measure the magnetic linear birefringence at a specified point on the basal plane of the crystal and to visually observe the magnetic state of the crystal under the microscope (with an additional source of white light).

3. EXPERIMENTAL RESULTS AND DISCUSSION

Figure 1 shows the integral field dependences (i.e., the dependences measured under illumination of the whole surface of the sample) of the magnetic linear birefringence observed under conditions where the vector **H** in the basal plane of the $FeBO_3$: Mg ferromagnetic crystal was oriented parallel and perpendicular to one of the C_2 axes and the azimuthal angle of the polarizer was θ = 45°. (Since the effect has different signs for these two directions of the magnetization, Fig. 1 presents the field dependences of the magnetic linear birefringence in the form of $|\Phi|(H)$ for convenience of comparison.) It can be seen from Fig. 1 that, under conditions of technical saturation of the magnetization, the values of $|\Phi|$ along the above two directions coincide in accordance with relationships (1) but the curves $|\Phi|(H)$ differ significantly in the range of magnetic fields ($3 \le H \le 17$ Oe for $\mathbf{H} \perp C_2$ [1]) corresponding to the inhomogeneous magnetic state of the crystal. In particular, the quantity $|\Phi|$ for the orientation $\mathbf{H} \parallel C_2$ reaches its maximum in a magnetic field $H \approx 3$ Oe, whereas the

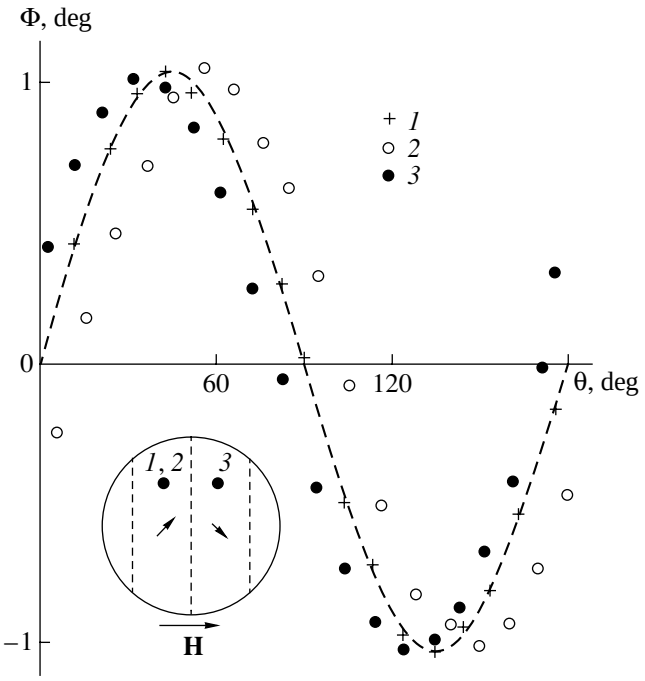

Fig. 2. Dependence of the magnetic linear birefringence of the $FeBO_3$: Mg ferromagnetic crystal on the azimuthal angle between the plane of light polarization and the direction of the applied magnetic field ($\mathbf{H} \perp C_2$). Magnetic field H: (*1*) 30 and (*2*, *3*) 6 Oe. The dashed line represents the dependence $\Phi \propto \sin 2\theta$, and the points are the experimental data. The inset schematically shows the magnetic inhomogeneity of the $FeBO_3$: Mg crystal: the dashed lines represent the boundaries of the light and dark fringes, which are visually observed on the image of the crystal in polarized light; the arrows inside the circle indicate the orientation of the local ferromagnetic moment at the center of the neighboring fringes; the points denoted by numerals are the positions of the light spots on the surface of the crystal at which the experimental dependences $\Phi(\theta)$ designated by the corresponding numerals were measured; and the arrow outside the circle indicates the direction of magnetization.

dependence $|\Phi|(H)$ obtained for the orientation $\mathbf{H} \perp C_2$ attains saturation considerably slower. It seems likely that this behavior is associated with the influence of magnetic inhomogeneities arising in the $FeBO_3$: Mg crystal on the process of magnetization along the hard magnetic axis. It should be noted that, within the limits of experimental error, the curve $|\Phi|(H)$ measured at room temperature does not depend on the orientation of the vector **H** in the basal plane of the crystal over the entire range of magnetic fields studied.

Figure 2 presents the local orientation dependences (the light is focused at different points on the crystal surface) of the magnetic linear birefringence of the $FeBO_3$: Mg ferromagnetic crystal for two values of the magnetic field ($\mathbf{H} \perp C_2$): (i) in a magnetic field $H_1 = 6$ Oe, in which the inhomogeneous magnetic state is observed in the crystal, and (ii) in a magnetic field $H_2 = 30$ Oe, in which the ferromagnetic moment is known to be homogeneous and lies in the basal plane aligned parallel to

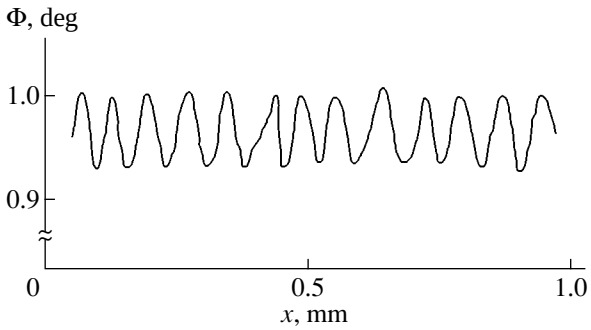

Fig. 3. Coordinate dependence of the magnetic linear birefringence of the $FeBO_3$: Mg ferromagnetic crystal upon scanning of the crystal surface by a focused laser beam along the direction of the applied magnetic field ($H = 6$ Oe, $\mathbf{H} \perp C_2$). The scanning velocity is approximately equal to 2 mm/min.

the axis of magnetization (perpendicular to the C_2 axis). It can be seen from this figure that the experimental dependences $\Phi(\theta)$ are adequately described by harmonic functions of the angle 2θ with an amplitude that is virtually independent of the magnetic field strength. This suggests that, in the inhomogeneous magnetic state, the magnetization of the crystal is homogeneous throughout the crystal thickness and the vector **m** does not deviate from the basal plane. It follows from relationships (1) that, in this case [at $\varphi(z) = \text{const}$], the dependences $\Phi(\theta)$ are characterized by the extreme values $\Phi = \pm A_0$ at the point (x, y) for $\theta = \varphi \pm 45°$. This condition allows one to determine the angle φ directly from the dependences $\Phi(\theta)$ shown in Fig. 2, i.e., to determine the azimuth of the vector **m** at specified points of the crystal surface. Recall that the points on the surface of the crystal in the measurements of the magnetic linear birefringence were chosen at the center of neighboring fringes of different magneto-optical contrasts that were observed visually with a microscope. Therefore, it can be concluded that, in the inhomogeneous magnetic state of the $FeBO_3$: Mg crystal, the angle of deviation of the vector **m** from the direction of magnetization in the magnetic field $H = 6$ Oe is approximately equal to 10°.

In order to reconstruct the spatial distribution of the vector **m** in the inhomogeneous magnetic state of the crystal, we analyze the coordinate dependence of the magnetic linear birefringence (Fig. 3) obtained by scanning the crystal surface with a focused laser beam along the direction of the applied magnetic field **H** ($H = 6$ Oe, $\mathbf{H} \perp C_2$, $\theta = 45°$).[2] It can be seen that the dependence $\Phi(x)$ exhibits an oscillatory behavior. The mean period of modulation of the magnetic linear birefringence is two times less than the spatial period of the system of light and dark fringes visually observed on the image of the sample in polarized light (see [1]). Hence, it follows from relationships (1) that the azimuth of the local fer-

[2] The scanning of the crystal surface in the direction perpendicular to the magnetic field **H** demonstrated that $\Phi(y) \approx \text{const}$.

romagnetic vector in the inhomogeneous magnetic state of the $FeBO_3$: Mg crystal can be approximately described by the relationship

$$\varphi = \varphi_0 \cos(2\pi x/D),$$

where φ_0 is the amplitude of the deviation of the vector **m** from the axis of magnetization and D is the period of the magnetic inhomogeneity.

4. CONCLUSIONS

Thus, the above investigation has confirmed the assumption made in [1] that, in the inhomogeneous magnetic state of the $FeBO_3$: Mg crystal, the local vector **m** does not deviate (as in the homogeneous magnetic phase) from the basal plane and the azimuth of this vector is described by a periodic function of the spatial coordinate along the direction perpendicular to one of the C_2 axes.

REFERENCES

1. A. T. Karaev, B. Yu. Sokolov, and Yu. M. Fedorov, Fiz. Tverd. Tela (St. Petersburg) **42**, 2036 (2000) [Phys. Solid State **42**, 2097 (2000)].
2. G. A. Smolenskiĭ, R. V. Pisarev, and I. G. Siniĭ, Usp. Fiz. Nauk **116** (2), 231 (1975) [Sov. Phys. Usp. **18**, 410 (1975)].
3. Yu. M. Fedorov, O. V. Vorotynova, and A. A. Leksikov, Fiz. Tverd. Tela (Leningrad) **31** (5), 192 (1989) [Sov. Phys. Solid State **31**, 829 (1989)].
4. J. Ferre and G. A. Gehring, Rep. Prog. Phys. **47**, 531 (1984).

Translated by O. Moskalev

Physics of the Solid State, Vol. 47, No. 2, 2005, pp. 267–271. Translated from Fizika Tverdogo Tela, Vol. 47, No. 2, 2005, pp. 255–259.

MAGNETISM AND FERROELECTRICITY

Domain Structure and Charge Ordering in a Layered Manganite $La_{1.2}Sr_{1.8}Mn_2O_7$ Crystal

S. F. Dubinin*, V. E. Arkhipov*, S. G. Teploukhov*, V. D. Parkhomenko*, Ya. M. Mukovskiĭ, and É. A. Neĭfel'd****

**Institute of Metal Physics, Ural Division, Russian Academy of Science, ul. S. Kovalevskoĭ 18, Yekaterinburg, 620219 Russia*
e-mail: dubinin@uraltc.ru

***Moscow State Institute of Steel and Alloys, Leninskiĭ pr. 4, Moscow, 117935 Russia*

Received April 26, 2004

Abstract—Charge ordering in a layered manganite $La_{1.2}Sr_{1.8}Mn_2O_7$ crystal with structural domains was studied using neutron diffraction in the temperature range 175–700 K. The wave vector of the charge ordering in the crystal is found to be $q \cong \{0.2, 0, 0\}2\pi/a$. It is argued that the actual domain structure of the anisotropic crystal affects its charge-ordering state. © *2005 Pleiades Publishing, Inc.*

A significant part of the interest in studying manganites of the type

$$(La, Sr)_{n+1}Mn_nO_{3n+1} \quad (1)$$

stems from the wide variety of charge-ordering states that occur in these compounds [1]. The charge ordering is typical of many strongly correlated systems where the interaction energy between electrons exceeds their kinetic energy. In the present paper, we concentrate on the influence of the actual macroscopic structure (domain structure) of compounds (1) on their charge-ordering state.

Let us start from what we consider a very typical example. Charge ordering in manganite crystals $La_{1-x}Sr_xMnO_3$ (corresponding to $n \longrightarrow \infty$ in (1); x = 0.1, 0.15) was studied in [2] by means of neutron diffraction. The most remarkable observation in [2] was that the charge ordering in the crystals under study manifested itself in the diffraction patterns as a well-developed superstructure. The superstructure was specified by the set of wave vectors

$$\mathbf{q}_1 = (0, 0, 1/2) \quad \text{in the } a^*c^* \text{ plane of the orthorhombic reciprocal lattice;}$$
$$\mathbf{q}_2 = (1/4, 1/4, 0) \quad \text{in the } a^*b^* \text{ plane of the orthorhombic reciprocal lattice.} \quad (2)$$

The magnetic and atomic structure of a $La_{0.85}Sr_{0.15}MnO_3$ crystal were also studied in detail in [3, 4], but no superstructure peaks of type (2) were observed in those studies. Wide and weak maxima of type (2) were found in [3] only in experiments with a powerful x-ray synchrotron source. In [4], it was argued that the charge ordering in $La_{0.85}Sr_{0.15}MnO_3$ manganite was specified by the wave vectors

$$\mathbf{q}_1 = (0, 0, 1) \quad \text{in the } a^*c^* \text{ plane;}$$
$$\mathbf{q}_2 = (1/2, 1/2, 0) \quad \text{in the } a^*b^* \text{ plane.} \quad (3)$$

In our opinion, the drastic difference in the results of the experiments reported in [2] and [3, 4] is due to the different domain structures of the crystals studied in those papers.

For example, the diffraction measurements in [4] were performed using a relatively perfect $La_{0.85}Sr_{0.15}MnO_3$ crystal, whereas the experiments in [2] involved La–Sr crystals with a highly developed domain structure. In other words, a chaotic mosaic of structural twin domains randomly oriented with respect to the cubic perovskite lattice axes was produced during the growth of these crystals. Macroscopically, a domain crystal can be considered to be pseudocubic. In such a crystal, elastic strains must arise in the vicinity of domain walls due to the mismatch between the lattice parameters of neighboring regions, and it is these strains that determine the metastable crystal structure of an individual domain. It is natural to assume that the increase in the elastic energy of a manganite crystal caused by the domain structure can be partially compensated for (due to the strong electron–lattice interaction) by a suitable change in the charge ordering. We suggest that this was the case in [2].

In the present work, we concentrate on the possible relation between the domain structure and charge (polaron) state of strongly anisotropic (layered) manganite $La_{1.2}Sr_{1.8}Mn_2O_7$ [corresponding to n = 2 in (1)]. The atomic and magnetic structure of this manganite has been studied reasonably well (see, e.g., [5, 6]). It will be recalled that the crystal lattice of $La_{1.2}Sr_{1.8}Mn_2O_7$ has a body-centered tetragonal unit cell (space group $I4/mmm$) with lattice parameters $a \cong$ 3.87 Å and $c \cong$ 20.14 Å. The unit cell can be considered to consist of several parallel layers: on the top and at the bottom, the cell has MnO_2 layers, and in the central part there are two $LaMnO_3$ layers separated by $(La, Sr)_2O_2$ layers from the layers of MnO_2.

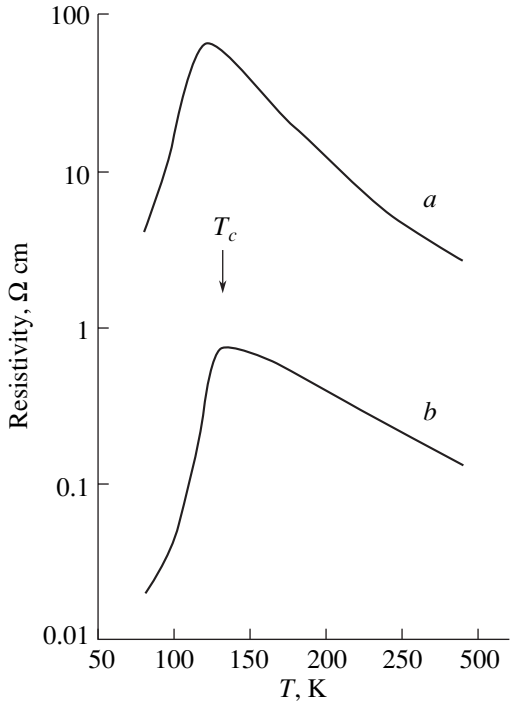

Fig. 1. Temperature dependences of the resistivity of the $La_{1.2}Sr_{1.8}Mn_2O_7$ crystal (*a*) along the *c* direction and (*b*) in the *ab* plane.

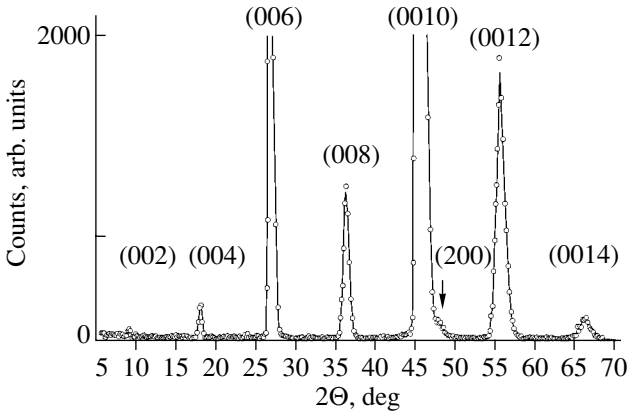

Fig. 2. Neutron diffraction pattern of the manganite $La_{1.2}Sr_{1.8}Mn_2O_7$ crystal taken at 300 K along the *c** direction.

For our experiment, we chose an $La_{1.2}Sr_{1.8}Mn_2O_7$ crystal grown by zone smelting. Thermal-neutron diffraction measurements were performed using a multichannel diffractometer specifically designed for studying single crystals. The wavelength of the incident neutron beam λ was 1.567 Å and was defined by a double-crystal monochromator made of pyrolytic graphite and strained germanium. The effective monochromatization of the primary beam and a well-advised choice of the wavelength of monochromatic neutrons enabled us to eliminate multiple harmonics in the diffraction patterns of the single crystal.

The temperature dependences of electrical resistivity in the *ab* plane and along the *c* axis are very characteristic physical properties of layered manganites. The data for our crystal are presented in Fig. 1. They agree well with analogous data from [5]. It can be seen from Fig. 1 that the resistivity is strongly anisotropic relative to the specific [001] direction in the manganite lattice. It is well known that, in terms of the electronic state, the maxima of $\rho_c(T)$ and $\rho_{ab}(T)$ correspond to the metal–insulator transition and in terms of the magnetic state, to the ferromagnetic Curie point T_C of manganite $La_{1.2}Sr_{1.8}Mn_2O_7$. The value of T_C of our crystal is 125 K, which agrees well with the data from [5] but is somewhat higher than the T_C value of 112 K found for the LaSr-manganite studied in [6]. In our opinion, this means that the layered manganites studied in those papers have almost the same chemical composition:

$$La_{2-2x}Sr_{1+2x}Mn_2O_7 \quad (x \cong 0.4). \tag{4}$$

The value of *x* in Eq. (4) means that about 40% of the Mn sites of the manganite crystal lattice are occupied by Mn^{4+} ions.

Before discussing the charge-ordering state, we will analyze the domain structure of our crystal. We obtained structural information from neutron diffraction data. Figure 2 presents the neutron diffraction pattern for the manganite crystal recorded along the *c** direction at 300 K. It can be seen that, in addition to Bragg reflections (0, 0, 2*n*) (*n* = 1, 2, 3, …) corresponding to the longer period of the layered manganite (*c* = 20.14 Å), the pattern shows a structural (200) peak corresponding to the lattice constant *a* = 3.87 Å. The intensity of the (200) reflection reaches a maximum at a deviation of approximately 1° from the [001] direction on the rocking curve of the crystal. The occurrence of the (200) reflection (seen in Fig. 2) supports the presence of structural domains in the manganite crystal. The orientation of the structural domains relative to the bulk crystal lattice follows unambiguously from the diffraction pattern presented in Fig. 3. The open circles in Fig. 3 show a neutron diffraction pattern from the layered manganite recorded near the (200) Bragg reflection along the *a** direction at 300 K. Alongside the main structural (200) reflection, this pattern exhibits a weak (0, 0, 10) reflection, the intensity of which reaches a maximum at a deviation of approximately 1° from the symmetry direction on the rocking curve of the crystal (as in the case shown in Fig. 2). Hence, the orientation relations of the structural domains (*d*) relative to the main part (*m*) of the anisotropic crystal can be written as

$$[100]_d \parallel [001]_m, \quad [001]_d \parallel [100]_m. \tag{5}$$

It follows from Eq. (5) that the structural domains found in crystal (4) are not twinned. The volume fraction (ν) of these domains in a sample can be estimated, for example, from the relative intensity $I\{(200)_d\}/I\{(0,$

$0, 10)_m\} = \nu F^2(200)/(1-\nu)F^2(0, 0, 10)$, where $F^2(200)$ and $F^2(0, 0, 10)$ are the respective structure factors. In our case, ν is about 5%.

The presence of the relatively small fraction of structural domains in the layered crystal has virtually no effect on $\rho_c(T)$ and $\rho_{ab}(T)$ in Fig. 1 in comparison with the resistivity data cited in [5]. We believe that structural domains (5) should exert a significant effect on the mechanical properties of $La_{1.2}Sr_{1.8}Mn_2O_7$; more specifically, they should reduce its strength. The physical reason for this reduction in strength is the presence of boundaries between domains and the main lattice, which have different lattice constants and atomic packing densities. Indeed, it is well known that, due to high local strains, atomic bonds in such regions of the crystal structure of solids can be broken the most easily, with the result that the continuousness of a crystal is disturbed. The growth and merging of the disturbances can lead to macroscopic cracks. The sample for our studies was chosen on this basis.

Let us consider now the physical factors that, in our opinion, stabilize the crystal structure of a layered crystal containing structural domains (5). We are concerned now with the data describing the charge ordering in layered manganite. According to [6], the charge (polaron) ordering in manganites (4) exists only in the paramagnetic phase and its influence on diffraction patterns is the strongest just above T_C and then gradually decreases as the temperature is increased. Charge (polaron) correlations have an effect on neutron diffraction patterns of the crystal because the Mn^{4+} ion does not distort the oxygen octahedron around it (this ion has no orbital angular momentum), whereas the Jahn–Teller ion Mn^{3+} strongly deforms the unit cell due to the interaction of the ionic $d(z^2)$ orbital with the lattice.

The results from [6] that are of special interest to us are the following: the charge ordering in the layered manganite corresponds to the wave vector

$$q = (0.3, 0, 1) \qquad (6)$$

(in units of $2\pi/a$ and $2\pi/c$), and the correlation length for this ordering in the [100] direction is $\xi \cong 26.4$ Å.

In the present work, the charge ordering is also studied in the paramagnetic phase of multidomain crystal (4). In Fig. 3, filled circles show neutron diffraction data taken from layered manganite near the (200) Bragg reflection along the a^* direction at 175 K. It can be seen that there are two diffraction maxima, (1.8, 0, 0) and (2.2, 0, 0), to the left and to the right of the structural (200) reflection. These maxima decrease slowly in intensity with increasing temperature and vanish completely at about 550 K. For comparison, the open circles in Fig. 3 show diffraction data taken at 300 K. The positions of the maxima in the reciprocal lattice are given with a higher precision in Fig. 4, which presents diffraction data for the multidomain crystal taken at 300 K near the (1.8, 0, 0) and (2.2, 0, 0) points of the reciprocal lattice along the c^* direction. It can be seen that the wave vector of the superstructural reflections has a

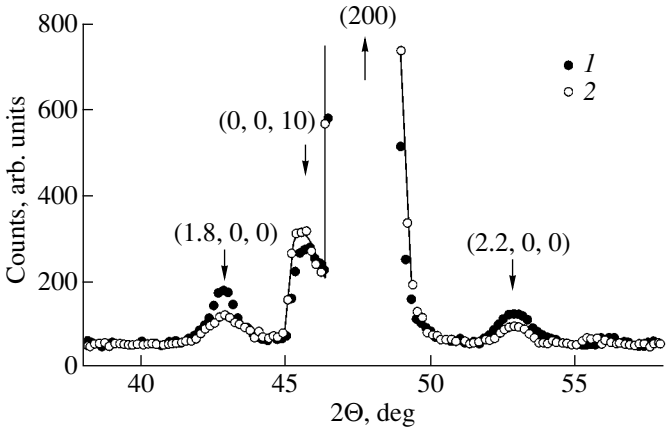

Fig. 3. Neutron diffraction patterns of multidomain crystal $La_{1.2}Sr_{1.8}Mn_2O_7$ taken near the (200) Bragg reflection along the a^* direction at (*1*) 175 and (*2*) 300 K.

small ($\cong 0.2\pi/c$) incommensurate component along the [001] direction. The wave vector (without the incommensurate correction) and the correlation length of the superstructure measured along the [100] direction in the multidomain crystal are

$$q \cong (0.2, 0, 0)2\pi/a;$$
$$\xi \sim 100 \text{ Å} \quad \text{along the [100] direction.} \qquad (7)$$

We believe that superstructure (7) can be associated only with charge ordering in the multidomain layered manganite, because the antiferromagnetic short-range order, which also exists in $La_{1.2}Sr_{1.8}Mn_2O_7$ above T_C [5], corresponds to the wave vector $(0.5, 0, 0)2\pi/a$. According to (7), the charge-ordering period in the [100] direction is five times the lattice constant a; i.e., it is equal to 19.4 Å. Taking into account the chemical composition of the compound ($x = 0.4$), we can conclude that two out of the five manganese ions situated along the long period of the superstructure unit cell are tetravalent.

Thus, the main charge-ordering parameters in the multidomain layered manganite given by Eq. (7) differ significantly from those in Eq. (6). The reason for this difference could be the charge density gradients appearing at the boundaries between the main lattice and structural domains. In this case, the type of equilibrium charge ordering in a particular multidomain crystal is determined by the condition that the charge density gradient be minimum. If, for example, the parameters of charge correlations in a $La_{1.2}Sr_{1.8}Mn_2O_7$ crystal with domains of type (5) are given by Eq. (6), then the periods of charge correlations in the $[100]_m$ direction near the boundaries between the main lattice and domains would be incommensurate and equal to $a/0.3 = 3.3a = 12.8$ Å and $c = 20.14$ Å, respectively. It is clear that strong charge density gradients would appear in this case.

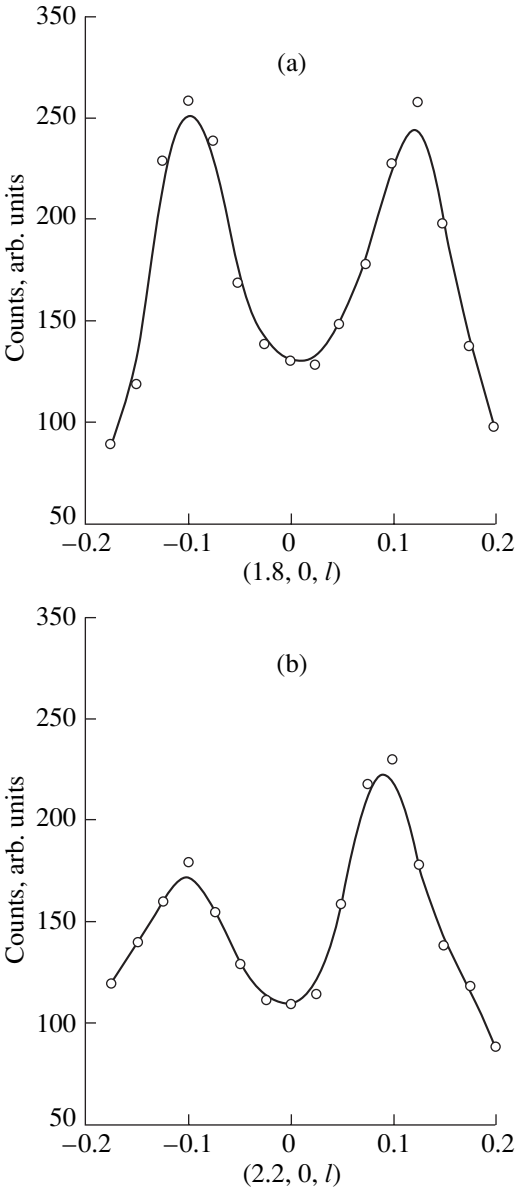

Fig. 4. Neutron diffraction patterns of multidomain manganite crystal $La_{1.2}Sr_{1.8}Mn_2O_7$ taken along the n^* direction at 300 K near the (*a*) (1.8, 0, 0) and (*b*) (2.2, 0, 0) points of the reciprocal lattice.

In contrast to the case of Eq. (6), the periods of charge correlations along $[100]_m$ and $[001]_m$ defined by Eq. (7) are similar ($a/0.2 = 19.4$ Å $\cong c = 20.14$ Å), so there should not be any strong charge density gradients in our crystal. Therefore, this type of charge ordering in the multidomain crystal can be a factor that stabilizes the crystal structure.

Experimental data (Fig. 5) give evidence that supports this conclusion. Figure 5 presents profiles of the (200) and (006) structural reflections in neutron diffraction patterns of multidomain crystal $La_{1.2}Sr_{1.8}Mn_2O_7$ taken at three characteristic temperatures: 175, 300, and 700 K. It can be seen that the profile of the (006) reflection does not change in this temperature range, whereas the (200) reflection is significantly altered. Even at 300 K, the half-width of the latter reflection shows an increase of 10% as compared to that at 175 K. We note that this effect is reversible in temperature; therefore, the strains arising in the multidomain crystal at 300 K are elastic. At 700 K, there are no charge correlations and the periodicity of the crystal along the [100] direction is strongly disturbed. The (200) reflection transforms into a wide diffuse maximum. This effect can only be due to anisotropic fragmentation of the crystal in the *ab* plane into large blocks, each of which is disoriented relative to the incident neutron beam. Readjustment of the sample and repeated heating to 700 K leads to further deterioration of the sample quality.

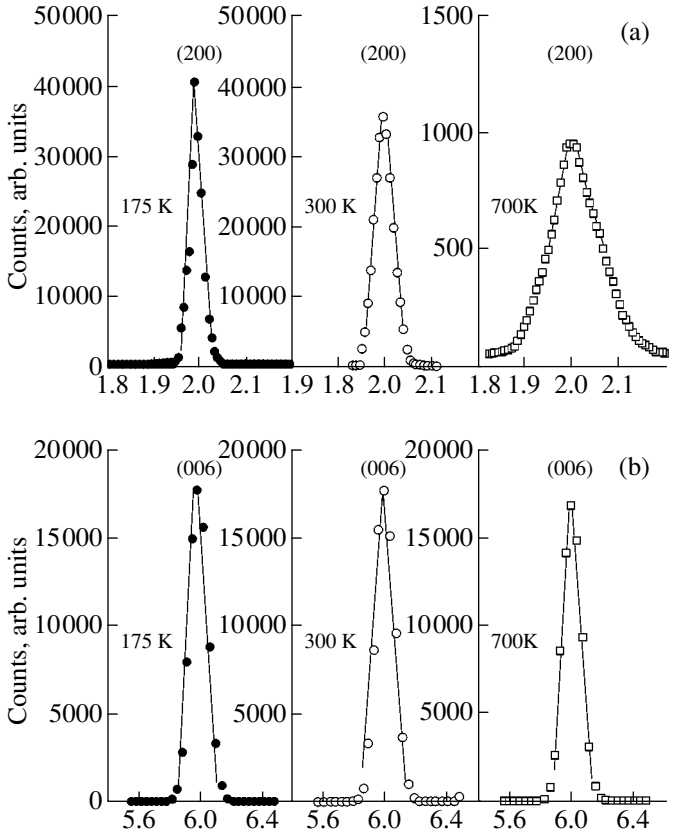

Fig. 5. Bragg reflections (a) (200) and (b) (006) in neutron diffraction patterns of multidomain crystal $La_{1.2}Sr_{1.8}Mn_2O_7$ taken along the scattering vector at 175, 300, and 700 K.

To conclude, in the present work, a new question has been raised regarding the relation between the macroscopic structure and charge ordering in solid solutions of manganites of type (1).

ACKNOWLEDGMENTS

This work was supported by the Ministry of Industry, Science, and Technology of the Russian Federation (project no. 40.012.1.1.1150), the Department of Phys-

ical Sciences of the RAS (program "Neutron Study of Material Structure and Basic Properties of Matter"), the federal program of support for leading scientific schools (project no. NSh-639.2003.2), and the Russian Foundation for Basic Research (project no. 02-02-16425).

REFERENCES

1. M. Yu. Kagan and K. I. Kugel', Usp. Fiz. Nauk **171**, 577 (2001) [Phys. Usp. **44**, 553 (2001)].
2. Y. Yamada, O. Hino, S. Nohdo, R. Kanao, T. Inami, and S. Katano, Phys. Rev. Lett. **77** (5), 904 (1996).
3. L. Vasiliu-Doloc, J. W. Lynn, A. H. Moudden, A. M. Leon-Gueravra, and A. Revcolevschi, Phys. Rev. B **58** (22), 14913 (1998).
4. S. F. Dubinin, V. E. Arkhipov, S. G. Teploukhov, and Ya. M. Mukovskiĭ, Fiz. Tverd. Tela (St. Petersburg) **45** (1), 113 (2003) [Phys. Solid State **45**, 118 (2003)].
5. T. G. Perring, G. Aeppli, Y. Moritomo, and Y. Tokura, Phys. Rev. Lett. **78** (16), 3197 (1997).
6. L. Vasiliu-Doloc, S. Rosenkranz, R. Osborn, S. K. Sinha, J. W. Lynn, J. Mesot, O. H. Seeck, G. Preosti, A. J. Fedro, and J. F. Mitchell, Phys. Rev. Lett. **83** (21), 4393 (1999).

Translated by G. Tsydynzhapov

Physics of the Solid State, Vol. 47, No. 2, 2005, pp. 272–280. Translated from Fizika Tverdogo Tela, Vol. 47, No. 2, 2005, pp. 260–267.

MAGNETISM AND FERROELECTRICITY

Dependence of the Magnetization Relaxation Time of Single-Domain Ferromagnetic Particles on Damping in the Brown Model

Yu. P. Kalmykov*, W. T. Coffey, and S. V. Titov*****

** Laboratoire Mathématiques et Physique pour les Systémes, Université de Perpignan, Perpignan Cedex, 66860 France*
e-mail: kalmykov@univ-perp.fr

*** Department of Electronic and Electrical Engineering, Trinity College, Dublin 2, Ireland*
e-mail: wcoffey@mee.tcd.ie

**** Institute of Radio Engineering and Electronics, Russian Academy of Science, pl. Vvedenskogo 1, Fryazino, Moscow oblast, 141190 Russia*
e-mail: svt245@ire216.msk.su

Received January 20, 2004; in final form, April 27, 2004

Abstract—Analytical expressions for the magnetization relaxation time τ of single-domain ferromagnetic particles with cubic or uniaxial anisotropy in a static transverse magnetic field are derived. The derivation is based on calculating the escape rate of a Brownian particle from a potential well; this technique is applicable at any damping and is generalized to the case of magnetic relaxation of superparamagnetic particles. The validity of the expressions obtained for τ is checked against a numerical solution of the Landau–Lifshitz–Gilbert equation over the whole range of damping (very low, intermediate, and high damping and the crossover region between low and intermediate damping). © *2005 Pleiades Publishing, Inc.*

1. INTRODUCTION

In order to achieve maximum density of magnetic recording, the size of magnetic particles (which carry bits of information) has to be reduced as much as possible. However, as the particle size decreases to several nanometers, thermal fluctuations start to affect the magnetic properties of particles [1]. It is the thermal fluctuations that determine the magnetization relaxation time of a nanoparticle and, consequently, influence the information storage reliability. Thermal instability of magnetization leads to the phenomenon of superparamagnetism [1–3], since each particle behaves like a paramagnetic atom possessing a magnetic moment of the order of ~10^4–10^5 Bohr magnetons. The dynamics of magnetization **M** of superparamagnetic particles is similar to Brownian rotation of a macromolecule in liquid and can be described (in terms of the Brown diffusion model [3, 4]) by the Fokker–Planck equation for the magnetization distribution function $W(\mathbf{M}, t)$:

$$\frac{\partial}{\partial t}W = L_{\mathrm{FP}}W = \frac{1}{2\tau_N}\{\beta[\alpha^{-1}\mathbf{u}\cdot(\nabla V\times\nabla W) + \nabla\cdot(W\nabla V)] + \Delta W\}. \quad (1)$$

Here, L_{FP} is the Fokker–Planck operator; Δ and ∇ are the Laplacian and gradient operators, respectively, on the surface of a unit sphere; V is the free-energy density of the particle; **u** is a unit vector parallel to the magnetization vector **M**; $\beta = v/kT$, v is the volume of the particle; k is the Boltzmann constant; T is the temperature;

$$\tau_N = \beta M_S(1+\alpha^2)/(2\gamma\alpha) \quad (2)$$

is the characteristic (diffusion) time; M_S is the magnetization of the particle; $\alpha = \gamma\eta M_S$ is the dimensionless damping factor characterizing the intensity of thermal fluctuations; γ is the gyromagnetic ratio; and η is the constant of friction. The Fokker–Planck equation (1) can be derived either from the Landau–Lifshitz equation [5] or from the analogous Gilbert equation [6] with a fluctuating field $\mathbf{h}(t)$, which takes into account thermal fluctuations of the magnetization of a single particle (the Langevin equation):

$$\dot{\mathbf{M}}(t) = \gamma\{\mathbf{M}(t)\times[\mathbf{H}(t) + \mathbf{h}(t) - \eta\dot{\mathbf{M}}(t)]\}, \quad (3)$$

where the magnetic field $\mathbf{H} = -\partial V/\partial\mathbf{M}$ includes the external and magnetic anisotropy fields. In order of magnitude, the amplitude of $\mathbf{h}(t)$ can be estimated to be $(\beta M_S)^{-1}$, which is ≥100 Oe at room temperature (so the random field is comparable to the anisotropy field) [7]. In deriving Eq. (1), it was assumed that the magnetization **M** is always uniform and that only its direction, and not its magnitude, changed; Furthermore, the interparticle interaction and memory effects were neglected. A detailed discussion of the range of validity of the Fokker–Planck (1) and Gilbert (3) equations can be found, for example, in [4, 7–9].

To estimate the magnetization relaxation time, Brown [3, 4] generalized the Kramers method [10] for calculating the escape rate Γ of a Brownian particle from a potential well with barrier height ΔU:

$$\Gamma = A\frac{\omega_a}{2\pi}e^{-\Delta U/kT}, \quad (4)$$

where ω_a is the cyclic frequency of oscillatory motion of the Brownian particle at the bottom of the potential well [11, 12] and the factor A characterizes the energy exchange between the particle and environment. The central part of the Kramers method is the calculation of the factor A in Eq. (4) for various dissipation conditions, namely, weak, strong, or moderate dissipation. Kramers [10] derived expressions for the escape rate of a Brownian particle from a potential well for intermediate-to-high and very low damping under the assumption that, in both cases, the potential-barrier height ΔU is much greater than the thermal energy. However, he was not able to obtain an expression that was valid over the whole range of variation of the damping parameter. This problem was solved later by Mel'nikov and Meshkov [13, 14], who derived a universal expression for Γ. Their approach is to transform the Fokker–Planck equation into the integral Wiener–Hopf equation by passing over to new variables (energy and action). The energy distribution function is taken at a given value of action S, which in this case is considered a free parameter. Then, the Wiener–Hopf equation is solved explicitly. The solution found allows one to calculate the escape rate Γ over the entire range of values of the dissipation parameter [13, 14].

In his first paper [3], Brown used the Kramers approach to calculate the relaxation time $\tau \sim \Gamma^{-1}$ of the longitudinal magnetization M_Z and limited himself to the case of an axially symmetric potential of magnetocrystalline anisotropy. In this case, the longitudinal and transverse modes of **M** rotation can be considered independently. The longitudinal modes are characterized only by the polar angle ϑ (the azimuthal angle φ describes precession of **M**), and the probability density function W depends only on ϑ. This is the only case where the Kramers theory [10] (developed for a classical Brownian particle in the strong dissipation limit) can be used to calculate τ for all values of the damping factor α. It should be noted, however, that the Fokker–Planck equation for the probability density function W of the M_Z distribution becomes one-dimensional due to the axial symmetry of the free energy V and not because of high damping, as in the case of a Brownian particle. If the free energy density $V(\vartheta, \varphi)$ is not axially symmetric, the calculation of the reorientation rate of the superparamagnetic-particle magnetization **M** differs in several important points from the calculation of the escape rate of a classical Brownian particle. First, the free energy of the magnetic particle has two degrees of freedom, ϑ and φ, and in general these variables cannot be separated. Second, the magnetization of the particle has no inertia, and the magnetization dynamics equation contains a gyromagnetic term. It is the gyromagnetic term that mixes the longitudinal and transverse modes in the case where the symmetry of the free energy is nonaxial. Similar to the situation with a classical Brownian particle, three distinct ranges of α can be considered in this case [12]:

(i) $\alpha \geq 1$, intermediate-to-high damping (IHD). In this case, the distribution function inside the potential well almost coincides with the equilibrium Boltzmann distribution. There are only small deviations at the barrier energy due to the particle leak over the barrier.

(ii) $\alpha \ll 1$, very low damping (VLD). In this case, the Fokker–Planck equation (1) can be transformed into new variables, namely, action (slow variable) and angle (fast variable), and then the distribution function can be averaged over the fast variable along the precession trajectory inside the potential well.

(iii) $0.01 < \alpha \leq 1$, crossover region. In this case, the expressions derived for low damping and intermediate-to-high damping are inapplicable. In particular, unlike the low-damping case, it is impossible here to average over the fast variable.

An analytical expression for the reorientation rate Γ of the particle magnetization in the case of intermediate-to-high damping ($\alpha \geq 1$) has been derived by Smith and de Rozario [15] and Brown [4]. An expression for the case of very low damping ($\alpha \ll 1$) has been obtained by Klik and Gunther [9]. (It should be noted that the method for calculating Γ in the IHD range [4, 15] is a special case of the Langer theory developed for calculating the temporal characteristics of the relaxation processes in metastable states of a system with many degrees of freedom [16]). In [12, 17], the Mel'nikov–Meshkov method [13] was generalized for calculating the reorientation rate Γ of the particle magnetization in the crossover region $0.01 < \alpha < 1$. The method developed in [12, 17] allows one to calculate Γ over the whole range of values of the damping factor α. In the present paper, this method is applied to two particular cases: cubic anisotropy and uniaxial anisotropy in the presence of a transverse magnetic field [12, 17]. In these cases, the free energy V describes equivalent metastable states, which greatly simplifies calculations (the case of nonequivalent states will be considered in a future publication). The relaxation times for similar systems in the IHD and VLD ranges were calculated, for example, in [4, 9, 15, 18, 19]. However, according to experimental and theoretical estimations, actual values of the damping factor α lie in the crossover region 0.01–0.1 (see, e.g., [8, 9, 20, 21]). In this region, as was already mentioned, neither IHD nor VLD expressions are applicable for obtaining quantitative results [22, 23]. In the present paper, we derive expressions for the magnetization relaxation time that are valid throughout the range of α. The accuracy of the formulas obtained is demonstrated by comparing the results with a numerical solution to the Fokker–Planck equation (1).

2. BASIC RELATIONS

Let us suppose that the free energy density $V(\mathbf{M})$ of a single-domain ferromagnetic particle has minima in the directions $\mathbf{n}_i$ and $\mathbf{n}_j$, separated by a potential barrier with a saddle point in the direction $\mathbf{n}_0$; the barrier is assumed to be much higher than the thermal energy. We introduce the directional cosines of the vector $\mathbf{M}$

$$u_1^{(k)} = \sin\vartheta_k\cos\varphi_k, \quad u_2^{(k)} = \sin\vartheta_k\sin\varphi_k,$$
$$u_3^{(k)} = \cos\vartheta_k$$

in a coordinate frame with its origin at the stationary point k ($k = 0, i, j$) and with the z axis normal to the $V(\mathbf{M})$ surface. At the point $\mathbf{n}_k$, the function $V(\mathbf{M})$ can be expanded into a Taylor series in $u_1^{(k)}$ and $u_2^{(k)}$. Up to second-order terms, the series is given [4, 24] by

$$V = V_k + \frac{1}{2}[c_1^{(k)}(u_1^{(k)})^2 + c_2^{(k)}(u_2^{(k)})^2],$$
$$c_1^{(k)} = \frac{\partial^2 V}{\partial u_1^{(k)2}}, \quad c_2^{(k)} = \frac{\partial^2 V}{\partial u_2^{(k)2}}. \tag{5}$$

Substituting Eq. (5) into Eq. (1), we can solve the Fokker–Planck equation in the vicinity of the saddle point [4]. The solution allows us to calculate the escape rate $\Gamma_{ij}^{\mathrm{IHD}}$ from the i-th potential well in the case of intermediate-to-high damping [4, 12, 24]:

$$\Gamma_{ij}^{\mathrm{IHD}} \sim \frac{\Omega_0\omega_i}{2\pi\omega_0}e^{-\beta(V_0 - V_i)}, \tag{6}$$

where $\omega_i = (\gamma/M_S)\sqrt{c_1^{(i)}c_2^{(i)}}$ and $\omega_0 = (\gamma/M_S)\sqrt{-c_1^{(0)}c_2^{(0)}}$ are the cyclic frequencies of librations of $\mathbf{M}$ at the bottom of the well and at the saddle point, respectively, and

$$\Omega_0 = \frac{\beta}{4\tau_N}[-c_1^{(0)} - c_2^{(0)}$$
$$+ \sqrt{(c_2^{(0)} - c_1^{(0)})^2 - 4\alpha^{-2}c_1^{(0)}c_2^{(0)}}].$$

For the case of very low damping ($\alpha \ll 1$, or, more precisely, $\alpha < 0.001$, according to the numerical calculations from [22, 23]), the escape rate from the i-th potential well $\Gamma_{ij}^{\mathrm{VLD}}$ was calculated in [9] (see also review [12]). The result is

$$\Gamma_{ij}^{\mathrm{VLD}} \sim \frac{\omega_i\alpha S_i}{2\pi}e^{-\beta(V_0 - V_i)}, \tag{7}$$

where S_i is the dimensionless action at the saddle point, which is defined by

$$S_i = \beta \oint_{V(\vartheta,\varphi) = V_0} \Big[(1 - \cos^2\vartheta)\frac{\partial}{\partial\cos\vartheta}V(\vartheta,\varphi)d\varphi$$
$$- (1 - \cos^2\vartheta)^{-1}\frac{\partial}{\partial\varphi}V(\vartheta,\varphi)d\cos\vartheta\Big]. \tag{8}$$

If there is only one saddle point, the contour integral in Eq. (8) is taken over a closed critical path $\vartheta(\varphi)|_{V = V_0}$, which passes through the saddle point and is defined by the equation $V(\vartheta, \varphi) = V_0$. If there are several equivalent saddle points, the critical path $\vartheta(\varphi)|_{V = V_0}$ connects two adjacent saddle points. By staying in the critical path $V(\vartheta, \varphi) = V_0$, the magnetization vector $\mathbf{M}$ can reach another metastable state.

For the crossover region ($0.01 < \alpha < 1$), the escape rate Γ_{ij} is given by [12 17]

$$\Gamma_{ij} = A(\alpha S_i)\Gamma_{ij}^{\mathrm{IHD}}, \tag{9}$$

where S_i is given by Eq. (8) and

$$A(\alpha S_i)$$
$$= \exp\left[\frac{1}{\pi}\int_0^\infty \frac{\ln[1 - \exp\{-\alpha S_i(\lambda^2 + 1/4)\}]}{\lambda^2 + 1/4}d\lambda\right]. \tag{10}$$

For Eq. (10), we have [13]

$$\lim_{\alpha\to\infty} A(\alpha S_i) = 1, \quad \lim_{\alpha\to 0} A(\alpha S_i)/\alpha = S_i. \tag{11}$$

Taking into consideration the limits in Eq. (11), we find that Eq. (9) reduces to Eqs. (6) and (7) in the IHD and VLD regions, respectively.

3. METHOD OF MATRIX CONTINUED FRACTIONS

Relation (9) can be used to estimate the longest relaxation time $\tau \sim \Gamma_{ij}^{-1}$. In turn, τ can be used to estimate the correlation time $\tau_\parallel$ of the equilibrium correlation function $C(t)$ of the longitudinal magnetization component, which is defined by

$$C(t) = \frac{\langle M_Z(0)M_Z(t)\rangle_0}{\langle M_Z^2(0)\rangle_0} = \frac{\langle\cos\vartheta(0)\cos\vartheta(t)\rangle_0}{\langle\cos^2\vartheta(0)\rangle_0} \tag{12}$$

where angle brackets denote the ensemble averaging. The correlation time $\tau_\parallel$ is given by [24]

$$\tau_\parallel = \int_0^\infty C(t)dt. \tag{13}$$

In other words, the correlation time is equal to the area under the $C(t)$ curve, which gives it another name, the

integrated relaxation time. The time $\tau_\parallel$ can also be expressed in terms of the eigenvalues λ_k of the Fokker–Planck operator L_{FP} from Eq. (1), because $C(t)$ can be formally expressed as a series of relaxation modes,

$$C(t) = \sum_k c_k e^{-\lambda_k t}. \quad (14)$$

Combining Eqs. (13) and (14), we get

$$\tau_\parallel = \sum_k c_k/\lambda_k, \quad (15)$$

where $\sum_k c_k = 1$. According to Eq. (15), the correlation time $\tau_\parallel$ depends on all the eigenvalues. The lowest eigenvalue, λ_1, characterizes reorientation of the magnetization **M** over potential barriers, and the other eigenvalues, λ_k ($k \neq 1$), correspond to high-frequency intrawell modes. In general, all λ_k and c_k are required to calculate $C(t)$ and $\tau_\parallel$. However, in the low-temperature limit, we have $\lambda_1 \ll \lambda_k$ and $c_1 \approx 1 \gg c_k$ ($k \neq 1$) (assuming that the potential wells are equal or almost equal). In this case, $1/\lambda_1$ is a good approximation to the correlation time $\tau_\parallel$.

To calculate the correlation time $\tau_\parallel$, the method of matrix continued fractions developed in [25–27] can be employed. In this method, the Fokker–Planck equation (1) [or the Gilbert equation (3)] is reduced to an infinite set of differential recurrence equations for the correlation functions $c_{l,m}(t) = \langle \cos\vartheta(0) Y_{l,m}[\vartheta(t), \varphi(t)]\rangle_0$ [24]:

$$\frac{d}{dt}c_{l,m}(t) = \sum_{l',m'} d_{l',m',l,m} c_{l,m}(t), \quad (16)$$

where $d_{l',m',l,m}$ are matrix elements of the Fokker–Planck operator and $Y_{l,m}(\vartheta, \varphi)$ are spherical harmonics [therefore, $c_{1,0}(t)/c_{1,0}(0) = C(t)$]. Equations (16) for the free energy of an arbitrary form are derived in [28, 29] (see also [24, Chapter 7]). Equations (16) can be transformed into a matrix recurrence equation [24–27],

$$\tau_N \frac{d}{dt}\mathbf{C}_n(t) = \mathbf{Q}_n^- \mathbf{C}_{n-1}(t) + \mathbf{Q}_n \mathbf{C}_n(t) + \mathbf{Q}_n^+ \mathbf{C}_{n+1}(t) \quad (n \geq 1), \quad (17)$$

where $\mathbf{C}_n(t)$ [$\mathbf{C}_0(t) = 0$] is a vector consisting of elements $c_{l,m}(t)$, and $\mathbf{Q}_n^-$, $\mathbf{Q}_n$, and $\mathbf{Q}_n^+$ are matrices consisting of elements $d_{l',m',l,m}$. The exact solution to Eq. (17) for the Laplace transform of the vector $\mathbf{C}_1(t)$ is [24]

$$\tilde{\mathbf{C}}_1(s) = \tau_N \Delta_1 \left\{ \mathbf{C}_1(0) + \sum_{n=2}^{\infty} \left[\prod_{k=2}^{n} \mathbf{Q}_{k-1}^+ \Delta_k \right] \mathbf{C}_n(0) \right\}, \quad (18)$$

where the matrix fraction $\Delta_n(s)$ is given by

$$\Delta_n(s) = \cfrac{\mathbf{I}}{\tau_N s\mathbf{I} - \mathbf{Q}_n - \mathbf{Q}_n^+ \cfrac{\mathbf{I}}{\tau_N s\mathbf{I} - \mathbf{Q}_{n+1} - \mathbf{Q}_{n+1}^+ \cfrac{\mathbf{I}}{\tau_N s\mathbf{I} - \mathbf{Q}_{n+2} - \ldots} \mathbf{Q}_{n+2}^-} \mathbf{Q}_{n+1}^-}.$$

Here, **I** is the identity matrix and the fraction bar denotes matrix inversion. Given $\tilde{\mathbf{C}}_1(s)$, we can find the correlation time

$$\tau_\parallel = \tilde{C}(0) = \tilde{c}_{1,0}(0)/c_{1,0}(0) \quad (19)$$

and the spectrum of the correlation function, $\tilde{C}(\omega) = \tilde{c}_{1,0}(i\omega)/c_{1,0}(0)$. Furthermore, we can estimate the lowest eigenvalue λ_1 from the equation $\det(\lambda_1\mathbf{I} - \mathbf{S}) = 0$, where the matrix **S** is defined as [23]

$$\mathbf{S} = -\tau_N^{-1}[\mathbf{Q}_1 + \mathbf{Q}_1^+ \Delta_2(0)\mathbf{Q}_2^-] \times \left[\mathbf{I} + \sum_{n=2}^{\infty} \prod_{m=1}^{n-1} \mathbf{Q}_m^+ \prod_{k=1}^{n-1} \Delta_{n-k+1}^2(0) \mathbf{Q}_{n-k+1}^- \right]^{-1}. \quad (20)$$

In other words, λ_1 is the lowest eigenvalue of the matrix **S**. For the cases of cubic anisotropy and of uniaxial anisotropy in the presence of a static magnetic field, the method of matrix continued fractions was developed in [23–27]. Here, we use this method mainly to estimate the accuracy of asymptotic expressions for the magnetization relaxation time.

4. UNIAXIAL PARTICLE IN A TRANSVERSE EXTERNAL FIELD

The free energy of a particle with uniaxial symmetry in the presence of a static external transverse field $\mathbf{H}_0$ is given by [12]

$$\beta V = \sigma(u_1^2 + u_2^2) - \xi u_1 = \sigma(\sin^2\vartheta - 2h\sin\vartheta\cos\varphi), \quad (21)$$

where $\sigma = \beta K$ is a dimensionless parameter characterizing the barrier height, K is the anisotropy constant, $\xi = \beta M_S H_0$ is a parameter characterizing the external field, and $h = \xi/2\sigma$. For $0 < h < 1$, the potential in Eq. (21) has one saddle point at $(\pi/2, 0)$ and two equiv-

alent minima at (arcsin$h$, 0) and (π – arcsin$h$, 0). The case of $h = 0$ corresponds to easy-axis anisotropy.

In order to estimate the lowest eigenvalue λ_1 in the IHD region ($\alpha \geq 1$) in the case of two or more metastable states, it is necessary to find all possible escape routes by using the discrete-orientation model [4, 15]. Analysis shows that the average magnetization of a crystal with uniaxial anisotropy in the presence of a static transverse external field decays with the characteristic time $1/2\Gamma_{ij}^{\mathrm{IHD}}$ [12], where the escape rate $\Gamma_{ij}^{\mathrm{IHD}}$ is given by Eq. (6). Taking into account that

$$\beta(V_0 - V_i) = \sigma(1-h)^2, \quad \beta c_1^{(1)} = \beta c_1^{(2)} = 2\sigma,$$

$$\beta c_2^{(1)} = \beta c_2^{(2)} = 2\sigma(1-h^2), \quad \beta c_1^{(0)} = 2\sigma h,$$

$$\beta c_2^{(0)} = -2\sigma(1-h),$$

we get [12, 22]

$$\tau_{\mathrm{IHD}} \sim \frac{1}{2\Gamma_{12}^{\mathrm{IHD}}} = \frac{2\tau_N \pi \sqrt{h} e^{\sigma(1-h)^2}}{\sigma\sqrt{1+h}(1-2h+\sqrt{1+4h(1-h)\alpha^{-2}})}. \quad (22)$$

The longest relaxation time $\tau = 1/\lambda_1$ in the case of two equivalent potential wells i and j (with $V_i = V_j$, $S_i = S_j$) is given by [17]

$$\tau = \frac{A(2\alpha S_i)}{A^2(\alpha S_i)}\tau_{\mathrm{IHD}}, \quad (23)$$

where the action S_i is given by Eq. (8). To find S_i, we need to know the critical path $\vartheta(\varphi)|_{V=V_0}$. This path can be found by solving the trigonometric equation

$$\sin^2\vartheta - 2h\sin\vartheta\cos\varphi = 1 - 2h,$$

and, for the minimum at the point $\vartheta = \arcsin h$, is given by

$$\vartheta(\varphi)|_{V=V_0} = \arccos\left[\sqrt{2h(1-h\cos^2\varphi - \cos\varphi\sqrt{1-2h+h^2\cos^2\varphi})}\right]. \quad (24)$$

From Eqs. (8) and (24) we get

$$S_i = \beta\int_0^{2\pi}\left\{\sin^2\vartheta_i(\varphi)\frac{\partial V}{\partial\cos\vartheta} + \frac{1}{\sin\vartheta_i(\varphi)}\frac{\partial V}{\partial\varphi}\right\}d\varphi = 16\sigma\sqrt{h}\left[1 - \frac{13}{6}h + \frac{11}{8}h^2 - \frac{3}{16}h^3 + \frac{7}{384}h^4 + \frac{h^5}{256} + O(h^6)\right]. \quad (25)$$

With Eqs. (22), (23), and (25), we get a universal expression for the time τ,

$$\tau \sim \frac{2\tau_N\pi\sqrt{h}e^{\sigma(1-h)^2}A(2\alpha S_i)}{\sigma\sqrt{1+h}(1-2h+\sqrt{1+4h(1-h)\alpha^{-2}})A^2(\alpha S_i)}, \quad (26)$$

where the dependence of the diffusion time τ_N on the damping factor α is given by Eq. (2). For very low damping ($\alpha < 0.001$), Eq. (26) coincides with the VLD asymptote:

$$\tau_{\mathrm{VLD}} \sim \frac{1}{2\Gamma_{12}^{\mathrm{VLD}}} = \frac{\pi\tau_N e^{\sigma(1-h)^2}}{8\sigma^2\sqrt{h(1-h)}}\left[1 - \frac{13}{6}h + \frac{11}{8}h^2 - \frac{3}{16}h^3 + \frac{7}{384}h^4 + \frac{h^5}{256} + O(h^6)\right]^{-1}. \quad (27)$$

The relaxation time τ, given by universal relation Eq. (26), and the inverse lowest eigenvalue $1/\lambda_1$, as calculated using the method of matrix continued fractions, are presented in Figs.1–4. It is seen from these figures that Eq. (26) agrees well with the results of numerical calculations over the whole range of α for the anisotropy factor $\sigma \gtrsim 4$. It should be stressed that Eq. (26) is not applicable for calculating τ in low fields, $4\sigma h \lesssim 1$. In this case (studied in detail in [12, 22]), the free energy density V depends on the azimuthal angle only weakly [i.e., potential (21) is almost axially symmetric] and all escape paths from the potential wells are roughly equivalent. To estimate τ for this case, we can use the following relation obtained in [22] using perturbation theory:

$$\tau \cong \tau_B\left\{1 + h^2\sigma^2\left[1 + 2(2\sigma\alpha^2 e)^{1/(2\sigma\alpha^2)} \times \gamma\left(1 + \frac{1}{2\sigma\alpha^2}, \frac{1}{2\sigma\alpha^2}\right)\right]\right\}^{-1}, \quad (28)$$

where

$$\tau_B \sim \tau_N\sqrt{\pi}\sigma^{-3/2}e^{\sigma}/2 \quad (29)$$

is the relaxation time for a uniaxial (axially symmetric) potential [3, 4] (asymptotic expression (29) is presented in Figs. 2, 3 for comparison) and $\gamma(a, z) = \int_0^z t^{a-1}e^{-t}dt$ is the incomplete gamma function. It can be shown [22]

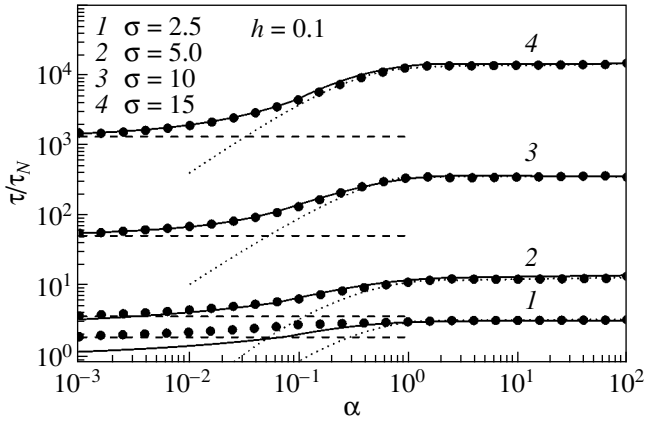

Fig. 1. Dependences of τ/τ_N on α for $h = 0.1$ and different values of σ. Solid lines are exact solutions found using the method of matrix continued fractions [26], dash lines are plotted according to Eq. (27), dotted lines correspond to Eq. (22), and circles correspond to universal relation (26).

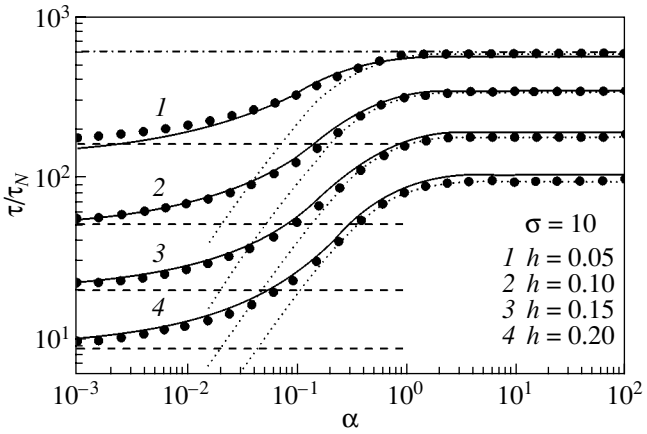

Fig. 2. Dependences of τ/τ_N on α for $\sigma = 10$ and different values of h. The notation is the same as in Fig. 1. The dash-dotted line represents τ/τ_N for a uniaxial crystal, Eq. (29).

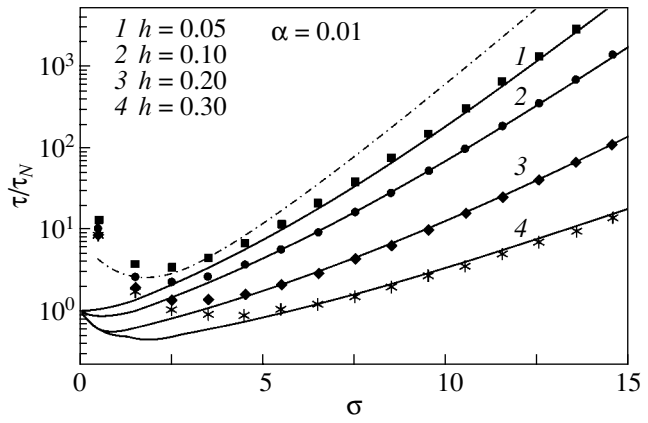

Fig. 3. Dependence of τ/τ_N on σ for $\alpha = 0.01$ and different values of h. Solid lines are exact solutions found using the method of matrix continued fractions [26], symbols correspond to universal relation (26), and the dash-dotted line represents τ/τ_N for a uniaxial crystal, Eq. (29).

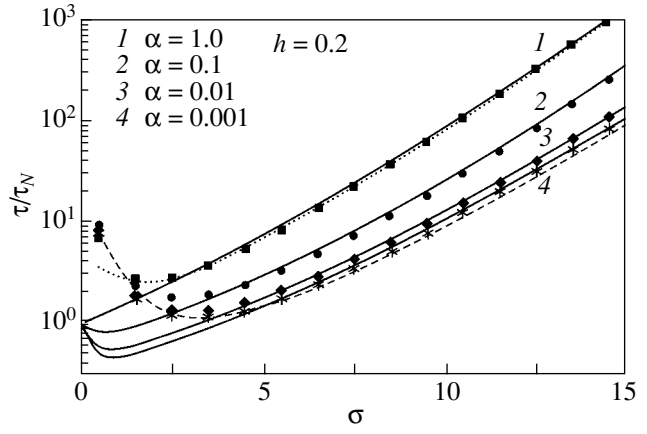

Fig. 4. Dependence of τ/τ_N on σ for $h = 0.2$ and different values of α. Solid lines are exact solutions found using the method of matrix continued fractions [26], symbols correspond to universal relation (26), the dotted line corresponds to Eq. (22) for $\alpha = 1$, and the dashed line represents Eq. (27) for the case of very low damping.

that the expression in square brackets in Eq. (28) is about 1 for $\alpha \gg 1$ and about $\alpha^{-1}\sqrt{\pi/\sigma}$ for $\alpha \ll 1$. The range of validity of Eq. (28) is determined by inequalities $h^2\sigma^2 \ll 1$, $\alpha > 4h^2\sigma^{3/2}$, and $\sigma \gtrsim 4$.

5. CUBIC ANISOTROPY

The free energy of a crystal with cubic anisotropy is given by [4, 15]

$$\begin{aligned}\beta V &= 4\sigma(u_1^2u_2^2 + u_2^2u_3^2 + u_3^2u_1^2)\\ &= \sigma(\sin^4\vartheta\sin^2 2\varphi + \sin^2 2\vartheta),\end{aligned} \tag{30}$$

where $\sigma = \beta K/4$ is a dimensionless parameter characterizing the height of the potential barrier and K is the anisotropy constant, which can be positive or negative. If $K > 0$ (Fe-like crystals), then the free energy in Eq. (30) has six minima (potential wells), eight maxima, and twelve saddle points. If $K < 0$ (Ni-like crystals), the minima become maxima and vise versa. According to the discrete-orientation model, the average magnetization of a crystal with cubic anisotropy decays with characteristic times $1/4\Gamma_{ij}^{\mathrm{IHD}}$ and $1/2\Gamma_{ij}^{\mathrm{IHD}}$ for $K > 0$ and $K < 0$, respectively [4]. The escape rate $\Gamma_{ij}^{\mathrm{IHD}}$ is given by Eq. (6), where

$$\beta(V_0 - V_i) = \sigma, \quad \beta c_1^{(i)} = \beta c_2^{(i)} = 8\sigma,$$

$$\beta c_1^{(0)} = 4\sigma, \quad \beta c_2^{(0)} = -8\sigma \quad \text{for} \quad K > 0$$

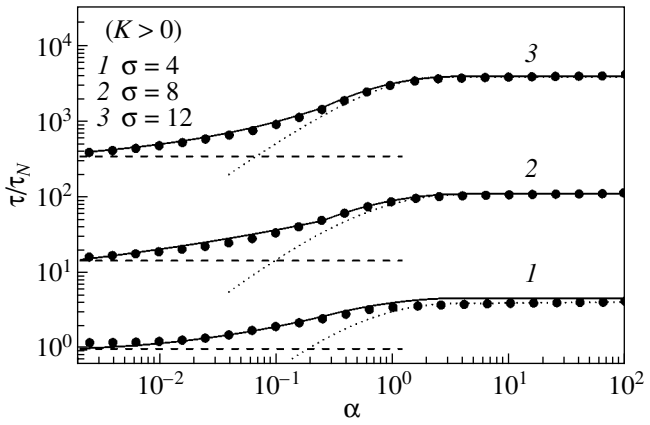

Fig. 5. Dependence of τ/τ_N on α for different values of σ ($K > 0$). Solid lines are exact solutions found using the method of matrix continued fractions for the correlation time $\tau_{||}$, dashed lines correspond to Eq. (38), dotted lines correspond to Eq. (31), and circles correspond to universal relation (36).

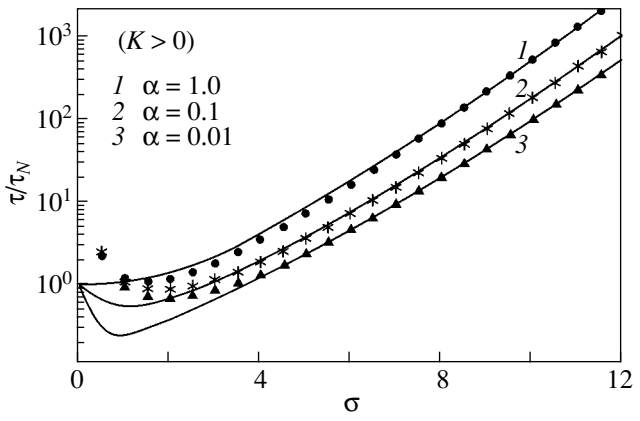

Fig. 6. Dependences of τ/τ_N on σ for different values of α in the crossover region for $K > 0$. Solid lines are exact solutions found using the method of matrix continued fractions for the correlation time $\tau_{||}$ and symbols correspond to universal relation (36).

and

$$\beta(V_0 - V_i) = -\sigma/3, \quad \beta c_1^{(i)} = \beta c_2^{(i)} = 16|\sigma|/3,$$

$$\beta c_1^{(0)} = 8|\sigma|, \quad \beta c_2^{(0)} = -4|\sigma| \quad \text{for} \quad K < 0.$$

Thus, we get [4, 15]

$$\tau_{\text{IHD}} \sim \frac{1}{4\Gamma_{ij}^{\text{IHD}}} = \frac{\tau_N \pi e^{\sigma}}{2\sqrt{2}\sigma(\sqrt{9 + 8/\alpha^2} + 1)} \quad (K > 0) \quad (31)$$

and

$$\tau_{\text{IHD}} \sim \frac{1}{2\Gamma_{ij}^{\text{IHD}}} = \frac{3\tau_N \pi e^{-|\sigma|/3}}{2\sqrt{2}|\sigma|(\sqrt{9 + 8/\alpha^2} - 1)} \quad (K < 0). \quad (32)$$

A universal equation for τ can be written as

$$\tau \sim \frac{\tau_{\text{IHD}}}{A(\alpha S_i)}. \quad (33)$$

To estimate S_i from Eq. (8), we need to find the critical path $\vartheta(\varphi)|_{V = V_0}$. For the minimum at $\vartheta = 0$ ($K > 0$) and for the minimum at $(\arccos(1/\sqrt{3}), \pi/4)$ ($K < 0$), the desired path goes through the two adjacent saddle points $(\arccos(1/\sqrt{2}), 0)$ and $(\arccos(1/\sqrt{2}), \pi/2)$ and satisfies the equation

$$\sin^4\vartheta \sin^2 2\varphi + \sin^2 2\vartheta = 1.$$

The solution to this equation is

$$\vartheta(\varphi)|_{V = V_0} = \arccos\sqrt{\frac{1 + \sin 2\varphi}{2 + \sin 2\varphi}}. \quad (34)$$

Thus, from Eqs. (8) and (34), we get

$$S_i = 12|\sigma| \int_0^{\pi/2} \frac{\sin 2\varphi \sqrt{1 + \sin 2\varphi}}{(2 + \sin 2\varphi)^{5/2}} d\varphi = 8\sqrt{2}|\sigma|/9. \quad (35)$$

Combining Eqs. (33)–(35), we get

$$\tau \sim \frac{\tau_N \pi e^{\sigma}}{2\sqrt{2}\sigma(\sqrt{9 + 8/\alpha^2} + 1)A(8\sqrt{2}\sigma\alpha/9)} \quad (K > 0) \quad (36)$$

and

$$\tau \sim \frac{3\tau_N \pi e^{|\sigma|/3}}{2\sqrt{2}|\sigma|(\sqrt{9 + 8/\alpha^2} - 1)A(\alpha|\sigma|8\sqrt{2}/9)} \quad (K < 0). \quad (37)$$

For $\alpha \ll 1$, Eqs. (36) and (37) coincide with the respective VLD asymptotic expressions

$$\tau_{\text{VLD}} \sim \frac{1}{4\Gamma_i^{\text{VLD}}} = \frac{\pi e^{\sigma}}{2\alpha\omega_i S_i} = \frac{9\pi e^{\sigma}}{64\sqrt{2}\sigma^2}\tau_N \quad (K > 0), \quad (38)$$

$$\tau_{\text{VLD}} \sim \frac{1}{2\Gamma_i^{\text{VLD}}} = \frac{\pi e^{|\sigma|/3}}{\omega_i \alpha S_i} \sim \frac{27\pi e^{|\sigma|/3}}{64\sqrt{2}\sigma^2}\tau_N \quad (K < 0). \quad (39)$$

The correlation time $\tau_{||}$ (calculated using the method of matrix continued fractions [26, 27]) and the relaxation time τ, given by universal relations (36) and (37), are presented in Figs. 5–8 as functions of α and σ. For comparison, the asymptotic expressions for the IHD and VLD regions given by Eqs. (31), (32), (38), and (39) are also presented in the figures. It can be seen that universal relations (36) and (37) agree well with the results of numerical calculations over the whole range of the parameter α, including the IHD, VLD, and crossover

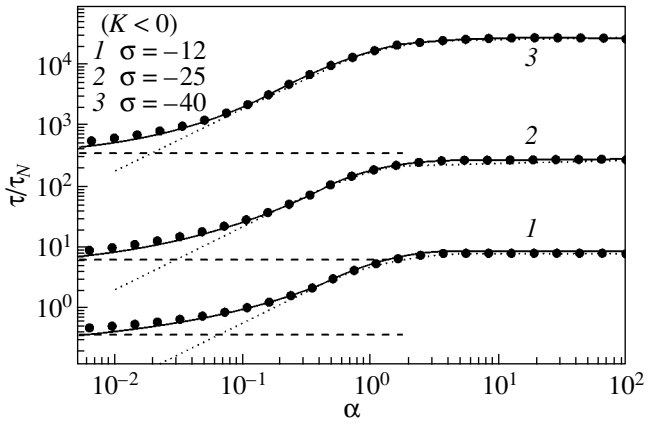

Fig. 7. Dependences of τ/τ_N on α for different values of σ ($K < 0$).

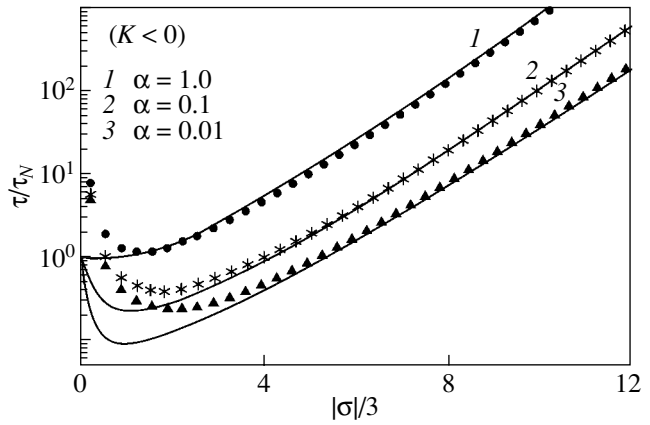

Fig. 8. Dependence of τ/τ_N on σ for different values of α ($K < 0$).

regions. The agreement is satisfactory starting from moderate values of the potential barrier ($\sigma \gtrsim 3$ for $K > 0$ and $|\sigma| \gtrsim 10$ for $K < 0$).

6. CONCLUSIONS

The method developed in [13] for calculating the escape rate of a classical Brownian particle from a potential well and generalized in [12, 17] to superparamagnetic particles enables one to find simple asymptotic expressions for the magnetization relaxation time τ. The results of calculations with these expressions agree well with the numerical solutions to the Landau–Lifshitz–Gilbert equation found using the method of matrix continued fractions over the whole range of values of the dissipation parameter (very low and intermediate-to-high damping and the crossover region between low and intermediate damping). Equations (26), (36), and (37), thus obtained for the magnetization relaxation time τ for the cases of cubic anisotropy and of uniaxial anisotropy in the presence of a static transverse field, allow one to easily estimate τ for any value of α with a good accuracy. The accuracy is good for the following reasons. The variation of the relaxation time τ with the potential barrier height ΔU is well fitted for large ΔU by the exponent $\tau \sim \tau_0 e^{\beta \Delta U}$ due to the equilibrium properties of the system, namely, the Boltzmann distribution at the bottom of the potential well. On the other hand, the dependence of the relaxation time τ on the damping factor α is conditioned by nonequilibrium (dynamic) properties of the system and is contained in the preexponential factor τ_0, which is strongly dependent on simplifications made during estimations. So, it will not suffice to assume there is a Boltzmann distribution at the bottom of the potential. It is also necessary to set the distribution function at the saddle points of the free energy. As noted by Kramers [10], the accuracy of the expressions derived for the escape rate is not really essential from the experimental viewpoint, because experimental methods are usually aimed at measuring the factor τ_0 and do this with some degree of accuracy. However, it is very important to find the analytical dependence of the relaxation time on the damping factor α, because it makes it possible to judge the relaxation mechanisms in magnetic systems.

7. ACKNOWLEDGMENTS

This work was supported by INTAS, grant no. 01-2341.

REFERENCES

1. L. Néel, Ann. Geophys. **5** (1), 99 (1949).
2. C. P. Pean and J. D. Livingston, J. Appl. Phys. **30** (Suppl. 1), 120S (1959).
3. W. F. Brown, Jr., Phys. Rev. **130** (5), 1677 (1963).
4. W. F. Brown, Jr., IEEE Trans. Magn. **15** (5), 1196 (1979).
5. L. D. Landau and E. M. Lifshitz, Phys. Z. Sowjetunion **8** (1), 153 (1935).
6. T. L. Gilbert, Phys. Rev. **100** (5), 1243 (1956).
7. Yu. L. Raikher and M. I. Shliomis, Adv. Chem. Phys. **87**, 595 (1994).
8. W. T. Coffey, P. J. Cregg, and Yu. P. Kalmykov, Adv. Chem. Phys. **83**, 263 (1993).
9. I. Klik and L. Gunther, J. Stat. Phys. **60** (3–4), 473 (1990); J. Appl. Phys. **67** (9), 4505 (1990).
10. H. A. Kramers, Physica (Utrecht) **7** (4), 284 (1940).
11. P. Hänggi, P. Talkner, and M. Borkovec, Rev. Mod. Phys. **62** (2), 251 (1990).
12. W. T. Coffey, D. A. Garanin, and D. McCarthy, Adv. Chem. Phys. **117**, 528 (2001).
13. V. I. Mel'nikov and S. V. Meshkov, J. Chem. Phys. **85** (2), 1018 (1986).
14. V. I. Mel'nikov, Phys. Rep. **209** (1–2), 1 (1991).
15. D. A. Smith and F. A. de Rozario, J. Magn. Magn. Mater. **3** (3), 219 (1976).
16. J. S. Langer, Ann. Phys. (N.Y.) **54** (2), 258 (1969).

17. P. M. Déjardin, D. S. F. Crothers, W. T. Coffey, and D. J. McCarthy, Phys. Rev. E **63** (2), 021102 (2001).
18. I. Eisenstein and A. Aharoni, Phys. Rev. B **16** (3), 1278 (1977).
19. I. Eisenstein and A. Aharoni, Phys. Rev. B **16** (3), 1285 (1977).
20. W. Wernsdorfer, Adv. Chem. Phys. **118**, 99 (2001).
21. W. T. Coffey, D. S. F. Crothers, J. L. Dormann, Yu. P. Kalmykov, E. C. Kennedy, and W. Wernsdorfer, Phys. Rev. Lett. **80** (25), 5655 (1998).
22. D. A. Garanin, E. C. Kennedy, D. S. F. Crothers, and W. T. Coffey, Phys. Rev. E **60** (6), 6499 (1999).
23. Yu. P. Kalmykov, Phys. Rev. E **62** (1), 227 (2000).
24. W. T. Coffey, Yu. P. Kalmykov, and J. T. Waldron, *The Langevin Equation*, 2nd ed. (World Sci., Singapore, 2004).
25. Yu. P. Kalmykov and S. V. Titov, Fiz. Tverd. Tela (St. Petersburg) **40** (9), 1642 (1998) [Phys. Solid State **40**, 1492 (1998)].
26. Yu. P. Kalmykov and S. V. Titov, Zh. Éksp. Teor. Fiz. **115** (1), 101 (1999) [JETP **88**, 58 (1999)].
27. Yu. P. Kalmykov, S. V. Titov, and W. T. Coffey, Phys. Rev. B **58** (6), 3267 (1998).
28. Yu. P. Kalmykov and S. V. Titov, Phys. Rev. Lett. **82** (14), 2967 (1999).
29. Yu. P. Kalmykov and S. V. Titov, J. Magn. Magn. Mater. **210** (1–2), 233 (2000).

Translated by G. Tsydynzhapov

Physics of the Solid State, Vol. 47, No. 2, 2005, pp. 281–286. Translated from Fizika Tverdogo Tela, Vol. 47, No. 2, 2005, pp. 268–273.

MAGNETISM AND FERROELECTRICITY

Magnetorefractive Effect in Granular Alloys with Tunneling Magnetoresistance

I. V. Bykov*, E. A. Gan'shina*, A. B. Granovsky*, V. S. Gushchin*, A. A. Kozlov*, T. Masumoto, and S. Ohnuma****

** Moscow State University, Vorob'evy gory, Moscow, 119992 Russia*
e-mail: granov@magn.ru
***Research Institute for Electric and Magnetic Materials 2-1-1, Yagiymaminami, Taihakuku, Sendai, 982-0807 Japan*
Received May 20, 2004

Abstract—The magnetorefractive effect and optical reflectivity are studied in granular Co–Al–O, Co–Si–O, and Co–Ti–O metal–insulator alloys exhibiting tunneling magnetoresistance for compositions close to the percolation threshold. The dependences of these effects on frequency, angle of incidence, and light polarization were measured. The experimental data obtained suggest that the major MRE mechanism in these systems is spin-dependent tunneling at optical frequencies. © *2005 Pleiades Publishing, Inc.*

1. INTRODUCTION

The magnetorefractive effect (MRE) is a new magneto-optical phenomenon consisting in a variation of the optical properties of magnets with a large magnetoresistance (MR) induced by their magnetization [1, 2]. It should be stressed that the MRE is a frequency analog of the MR. Therefore, on the one hand, this effect is even in magnetization and is not gyrotropic, which distinguishes it from traditional magneto-optical phenomena, while on the other hand, the correlation with the MR (not necessarily linear) separates this effect from other possible magnetically induced variations in the optical properties of magnetic and nonmagnetic materials. In systems with tunneling MR, a remarkable example of which is given by granular ferromagnetic-metal–insulator films with a metal content close to the percolation threshold, the nature of the MRE is conceivably related to spin-dependent tunneling at optical frequencies [1, 2].

The MRE in granular metal–insulator films (or nanocomposites) was first reported in [3] and subsequently studied by a number of researchers [1, 2, 4–6]; the data obtained are largely consistent with the above concept of the MRE and the relevant theory [1, 7]. The MRE in nanocomposites exceeds the traditional magneto-optical effects by about two orders of magnitude. The room-temperature MRE in a (CoFe)–(MgF) sample with a volume concentration of the magnetic phase of 48% can be as high as 1.5% [5]. As far as we know, this is a record-high value. A number of issues remain, however, either unclear or debatable. In particular, no correlation between the field dependences of the MRE and MR has been corroborated experimentally, the part played by the dielectric matrix in the formation of the effect has not been clarified (a noticeable MRE was recently revealed at certain frequencies in the nonmagnetic crystalline dielectric Al_2O_3 [6]), and the dependence of the MRE on the polarization and angle of incidence of light have not been studied adequately. Finally, no attempts have thus far been undertaken to quantitatively test the theory of the MRE in nanocomposites. It is these issues that will be addressed in the present communication.

2. SAMPLES, METHODS OF INVESTIGATION, AND DETAILS OF THE EXPERIMENT

Thin-film ferromagnetic-metal–insulator Co–Al–O, Co–Si–O, and Co–Ti–O nanocomposites were prepared by rf magnetron cosputtering in an argon atmosphere (~8 mTorr) of insulator and Co metal targets onto uncooled substrates of Corning Glass 7059. The compositions of the samples studied, their thicknesses, and the magnitudes of the MR and MRE in them obtained in these studies in fields of 10 and 1.6 kOe,

Compositions of samples, their thicknesses, magnetoresistance, and magnetorefractive effect

Sample composition	Film thickness, μm	MR, % (10 kOe)	MRE (1.6 kOe)	
			ξ(ν), %	ν, cm^{-1}
$Co_{43}Al_{22}O_{35}^{*}$	2	8.5	0.8	1100
$Co_{50.3}Al_{20.4}O_{29.3}$	2.62	9.2	–1.0	1200
$Co_{51.5}Al_{19.5}O_{29}$	1.91	9.2	–0.9	1100
$Co_{55.2}Al_{19}O_{25.8}$	2.62	4.8	–0.6	1000
$Co_{52.3}Si_{12.2}O_{35.5}$	1.67	4.1	+0.7	1300
$Co_{50.2}Ti_{9.1}O_{40.7}$	2.02	5.8	–0.7	1030

* at. %

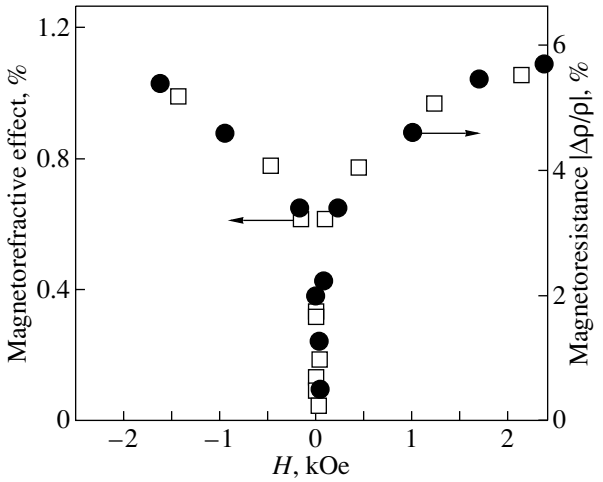

Fig. 1. Field dependence of the magnetorefractive effect and magnetoresistance of the $Co_{43}Al_{22}O_{35}$ nanocomposite for $\phi = 10°$ and $\nu = 1130$ cm^{-1}.

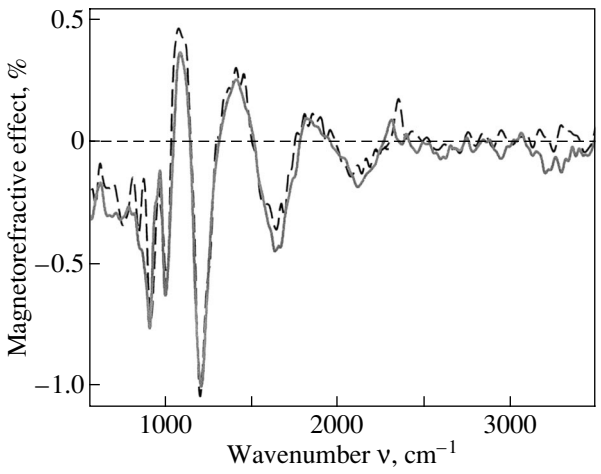

Fig. 2. MRE dispersion in the $Co_{50.3}Al_{20.4}O_{29.3}$ nanocomposite obtained for *p*-polarized light under equatorial (dashed line) and meridional (solid line) sample magnetization; $\phi = 45°$.

respectively, are listed in the table. A detailed description of the sample preparation procedure and the methods and results of measurements of their chemical composition and structural, electrical, and magnetic parameters can be found in [8, 9]. Both in the text and in the table, the content of the components is given in units of volume concentration.

The spectra of optical reflectivity $R(\nu)$ and of the magnetorefractive effect in reflection, $\xi(\nu)$, were studied over a broad wavelength interval, from 2 to 20 μm (5000–500 cm^{-1}), with a FTIR PU9800 commercial Fourier spectrometer having a spectral resolution *Res* ~ 4 cm^{-1}. The reflectivity spectra presented below are normalized against those of a gold mirror. The MRE was calculated as the ratio of the change in the reflected intensity induced by sample magnetization to the reflected intensity of the demagnetized sample:

$$\xi(\nu, H) = \frac{\Delta R}{R} = \frac{R(\nu, H = 0) - R(\nu, H)}{R(\nu, H = 0)}; \qquad (1)$$

where $R(\nu, H = 0)$ and $R(\nu, H)$ are the sample reflectivities in the demagnetized state and in a field H, respectively.

The magnetorefractive effect was measured on a setup described in [1, 5], with the magneto-optical attachment modified by replacing the aspherical mirrors by plane mirrors; this change made it possible to measure the MRE not only at a close-to-normal angle of incidence ($\phi \sim 8°$) but also at 20° and 45°. The specific design of the electromagnet did not allow us to increase the angle of incidence of light. The light was polarized with a KRS-5 grid polarizer, which was introduced into the incident beam (before the magnet) and was also located in the magneto-optical module of the setup.

The resulting spectrum of the effect was obtained by averaging over 600–1000 scans. The noise level was 1×10^{-4} in the interval 1000–3000 cm^{-1} and 3×10^{-4} elsewhere in the range covered.

All our measurements were performed at room temperature.

3. EXPERIMENTAL RESULTS AND DISCUSSION

To determine the nature of the MRE in nanocomposites, it is essential to obtain experimental evidence that the MRE in these systems originates from tunneling MR rather than being a consequence of any other causes, for instance, of the even and odd magneto-optical Kerr effects or of the effect of a magnetic field on the optical properties of the dielectric matrix. Direct evidence could be furnished by checking the correlation between the field dependences of the MRE and MR measured on the same samples in a dc magnetic field varied from 0 to 2.2 kOe [3]. Figure 1 exemplifies experimental data on the $Co_{43}Al_{22}O_{35}$ nanocomposite and demonstrates good agreement between the MRE and MR field dependences, which supports the validity of the relations derived in [4, 10].

To make certain that the MRE is indeed not related to odd magneto-optical effects, we determined the MRE parameter as the arithmetic mean of a number of measurements performed under two opposite orientations of a magnetic field. MRE measurements carried out in polarized light with the external magnetic field **H** oriented differently relative to the plane of polarization of light, namely, $\mathbf{H} \parallel \mathbf{M}$, $\mathbf{E} \perp \mathbf{M}$ and $\mathbf{H} \parallel \mathbf{M}$, $\mathbf{E} \parallel \mathbf{M}$ (**M** is the magnetization vector, and **E** is the electric-field vector of the *p*-polarized light), likewise did not reveal any differences between the MRE spectra obtained in the equatorial and meridional geometries. This can be seen from Fig. 2, which displays data on the magnetorefrac-

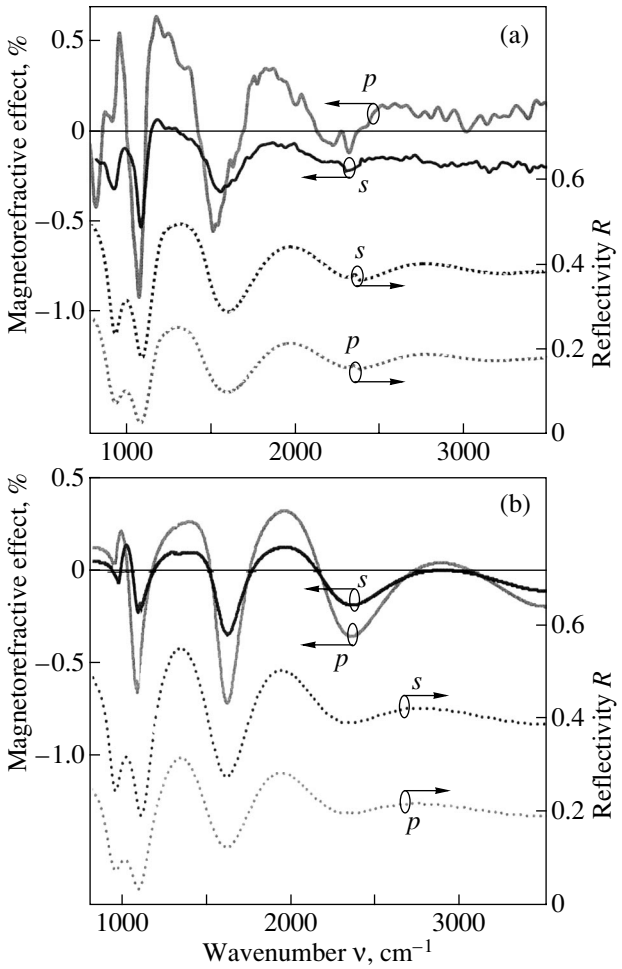

Fig. 3. Dispersion of the MRE (solid line) and reflectivity R (dashed line) for the $Co_{51.5}Al_{19.5}O_{29}$ nanocomposite obtained with *s*- and *p*-polarized light for $H = 1600$ Oe and $\phi = 45°$; (a) experiment, and (b) theoretical calculation.

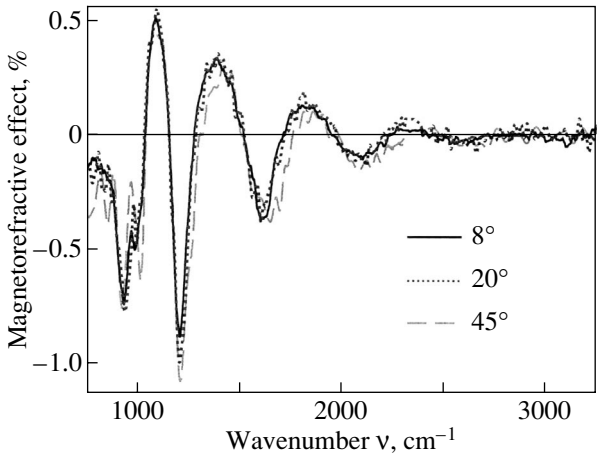

Fig. 4. MRE dispersion of the $Co_{50.3}Al_{20.4}O_{29.3}$ nanocomposite measured for *p*-polarized light at three angles of incidence.

tive response of the $Co_{50.3}Al_{20.4}O_{29.3}$ nanocomposite obtained for an angle of incidence of light $\phi = 45°$.

The pronounced magnetically induced variation in the optical properties of Al_2O_3 observed in [6] within a narrow wavelength interval near $\lambda = 9$ μm at an angle of incidence of *p*-polarized light $\phi = 65°$ (which was also termed the MRE) requires separate analysis. Note that the above conditions of observation ($\lambda = 9$ μm, $\phi = 65°$) correspond to fairly weak reflection, under which it would possibly be more reasonable to measure the difference ΔR than the MRE parameter. We performed measurements of both ξ and ΔR in single-crystal Al_2O_3 throughout the spectral range covered in fields of up to 1.6 kOe and for angles of incidence of 8°–45° (the frequency dependence of optical reflectivity $R(\nu)$ for sapphire is shown in Fig. 5); to within the error of measurement, no differences in the spectral dependence of reflectivity caused by sample magnetization were found. Therefore, it can be said with confidence that, under our conditions ($\phi = 45°$, *p* and *s* components, $H =$ 1.6 kOe), the Al_2O_3 insulating matrix does not contribute to the measured MRE signal. Furthermore, magneto-optical studies of nanocomposites of cobalt inserted into various matrices (see table) have also not revealed any additional contributions of the dielectric matrix to the MRE. One may conclude that the material of the crystalline dielectric matrix (Al_2O_3, SiO_2, TiO_2) influences the optical parameters of the nanocomposite and the tunneling MR and indirectly changes the MRE, an aspect which will be analyzed in detail below. One may also expect the impurities dissolved in the matrix or the localized states to give rise to an enhanced MR and, hence, an enhanced MRE, although no such effects have been revealed.

Figure 3a presents frequency spectra of the MRE and optical reflectivity of the $Co_{51.5}Al_{19.5}O_{29}$ nanocomposite obtained for *s*- and *p*-polarized light at an angle of incidence $\phi = 45°$. The effect is the largest near the frequency $\nu \sim 1100$ cm^{-1} and reaches $\xi_p = 0.9\%$ and $\xi_s = 0.53\%$ for the *p* and *s* polarization, respectively. Similar results were obtained for a nanocomposite of almost the same composition, $Co_{50.3}Al_{20.4}O_{29.3}$, exhibiting the same MR (cf. Fig. 4 and table). As seen from Fig. 5, the absolute value of the MRE of this sample for the *p* polarization measured at a frequency $\nu \simeq 1200$ cm^{-1} can be as high as 1%. Large values of the MRE for the nanocomposites studied here in the *p*- and *s*-polarized light fall in the frequency region 800–1800 cm^{-1}, where minima and maxima of the reflectivity $R(\nu)$ are observed (Fig. 3a).

Our measurements of the angular dependence of the MRE made on all the samples showed the absolute values of the effect in the *p* polarization to be slightly larger than those in the *s* polarization. As one goes over to large angles of incidence (up to 45° in our experiments), the *s*-component MRE decreases, while ξ_p remains almost the same. This is exemplified in Fig. 4 by the frequency spectra $\xi(\nu)$ of the $Co_{50.3}Al_{20.4}O_{29.3}$

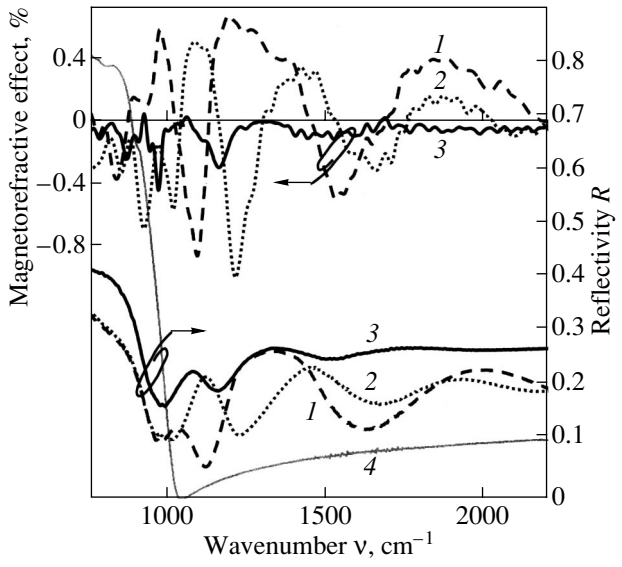

Fig. 5. Dispersion of the MRE and of the reflectivity R measured for p-polarized light for nanocomposites (*1*) $Co_{51.5}Al_{19.5}O_{29}$, (*2*) $Co_{50.3}Al_{20.4}O_{29.3}$, (*3*) $Co_{55.2}Al_{19}O_{25.8}$, and (*4*) Al_2O_3; $\phi = 45°$.

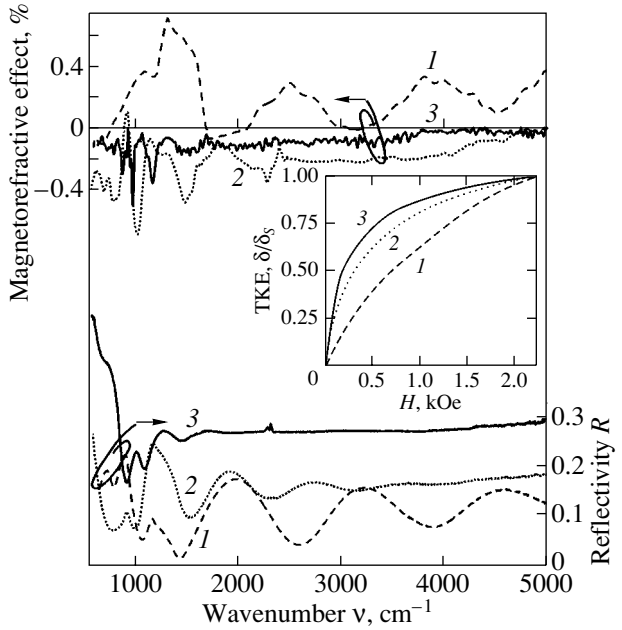

Fig. 6. Dispersion of the MRE and R measured in p-polarized light for the nanocomposites (*1*) $Co_{52.3}Si_{12.2}O_{35.5}$, (*2*) $Co_{50.2}Ti_{9.1}O_{40.7}$, and (*3*) $Co_{55.2}Al_{19}O_{25.8}$; $\phi = 45°$. The inset shows the magnetic-field dependence of the equatorial Kerr effect δ reduced to the maximum value of the effect δ_s obtained in the field $H = 2.25$ kOe.

nanocomposite obtained with p-polarized light at three angles of incidence. Similar spectra were also obtained for the other samples. Figure 3a also shows that, at $\phi = 45°$, the values of ξ_s (for $Co_{51.5}Al_{19.5}O_{29}$) are slightly smaller than those of ξ_p. Thus, the experimental data obtained on the angular and polarization dependences of the MRE are in good agreement with theoretical analysis [7].

The frequency dependences of reflectivity and the MRE obtained on a number of nanocomposites (Fig. 5) exhibit oscillations. The oscillation periods are largely the same, and no dependence of their length on the sample composition was revealed. A thinner $Co_{51.5}Al_{19.5}O_{29}$ sample shows a longer oscillation period both in the MRE and the reflectivity. The character of the $R(\nu)$ and $\xi(\nu)$ spectra and the oscillation periods evaluated theoretically (Fig. 3b) with due account of the actual thicknesses and actual complex refractive indices of these nanocomposites argue convincingly that the oscillations of $R(\nu)$ and particularly of $\xi(\nu)$ originate from interference. This is also suggested by studies of the spectra of samples containing ferromagnetic particles dispersed in various dielectric matrices.

The frequency spectra of the MRE and optical reflectivity of Co nanoclusters embedded in silicon, titanium, and aluminum oxide matrices are displayed in Fig. 6. The reflectivity spectra of all samples exhibit a number of phonon modes of the dielectric matrix and corresponding spikes in the magnetorefractive effect. The maximum MRE values of the $Co_{52.3}Si_{12.2}O_{35.5}$ nanocomposite obtained in the p-polarized light, which reach as high as $\xi_p = 0.7\%$, fall in the frequency range 1250–1320 cm^{-1}, where the reflectivity is $R \simeq 0.5\%$. For the s polarization, the MRE value of this nanocomposite measured in the same wavelength interval does not exceed 0.3% but the reflectivity is higher, $R \simeq 3\%$. Granular nanocomposites of ferromagnetic Co dispersed in TiO_2 and Al_2O_3 matrices exhibit a similar behavior of the MRE and reflectivity spectra. More pronounced oscillations are seen in the magneto-optical spectra, i.e., with a magnetic field acting upon the ferromagnetic nanocomposite, with the effects bearing a distinct interference character. Note also that the MRE effect of the $Co_{52.3}Si_{12.2}O_{35.5}$ nanocomposite, unlike that of the other samples, is always positive. This sample reveals a large magnetoresistance (4.1%). However, as follows from the data obtained for the equatorial Kerr effect (see inset to Fig. 6) in the visible region, the magnetization curve of this sample suggests that the sample has not yet reached the percolation threshold. A similar reversal of the MRE sign in granular $(Co_{50}Fe_{50})_x(Al_2O_3)_{100-x}$ films in the prepercolation region was reported to occur in [6].

The above results can be interpreted in terms of a model [1, 5] that takes into account the attenuation and interference effects in the nanocomposite and substrate layers. When the optical parameters of the substrate material are included, the agreement between theory and experiment is the best.

Let us consider a four-layer system (Fig. 7) consisting of a nanocomposite film (with thickness d_2 and complex refractive index $\eta_2 = n_2^0 - ik_2^0$) deposited on a

substrate (with thickness d_3 and refractive index $\eta_3 = n_3 - ik_3$); the system is in vacuum ($n_{1,4} = 1$, $k_{1,4} = 0$). It is known [11] that the reflectivity r and transmission t for s- and p-polarized waves incident on the interface between the jth and kth media having complex refractive indices η_j and η_k, respectively, can be written as

$$r_{jk}^{p} = \frac{g_j\eta_k^2 - g_k\eta_j^2}{g_j\eta_k^2 + g_k\eta_j^2}, \quad r_{jk}^{s} = \frac{g_j - g_k}{g_j + g_k},$$
$$t_{jk}^{p} = \frac{2g_j\eta_k\eta_j}{g_j\eta_k^2 + g_k\eta_j^2}, \quad t_{jk}^{s} = \frac{2g_j}{g_j + g_k}, \tag{2}$$

where

$$g_{j(k)} = \sqrt{\eta_{j(k)}^2 - \eta_1^2\sin^2\phi_0}.$$

The reflectivity $R^{p(s)}$ and transmission $T^{p(s)}$ of the four-layer system can be cast using the recurrent relations

$$R^{p(s)} = \left|r_{jklm}^{p(s)}\right|^2, \quad T^{p(s)} = \left|t_{jklm}^{p(s)}\right|^2,$$
$$r_{jklm}^{p(s)} = \frac{r_{jk}^{p(s)} + F_k^2 r_{klm}^{p(s)}}{1 + F_k^2 r_{jk}^{p(s)} r_{klm}^{p(s)}}, \quad t_{jklm}^{p(s)} = \frac{t_{jk}^{p(s)} + t_{klm}^{p(s)} F_k}{1 + F_k^2 r_{jk}^{p(s)} r_{klm}^{p(s)}}, \tag{3}$$
$$r_{jkl}^{p(s)} = \frac{r_{jk}^{p(s)} + F_k^2 r_{kl}^{p(s)}}{1 + F_k^2 r_{jk}^{p(s)} r_{kl}^{p(s)}}, \quad t_{jkl}^{p(s)} = \frac{t_{jk}^{p(s)} + t_{kl}^{p(s)} F_k}{1 + F_k^2 r_{jk}^{p(s)} r_{kl}^{p(s)}},$$
$$F_k = \exp(-2\pi i\nu g_k d_k),$$

where j, k, l, and m label the media; F_k is the phase factor of the kth layer responsible for the interference and attenuation of light in the film and the substrate; and $\nu = 1/\lambda$ is the wavenumber.

As follows from the theory of the MRE, the refractive index n_2 and the extinction coefficient k_2 of the nanocomposite film in the case where the sample is magnetized can be written as [1]

$$n_2 = n_2^0\left(1 + \frac{\Delta\rho}{\rho}\frac{(k_2^0)^2}{(k_2^0)^2 + (n_2^0)^2}\right),$$
$$k_2 = k_2^0\left(1 + \frac{\Delta\rho}{\rho}\frac{(n_2^0)^2}{(k_2^0)^2 + (n_2^0)^2}\right), \tag{4}$$

where $\Delta\rho/\rho$ is the absolute value of the MR under a magnetic field H. Equations (2) and (3), combined with Eqs. (4) for the film optical parameters, fully determine the MRE and optical reflectivity of the nanocomposite for p- and s-polarized light.

In order to determine the optical parameters of the $Co_{51.5}Al_{19.5}O_{29}$ nanocomposite, we measured the transmission $T(\nu)$ ($\phi = 0°$) and reflectivity $R^s(\nu)$ ($\phi = 20°$) spectra for s-polarized light for a ferromagnetic sample and a glass substrate (Fig. 8). By solving the inverse problem, one can find the optical parameters n_i and k_i of the sample and the substrate. In the range 3000–6000 cm^{-1}, the substrate has a small extinction coefficient $k_3 \sim 10^{-4}$–10^{-5} for a refractive index n_3 varying from 1.5 to 1.3. At frequencies below 2000 cm^{-1}, the absorption of the substrate increases substantially, thus precluding accurate determination of the optical constants in this spectral region. The absorption band of the Al_2O_3 matrix in the $Co_{51.5}Al_{19.5}O_{29}$ nanocomposite is centered at $\nu \sim 1025$ cm^{-1}. In pure Al_2O_3, this band is shifted to lower frequencies down to 950 cm^{-1}. Figure 9

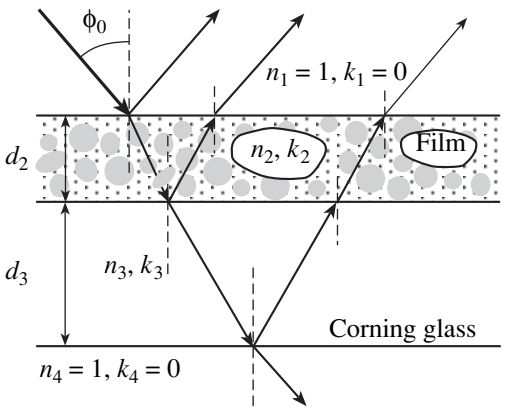

Fig. 7. Ray propagation in the air–film–substrate–air system (schematic).

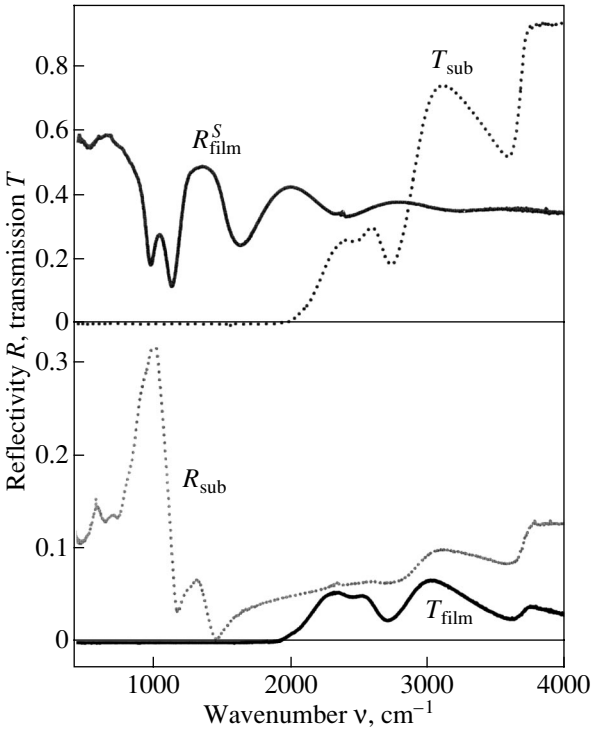

Fig. 8. Frequency dependences of the transmission and reflectivity of the substrate, T_{sub} and R^s_{sub} (dashed line), and of a $Co_{51.5}Al_{19.5}O_{29}$ film, T_{film} and R^s_{film} (solid line).

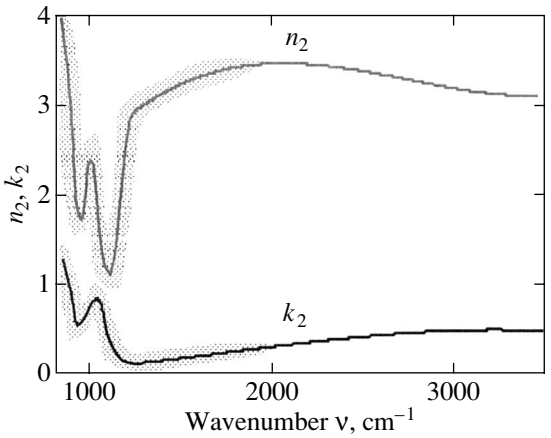

Fig. 9. Dispersion of the refractive index n_2 and of the extinction coefficient k_2 of a $Co_{51.5}Al_{19.5}O_{29}$ film.

plots the dispersion of the refractive index n_2 and of the extinction coefficient k_2 of the nanocomposite under study. The shaded region identifies the scatter of possible values of optical constants obtained in calculations with inclusion of the errors in experimental reflectivity and transmission data.

The experimental optical parameters and magnetoresistance were used to calculate the MRE from Eqs. (2)–(4). The calculated optical-reflectivity and MRE spectra obtained at $H = 1600$ Oe and $\phi = 45°$ are displayed in Fig. 3b. The calculated spectra correlate well with the experimental data (Fig. 3a) both in their structure and the magnitude of $\xi(\nu)$ and $R(\nu)$. Both the $R(\nu)$ and $\xi(\nu)$ spectra exhibit oscillations due to interference with a periodicity of $\simeq 700$ cm^{-1}. The sign of the MRE undergoes a sharp reversal in the region of the absorption band. These experimental findings find adequate interpretation in the theory.

The experimental data accumulated for the field, angular, polarization, and frequency dependences of the MRE in granular Co–Al–O, Co–Si–O, and Co–Ti–O metal–insulator alloys are fully consistent with present concepts regarding the nature of MRE in systems with tunneling contacts that exhibit high-frequency spin-dependent tunneling. A simple MRE model in which the tunneling contact between grains of a percolation cluster is described in terms of a parallel-connected capacitance and tunneling resistance circuit with inclusion of dispersion of the optical parameters of the film and substrate, as well as of light interference processes, makes it possible to interpret the experimentally observed features on a quantitative level. This agreement indicates that spin-dependent tunneling persists up to optical frequencies. The magnitude of the MRE in nanocomposites depends on many factors in a complex manner, primarily on the MR and optical parameters, and, therefore, varies over a fairly broad range, from 0.1 to 1.5%. Because the potential of increasing the magnetoresistance of nanocomposites in weak fields has been practically exhausted, it appears important, from the standpoint of both increasing the magnetorefractive effect and testing the theory, to study this effect in spin-gate tunneling contacts.

ACKNOWLEDGMENTS

This study was supported by the Russian Foundation for Basic Research (project no. 03-02-16127) and the program “Universities of Russia.”

REFERENCES

1. A. B. Granovskiĭ, I. V. Bykov, E. A. Gan’shina, V. S. Gushchin, M. Inoue, Yu. E. Kalinin, A. A. Kozlov, and A. N. Yurasov, Zh. Éksp. Teor. Fiz. **123** (6), 1256 (2003) [JETP **96**, 1104 (2003)].
2. A. Granovsky and M. Inoue, J. Magn. Magn. Mater. **272–276** (Suppl. 1), E1601 (2004).
3. I. V. Bykov, E. A. Gan’shina, A. B. Granovskiĭ, and V. S. Gushchin, Fiz. Tverd. Tela (St. Petersburg) **42** (3), 487 (2000) [Phys. Solid State **42**, 498 (2000)].
4. D. Bozec, V. G. Kravets, J. A. D. Matthew, and S. M. Thompson, J. Appl. Phys. **91** (10), 8795 (2002).
5. A. B. Granovskiĭ, V. S. Gushchin, I. V. Bykov, N. Kobayashi, A. A. Kozlov, S. Ohnuma, T. Masumoto, and M. Inoue, Fiz. Tverd. Tela (St. Petersburg) **45** (5), 868 (2003) [Phys. Solid State **45**, 911 (2003)].
6. V. G. Kravets, A. N. Pogorelyĭ, A. F. Kravets, A. Ya. Vovk, and Yu. I. Dzhezherya, Fiz. Tverd. Tela (St. Petersburg) **45** (8), 1456 (2003) [Phys. Solid State **45**, 1530 (2003)].
7. A. B. Granovsky, M. Inoue, J. P. Clerc, and A. N. Yurasov, Fiz. Tverd. Tela (St. Petersburg) **46** (3), 484 (2004) [Phys. Solid State **46**, 498 (2004)].
8. N. Kobayashi, S. Ohnuma, T. Masumoto, and H. Fujimori, J. Appl. Phys. **90**, 4159 (2001).
9. S. Ohnuma, K. Hono, E. Abe, H. Onodera, S. Mitani, and H. Fujimori, J. Appl. Phys. **82** (11), 5646 (1997).
10. A. B. Granovskiĭ, M. V. Kuzmichev, and J. P. Clerc, Zh. Éksp. Teor. Fiz. **116** (5), 1762 (1999) [JETP **89**, 955 (1999)].
11. V. M. Maevskiĭ, Fiz. Met. Metalloved. **59** (2), 213 (1985).
12. P. Bruesch, R. Kotz, H. Neff, and L. Pietronero, Phys. Rev. B **29** (8), 4691 (1984).

Translated by G. Skrebtsov

Physics of the Solid State, Vol. 47, No. 2, 2005, pp. 287–292. Translated from Fizika Tverdogo Tela, Vol. 47, No. 2, 2005, pp. 274–280.

MAGNETISM AND FERROELECTRICITY

Response of the Electrical Resistivity and Magnetoresistance of $La_{0.67}Ca_{0.33}MnO_3$ Films to Biaxial Tensile Strains

Yu. A. Boĭkov* and T. Claeson**

**Ioffe Physicotechnical Institute, Russian Academy of Sciences, Politekhnicheskaya ul. 26, St. Petersburg, 194021 Russia*
e-mail: yu.boikov@mail.ioffe.ru
***Chalmers Technological University, Göteborg, SE-41296 Sweden*

Received May 27, 2004

Abstract—The structure, electrical resistivity, and magnetoresistance of (50-nm)$La_{0.67}Ca_{0.33}MnO_3$ epitaxial films grown on a [(80 nm)$Ba_{0.25}Sr_{0.75}TiO_3$/$La_{0.3}Sr_{0.7}Al_{0.65}Ta_{0.35}O_3$] substrate with a substantial positive lattice misfit have been studied. The tensile biaxial strains are shown to account for the increase in the cell volume and in the relative concentration of Mn^{+3} ions in the manganite films as compared to those for the original material (33%). The peak in the temperature dependence of the resistivity ρ of $La_{0.67}Ca_{0.33}MnO_3$ films was shifted by 30–35 K toward lower temperatures relative to its position in the ρ(*T*) graph for a manganite film grown on (001)$La_{0.3}Sr_{0.7}Al_{0.65}Ta_{0.35}O_3$. For $T < 150$ K, the temperature dependences of ρ of $La_{0.67}Ca_{0.33}MnO_3$/$Ba_{0.25}Sr_{0.75}TiO_3$/$La_{0.3}Sr_{0.7}Al_{0.65}Ta_{0.35}O_3$ films could be well fitted by the relation $\rho = \rho_0 + \rho_1 T^{4.5}$, where $\rho_0 = 0.35$ mΩ cm and the coefficient ρ_1 decreases linearly with increasing magnetic field. In the temperature interval 4.2–300 K, the magnetoresistance of manganite films was within the interval 15–95% ($\mu_0 H = 5$ T). © *2005 Pleiades Publishing, Inc.*

1. INTRODUCTION

Considerable interest has been expressed in $La_{1-x}(Ca,Sr)_xMnO_3$ thin films in recent years due to their potential application in hard-disk read heads [1], magnetic memory cells [2], IR detectors [3], as coatings capable of efficient absorption of microwaves [4], etc.

The electron transport and magnetic properties of $La_{1-x}(Ca,Sr)_xMnO_3$ are governed by the degree of charge and spin ordering in the 3*d* electronic shells of the tri- and quadrivalent manganese ions. Investigation of the mechanisms affecting the character and extent of interrelation between the electrical and magnetic properties of perovskite-like manganites, which belong to the group of materials with strongly correlated electrons, is of considerable scientific interest.

In addition to the structure and chemical doping, strains exert a marked influence on the parameters of $La_{1-x}(Ca,Sr)_xMnO_3$ heteroepitaxial films. The differences between the lattice parameters and temperature coefficients of linear expansion of the substrate and film are the main reasons accounting for the generation of biaxial strains in the latter. Until recently, the effect of strains on electron spin ordering in manganite films had not been studied sufficiently. This has complicated the use of biaxial strains for optimizing the electrical and magnetic parameters of thin manganite layers.

We report here on a study of $La_{0.67}Ca_{0.33}MnO_3$ (LCMO) films grown on a $La_{0.3}Sr_{0.7}Al_{0.65}Ta_{0.35}O_3$ (LSATO) substrate coated with a $Ba_{0.25}Sr_{0.75}TiO_3$ (BSTO) buffer layer, whose lattice parameter exceeds those of LCMO and LSATO. As shown by us earlier [5, 6], the temperature dependences of the resistivity and magnetoresistance of LCMO epitaxial films grown on single-crystal substrates (LSATO, $NdGaO_3$) with a small lattice misfit and small difference between the temperature coefficients of linear expansion agree well with those for the corresponding stoichiometric bulk samples.

2. EXPERIMENT

A thin BSTO buffer layer was employed to increase the effective lattice misfit *m* between the manganite film and the substrate [$m = (a_S - a_L)/a_S$, where a_S and a_L are the substrate and lattice parameters, respectively]. In the case of a BSTO film (cubic unit cell at 300 K, $a_1 = 3.930$ Å [7]) and an LSATO substrate (pseudocubic at 300 K, $a_2 = 3.868$ Å [7]), we have $m \approx -1.6\%$. The unit cell constant of pseudocubic stoichiometric bulk LCMO samples is 3.858 Å [8]. The LCMO, BSTO, and LSATO have similar temperature coefficients of linear expansion [7, 9].

The (80-nm)BSTO buffer and the (50-nm)LCMO film were successively deposited on the (001)LSATO surface by laser ablation (ComPex 205, KrF, λ = 248 nm, τ = 30 ns). The substrate temperature during the BSTO and LCMO growth was 760°C. The density of the laser intensity on the target surface was 2 J/cm^2, and the oxygen pressure in the growth chamber was maintained at a level $p_0 = 0.3$ mbar. The effective growth rate *v* of the BSTO and LCMO films was 0.7 and 0.2 Å/pulse, respectively. On termination of the manganite film deposition, the heterostructure thus formed was cooled in

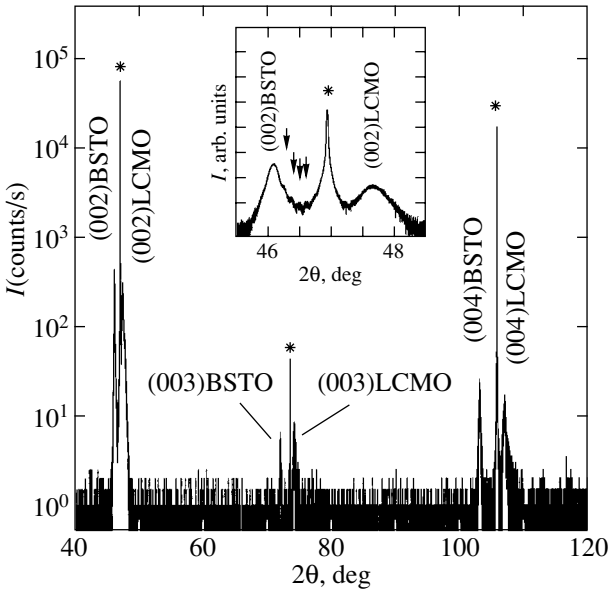

Fig. 1. X-ray diffractogram (CuK_{α_1} radiation, ω/2θ scan) of the (50-nm)LCMO/(80-nm)BSTO/(001)LSATO heterostructure obtained with the incident and reflected x-ray beams confined in a plane perpendicular to (001)LSATO. The asterisks identify x-ray peaks from the substrate. The inset shows the fragment of this diffractogram that contains (002) reflections from the manganite film, buffer layer, and substrate. Arrows specify the Laue satellite peaks.

an oxygen environment (p_O = 1 atm) to room temperature at a rate of 20°C/min.

The phase composition, orientation, and structure of the grown layers were studied by x-ray diffraction (Philips Eppert MRD, 2θ and ϕ scans, rocking curves). The x-ray scans were visualized using high-precision x-ray optics (a (220)Ge four-crystal monochromator served to form the incident x-ray beam, and the angle 2θ was measured with a plane graphite monochromator). To determine the lattice cell parameters of the grown layers in the substrate plane and along the normal to its surface, ω/2θ scans were performed in the geometry where the plane confining the incident and reflected x-ray beams was oriented orthogonal to (101) or (001)LSATO. The thicknesses of the buffer layer and of the manganite film in the LCMO/BSTO/LSATO heterostructure were derived from the Laue satellite peak widths in the measured x-ray diffractograms.

The resistance R of LCMO films was measured in the van der Pauw geometry in the temperature range 4.2–300 K, both with and without a magnetic field applied ($\mu_0 H$ up to 5 T, with the magnetic field oriented parallel to the substrate plane but perpendicular to the current flow direction). Four silver contacts arranged at the corners of a square were deposited on the LCMO film surface. The resistivity ρ of the films was calculated from the relation $\rho = \pi R d/\ln 2$ [10], where d = 50 nm is the manganite layer thickness.

3. RESULTS AND DISCUSSION

We prepared and studied five LCMO/BSTO/(001)LSATO heterostructures. The scatter among the structural, electrical, and magnetic parameters of the LCMO films in the bilayer systems grown was very small. In particular, the relative shift of the peak in the $\rho(T, H = 0)$ curves of the manganite films in our heterostructures did not exceed 5 K and the rocking curve half-widths η for the (002) x-ray peak due to the corresponding layers differ by less than 8%.

3.1. Structure of the BSTO and LCMO Layers

The x-ray data suggest that the LCMO film and the BSTO buffer in the LCMO/BSTO/LSATO heterostructure were free of microinclusions of secondary phases (Fig. 1). In x-ray ϕ scans of the (101) reflections, the BSTO buffer layer and the LCMO film produced four equidistant (90°-spaced) peaks each. The layers making up the heterostructure were preferentially oriented both relative to the substrate normal and azimuthally, with the (001) planes and the [010] directions in LCMO and BSTO being parallel to (001) and [010]LSATO, respectively. The cell parameters of the BSTO layer measured in the substrate plane, $a_\parallel$, and along the normal to this plane, $a_\perp$, differed only slightly (see table). Relaxation of strains in the buffer layer occurred primarily during its growth and oxygen saturation. The effective cell volume of the buffer layer, $V_{eff} = a_\perp \times a_\parallel^2$ = 60.73 Å^3, agrees well with the data available from the literature for the corresponding bulk samples [11].

The lattice misfit between LCMO and LSATO is $m \approx$ +0.3%. In the case of an LCMO film and an LSATO substrate coated with a (80-nm)BSTO buffer, the misfit m increases sixfold to about +1.8%. The cell parameter of the LCMO film grown on BSTO/LSATO was measured to be 3.812 ± 0.003 Å along the substrate normal,

Parameters of BSTO and LCMO films in the LCMO/BSTO/(001)LSATO heterostructure

Film material	Layer thickness, nm	v, Å/pulse	$a_\perp$, Å	$a_\parallel$, Å	V_{eff}, Å^3	$\Delta a/a$, 10^{-3}	t, nm	∂ϕ, deg	η, deg
BSTO	80	0.7	3.934	3.929	60.73	1.1	90	1	0.09
LCMO	50	0.2	3.812	3.883	57.48	1.6	70	1	0.17

which is substantially smaller than that measured in the substrate plane, 3.883 ± 0.003 Å. The (50-nm)LCMO film grown on BSTO/LSATO was subjected to in-plane tensile strains. A comparison of the $a_{\parallel}$ parameters for the layers making up the LCMO/BSTO bilayer heterostructure grown on (001)LSATO (see table) suggests that the strains in the manganite film have partially relaxed. The noticeable width of the rocking curve obtained for the (002)LCMO x-ray peak (see table) indicates nonuniform relaxation of strains in the manganite film. The effective cell volume (~57.48 Å^3) of the LCMO/BSTO/LSATO film was larger than that for bulk stoichiometric LCMO samples (~57.39 Å^3 [9]).

The larger value of V_{eff} in the LCMO films grown on BSTO/LSATO should be assigned to a high oxygen vacancy concentration in their volume and/or calcium depletion. The nuclei forming in the initial stage of growth of a manganite film on the BSTO/LSATO surface are either of a stoichiometric composition or depleted or enriched in oxygen (calcium). Oxygen (calcium)-deficient LCMO nuclei have a lower elastic strain energy as compared with nuclei with a stoichiometric composition, because the lattice parameter of a perovskite-like manganite increases when depleted in oxygen (calcium). For this reason, the nuclei depleted in oxygen (calcium) are the first to become stable. A calcium-enriched phase can precipitate on the outer boundaries of growing LCMO islands. Therefore, intergrain layers in a LCMO/BSTO/LSATO film may differ somewhat in composition from the bulk of a crystallite. As a result of these features in the nucleation and growth of perovskite-like manganites, the effective cell volume of LCMO films grown on a substrate with a noticeable positive lattice misfit turns out to be larger than V_{eff} for the corresponding single crystals. In full agreement with the above model, the cell volume in (40-nm)LCMO films [12] grown under biaxial compressive stresses was smaller than V_{eff} for stoichiometric bulk samples.

The effective crystal grain dimensions t and the average relative lattice parameter distortion $\Delta a/a$ in the layers making up the LCMO/BSTO/LSATO heterostructure were estimated from the dependence of the FWHM of the (00n) peaks in an x-ray $\omega/2\theta$ scan on θ, which, according to [13], is given by

$$\text{FWHM} \times \cos\theta = 0.9\lambda_1/t + 2(\Delta a/a)\sin\theta, \qquad (1)$$

where $\lambda_1 = 1.54056$ Å is the x-ray wavelength. As follows from the data displayed in Fig. 2, the values of $0.9\lambda_1/t$ for the BSTO layer and the LCMO film for $\theta = 0$ are 1.6×10^{-3} and 1.9×10^{-3}, respectively. It follows that the effective size of crystal grains in the buffer layer is 90 nm and in the manganite film, 70 nm. The values of $\Delta a/a$ derived for the BSTO and LCMO layers from the slope of the FWHM × cosθ vs. sinθ graphs in Fig. 2 are listed in the table. The average lattice cell distortion in the (80-nm)BSTO layer ($\Delta a/a \approx 1.1 \times 10^{-3}$) is approximately twice that obtained for thick (700-nm)BSTO epitaxial films grown on $SrRuO_3$ [7].

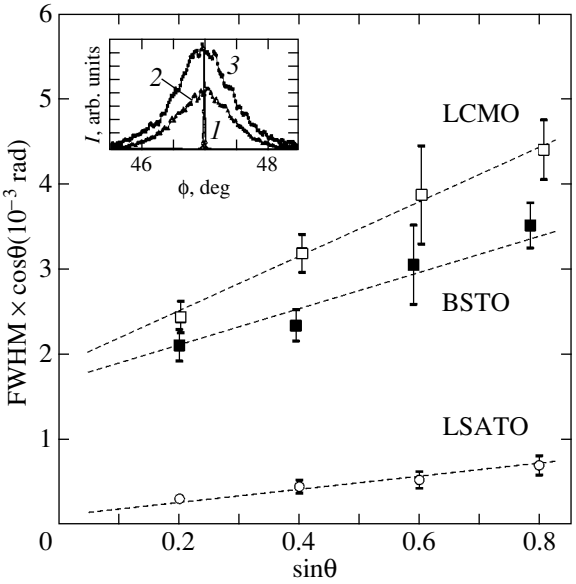

Fig. 2. The product FWHM × cosθ plotted vs. sinθ for the manganite film, the buffer layer, and the substrate in the (50-nm)LCMO/(80-nm)BSTO/(001)LSATO heterostructure. Inset shows peaks in x-ray ϕ scans for the (101) reflections from (*1*) the LSATO substrate, (*2*) LCMO film, and (*3*) BSTO buffer.

The fairly large value $\Delta a/a \approx 1.6 \times 10^{-3}$ for the LCMO film in the LCMO/BSTO/LSATO heterostructure indicates that the strains acting in its volume are nonuniformly distributed.

The misfit between the BSTO and LSATO lattices accounts for the noticeable azimuthal misorientation $\partial\phi \approx 1°$ between the crystal grains forming in the buffer layer and the manganite film grown on its surface. The magnitude of $\partial\phi$ was estimated with due account of the peak FWHM in the ϕ scans obtained for the (101)BSTO and (101)LCMO x-ray reflections from the LCMO/BSTO/LSATO heterostructure. The corresponding x-ray peaks are shown in the inset to Fig. 2. Also shown for comparison is a peak in an x-ray ϕ scan measured for the (101) reflection from a single-crystal LSATO substrate ($\partial\phi \approx 0.02°$).

3.2. Dependence of the LCMO Film Electrical Resistivity on Temperature and Magnetic Field

For $H = 0$, the maximum in the temperature dependence of the resistivity of LCMO films grown on BSTO/LSATO was observed at $T_M = 225$–230 K (Fig. 3). This value is about 35 K lower than the temperature at which the resistivity of bulk stoichiometric samples and of LCMO epitaxial films grown on (001)LSATO passes through a maximum [5]. (T_M for bulk LCMO crystals differs very little from the Curie temperature T_C [14].) The lower values of T_M for the LCMO/BSTO/LSATO films may be partially due to their deviation from stoichiometry. The depletion of an LCMO film in oxygen

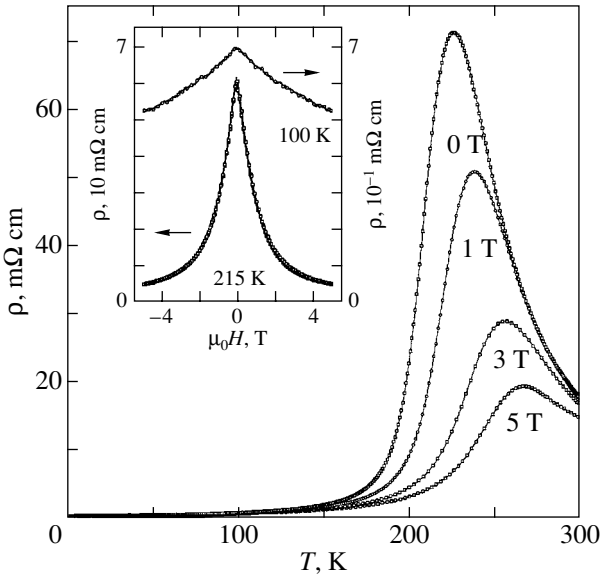

Fig. 3. Temperature dependences of the resistivity ρ of a (50-nm)LCMO film in an LCMO/BSTO/(001)LSATO heterostructure measured at various magnetic fields. Inset shows the magnetic field dependences of ρ obtained at 100 and 215 K.

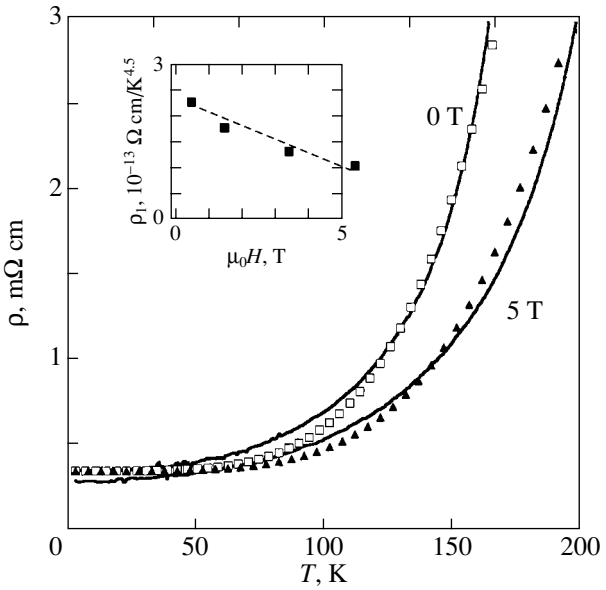

Fig. 4. Temperature dependences of the resistivity ρ of a (50-nm)LCMO/(80-nm)BSTO/(001)LSATO film measured in the range 4.2–200 K at $\mu_0 H$ = 0 and 5 T (solid curves). The values of ρ calculated using Eq. (2) for $\mu_0 H$ = 0 (squares) and $\mu_0 H$ = 5 T (triangles) fit the experimental data well. The inset shows the magnetic field dependence of the coefficient ρ_1 obtained for the same film.

(calcium) is accompanied by an increase in the relative concentration of Mn^{+3} ions in its volume, which, according to the phase diagram obtained for $La_{1-x}Ca_xMnO_3$ ceramic samples [15], should bring about a lowering of the ferromagnetic ordering temperature of manganese ion spins. Nonuniform elastic strains in a manganite film increase the scatter in the effective manganese–oxygen bond length, which also contributes to the decrease in T_M [16].

The presence of a magnetic field is conducive to ferromagnetic spin ordering in a manganite film and an increase in T_M. As $\mu_0 H$ increased from 0 to 5 T, the maximum in the ρ(*T*, *H*) graphs for the LCMO/BSTO/LSATO films shifted toward higher temperatures (by 45 K at $\mu_0 H$ = 5 T) and the peak value of resistivity decreased by a factor of 3–4 (Fig. 3).

For $T < T_C$, the resistivity of 3*d* ferromagnetic metals is contributed (in addition to electron–electron interaction and electron scattering from phonons and structural defects) by spin disorder [17]. According to [18], the spontaneous magnetization vector in an LCMO film strained biaxially (tension) by the substrate becomes oriented preferentially parallel to the plane of the latter. The nonuniformity of the strains, as well as the azimuthal misorientation of crystal grains, intensifies disorder in the manganese-ion electron spin system. The contribution of electron–magnon scattering to the resistivity of a manganite film should become significant when most of its volume is in the ferromagnetic state, i.e., for $T \ll T_C$. In conditions where the relaxation of carriers is dominated by their interaction with spin waves, the resistivity of a ferromagnet, according to [19], should obey the relation $\rho \sim \rho_1 T^{4.5}$, where ρ_1 is a coefficient that is dependent on magnetic field but independent of temperature. The temperature dependences of the resistivity of an LCMO/BSTO/LSATO film measured at $\mu_0 H$ of 0 and 5 T are presented graphically in Fig. 4 (solid curves). For $T < 200$ K and $\mu_0 H$ = 0–5 T, the experimental ρ(*T*, *H*) relations can be satisfactorily fitted by

$$\rho(T, H) = \rho_0 + \rho_1(H) T^{4.5}, \qquad (2)$$

where ρ_0 = 3.5 mΩ cm is a constant independent of temperature and magnetic field. The coefficient $\rho_1(H)$ was determined at different magnetic fields from the slope of experimental $\rho \sim T^{4.5}$ relations within the range 4.2–50 K. It was found that ρ_1 falls off approximately linearly with increasing magnetic field (see inset to Fig. 4). A similar dependence of the coefficient ρ_1 on magnetic field was reported in [14]. Figure 4 presents the values of ρ for an LCMO/BSTO/LSATO film calculated from Eq. (2) for $\mu_0 H$ = 0 (squares) and $\mu_0 H$ = 5 T (triangles). In [14], when fitting the ρ(*T*) curves for LCMO films subjected to heat treatment in an oxygen environment, a term proportional to T^2 was added to the right-hand side of Eq. (2) to account for the contribution from electron–electron interaction to carrier relaxation.

Within the temperature interval 200 K–T_M, the resistivity of the LCMO/BSTO/LSATO film increased with

temperature faster than predicted by Eq. (2). This is caused by an increasing concentration of a nonferromagnetic phase in its volume, which is accompanied by a decrease in size and density of the highly conducting (ferromagnetic) "percolation channels." The coexistence of inclusions of a ferromagnetic (high-conductivity) and a paramagnetic (low-conductivity) phase in the bulk of a manganite film at the temperatures specified above manifests itself clearly in the response of the electrical resistivity of the film to a magnetic field. The $\rho(H)$ curves measured on an LCMO/BSTO/LSATO film at $T = 215$ and 100 K are shown in the inset to Fig. 3. As follows from the $\rho(H, 215\ \text{K})$ graph, the absolute value of the $d\rho/dH$ derivative for $\mu_0 H < 1.5$ T greatly exceeds those obtained for $\mu_0 H > 3.5$ T. The fast drop in the resistivity of the LCMO/BSTO/LSATO film observed to occur with increasing magnetic field ($\mu_0 H < 1.5$ T) results from the increasing concentration of the ferromagnetic phase (an increase in the percolation channel density). For $\mu_0 H > 3.5$ T, the greater part of the LCMO/BSTO/LSATO film volume is in the ferromagnetic state and the observed relatively weak (approximately linear) decrease in its resistivity with increasing $\mu_0 H$ is caused by the electron–magnon coupling weakening as a result of spatial ordering of manganese electronic spins. At low temperatures ($T \le 150$ K), inclusions of the paramagnetic phase make up an insignificant volume fraction already at $H = 0$; therefore, the resistivity of the film varies almost linearly with increasing $\mu_0 H$ in the range 0–5 T (see inset to Fig. 3). This correlates well with the corresponding data available for bulk samples of 3*d* ferromagnetic metals [17].

In the temperature interval T_M–300 K, the resistivity of the LCMO film obeyed the relation $\ln\rho(H = 0) \sim E_A/k_B T$, with $E_A = 0.14$ eV (k_B is the Boltzmann constant). This pattern of the temperature dependence of the paramagnetic phase in manganites ($T > T_C$) may be caused by the formation of small-radius polarons in their bulk [20, 21], whose mobility grows exponentially with temperature. Structural studies [22] provide supportive evidence for the presence of substantial distortions in the LCMO lattice for $T > T_C$, which largely disappear for $T < T_C$.

Turning now to analysis of the data obtained on the magnetoresistance of LCMO/BSTO/LSATO films, we can note that the strength of electron–electron and electron–phonon coupling does not depend significantly on magnetic field [14, 17]. Among the mechanisms conducive to a decrease in the resistivity of LCMO/BSTO/LSATO films with increasing *H*, the following three stand out: (i) for $T < T_C$, the magnetic field amplifies spin-wave damping, which favors an increased carrier (hole) relaxation time; (ii) at temperatures close to T_C, the magnetic field increases the density of the ferromagnetic high-conductivity percolation channels in the bulk of a manganite film; and (iii) the magnetic field fosters a reduction in the relative misorientation of spins in grain spacers as compared to their orientation in the bulk of the crystallites.

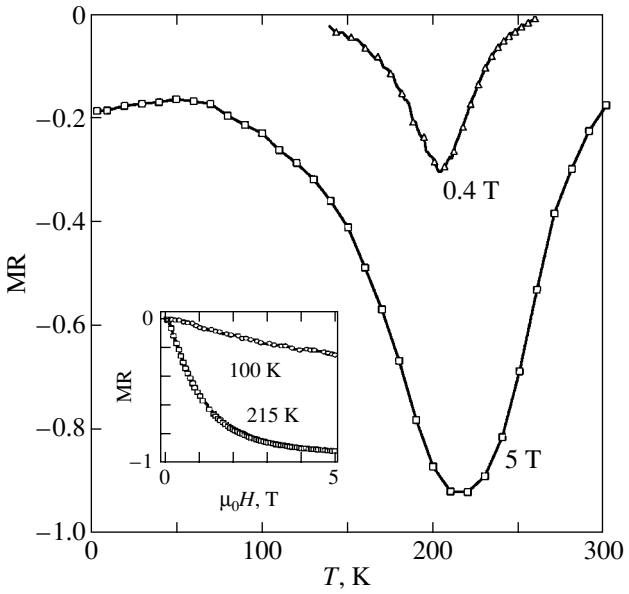

Fig. 5. Temperature dependences of the magnetoresistance $MR = [\rho(\mu_0 H) - \rho(0)]/\rho(0)$ of a manganite film in a (50-nm)LCMO/(80-nm)BSTO/(001)LSATO heterostructure measured at $\mu_0 H = 0.4$ and 5 T. The inset shows the magnetic field dependences of the magnetoresistance of the same film obtained at 100 and 215 K.

Figure 5 displays the temperature dependences of magnetoresistance $MR = [\rho(\mu_0 H) - \rho(0)]/\rho(0)$ measured on an LCMO/BSTO/LSATO film in magnetic fields of 0.4 and 5 T. At $\mu_0 H = 0.4$ T, the manganite films exhibited the maximum magnitude of negative magnetoresistance in the vicinity of 205 K. As *H* increased, the peak in the $MR(T, H)$ curve shifted toward higher temperatures. The FWHM of the peak in the $MR(T, H)$ dependence obtained for LCMO/BSTO/LSATO films exceeded by several times the corresponding value for LCMO films grown on substrates with a small *m* [5]. Furthermore, the values of MR obtained for the LCMO/BSTO/LSATO films at low temperatures ($T < 10$ K) greatly exceeded the magnetoresistance of the LCMO films grown on substrates with a small *m* that were heat-treated in oxygen [6]. This finding can be partially assigned to the existence of grain boundaries with off-stoichiometry in the LCMO/BSTO/LSATO films [23].

The magnetic field dependences of the magnetoresistance of an LCMO/BSTO/LSATO film measured at $T = 215$ and 100 K are displayed in the inset to Fig. 5. At $T = 100$ K, negative MR of the LCMO/BSTO/LSATO film increased almost linearly with increasing $\mu_0 H$, which fits with the dependence of the coefficient ρ_1 [defined in Eq. (2)] on magnetic field (see inset to Fig. 4). Thus, in the range $0 < \mu_0 H < 5$ T, the $MR(H, 100\ \text{K})$ relation is determined to a considerable extent by carrier (hole) scattering from magnons. At temperatures close to T_M, the effect of scattering by magnons on the character of the magnetic field depen-

dence of resistivity of the LCMO/BSTO/LSATO film becomes dominant only for $\mu_0 H > 3.5$ T [see inset to Fig. 5, MR(H, T = 215 K)]. The anomalously strong growth of the negative magnetoresistance in magnitude with increasing H for a relatively weak magnetic field ($\mu_0 H < 1.5$ T) is largely due to the increasing density of ferromagnetic, highly conducting percolation channels in the bulk of a manganite film.

4. CONCLUSIONS

Tensile strains acting in the course of nucleation and growth of (50-nm)LCMO manganite films are conducive to the onset of off-stoichiometric distortions in the latter (depletion in oxygen and/or calcium), which becomes manifest in an increase in the unit cell volume and brings about a decrease in the relative concentration of quadrivalent manganese ions. An increase in the Mn^{3+} ion concentration in a manganite film weakens the ferromagnetic interaction between manganese ions, which involves double exchange of electrons between Mn^{3+} and Mn^{4+} mediated by the oxygen ion. This weakening may account, to a certain extent, for the shift of the maximum in the temperature dependence of the resistivity of the (50-nm)LCMO/(80-nm)BSTO/LSATO film toward lower temperatures relative to its position on the $\rho(T, H = 0)$ curve for bulk stoichiometric LCMO samples. For $T < T_C$, the nonuniform distribution of strains, density fluctuations of oxygen vacancies and vacancies on the cation sublattice, and azimuthal misorientation of crystal grains in the LCMO/BSTO/LSATO film enhance misorientation of the electronic spins of the manganese ions, thus increasing the spin-wave contribution to the carrier relaxation. At temperatures close to the ferromagnetic phase transition, the magnetic field increases the relative concentration of inclusions of the ferromagnetic phase in the bulk of a manganite film. The magnetic field also enhances spin-wave damping and reduces spatial misorientation of the electron spins of the manganese ions at grain boundaries and in the bulk of the crystallites.

ACKNOWLEDGMENTS

This study was carried out in the framework of scientific cooperation between the Russian and Royal Swedish Academies of Sciences and was also partially supported by the Russian Foundation for Basic Research (project no. 04-02-16212) and the program of the Presidium of the RAS “Low-Dimensional Quantum Structures” (project no. 9B19).

REFERENCES

1. Y. Tokura, in *Colossal Magnetoresistive Oxides*, Ed. by Y. Tokura (Gordon and Breach, Amsterdam, 2000), p. 2.
2. S. S. P. Parkin, K. P. Roche, M. G. Samant, P. M. Rice, R. B. Beyers, R. E. Scheuerlein, E. J. O’Sullivan, S. L. Brown, J. Bucchigano, D. W. Abraham, Yu. Lu, M. Rooks, P. L. Trouilloud, R. A. Wanner, and W. J. Gallagher, J. Appl. Phys. **85** (8), 5828 (1999).
3. A. Goyal, M. Rajeswari, R. Shreekala, S. E. Lofland, S. M. Bhagat, T. Boettcher, C. Kwon, R. Ramesh, and T. Venkatesan, Appl. Phys. Lett. **71** (17), 2535 (1997).
4. V. V. Srinivasu, S. E. Lofland, S. M. Bhagat, K. Ghosh, and S. D. Tyagi, J. Appl. Phys. **86** (2), 1067 (1999).
5. Yu. A. Boĭkov, T. Claeson, and A. Yu. Boĭkov, Zh. Tekh. Fiz. **71** (10), 54 (2001) [Tech. Phys. **46**, 1260 (2001)].
6. Yu. A. Boĭkov, V. A. Danilov, and A. Yu. Boĭkov, Fiz. Tverd. Tela (St. Petersburg) **45** (4), 649 (2003) [Phys. Solid State **45**, 681 (2003)].
7. Yu. A. Boikov and T. Claeson, Physica B (Amsterdam) **311** (3–4), 250 (2002).
8. C. J. Lu, Z. L. Wang, C. Kwon, and Q. X. Jia, J. Appl. Phys. **88** (7), 4032 (2000).
9. K. H. Kim, J. Y. Gu, H. S. Choi, G. W. Parjk, T. W. Park, and T. W. Noh, Phys. Rev. Lett. **77** (9), 1877 (1996).
10. T. I. Kamins, J. Appl. Phys. **42** (9), 4357 (1971).
11. A. von Hippel, Rev. Mod. Phys. **22** (3), 221 (1950).
12. Yu. A. Boĭkov, T. Claeson, and A. Yu. Boĭkov, Fiz. Tverd. Tela (St. Petersburg) **45** (6), 1040 (2003) [Phys. Solid State **45**, 1090 (2003)].
13. E. D. Specht, T. E. Clausing, and L. Heatherly, J. Mater. Res. **5** (11), 2351 (1990).
14. G. J. Snyder, R. Hiskes, S. DiCarolis, M. R. Beasley, and T. H. Geballe, Phys. Rev. B **53** (21), 14 434 (1996).
15. P. Shieffer, A. P. Ramirez, W. Bao, and S.-W. Cheong, Phys. Rev. Lett. **75** (18), 3336 (1995).
16. L. M. Rodriguez-Martinez and J. P. Attfield, Phys. Rev. B **54** (22), R15622 (1996).
17. B. Raquet, M. Viret, J. M. Broto, E. Sondergard, O. Cespedes, and R. Many, J. Appl. Phys. **91** (10), 8129 (2002).
18. Y.-A. Soh, G. Aeppli, N. D. Mathur, and M. G. Blamire, J. Appl. Phys. **87** (9), 6743 (2000).
19. K. Kubo and N. Ohata, J. Phys. Soc. Jpn. **33** (1), 21 (1972).
20. M. Jaine, M. B. Salamon, M. Rubinstein, R. E. Treece, J. S. Horwitz, and D. B. Chrisey, Phys. Rev. B **54** (17), 11 914 (1996).
21. G. Zhao, Y. S. Wang, D. J. Kang, W. Prellier, M. Rajeswari, H. Keller, T. Venkatesan, C. W. Chu, and R. L. Creene, Phys. Rev. B **62** (18), R11949 (2000).
22. P. J. Radaelli, M. Marezio, H. Y. Hwang, S.-W. Cheomg, and B. Batlogg, Phys. Rev. B **54** (13), 8992 (1996).
23. R. Mahesh, R. Mahendiran, A. K. Raychaudhuri, and C. N. R. Rao, Appl. Phys. Lett. **68** (16), 2291 (1996).

Translated by G. Skrebtsov

Physics of the Solid State, Vol. 47, No. 2, 2005, pp. 293–297. Translated from Fizika Tverdogo Tela, Vol. 47, No. 2, 2005, pp. 281–285.

MAGNETISM AND FERROELECTRICITY

Temperature Dependence of Magnetooptic Effects in Rare-Earth Magnetic Semiconductor γ-Dy_2S_3

B. B. Krichevtsov* and H.-J. Weber**

**Ioffe Physicotechnical Institute, Russian Academy of Sciences, Politekhnicheskaya ul. 26, St. Petersburg, 194021 Russia*

***Dortmund University, Dortmund, 44221 Germany*

Received June 9, 2004

Abstract—Temperature dependences of the Faraday effect (FE), which is linear in a magnetic field **B**; of the nonreciprocal linear birefringence (NB) associated with magnetic field–induced spatial dispersion; and of the Cotton–Mouton effect (CME), which is quadratic in a magnetic field **B**, have been studied in the transmission region of the γ-Dy_2S_3 cubic magnetic semiconductor (T_d symmetry class) at wavelength λ = 633 nm in the temperature range T = 25–294 K. As the temperature is lowered, the magnitudes of the FE and of the two main NB components, α_{001} and α_{011}, increase in proportion to the magnetic susceptibility χ. This behavior implies that the magnitude of these effects is determined by the magnetic moment **m** of the Dy^{3+} ion induced by the magnetic field **B**. The CME component β_{001} (**k** ∥ [1$\bar{1}$0], **B** ∥ [001]) grows in proportion to the magnetic susceptibility squared, χ^2; i.e., $\beta_{001} \sim \mathbf{m}^2$. By contrast, the component β_{111} (**k** ∥ [1$\bar{1}$0], **B** ∥ [111])) exhibits a weaker temperature dependence, which indicates the manifestation of microscopic mechanisms in the CME component β_{111} that differ from those for β_{001}. *© 2005 Pleiades Publishing, Inc.*

1. INTRODUCTION

Investigation of semiconducting compounds with a large bandgap E_g has been recently attracting considerable attention. Among these compounds are, in particular, the rare-earth sesquisulfides γ-Ln_2S_3, which are magnetic semiconductors with a bandgap $E_g \approx 3$ eV [1]. They crystallize in a noncentrosymmetric cubic structure (T_d crystal class) and exhibit properties stemming from the absence of an inversion center. For instance, crystals of the γ-Ln_2S_3 family were found to exhibit a large electro-optical effect [2], photogalvanic effect [3], piezoelectric effect [4], etc. The presence of the rare-earth (RE) ions in the structure accounts for the magnetic properties and the relatively high intensity of the magneto-optic effects. For instance, the Faraday effect (FE) seen in the transmission window of some sesquisulfides is as high as ≈10^3 deg/cm T [5].

Rare-earth sesquisulfides have been recently observed to exhibit magnetic linear birefringence (MLB) [6]. Unlike crystals with a center of inversion, MLB in γ-Ln_2S_3 is determined not only by the Cotton–Mouton effect (CME), which is quadratic in a magnetic field **B**, but also by nonreciprocal birefringence (NB), which is linearly dependent on magnetic field **B**. The nature of the latter is mediated by magnetically induced spatial dispersion and is directly associated with the crystal structure lacking inversion symmetry [7].

In contrast to the FE, the CME and NB are anisotropic in a cubic crystal, so in order to describe these effects, one has to determine the magnitude of the CME and NB for at least two different orientations of magnetic field **B** relative to the crystallographic axes. MLB studies performed in the transmission window of γ-Dy_2S_3 have shown that the fundamental CME components, β_{001} (**k** ∥ [110], **B** ∥ [001]) and β_{111} (**k** ∥ [110], **B** ∥ [111]), are opposite in sign and differ in dispersion [8]. The energy of the effective oscillator determining the dispersion of $\beta_{001}(E)$ is $E_{\text{eff}} \approx 3.4$ eV, which is about 0.6 eV above the fundamental absorption edge. The β_{111} component depends only weakly on photon energy E and does not exhibit a resonant increase with increasing E within the energy interval E = 1.5–2.5 eV. The main NB components of γ-Dy_2S_3, namely, α_{001} (**k** ∥ [1$\bar{1}$0], **B** ∥ [001]) and α_{011} (**k** ∥ [1$\bar{1}$0], **B** ∥ [011]), also reveal differences in their spectral response. Indeed, while α_{011}, just as β_{001}, grows resonantly with photon energy E and derives from transitions with energy $E \approx 3.4$ eV, α_{001}, similar to β_{111}, is weakly dependent on E. The difference in the spectral response of the MLB components indicates that they originate from electronic transitions with different energies. The energy of the transitions responsible for the components of CME β_{111} and NB α_{001} should be substantially larger ($E \gg 3.4$ eV) than that for β_{001} and α_{011}. The transitions governing the magneto-optical properties in sesquisulfides have not been assigned unambiguously to date. Nevertheless, it can be assumed that the electron transitions responsible for the magneto-optical effects in γ-Dy_2S_3 originate from the Dy^{3+} ground state ($^6H_{15/2}$) and that their behavior is largely governed by the magnetic field–induced splitting of this state. Therefore, it appeared of interest

1063-7834/05/4702-0293$26.00

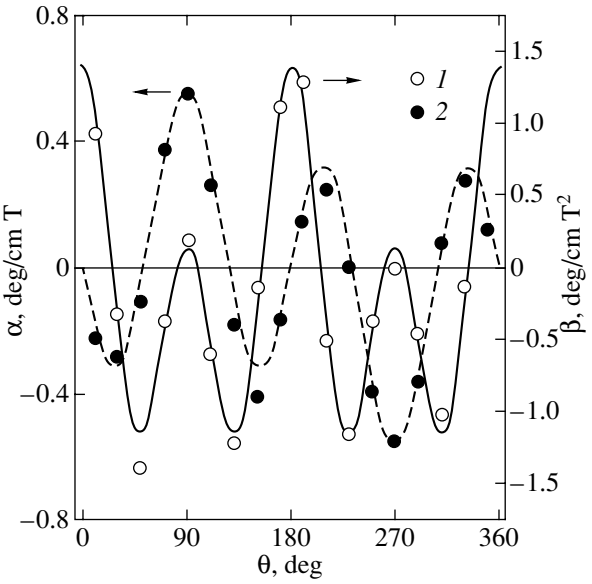

Fig. 1. Angular dependences of (*1*) the CME (β) and (*2*) NB (α) measured in γ-Dy_2S_3 in the **E**45**B** geometry in the (110) plane at λ = 633 nm. The solid line is a plot of the CME relation $\beta(\theta) = a_1 + b_1\cos 2\theta + c_1\cos 4\theta$. The dashed line is NB calculated from the relation $\alpha(\theta) = a_2\sin\theta + b_2\sin 3\theta$.

to find the relation between the magnitudes of the linear and quadratic magneto-optical effects in γ-Dy_2S_3 and the magnetic moment **m** of the rare-earth sublattice induced by an external magnetic field. This moment is known to be determined by the population of the ground state levels of the RE ion in a magnetic field. This relation can be derived by comparing the temperature dependences of the magneto-optical effects and of the magnetic susceptibility. As far as we know, investigation into the magneto-optical properties in γ-Ln_2S_3 has thus far been limited to their spectral response at fixed temperatures. The present communication reports on a study of the temperature dependences of magneto-optical effects in γ-Dy_2S_3 that are linear (FE, NB) or quadratic (CME) in magnetic field and on their comparison with the temperature dependence of the magnetic susceptibility.

2. MEASUREMENT TECHNIQUES AND SAMPLES

The FE and MLB were studied using the polarimetric technique [9] at a light wavelength λ = 633 nm. We measured the change in the angle of rotation of the plane of polarization ξ of light (for FE) or in its ellipticity φ (in the case of MLB) induced by the application of an external magnetic field **B** to the crystal. The MLB measurements were conducted in the **k** ⊥ **B** geometry. The maximum magnetic field **B** that could be generated by an electromagnet was ±0.5 T. The angular dependences of CME and NB were measured at a temperature T = 294 K in the **E** || **B** and **E**45**B** geometries [8, 9], with the sample azimuth θ (the angle between the magnetic field **B** and a [001]-type crystallographic axis) being varied in the range 0–360° and measured to within ~0.1°. To separate the CME from NB (which are even and odd in the magnetic field, respectively) for a given angle θ, we measured the angle φ at **B** = 0 (φ_0) and **B** = ±0.5T ($\varphi_\pm$). The magnitudes of the CME (β) and NB (α) were found from the relations

$$\beta = \frac{\varphi_+ + \varphi_- - 2\varphi_0}{2dB^2}, \quad (1)$$

$$\alpha = \frac{\varphi_+ - \varphi_-}{2dB}, \quad (2)$$

where d is the sample thickness. The quantity φ_0 is due to the existence of magnetic field–independent spontaneous birefringence in a crystal originating from internal stresses and defects.

Studies of the temperature dependence were carried out in a closed-cycle optical cryostat within the temperature interval T = 25–294 K, with the temperature stable within ~0.5 K. The crystal was placed on a cooled holder in vacuum. The CME was measured at **B** || [001] (θ = 0) and **B** || [111] (θ = 55°) in the **E**45**B** geometry, and the NB was measured at **B** || [001] in the **E** || **B** geometry (α_{001}) and at **B** || [110] in the **E**45**B** geometry (α_{110}). The crystallographic axes were oriented relative to the magnetic field with Δθ no worse than 5°. To exclude the FE, which may appear as a result of inaccuracies in the orientation of the magnetic field **B** perpendicular to the direction of **k**, the magnet was adjusted carefully before MLB measurements. To do this, the quarter-wave plate was removed from the optical arrangement and the magnet was turned such that the application of a magnetic field did not cause any rotation of the plane of polarization. The sensitivity of measuring the rotation of the plane of polarization was ~10″.

The γ-Dy_2S_3 samples were polished, plane-parallel plates cut in the (110) plane with dimensions ~3 × 3 × 1 mm. The samples were oriented by means of x rays. The orientation accuracy was ~3°. The spontaneous crystal birefringence associated with internal strains and with the existence of defects did not exceed $\Delta n = 10^{-6}$. The presence of such birefringence did not exert noticeable effects on the magnitude of the MLB and FE [6]. When measuring the temperature dependences of the FE, a magnetic field B = ±0.01 T was applied along the direction of light propagation, **k**. The magnet was mounted inside the cryostat to preclude the FE originating from the cryostat windows. The Verde parameter V[deg/cm T] characterizing the FE was determined from the relation $V = (\xi_+ - \xi_-)/dB$.

3. EXPERIMENTAL RESULTS

Figure 1 plots typical angular dependences of the CME (β) and NB (α) measured in γ-Dy_2S_3 in a (110)-type plane in the **E**45**B** geometry. The angular

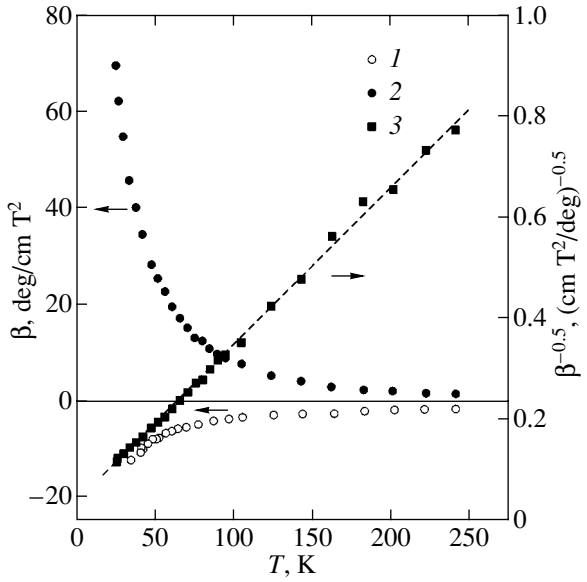

Fig. 2. Temperature dependences (*1*, *2*) of the CME components (*1*) β_{001} and (*2*) β_{111} and (*3*) of $\beta_{001}^{-0.5}$. The dashed line is a linear fit.

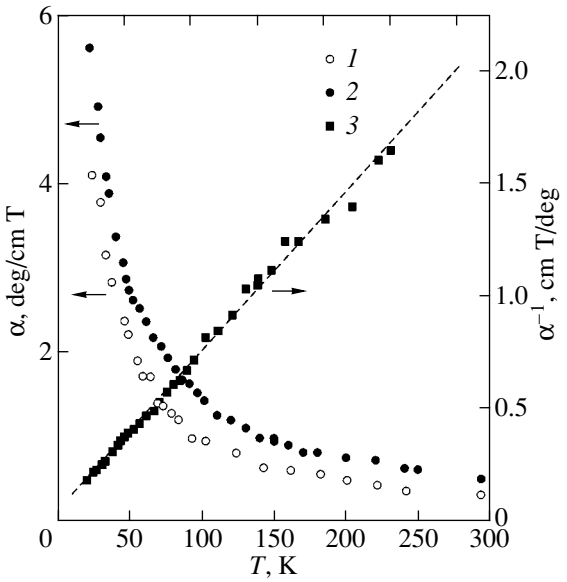

Fig. 3. Temperature dependences (*1*, *2*) of the NB components (*1*) α_{011} (**E**45**B** geometry, **B** ∥ [011]) and (*2*) α_{001} (**E** ∥ **B** geometry, **B** ∥ [001]) and (*3*) of α_{011}^{-1}. The dashed line is a linear fit.

dependence of the quadratic-in-magnetic-field CME $\beta(\theta)$ in this plane is described by a combination of the zeroth-, second-, and fourth-order harmonics, $\beta(\theta) = a_1 + b_1\cos 2\theta + c_1\cos 4\theta$. The anisotropy of the odd-in-**B** NB is approximated by harmonics of the first and third orders, $\alpha(\theta) = a_2\sin\theta + b_2\sin 3\theta$. In accordance with the phenomenological description of quadratic magneto-optical effects in a cubic crystal of the T_d crystal class, the CME components measured in the **E**45**B** geometry, namely, β_{001} (**B** ∥ [001]) and β_{111} (**B** ∥ [111]), are determined by a fourth-rank tensor ρ_{ijkl} that is symmetric in two pairs of indices [10]: $\beta_{001} = -\pi(1/2)n^3(\rho_{11} - \rho_{12})/\lambda$ and $\beta_{111} = -\pi n^3\rho_{44}/\lambda$. The NB measured in the **E**45**B** geometry is determined for **B** ∥ [011] (α_{011}) by the components A and g of the tensor γ_{ijkl} describing the relation between the components of the permittivity tensor ε_{ij}, the wave vector **k**, and magnetic field **B** ($\delta\varepsilon_{ij} = \gamma_{ijml}k_mB_l$), $\alpha_{011} = \pi(3A + 2g)k/4n\lambda$. When measured in the **E** ∥ **B** geometry with **B** ∥ [001], the NB (α_{001}) is determined only by the component g: $\alpha_{001} = \pi gk/n\lambda$ [9]. The components β_{001}, β_{111}, α_{001}, and α_{011} completely determine the MLB of a cubic crystal, so we studied the temperature dependences of only these components.

Figure 2 plots temperature dependences of the CME components β_{001} and β_{111} in γ-Dy_2S_3. As the temperature decreases, both components grow monotonically in magnitude. At T = 25 K, β_{001} reaches as high as ~70 deg/cm T², which is 45 times the value of β_{001} at T = 294 K. In contrast to β_{001}, the component β_{111} grows much more weakly with decreasing temperature. At T = 25 K, its value ($\beta_{111} \approx -15$ deg/cm T²) is only 15 times that at room temperature.

Figure 3 displays the temperature dependence of the NB components $\alpha_{001}(T)$ and $\alpha_{011}(T)$. Both NB components increase with decreasing temperature in almost identical fashion, and their values at T = 25 K are approximately an order of magnitude larger than those at T = 294 K.

Figure 4 shows the temperature dependence of the FE in γ-Dy_2S_3. The $V(T)$ relation is similar to the temperature dependence of the NB components $\alpha_{001}(T)$ and $\alpha_{011}(T)$. The FE grows monotonically in magnitude with decreasing temperature to reach values of ~3000 deg/cm T at T = 25 K.

Thus, a decrease in temperature gives rise to strongly increased linear and quadratic magneto-optical effects in γ-Dy_2S_3. The FE and NB, which are linear in magnetic field, grow similarly with a decrease in temperature, and their magnitude at T = 25 K is about an order of magnitude larger than that at T = 294 K. The CME components that are quadratic in magnetic field (β_{001}, β_{111}) behave differently with decreasing temperature. The component β_{001} increases by nearly two orders of magnitude, while β_{111} grows only by an order of magnitude.

4. DISCUSSION OF THE RESULTS

The relatively large magnitude of the linear and quadratic magneto-optical effects observed in rare-earth sesquisulfides γ-Ln_2S_3, in particular, at T = 294 K, is due to their structure including trivalent RE ions with an unfilled $4f^N$ shell, which is responsible for the paramagnetism of these compounds, as well as to the spe-

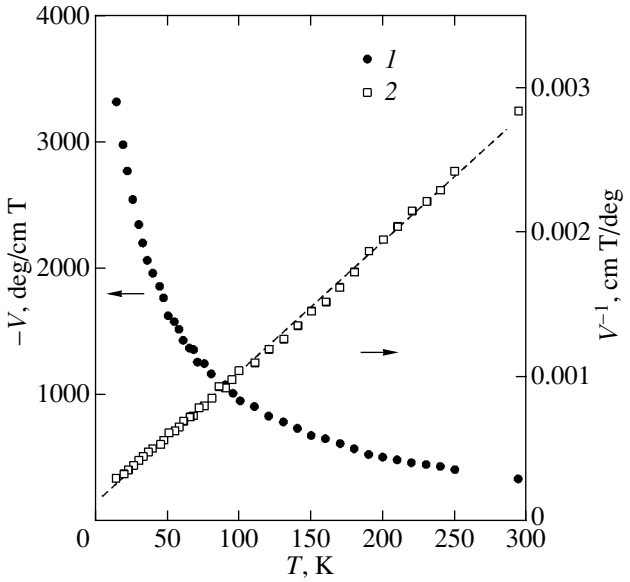

Fig. 4. Temperature dependences of (*1*) the FE V and (*2*) V^{-1} measured in γ-Dy_2S_3 at λ = 633 nm. The dashed line is a linear fit to $V^{-1}(T)$.

cific features of their electronic structure. In contrast to paramagnetic dielectrics, which contain RE ions (for instance, gallate and aluminate garnets, phosphate and silicate glasses) whose energy of optical transitions $4f^N \longrightarrow 4f^{N-1}5d$ between the states of the RE ions responsible for the magneto-optical effects lies in the region $E \sim 5$–7 eV [11], the optical transition energy in rare-earth semiconductors γ-Ln_2S_3 is substantially smaller (E = 3.5–4.0 eV) and its magnitude correlates with the bandgap width E_g [12]. Among crystals of the sesquisulfide family, the paramagnetic properties are particularly strongly manifest in γ-Dy_2S_3 due to the large magnetic moment of the Dy^{3+} ion ($10.6\mu_B$) in the ground state ($^6H_{15/2}$). In this family, γ-Dy_2S_3 also stands out as having the largest magneto-optical oscillator strength B_{eff}, which enters the expression for the FE dispersion in the single-oscillator model, $V(E) = B_{\text{eff}}E^2/(E_{\text{eff}}^2 - E^2)$ [5].

The temperature dependence of the magneto-optical effects in paramagnets observed in transmission regions at frequencies far from resonances is determined by various mechanisms. The mixing and diamagnetic mechanisms account for the temperature-independent part of the FE, while the paramagnetic mechanism is responsible for the temperature-dependent FE [13]. In weak magnetic fields, i.e., in the case where the **m**(**B**) dependence is linear, the paramagnetic mechanism provides a linear relation between the FE and the magnetic moment **m** of the rare-earth sublattice induced by a magnetic field **B**:

$$V = Am(T)/B = A\chi(T), \qquad (3)$$

where $\chi(T)$ is the magnetic susceptibility and A is the magneto-optical susceptibility.

In crystals containing RE ions with a nonzero ground-state orbital angular momentum, the paramagnetic contribution to the magnetic susceptibility of the rare-earth sublattice usually substantially exceeds the diamagnetic and the Van Vleck terms. The temperature dependence of the FE in these crystals is dominated by the paramagnetic mechanism, i.e., by the temperature dependence of the magnetic susceptibility $\chi(T)$ [13]. The magneto-optical susceptibility A in Eq. (3) is determined by the energy of the optical transitions responsible for the FE, by matrix elements of the $\text{Im}\{d_{ab}d_{ba}\}$ type (where a and b label the ground and excited states of an optical transition and d_{ab} is the dipole moment operator), and by the refractive index n. In γ-Gd_2S_3, in which the RE ion resides in the S state, and in the diamagnetic γ-La_2S_3, the values of NB and CME at T = 294 K are at least an order of magnitude smaller than those in γ-Dy_2S_3 and γ-Pr_2S_3 [6]. Therefore, we may expect the paramagnetic mechanism to also govern the temperature dependence of the linear-in-magnetic-field NB in γ-Dy_2S_3,

$$\alpha = Cm(T)/B = C\chi(T) \qquad (4)$$

and of the quadratic CME,

$$\beta = Dm^2(T)/B^2 = D\chi^2(T), \qquad (5)$$

where C and D are the magneto-optical susceptibilities.

It should be stressed that Eqs. (3)–(5) are valid only in the region where the **m**(**B**) relation is linear, i.e., where the condition $g\mu_B B \ll kT$ holds (g is the ground-state spectroscopic splitting factor). Breakdown of this condition may give rise to the appearance of the FE in a cubic crystal in a transverse magnetic field **B** (due to g-factor anisotropy) [14], a dependence of the magnitude of the FE on the direction of light propagation **k**, a violation of the rule of even effects in CME, anisotropy in the magnetic susceptibility [15], the appearance of a linear dependence of the CME on magnetic field [16], etc. In the present study, the $g\mu_B B \ll kT$ condition was met in the temperature and magnetic-field ranges covered.

A study of the temperature dependence of the magnetic susceptibility of γ-Dy_2S_3 carried out on crushed single crystals revealed that this crystal persists in the paramagnetic state down to liquid-helium temperature (T = 4.2 K) and that the temperature dependence of the inverse magnetic susceptibility χ^{-1} can be roughly fitted by a linear function of temperature $\chi^{-1} = C_m(T - \theta_m)$, where $\theta_m \cong 5$ K [17]. Figures 3 and 4 display the temperature dependences of the reciprocal values of NB, $\gamma_{001}^{-1}(T)$, and FE, $V^{-1}(T)$, for γ-Dy_2S_3. These relations are well fitted by linear functions of temperature. This implies that the main contribution to both the FE and NB is determined by the paramagnetic mechanism. Figure 2 plots the temperature dependence of the

square root of the inverse CME, $\beta_{001}^{-0.5}(T)$. The $\beta_{001}^{-0.5}(T)$ relation is linear in temperature; i.e., the CME component β_{001}, just as NB and FE, is dominated by the paramagnetic mechanism. Note that the crossings of the $V^{-1}(T)$, $\alpha_{001}^{-1}(T)$, and $\alpha_{011}^{-1}(T)$ graphs with the horizontal axis (Figs. 3, 4) are shifted toward negative temperatures by about 10 K. Negative values of the Curie temperature θ_m are known to be characteristic of antiferromagnets; therefore, although the temperature dependence of magneto-optical effects can be affected by the temperature dependence of the magneto-optical susceptibilities *A*, *C*, and *D* and of the refractive index *n* due to the temperature-induced shift of the bandgap edge, $E_g(T)$, one cannot disregard the possibility of a γ-Dy_2S_3 transition to the antiferromagnetic state at temperatures $T < 4.2$ K. Note that antiferromagnetic ordering at low temperatures ($T \approx 2.5$ K) is observed to occur in dielectric crystals $Dy_3Al_5O_{12}$ and $Dy_3Ga_5O_{12}$.

The temperature dependence of the CME component $\beta_{111}(T)$ differs from that of $\beta_{001}(T)$. While the ratio $\beta_{001}(T)/V(T)^2 = 9.1 \times 10^{-6}$ cm/deg remains constant to within 10% over the temperature range $T = 25$–300 K, the ratio $\beta_{111}(T)/V(T)^2$, as measured in the same temperature range, varies by several times. The temperature dependence of $\beta_{111}^{-0.5}(T)$ is not linear and, hence, is not governed by the paramagnetic mechanism alone. The difference between the temperature dependences of $\beta_{111}(T)$ and $\mathbf{m}^2(T)$ may originate from the existence of a small temperature-independent contribution due to the diamagnetic or Van Vleck mechanism or from a mechanism associated with combined action of the quadratic magneto-optical effect and the Pockels effect [8]. In the latter case, the temperature dependence of $\beta_{111}(T)$ should be determined by the product of the second-order magnetoelectric susceptibility and the linear electro-optical coefficient and can differ from the $\beta_{001}(T)$ dependence.

5. CONCLUSIONS

Thus, our study has shown that, over the temperature and magnetic-field ranges covered, the components of the linear-in-magnetic-field NB effect (α_{001}, α_{011}) in γ-Dy_2S_3 vary, just as the FE, in proportion to the rare-earth sublattice magnetization; i.e., they are mediated by the paramagnetic mechanism. The component of the quadratic CME, β_{001}, varies in proportion to the magnetization squared, and the component β_{111} follows a weaker temperature dependence. The difference between the spectral and temperature dependences of β_{001} and β_{111} suggests the manifestation of different microscopic mechanisms for these CME components.

ACKNOWLEDGMENTS

This study was supported by the Russian Foundation for Basic Research in cooperation with Deutsche Forschungsgemeinschaft (Germany), project no. 02-02-04003.

REFERENCES

1. V. P. Zhuze and A. I. Shchelykh, Fiz. Tekh. Poluprovodn. (Leningrad) **23** (3), 393 (1989) [Sov. Phys. Semicond. **23**, 245 (1989)].
2. V. P. Zhuze, A. A. Kamarzin, V. V. Sokolov, T. I. Volkonskaya, I. A. Smirnov, and A. I. Shelykh, Pis'ma Zh. Tekh. Fiz. **7**, 1435 (1981) [Sov. Tech. Phys. Lett. **7**, 613 (1981)].
3. T. M. Batirov, K. A. Verkhovskaya, A. A. Kamarzin, Yu. N. Malovitskiĭ, V. I. Lisovaĭn, and V. M. Fridkin, Fiz. Tverd. Tela (Leningrad) **24**, 1313 (1982) [Sov. Phys. Solid State **24**, 746 (1982)].
4. T. I. Volkonskaya, A. I. Shelykh, A. V. Sotnikov, V. V. Sokolov, and F. R. Akhmedzhanov, Fiz. Tverd. Tela (Leningrad) **29** (2), 559 (1987) [Sov. Phys. Solid State **29**, 318 (1987)].
5. R. Dagis, G. Barbonas, and G. Pukinskas, Litov. Fiz. Sb. **28** (5), 559 (1988).
6. B. B. Krichevtsov, Zh. Éksp. Teor. Fiz. **119**, 954 (2001) [JETP **92**, 830 (2001)].
7. D. L. Portigal and E. Burstein, J. Phys. Chem. Solids **32**, 1396 (1975).
8. B. B. Krichevtsov and H.-J. Weber, Fiz. Tverd. Tela (St. Petersburg) **46**, 488 (2004) [Phys. Solid State **46**, 502 (2004)].
9. B. B. Krichevtsov, R. V. Pisarev, A. A. Rzhevskiĭ, and H.-J. Weber, Zh. Éksp. Teor. Fiz. **114** (3), 1018 (1998) [JETP **87**, 553 (1998)].
10. R. V. Pisarev, in *Physics of Magnetic Dielectrics* (Nauka, Leningrad, 1974) [in Russian].
11. A. K. Zvezdin, V. M. Matveev, A. A. Mukhin, and A. I. Popov, *Rare-Earth Ions in Magnetic-Ordered Crystals* (Nauka, Moscow, 1985) [in Russian].
12. G. Babonas, R. Dagis, and G. Pukinskas, Phys. Status Solidi B **153**, 741 (1989).
13. A. K. Zvezdin and V. A. Kotov, *Modern Magnetooptics and Magnetooptical Materials* (Inst. of Physics, Bristol–Philadelphia, 1997).
14. V. M. Zapasskiĭ, Fiz. Tverd. Tela (Leningrad) **19**, 964 (1977) [Sov. Phys. Solid State **19**, 561 (1977)].
15. A. K. Zvezdin, A. I. Popov, and Kh. I. Turkmenov, Fiz. Tverd. Tela (Leningrad) **28**, 1760 (1986) [Sov. Phys. Solid State **28**, 974 (1986)].
16. N. F. Vedernikov, A. K. Zvezdin, S. V. Koptsik, R. Z. Levitin, K. M. Mukimov, A. P. Petrov, A. I. Popov, and Kh. I. Turkmenov, Pis'ma Zh. Éksp. Teor. Fiz. **43** (1), 38 (1986) [JETP Lett. **43**, 48 (1986)].
17. H. L. Beeler and J. B. Gruber, Chem. Phys. **13**, 359 (1976).

Translated by G. Skrebtsov

Physics of the Solid State, Vol. 47, No. 2, 2005, pp. 298–304. Translated from Fizika Tverdogo Tela, Vol. 47, No. 2, 2005, pp. 286–292.

MAGNETISM AND FERROELECTRICITY

Polarization Kinetics of a Photosensitive Relaxor Ferroelectric

V. V. Gladkiĭ, V. A. Kirikov, T. R. Volk, E. S. Ivanova, and L. I. Ivleva

Shubnikov Institute of Crystallography, Russian Academy of Sciences, Leninskiĭ pr. 59, Moscow, 119333 Russia

e-mail: glad@ns.crys.ras.ru

Received April 28, 2004

Abstract—Polarization switching in alternating quasi-static electric fields of frequency 10^{-4} Hz and polarization relaxation in dc fields were studied in a photosensitive La- and Ce-doped barium–strontium niobate relaxor ferroelectric. Experimental data obtained in the thermal activation stage of the relaxation were used to reconstruct the relaxation time distribution spectrum. The characteristics of the polarization kinetics of an illuminated and a dark crystal are compared. It is shown that, in the crystal illuminated by light, the photoconductivity compensates for random electric and depolarization fields, thereby giving rise to a growth in amplitude of the dielectric hysteresis loops in the polarization versus field relation and to longer polarization relaxation times or increased heights of the potential barriers separating stable states from metastable states. *© 2005 Pleiades Publishing, Inc.*

1. INTRODUCTION

Relaxor ferroelectrics (relaxors)—crystalline solid solutions of lead magnesium niobate (PMN) [1] or barium–strontium niobate (SBN) [2]—are essentially disordered systems. Unlike the conventional uniform ferroelectrics, relaxors feature specific characteristics [3]. The phase transition to the polar state and the temperature-induced variations of all physical properties undergo strong broadening at the phase transition within a broad temperature range (the Curie region). Quasi-static dielectric hysteresis loops exhibit clearly pronounced anomalies in that their cycles are not closed and do not reproduce one another, with reproducible loop trajectories appearing only after a few polarization switching cycles [4–7]. The coercive field does not have a definite value and is distributed over the crystal volume within a broad range of values [8]. The relaxation time spectra measured under polarization and depolarization are extremely broad and include giant times [6–8]. The above specific dielectric properties of relaxors, which are a distinctive feature and a measure of their structural disorder, may originate from an internal electric field E_i distributed in a random manner in direction and magnitude over a nonuniform crystal [3]. These fields spread out the phase transition [1–3], and the symmetric curve of the local free energy of the crystal is distorted into an asymmetric double-minimum curve [3] with parameters that are dependent on the local values of E_i, which accounts for the observed anomalies on the loops and polarization processes [6, 8].

The properties of a ferroelectric are known to depend on depolarization field screening by free charge carriers (equilibrium or not), i.e., on the electrical conductivity [9]. In photosensitive relaxor ferroelectrics, the screening of an internal field E_i distributed nonuniformly over the crystal volume should govern the specific features of photoinduced effects. In the equilibrium state, E_i is naturally screened completely by the equilibrium (dark) carriers. In a nonequilibrium state, which may arise, for instance, under the action of an external electric field or under photoexcitation, free carriers produce an additional contribution, so the kinetics of the polarization process should depend on conductivity. Comparison of the polarization kinetics of two SBN compositions with different dark conductivities [6] revealed that an increase in the conductivity brings about a decrease in the polarization anomalies and hysteresis loops typical of relaxors. There are indications that photoexcitation slows down depolarization processes in the photosensitive SBN : Ce relaxor ferroelectric [10]. Investigating the effect of photoconductivity on polarization kinetics in SBN crystals is of interest not only from the standpoint of relaxor physics but may also have application potential for hologram recording, a process closely connected with the interaction of polarization switching with the fields of space charges generated in the course of hologram recording [11–13].

This communication reports on a comprehensive investigation of the effect of photoactive light on the polarization kinetics of a $Sr_{0.61}Ba_{0.39}Nb_2O_6$ (SBN-0.61) photosensitive relaxor ferroelectric codoped by La and Ce ions.

2. CRYSTALS AND THE MEASUREMENT TECHNIQUE

An SBN crystal was grown by a modified Stepanov method at the Institute of General Physics, Russian Academy of Sciences [14]. The crystal was codoped by 1 wt % La_2O_3 and 0.1 wt % Ce_2O_3 in the melt, and the impurity concentrations in the crystal, as measured by

a Comebax microprobe analyzer, were 0.44 at. % La and 0.023 at. % Ce. The sample chosen for study was a polished crystal plate measuring $3 \times 2 \times 0.9$ mm. Silver paste electrodes were fired onto the sample surface perpendicular to the polar direction along the shortest edge (the *Z* axis). All measurements were carried out at room temperature.

The crystal polarization *P* and its dependence on time *t* and electric field *E* were derived from the magnitude of the charge *Q* measured with an electrometric bridge by a high-precision compensation technique described in considerable detail in [15]. The electric charge *Q* that builds up on the crystal electrodes when the bridge is balanced by a compensating voltage $v(t)$ can be written as

$$Q(t) = Cv(t) = P(t) + Q_c, \quad (1)$$

where Q_c is the charge due to conductivity,

$$Q_c = \frac{VSt\sigma}{d}, \quad (2)$$

d is the sample thickness, *S* is the electrode area, σ is the electrical conductivity, and *C* is a reference capacitance. If the conductivity is low, then the second term in Eq. (1), Q_c, can be neglected, in which case all of the measured charge will be associated with the change in polarization *P* only. In the experiments reported on in this communication, the conductivity exerts a significant effect on the charge *Q* and, therefore, a correction for the conductivity is necessary.

The charge *Q* was measured in three regimes, namely, in an ac sawtooth quasi-static electric field (dielectric hysteresis loops), under application of a dc field (polarization relaxation), and with the dc field removed (depolarization relaxation). The dielectric hysteresis loops were measured by applying a sawtooth voltage *V* varying within the range of +300 to –300 V in steps multiple of 1 V at time intervals multiple of 1 s; the maximum number of steps was 1200. Several polarization switching cycles were measured. The relaxation study was carried out by measuring the charge in intervals of 0.25 to 1 min.

The electric charge *Q* building up on the electrodes due to conductivity and the electrical conductivity of the sample were estimated from the evolution of *Q* in long-time measurements, i.e., under conditions where the relaxation *P* practically stops and the time dependence of *Q*, according to Eq. (2), is a straight line.

The effect of photoconductivity was studied with white light generated by an OI-18 mercury lamp equipped with an S3S14 filter (spectral interval 400–700 nm) and having an output of 0.3–25 mW/cm^2. To preclude screening of the external field, the cross-sectional area of the beam was chosen to be in considerable excess of that of the crystal entrance plane. Figure 1 presents the absorption spectrum of the SBN-0.61 (La + Ce) crystals studied; the broad absorption band standing out in the visible region of the spectrum derives from the photoactive Ce impurity. Estimates made from measurements of the permittivity ε_{33} at 1 kHz under illumination show that the increase in sample temperature caused by the absorption of light does not exceed 2°C; i.e., all the effects described below originate from the contribution of photoconductivity rather than from heating.

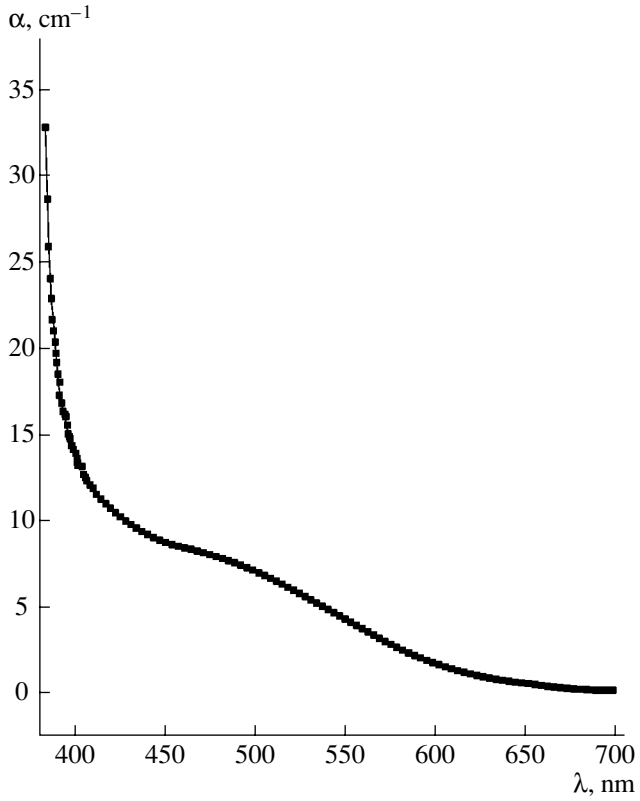

Fig. 1. Absorption spectrum of SBN-0.61 (La + Ce) crystals.

3. EXPERIMENTAL RESULTS

3.1. Quasi-Static Dielectric Hysteresis Loops

Figure 2 displays quasi-static dielectric hysteresis loops measured under the application and removal of illumination of different intensities. Switching on the light strongly increases the crystal conductivity, which provides a sizable contribution, given by Eq. (2), to the measured charge density Q_c. Because *E* varies in a sawtooth manner, i.e., grows linearly with *t*, $E = E_0 t$, up to a maximum value $E_m = E_0 t_m$ and subsequently falls off also linearly with *t*, $E = E_m - E_0 t$, the contributions $Q_c = (E_m t_m \sigma/2)(E/E_m)^2$ and $Q_c = (E_m t_m \sigma/2)(2 - E/E_m)^2$ always increase parabolically with increasing and decreasing *E*, respectively. The total contribution accumulated in one-half of the field period, $2t_m = T/2$, is $Q_c = E_m t_m \sigma$, and that for the next half-period is $Q_c = 0$. For this reason, the field dependence of the total charge $Q(E)$

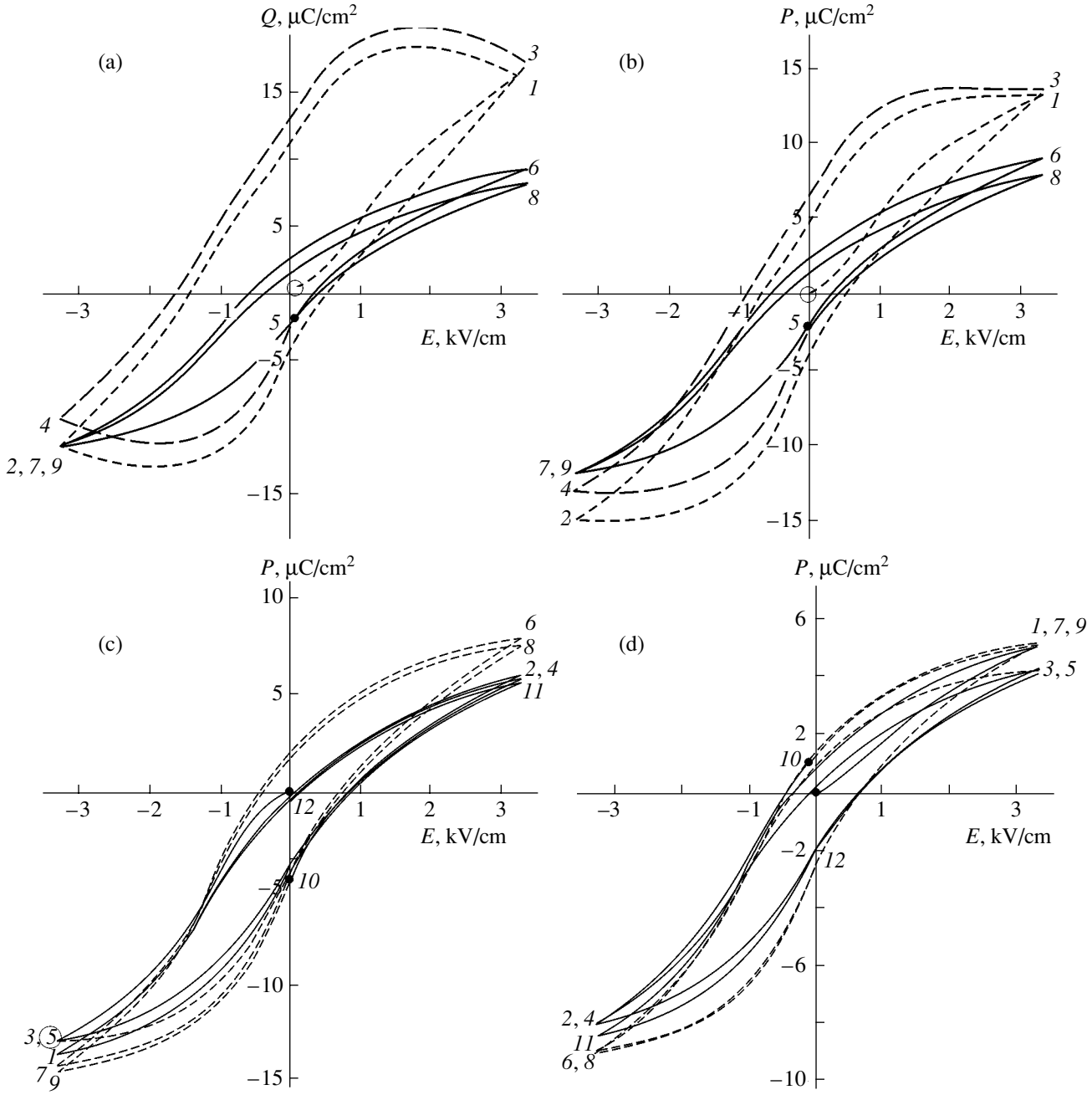

Fig. 2. Dielectric hysteresis loops of (a) charge Q and (b–d) polarization P in an SBN-0.61 (La + Ce) photosensitive relaxor ferroelectric plotted vs. applied ac electric field E and measured under illumination and in the dark. Solid lines are trajectories obtained in the dark. Dashed lines are obtained under illumination. Figures adjoining the curves identify the sequence of Q and P variation.

within the intervals where the field E decreases is a bell-shaped function. Knowing the sample conductivity σ, one can calculate the dependence of the polarization $P(E)$ on field E. Estimates of σ from measurements of Q in dc fields are presented below. The $P(E)$ function, as derived from data on Q (corrected for the conductivity), is shown graphically in Fig. 2b. The figures next to the curves indicate the sequence of variation of Q and P. The open circles identify the application of illumination. Dashed lines plot the variation in Q and P of the illuminated sample, and the solid lines, that of the dark sample. The illumination power density is ~20 ± 5 mW/cm^2, and the corresponding electrical conductivity of the sample is $\sigma \sim 2 \times 10^{-12}$ (Ω cm)$^{-1}$. Figures 2c and 2d display hysteresis loops measured with a different sequence of switching the light on and off and at a lower illumination power density of ~2 mW/cm^2.

Polarization relaxation parameters

Process	E, kV/cm	I, mW/cm^2	a, min	n	P_0, μC/cm^2	P_e, μC/cm^2	σ, Ω^{-1} cm^{-1}	τ_m, min	Δτ, min
Polarization	2	0	0.137 ± 0.006	0.083 ± 0.006	5.65	7.9 ± 0.1	2×10^{-14}	0.127 ± 0.006	0.5
	2	2 ± 1	6.2 ± 0.9	0.21 ± 0.08	7.22	19.7 ± 3.4	2×10^{-13}	5.0 ± 1.1	16.5
	2.8	0	0.2100 ± 0.0002	0.1040 ± 0.0002	6.85	0		0.1900 ± 0.0002	0.7
Depolarization	2.8	2 ± 1	3.1 ± 0.1	0.350 ± 0.005	7.27	0		2.32 ± 0.08	7
	5	2 ± 1	5.1 ± 0.3	0.46 ± 0.02	9.45	0		3.5 ± 0.2	10

All hysteresis loops follow a pattern characteristic of relaxor ferroelectrics, which can be revealed using a variety of methods [4–7, 16]. The trajectories of the first several loop cycles represent unclosing and noncoincident curves with a decreasing amplitude; the hysteresis loops start to coincide and reproduce one another only after a few polarization switching cycles. A comparison of the curves shown in Figs. 2a–2d shows convincingly that, irrespective of the total time of cycling in the dark and under illumination, the amplitude of the hysteresis loop $P(E)$ (polarization-switching amplitude) increases under illumination and that this effect becomes more enhanced as the intensity of illumination increases (photoconductivity). The effect of photoactive light on hysteresis loops in SBN : Ce was reported in [10]to be qualitatively similar.

3.2. Polarization Relaxation in DC Electric Fields

Polarization relaxation of a relaxor ferroelectric in a dc field occurs, as a rule, in two stages [6–8]; a fast stage (a "jump"), which is primarily due to over-barrier motion of domain walls in the crystal without a clearly pronounced coercive field, and a slow (thermally activated) stage, with domain-wall motion through the barriers separating the stable states from metastable states.

Analysis of the polarization relaxation in dc electric fields and of depolarization following the removal of the applied field can provide quantitative information on the structure of the energy barriers between the metastable and stable states in crystals. The height of the barriers depends on several relaxation parameters. The accuracy of determination of these parameters is higher, the longer the time of relaxation measurement [17]. As has been shown more than once for relaxor ferroelectrics [4–8], the kinetics of the slow polarization $P(t)$ following the thermal activation mechanism satisfactorily follows a power law:

$$p(t) = \frac{P_e - P(t)}{P_e - P_0} = \frac{1}{(1 + t/a)^n}, \qquad (3)$$

where P_0 is the initial polarization; the equilibrium polarization P_e and constants a and n are three independent parameters. Equation (3) is an empirical power law and apparently holds for various inhomogeneous systems with nonexponential relaxation, because for certain values of the parameters a and n this equation coincides very closely with the analogous linear [18], logarithmic [19], or power-law [18] relations observed in earlier experiments. Unlike the well-known Kohlrausch law [18], the power-law relation (3), first, better fits the relaxation observed over short times, where its rate is the highest but finite, and, second, Eq. (3) corresponds to a simple distribution function $f(\tau)$ for relaxation times τ, which is related to Eq. (3) through the Laplace transform. Assuming the relaxation centers to be independent, their contributions to the total polarization should be additive, with the dimensionless polarization $p(t)$ being a sum of exponentials,

$$p(t) = \int_0^\infty f(\tau)\exp(-t/\tau)d\tau.$$

If $p(t)$ is a power-law function (3), then [20]

$$f(\tau) = \{a^n/\Gamma(n)\}(1/\tau)^{n+1}\exp(-a/\tau), \qquad (4)$$

where $\Gamma(n)$ is the gamma function. The function $f(\tau)$ is normalized; i.e., $\int_0^\infty f(\tau)d\tau = 1$. More convenient for use is a dimensionless normalized function $g(\tau) = \tau f(\tau)$, which is the density of distribution of lnτ or of the barrier energy U in the sample, because $\ln(\tau/\tau_0) = U/kT$, where τ_0 is a kinetic coefficient. The distributions of these functions have maxima at $\tau_m = a/(1 + n)$ for $f(\tau)$ and at $\tau_m = a/n$ for $g(\tau)$ [6].

Thus, the effects of illumination on the kinetics of polarization and depolarization can be described in terms of a variation in the barrier energy distribution spectrum (or, which is exactly the same, in the relaxation time distribution spectrum). The free parameters P_e, a, and n, as well as the conductivities and some other characteristics, are listed in the table.

3.3. Analysis of the Polarization Relaxation Process

The polarization relaxation was measured in a dc electric field E = 2 kV/cm in the dark and under illumination with a power density of ~2 mW/cm^2. In the initial fast stage (jump in P), which lasted ~15 s, the polar-

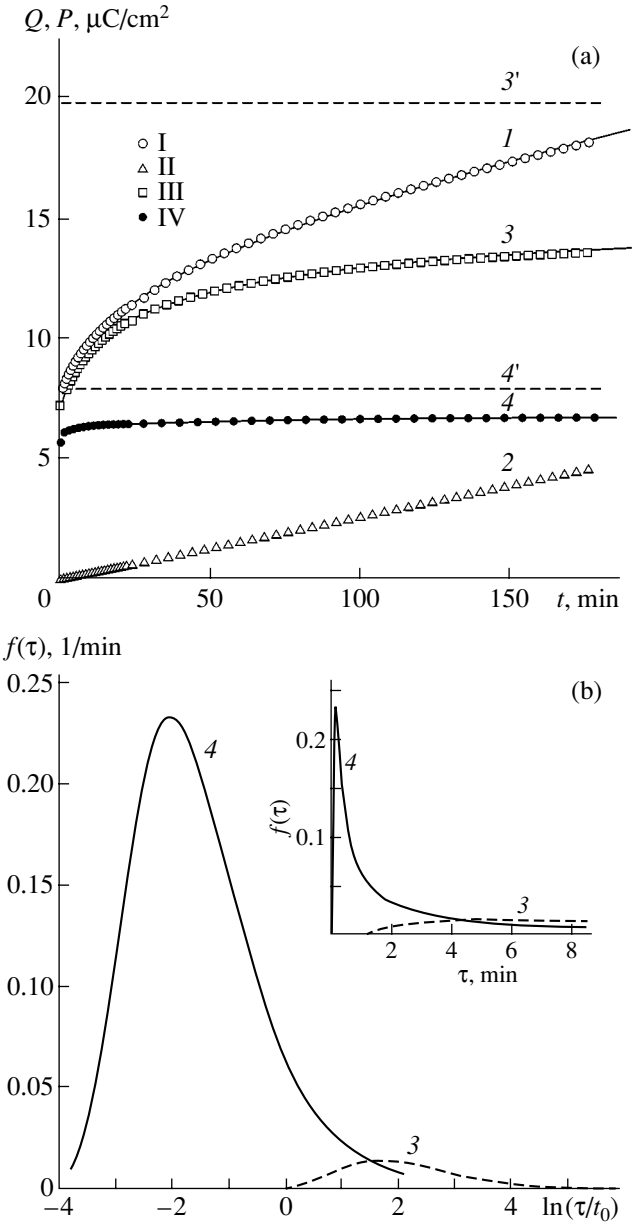

Fig. 3. (a) Relaxation of (*1*) measured charge Q, (*2*) the charge generated by photoconductivity Q_c, and (*3*, *4*) polarization P in a dc electric field E = 2.0 kV/cm and (b) relaxation time distribution spectra $f(\tau)$ of an SBN-0.61 (La + Ce) relaxor ferroelectric measured with illumination (*4*) removed and (*1*–*3*) turned on. (*3*', *4*') Equilibrium values of polarization P_e; t_0 = 1 min. The inset shows spectra $f(\tau)$ drawn on a time scale.

ization relaxation was 5.65 and 7.23 μC/cm² in the first and second cases, respectively. Figure 3a illustrates the effect of illumination on the slow polarization relaxation. Curves *1* and *4* plot the time variation of the measured charge Q under illumination and in the dark, respectively. From the linear dependence of charge Q at long times observed under illumination (curve *1*), we can estimate the photoconductivity σ using Eq. (2) and isolate the polarization variation $P(t)$ from the experimentally measured charge $Q(t)$ by subtracting the ohmic-current charge Q_c (curve *2*). Curve 3 in Fig. 3a is a graphical representation of the $P(t)$ relation obtained in this way (by subtracting curve *2* from curve *1*). The experimental data amassed for the sample kept in the dark were subjected to the same treatment. However, due to the low dark conductivity σ, the $P(t)$ graph (curve *4*) is almost identical to the experimental $Q(t)$ relation. Solid curves *3* and *4* in Fig. 3a are the fit of Eq. (3) to the experimental data, and dashed horizontal straight lines *3*' and *4*' plot the equilibrium values of polarization P_e to which the P relaxation curves tend asymptotically under illumination and in the dark, respectively. Symbols I through IV refer to experimental data.

Figure 3b shows spectra $f(\tau)$ obtained for an illuminated (curve *3*) and an unilluminated (curve *4*) sample; the inset presents the same spectra redrawn on the time scale. The half-width of the spectra is 16.5 and 0.5 min, respectively.

3.4. Analysis of the Depolarization Relaxation Process

The depolarization was measured after application of a field of 2.8 and 5 kV/cm to the crystal for 15 min. Figure 4a plots the charge Q in the dark (curve *1*) and under illumination at I = 1 mW/cm² (curve *2*) measured after polarization by a field of 2.8 kV/cm. Slow relaxation starts after a jump in P down to 6.85 and 7.97 μC/cm² with the crystal in the dark and under illumination, respectively. The accuracy of depolarization measurements is high enough, because, in contrast to the polarization kinetics in an external field, there is no need to isolate the linear component of the ohmic-current charge. The transient signal of a photovoltaic current generated in a photosensitive medium under illumination [9] has a very fast response time, which makes its contribution to a measured charge negligible.

In Fig. 4a, symbols I and II refer to experimental data and the solid lines are fits of the power-law time dependence (3) to these data. The fit is extremely good. The relaxation time distribution spectra $f(\tau)$ are displayed in Fig. 4b for the cases of the dark (curve *1*) and illuminated (curve *2*) crystals; the inset shows the same spectra presented on the time scale. Also given for comparison is a spectrum $f(\tau)$ derived from a depolarization curve under illumination after application of a polarizing field of 5 kV/cm (curve *3*). The half-width $\Delta\tau$ of the distribution spectra drawn on the time scale is 0.7 min for the unilluminated sample and 7 and 10 min for the illuminated sample subjected to polarizing fields of 2.8 and 5 kV/cm, respectively. The shifts of the spectra toward longer relaxation times for the two polarizing fields are almost the same (curves *2*, *3* in Fig. 4b). Note that the depolarization process occurring under illumination is anomalous. Indeed, in most relaxor ferroelec-

trics, the relaxation rate dP/dt of a dark crystal decreases as the most probable relaxation time $\tau_m = a/(1 + n)$ increases [6, 7]; in our case, the rate grows with increasing τ_m, and this occurs, as can be readily verified, primarily through an increase in the exponent n in the power-law relation (3).

4. DISCUSSION

As follows from the table and Figs. 3 and 4, illumination increases the parameters P_e, a, and n in the kinetic relation (3). The increase in the equilibrium polarization P_e, which the P relaxation curve approaches asymptotically under application of a given dc field (curves *3*,' *4*' in Fig. 3a), implies that the crystal volume involved in the polarization process grows under illumination. This conclusion fits with the increase in the switched charge under illumination, an observation derived from the $P(E)$ hysteresis loops (Fig. 2). The spectra $f(\tau)$ broaden and shift toward longer relaxation times τ; i.e., crystal regions with longer times τ start to play a more active role in the spectrum under illumination. As the light intensity increases, the spectrum $f(\tau)$ grows in half-width. The shift of the spectral maximum $\tau_m = a/(1 + n)$ toward longer times should be assigned primarily to an increase in a for a comparatively small increase in n. Comparatively low light intensities (corresponding to a change in conductivity by about an order of magnitude) exert a pronounced effect on the relaxation time distribution spectrum; indeed, the most probable relaxation time τ_m for polarization and depolarization increases from 10–20 s to a few minutes (see insets to Figs. 3b, 4b), the half-width of the spectrum likewise increases by an order of magnitude, etc. The kinetics of depolarization in SBN : Ce was reported in [10] to slow down under illumination. Interestingly, despite the increase in the time τ, illumination increases the polarization relaxation rate dP/dt, which can be traced to a considerable increase in P_e in the case of polarization and an increase in the exponent n in the case of depolarization.

The photoinduced effects observed to occur in relaxor ferroelectrics can be qualitatively interpreted as being due to screening of the nonuniformly distributed internal field E_i by nonequilibrium carriers. Screening gives rise to a slowing down of the polarization and depolarization processes and to a "leveling off" of the spatial variation in the redistributing field E_i, or, in other words, to a weakening of asymmetry in the local free energy. This weakens the "freezing" [4, 6] or "pinning" [5] effects characteristic of relaxor ferroelectrics under application of an external field, so the part of the crystal volume involved in switching in the given field (i.e., the equilibrium polarization P_e) increases. This increase is accompanied by a shift of the spectrum $f(\tau)$ to longer relaxation times and by a broadening of the spectrum.

One of the factors governing the effect of illumination is the dielectric relaxation (screening) time $\tau_s = \varepsilon/4\pi\sigma$. In particular, the relationship between the rate of polarizing-field variation and $1/\tau_s$ plays a certain role in determining the shape of the $P(E)$ loop. If the field variation rate is much slower than $1/\tau_s$, the screening comes to an end and the internal-field distribution does indeed level off. Accepting rough estimates of τ_s for the inten-

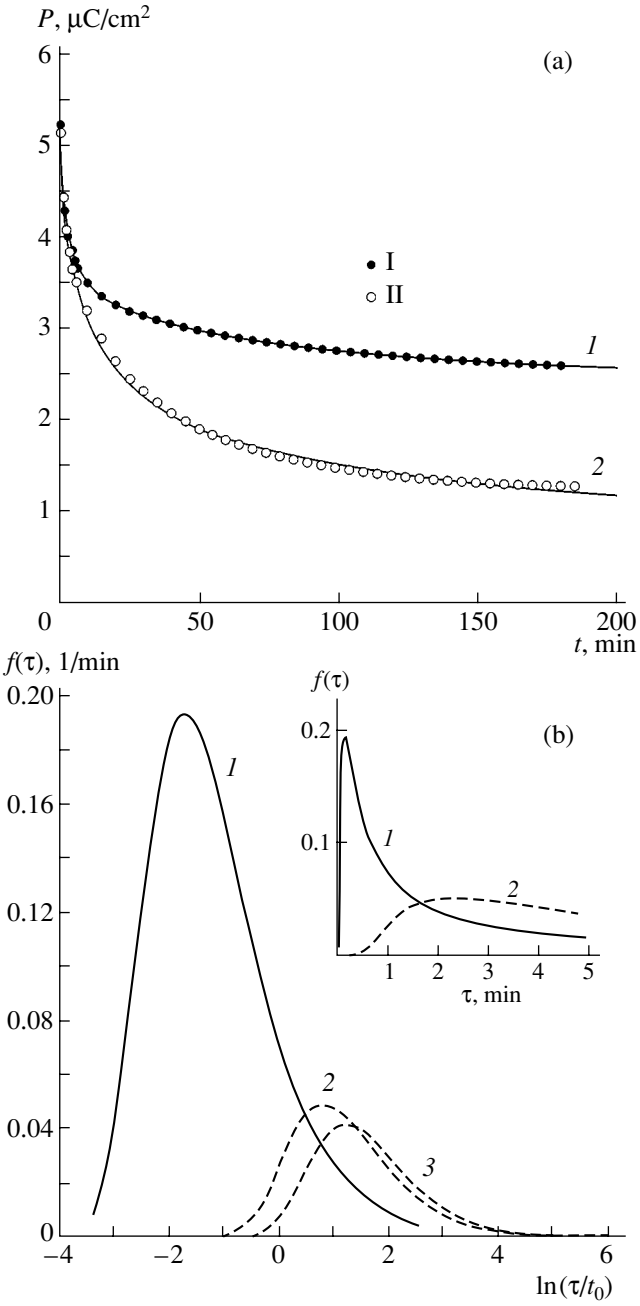

Fig. 4. (a) Depolarization relaxation and (b) depolarization spectra $f(\tau)$ of an SBN-0.61 (La + Ce) relaxor ferroelectric measured with illumination (*1*) removed and (*2*, *3*) turned on. The preliminary polarization electric field E is equal to (*1*, *2*) 2.8 and (*3*) 5 kV/cm; $t_0 = 1$ min. The inset shows spectra $f(\tau)$ drawn on a time scale.

sities employed (on the order of a few minutes and tens of seconds for $I = 2$ and 20 mW/cm^2, respectively), we find that, for the higher intensity, complete screening of E_i takes place and the illumination effect is very pronounced. These qualitative considerations suggest that, when measuring $P(E)$ loops at higher frequencies, the effect of nonequilibrium conductivity should be less noticeable.

4. CONCLUSIONS

Experiments involving the effect of light on polarization have indicated that photoconductivity plays an essential part in these processes. The increase in the polarization switching amplitude observed to occur under illumination should be considered another argument for the existence in relaxor ferroelectrics of a randomly distributed internal electric field, which decreases when the nonuniform polarization is screened. The increase in the polarization relaxation time in dc electric fields under illumination provides more proof that polarization screening favors a decrease in the depolarizing electric fields, which are one of the reasons for the rearrangement of the crystal domain structure.

ACKNOWLEDGMENTS

This study was supported by the Russian Foundation for Basic Research (project no. 02-02-16823) and INTAS (project no. 01-173).

REFERENCES

1. G. A. Smolenskiĭ, V. A. Bokov, V. A. Isupov, N. N. Kraĭnik, R. E. Pasynkov, and M. S. Shur, *Ferroelectrics and Antiferroelectrics* (Nauka, Leningrad, 1971), p. 355 [in Russian].
2. M. E. Lines and A. M. Glass, *Principles and Applications of Ferroelectrics and Related Materials* (Clarendon, Oxford, 1977; Mir, Moscow, 1981).
3. L. E. Cross, Ferroelectrics **76**, 241 (1987).
4. V. V. Gladkiĭ, V. A. Kirikov, S. V. Nekhlyudov, T. R. Volk, and L. I. Ivleva, Pis'ma Zh. Éksp. Teor. Fiz. **71** (1), 38 (2000) [JETP Lett. **71**, 24 (2000)].
5. T. Granzow, V. Dorfler, Th. Woike, M. Wohleke, R. Pankrath, M. Imlau, and W. Kleeman, Phys. Rev. B **63**, 174101 (2001).
6. V. V. Gladkiĭ, V. A. Kirikov, T. R. Volk, and L. I. Ivleva, Zh. Éksp. Teor. Fiz. **120** (3), 678 (2001) [JETP **93**, 596 (2001)].
7. V. V. Gladkiĭ, V. A. Kirikov, S. V. Nekhlyudov, T. R. Volk, and L. I. Ivleva, Fiz. Tverd. Tela (St. Petersburg) **42** (7), 1296 (2000) [Phys. Solid State **42**, 1334 (2000)].
8. V. V. Gladkiĭ, V. A. Kirikov, T. R. Volk, D. V. Isakov, and E. S. Ivanova, Fiz. Tverd. Tela (St. Petersburg) **45** (11), 2067 (2003) [Phys. Solid State **45**, 2171 (2003)].
9. V. M. Fridkin, *Photoferroelectrics* (Nauka, Moscow, 1976; Springer, Berlin, 1979).
10. T. Granzow, V. Dorfler, Th. Woike, M. Wohlecke, R. Pankrath, M. Imlau, and W. Kleeman, Europhys. Lett. **57** (4), 597 (2002).
11. F. Micheron and G. Bismuth, Appl. Phys. Lett. **23**, 71 (1973).
12. Y. Qiao, S. Orlov, D. Psaltis, and R. R. Neurgaonkar, Opt. Lett. **18** (12), 1004 (1993).
13. M. Hisaka, H. Ishitobi, and S. Kawata, J. Opt. Soc. Am. B **17** (3), 422 (2000).
14. L. I. Ivleva, N. V. Bogodaev, N. M. Polozkov, and V. V. Osiko, Opt. Mater. **4**, 168 (1995).
15. V. V. Gladkiĭ, V. A. Kirikov, S. V. Nekhlyudov, and E. S. Ivanova, Fiz. Tverd. Tela (St. Petersburg) 39 (11), 2046 (1997) [Phys. Solid State **39**, 1829 (1997)].
16. M. Y. Goulkov, T. Granzow, U. Doerfler, Th. Woike, M. Imlau, and R. Pankrath, Appl. Phys. B **76** (4), 407 (2003).
17. V. V. Gladkiĭ, V. A. Kirikov, E. S. Ivanova, and S. V. Nekhlyudov, Fiz. Tverd. Tela (St. Petersburg) **41** (3), 499 (1999) [Phys. Solid State **41**, 447 (1999)].
18. A. K. Jonscher, *Dielectric Relaxation in Solids* (Chelsea Dielectric, London, 1983).
19. V. V. Gladkiĭ, V. A. Kirikov, and E. S. Ivanova, Zh. Éksp. Teor. Fiz. **110** (1), 298 (1996) [JETP **83**, 161 (1996)].
20. V. A. Ditkin and A. P. Prudnikov, *Reference Book on Operational Calculus* (Vysshaya Shkola, Moscow, 1965), p. 466 [in Russian].

Translated by G. Skrebtsov

Physics of the Solid State, Vol. 47, No. 2, 2005, pp. 305–311. Translated from Fizika Tverdogo Tela, Vol. 47, No. 2, 2005, pp. 293–299.

MAGNETISM AND FERROELECTRICITY

Electro-Optical Properties of Strontium–Barium Niobate Crystals and Their Relation to the Domain Structure of the Crystals

T. R. Volk*, N. R. Ivanov*, D. V. Isakov*, L. I. Ivleva, and P. A. Lykov****

** Shubnikov Institute of Crystallography, Russian Academy of Sciences, Leninskiĭ pr. 59, Moscow, 119333 Russia*
e-mail: volk@ns.crys.ras.ru

*** Scientific Center of Laser Materials and Technologies, Institute of General Physics, Russian Academy of Sciences, ul. Vavilova 38, Moscow, 117942 Russia*

Received May 11, 2004

Abstract—The electro-optical coefficients r_{ij} and half-wave voltage $V_{\lambda/2}$ of strontium–barium niobate crystals poled in the ferroelectric phase are shown to vary along the polar axis. The $r_{ij}(z)$ and $V_{\lambda/2}(z)$ dependences indicate the presence of a residual domain density $D(z)$ and clearly depend on the sign of the polarizing field, with r_{ij} being minimum (D being maximum) near the negative electrode. This character of the $D(z)$ distribution and, hence, the $r_{ij}(z)$ and $V_{\lambda/2}(z)$ coordinate dependences can be explained by predominant domain nucleation near the negative electrode, which is revealed when the switching processes are studied using 90° (Rayleigh) light scattering from domain walls. © *2005 Pleiades Publishing, Inc.*

1. INTRODUCTION

Ferroelectric crystals of $Sr_xBa_{1-x}Nb_2O_6$ (SBN-x) solid solutions have high optical properties and, therefore, are promising for various optical applications [1]. For example, SBN-0.75 and SBN-0.61 : (Ce,La) exhibit extremely high electro-optical coefficients: r_{33} = 1240 [1] and 1000 pm/V [2], respectively. In certain compositions, the two-beam coupling gain factors are high ($\Gamma \geq 20$ cm^{-1} in SBN-0.61 : Ce [3] and SBN-0.61 : Cr [4]), which makes these materials attractive for dynamic photorefractive holography. The high values of nonlinear optical coefficients [5] and comparatively low coercive fields (~1 kV/cm) have motivated a search for ways to create regular domain structures based on these materials in order to convert optical frequencies in the quasi-phase-matching mode [6] (true phase matching cannot be realized in SBN due to the small birefringence).

However, the irreproducibility of the parameters mentioned above and the large scatter of their values given in the literature complicate the practical application of SBN crystals. These negative factors correlate with the anomalies of the ferroelectric properties detected in SBN crystals, in particular, with the degradation of dielectric $P(E)$ hysteresis loops (a decrease in the loop amplitude during sequential field reversal) [7, 8] and with the coercive field that is widely distributed in value over the volume of an SBN crystal [9]. These anomalies are undoubtedly caused by the specific features of the SBN structure (disordering due to the unfilled one-sixth fraction of A-cation positions in the tetragonal potassium–tungsten bronze structure [1]), which are responsible for the relaxor properties of this SBN solid solution [10]. However, in spite of this major cause of the negative qualities of SBN crystals, it is worthwhile to search for methods for optimizing and controlling their properties.

The goal of this work is to analyze the electro-optical (EO) properties of SBN crystals and their relation to switching processes and to the dynamics of the domain structure, studied using 90° (Rayleigh) scattering by domain walls.

2. EXPERIMENTAL

2.1. Crystals

SBN crystals were grown using the modified Stepanov method at the Institute of General Physics, Russian Academy of Sciences [11]. We studied the following compositions: SBN-0.75, SBN-0.61, SBN-0.61 : 0.1 wt % Ce (SBN-Ce), SBN-0.61 : (0.1 wt % Ce, 1 wt % La) (SBN-Ce,La), and SBN-0.61 : 0.01 wt % Cr (SBN-Cr). The last three compositions have applications as holographic materials [2–4]. The samples were optically polished plates of different shape. We used a silver paste for the electrodes. The EO coefficients were measured in samples less than 2.5-mm thin (in the beam propagation direction), since such measurements in thicker crystals are difficult to perform because of the high values of r_{ij}. Optical elements with linear dimensions of about 10 mm were used to measure half-wave voltages $V_{\lambda/2}$.

1063-7834/05/4702-0305$26.00

2.2. Electro-Optical Methods

Linear EO coefficients r_{ij} are defined by linearizing the quadratic EO coefficients [12] and can be expressed as

$$r_{33} = 2g_{33}P_s\varepsilon_{33}\varepsilon_0, \quad (1)$$

$$r_{13} = 2g_{13}P_s\varepsilon_{33}\varepsilon_0, \quad (2)$$

where P_s is the spontaneous polarization and g_{ij} are the coefficients of a quadratic EO effect in the centrosymmetric phase. It is obvious from Eqs. (1) and (2) that the $r(E)$ dependence looks as a hysteresis loop. In a multidomain crystal, the effective coefficient r is less than r_0, where r_0 is the EO coefficient in a single-domain crystal. In this work, we normalized the $r(E)$ loop to ±1 by dividing r into $r_0(E = 0)$; r_0 was taken to be the maximum value of the EO coefficient in the given crystal even if this value was reached only once. The half-wave voltages are defined as

$$V_{\lambda/2} = (\lambda/r_0 n_e^3)d/l \quad (3)$$

(for $d/l = 1$, where d and l are the sample dimensions). As follows from Eqs. (1)–(3), $V_{\lambda/2}$ has a hysteretic field dependence.

A convenient parameter characterizing the dependence on the domain structure of a crystal is the domain density D. Let ν^+ and ν^- be the volumes of "plus" and "minus" domains, respectively. Then, we have $\nu^+ + \nu^- = \nu$, where ν is the crystal volume. For example, a positive domain density in a negative matrix is $D^+ = \nu^+/\nu$ and an EO signal is related to the volume degree of polarization as $r/r_0 = (\nu^- - \nu^+)/\nu$; that is, we have a linear relation

$$r/r_0 = 1 - 2D^+. \quad (4)$$

As D increases, r decreases and $V_{\lambda/2}$ increases. Thus, any changes in r and $V_{\lambda/2}$ caused by the application of a field to the crystal can be interpreted as a change in the domain density D (under the assumption that r_0 = const). The $r(z)$ and $r(x, y)$ distributions obtained with a beam scanned along the crystallographic directions give one- and two-dimensional D^+ or D^- distributions, respectively.

The EO coefficients and half-wave voltages were measured with a He–Ne laser at $\lambda = 633$ nm. The EO coefficients were measured using a dynamic method with a high phase sensitivity ($2\pi \times 10^{-6}$). An EO signal was excited by an ac measuring field with an effective strength of 6 V/cm and a frequency of 1000 Hz (the case of an unclamped crystal). A sawtooth field E with a period of 27 min and an amplitude of ±5.6 kV/cm, which is higher than $|E_c| \le$ (2.0–2.5) kV/cm, was applied to a crystal. As noted above, the $r(E)$ dependence normalized to ±1 has the form of a hysteresis loop, whose shape in saturation differs slightly from that of saturated loops of dielectric $P(E)$ hysteresis due to the contribution from the quadratic EO effect [which results in a descending, almost linear $r_0(E)$ dependence]. To determine the spatial distribution of the EO coefficients, we scanned a sample using a thin (0.1 mm in diameter), almost parallel beam. We used the transverse geometry ($\mathbf{E} \parallel z$, $\mathbf{k} \perp z$) to measure the linear EO coefficient,

$$r_c = \left|r_{33} - (n_0/n_e)^3 r_{13}\right|. \quad (5)$$

The corresponding values of $V_{\lambda/2}$ were measured using a standard polarization-optical technique. Investigations were carried out using a dynamic method and a sinusoidal 50-Hz field in the transverse geometry ($\mathbf{E} \parallel z$, $\mathbf{k} \perp z$); the polarization vector of light made an angle of 45° with the directions of crossed polarizers.

2.3. Method of 90° Scattering of Light by Domains

SBN crystals exhibit significant 90° scattering of a laser beam propagating perpendicular to the polar axis [13–15]. The scattering intensity decreases sharply after poling the crystal or in the paraelectric phase [14]; the characteristics of scattering dynamics in pulsed fields correlate with the kinetic characteristics of pulsed switching [15]. Thus, 90° light scattering is related to the presence of domains and can serve as a tool for studying their dynamics. Scattering centers are domain walls that are regions having nonuniform refractive indices n_i. A domain wall can be considered a local sandwich-like nonuniformity of n_i [16]. If the wave vector $\mathbf{k}_i$ of the incident light is normal to the polar axis, then the wave vector of light partially reflected by a domain wall is $\mathbf{k}_r = \mathbf{k}_i + 2(\mathbf{k}_i\mathbf{q}_m)\mathbf{q}_m$, where $\mathbf{q}_m$ is the unit normal vector to the domain wall [15]. If the refractive index increases by dn and the wall area is dA, then the amplitude of the reflected light is[15]

$$dE_r = E_i|\mathbf{k}_i|H\frac{dn}{2n}dA, \quad (6)$$

where H is the domain-wall thickness (for $|\mathbf{k}_i|H \ll 1$). By integrating dE_r, we find that the 90° light-scattering intensity depends on three factors, namely, the mean domain-wall thickness, the variation δn in the wall region, and the total area of the walls in the illuminated volume. In a first approximation, we assume that the wall thickness and δn depend only weakly on the applied field; therefore, the light-scattering intensity is considered to be proportional to the total domain-wall area, i.e., the domain density and size.

The method of measuring 90° light scattering allows us to probe a volume using a thin beam, which makes it possible to study the spatial distribution of processes related to the domain dynamics. In this work, we study the spatial distribution of the domain density by applying pulsed switching fields to a crystal. The following geometry was used: a focused He–Ne laser beam (λ = 633 nm) was propagated along a direction (x or y axis)

normal to the polar axis, and the scattered light was recorded in an orthogonal direction (*y* or *x* axis, respectively) using a diaphragm located immediately behind a sample. In other words, only a small fraction of the scattered light was separated. The incident beam was polarized parallel to the ||*z* axis, and the scattered beam passed through an analyzer that was also parallel to the ||*z* axis [the so-called *x*(*zz*)*y* or *y*(*zz*)*x* configuration]. The incident light intensity did not exceed 0.05 W/cm^2 in order to avoid photorefraction in an applied field. Along the polar axis, field pulses with a pulse rise time of 1 μs and a pulse duration of 4–20 μs were applied.

Figure 1 shows an example of the light-scattering kinetics (curve *1*) when a field pulse was applied (curve *2*). The light-scattering intensity was measured in the case where a field pulse train with a constant polarity, a constant pulse period-to-pulse duration ratio, and an increasing amplitude were applied along the *z* axis (see inset to Fig. 1). As can be seen from Fig. 1, the application of a field pulse is accompanied by a change in the light-scattering intensity by $\Delta I = I_s - I_b$, where I_s and I_b are the light intensities in a field and in the absence of a field, respectively (at $E = 0$, there always exists a certain background scattering intensity $I_b \neq 0$, which is mainly related to crystal inhomogeneity). Hereafter, $+\Delta I$ and $-\Delta I$ are an increase and a decrease, respectively, in the light intensity with respect to I_b. The $\Delta I(t)$ dependence is substantially delayed with respect to the pulse front. If the variation in scattering were partly caused by a change in the refractive indices in antiparallel domains due to the EO effect, $n_O^E = n_O \pm (1/2) n_O^3 r_{13} E_3$ (where n_O and n_O^E are the ordinary refractive indices in the absence and in the presence of a field E_3, respectively), then there would be a scattering component that is synchronous with the pulse rise. The absence of this component indicates that the contribution from the EO effect is small and that the light-scattering kinetics $\Delta I(t)$ associated with the application of a field can only be related to the domain dynamics [15]. The $\Delta I(E)$ distributions in the bulk of a crystal were used to make a qualitative *in-situ* estimation of the domain-density distribution $D(z)$ in an applied field.

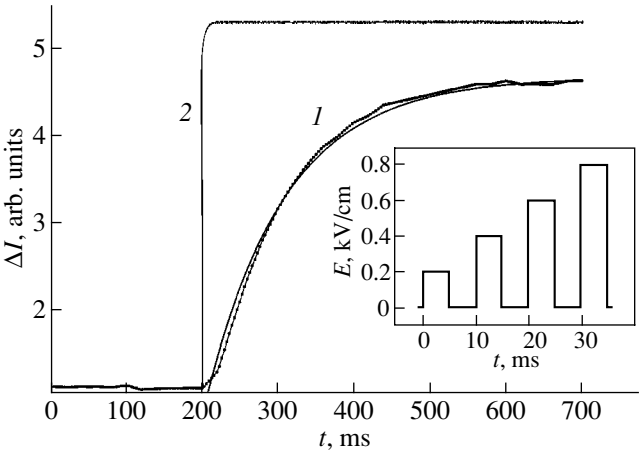

Fig. 1. Example of the scattering intensity kinetics (curve *1*) induced by a Π-shape pulse (curve *2*). Solid line *1* is a fitting of $\Delta I(t)$ by an exponential function. The inset shows the shape of the field pulse train used.

3. EXPERIMENTAL RESULTS

3.1. Results of the Electro-Optical Measurements

The spatial distributions of the EO coefficient and $V_{\lambda/2}$ were studied in the as-grown crystals poled by an applied field $E > E_c$ at room temperature. Figure 2 shows the distributions of the EO signal along the polar (001) and nonpolar (110) directions in an SBN-0.61 crystal polarized in a field of 5.6 kV/cm. The upper and lower curves in Figs. 2a and 2b were obtained after poling in fields opposite in sign. The points indicate experimental results, and the solid lines are the results of independent linear regression. For the (001) direction (Fig. 2a), scanning was performed approximately along the central axis of the sample. For the (110) direction (Fig. 2b), we conducted scanning at the three fixed *z* values given in Fig. 2a. We could not reach complete poling of the SBN crystals: in all cases, we have $r/r_0 < 1$, which indicates that there is a residual domain density.

As follows from Fig. 2a, the EO coefficient depends almost linearly on the *z* coordinate and the $r_c(z)$ dependence is reversed (dr_c/dz changes sign with respect to the coordinate system) when the sign of the polarizing field changes. Thus, the gradient of the EO coefficient along the *z* axis results from the application of the field rather than from possible growth causes (e.g., from a smooth change in the composition). This means that the field causes a stable linear distribution of the residual domain density along the polar axis. The domain density is always maximum (the EO coefficient is minimum) near the negative electrode (Fig. 2a).

In the nonpolar direction, $r_c(x)$ tends to decrease near the lateral faces of the crystal (Fig. 2b). Since the linear dimensions of the sample in this direction are significantly smaller than the diameter of the crystalline boule grown, the decrease in r_c (an increase in the domain density) is again not related to growth causes and is caused by the properties of the lateral surfaces (apparently, by the character of their mechanical treatment). The domain-density spikes observed in $r_c(x)$ (Fig. 2b) and correlated in the *z* coordinate (Fig. 2a) and their size and polarity can be compared to the well-known stria-type macrodefects [1].

The spatial distributions of $V_{\lambda/2}$ are qualitatively similar to those of the EO coefficients. Figure 3 shows the $V_{\lambda/2}$ distributions in an SBN-0.61 : Cr crystal obtained after a field $E = 7$ kV/cm was applied for 14 h at room temperature. As is seen from Fig. 3, complete

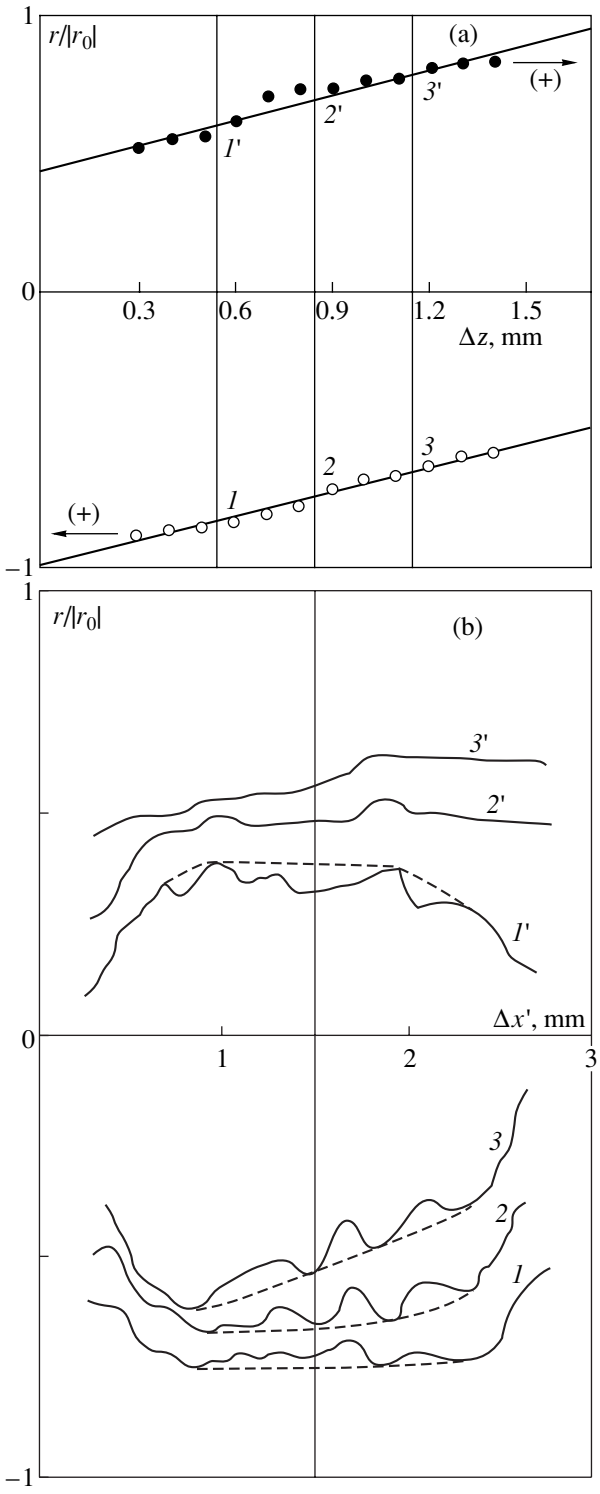

Fig. 2. Spatial distributions of the EO signal along (a) the polar [001] and (b) nonpolar [110] directions in an SBN-0.61 crystal poled in a field of 5.6 kV/cm at room temperature. (a) The upper and lower curves correspond to two directions of the poling field; the "+" arrow points to the electrode with a positive potential on the *z* axis. (b) Straight lines *1–1*', *2–2*', and *3–3*' show scanning lines along the nonpolar direction. Curves *1–3* and *1'–3'* in panel (b) are constructed for the three fixed *z* coordinates that are shown in panel (a) and correspond to the upper and lower branches, respectively, of the EO hysteresis loop shown in Fig. 4.

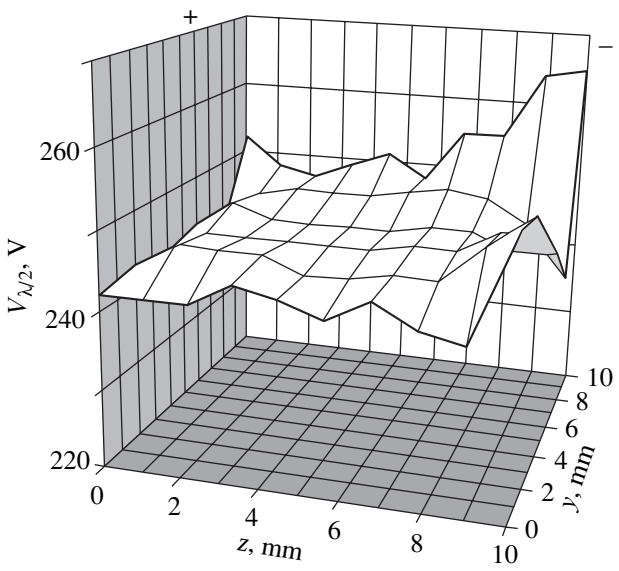

Fig. 3. Spatial distribution of the half-wave voltage $V_{\lambda/2}$ in an SBN-Cr crystal after poling in a field E = 7 kV/cm for 14 h at room temperature. The symbols "+"and "–" indicate the signs of the potentials applied to the electrodes.

poling is not achieved even under such severe conditions, since there is a nonuniform $V_{\lambda/2}$ distribution along the *z* axis, which indicates the presence of a residual domain density. Similar $V_{\lambda/2}(x, z)$ distributions were obtained in SBN-Ce and SBN-Ce,La crystals. The dependence of the $V_{\lambda/2}$ distribution on the field sign is identical to that of the EO coefficient: $V_{\lambda/2}$ is always maximum (the domain density is maximum) near the negative electrode. The nature of this dependence will be explained in terms of the domain dynamics, which was studied by measuring the intensity of 90° light scattering and is described in the next subsection.

EO hysteresis loops degrade (their amplitudes decrease) during sequential cycling in a field. Figure 4 shows the variation of EO hysteresis loops in an as-grown SBN-0.61 crystal in sequential half-cycles of switching by a sawtooth voltage and with a change in the sawtooth-voltage amplitude from ~E_c to ~$2E_c$. The degradation of hysteresis loops (fatigue) in a strong field, which was detected by other optical [17, 18] and electrical [7, 8] methods in SBN crystals of various compositions, is a fundamental property of relaxor ferroelectrics.

3.2. Results of 90° Light-Scattering Measurements

The field dependences of the light-scattering intensity were measured in multidomain crystals after annealing in the paraelectric phase followed by slow cooling to the ferroelectric phase. Figure 5 shows the field dependence of the light-scattering intensity ΔI in an SBN-0.75 crystal. The right-hand and left-hand branches of the curve were obtained for field pulse

trains (Fig. 1, inset) of opposite polarities (the field signs "+" and "–" are unambiguously set in the crystal holder irrespective of the crystal). Before each application of a field pulse train of a certain sign, the crystal was annealed in the paraelectric phase; that is, the $+E$ and $-E$ branches of the $\Delta I(E)$ curve were constructed under identical conditions in the initially multidomain crystal. Without focusing on analyzing the $\Delta I(E)$ curve (which was made in [15]), we note that the main feature of this dependence is the existence of threshold fields $E^{\pm}_{\max}$ at which the scattering intensity increases sharply and $\Delta I(E)$ passes through maxima. The $+E$ and $-E$ branches are asymmetric; more specifically, the fields $E^{+}_{\max}$ and $E^{-}_{\max}$ and the corresponding maximum values of $\Delta I(E)$ are somewhat different. Since ΔI is assumed to characterize the domain-wall area, the fields $E^{\pm}_{\max}$ have the meaning of the coercive field E_c. Indeed, the average value of $E_{\max}$ (~2 kV/cm) in SBN-0.75 correlates with $E_c \sim 1.5$–2.0 kV/cm estimated from a quasi-static $P(E)$ hysteresis loop for the same SBN-0.75 crystal [9, 15]. The same $\Delta I(E)$ dependences and similar values of $E_{\max}$ and E_c have been observed in other SBN compositions [15]. In terms of ferroelectricity, the shape of the $\Delta I(\pm E)$ curve means a weak response of the initial domain structure to a field $|E| < |E_{\max}|$ and a sharp increase in the domain-wall area followed by its decrease at $|E| \geq |E_{\max}|$. The difference in the values of $E^{+}_{\max}$ and $E^{-}_{\max}$ characterizes the unipolarity of a crystal. We will refer to the quantity $E_b = (|E^{+}_{\max} - E^{-}_{\max}|)/2$ as the bias field. For SBN-0.75, this field is $E_b \approx 0.3$ kV/cm, which agrees well with E_b measured by the ordinary method from the $P(E)$ loop for the same crystal. Unipolarity in the multidomain state is characteristic of SBN crystals [7, 9] and is caused by their relaxor properties.

In essence, the $\Delta I(E)$ dependence is identical to the field dependence of the switching current $i_s(\pm E)$). In this connection, we should emphasize the radical differences between the pulsed switching (polarization) of SBN crystals and the model scenario [19]. In [20, 21], switching currents were studied in SBN crystals and it was found that the application of short pulses with much higher amplitudes than E_c led to switching (polarization) of only an insignificant portion of the crystal volume; its complete repolarization (polarization) requires pulses as long as tens of seconds. Therefore, in our case (when the pulse durations fall in the millisecond range), the $\Delta I(E)$ maxima correspond to polarization of a very small portion of the volume; i.e., the switched charge is $Q_s \ll P_s$ [20, 21].

The probing of the central zone of this crystal along the nonpolar axis revealed virtually identical $\Delta I(E)$ dependences with a small scatter of the $E^{\pm}_{\max}$ values (Fig. 5). However, the character of the $\Delta I(E)$ dependence changes qualitatively as we approach the electrodes. Figure 6 shows the $\Delta I(E)$ curves constructed at a distance of about 0.5 mm from the top electrode (curve *1*) and from the bottom electrode (curve *2*) for the same SBN-0.75 sample [see inset (*a*) to Fig. 6]. The $\Delta I(\pm E)$ branches were again obtained under identical conditions after annealing of the crystal in the paraelectric phase before the application of a field pulse train of the same polarity. As is seen from Fig. 6, the $\Delta I(\pm E)$ dependences are sharply asymmetric in both near-electrode spaces. When a positive potential is applied to an

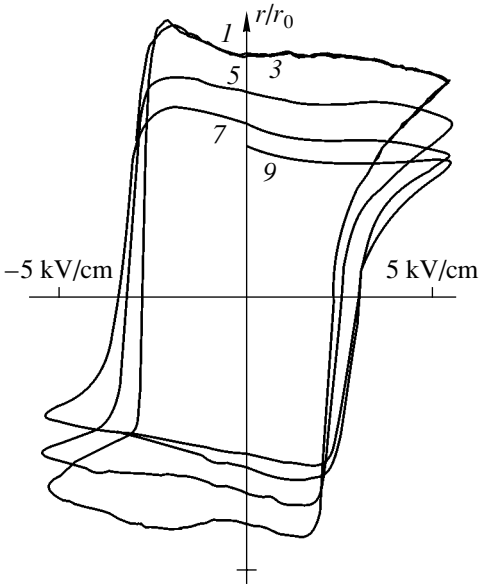

Fig. 4. Degradation of EO hysteresis loops in an SBN-0.61 crystal upon switching by a sawtooth voltage. Numbering corresponds to half-cycles, and some curves are omitted.

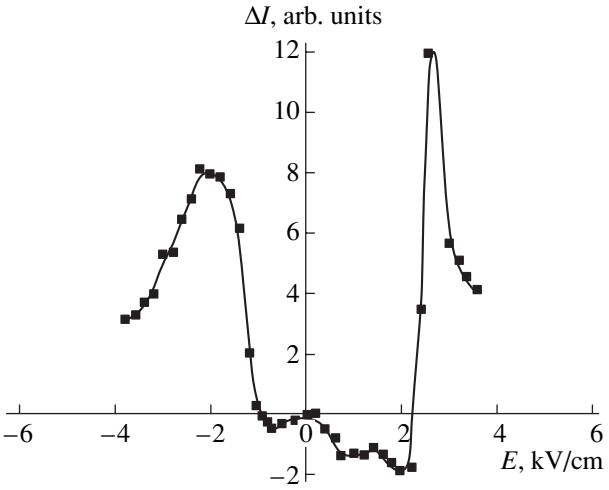

Fig. 5. Dependence of the 90° light-scattering intensity in a multidomain SBN-0.75 crystal on the filed pulse amplitude (the shape of the pulse trains of two polarities applied to the crystal is shown in the inset to Fig. 1). The dependence is obtained in the central zone of the crystal.

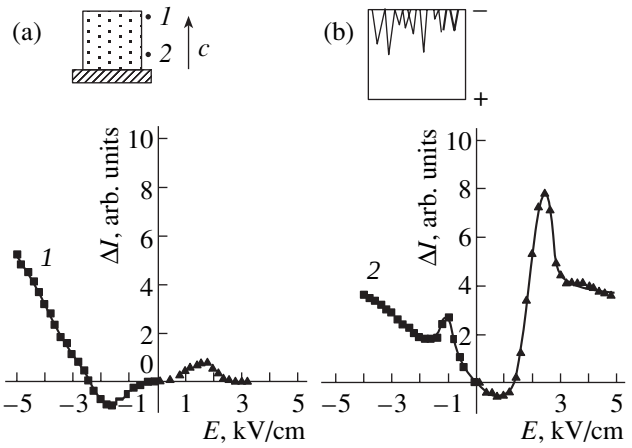

Fig. 6. Dependence of the 90° light-scattering intensity in a multidomain SBN-0.75 crystal on the field pulse amplitude in near-electrode spaces. Curves *1* and *2* correspond to the points shown in inset (a) (near the top and bottom electrodes, respectively). Inset (b) schematically shows the process that occurs during the application of field pulses; specifically, predominant domain nucleation occurs near the negative electrode, which is the cause of the increase in $\Delta I(-E)$ observed in curves *1* and *2*.

electrode, the $\Delta I(+E)$ dependence qualitatively resembles the analogous curve in the central zone of the crystal (Fig. 5) and $E^{+}_{\max}$ agrees with the average value of $E^{\pm}_{\max}$. In contrast, when a negative potential is applied to an electrode (the left-hand branches of the curves in Fig. 6), ΔI passes through a weak maximum and continues to increase smoothly with increasing $E > E^{\pm}_{\max}$ without exhibiting a tendency toward decreasing or leveling off. It should be noted that the character of the $\Delta I(E)$ dependence near the electrodes is unambiguously determined by the electrode polarity: a smooth increase in $\Delta I(E)$ is always observed near the negative electrode. The asymmetry of the $\Delta I(\pm E)$ curves in the near-electrode spaces indicates that, when a field is applied, the domain-wall area (the domain density D) near the negative electrode is always greater than that near the positive electrode. This means that domains nucleate mainly near the negative electrode [this process is shown schematically in inset (b) to Fig. 6]. Such asymmetry of the domain nucleation is characteristic of certain ferroelectrics; for example, in $LiNbO_3$, the appearance of domains in lower fields was also detected near the negative electrode [22]. The causes of this asymmetric domain nucleation are obviously related to the difference between the surface layers at the "+" and "–" ferroelectric surfaces.

4. DISCUSSION OF THE RESULTS

It will be recalled that all the results presented above were obtained for crystals polarized by a field $E > E_c$ in the ferroelectric phase (at room temperature). The measurements show that this poling mode in the ferroelectric phase (even under very severe conditions) results in gradients of r_c and $V_{\lambda/2}$ along the polar axis, i.e., in a residual domain-density distribution. There is a clear relationship between the $r_c(z)$ and $V_{\lambda/2}(z)$ distributions and the sign of the polarizing field: the minimum r_c and the maximum $V_{\lambda/2}$, i.e., the maximum residual domain density D, are observed at the negative electrode. This relationship is explained by the predominant domain nucleation at the negative electrode, which was revealed by studying the domain density $D(z)$ using 90° light scattering (Fig. 6). The smooth increase in $\Delta I(-E)$ observed with increasing pulse amplitude (Fig. 6, left-hand branches) can be explained qualitatively as follows. SBN crystals have needlelike domains, namely, tetrahedral pyramids that have a cross-sectional dimension of several microns, a length of 0.2–0.5 mm, and an apex angle of about 0.5° [23–25]. When a field is applied, their frontal growth is predominant and the stage of the lateral motion of domain walls and the coalescence of domains is weakly pronounced [25]. Thus, as the field amplitude increases, the nucleation and subsequent frontal growth of needlelike domains into the bulk occur near the negative electrode. Therefore, the domain-wall area (and, hence, ΔI) increases. Near the positive electrode, the domain density remains unchanged under the action of fields of the same amplitude (the right-hand branches of the $\Delta I(E)$ curves in Fig. 6). This situation is shown schematically in inset (b) to Fig. 6. The domain-density distribution with a maximum near the negative electrode exists even after very long field actions (Fig. 3); that is, $D(z)$ does not level off. The shape of the EO hysteresis loops (Fig. 4) also indicates the presence of a "superslow" switching (or polarization) component under fields $E > E_c$ with a lifetime of up to several hours. Even after such a long field effect, we have $r/r_0 < 1$.

Anomalously long polarization times of SBN crystals are a fundamental property of relaxor ferroelectrics [7]. In contrast to ordinary ferroelectrics [19], the polarization kinetics of such crystals (reaching a quasi-equilibrium state that corresponds to the applied field) is described by the power law [7]

$$p(t) = 1/(1 + t/a)^n \qquad (7)$$

with characteristic times specified by the potential-barrier distribution [the distribution of internal fields characteristic of an inhomogeneous (relaxor) ferroelectric]. These times can reach giant values [7], which means that a crystal cannot be completely poled within reasonable real times with a polarizing field applied in the ferroelectric phase. Along with this major cause, such long polarization times can be partly accounted for by the difficult frontal growth of domains with tilt walls in crystals with high values of piezoelectric coefficients.

Thus, the distributions of EO coefficients and $V_{\lambda/2}(z)$ along the polar axis in SBN crystals, i.e., the presence

of a residual domain density near the negative electrode after a field has been applied in the ferroelectric phase, are caused by a few factors: the appearance of domains only near the negative electrode over a wide range of fields $E > E_c$, specific domain dynamics (predominant frontal growth in the field), and extremely long polarization times. The coordinate dependence of the EO coefficients in SBN crystals and the degradation of their values when a field is repeatedly applied are likely to be the main causes of their irreproducibility and the scatter of their reported values.

5. CONCLUSIONS

When a field is applied to SBN crystals in the ferroelectric phase, domains nucleate and grow predominantly near the negative electrode over a wide range of fields $E > E_c$. A residual domain density $D(z)$ is retained after a very long effect of the field. Therefore, all SBN crystals poled in the ferroelectric phase always exhibit coordinate dependences of the electro-optical coefficients r_{ij} and the half-wave voltage $V_{\lambda/2}$ along the polar axis. The $r_{ij}(z)$ and $V_{\lambda/2}(z)$ distributions follow the $D(z)$ distribution and are determined by the sign of the polarizing field; more specifically, r_{ij} is minimum ($V_{\lambda/2}$ is maximum) near the negative electrode. Note that 90° light scattering can be used effectively to track switching processes in local volumes of ferroelectrics, as was demonstrated in this work.

ACKNOWLEDGMENTS

This work was supported by the Russian Foundation for Basic Research (project no. 03-02-13272) and INTAS (project no. 01-0173).

REFERENCES

1. Yu. S. Kuz'minov, *Ferroelectric Crystals for Laser Radiation Control* (Nauka, Moscow, 1982) [in Russian].
2. T. Volk, L. Ivleva, P. Lykov, D. Isakov, V. Osiko, and M. Woehlecke, Appl. Phys. Lett. **79** (6), 854 (2001).
3. M. D. Ewbank, R. R. Neurgaonkar, W. K. Cory, and J. Feinberg, J. Appl. Phys. **62** (2), 374 (1987).
4. K. Sayano, A. Yariv, and R. R. Neurgaonkar, Appl. Phys. Lett. **55** (4), 328 (1989).
5. A. E. Andreĭchuk, L. M. Dorozhkin, Yu. S. Kuz'minov, I. A. Maslyanitsyn, V. N. Molchanov, A. I. Rusakov, V. I. Simonov, V. D. Shigorin, and G. P. Shipulo, Kristallografiya **29** (6), 1094 (1984) [Sov. Phys. Crystallogr. **29**, 641 (1984)].
6. Y. Y. Zhu, R. F. Xiao, J. S. Fu, G. K. L. Wong, and N. Ming, Opt. Lett. **22** (18), 1382 (1997).
7. V. V. Gladkiĭ, V. A. Kirikov, T. R. Volk, and L. I. Ivleva, Zh. Éksp. Teor. Fiz. **120** (3), 678 (2001) [JETP **93**, 596 (2001)].
8. T. Granzow, V. Doerfler, Th. Woike, M. Woehlecke, R. Pankrath, M. Imlau, and W. Kleemann, Phys. Rev. B **63**, 174101 (2001).
9. V. V. Gladkiĭ, V. A. Kirikov, T. R. Volk, D. V. Isakov, and E. S. Ivanova, Fiz. Tverd. Tela (St. Petersburg) **45** (11), 2067 (2003) [Phys. Solid State **45**, 2171 (2003)].
10. L. E. Cross, Ferroelectrics **76**, 241 (1987).
11. L. I. Ivleva, N. V. Bogodaev, N. M. Polozkov, and V. V. Osiko, Opt. Mater. **4**, 168 (1995).
12. M. DiDomenico and S. H. Wemple, J. Appl. Phys. **40** (3), 720 (1969).
13. A. I. Bezhanova, V. G. Silvestrov, G. A. Zeinalova, and T. R. Volk, Ferroelectrics B **111**, 299 (1990).
14. J. P. Wilde and R. E. Wilde, J. Appl. Phys. **71** (1), 418 (1992).
15. D. Isakov, T. Volk, L. Ivleva, K. Betzler, C. David, A. Tunyagi, and M. Woehlecke, Pis'ma Zh. Éksp. Teor. Fiz. **80** (4), 289 (2004) [JETP Lett. **80**, 258 (2004)].
16. S. Kawai, T. Ogawa, H. S. Lee, R. C. DeMattei, and R. S. Feigelson, Appl. Phys. Lett. **73** (6), 768 (1998).
17. M. Y. Goulkov, T. Granzow, U. Doerfler, Th. Woike, M. Imlau, and R. Pankrath, Appl. Phys. B **76** (4), 407 (2003).
18. U. Doerfler, T. Granzow, Th. Woike, M. Woehlecke, R. Pankrath, and M. Imlau, Appl. Phys. B **78** (2), 211 (2004).
19. M. E. Lines and A. M. Glass, *Principles and Applications of Ferroelectrics and Related Materials* (Clarendon, Oxford, 1977; Mir, Moscow, 1981).
20. T. Volk, D. Isakov, L. Ivleva, and M. Woehlecke, Appl. Phys. Lett. **83** (11), 2220 (2003).
21. T. R. Volk, D. V. Isakov, and L. I. Ivleva, Fiz. Tverd. Tela (St. Petersburg) **45** (8), 1463 (2003) [Phys. Solid State **45**, 1537 (2003)].
22. N. F. Evlanova, Candidate's Dissertation (Moscow State Univ., Moscow, 1978).
23. L. A. Bursill and P. J. Lin, Philos. Mag. B **54**, 157 (1986).
24. G. Fogarty, B. Steiner, M. Cronin-Golomb, U. Laor, M. H. Garett, J. Martin, and R. Uhrin, J. Opt. Soc. Am. B **13** (11), 2636 (1996).
25. N. R. Ivanov, T. R. Volk, L. I. Ivleva, S. P. Chumakova, and A. V. Ginzberg, Kristallografiya **47** (6), 1065 (2002) [Crystallogr. Rep. **47**, 1023 (2002)].

Translated by K. Shakhlevich

Physics of the Solid State, Vol. 47, No. 2, 2005, pp. 312–323. Translated from Fizika Tverdogo Tela, Vol. 47, No. 2, 2005, pp. 300–310.

LATTICE DYNAMICS AND PHASE TRANSITIONS

Longitudinal-Phonon Relaxation Mechanisms in Cubic Crystals of Germanium, Silicon, and Diamond

I. G. Kuleev and I. I. Kuleev

Institute of Metal Physics, Ural Division, Russian Academy of Sciences, ul. S. Kovalevskoĭ 18, Yekaterinburg, 620219 Russia
e-mail: kuleev@imp.uran.ru

Received March 30, 2004; in final form, May 19, 2004

Abstract—The relaxation rates of thermal and high-frequency longitudinal phonons are calculated using an anisotropic-continuum model. Three-phonon scattering mechanisms ($L \longleftrightarrow L + L$, $L \longleftrightarrow T + L$) for the phonon relaxation are considered. Anisotropic anharmonic phonon scattering in cubic crystals is described in terms of the second- and third-order elastic moduli. The parameters determining the longitudinal-phonon relaxation rates are found for germanium, silicon, and diamond crystals. The long-wavelength limit and the transition to the isotropic-medium model are considered, and the dependences of the relaxation rates of thermal and high-frequency phonons on temperature and phonon wave vector are analyzed for these crystals. © *2005 Pleiades Publishing, Inc.*

1. INTRODUCTION

Understanding the phonon relaxation mechanisms operating in anharmonic scattering processes is of importance in studying the lattice thermal conductivity of crystals [1] and kinetic effects, such as the attenuation of ultrasonic waves [2] and the electron–phonon drag thermopower [3]. Experimental studies of the isotope effects in the thermal conductivity of germanium, silicon, and diamond [4–8] and theoretical analysis of the results obtained [9, 10] have shown that normal processes (N processes) of phonon–phonon scattering are important in the lattice thermal conductivity of isotopically enriched and chemically pure crystals. These processes (conserving the energy of colliding phonons) and boundary phonon scattering are the main mechanisms that limit the maximum values of the thermal conductivity of isotopically highly enriched crystals [9, 10].

In calculating the thermal conductivity using the relaxation method [4–12], the phonon relaxation rates in N processes are usually found within the long-wavelength approximation, $z_{q\lambda} = \hbar\omega_{q\lambda}/k_B T \ll 1$, where $\hbar\omega_{q\lambda}$ is the energy of a phonon with wave vector $\mathbf{q}$ and polarization λ. The application of this approximation for calculating the attenuation of long-wavelength ultrasonic waves and the electron–phonon drag thermopower is well founded, because the electrons in semiconductor crystals can interact with long-wavelength phonons only. However, the lattice thermal conductivity of Ge and Si crystals with a natural isotopic composition is mainly due to thermal phonons with $z_{q\lambda} \approx 1$, while that of isotopically enriched crystals is dominated by thermal phonons with $z_{q\lambda} \approx 2$–4. Therefore, the long-wavelength approximation to phonon relaxation rates cannot be used to calculate the thermal conductivity. In the relaxation method, the parameters that characterize the intensity of anharmonic processes are theoretical parameters and are determined by fitting the calculations to the experimental data [4–12]. To estimate the probability of anharmonic scattering processes, the isotropic-medium model is usually used. However, this model is inadequate for germanium, silicon, and diamond crystals, as well as for extensively studied cubic crystals, such as InSb, GaAs, and CaF_2, which exhibit significant elastic anisotropy characterized by the second- and third-order elastic moduli.

The objective of our study is to determine the phonon relaxation rates due to anharmonic scattering processes from the experimental data on the second- and third-order elastic moduli. By determining the dependences of the phonon relaxation rates on temperature and phonon wave vector in Ge, Si, and diamond crystals, we can, first, find the absorption coefficients for both long-wavelength ($z_{q\lambda} \ll 1$) and high-frequency ($z_{q\lambda} \gg 1$) ultrasonic waves and, second, specify the dominant thermal-phonon relaxation mechanisms and avoid the necessity of fitting the two parameters of the theory when calculating the thermal conductivity of these crystals.

In this paper, we consider the longitudinal-phonon relaxation due to anharmonic scattering processes in cubic crystals. In Section 2, the elastic energy of a cubic crystal is expressed in terms of the second- and third-order elastic moduli. This energy determines the probabilities of various anharmonic three-phonon scattering processes. In Section 3, we calculate the rates of relaxation of thermal and high-frequency longitudinal phonons via the $L \rightleftharpoons L + L$ and $L \rightleftharpoons T + L$ processes in cubic crystals. The formulas obtained make it possible to determine the rates of longitudinal-phonon relax-

1063-7834/05/4702-0312$26.00

Table 1. Thermodynamic elastic moduli of Ge, Si, and diamond (in units of 10^{12} dyn/cm^2)

	c_{11}	c_{12}	c_{44}	c_{111}	c_{112}	c_{123}	c_{144}	c_{155}	c_{456}
Ge	1.289	0.483	0.671	–7.10	–3.89	–0.18	–0.23	–2.92	–0.53
Si	1.657	0.638	0.796	–8.25	–4.51	–0.64	0.12	–3.10	–0.64
Diamond	10.76	1.25	5.758	–62.6	–22.6	1.12	–6.74	–28.6	–8.23

ation due to anharmonic scattering processes from the experimental data on the elastic moduli. The dependences of the phonon relaxation rates on temperature and phonon wave vector in germanium, silicon, and diamond crystals are analyzed in Section 4. The long-wavelength limit and the transition to the isotropic-medium model are considered. The results obtained in this work are compared with earlier results obtained within the isotropic-medium model.

2. THE ELASTIC ENERGY OF THE CUBIC CRYSTAL

The expression for the elastic energy of a cubic crystal was obtained in [13] (see also [14]) to terms of the third order in the strain tensor η_{ij}. We transform that expression in much the same way as was done in [15], within the isotropic-medium model. Since the experimentally determined quantities in [16–19] were the thermodynamic third-order elastic moduli c_{ijk}, we use the normalization of the moduli c_{ijk} introduced by Brugger [20]. In this case, the expression for the elastic energy density derived in [13] can be written in the following form convenient for calculations:

$$\begin{aligned} W &= \frac{1}{2}c_{11}\left(\sum_i \eta_{ii}\right)^2 + \frac{1}{2}(c_{11}-c_{12}-c_{44})\sum_i \eta_{ii}^2 \\ &+ c_{44}\sum_i \eta_{ik}^2 + \frac{1}{6}\left\{\tilde{c}_{111}\sum_i \eta_{ii}^3 + 3\tilde{c}_{112}\sum_{i,k}\eta_{ii}^2\eta_{kk}\right. \\ &+ c_{123}\left(\sum_i \eta_{ii}\right)^3 + 6c_{144}\sum_{i,k}\eta_{ii}^2\eta_{jk} \\ &\left. + 8c_{456}\sum_{i,k}\eta_{ik}\eta_{kj}\eta_{ji} + 12\tilde{c}_{155}\sum_{i,k}\eta_{ii}\eta_{ik}^2\right\}. \end{aligned} \tag{1}$$

Here,

$$\begin{aligned} \tilde{c}_{111} &= c_{111} - 3c_{112} + 2c_{123} + 12c_{144} \\ &\quad - 12c_{155} + 16c_{456}, \\ \tilde{c}_{112} &= c_{112} - c_{123} - 2c_{144}, \\ \tilde{c}_{155} &= c_{155} - c_{144} - 2c_{456}. \end{aligned} \tag{2}$$

The relationships between the thermodynamic moduli c_{ijk} and the normalized moduli c_{ijk}^{B} used by Birch [13] are

$$\begin{aligned} &c_{111} = 6c_{111}^{\mathrm{B}}, \quad c_{112} = 2c_{112}^{\mathrm{B}}, \quad c_{123} = c_{123}^{\mathrm{B}}, \\ &c_{144} = \frac{1}{2}c_{144}^{\mathrm{B}}, \quad c_{155} = \frac{1}{2}c_{155}^{\mathrm{B}}, \quad c_{456} = \frac{1}{4}c_{456}^{\mathrm{B}}. \end{aligned} \tag{3}$$

It should be noted that in [19] the coefficient indicated in the relationship between the thermodynamic modulus c_{456} and the corresponding modulus used by Birch is erroneous, 1/8 (see also [20, 21]). The normalized moduli used by Tucker and Rampton [15] are

$$c_{ijk}^{TR} = \frac{1}{6}c_{ijk}. \tag{3a}$$

The second- (c_{ik}) and third-order (c_{ijk}) elastic moduli of Ge, Si, and diamond crystals are listed in Table 1.

The strain tensor η_{ik} can be expressed in terms of the distortion tensor ξ_{ik} [22] as

$$\begin{aligned} \eta_{ik} &= \frac{1}{2}\left(\frac{\partial u_i}{\partial x_k} + \frac{\partial u_k}{\partial x_i} + \sum_j \frac{\partial u_j}{\partial x_i}\frac{\partial u_j}{\partial x_k}\right) \\ &\equiv \frac{1}{2}\left(\xi_{ik} + \xi_{ki} + \sum_j \xi_{ji}\xi_{jk}\right). \end{aligned} \tag{4}$$

Substituting Eq. (4) into Eq. (1) gives

$$\begin{aligned} W &= \frac{1}{2}c_{11}\left(\sum_i \xi_{ii}\right)^2 + \frac{1}{2}(c_{11}-c_{12}-2c_{44})\sum_i \xi_{ii}^2 \\ &+ \frac{1}{4}c_{44}\sum_i (\xi_{ik}+\xi_{ki})^2 + \frac{1}{6}\left\{\tilde{c}_{111}\sum_i \xi_{ii}^3 + 3\tilde{c}_{112}\sum_{i,k}\xi_{ii}^2\xi_{kk}\right. \\ &+ c_{123}\left(\sum_i \xi_{ii}\right)^3 + 3c_{144}\sum_{i,j,k}\xi_{ii}\xi_{jk}\xi_{kj} \\ &+ 3(c_{144}+c_{12})\sum_{i,j,k}\xi_{ii}\xi_{jk}^2 + 2c_{456}\sum_{i,j,k}\xi_{ik}\xi_{kj}\xi_{ji} \\ &+ 6(c_{44}+c_{456})\sum_{i,j,k}\xi_{ik}\xi_{ji}\xi_{jk} \\ &\left. + 3\tilde{c}_{155}\sum_{i,k}(\xi_{ii}\xi_{ik}^2 + 2\xi_{ii}\xi_{ik}\xi_{ki})\right) \end{aligned} \tag{5}$$

Table 2. Elastic moduli ΔC, $\tilde{c}_{111}$, $\tilde{c}_{112}$, and $\tilde{c}_{155}$ of Ge, Si, and diamond (in units of 10^{12} dyn/cm^2)

	Ge	Si	Diamond
ΔC	–0.54	–0.57	–2.01
$\tilde{c}_{155}$	–1.63	–1.9	–5.4
$\tilde{c}_{112}$	–3.25	–4.1	–10.24
$\tilde{c}_{111}$	28.01	32.4	138.1

$$+ 3[\tilde{c}_{155} + (c_{11} - c_{12} - 2c_{44})]\sum_{i,k}\xi_{ii}\xi_{ki}^2\Bigg\}.$$

The terms cubic in ξ_{ik} in Eq. (5) account for interaction between phonons. It follows from Eq. (5) that, due to the nonlinear coupling between the strain tensor η_{ik} and the distortion tensor ξ_{ik}, the phonon relaxation involves not only the third-order elastic moduli but also the second-order elastic moduli. Let us consider the transition from the elastic energy of the cubic crystal to the elastic energy of the isotropic medium W_{iso}, whose expression was derived in [15, Eq. (4.6)]. From the condition $\Delta W = W_k - W_{\text{iso}} = 0$, we find that

$$\begin{aligned}
\Delta C &= c_{11} - c_{12} - 2c_{44} = 0,\\
\tilde{c}_{112} &= c_{112} - c_{123} - 2c_{144} = 0,\\
\tilde{c}_{155} &= c_{155} - c_{144} - 2c_{456} = 0,\\
\tilde{c}_{111} &= c_{111} - 3c_{112} + 2c_{123}\\
&+ 12c_{144} - 12c_{155} + 16c_{456} = 0.
\end{aligned} \tag{6}$$

Let us write the displacement of a particle in the standard form [15]:

$$u_i(x) = i\sum_{\mathbf{q}}\left(\frac{\hbar}{2\rho V\omega_{\mathbf{q}\lambda}}\right)^{1/2} e_i^{\lambda} e^{i\mathbf{qr}}(b_{\mathbf{q}\lambda} - b_{-\mathbf{q}\lambda}^{+}), \tag{7}$$

where $b_{-\mathbf{q}\lambda}^{+}$ and $b_{\mathbf{q}\lambda}$ are the phonon creation and annihilation operators, respectively; ρ is the density; V is the normalization volume; $\mathbf{e}$ is the polarization vector; and $\omega_{\mathbf{q}\lambda}$ is the frequency of a phonon with wave vector $\mathbf{q}$ and polarization λ. It is seen from Eq. (7) that each tensor component ξ_{ij} is characterized by the coefficient $e_i q_j$. Substituting Eq. (7) into Eq. (5) gives the following expression for the anharmonic contribution to the energy density of lattice vibrations:

$$W = -\frac{i}{6}\sum_{\substack{\mathbf{q}_1,\mathbf{q}_2,\mathbf{q}_3\\ \lambda_1\lambda_2\lambda_3}}\left(\frac{\hbar}{2\rho V}\right)^{3/2}(\omega_{\mathbf{q}_1\lambda_1}\omega_{\mathbf{q}_2\lambda_2}\omega_{\mathbf{q}_3\lambda_3})^{-1/2}$$

$$\times (b_{\mathbf{q}_1\lambda_1} - b_{-\mathbf{q}_1\lambda_1}^{+})(b_{\mathbf{q}_2\lambda_2} - b_{-\mathbf{q}_2\lambda_2}^{+})(b_{\mathbf{q}_3\lambda_3} - b_{-\mathbf{q}_3\lambda_3}^{+})$$

$$\times \exp(i(\mathbf{q}_1 + \mathbf{q}_2 + \mathbf{q}_3)\mathbf{r})V_{\mathbf{q}_1\mathbf{q}_2\mathbf{q}_3}^{\lambda_1\lambda_2\lambda_3},$$

$$\begin{aligned}
V_{\mathbf{q}_1\mathbf{q}_2\mathbf{q}_3}^{\lambda_1\lambda_2\lambda_3} &= \tilde{c}_{111}\sum_i e_{1i}q_{1i}e_{2i}q_{2i}e_{3i}q_{3i}\\
&+ c_{123}(\mathbf{e}_1\mathbf{q}_1)(\mathbf{e}_2\mathbf{q}_2)(\mathbf{e}_3\mathbf{q}_3)\\
&+ \tilde{c}_{112}\sum_i[(\mathbf{e}_1\mathbf{q}_1)e_{2i}q_{2i}e_{3i}q_{3i} + (\mathbf{e}_2\mathbf{q}_2)e_{1i}q_{1i}e_{3i}q_{3i}\\
&+ (\mathbf{e}_3\mathbf{q}_3)e_{1i}q_{1i}e_{2i}q_{2i}] + c_{144}[(\mathbf{e}_1\mathbf{q}_1)(\mathbf{e}_2\mathbf{q}_3)(\mathbf{e}_3\mathbf{q}_2)\\
&+ (\mathbf{e}_2\mathbf{q}_2)(\mathbf{e}_1\mathbf{q}_3)(\mathbf{e}_3\mathbf{q}_1) + (\mathbf{e}_3\mathbf{q}_3)(\mathbf{e}_1\mathbf{q}_2)(\mathbf{e}_2\mathbf{q}_1)]\\
&+ (c_{12} + c_{144})[(\mathbf{e}_1\mathbf{q}_1)(\mathbf{e}_2\mathbf{e}_3)(\mathbf{q}_3\mathbf{q}_2)\\
&+ (\mathbf{e}_2\mathbf{q}_2)(\mathbf{e}_1\mathbf{e}_3)(\mathbf{q}_3\mathbf{q}_1) + (\mathbf{e}_3\mathbf{q}_3)(\mathbf{e}_1\mathbf{e}_2)(\mathbf{q}_1\mathbf{q}_2)]\\
&+ c_{456}[(\mathbf{e}_1\mathbf{q}_3)(\mathbf{e}_2\mathbf{q}_1)(\mathbf{e}_3\mathbf{q}_2) + (\mathbf{e}_1\mathbf{q}_2)(\mathbf{e}_2\mathbf{q}_3)(\mathbf{e}_3\mathbf{q}_1)]\\
&+ (c_{44} + c_{456})[(\mathbf{e}_1\mathbf{q}_2)(\mathbf{q}_1\mathbf{q}_3)(\mathbf{e}_2\mathbf{e}_3)\\
&+ (\mathbf{e}_2\mathbf{q}_3)(\mathbf{q}_1\mathbf{q}_2)(\mathbf{e}_1\mathbf{e}_3) + (\mathbf{e}_3\mathbf{q}_1)(\mathbf{q}_2\mathbf{q}_3)(\mathbf{e}_1\mathbf{e}_2)\\
&+ (\mathbf{e}_1\mathbf{q}_3)(\mathbf{q}_1\mathbf{q}_2)(\mathbf{e}_2\mathbf{e}_3) + (\mathbf{e}_2\mathbf{q}_1)(\mathbf{q}_2\mathbf{q}_3)(\mathbf{e}_1\mathbf{e}_3)\\
&+ (\mathbf{e}_3\mathbf{q}_2)(\mathbf{q}_1\mathbf{q}_3)(\mathbf{e}_1\mathbf{e}_2)]\\
&+ \tilde{c}_{155}\sum_i\{e_{1i}e_{2i}e_{3i}(q_{1i}(\mathbf{q}_2\mathbf{q}_3) + q_{2i}(\mathbf{q}_1\mathbf{q}_3) + q_{3i}(\mathbf{q}_1\mathbf{q}_2))\\
&+ e_{1i}q_{1i}[e_{2i}q_{3i}(\mathbf{e}_3\mathbf{q}_2) + e_{3i}q_{2i}(\mathbf{e}_2\mathbf{q}_3)]\\
&+ e_{2i}q_{2i}[e_{1i}q_{3i}(\mathbf{e}_3\mathbf{q}_1) + e_{3i}q_{1i}(\mathbf{e}_1\mathbf{q}_3)]\\
&+ e_{3i}q_{3i}[e_{1i}q_{2i}(\mathbf{e}_2\mathbf{q}_1) + e_{2i}q_{1i}(\mathbf{e}_1\mathbf{q}_2)]\}\\
&+ [\tilde{c}_{155} + \Delta C]\sum_i q_{1i}q_{2i}q_{3i}[e_{1i}(\mathbf{e}_2\mathbf{e}_3)\\
&+ e_{2i}(\mathbf{e}_1\mathbf{e}_3) + e_{3i}(\mathbf{e}_1\mathbf{e}_2)].
\end{aligned} \tag{8}$$

Under conditions (6), Eq. (8) gives the anharmonic contribution to the energy density for the isotropic medium [15, Eq. (4.22)]. The cubic crystal differs from the isotropic medium in the terms containing the third-order elastic moduli $\tilde{c}_{111}$, $\tilde{c}_{112}$, and $\tilde{c}_{155}$. Let us consider conditions (6) for Ge, Si, and diamond crystals using the experimental data on the second- and third-order elastic moduli given in Table 1. Analysis shows (Table 2) that, for these crystals, conditions (6) are not satisfied for both the second- and third-order elastic moduli; indeed, $|\Delta C| \sim c_{12}$ and $\tilde{c}_{155}$ is approximately two times less than the initial elastic modulus c_{155}. The deviation from the isotropic-medium model is the largest for the elastic modulus $\tilde{c}_{111}$; this modulus is much larger than the other third-order moduli for Ge, Si, and diamond and is opposite in sign to the initial modulus c_{111}. Therefore, the largest deviation from the isotropic-medium model will be observed for the relaxation rates involving the

elastic modulus $\tilde{c}_{111}$. Integrating over the normalization volume, we obtain the matrix element $V^{\lambda_1\lambda_2\lambda_3}_{\mathbf{q}_1\mathbf{q}_2\mathbf{q}_3}$, whose modulus squared determines the probability of phonon scattering due to anharmonic scattering processes. With Eq. (8), we can study various three-phonon scattering mechanisms and calculate the phonon relaxation rates due to anharmonic scattering processes in cubic crystals.

3. LONGITUDINAL-PHONON RELAXATION MECHANISMS IN CUBIC CRYSTALS

The main longitudinal-phonon relaxation mechanisms operating in cubic crystals are associated with the following processes [15, 23]:

$$\begin{aligned}
&(1)\quad L + L \longrightarrow L, \quad \omega^L_{\mathbf{q}_3} = \omega^L_{\mathbf{q}_1} + \omega^L_{\mathbf{q}_2},\\
&\qquad L \longrightarrow L + L, \quad \omega^L_{\mathbf{q}_1} = \omega^L_{\mathbf{q}_2} + \omega^L_{\mathbf{q}_3},\\
&(2)\quad L + T \longrightarrow L, \quad \omega^L_{\mathbf{q}_3} = \omega^L_{\mathbf{q}_1} + \omega^T_{\mathbf{q}_2},\\
&\qquad L \longrightarrow T + L, \quad \omega^L_{\mathbf{q}_1} = \omega^T_{\mathbf{q}_2} + \omega^L_{\mathbf{q}_3},\\
&(3)\quad L + T \longrightarrow T, \quad \omega^T_{\mathbf{q}_3} = \omega^L_{\mathbf{q}_1} + \omega^T_{\mathbf{q}_2},\\
&\qquad L \longrightarrow T + T, \quad \omega^L_{\mathbf{q}_1} = \omega^T_{\mathbf{q}_2} + \omega^T_{\mathbf{q}_3}.
\end{aligned} \tag{9}$$

The first row for each case represents the fusion (*S* process) of a longitudinal phonon with a longitudinal [case (i)] or transverse phonon [case (ii), (iii)] into a longitudinal [cases (i), (ii)] or transverse phonon [case (iii)]. The second row for each case represents the decay (*R* process) of a longitudinal phonon into two longitudinal phonons [case (i)], a transverse and a longitudinal phonon [case (ii)], or two transverse phonons [case (iii)].

Below, we calculate the phonon relaxation rate in cubic crystals for cases (i) and (ii) and determine their values and dependences on temperature and phonon wave vector using the data on the elastic moduli from Tables 1 and 2. According to [12], the phonon relaxation rate is given by

$$\begin{aligned}
&\nu_{\mathrm{phN}}(q_1, \lambda_1)\\
&= \frac{\pi\hbar^4}{(2\rho k_B T)^3}\frac{1}{V}\sum_{\substack{\mathbf{q}_2\mathbf{q}_3\\ \lambda_2\lambda_3}}\frac{\sinh\left(\frac{z_1}{2}\right)\delta_{\mathbf{q}_1+\mathbf{q}_2+\mathbf{q}_3,0}}{z_1z_2z_3\sinh\left(\frac{z_2}{2}\right)\sinh\left(\frac{z_3}{2}\right)}\\
&\times\left|V^{\lambda_1\lambda_2\lambda_3}_{\mathbf{q}_1\mathbf{q}_2\mathbf{q}_3}\right|^2\{2\delta(\omega_{\mathbf{q}_1\lambda_1} + \omega_{\mathbf{q}_2\lambda_2} - \omega_{\mathbf{q}_3\lambda_3})\\
&\quad + \delta(\omega_{\mathbf{q}_1\lambda_1} - \omega_{\mathbf{q}_2\lambda_2} - \omega_{\mathbf{q}_3\lambda_3})\}.
\end{aligned} \tag{10}$$

In curly brackets, the first term is due to *S* processes and the second to *R* processes.

For the *LLL* relaxation mechanism [case (i)], we have in Eq. (8)

$$\begin{aligned}
&(\mathbf{e}_1\mathbf{q}_1) = q_1, \quad (\mathbf{e}_2\mathbf{q}_2) = q_2, \quad (\mathbf{e}_3\mathbf{q}_3) = q_3,\\
&\mathbf{q}_1 + \mathbf{q}_2 = \mathbf{q}_3 \quad (S\text{ process});\\
&\mathbf{q}_1 = \mathbf{q}_2 + \mathbf{q}_3 \quad (R\text{ process}).
\end{aligned} \tag{11}$$

Using Eqs. (11), we express matrix element (8) for the *R* and *S* processes for the *LLL* mechanism in terms of the magnitudes of the vectors $\mathbf{q}_1$ and $\mathbf{q}_2$, the angle θ between them, and the azimuthal angle φ of the vector $\mathbf{q}_2$:

$$\begin{aligned}
V^{LLL}_{S,R} &= q_1q_2q_3\Bigg\{(c_{123} + c_{12} + 2c_{144})\\
&+\left(\frac{q_2}{q_3}\right)^2\Bigg[\cos\theta\left(\frac{q_1}{q_2} \pm \cos\theta\right)\\
&\times\left\{(2A_{\mathrm{cub}} + 4\tilde{c}_{155} + \Delta C)\left(\frac{q_1}{q_2}\cos\theta \pm 1\right)\right\}\\
&+ (4\tilde{c}_{155} + \Delta C + \tilde{c}_{111} + 2\tilde{c}_{112})\\
&\times\left(\cos\theta\left(\frac{q_1}{q_2} \pm \cos\theta\right)\right)^2 + \tilde{c}_{112}\left(\left(\frac{q_1}{q_2} \pm \cos\theta\right)^2\right.\\
&\left.+ (\cos\theta\sin\theta)^2 + (\sin\theta)^4((\sin\varphi)^4 + (\cos\varphi)^4)\right)\Bigg]\Bigg\}.
\end{aligned} \tag{12}$$

In Eq. (12), the first term and the terms containing the coefficient A_{cub} account for isotropic scattering of longitudinal phonons. The other terms are associated with cubic anisotropy and vanish in the isotropic medium. For the cubic crystal, we have

$$A_{\mathrm{cub}} = c_{12} + 3c_{44} + 2c_{144} + 4c_{456}. \tag{13}$$

For the isotropic medium, using Eqs. (6), we find that the expression for A_{cub} becomes identical to that derived in [15]:

$$\begin{aligned}
A_{\mathrm{cub}} &= A_{\mathrm{iso}} = A_1 + 3A_2 + A_3 + A_4\\
&= 1.5c_{11} - 0.5c_{12} + 2c_{155}\\
&= 1.5c_{11} - 0.5c_{12} + 12c^{TR}_{155}
\end{aligned} \tag{13a}$$

(the coefficients A_1, A_2, A_3, A_4 are defined in [15]).

From the conservation of energy, it follows that, in the Debye approximation for the phonon spectrum, only collinear phonons can interact via the *LLL* mechanism [1, 23]. If the dispersion of phonons is taken into account, the probability of phonon scattering via this

mechanism vanishes. However, the phonon lifetime remains finite due to anharmonic scattering processes and scattering from defects, impurities, and boundaries. The decay of phonon states can be taken into account by substituting a Lorentzian for the δ functions that ensure the energy conservation in the fusion and decay of longitudinal phonons [1, 22]. In order to analyze the effect of the decay of phonon states via the *LLL* mechanism, we find the total longitudinal-phonon relaxation rate determined by all relaxation processes (9). If the collision-induced broadening of phonon states $\gamma_L(q_1)$ is much smaller than the phonon energies $(\hbar\omega_{\mathbf{q}_2})$, $(\hbar\omega_{\mathbf{q}_3})$, the Lorentzian is sharply peaked at $\cos\theta \approx 1$. We restrict our calculations to this approximation and put $\cos\theta \approx 1$. For the cubic crystal, the matrix element for the *LLL* scattering mechanism thus obtained is

$$V_{S,R}^{LLL} = (3c_{11} + c_{111})q_1q_2(q_1 \pm q_2). \tag{14}$$

This expression is also valid for the isotropic medium, which can be verified using Eqs. (6). Substituting Eq. (13) into Eq. (10) gives the following expression for the phonon relaxation rate due to the *LLL* mechanism:

$$\nu_{\text{phN}}^{LLL} = B_{LLL}T^5\sinh(z_1/2) \times\left\{2\int_0^{z_{DL}} dz_2 \frac{z_2^2(z_1+z_2)^2}{\sinh\left(\frac{z_2}{2}\right)\sinh\left(\frac{z_1+z_2}{2}\right)} + \int_0^{z_1} dz_2 \frac{z_2^2(z_1-z_2)^2}{\sinh\left(\frac{z_2}{2}\right)\sinh\left(\frac{z_1-z_2}{2}\right)}\right\}, \tag{15}$$

$$B_{LLL} = \frac{(3c_{11}+c_{111})^2(k_B)^5}{32\pi\hbar^4\rho^3 S_L^9}.$$

Using Eq. (15), we find the dependence of the phonon relaxation rate on temperature and phonon wave vector for a cubic crystal in which the *LLL* scattering mechanism is operative and the decay of phonons is weak.

For the *LTL* phonon relaxation mechanism [case (ii) in Eqs. (9)], we have

$$(\mathbf{e}_1\mathbf{q}_1) = q_1, \quad (\mathbf{e}_2\mathbf{q}_2) = 0, \quad (\mathbf{e}_3\mathbf{q}_3) = q_3, \quad (\mathbf{e}_2\mathbf{q}_1) = (\mathbf{e}_2\mathbf{q}_3); \tag{16}$$
$$\mathbf{q}_1 + \mathbf{q}_2 = \mathbf{q}_3\ (S), \quad \mathbf{q}_1 = \mathbf{q}_2 + \mathbf{q}_3\ (R).$$

Using Eqs. (16), we express matrix element (8) for the *S* and *R* processes of the *LTL* relaxation mechanism in terms of the longitudinal-phonon polarization vector $\mathbf{e}_2$ and the angular coordinates θ and φ of the vector $\mathbf{q}_2$:

$$V_{S,R}^{LTL} = \pm\frac{q_1^3q_2}{q_3}\{A_{S,R}(\theta)e_{2z} + b_{(S,R)} \times\left[e_{2x}\left(\frac{q_{2x}}{q_2}\right)^3 + e_{2y}\left(\frac{q_{2y}}{q_2}\right)^3\right]\}, \tag{17}$$

$$A_{S,R}(\theta) = \cos\theta\{(\tilde{c}_{111} + \tilde{c}_{112} + 8\tilde{c}_{155} + 2\Delta C) \times\left(1 \pm \frac{q_2}{q_1}\cos\theta\right)^2 + \tilde{c}_{112}\left(\frac{q_3}{q_1}\right)^2\} + \left(1 \pm \frac{q_2}{q_1}\cos\theta\right) \times\left\{(A_{\text{cub}} + 2\tilde{c}_{155})\left(2\cos\theta \pm \frac{q_2}{q_1}\right) + \Delta C\cos\theta\right\}, \tag{18}$$

$$b_{(S,R)} = \tilde{c}_{112}\left(\frac{q_2}{q_1}\right)^2.$$

In Eq. (18), the terms containing the coefficient A_{cub} [given by Eqs. (13), (13a)] account for isotropic phonon scattering; the other terms are associated with cubic anisotropy and vanish in the isotropic medium characterized by Eqs. (6).

It is seen from Eq. (17) that the square of the modulus of the matrix element that determines the probability of three-phonon scattering of the *LTL* type depends on the products of the components of the polarization vector $\mathbf{e}_2$ times the components of the phonon wave vector $\mathbf{q}_2$. In general, both the relaxation rate ν_{phN}^{LTL} and the phonon eigenfrequencies depend on the direction of longitudinal-phonon propagation relative to the crystallographic axes. In what follows, we consider one of the symmetry axes, such as [100], [001], and [111], and take the *z* axis and the phonon wave vector $\mathbf{q}_1$ to be along this axis. Using the relation $\mathbf{e}_2\mathbf{q}_2 = 0$, we express the components of the longitudinal-phonon polarization vector $\mathbf{e}_2$ in terms of the angular coordinates θ and φ of the vector $\mathbf{q}_2$:

$$e_{2x} = \cos\theta\cos\varphi\cos\varphi_e - \sin\varphi_e\sin\varphi,$$
$$e_{2y} = \cos\theta\sin\varphi\cos\varphi_e + \sin\varphi_e\cos\varphi, \tag{19}$$
$$e_{2z} = -\sin\theta\cos\varphi_e.$$

The angle φ_e defines the direction of the polarization vector $\mathbf{e}_2$ in the plane perpendicular to the vector $\mathbf{q}_2$. Let us discuss the procedure for averaging the probability of phonon scattering via the *LTL* mechanism over the polarization vector of the transverse phonon. This procedure has not been described in the literature. Sometimes, in calculating the relaxation rate within the isotropic-medium model, the direction of the transverse-phonon polarization vector $\mathbf{e}_2$ relative to the vectors $\mathbf{q}_1$ and $\mathbf{q}_2$ is specified. For example, Tamura [24] assumed

the vector $\mathbf{e}_2$ to lie in the plane of the vectors $\mathbf{q}_1$ and $\mathbf{q}_2$. This assumption causes a factor of 1/2 to be missing for the *LTL* relaxation mechanism in the isotropic medium [24] and does not take into account important terms in the probability of three-phonon scattering processes in cubic crystals. We averaged the squared magnitude of matrix element (17) over the polarization vector $\mathbf{e}_2$ and the angle φ to obtain

$$\langle (e_{2z})^2 \rangle_{\varphi_2, \varphi_e} = \int_0^{2\pi} d\varphi_2 \int_0^{2\pi} d\varphi_e (e_{2z})^2 = \pi \sin^2\theta,$$

$$\left\langle (e_{2x})^2 \left(\frac{q_{2x}}{q_2}\right)^6 \right\rangle = \left\langle (e_{2y})^2 \left(\frac{q_{2y}}{q_2}\right)^6 \right\rangle = \frac{5\pi}{16}\sin^6\theta\left(1 - \frac{7}{8}\sin^2\theta\right), \quad (20)$$

$$2\left\langle e_{2z}\left[e_{2x}\left(\frac{q_{2x}}{q_2}\right)^3 + e_{2y}\left(\frac{q_{2y}}{q_2}\right)^3\right]\right\rangle = -\frac{3\pi}{2}\sin^4\theta\cos\theta,$$

$$2\left\langle e_{2x}e_{2y}\left(\frac{q_{2x}q_{2y}}{q_2^2}\right)^3\right\rangle = -\frac{3\pi}{64}\sin^8\theta.$$

When averaged over the angles φ_e and φ, the probability of phonon scattering depends only on the magnitudes of the vectors $\mathbf{q}_1$ and $\mathbf{q}_2$ and the angle θ between them. The integral over θ in Eq. (10) can easily be evaluated using the δ function that ensures energy conservation in the fusion and decay of longitudinal phonons, and we have

$$\cos\theta_R = S^* + \frac{q_2}{2q_1}(1 - S^{*2}) = S^*\left(1 + \frac{z_2}{2z_1}\left(\frac{1}{S^{*2}} - 1\right)\right),$$

$$z_2 \le z_{2mR},$$

$$\cos\theta_S = S^* - \frac{q_2}{2q_1}(1 - S^{*2}) = S^*\left(1 - \frac{z_2}{2z_1}\left(\frac{1}{S^{*2}} - 1\right)\right), \quad (21)$$

$$z_2 \le z_{2mS},$$

$$z_{2mR} = \frac{2S^*z_1}{1 + S^*}, \quad z_{2mS} = \frac{2S^*z_1}{1 - S^*}, \quad S^* = \frac{S_t}{S_L},$$

$$z_2 = \frac{\hbar\omega_{q2}}{k_B T}, \quad z_1 = \frac{\hbar\omega_{q1}}{k_B T},$$

where S_t and S_L are the velocities of transverse and longitudinal phonons, respectively.

After substituting Eqs. (18)–(21) into Eq. (10), the probability of phonon scattering via the *LTL* mechanism will be a function of the ratio of the reduced wave vectors z_1 and z_2. In order to simplify the final expression for the relaxation rate ν_{phN}^{LTL}, we transform the remaining integrals by using the substitutions

$$z_2 = \frac{2S^*z_1}{1 + S^*}y \quad (\text{for } R \text{ processes}),$$
$$z_2 = \frac{2S^*z_1}{1 - S^*}y \quad (\text{for } S \text{ processes}). \quad (22)$$

After simple algebra, we obtain

$$\nu_{\text{phN}}^{LTL} = B_{LTL}T^5 z_1^5 \sinh(z_1/2)\{2(1 + S^*)J_S + (1 - S^*)J_R\},$$

$$J_{S,R} = \int_0^1 dy \frac{y^2 B_{S,R}(y)\varphi_{1S,R}(y)}{\left(\frac{(1 \mp S^*)}{2S^*} \pm y\right)^2 \sinh\left(\frac{S^*z_1 y}{(1 \mp S^*)}\right)\sinh\left(\frac{z_1}{2}\left(1 \pm \frac{2S^*y}{(1 \mp S^*)}\right)\right)}; \quad (23)$$

$$B_{LTL} = \frac{(C_A)^2 (k_B)^5}{16\pi\hbar^4\rho^3 S_t S_L^8}, \quad C_A = \tilde{c}_{111} + \tilde{c}_{112} + 8\tilde{c}_{155} + 2\Delta C.$$

The functions $B_S(y)$ and $B_R(y)$ are defined as

$$B_S(y) = A_S(y)\left[A_S(y) - 6P_{112}\frac{1 + S^*}{1 - S^*}y^2\varphi_{0S}\varphi_{1S}\right] + 10\left(P_{112}\frac{1 + S^*}{S^*(1 - S^*)}\right)^2 y^4\varphi_{1S}^2\left(1 - \frac{19}{20}(1 - S^{*2})\varphi_{1S}\right), \quad (24)$$

$$B_R(y) = A_R(y)\left[A_R(y) - 6P_{112}\frac{1 - S^*}{1 + S^*}y^2\varphi_{0R}\varphi_{1R}\right] + 10\left(P_{112}\frac{1 - S^*}{S^*(1 + S^*)}\right)^2 y^4\varphi_{1R}^2\left(1 - \frac{19}{20}(1 - S^{*2})\varphi_{1R}\right),$$

$$A_S(y) = \varphi_{0S}(y)\left[(\varphi_{2S}(y))^2 + P_{112}\left(1 + \frac{2S^*}{1 - S^*}y\right)^2\right] + \varphi_{2S}(y)[P_{AC}\varphi_{3S}(y) + P_\Delta\varphi_{0S}(y)],$$

$$A_R(y) = \varphi_{0R}(y)\left[(\varphi_{2R}(y))^2 + P_{112}\left(1 + \frac{2S^*}{1 + S^*}y\right)^2\right] + \varphi_{2R}(y)[P_{AC}\varphi_{3R}(y) + P_\Delta\varphi_{0R}(y)], \quad (25)$$

$$P_{112} = \frac{\tilde{c}_{112}}{C_A}, \quad P_{AC} = \frac{A_{\text{cub}} + 2\tilde{c}_{155}}{C_A}, \quad P_\Delta^+ = \frac{\Delta C}{C_A}.$$

The functions φ_{nS} and φ_{nR} originate from the angular dependence of the matrix element [see Eqs. (17), (18)]. After substituting Eqs. (21), they become functions of the ratio of reduced wave vectors (22). Some of these functions have zeros within the range of integration. For this reason, the contributions from the third-order elastic moduli to the relaxation rate vary significantly and the probability of longitudinal-phonon scattering is a complicated nonmonotonic function of the ratio of the reduced wave vectors. These functions have the form

$$\begin{aligned}
\varphi_{0S}(y) &= 1 - \frac{1+S^*}{S^*}y,\\
\varphi_{1S}(y) &= (1-y)\left(1 + y\frac{1+S^*}{1-S^*}\right),\\
\varphi_{2S}(y) &= \left(1 - y\left(\frac{\sqrt{2-(S^*)^2}-S^*}{1-S^*}\right)\right)\\
&\times\left(1 + y\left(\frac{\sqrt{2-(S^*)^2}+S^*}{1-S^*}\right)\right),\\
\varphi_{3S}(y) &= 2 + \frac{2S^*y}{1-S^*},\\
\varphi_{0R}(y) &= 1 + \frac{1-S^*}{S^*}y,\\
\varphi_{1R}(y) &= (1-y)\left(1 + y\frac{1-S^*}{1+S^*}\right),\\
\varphi_{2R}(y) &= \left(1 - y\left(\frac{\sqrt{2-(S^*)^2}+S^*}{1+S^*}\right)\right)\\
&\times\left(1 + y\left(\frac{\sqrt{2-(S^*)^2}-S^*}{1+S^*}\right)\right),\\
\varphi_{3R}(y) &= 2 - \frac{2S^*y}{1+S^*}.
\end{aligned} \tag{26}$$

Using Eqs. (23)–(26), we will investigate the dependence of the relaxation rate due to the *LTL* mechanism on temperature and phonon wave vector for cubic crystals.

4. RESULTS OF NUMERICAL CALCULATIONS OF THE LONGITUDINAL-PHONON RELAXATION RATES FOR GERMANIUM, SILICON, AND DIAMOND CRYSTALS

Let us consider the dependence of the longitudinal-phonon relaxation rates due to the *LLL* and *LTL* mechanisms on temperature and phonon wave vector for cubic crystals of germanium, silicon, and diamond. For the *LLL* mechanism in the long-wavelength limit $z_1 \ll 1$, Eq. (15) gives

$$\begin{aligned}
\nu_{\mathrm{phN}}^{LLL} &\cong B_{LLL}^0 T^5 z_1,\\
B_{LLL}^0 &\cong \frac{16\pi^4}{15}B_{LLL} = \frac{\pi^3(3c_{11}+c_{111})^2 k_\mathrm{B}^5}{30\hbar^4\rho^3 S_L^9}.
\end{aligned} \tag{27}$$

In this case, the dominant contribution to the relaxation rate of longitudinal phonons comes from the fusion of phonons and the rate ν_{phN}^{LLL} is a linear function of the phonon wave vector, as is the case for the isotropic medium [2, 23]. The coefficient B_{LLL}^0 given by Eq. (27) is four times greater than that derived by Maris for the isotropic medium (see [23, Eq. (239)]). This difference is due to the fact that the factor of 1/4 that appears when the square of the generalized Grüneisen parameter is averaged over the angular variables (see [23, Eqs. (238), (239)]) is absent from the averaged square of the matrix element given by Eq. (14). It seems likely that the procedure that is based on the generalized Grüneisen parameter [23] is not adequate for cubic crystals.

We are now in a position to discuss the dependence of the relaxation rate ν_{phN}^{LLL} on the phonon wave vector for thermal and high-frequency phonons ($z_1 > 1$) in cubic crystals. It can be seen from Eq. (15) that the quantity

$$\nu_{LLL}^*(z_1) = \frac{\nu_{\mathrm{phN}}^{LLL}(z_z, T)}{B_{LLL}^0 T^5} = \nu_{LLL}^{*(S)}(z_1) + \nu_{LLL}^{*(R)}(z_1) \tag{28}$$

depends only on the reduced phonon wave vector z_1 for all crystals in question. The functions $\nu_{LLL}^*(z_1)$, $\nu_{LLL}^{*(S)}(z_1)$, and $\nu_{LLL}^{*(R)}(z_1)$ are plotted in Fig. 1. The total relaxation rate $\nu_{LLL}^*(z_1)$ is seen to be a monotonically increasing function of z_1. For $z_1 < 2.5$, the total rate is dominated by the *S* processes and is approximately a linear function (curve *2a* in Fig. 1). In this range, the contribution from the *R* processes is given by

$$\nu_{LLL}^{*(R)}(z_1) \cong \frac{5}{4\pi^4}z_1^4. \tag{29}$$

At $z_1 = 1$, this contribution is 312 times less than that from the *S* processes. However, as the phonon wave vector increases, the contribution from the decay processes increases rapidly and the rates $\nu_{LLL}^{*(S)}(z_1)$ and $\nu_{LLL}^{*(R)}(z_1)$ become equal at $z_1 = 6.3$. At $z_1 \gg 1$, the dominant contribution to the longitudinal-phonon relaxation rate in Ge, Si, and diamond crystals comes from

the *R* processes (curve *3* in Fig. 1). The contribution from these processes varies as the fifth power of the phonon wave vector

$$\nu_{\text{phN}}^{LLL(R)} \cong B_{LLL}^{(R)} T^5 z_1^5, \quad B_{LLL}^{(R)} = \frac{1}{15} B_{LLL},$$
$$\nu_{LLL}^{*(R)}(z_1) \cong \frac{1}{16\pi^4} z_1^5. \tag{30}$$

In this limiting case, the contribution from the *S* processes increases far more slowly, in proportion to the square of the wave vector,

$$\nu_{\text{phN}}^{LLL}(z_1) \cong \frac{15 J_2}{4\pi^4} z_1^2,$$
$$J_2 = \int_0^{z_{DL}} dz_2 \frac{z_2^2}{\exp(z_2) - 1} \cong 2.4. \tag{30a}$$

As might be expected in the approximation used, the calculated dependences of the longitudinal-phonon relaxation rate due to the *LLL* mechanism in the cubic crystals, Eqs. (27) and (30), are identical to those in the isotropic medium [25]. The values of the coefficients B_{LLL}^0 and $B_{LLL}^{(R)}$ for germanium, silicon, and diamond crystals are listed in Table 3 for various crystallographic directions. It follows from Table 3 that, at T = 10 K and z_1 = 1, the relaxation rate ν_{phN}^{LLL} for the [100] direction is 1.72×10^5, 1.66×10^4, and 5.79×10^2 s^{-1} for Ge, Si, and diamond, respectively. As we go from the [100] to [111] direction, the relaxation rate ν_{phN}^{LLL} decreases by a factor of approximately 3 for Ge and 2 for Si and diamond.

In calculating the thermal conductivity of the cubic crystals, it should be taken into account that the energy of phonons that are important in this case is restricted by the inequality $z_1 < 4$–5, because the contribution from higher energy phonons is cut off by the Planck distribution function. For this energy range, Eq. (15) for the phonon relaxation rate due to the *LLL* mechanism can be approximated by the simple expression

$$\nu_{\text{phN}}^{LLL} \cong B_{LLL}^0 T^5 z_1 (1 + 0.03 z_1 + 0.00084 z_1^4), \tag{31}$$

which is close to Eq. (15) in the range $0 < z_1 < 6$ (curve *1a* in Fig 1).

Now, let us consider the longitudinal-phonon relaxation via the *LTL* scattering mechanism for Ge, Si, and diamond crystals. In the long-wavelength limit, $z_1 \ll 1$, we have from Eq. (23) for this mechanism

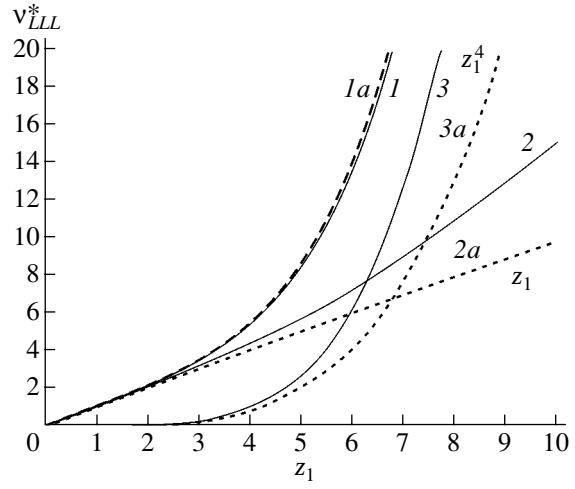

Fig. 1. Dependences of the longitudinal-phonon relaxation rate due to *LLL* processes on the reduced phonon wave vector. (*1*) Function $\nu_{LLL}^*(z_1)$, (*2*) contribution from *S* processes, and (*3*) contribution from *R* processes. Dashed lines represent approximations for (*1a*) function $\nu_{LLL}^*(z_1)$ for thermal phonons given by Eq. (31), (*2a*) the contribution from *S* processes given by Eq. (27), and (*3a*) the contribution from *R* processes given by Eq. (29).

$$\nu_{\text{phN}}^{LTL} \cong B_{LTL}^0 T^5 z_1^4,$$
$$B_{LTL}^0 = B_{LTL}\left(\left(\frac{1 - S^*}{S^*}\right)^2 (1 + S^*) J_{0S} + \frac{(1 - S^*)(1 + S^*)^2}{2S^{*2}} J_{0R}\right), \tag{32}$$
$$J_{0S} \cong \int_0^1 dy \frac{y \varphi_{1S}(y) B_S(y)}{\left(\frac{1 - S^*}{2S^*} + y\right)^3}, \quad J_{0R} \cong \int_0^1 dy \frac{y \varphi_{1S}(y) B_S(y)}{\left(\frac{1 + S^*}{2S^*} - y\right)^3}.$$

For Ge, we have $J_{0S} \approx 8$ and $J_{0R} \approx 4.7 \times 10^{-3}$, and for Si and diamond, we have $J_{0R}/J_{0S} \approx 10^{-3}$. Therefore, in this limit, the dominant contribution to the longitudinal-phonon relaxation comes from the fusion of phonons and the contribution from the decay processes is negligibly small. For this reason, the longitudinal-phonon relaxation rate due to the *LTL* mechanism in the long-wavelength limit varies in proportion to the fourth power of the phonon wave vector in the cubic crystals, as is the case in the isotropic medium [12, 23]. The contribution from this scattering mechanism to the attenuation of long-wavelength ultrasonic waves is significantly less than that from the *LLL* mechanism considered above [see Eq. (27)].

The values of the coefficients B_{LTL}^0 for the Ge, Si, and diamond crystals are listed in Table 4 for various

Table 3. Parameters determining the relaxation rate of longitudinal phonons via the *LLL* processes in Ge, Si, and diamond

	B^0_{LLL}, $s^{-1}\,K^{-5}$ [100]	B^0_{LLL}, $s^{-1}\,K^{-5}$ [110]	B^0_{LLL}, $s^{-1}\,K^{-5}$ [111]	B^R_{LLL}, $s^{-1}\,K^{-5}$ [100]	B^R_{LLL}, $s^{-1}\,K^{-5}$ [110]	B^R_{LLL}, $s^{-1}\,K^{-5}$ [111]
Ge	1.72	0.73	0.57	1.11×10^{-3}	4.72×10^{-4}	3.69×10^{-4}
Si	0.166	0.081	0.065	1.07×10^{-4}	5.2×10^{-5}	4.2×10^{-5}
Diamond	5.79×10^{-3}	3.87×10^{-3}	3.35×10^{-3}	3.72×10^{-6}	2.49×10^{-6}	2.15×10^{-6}

Table 4. Parameters determining the relaxation rate of longitudinal phonons via the *LTL* processes in Ge, Si, and diamond

	B^0_{LTL}, $s^{-1}\,K^{-5}$ [100]	B^0_{LTL}, $s^{-1}\,K^{-5}$ [110]	B^0_{LTL}, $s^{-1}\,K^{-5}$ [111]	B^R_{LTL}, $s^{-1}\,K^{-5}$ [100]	B^R_{LTL}, $s^{-1}\,K^{-5}$ [110]	B^R_{LTL}, $s^{-1}\,K^{-5}$ [111]
Ge	1.02	0.26	0.092	4.16×10^{-4}	3.72×10^{-4}	2.43×10^{-4}
Si	0.09	0.02	0.018	3.82×10^{-5}	4.09×10^{-5}	2.77×10^{-5}
Diamond	0.0032	0.0012	0.0011	1.99×10^{-6}	1.54×10^{-6}	1.33×10^{-6}

crystallographic directions. It follows from Table 4 that, at $T = 10$ K and $z_1 = 1$, the rate $\nu^{LTL}_{\rm phN}$ for the [100] direction is 1.02×10^5, 0.9×10^4, and 0.32×10^3 s^{-1} for Ge, Si, and diamond, respectively. It is also seen from Table 4 that, in the long-wavelength limit, the effect of the cubic anisotropy on $\nu^{LTL}_{\rm phN}$ is greater than that on $\nu^{LLL}_{\rm phN}$. As we go from the [100] to [111] direction, the coefficient B^0_{LTL} decreases by a factor of more than 10 for Ge, 5 for Si, and nearly 3 for diamond.

Now, we consider the dependence of the relaxation rate $\nu^{LTL}_{\rm phN}$ on temperature and phonon wave vector for thermal and high-frequency phonons ($z_1 > 1$). It follows from Eq. (23) that the quantity

$$\nu^*_{LTL}(z_1) = \frac{\nu^{LTL}_{\rm phN}(z_1, T)}{B^0_{LTL}T^5} = \nu^{*(S)}_{LTL}(z_1) + \nu^{*(R)}_{LTL}(z_1) \quad (33)$$

depends only on the reduced phonon wave vector z_1. The functions $\nu^*_{LTL}(z_1)$, $\nu^{*(S)}_{LTL}(z_1)$, and $\nu^{*(R)}_{LTL}(z_1)$ for the Ge, Si, and diamond crystals are plotted in Fig. 2. It can be seen that the contribution from the *S* processes $\nu^{*(S)}_{LTL}(z_1)$ for these crystals is a nonmonotonic function of z_1. The quantity $\nu^{*(S)}_{LTL}(z_1)$ first increases sharply, in proportion to z_1^4; then passes through a maximum at $z_1 \approx 4$ and decreases, reaching a minimum at $z_1 \approx 20$, 14, and 9 for Ge, Si, and diamond, respectively; and then increases monotonically at larger values of z_1. For the decay processes, the relaxation rate $\nu^{*(R)}_{LTL}(z_1)$ increases monotonically with z_1, in proportion to z_1^4 at $z_1 \ll 1$ [see Eq. (23)] and in proportion to q_1^5 at $z_1 > 10$, as in the isotropic medium [26, 27]. In the latter case, the rate $\nu^{LTL(R)}_{\rm phN}$ does not depend on temperature and varies in proportion to q_1^5:

$$\nu^{LTL(R)}_{{\rm ph}N} \cong B^R_{LTL}T^5z_1^5, \quad B^{(R)}_{LTL} = B_{LTL}(1-S^*)J_R,$$
$$J_R \cong \int_0^1 dy \frac{y^2 B_R(y)\varphi_{1R}(y)}{\left(\frac{1\mp S^*}{2S^*} \pm y\right)^2}, \quad (34)$$

where the function $B_R(y)$ is defined by Eqs. (23)–(25). The values of the coefficient $B^{(R)}_{LTL}$ for the Ge, Si, and diamond crystals are listed in Table 4, from which it follows that the cubic anisotropy of the relaxation rate $\nu^{LTL}_{\rm phN}$ for high-frequency phonons is significantly less than that for long-wavelength phonons. As we go from the [100] to [111] direction, the coefficient B^R_{LTL} decreases by a factor of 1.7 for Ge and approximately 1.4 for Si and diamond. We note that the decay processes are insignificant in the long-wavelength limit, as well as for thermal phonons with $z_1 \approx 1$–2. The contributions from the *R* and *S* processes become equal at $z_1 \approx 5.4$ for Ge and $z_1 \approx 5.8$ for Si and diamond; at higher values of the wave vector z_1, the dominant contribution to the relaxation rate $\nu^{LTL}_{\rm phN}$ comes from the *R* processes.

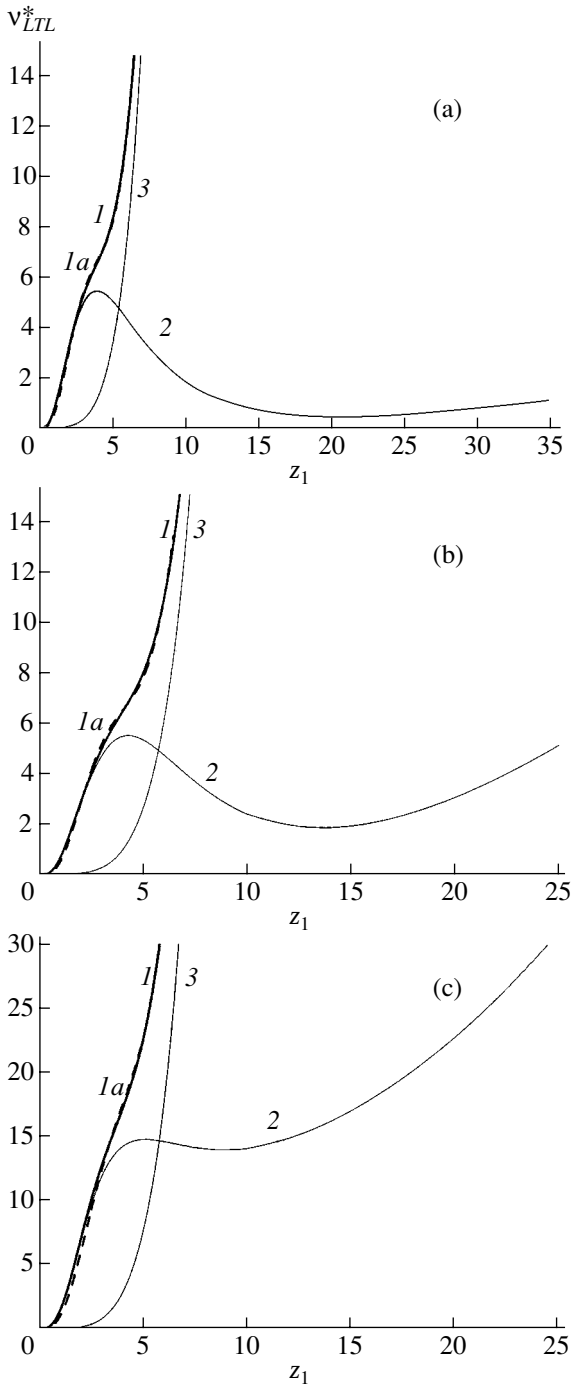

Fig. 2. Dependences of the phonon relaxation rate due to *LTL* processes on the reduced phonon wave vector for (a) Ge, (b) Si, and (c) diamond for the [100] direction. (*1*) Function $\nu^*_{LTL}(z_1)$, (*2*) the contribution from *S* processes to the relaxation rate, and (*3*) the contribution from *R* processes. Dashed lines *1a* plot Eq. (35) for thermal phonons.

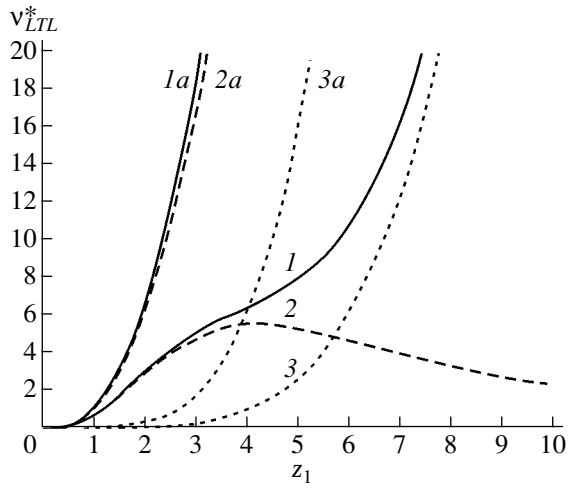

Fig. 3. Dependences of the phonon relaxation rate due to *LTL* processes on the reduced phonon wave vector (*1*, *2*, *3*) for the [100] direction in the cubic Si crystal and (*1a*, *2a*, *3a*) for Si in the isotropic approximation. (*1*, *1a*) Function $\nu^*_{LTL}(z_1)$, (*2*, *2a*) the contribution from *S* processes, and (*3*, *3a*) the contribution from *R* processes.

Equations (23)–(26) for the rate ν^{LTL}_{phN} are too cumbersome to be used to analyze the heat conductivity of the cubic crystals. Since the lattice thermal conductivity is determined by phonons with $z_1 < 4$–5, we use an approximate expression for the phonon relaxation rate ν^{LTL}_{phN} in this range:

$$\nu^{LTL}_{\text{phN}} \cong D_i B^0_{LTL} T^5 z_1^4 \times (\exp(-\alpha_i z_1) + c_i\beta + 0.9\gamma_i z_1),$$
$$\beta = \frac{B_{LTL}}{B^0_{LTL}} \frac{(1-S^*)(1+S^*)^2}{2S^{*2}} J_{0R}, \quad \gamma = \frac{B^{(R)}_{LTL}}{B^0_{LTL}}, \tag{35}$$

where the parameters D_i, α_i, and c_i for Ge, Si, and diamond are D_i = 1.61, 1.4, and 2.09, α_i = 1.09, 1.06, and 0.9, and c_i = 1.12, 0.98, and 0, respectively. It can be seen from Fig. 2 (curves *1a*) that approximation (35) agrees well with the calculations based on Eqs. (23)–(26) in the range $0 < z_1 < 6$. We note that the relaxation rates due to the *LTL* and *LLL* scattering mechanisms are of the same order of magnitude for thermal phonons and, hence, must be taken into account in calculating the thermal conductivity of the Ge, Si, and diamond crystals.

Now, we compare the calculated relaxation rates due to the *LTL* mechanism in the Ge, Si, and diamond crystals with those obtained for the isotropic medium. For this purpose, we substitute Eqs. (6) into Eqs. (23) and (24). It can be seen that, in the functions $B_S(y)$ and $B_R(y)$, only the terms containing the coefficient A_{cub} [given by Eq. (13a)] remain in the isotropic approximation. Figure 3 compares the $\nu^*_{LTL}(z_1)$, $\nu^{*(S)}_{LTL}(z_1)$, and $\nu^{*(R)}_{LTL}(z_1)$ dependences calculated for the cubic Si crys-

tal and for Si in the isotropic approximation. It can be seen that the calculated $\nu^*_{LTL}(z_1)$ for the cubic crystal differs significantly from that for the isotropic medium (Fig. 3, curves *1*, *1a*). For the decay processes, the $\nu^{*(R)}_{LTL}(z_1)$ dependences are similar (curves *3*, *3a*), although at $z_1 \gg 1$ the values of $\nu^{*(R)}_{LTL}(z_1)$ calculated in the isotropic approximation are 8.8 times greater than those for the cubic crystal. The results for the fusion processes differ more significantly (Fig. 3, curves *2*, *2a*). First, in the long-wavelength limit, the coefficient B^0_{LTL} for Si calculated in the isotropic approximation is 1.9 times greater than that for the cubic crystal. Second, the relaxation rate $\nu^{*(S)}_{LTL}(z_1)$ calculated in the isotropic approximation increases monotonically with z_1 (curve *2a* in Fig. 3), whereas for all cubic crystals this rate exhibits a nonmonotonic behavior (curves *2* in Fig. 2). An analysis shows that these features of the longitudinal-phonon relaxation rate $\nu^{*(S)}_{LTL}(z_1)$ are due to the angular dependence of the probability of anharmonic scattering [Eqs. (17), (18); (23), (25)] and to the anisotropy in the elastic properties of the Ge, Si, and diamond crystals. Obviously, the isotropic-medium approximation cannot be used to calculate the longitudinal-phonon relaxation rate due to the *LTL* mechanism.

5. CONCLUSIONS

We have considered the longitudinal-phonon relaxation via the $L \rightleftharpoons L + L$ and $L \rightleftharpoons T + L$ processes in cubic crystals. The elastic energy associated with the anharmonicity of lattice vibrations in cubic crystals has been expressed in terms of the second- and third-order elastic moduli. Using the experimental values of the second- and third-order elastic moduli, we have found the parameters that determine the relaxation rate of longitudinal phonons in the Ge, Si, and diamond crystals. The dependences of the phonon relaxation rate on temperature and phonon wave vector were found for germanium, silicon, and diamond. It has been shown that, under the assumption of weak phonon damping and the absence of dispersion, the phonon relaxation rates due to the $L \rightleftharpoons L + L$ processes in the cubic crystals coincide with those calculated for the respective isotropic media. In contrast, the dependences of the relaxation rates due to the $L \rightleftharpoons T + L$ processes on the phonon wave vector calculated for the cubic crystals differ significantly from those for the isotropic media. The relaxation rate due to the fusion of phonons calculated in the isotropic approximation increases monotonically with the phonon wave vector, whereas the analogous relaxation rate for the [100] direction in the cubic crystals varies nonmonotonically. The specific features of the relaxation rate of longitudinal phonons via the $L \rightleftharpoons T + L$ processes have been established to be due to the angular dependence of the probability of anharmonic scattering and to the anisotropy in the elastic properties of the crystals under study.

ACKNOWLEDGMENTS

The authors are grateful to A.P. Tankeev for discussing the results and helpful remarks.

This work was supported by a grant of the President of the Russian Federation (project NSh-1380.2003.2), the Ural Division of the RAS (youth grant no. 15-02-04), the Dinastiya Fund, and the International Center for Fundamental Physics in Moscow.

REFERENCES

1. V. L. Gurevich, *Kinetics of Phonon Systems* (Nauka, Moscow, 1980) [in Russian].
2. B. Truell, C. Elbaum, and B. B. Chick, *Ultrasonic Methods in Solid State Physics* (Academic, New York, 1969; Mir, Moscow, 1972).
3. V. M. Askerov, *Electron Transport Phenomena in Semiconductors* (Nauka, Moscow, 1985) [in Russian].
4. A. P. Zhernov and A. V. Inyushkin, *Isotope Effects in Solids* (Ross. Nauchn. Tsentr "Kurchatovskiĭ Institut", Moscow, 2001) [in Russian].
5. M. Asen-Palmer, K. Bartkowski, E. Gmelin, M. Cardona, A. P. Zhernov, A. V. Inyushkin, A. N. Taldenkov, V. I. Ozhogin, K. M. Itoh, and E. E. Haller, Phys. Rev. B **56** (15), 9431 (1997).
6. T. Ruf, R. W. Henn, M. Asen-Palmer, E. Gmelin, M. Cardona, H.-J. Pohl, G. G. Devyatych, and P. G. Sennikov, Solid State Commun. **115** (5), 243 (2000).
7. J. E. Graebner, M. E. Reiss, L. Seibles, T. M. Hartnett, R. P. Miller, and C. J. Robinson, Phys. Rev. B **50** (6), 3702 (1994).
8. J. R. Olson, R. O. Pohl, J. W. Vandersande, A. Zolten, T. R. Anthony, and W. F. Banholzer, Phys. Rev. B **47** (22), 14850 (1993).
9. I. G. Kuleev and I. I. Kuleev, Zh. Éksp. Teor. Fiz. **120** (6), 649 (2001) [JETP **93**, 568 (2001)].
10. I. G. Kuleev and I. I. Kuleev, Zh. Éksp. Teor. Fiz. **122**, 558 (2002) [JETP **95**, 480 (2002)].
11. R. Berman, *Thermal Conduction in Solids* (Clarendon, Oxford, 1976; Mir, Moscow, 1979).
12. B. M. Mogilevskiĭ and A. F. Chudnovskiĭ, *Thermal Conductivity of Semiconductors* (Nauka, Moscow, 1972) [in Russian].
13. F. Birch, Phys. Rev. **71** (11), 809 (1947).
14. L. K. Zarembo and V. A. Krasil'nikov, *Introduction to Nonlinear Physical Acoustics* (Nauka, Moscow, 1966) [in Russian].
15. J. W. Tucker and V. W. Rampton, *Microwave Ultrasonics in Solid State Physics* (North-Holland, Amsterdam, 1972; Mir, Moscow, 1975).
16. T. Bateman, W. P. Mason, and H. J. McSkimin, J. Appl. Phys. **32** (5), 928 (1961); H. J. McSkimin and P. Andreath, J. Appl. Phys. **35** (11), 3312 (1964).

17. M. H. Grimsditch, E. Anastassakis, and M. Cardona, Phys. Rev. B **18** (2), 901 (1978).

18. W. P. Mason, in *Physical Acoustics. Principles and Methods*, Ed. by W. P. Mason (Academic, New York, 1965; Mir, Moscow, 1968), Vol. 3, Part B, p. 235.

19. I. N. Frantsevich, F. F. Voronov, and S. A. Bakuta, *A Handbook of the Elastic Constants and Elastic Moduli of Metals and Nonmetals* (Naukova Dumka, Kiev, 1982) [in Russian].

20. K. Brugger, Phys. Rev. A **133** (6), 1611 (1964).

21. R. N. Thurston, in *Physical Acoustics. Principle and Methods*, Ed. by W. P. Mason (Academic, New York, 1964; Mir, Moscow, 1966), Vol. 1, Part A, p. 235.

22. L. D. Landau and E. M. Lifshitz, *Course of Theoretical Physics*, Vol. 7: *Theory of Elasticity*, 4th ed. (Nauka, Moscow, 1987; Pergamon, New York, 1986).

23. H. J. Maris, in *Physical Acoustics. Principle and Methods*, Ed. by W. P. Mason (Academic, New York, 1971), Vol. 7, p. 280.

24. S. Tamura, Phys. Rev. B **31** (4), 2574 (1985).

25. P. S. Zyryanov and G. G. Taluts, Zh. Éksp. Teor. Fiz. **49** (6), 1942 (1965) [Sov. Phys. JETP **22**, 1326 (1966)].

26. G. L. Slonimskiĭ, Zh. Éksp. Teor. Fiz. **7** (12), 1457 (1937).

27. R. Orbach and L. A. Vredevoe, Physics (Long Island City, New York) **1** (2), 91 (1964).

Translated by Yu. Epifanov

Physics of the Solid State, Vol. 47, No. 2, 2005, pp. 324–326. Translated from Fizika Tverdogo Tela, Vol. 47, No. 2, 2005, pp. 311–313.

LATTICE DYNAMICS AND PHASE TRANSITIONS

Electric Field–Induced Formation of a New Commensurate Phase of the $[N(CH_3)_4]_2CuCl_4$ Crystal

D. G. Sannikov

Shubnikov Institute of Crystallography, Russian Academy of Sciences, Leninskiĭ pr. 59, Moscow, 119333 Russia

e-mail: sannikov@ns.crys.ras.ru

Received May 27, 2004

Abstract—The formation of a new commensurate phase with a dimensionless wave number $q = 1/3$ in an $[N(CH_3)_4]_2CuCl_4$ crystal under the action of an external electric field is analyzed theoretically. The phase diagram is constructed on a plane specified by two coefficients of the thermodynamic potential in the presence and in the absence of an external electric field. © *2005 Pleiades Publishing, Inc.*

1. INTRODUCTION

In [1, 2], we constructed the theoretical pressure–temperature (*P–T*) phase diagrams for an $[N(CH_3)_4]_2CuCl_4$ (*TMA*–CuCl) crystal, where *TMA* is tetramethylammonium. These diagrams are in good agreement with the experimental *P–T* diagrams measured in [3–5]. The phases revealed in the *P–T* diagrams are as follows: the initial *C* phase (*Pmcn* symmetry), the incommensurate *IC* phase, and the commensurate $C_{m/l}$ phase, where *m*/*l* stands for the dimensionless wave number $q_{m/l}$ characterizing the phase. For each of the $C_{m/l}$ phases (except for the $C_{0/l}$ phase with dimensionless wave number $q_{0/l} = 0$), there are two different solutions and, accordingly, there can exist two different phases with different symmetries (see table in [1, 2]; the feasible but improbable third solution will not concern us in this study). The specific solution (or phase) is determined by the sign of the coefficient of the anisotropic invariant in the thermodynamic potential (see below).

Under an external action (electric field, mechanical stress), another phase with the same dimensionless wave number $q_{m/l}$ can be induced in the crystal. Consequently, a new $C_{m/l}$ commensurate phase will be observed in the *P–T* phase diagram. The purpose of this work is to analyze theoretically the formation of a new $C_{1/3}$ commensurate phase under the action of an external electric field.

2. THERMODYNAMIC POTENTIALS

A theoretical approach to the construction of *P–T* phase diagrams for the family of *TMA* crystals was described in [2] (see also [1, 6, 7]). Let us write the thermodynamic potentials for the $C_{1/3}$ and *IC* phases of the *TMA*–CuCl crystal in the presence of an electric field E_x (where P_x is the polarization oriented along the *x* axis):

$$\begin{aligned}\Phi_{1/3} &= \alpha(q_{1/3})\rho^2 + \beta\rho^4 + \gamma\rho^6 - \alpha'_3\rho^6\cos 6\varphi \\ &\quad - g_3P_x\rho^3\cos 3\varphi + sP_x^2 - P_xE_x, \\ \Phi_{IC} &= \alpha(b)\rho^2 + \beta\rho^4 + \gamma\rho^6 + sP_x^2 - P_xE_x.\end{aligned} \tag{1}$$

Here, $\beta > 0$, $\gamma > 0$, and $s > 0$ are coefficients. Formulas (1) for parameters $E_x = 0$ and $P_x = 0$ coincide with relationships (1) and (2) given in [1].

The dependence of the coefficient of elasticity $\alpha(q)$ for the soft branch of the normal oscillation spectrum of the crystal on the dimensionless wave number $q = k_z/c^*$ can be described by the expression

$$\begin{aligned}\alpha(q) &= \alpha - \delta q^2 - \kappa q^4 + \tau q^6 \\ &(\kappa > 0, \tau > 0).\end{aligned} \tag{2}$$

This expression can be rewritten in the form

$$\begin{aligned}\alpha(q) &= a + \Delta(q), \\ \Delta(q) &= \tau(b^2 - q^2)^2[q^2 + 2(b^2 - q_L^2)], \\ \delta &= \tau b^2(3b^2 - 4q_L^2), \quad q_L^2 \equiv \kappa/2\tau, \\ \Delta_3 &= \Delta(q_{1/3}),\end{aligned} \tag{3}$$

where *a* and *b* are the coordinates of the minimum in the soft branch [described by relationship (2)] at an arbitrary point of the Brillouin zone.

It is convenient to change over to the dimensionless variables ϕ, *R*, *P*, and *E* and the parameters A_γ, A_3, *g*, *G*, *B*, *D*, Q_L, *A*, and D_3 (*Q* is a number):

$$\Phi = \phi\Phi_0, \quad \rho = RR_0, \quad P_x = PP_0, \quad E_x = EE_0,$$
$$\Phi_0 = P_0^2 = E_0^2 = (\tau Q^6)^2/\beta, \quad R_0^2 = \tau Q^6/\beta,$$
$$\gamma = 4\beta^2 A_\gamma/\tau Q^6, \quad |\alpha_3'| = 4\beta^2 A_3/\tau Q^6,$$
$$g_3^2 = 4\beta^2 g^2/\tau Q^6, \quad G = g^2/8s, \quad b = BQ, \tag{4}$$
$$q_L = Q_L Q, \quad \delta = D\tau Q^4,$$
$$a = -A\tau Q^6, \quad \Delta_3 = D_3\tau Q^6.$$

The thermodynamic potentials defined by formulas (1) take the following form (it is assumed that $\alpha_3' < 0$; see below):

$$\phi_{1/3} = -(A - D_3)R^2 + R^4 + 4A_\gamma R^6 + 4A_3 R^6\cos 6\varphi$$
$$- 2gPR^3\cos 3\varphi + sP^2 - PE, \tag{5}$$
$$\phi_{IC} = -AR^2 + R^4 + 4A_\gamma R^6 + sP^2 - PE.$$

3. EQUILIBRIUM VALUES OF THE PARAMETERS

By varying the dimensionless parameters φ and P in expression (5) for the thermodynamic potential $\phi_{1/3}$, we obtain the following two solutions corresponding to the c_1 and c_2 phases:

$$\text{for the } c_1 \text{ phase:} \quad \cos 3\varphi = gE/16s(A_3 - G)R^3,$$
$$P_1 = A_3 E/2s(A_3 - G);$$
$$\text{for the } c_2 \text{ phase:} \quad \cos 3\varphi = g/|g|, \tag{6}$$
$$P_2 = |g|R^3/s + E/2s.$$

The sign of the coefficient α_3' is chosen so ($\alpha_3' < 0$) that, in the absence of an external electric field ($E = 0$), there exists a solution corresponding to the c_1 phase ($P12_1c1$ symmetry; see table in [1] or [2]). The first term in the expression for the parameter P_2 is the spontaneous polarization. In this case, the c_2 phase is the improper ferroelectric phase with $P2_1cn$ symmetry.

Substituting relationship (6) into expression (5) gives

$$\phi_1 = -(A - D_3)R^2 + R^4 + 4(A_\gamma - A_3)R^6$$
$$- GE^2/4s(A_3 - G) - E^2/4s,$$
$$\phi_2 = -(A - D_3)R^2 + R^4 + 4(A_\gamma + A_3 - 2G)R^6 \tag{7}$$
$$- |g|ER^3/s - E^2/4s.$$

By varying the dimensionless parameter P in expression (5) for the thermodynamic potential ϕ_{IC} and substituting the obtained value of P into formula (5), we derive the following expressions:

$$P = E/2s, \quad \phi_C = -E^2/4s,$$
$$\phi_{IC} = -AR^2 + R^4 + 4A_\gamma R^6 - E^2/4s. \tag{8}$$

Here, we added the thermodynamic potential ϕ_C for the initial phase. Note that the term $E^2/4s$ is identical for all the phases under consideration (hence, in what follows, this term will be discarded).

By varying the dimensionless parameter R in formulas (7) and (8) for the thermodynamic potentials and substituting the expressions obtained for the parameter R into the relationship for ϕ, we find

$$\phi_1 = -1/4(A - D_3)^2\{1 - 2(A_\gamma - A_3)(A - D_3)\}$$
$$- GE^2/4s(A_3 - G),$$
$$\phi_2 = -1/4(A - D_3)^2\{1 - 2(A_\gamma + A_3 - 2G)(A - D_3) \tag{9}$$
$$+ 8[GE^2/4s(A - D_3)]^{1/2}\},$$
$$\phi_{IC} = -1/4A^2\{1 - 2A_\gamma A\}.$$

In expressions (9), we carried out expansions into series with respect to small terms. It is assumed that $A_\gamma A \ll 1$ and $E^2/4s \ll 1$. It should be noted that expression (9) for the thermodynamic potential ϕ_2 is satisfied only under the condition $A - D_3 > 0$.

4. BOUNDARIES BETWEEN THE PHASES AND THE PHASE DIAGRAM

By equating the thermodynamic potentials described by relationships (9) and again using the expansions with respect to small terms, we obtain the following expressions for the boundaries between the phases.

For the *C–IC* boundary, $A = 0$.

For the c_1–*IC* boundary, $D_3 = A_3A^2 + 2GE^2/4s(A_3 - G)A$.

For the *C*–c_2 boundary,

$$-A = -D_3 + 8GE^2/4s, \quad (A < 0).$$

For the c_1–c_2 boundary,

$$A = D_3 + [GE^2/4s(A_3 - G)^2]^{1/3}.$$

For the c_2–*IC* boundary,

$$D_3 = -(A_3 - 2G)A^2 + 4[(GE^2/4s)A]^{1/2}$$
$$(A > D_3).$$

For the c_2–*IC* boundary, $D_3 = A + 8GE^2/4s$. (10)

The last expression for the c_2–*IC* phase boundary is obtained in the vicinity of the point *K* (see figure). The coordinates of the points *K*, *N*, and *O* can be determined

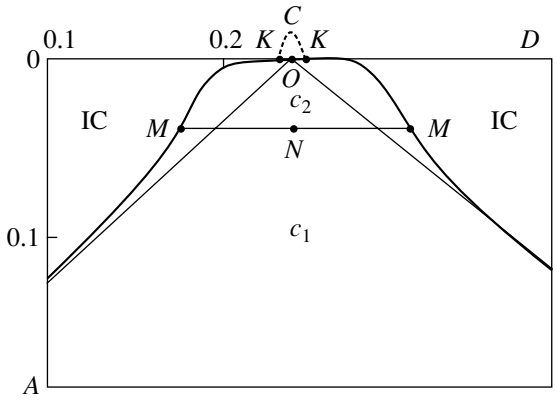

Phase diagram on a plane specified by two dimensionless coefficients (D and A) of the thermodynamic potential. The inclined straight lines emanating from the point O represent the IC–$C_{1/3}$ phase boundary in the absence of an external electric field ($E = 0$). The dotted line indicates the C–c_2 phase boundary, which is enlarged along the A axis by a factor of 10^3.

from expressions (10) for the C–c_2 and c_1–c_2 phase boundaries under the assumption that $D_3 = 0$ (for the points N and O) and $A = 0$ (for the point K). The coordinates of the points M are as follows (see figure):

$$A = [GE^2/4s(A_3 - G)^2]^{1/3},$$
$$D_3 = (3A_3 - 2G)[GE^2/4s(A_3 - G)^2]^{2/3}. \quad (11)$$

Note that the c_1–c_2 phase transition is a second-order transition.

Formulas (10) can be used to construct the phase diagram on the D–A plane. For this purpose, we choose the following values of the parameters (identical to those used in [1]):

$$Q_L^2 = 0.2, \quad A_\gamma = A_3 = 2G = 0.36, \quad Q = 0.5. \quad (12)$$

Let us assume that $E^2/4s = 10^{-5}$. For this value, the region of existence of the c_2 phase proves to be rather large in size (see figure). As follows from relationships (3), (4), and (11), the coordinates of the points M on the D axis correspond to dimensionless wave numbers $q = 0.317$ and 0.35 (the coordinate of the point O corresponds to $q = 0.333$). For $E^2/4s = 10^{-6}$, the parameter A decreases at the point N by a factor of $10^{1/3}$, between the points M by a factor of $10^{2/3}$, etc. [see expression (11)]. I hope that, in further experiments, it may become possible to achieve electric fields in which the size of the induced c_2 phase will be large enough to be observed on the experimental P–T phase diagram.

In this paper, the theoretical P–T phase diagram, which can be constructed on the basis of the phase diagram on the D–A plane (see figure), has not been presented, because these diagrams are very similar in shape (see [1, 2]).

ACKNOWLEDGMENTS

This work was supported by the Russian Foundation for Basic Research, project no. 03-02-16104.

REFERENCES

1. D. G. Sannikov, Fiz. Tverd. Tela (St. Petersburg) **42** (12), 2213 (2000) [Phys. Solid State **42**, 2282 (2000)].
2. H. Mashiyama, G. A. Kissenikh, and D. G. Sannikov, Ferroelectrics **283**, 109 (2003).
3. K. Gesi, J. Phys. Soc. Jpn. **65** (7), 1963 (1996).
4. S. Shimomura, H. Tarauchi, N. Hamaya, and Y. Fujii, Phys. Rev. B **54** (10), 6915 (1996).
5. K. Gesi, Kristallografiya **44** (1), 89 (1999) [Crystallogr. Rep. **44**, 84 (1999)].
6. D. G. Sannikov, G. A. Kissenikh, and H. Mashiyama, J. Phys. Soc. Jpn. **69** (1), 130 (2000); J. Phys. Soc. Jpn. **71** (6), 1435 (2002).
7. D. G. Sannikov and H. Mashiyama, J. Phys. Soc. Jpn. **71** (7), 1698 (2002); J. Phys. Soc. Jpn. **72** (6), 1423 (2003).

Translated by I. Volkov

Physics of the Solid State, Vol. 47, No. 2, 2005, pp. 327–331. Translated from Fizika Tverdogo Tela, Vol. 47, No. 2, 2005, pp. 314–318.

LATTICE DYNAMICS AND PHASE TRANSITIONS

Temperature Dependence of the Order Parameter and of Diffuse Scattering in the Hg_2Cl_2 Model Ferroelastics

Yu. F. Markov*, K. Knorr, and E. M. Roginskiĭ***

**Ioffe Physicotechnical Institute, Russian Academy of Sciences, Politekhnicheskaya ul. 26, St. Petersburg, 194021 Russia*

e-mail: yu.markov@mail.ioffe.ru

***Saarlandes University, Saarbrücken, Germany*

Received June 3, 2004

Abstract—The fundamental and diffuse x-ray reflections from Brillouin zone–edge *X* points of the paraelastic phase of Hg_2Cl_2 crystals (whose integrated intensity is related to the order parameter and its fluctuations) were studied. Information was obtained on the temperature dependence of the order parameter and of diffuse scattering, and the critical exponents were determined. The conclusion is drawn that the ferroelastic phase transition in these crystals is close to the tricritical point. © *2005 Pleiades Publishing, Inc.*

1. INTRODUCTION

Crystals of the mercurous halides Hg_2Hal_2 (*Hal* = Cl, Br, I) are isomorphic at room temperature and form a D_{4h}^{17} -symmetry body-centered tetragonal lattice with two molecules in the unit cell [1]. They have a specific crystal structure made up of parallel chains of linear molecules *Hal*–Hg–Hg–*Hal* weakly bound to one another. The chain structure of these crystals accounts for the very strong anisotropy of their physical properties. For instance, Hg_2Cl_2 crystals feature a transverse acoustic (TA) wave velocity $V_{[110]}^{[1\bar{1}0]} = 347$ m/s, which is record-low among solids; a record-high birefringence $\Delta n = +0.66$; and a very strong acousto-optical interaction ($M_2 = 640 \times 10^{-18}$ CGS units for a TA wave) [2]. These crystals are employed in technology as basic elements in acoustic delay lines, polarizers, acousto-optical filters, etc.

When cooled, at $T_c = 186$ K Hg_2Cl_2 crystals undergo improper ferroelastic phase transitions from the tetragonal to orthorhombic phase ($D_{4h}^{17} \longrightarrow D_{2h}^{17}$) driven by condensation of the slowest soft TA branch at the *X* points of the Brillouin zone (BZ) boundary of the tetragonal paraelastic phase. These transitions are accompanied (at $T \le T_c$) by unit cell doubling, $X \longrightarrow \Gamma$ zone folding, the onset of spontaneous strain, and the formation of ferroelastic domains [3]. Having a very simple crystal structure and featuring strongly pronounced phase transition effects, the mercurous halides serve as model objects in studies of general problems of structural phase transitions.

The present communication reports on a high-precision x-ray investigation of the temperature dependence of the order parameter and determination of the critical exponents carried out over a broad temperature range including $T_c = 186$ K. The attention was focused on studying the zone edge *X* points. X-ray reflections from these points in the high-temperature tetragonal (D_{4h}^{17}) paraelastic phase are forbidden by selection rules, and they should appear only in the low-temperature orthorhombic (D_{2h}^{17}) phase as a result of a phase transition, cell doubling, and $X \longrightarrow \Gamma$ zone folding, due to which the diffuse reflections at the *X* points of the paraelastic-phase BZ ($T > T_c$) transform into fundamental Bragg reflections at the zone center (Γ point) of the ferroelastic phase ($T < T_c$). Investigating the temperature dependence of integrated intensity of these fundamental reflections ($T < T_c$) permits one to find the temperature dependence of the phase transition order parameter and determine the critical exponent value. We may recall that the order parameter for Hg_2Cl_2 crystals corresponds to opposite displacements (along the [110] direction) of the centers of gravity of the nearest neighbor Hg_2Cl_2 molecules residing in adjacent {110} planes [3].

X-ray diffraction patterns of the high-temperature phase ($T > T_c$) exhibit, however, weak diffuse zone-edge reflections (in our case, at the *X* points) related to dynamic and static spatial–temporal order parameter fluctuations, which induce nucleation of clusters of the low-temperature orthorhombic phase in the high-temperature tetragonal matrix [4]. Quantitative investigation of the temperature dependence of the order parameter and determination of the critical exponent values is an intriguing major problem requiring specific, high-precision measurements, which form the core of the present work.

1063-7834/05/4702-0327$26.00 © 2005 Pleiades Publishing, Inc.

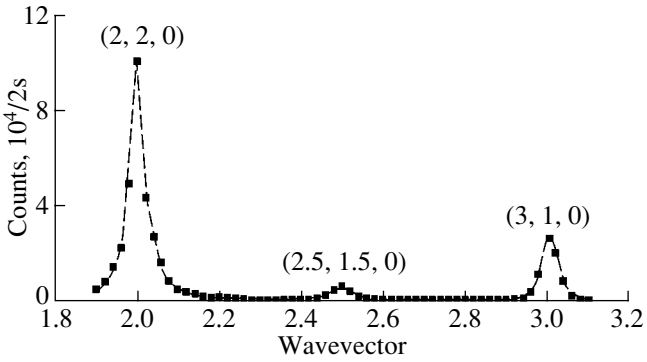

Fig. 1. Fundamental Bragg reflections (2, 2, 0) and (3, 1, 0) and a diffuse peak at the *X* point (2.5, 1.5, 0) of the BZ obtained in an extended Γ–*X*–Γ scan performed at T = 190 K.

2. EXPERIMENT

X-ray diffraction measurements were performed on a two-circle diffractometer with copper-anode CuK_α radiation. Low-temperature studies were carried out in a closed-cycle helium cryostat (Cryogenics) providing good temperature stabilization (≈0.1 K). The samples under study were high-quality mercurous chloride single crystals measuring $3 \times 3 \times 3$ mm. The crystals were cleaved along the {110} cleavage planes, cut along the (001) plane, and subsequently etched for a short time in a $1HNO_3 + 3HCl$ mixture. All measurements were conducted on the {110} planes.

3. EXPERIMENTAL RESULTS

We studied the behavior of x-ray (diffuse and Bragg) scattering at various points of BZ (reciprocal lattice) with half-integer indices h and k and $l = 0$ [primarily the points (3.5, 2.5, 0), (2.5, 3.5, 0), (2.5, 1.5, 0), (1.5, 2.5, 0)].[1] Figure 1 displays the results obtained in a typical extended scan made at T = 190 K in the Γ–*X*–Γ direction (2.5 + δ, 1.5 – δ, 0) in the reciprocal lattice (or in the BZ) of Hg_2Cl_2 crystals with the (2, 2, 0) and (3, 1, 0) Bragg reflections and a diffuse reflection at the (2.5, 1.5, 0) *X* point. This scanning coincides in direction with soft TA wave propagation. We can see that this extended Γ–*X*–Γ scan permits simultaneous observation of the weak diffuse (2.5, 1.5, 0) maximum and intense fundamental (Bragg) even ($h + k + l = 2n$) reflections (2, 2, 0) and (3, 1, 0), which are allowed for this body-centered tetragonal (D_{4h}^{17}) lattice of Hg_2Cl_2 crystals. While the odd Bragg reflections ($h + k + l = 2n + 1$) are forbidden by selection rules for this structure, an extended *ZE–X–EZ* scan orthogonal to the previous one and performed at temperatures close to T_c revealed broad weak (2, 1, 0) and (3, 2, 0) maxima, whose manifestation could be induced by the phase transition, as well as by structural imperfections (we do not show these weak odd reflections here).

When studying the temperature dependence of the integrated intensity of the newly appearing reflections (in our case, from the *X* points of the BZ) with the purpose of gaining information on the temperature dependence of the order parameter, one should use broad diffractometer slits and ω scan, which is performed by rotating the crystal alone, with the x-ray emitter and detector fixed in position. Note that the direction of this scanning in reciprocal space differs slightly from that of the Γ–*X*–Γ scan. Figure 2 displays typical diffuse ($T > T_c$) and fundamental ($T \le T_c$) (3.5, 2.5, 0) reflections obtained at different temperatures. Under cooling, the integrated intensity and amplitude of these reflections increase and their half-width decreases. The profile of these reflections can be fitted satisfactorily by a Lorentzian (Fig. 2),

$$I(\omega) = A\Delta^2/\{\Delta^2 + 4(\omega - \omega_x)^2\}, \qquad (1)$$

where A is the reflection intensity (amplitude), Δ is the reflection half-width (FWHM), and ω and ω_x are the angles.

From these data, one can extract with a high accuracy the main parameters (integrated intensity, amplitude, half-width, etc.) of these reflections. The large half-width of these diffuse reflections at the *X* points observed under scanning is primarily due to coupling to the soft TA branch. In the vicinity of the BZ *X* point, this branch has a small dispersion ($\lambda_1 = 8$ meV$^2 \times$ Å^2) in the Γ–*X*–Γ direction (which is close to ω scan) as compared to the dispersion of the TA branch in the orthogonal direction *ZE–X–EZ* ($\lambda_2 = 255$ meV$^2 \times$ Å^2) [5].

The profiles of these maxima recorded at different temperatures, down to liquid-helium temperature, were simulated to yield the temperature dependence of the reflection intensity. Figure 3a shows the temperature dependences of the integrated intensity for reflections from the *X* points of the BZ, (3.5, 2.5, 0) and (2.5, 3.5, 0). Recall that the reflections are diffuse at $T > T_c$ and that at $T \le T_c$ the phase transition, cell doubling, and $X \longrightarrow \Gamma$ zone folding transform them into fundamental Bragg reflections that are allowed in x-ray scattering, whose integrated intensity may serve as a characteristic of the behavior of the order parameter. As seen from Fig. 3a, the intensity does not undergo a jump at the transition point ($T = T_c$). Hence, this phase transition, rather than being first-order, is continuous and (in a first approximation) close to second-order.

The value of the order parameter is known to be proportional to the square root of the integrated intensity of the transition-induced reflections. Figure 3b displays the typical dependences of the order parameter η on temperature for two *X* points of the BZ. These graphs are smooth curves tending to saturation under deep cooling; i.e., the order parameter grows monotonically

[1] The reciprocal lattice indices and BZ high-symmetry points are given in the tetragonal phase notation.

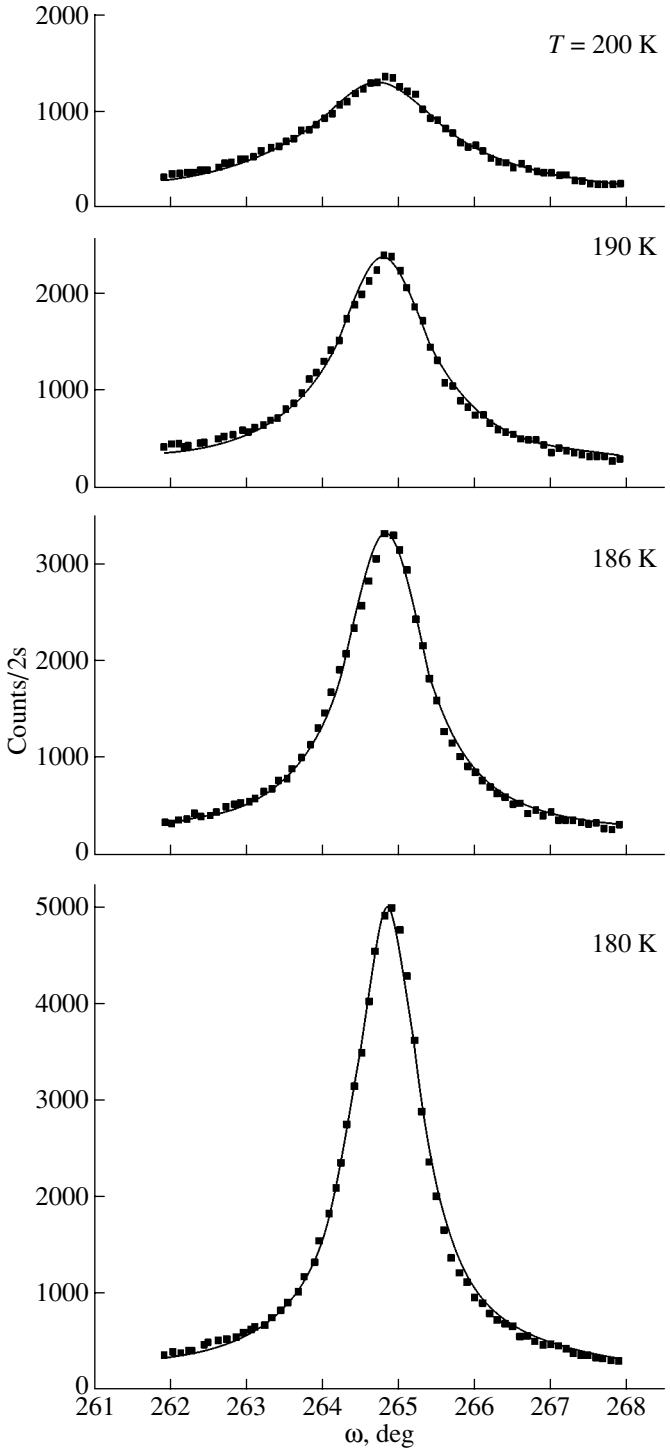

Fig. 2. Diffuse (at $T > T_c = 186$ K) and fundamental ($T \le T_c$) (3.5, 2.5, 0) reflections obtained at different temperatures in ω scan (points are experiment, solid lines are Lorentzians).

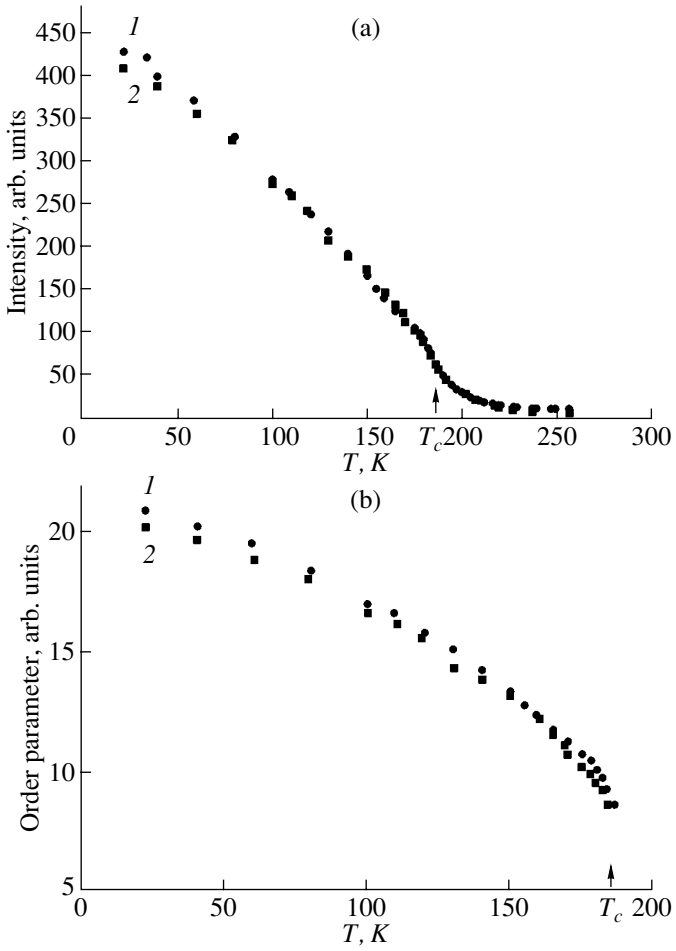

Fig. 3. (a) Temperature dependences of the integrated intensities of the diffuse (at $T > T_c$) and fundamental ($T < T_c$) reflections from the X points of the BZ boundary and (b) temperature dependence of the order parameter; (*1*) the (2.5, 3.5, 0) and (*2*) (3.5, 2.5, 0) reflections.

with cooling toward a final fixed value. To determine accurate values of the critical exponent β, however, these dependences ($\eta \sim \tau^{\beta}$) were redrawn as functions of reduced temperature $\tau = (T_c - T)/T_c$ on a log–log scale. Linear relations were obtained (Fig. 4), and their slopes were used to calculate the critical exponent β; its values were found to be 0.28 ± 0.02 and 0.29 ± 0.02 for the (3.5, 2.5, 0) and (2.5, 3.5, 0) X points, respectively. It seems worthwhile to explain that the deviation of several points of the graph from a straight line within a few degrees near T_c ($T < T_c$) is due to the contribution to the integrated intensity from the diffuse scattering induced by order parameter fluctuations, but now in the ferroelastic phase.

It is known that the diffuse scattering intensities in both the paraelastic and ferroelastic phases are proportional to order parameter fluctuations. In the paraelastic phase ($T > T_c$), only diffuse reflections are observed, which are induced by these fluctuations. For $T \le T_c$, i.e., at the phase transition and the $X \longrightarrow \Gamma$ zone folding in the BZ, the reflections from the X point of the BZ transform into fundamental (Bragg) reflections at the BZ center (the Γ point), which is active in x-ray diffraction. For $T \le T_c$, there also exists a temperature region over

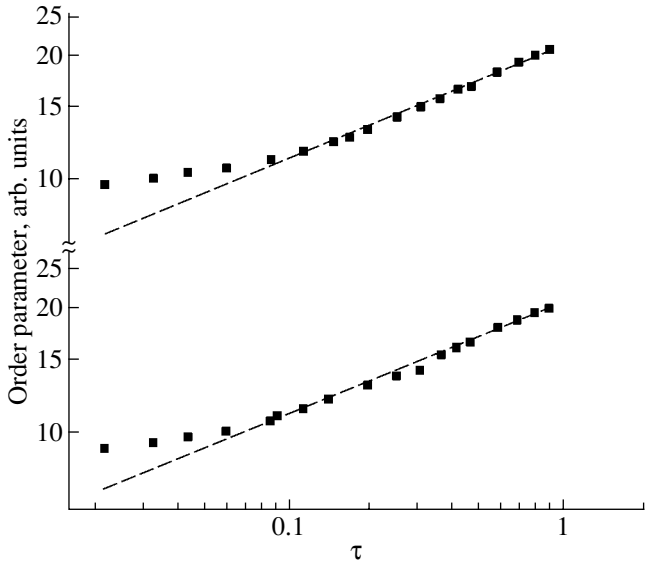

Fig. 4. Order parameter plotted vs. reduced temperature $\tau = (T_c - T)/T_c$ on a log–log scale. The top and bottom curves correspond to the (2.5, 3.5, 0) *X* point and the (3.5, 2.5, 0) point, respectively; symbols are experiment and the dashed line is a linear fit.

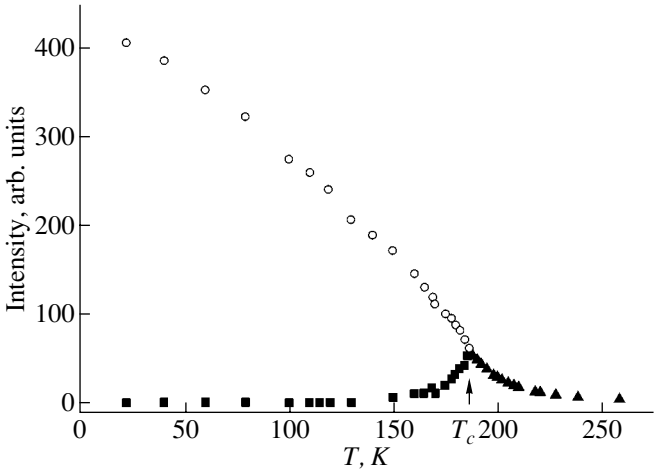

Fig. 5. Temperature dependence of the integrated intensity of diffuse scattering at the (3.5, 2.5, 0) *X* point in the paraelastic phase ($T > T_c$; triangles) and in the ferroelastic phase ($T < T_c$; squares); open circles relate to the behavior of the integrated intensity of this reflection for $T < T_c$.

which order parameter fluctuations manifest themselves in diffuse scattering. In the case of first-order phase transitions, the situation can be explained in a straightforward manner. When a sample is cooled, a narrow fundamental (Bragg) reflection appears abruptly on the broad diffuse peak at the transition point ($T = T_c$), and its intensity grows with a further decrease in temperature while the intensity of the diffuse reflection falls off. By simulating the profiles of these reflections, one can easily separate them and derive the temperature dependence of their main parameters. In the case of continuous (for example, second-order) phase transitions, one usually fails in rigorously extracting the contribution of diffuse scattering to the total intensity of the transition-induced reflection at $T \le T_c$. It is possible, however, to evaluate the contribution of diffuse scattering and its temperature dependence at $T \le T_c$ with a sufficiently high accuracy by analyzing the temperature dependence of the order parameter (and, hence, of the integrated intensity) drawn on a log–log scale. This contribution is directly related to the deviation of these graphs from a straight line near T_c at $T < T_c$ (Fig. 4).

Figure 5 plots the temperature dependences of the integrated intensity of diffuse scattering in the paraelastic phase ($T > T_c$) and in the ferroelastic phase ($T \le T_c$). This plot reveals that the temperature range of diffuse scattering in the low-temperature phase is significantly narrower than that in the high-temperature phase. In view of the close relation between order parameter fluctuations and the diffuse scattering intensity, one may conclude that the temperature region of order parameter fluctuations for $T < T_c$ is substantially smaller (by a factor of more than 2) than that for $T > T_c$, which does not conflict with theoretical predictions.

4. DISCUSSION OF THE RESULTS

Let us consider the temperature dependence of the order parameter in terms of the phenomenological theory of Landau for various types of phase transitions. For pure improper ferroelastics, the thermodynamic potential of Landau in the vicinity of a phase transition can be written as an expansion in a small order parameter η [6]:

$$\Phi = \Phi_0 + A\eta^2/2 + B\eta^4/4 + D\eta^6/6 + K\eta^2\varepsilon + C\varepsilon^2/2, \quad (2)$$

where Φ_0 is the thermodynamic potential of the high-temperature phase; *B*, *D*, and *K* are constants; ε is the lattice strain; and *C* is the elastic modulus. The coefficient of η^2 can be assumed to obey the simplest linear dependence on temperature, $A = \lambda(T - T_c)$. Upon renormalization and minimization in ε, thermodynamic potential (2) transforms to

$$\Phi = \Phi_0 + A\eta^2/2 + B'\eta^4/4 + D\eta^6/6, \quad (3)$$

$$B' = B - 2K^2/C. \quad (4)$$

The temperature dependence of the order parameter is given by

$$\eta^2 = \{[B'^2 + 4\lambda D(T_c - T)]^{1/2} - B'\}/2D. \quad (5)$$

For second-order phase transitions that are far from the tricritical point ($B'^2 \gg 4AD$), the temperature dependence of the order parameter follows the relation

$$\eta = [\lambda(T_c - T)/B']^{\beta}, \quad \text{where} \quad \beta = 0.5. \qquad (6)$$

If, however, $B'^2 \ll 4AD$ [which may result from a sufficiently strong coupling of the order parameter with strain; cf. Eqs. (3)–(5)], the phase transition in a crystal is close to the tricritical point [6]. In this case, the order parameter will depend on temperature with another critical exponent β

$$\eta = [\lambda(T_c - T)/D]^{\beta}, \quad \text{where} \quad \beta = 0.25. \qquad (7)$$

Thus, in the case of second-order phase transitions and transitions in the vicinity of the tricritical point, the theoretical values of the critical exponents β are 0.5 and 0.25, respectively. Analysis of the experimental results obtained reveals that critical-exponent values of 0.28 and 0.29 are inconsistent with the description of second-order phase transitions far from the tricritical point. The experimental values of β are close to 0.25, and they argue convincingly for the model of phase transitions in Hg_2Cl_2 crystals as occurring near the tricritical point. It is conceivable that the phase transition in these crystals occurs not directly at the tricritical point but in its immediate proximity. However, our experiments do not offer an unambiguous conclusion as to which side the phase transition is displaced from the tricritical point, namely, toward weak first-order or second-order phase transitions. We may recall that, in an earlier comprehensive and high-precision study of the temperature dependence of soft modes, heat capacity, spontaneous deformation, etc., of these crystals, we calculated the thermodynamic-potential parameters and determined the corresponding critical exponents, whose values suggested that the phase transition in these crystals are close to the tricritical point [7]. The proposed model of the phase transition provided an explanation for all the experimental results obtained in studies of the Hg_2Cl_2 crystals.

5. CONCLUSIONS

Our studies carried out on Hg_2Cl_2 single crystals have shown that the TA soft mode condenses at the X points of the BZ boundary and that the phase transition is accompanied by cell doubling and $X \longrightarrow \Gamma$ zone folding in the BZ. The monotonic growth of the integrated intensity of the diffuse reflections and the absence of any jumps at $T = T_c$ do not contradict the model of a continuous ferroelastic phase transition in the vicinity of the tricritical point [7]. The observed diffuse scattering induced by spatial–temporal order-parameter fluctuations is associated, at high temperatures ($T \gg T_c$), primarily with the nucleation of static clusters of the low-temperature orthorhombic phase in the high-temperature tetragonal matrix. As the crystal is cooled and approaches T_c, the dynamic effects increase of intensity, which should become manifest in an increase of the contribution of dynamic clusters to diffuse scattering. It is the latter effect that obviously takes place here, but we failed to separate the static from dynamic contributions. The direct relation between order parameter fluctuations and the diffuse scattering intensity provides a straightforward explanation for the narrowing (by a factor of more than 2) of the temperature region of order parameter fluctuations in the ferroelastic phase ($T < T_c$) as compared to that in the paraelastic phase ($T > T_c$).

ACKNOWLEDGMENTS

The authors are indebted to A.A. Kaplyanskiĭ for helpful discussions.

This work was supported in part by the program of the Department of Physical Sciences of the RAS.

REFERENCES

1. H. Mark and J. Steinbach, Z. Krystallogr. **64**, 78 (1926).
2. *Proceedings of 2nd International Symposium on Univalent Mercury Halides* (Trutnov, ČSFR, 1989).
3. A. A. Kaplyanskiĭ, Yu. F. Markov, and Ch. Barta, Izv. Akad. Nauk SSSR, Ser. Fiz. **43** (8), 1641 (1979).
4. Yu. F. Markov, K. Knorr, and E. M. Roginskii, Ferroelectrics **265**, 67 (2001).
5. J. P. Benoit, G. Hauret, and J. Lefebvre, J. Phys. (Paris) **43**, 641 (1982).
6. B. A. Strukov and A. P. Levanyuk, *Physical Principles of Ferroelectric Phenomena in Crystals* (Nauka, Moscow, 1995), p. 67 [in Russian].
7. M. E. Boiko, Yu. F. Markov, V. S. Vikhnin, A. S. Yurkov, and B. S. Zadokhin, Ferroelectrics **130**, 263 (1992).

Translated by G. Skrebtsov

Physics of the Solid State, Vol. 47, No. 2, 2005, pp. 332–336. Translated from Fizika Tverdogo Tela, Vol. 47, No. 2, 2005, pp. 319–323.

LATTICE DYNAMICS AND PHASE TRANSITIONS

Phase Transition in a KPb_2Br_5 Crystal

S. V. Mel'nikova*, L. I. Isaenko, V. M. Pashkov**, and I. V. Pevnev****

** Kirensky Institute of Physics, Siberian Division, Russian Academy of Sciences, Akademgorodok, Krasnoyarsk, 660036 Russia*

e-mail: msv@iph.krasn.ru

*** Institute of Mineralogy and Petrography, Siberian Division, Russian Academy of Sciences, Universitetskiĭ pr. 3, Novosibirsk, 630058 Russia*

e-mail: lisa@lea.nsk.ru

Received June 4, 2004

Abstract—Crystals of the KPb_2Br_5 compound are investigated using polarized light microscopy and calorimetry. The birefringence and the angle of rotation of the optical indicatrix are measured in the temperature range 270–620 K. It is found that the KPb_2Br_5 crystal undergoes a first-order ferroelastic phase transition at temperatures $T_{0\uparrow}$ = 519.5 K and $T_{0\downarrow}$ = 518.5 K with a change in the enthalpy $\Delta H = 1300 \pm 200$ J/mol. This transition is accompanied by both twinning and the symmetry change $mmm \longleftrightarrow P2_1/c$. It is revealed that the angle of rotation of the optical indicatrix exhibits an unusual behavior under variations in the temperature due to a strong temperature dependence of the birefringence. © *2005 Pleiades Publishing, Inc.*

1. INTRODUCTION

The search for new active media for solid-state lasers operating in the middle-infrared range [1] has given impetus to investigations of the crystal family of compounds with the general formula APb_2X_5 (A = Cs, Rb, K, NH_4; X = Cl, Br). It is known [2] that, depending on the ratios between the ionic radii A/X and Pb/X, all these compounds can form two structural modifications, namely, the monoclinic modification $NH_4Pb_2Cl_5$ and the tetragonal modification $NH_4Pb_2Br_5$. According to the phase diagram, the region of existence of KPb_2Br_5 crystals lies along the boundary between the regions corresponding to these two structures and, hence, the KPb_2Br_5 compound can exist in both modifications. The KPb_2Br_5 monoclinic crystals ($P2_1/c$) are formed upon high-temperature crystallization, whereas the tetragonal crystals ($I4/mcm$) grow from aqueous solutions [2, 3]. X-ray diffraction investigations of KPb_2Br_5 crystals at room temperature have established that the monoclinic unit cell is similar to a rectangular unit cell with parameters a = 9.264 Å, b = 8.380 Å, c = 13.063 Å, and Z = 4. The monoclinic angle is relatively small: $\beta = 90.06(12)°$ [2]. Furthermore, Cola *et al.* [3] assigned these crystals to the orthorhombic system. Nothing definite is known about phase transitions from the monoclinic structural modification to the tetragonal modification. However, according to the differential thermal analysis performed in [3], KPb_2Br_5 crystals in the monoclinic modification undergo a phase transition at a temperature T_0 = 515 K with a weak thermal effect (≈400 J/mol). On the other hand, the x-ray diffraction patterns at higher temperatures (T = 593 K) did not exhibit any noticeable changes, except for insignificant shifts of the peaks and small variations in their intensities. All the aforementioned facts indicate that KPb_2Br_5 monoclinic crystals can undergo a structural phase transition at high temperatures.

The purpose of this work was to reveal the hypothetical structural phase transition, to determine its type, and to elucidate the nature and symmetry of the initial high-temperature phase. In order to solve these problems, the KPb_2Br_5 crystal was studied using polarized light microscopy and measurements of the heat capacity and birefringence over a wide range of temperatures.

2. SAMPLE PREPARATION AND EXPERIMENTAL TECHNIQUE

Crystals of the KPb_2Br_5 compound were grown by the Bridgman method from a batch of stoichiometric composition at a temperature T = 655 K. The initial potassium and lead bromides (special-purity grade) were dried under dynamic vacuum and then repeatedly purified through directional crystallization. A vertical one-zone furnace with a temperature gradient of no less than 5 K/mm served as the growth apparatus. Single crystals up to 15 mm in diameter and 40 mm in length were grown in evacuated silica tubes at a mean rate of 2–4 mm/day.

The thermodynamic properties were investigated on a DSM-2M differential scanning microcalorimeter. The DSM signals were recorded and processed using a computer. The measurements with powder samples were carried out in the temperature range 340–600 K.

The birefringence of the KPb_2Br_5 crystal was measured on the (001), (010), and (100) sections. The mea-

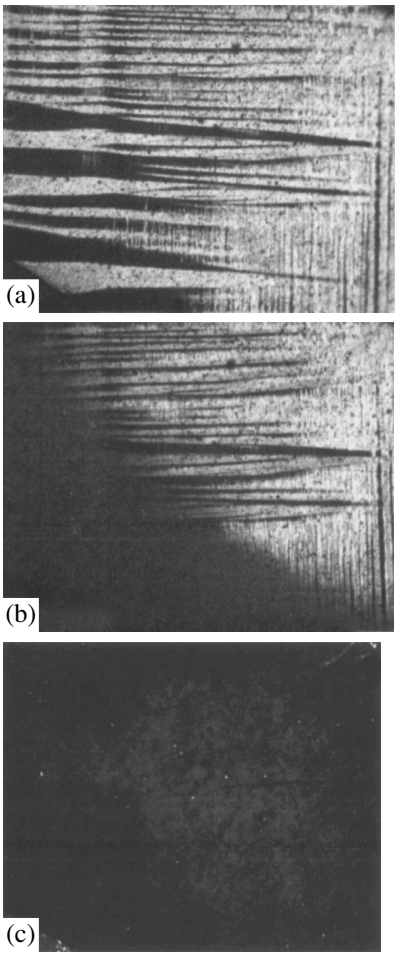

Fig. 1. Twinning of the KPb_2Br_5 crystal in the (010) section at temperatures T = (a) 518.5, (b) 519.5, and (c) 521.0 K.

surements were performed on a Berec compensator with an accuracy of $\cong 10^{-5}$ and a Senarmont compensator with a sensitivity of no less than $\cong 10^{-7}$ at a wavelength of 6328 Å. The former compensator was used to determine the birefringence magnitude, and the latter compensator made it possible to examine the temperature dependence of the birefringence. Observations in polarized light and measurements of the rotation angle of the optical indicatrix were carried out using an Axiolab polarizing microscope with an accuracy of ±0.5°. All the experiments were performed at temperatures ranging from 273 to 620 K.

3. EXPERIMENTAL RESULTS

Observations of the crystal plates in polarized light at room temperature revealed a streaky twin structure in the (010) section (Fig. 1). The structural components differ in the extinction positions by an angle 2φ. The twin boundaries are aligned parallel to the [100] and [001] directions. The width of twins is approximately equal to 10 μm. During heating, the twin pattern is

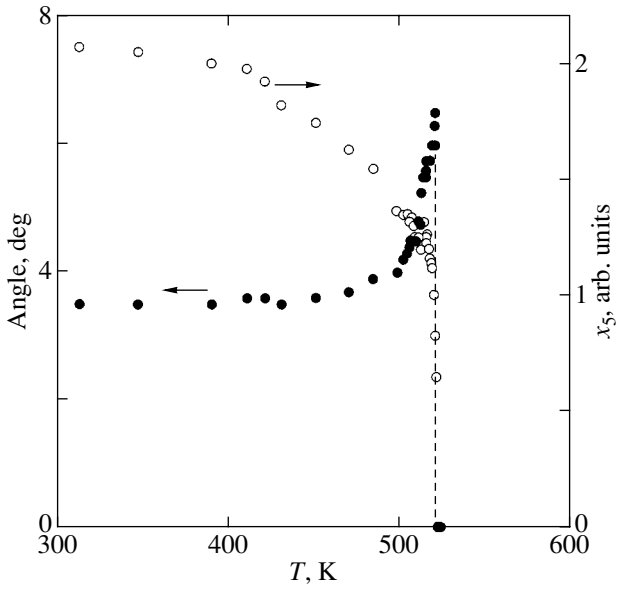

Fig. 2. Temperature dependences of the rotation angle of the optical indicatrix φ(T) and the component $x_5(T)$ of the shear spontaneous strain in the KPb_2Br_5 crystal.

observed up to a temperature of 519 K and then disappears. At temperatures above T = 520 K, the crystal is characterized by a uniform "straight" extinction and twins are absent. During cooling, twins again appear, but the pattern changes radically: there arise large-sized regions that occupy half the sample and differ in the extinction positions by an angle 2φ. The formation of these large-sized regions made it possible to measure the birefringence from the (010) section of the sample in a single-domain state. The original twin pattern is regained with time.

Figure 2 presents the angle of rotation of the optical indicatrix with respect to the [010] direction in a single twin as a function of temperature. The dependence φ(T) exhibits an unusual behavior. At room temperature, the angle of rotation of the optical indicatrix is small and approximately equal to 4°. During heating, the angle of rotation initially remains constant, increases to 7° only in the vicinity of the phase transition, and then sharply decreases to zero. With a further increase in the temperature, the extinction of the sample remains unchanged. In the range 525–545 K, an unusual coloration of the crystal is observed in polarized light: the crystal becomes colored and changes its color (beginning with red) at each temperature. At temperatures above 550 K, the coloration disappears.

The temperature dependences of the birefringences Δn_a, Δn_b, and Δn_c are depicted in Fig. 3. At room temperature, the birefringences are approximately identical and relatively large (≈0.06) for the (100) and (010) sections and close to zero for the (001) section. As the temperature increases, the difference in the refractive indices initially changes linearly and insignificantly. At

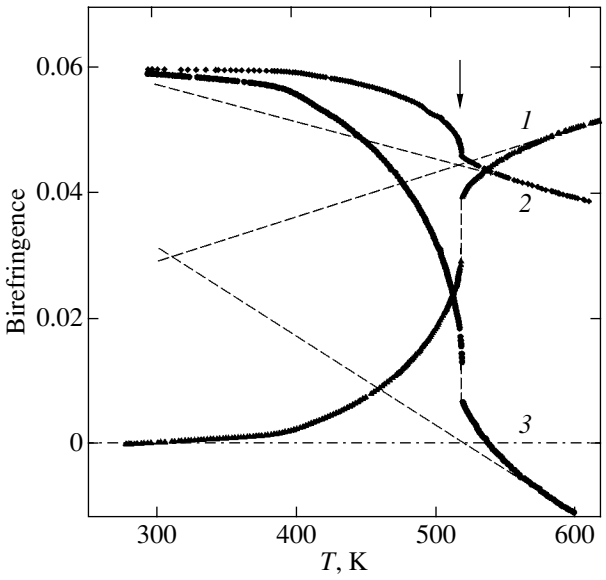

Fig. 3. Temperature dependences of the birefringence of the KPb_2Br_5 crystal: (*1*) Δn_c, (*2*) Δn_a, and (*3*) Δn_b.

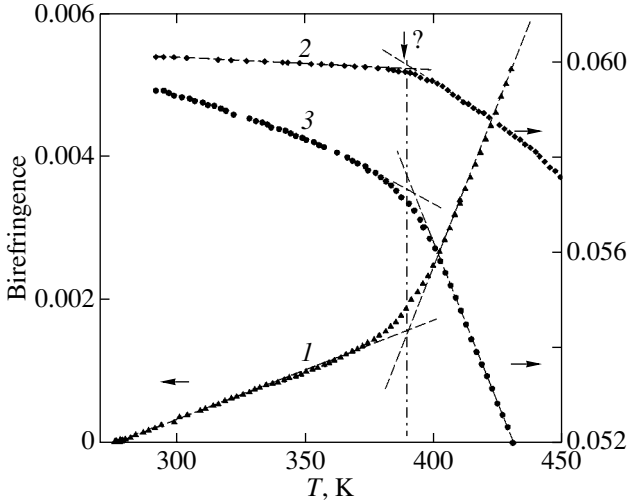

Fig. 4. Temperature dependences of the birefringence of the KPb_2Br_5 crystal at temperatures close to 400 K: (*1*) Δn_c, (*2*) Δn_a, and (*3*) Δn_b.

temperatures above $T \approx 390$ K, the dependences $\Delta n(T)$ exhibit an anomalous behavior for all the sections. It is worth noting that, at this temperature ($T \approx 390$ K), the dependences $\Delta n(T)$ for all three sections are characterized by a specific point (Fig. 4).

At temperatures $T_{0\uparrow} = 519.5$ K and $T_{0\downarrow} = 518.5$ K, the birefringence undergoes a jump with an insignificant temperature hysteresis ($\Delta T \approx 1$ K) (Fig. 3). As the temperature increases above 570 K, the temperature dependence of the birefringence exhibits a linear behavior. The dashed lines in Fig. 3 correspond to the extrapolation of the initial linear dependences of the birefringence. It can be seen from this figure that the KPb_2Br_5 crystal is characterized by pronounced pretransitional phenomena over a wide temperature range (≈60 K) above the phase transition point.

Slightly above the transition temperature, there is an "isotropic point" at which the birefringence Δn_b for the (010) section decreases to zero and then changes sign. It is in this temperature range that the continuous change in color of the crystal is observed in polarized light with a variation in the temperature. The birefringence of the crystal is characterized by a large dispersion (close to that of lithium niobate). This dispersion in the visible spectral range is approximately equal to 0.01. Hence, for each wavelength in the temperature range 525–545 K there is one zero point. Apart from the zero point for the (010) section, the zero point of the birefringence is observed for the (001) section below room temperature (Fig. 3).

Figure 5 shows the temperature dependence of the excess heat capacity associated with the phase transition according to the microcalorimetric data. The change in the enthalpy upon the phase transition was determined by integrating the function $\Delta C_p(T)$, where ΔC_p is the excess heat capacity. The obtained change in the enthalpy $\Delta H = 1300 \pm 200$ J/mol is nearly three times larger than that determined by the differential thermal analysis in [3] ($\Delta H \approx 400$ J/mol). This substantial difference in the values of ΔH can be caused by different accuracies of the methods used.

4. DISCUSSION

The investigations performed demonstrate that the KPb_2Br_5 crystal undergoes a phase transition at a temperature $T_0 \approx 519$ K. This transition is accompanied not only by a jump in the birefringence but also by a temperature hysteresis that is characteristic of first-order phase transitions. The twinning geometry and the angle of rotation of the optical indicatrix indicate that, at room temperature, the phase is monoclinic with the twofold axis parallel to the [010] direction. This is consistent with the symmetry group $P2_1/c$ [2]. Judging from the observations in polarized light, the high-temperature phase has orthorhombic symmetry. A considerable increase in the twin size upon repeated runs through the phase transition temperature T_0 suggests that the twin boundaries are sensitive to inhomogeneous internal stresses that arise upon the first-order phase transition and are responsible for the formation of a single-domain structure of the sample. Inhomogeneous strains relax with time, and the twins regain their original structure. Such a situation can be observed when the phase transition is ferroelectric in nature. These findings give grounds to assume that, at a temperature $T_0 \approx 519$ K, the crystal undergoes a first-order ferroelastic phase transition with the symmetry change

$mmm \longleftrightarrow P2_1/c$. This change in symmetry leads to the appearance of the component x_5 of the shear spontaneous strain and, hence, to the rotation of the optical indicatrix about the [010] axis.

It should be noted that no changes in the x-ray diffraction patterns above the phase transition temperature as compared to those at room temperature were revealed in [3]. This fact is not clear from the standpoint of the assumed symmetry change. The extinction laws are different for orthorhombic and monoclinic symmetries. Taking into account these circumstances, we repeated the experiment performed in [3]. For this purpose, we recorded the x-ray powder diffraction patterns at a temperature of 560 K and at room temperature and then compared them. According to our experimental data, a number of lines that do not satisfy the condition $(h + k + l) = 2n$ disappear at temperatures above the phase transition point. This suggests that the high-temperature phase of the KPb_2Br_5 crystal is orthorhombic and has the same unit cell but the cell is body-centered. The phase transition is not accompanied by a multiple change in the unit cell volume. This is typical of proper phase transitions. Most likely, the set of reflections observed in the x-ray diffraction pattern corresponds to a space group of the orthorhombic crystal system with a center of symmetry and a body-centered unit cell, i.e., to the space group *Immm* or *Imma*.

It is universally accepted that, upon proper ferroelectric phase transitions, the temperature dependence of the rotation angle of the optical indicatrix reflects the behavior of the shear spontaneous strain arising below the phase transition: $\varphi \sim x_s$. However, this is not always the case. As was shown by Aleksandrov *et al.* [4], this simplification holds true for small angles of rotation and for insignificant changes in the birefringence. In actual fact, upon transformation of the polarization tensor from one coordinate system to another coordinate system, we obtain $\tan 2\varphi = n^3 p_{55} x_5/\Delta n_b$, where p_{55} is the photoelasticity coefficient, n is the averaged refractive index, and x_5 is the shear strain component. The angle of rotation of the optical indicatrix is small and, hence, $\tan\varphi \approx \varphi$. However, it can be seen from Fig. 3 that the birefringence for the (010) section in the phase transition range varies from a maximum value to zero and even reverses sign. Therefore, in order to determine the temperature dependence of the shear strain $x_5(T)$ for the KPb_2Br_5 crystal from optical experiments, we should take into account the two dependences $\Delta n_b(T)$ and $\varphi(T)$. Figure 2 depicts the dependence $(\Delta n_b \tan 2\varphi)(T)$, which reflects the behavior of the shear strain $x_5(T)$ for the KPb_2Br_5 crystal under the assumption that the phase transition is purely ferroelastic in nature.

The temperature dependences of the anomalous component of the birefringence in the range below the phase transition point T_0 are plotted in Fig. 6. These dependences were obtained by subtracting the extrapolated linear portions of the temperature dependences of the birefringence for the initial phase from the curves $\Delta n(T)$ depicted in Fig. 3. As can be seen from Fig. 6, the KPb_2Br_5 crystal is characterized by pronounced pretransitional effects over a wide temperature range (≈60 K) above the phase transition point. The phase transition is accompanied by a jump in the birefringence, and then the birefringence increases gradually. However, at temperatures below $T \approx 400$ K, the value of $\delta(\Delta n)(T)$ begins to decrease. It is known that, below the phase transition temperature, the anomalous component of the birefringence measured in the orthorhombic setting is proportional to the transition parameter squared; i.e., $\delta(\Delta n)(T) \sim \eta^2$. Figure 7 shows these dependences for all three sections of the KPb_2Br_5 crystal. The transition parameter is taken as the strain component x_5 calculated according to the above procedure (Fig. 2). It can be seen from Fig. 7 that all the experimental points fall on a linear dependence passing through the origin of the coordinates. This implies that

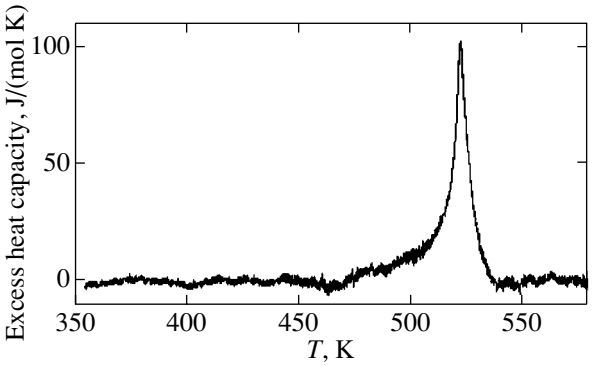

Fig. 5. Temperature dependences of the excess heat capacity of the KPb_2Br_5 crystal.

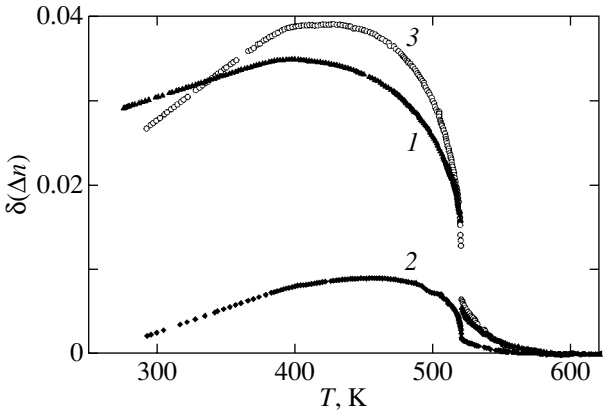

Fig. 6. Temperature dependences of the anomalous component of the birefringence for the KPb_2Br_5 crystal: (*1*) $\delta(\Delta n_c)$, (*2*) $\delta(\Delta n_a)$, and (*3*) $\delta(\Delta n_b)$.

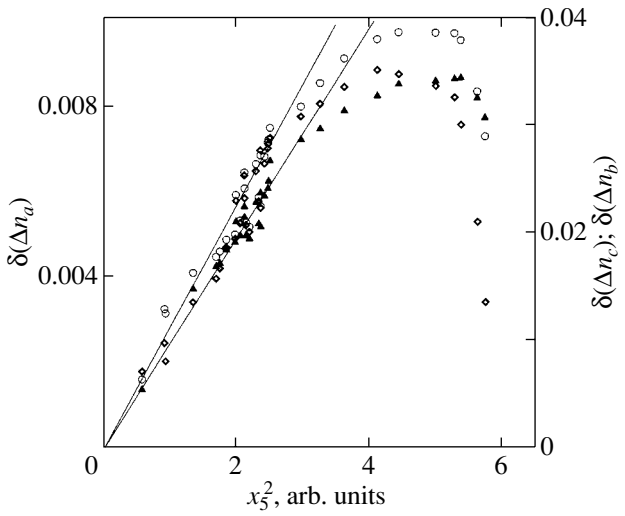

Fig. 7. Correlation between the anomalous component of the birefringence and the transition parameter squared at the corresponding temperatures. The point designations are the same as in Figs. 3, 4, and 6.

the anomalous birefringence is governed by the shear strain. However, at temperatures below 400 K, the anomalous birefringence considerably deviates from linear behavior.

5. CONCLUSIONS

Thus, the above investigations confirmed the assumption that the KPb_2Br_5 crystals undergoes a phase transition in the temperature range close to 515 K in which a weak thermal anomaly was revealed in [3]. This transition is not related to radical structural transformations that can occur upon the transition between two structural modifications of the crystal, namely, $P2_1/c$ and $I4/mcm$. The observed transition is accompanied by weak structural distortions and twinning typical of the change in crystal symmetry $mmm \longleftrightarrow P2_1/c$. The structural distortion is very small, and the monoclinic angle is determined within the limits of experimental error: $\beta = 90.06(12)°$ [2]. According to our experimental data, we can assume that the high-temperature phase is adequately described by the space group *Immm* or *Imma*.

The factors responsible for the inflection in the temperature dependences of the birefringence at a specific point in the vicinity of 390 K (Fig. 4) remain unclear. There are two possible variants. First, there can occur another phase transition. However, closer examination performed by differential scanning calorimetry did not reveal additional anomalies (Fig. 5). Second, the phase transition is pseudoproper in nature; i.e., there are two transition parameters that are linearly related but are characterized by different temperature dependences (as is the case with the $CsLiCrO_4$ compound [5]).

ACKNOWLEDGMENTS

We would like to thank A.F. Bovina for performing the x-ray diffraction experiments and A.V. Kartashov for his assistance in performing the calorimetric measurements.

This work was supported by the US Civilian Research and Development Foundation for the Independent States of the Former Soviet Union (CRDF), project no. +RE 2-2222.

REFERENCES

1. L. Isaenco, A. Yelisseyev, A. Tkachuk, S. Ivanova, S. Vatnik, A. Merkulov, S. Payne, R. Page, and M. Nostrand, Mater. Sci. Eng. B **81**, 188 (2001).
2. Y. P. Beck, G. Clicqué, and H. Nau, Z. Anorg. Allg. Chem. **536**, 35 (1986).
3. M. Cola, V. Massarotti, R. Riccardi, and C. Sinistri, Z. Naturforsch. A **26**, 1328 (1971).
4. K. S. Aleksandrov, S. V. Mel'nikova, A. I. Kruglik, S. M. Tret'yak, and V. V. Mitkevich, Kristallografiya **34**, 147 (1989) [Sov. Phys. Crystallogr. **34**, 85 (1989)].
5. I. Hashiguchi, Y. Kuroiwa, and A. Sawada, J. Phys. Soc. Jpn. **68** (8), 2673 (1999).

Translated by O. Borovik-Romanova

Physics of the Solid State, Vol. 47, No. 2, 2005, pp. 337–346. Translated from Fizika Tverdogo Tela, Vol. 47, No. 2, 2005, pp. 324–333.

LATTICE DYNAMICS AND PHASE TRANSITIONS

Raman Spectra of Cadmium Titanate

V. I. Torgashev,* Y. I. Yuzyuk,* V. B. Shirokov,* V. V. Lemanov, and I. E. Spektor*****

**Rostov State University, pr. Stachki 194, Rostov-on-Don, 344090 Russia*

***Ioffe Physicotechnical Institute, Russian Academy of Sciences, Politekhnicheskaya ul. 26, St. Petersburg, 194021 Russia*

****Institute of General Physics, Russian Academy of Sciences, ul. Vaviliva 38, 117942 Russia*

Received June 22, 2004

Abstract—Polarized Raman spectra of $CdTiO_3$ single crystals are recorded for the first time over the frequency range $5 < \nu < 1000$ cm^{-1} at temperatures of 10 to 1200 K. The emphasis was on the low-frequency range, where an anomalous temperature dependence of a few phonon modes was observed. At high temperatures, four phonon modes exhibiting a behavior typical of soft modes were found to exist. These phonon modes are assumed to restore the cubic symmetry of the lattice. Their extrapolated temperature dependences suggest that there exists a sequence of three hypothetical high-temperature phase transitions analogous to those observed in the genuine perovskite $CaTiO_3$. At temperatures below 78 K, the Raman spectrum exhibits new lines associated with polar distortions of the unit cell. At low frequencies, three lines are observed whose parameters exhibit an anomalous behavior typical of soft modes in a ferroelectric phase. Several different polar states are assumed to exist at low temperatures. © *2005 Pleiades Publishing, Inc.*

1. INTRODUCTION

There is continuing interest in perovskite and perovskite-structure crystals, which undergo various phase transitions (ferroelectric, antiferroelectric, with orbital or magnetic ordering, etc.). This interest is due to the fact that the fundamental nature of the phenomena observed in them is not yet well understood and also to the various applications of these compounds in engineering [1].

Cadmium titanate ($CdTiO_3$) has been very poorly studied in comparison with related compounds. The ferroelectric properties of $CdTiO_3$ below 50 K were discovered by Smolenskiĭ [2–4] and confirmed later by Hegenbarth [5, 6]. Recently, interest in experimental studies on $CdTiO_3$ has been rekindled. Both ceramic and single-crystal samples have been found to exhibit a peak in permittivity at temperatures of ~77 K [7–11]. Furthermore, dielectric hysteresis loops have been observed below these temperatures [7, 9–11]. The saturated spontaneous polarization was $P_s = 9 \times 10^{-7}$ C/cm^2, which is an order of magnitude less than P_s in barium titanate. This ferroelectric phase transition was assumed in [10] to occur near the tricritical point with a critical index $\beta = 0.25$. Studies on the birefringence (Δn_i) of single crystals over a wide temperature range have confirmed the occurrence of a phase transition at 83 K, where the monotonic temperature dependence of $\Delta n_i(T)$ changes sharply [12] and exhibits a hysteresis of approximately 3 K. In [12], this phase transition was assumed to be first-order. Note that the dielectric hysteresis is less than 1 K [10]. The birefringence $\Delta n_i(T)$ above T_c decreases monotonically as the temperature increases up to 1200 K [12], though a small discontinuity in slope was observed in [13] in the temperature range 473–523 K, where a sharp increase in permittivity was also observed; however, this behavior was assigned in [13] to the effect of structural defects.

X-ray diffraction studies on single-crystal $CdTiO_3$ have shown [14, 15] that this perovskite is centrosymmetric and belongs to the *Pnma* space group ($GdFeO_3$-type structure), which differs from the results from [13, 16]. The unit cell contains four $CdTiO_3$ formula units ($Z = 4$). The orthorhombic distortion is similar to that in the genuine perovskite $CaTiO_3$ [17] caused by several high-temperature phase transitions. We note, however, that high-temperature phase transitions in $CdTiO_3$ have not yet been detected reliably; the results reported in [18, 19] are not reliable, because the samples exhibited a high conductivity at high temperatures and were prone to reconstructive transformations into the ilmenite structure [20]. A specific feature of these high-temperature transitions is that the distortions caused by them can be adequately described by pure rotations of rigid octahedra TiO_6 around different crystallographic axes [21, 22].

There is little information available in the literature on the dynamic properties of the crystal lattice. We are aware of only fragmentary data on phonon spectra from [7, 23]. The vibrational spectra of the ilmenite modification of $CdTiO_3$ were studied in [24, 25].

In this paper, we report on the results of Raman scattering studies on single- and multidomain $CdTiO_3$ crystals over the temperature range 10–1200 K at frequencies of 5 to 1000 cm^{-1}. Particular emphasis was placed on the low-frequency spectral region. The temperature

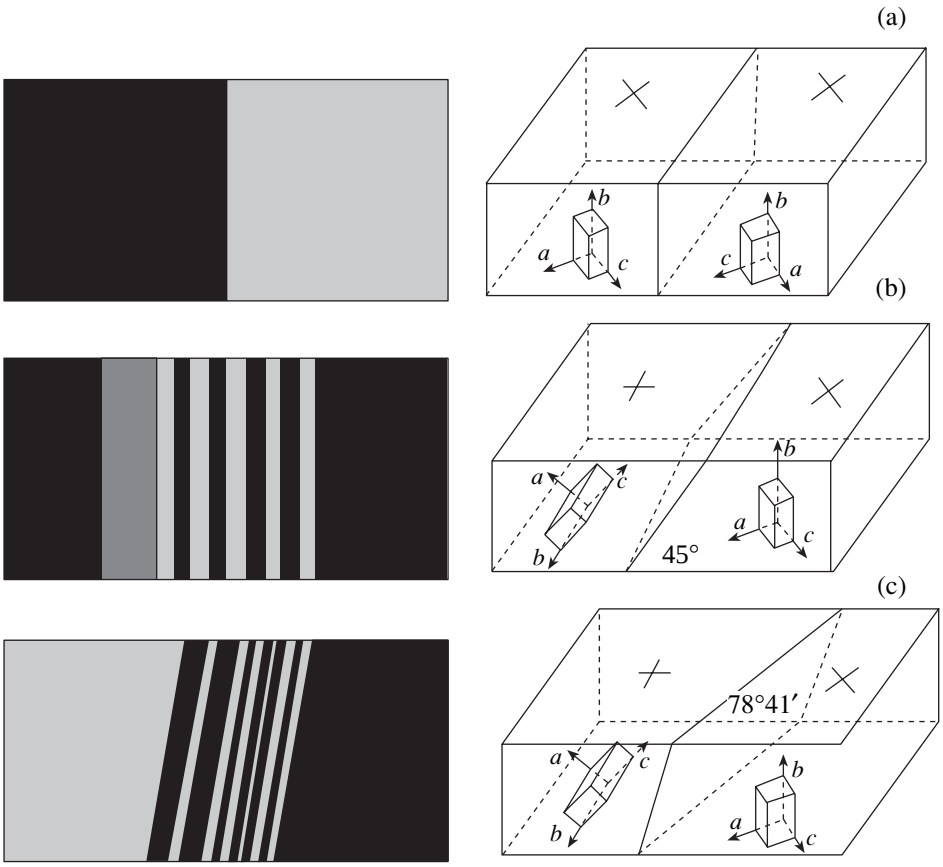

Fig. 1. Schematic microscopic images and the corresponding twins (the axes of the orthorhombic unit cell are indicated with respect to the $CdTiO_3$ crystal faces). (a) Type-I, (b) type-II, and (c) type-III twins. Crosses indicate the directions of extinction of light propagating perpendicular to the large face of the crystal platelet.

dependence of the phonon spectrum is described quantitatively in terms of an additive-oscillator model.

2. EXPERIMENT

Crystals were grown using a technique (described in [26, 27]) for crystallizing platelet-shaped perovskite-structure $CdTiO_3$ crystals. The KF–KVO_3 system was used as a solvent. Its eutectic melting temperature is approximately 770 K at 27 mol % KF, which made it possible to reduce the temperature at which crystallization begins to 1270 to 1300 K and thereby stabilize the melt.

Experiments were carried out in a platinum crucible 50 cm^3 in volume. The best crystals were obtained using the starting composition (in grams) 1.4 $CdTiO_3$: 6.9 KF : 2.5 KVO_3. A melt became homogeneous in 1.5 to 2 h at temperatures of 1290 to 1310 K under regular mixing and was cooled to 1140–1170 K at a rate of 6 to 8 K/h. After the mother melt was poured off, the crystals were cooled slowly and then washed with dilute HCl.

The crystals obtained were high optical–quality amber-colored transparent $CdTiO_3$ platelets up to 7×10 mm^2 in area and 10- to 200-μm thick. The composition of single crystals was determined with a combination scanning electron microscope–microprobe Camebax-Micro using a standard correcting technique (ZAF). The content of impurities was less than 0.1–0.15 mol %. X-ray diffraction studies did not reveal reflections from ilmenite-structure $CdTiO_3$. The parameters of the pseudomonoclinic perovskite-like unit cell were determined to be $a = c = 3.791$ Å, $b = 3.809$ Å, and $\beta = 91°11.6'$, which is close to the results from [14, 15].

Most very thin (up to 20 μm) $CdTiO_3$ single-crystal platelets, studied in polarized light at room temperature, were single domain. Thicker samples exhibited a domain structure. Facets of samples showed symmetrical extinction of light; however, there were also platelets for which parallel extinction was observed. Three types of twins were detected [26]. Type-I twins were observed to exist in crystals showing symmetric extinction. Polarized light was propagated along the [010] axis of the orthorhombic unit cell in both parts of a twin. The twinning plane was parallel to the (100) plane

of the pseudocubic unit cell. Type-II and III twins were detected in crystals that showed mixed extinction (with one part of a twin showing parallel extinction and the other part symmetric extinction). In a type-II twin, the twinning plane makes an angle of 45° with the developed face of the crystal and is parallel to the (110) plane of the pseudocubic unit cell. The twinning plane in type-III twins coincides with the (151) plane and makes an angle of 78°41′ with the developed face of the crystal [26]. The structure of twins is shown schematically in Fig. 1. The microscope-based Raman scattering technique made it possible to take spectra from individual "thick" twins.

Raman spectra were excited by polarized light from a Coherent-Innova 90 Ar^+ ion laser (λ = 514.5 nm) and analyzed with a Jobin Yvon T64000 spectrometer equipped with a CCD camera. Polarized spectra were taken from carefully oriented samples, with the axes of the laboratory coordinate system being parallel to those of the cubic-perovskite unit cell: $X \parallel [100]$, $Y \parallel [010]$, and $Z \parallel [001]$. Raman spectra were measured in backscattering geometry using a microscope to focus the light incident on the sample, which made it possible to collect scattered light from a spot approximately 2 μm in diameter. At high temperatures, a Linkam cell was utilized. Low-temperature measurements were performed using a closed-cycle gas flow cryostat with a temperature-stabilizing system (Oxford). Samples were naturally grown platelets approximately 3 × 4 mm^2 in area and 40-μm thick that were not subjected any mechanical treatment.

To obtain quantitative information on the parameters of Raman spectrum lines, we utilized a damped harmonic–oscillator model. Raman spectra were fitted (using the method of least squares) by the expression

$$I(\nu) = I_b + C[n(\nu, T) + 1]\sum_i \frac{\Delta\varepsilon_i \nu_i^2 \nu\gamma_i}{(\nu_i^2 - \nu^2)^2 + \gamma_i^2\nu^2}. \quad (1)$$

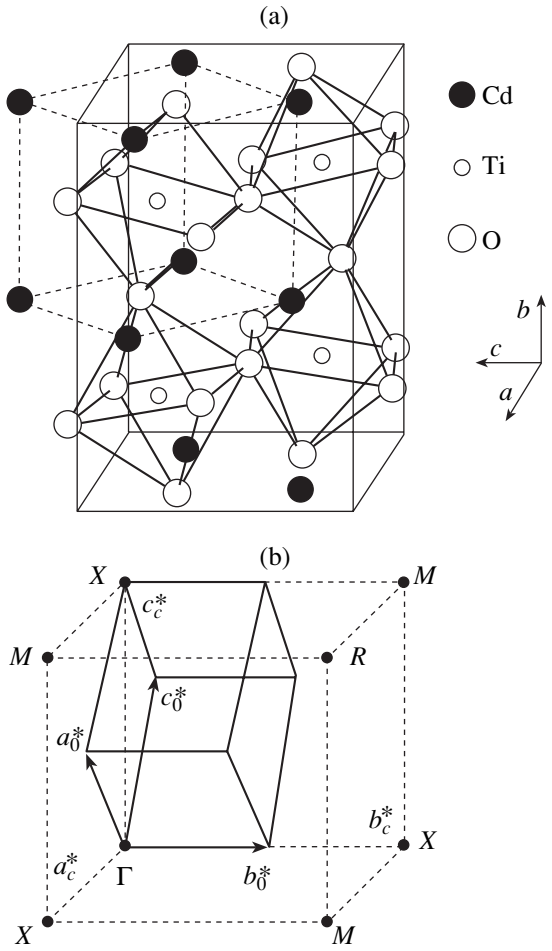

Fig. 2. (a) Unit cell and (b) Brillouin zone of the orthorhombic polymorphic modification of $CdTiO_3$ (solid lines) and their relation to the perfect cubic unit cell (dashed lines). In panel (b), the letters indicate the points of the cubic BZ that are transferred to the center of the orthorhombic BZ as a result of rotational structural distortions.

Here, I_b is a constant background; C is a constant; $[n(\nu, T) + 1]$ is the Bose–Einstein factor, characterizing the occupancy of phonon energy levels; and ν_i, γ_i, and

Composition of the representations for the atomic positions in the perovskite structure (space group *Pm3m*)

Position (wave vector)	Representation type	Zone-point representation composition			
		k_{10} (*X* point)	k_{11} (*M* point)	k_{13} (*R* point)	k_{12} (Γ point)
(*a*): (000)	Displacement	$\tau_4 + \tau_{10}$	$\tau_4 + \tau_{10}$	τ_{10}	τ_{10}
(*b*): (1/2 1/2 1/2)	Displacement	$\tau_1 + \tau_9$	$\tau_6 + \tau_{10}$	τ_7	τ_{10}
	Rotation	$\tau_2 + \tau_{10}$	$\tau_5 + \tau_9$	τ_8	τ_9
(*c*): (1/2 1/2 0)	Displacement	$\tau_1 + \tau_4 + \tau_6 + 2\tau_9 + \tau_{10}$	$\tau_1 + \tau_3 + \tau_5 + \tau_6 + \tau_7 + \tau_9 + \tau_{10}$	$\tau_4 + \tau_6 + \tau_8 + \tau_{10}$	$\tau_8 + 2\tau_{10}$
Total: (*a*), (*b*), (*c*)	Displacement	$2\tau_1 + 2\tau_4 + \tau_6 + 3\tau_9 + 2\tau_{10}$	$\tau_1 + \tau_3 + \tau_4 + \tau_5 + 2\tau_6 + \tau_7 + \tau_9 + 3\tau_{10}$	$\tau_4 + \tau_6 + \tau_7 + \tau_8 + 2\tau_{10}$	$\tau_8 + 4\tau_{10}$

Note: The labeling of representations and wave vectors is the same as that introduced in [29].

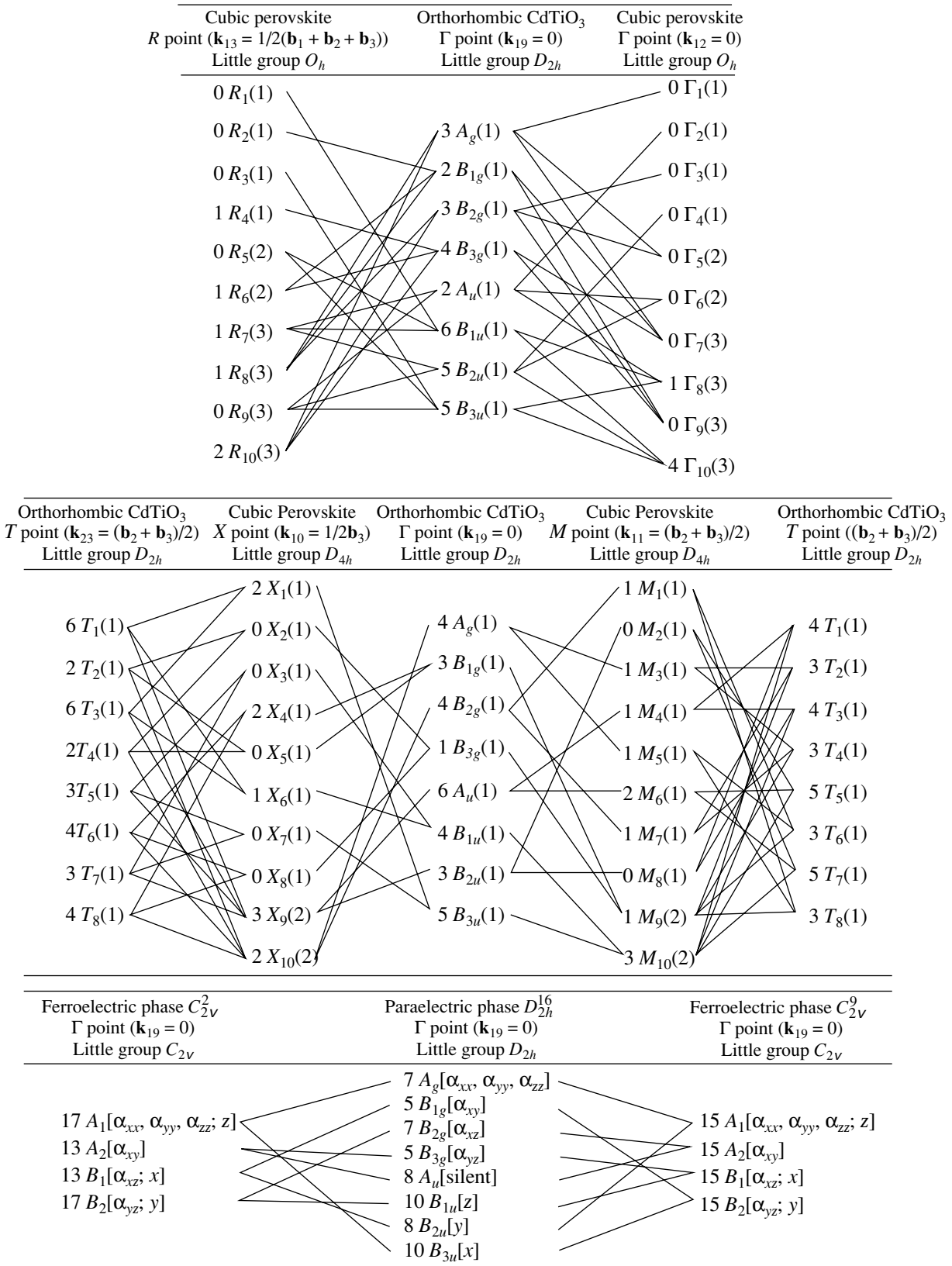

Fig. 3. Correlation between the representations corresponding to the Γ, *X*, *M*, *T*, and *R* points of the BZ of the "perfect" perovskite (O_h^1 symmetry) transferred to the BZ center of orthorhombic $CdTiO_3$ belonging to space group *Pnma* (D_{2h}^{16}). The numeral written in front of a representation symbol is the number of times this representation appears in the displacement representation. The numeral in parentheses after a representation symbol is the degeneracy of the mode. The origin of coordinates is at the Cd atom site.

$\Delta\varepsilon_i\nu_i^2$ are the natural frequency, damping constant, and oscillator strength of the *i*th mode, respectively.

3. THE CRYSTAL STRUCTURE OF $CdTiO_3$ AND FACTOR-GROUP ANALYSIS OF PHONON MODES

$CdTiO_3$ crystallizes in an orthorhombically distorted perovskite structure and belongs to the *Pnma* group [15]; its unit cell is shown schematically in Fig. 2.

The vibrational representation of perovskites has been analyzed in many papers (see, e.g., [28]) and is given in the table. We use the labeling of wave vectors and representations introduced by Kovalev [29]; this labeling is unambiguous and is preferable to that used in [21, 22, 28, 30], because the representations are often erroneously identified in the literature. We also added a rotation representation at the *b* position in order to separate the corresponding mechanism for rigid TiO_6 octahedra. Rotational distortions of the structure, which occur in $CdTiO_3$ at high temperatures, cause a folding of the Brillouin zone (BZ) and thereby transfer phonon modes from the *R*, *M*, and *X* points of the cubic-lattice BZ to the center of the orthorhombic BZ (Fig. 2b). The corresponding correlations are shown in Fig. 3.

4. EXPERIMENTAL RESULTS AND DISCUSSION

From the correlation diagram in Fig. 3, it follows that the phonon modes at the *R*, *M*, and *X* points in the Brillouin zone become active in first-order Raman scattering after the corresponding phase transitions occur, causing a multiplication of the unit cell volume. As a result, one might expect that the Raman spectrum at room temperature will contain 24 lines ($7A_g + 5B_{1g} + 7B_{2g} + 5B_{3g}$) and that 25 polar phonon modes ($9B_{1u} + 7B_{2u} + 9B_{3u}$) will be infrared-active due to the crystal being centrosymmetric. It should be stressed that all Raman-active phonons in $CdTiO_3$ originate from the phonon modes at the BZ boundary of the cubic phase.

4.1. The General Structure of the Raman Spectra and Symmetry Classification of Spectral Lines

Polarized Raman spectra from a $CdTiO_3$ single crystal were taken in a 180° scattering geometry for all possible orientations of the vectors **E** of the incident and scattering monochromatic laser light relative to the crystallographic axes of the crystal. As exemplified in Fig. 1, polarized spectra can be obtained from individual domains. Experimentally, it is convenient to investigate domains in which the *b* axis of the orthorhombic unit cell is normal to the large natural (010) face of a sample and the *a* and *c* axes make an angle of 45° with the other two natural faces. In this case, in order to analyze experimental Raman spectra, the common Raman

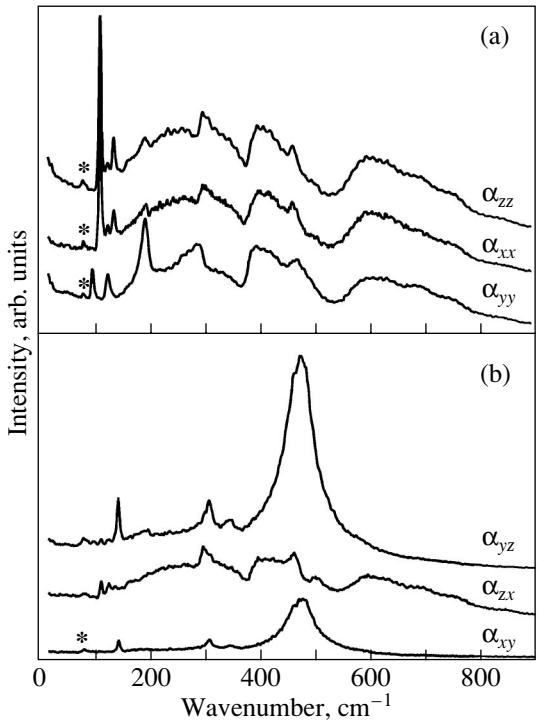

Fig. 4. Raman spectra of orthorhombic single-crystal $CdTiO_3$ taken in various scattering geometries at $T = 296$ K. The main Raman tensor components are indicated. Here and in Figs. 5 and 7, asterisks indicate the laser plasma line.

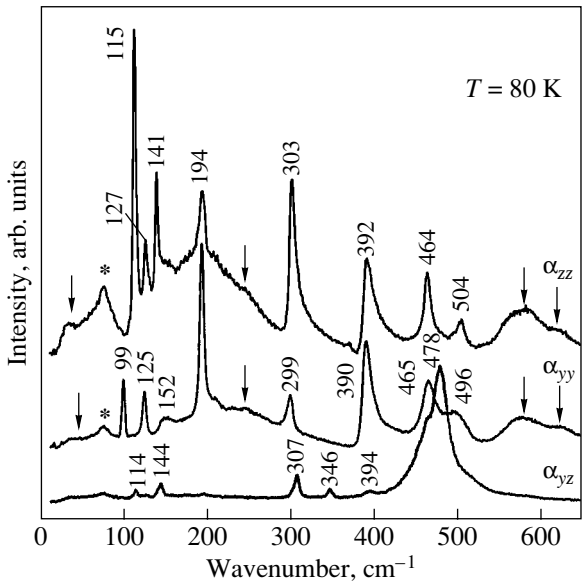

Fig. 5. Polarized Raman spectra of orthorhombic single-crystal $CdTiO_3$ taken at 80 K. Only A_g modes can be observed in the *yy* spectrum. The A_g and B_{2g} modes can appear simultaneously in the *zz* spectrum, and the B_{1g} and B_{3g} modes, in the *yz* spectrum. The second-order Raman bands are indicated by arrows.

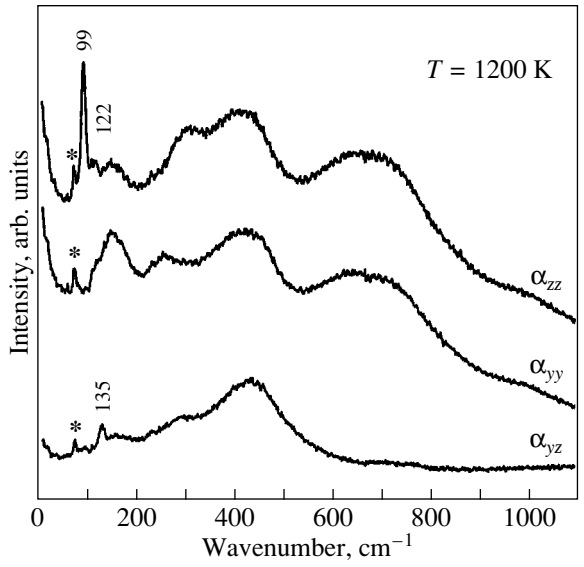

Fig. 6. Polarized Raman spectra of crystal $CdTiO_3$ taken at 1200 K. Asterisks indicate the laser plasma line. The second- and higher order Raman scattering is seen to dominate.

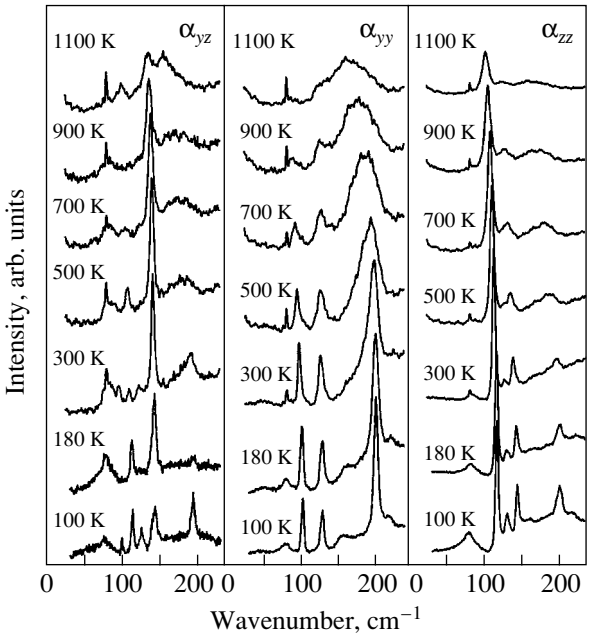

Fig. 7. Temperature dependence of the low-frequency Raman spectra of $CdTiO_3$ over the range 100–1100K.

tensors for the D_{2h} group should be subjected to the transformation corresponding to rotation through 45° about the *b* axis. This procedure gives the following Raman tensors attributed to the coordinate system associated with the natural facets of the crystal:

$$\begin{bmatrix} a & 0 & 0 \\ 0 & b & 0 \\ 0 & 0 & c \end{bmatrix} \Rightarrow \frac{1}{2}\begin{bmatrix} (a+c) & 0 & (a-c) \\ 0 & 2b & 0 \\ (a-c) & 0 & (a+c) \end{bmatrix} A_g;$$

$$\begin{bmatrix} 0 & 0 & e \\ 0 & 0 & 0 \\ e & 0 & 0 \end{bmatrix} \Rightarrow \begin{bmatrix} -e & 0 & 0 \\ 0 & 0 & 0 \\ 0 & 0 & e \end{bmatrix} B_{2g};$$

$$\begin{bmatrix} 0 & d & 0 \\ d & 0 & 0 \\ 0 & 0 & 0 \end{bmatrix} \Rightarrow \frac{1}{\sqrt{2}}\begin{bmatrix} 0 & d & 0 \\ d & 0 & d \\ 0 & d & 0 \end{bmatrix} B_{1g};$$

$$\begin{bmatrix} 0 & 0 & 0 \\ 0 & 0 & f \\ 0 & f & 0 \end{bmatrix} \Rightarrow \frac{1}{\sqrt{2}}\begin{bmatrix} 0 & -f & 0 \\ -f & 0 & f \\ 0 & f & 0 \end{bmatrix} B_{3g}.$$

Thus, the A_g modes can be observed in the *yy* and *xz* spectra, whereas both the A_g and B_{2g} modes can be seen simultaneously in the *xx* and *zz* spectra (in what follows, we use the small letters *x*, *y*, and *z* to denote the spectra described by the components of the transformed Raman tensors). Similarly, the B_{1g} and B_{3g} modes cannot be distinguished in experimental Raman spectra. Furthermore, since type-I twins are rotated about axis $Y \parallel b$ through 45° in opposite (clockwise and counterclockwise) directions, it is almost impossible to identify the modes in a multidomain sample in terms of symmetry. In our experiments, this problem is circumvented by carrying out microscope-based Raman measurements on individual domains.

Figure 4 shows polarized spectra taken in various scattering geometries at room temperature. It is seen that the spectra are very broad, highly structured bands typical of second-order spectra, with sharp first-order resonance peaks being seen against this background. We note that the Raman spectra of the $CdTiO_3$ single crystal are very similar to those of $CaTiO_3$ reported in [30], if it is considered that the latter were unpolarized.

As the sample is cooled, the intensity of the second-order bands decreases monotonically and the first-order lines narrow. Figure 5 shows a *yy* spectrum taken at 80 K, where seven narrow lines are seen against the still strong background of higher order Raman scattering. These narrow resonance lines can be identified with the predicted $7A_g$ phonon modes at the BZ center of the centrosymmetric orthorhombic unit cell of $CdTiO_3$ and are positioned at 99, 125, 194, 299, 390, 465, and 496 cm^{-1}. By comparing the *zz* and *yy* spectra in Fig. 5, the peaks at 115, 141, 303, 392, and 504 cm^{-1} can be assigned unambiguously to B_{2g} phonon modes. The other predicted B_{2g} peaks in the *zz* spectrum are close in frequency to the A_g lines in the *yy* spectrum and, there-

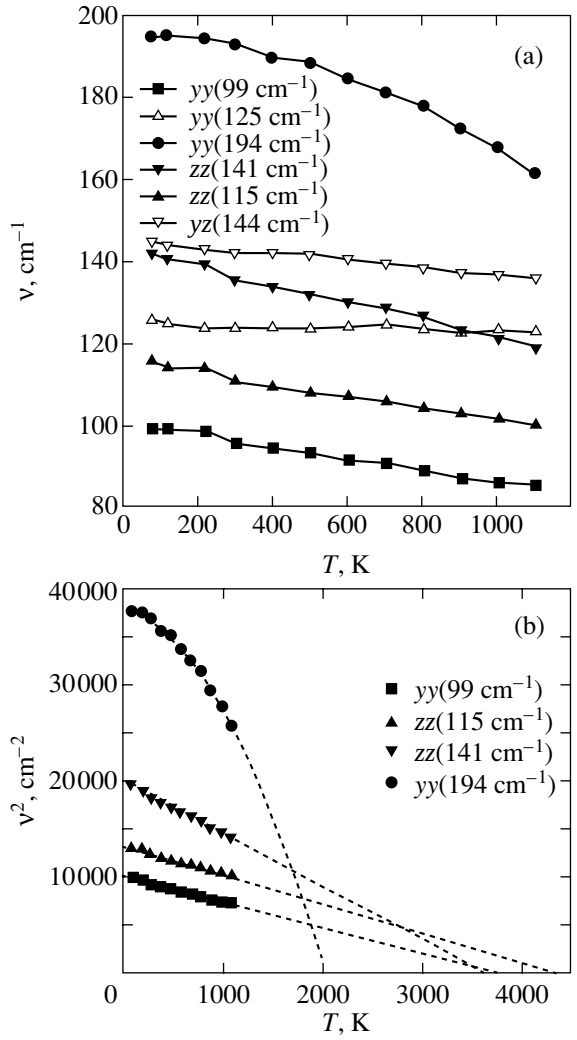

Fig. 8. Temperature dependences of (a) the frequencies and (b) the squares of the frequencies of the lowest frequency Raman lines from crystal $CdTiO_3$. By extrapolating the linear portions of the $\nu^2(T)$ curves, the temperatures of hypothetic second-order phase transitions are found to be $T_1 \approx 4350$ K and $T_2 \approx 3680$ K. For the 194-cm^{-1} mode, the $\nu^4(T)$ curve was extrapolated to obtain $T_3 \approx 2000$ K (panel b). The $\nu(T) = A(T_3 - T)^{1/4}$ dependence is typical of phase transitions close to the tricritical point.

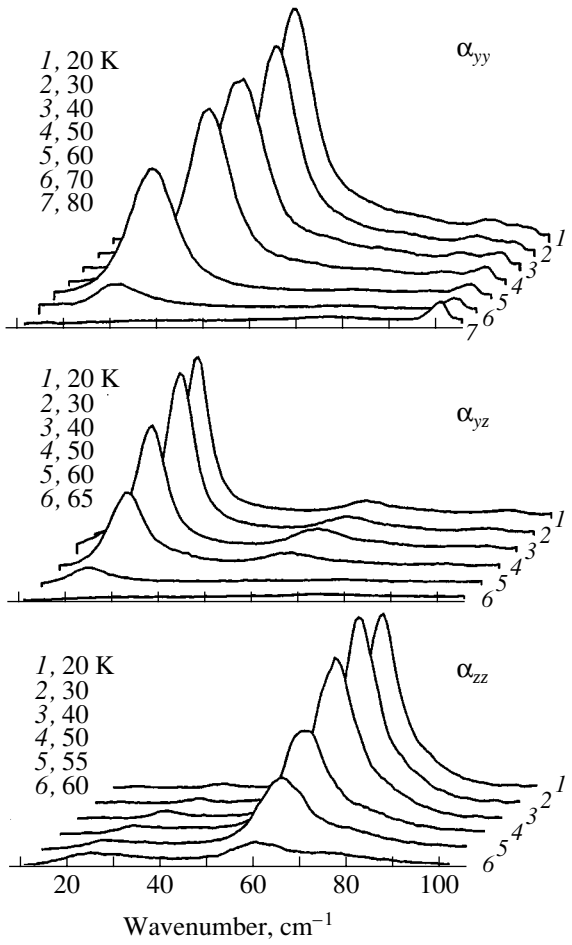

Fig. 9. Variations in the low-frequency Raman spectra with temperature decreasing from 80 to 20 K. New lines are seen to arise against the background of high-order Raman scattering.

fore, cannot be identified unambiguously due to possible small polarization distortions during measurements.

The *xy* and *yz* spectra are very similar but differ significantly in structure from the spectra corresponding to the other components of the Raman tensor (Fig. 4). According to factor-group analysis, the former spectra must contain five first-order lines of each symmetry type ($5B_{1g}$, $5B_{3g}$). However, reliable identification is hampered even at 80 K, because at this temperature there are six distinguishable resonances in both spectra (at 114, 144, 307, 346, 394, 478 cm^{-1}; Fig. 5). It should be noted that the weak peak at 114 cm^{-1} may be a leak from the very strong B_{2g} line. Certain of the B_{1g} and B_{3g} modes are very likely to be very close in frequency and cannot be resolved even at low temperatures because their profiles overlap. This conclusion was supported by recent *ab initio* calculations of the lattice dynamics of a related compound, $CaTiO_3$, in which lattice modes differing in symmetry were found to have very similar frequencies [30, 31]. Furthermore, it can be seen even visually that, e.g., the line peaked at 478 cm^{-1} has a complex structure, i.e., that it actually consists of several lines. The spectrum of the *yz* component of the Raman tensor was analyzed using Eq. (1), i.e., was fitted by a sum of damped harmonic oscillators. As a result, three independent lines were separated (at 459.3, 479.1, 509.4 cm^{-1}), whose combination fitted the experimental profile very closely. Attempts to resolve the other lines of these spectra within experimental error were not successful, and we identified them as singlets. Thus, eight out of the ten predicted B_{1g} and B_{3g} phonon modes were detected in the *xy* and *yz* spectra.

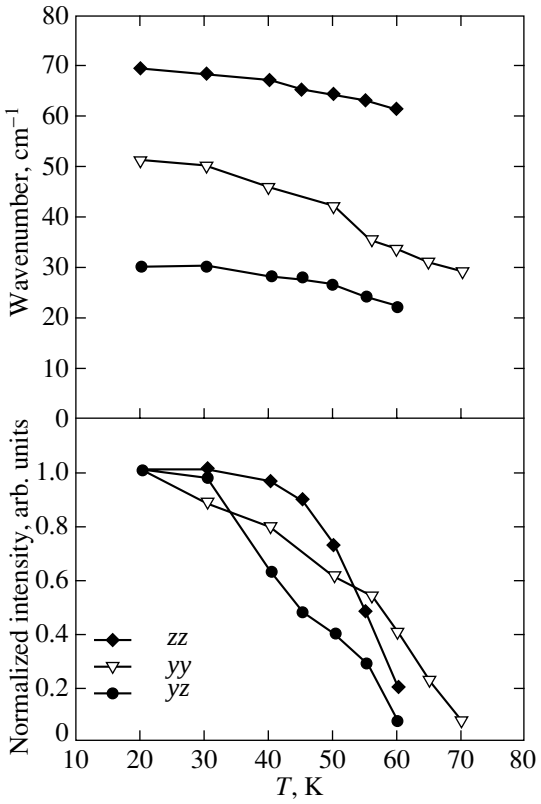

Fig. 10. Temperature dependences of the frequencies and integrated intensities (normalized to their values at T = 20 K) of the Raman lines shown in Fig. 9.

From the results presented above it follows that, despite the slight disagreement with the predictions from the factor-group analysis, the experimental polarized Raman spectra of $CdTiO_3$ are consistent with the *Pnma* symmetry of its crystal lattice.

4.2. The Temperature Dependence of the Raman Spectra

Figure 6 shows Raman spectra of $CdTiO_3$ taken at 1200 K. These spectra are also well polarized, as at lower temperatures, but now the second-order bands are dominant. Nevertheless, even at this temperature, the lowest frequency first-order lines remain relatively narrow in comparison with the high-frequency lines, which are almost obscured by the many-particle excitation continuum. Above 1200 K, the crystal surface begins to degrade, which makes observation of Raman spectra impossible; therefore, other methods should be applied to study the expected high-temperature phase transitions.

The temperature dependence of low-temperature Raman spectra taken at 100 to 1100 K is shown in Fig. 7. The lowest frequency first-order Raman lines are seen to shift noticeably to lower frequencies. The low-frequency A_g lines in the *yy* spectra are significantly broadened with sample heating, and the lowest two resonances become almost invisible in the spectra above 1000 K. It is significant that the temperature dependences of their frequencies are different (Fig. 8a). The lowest frequency peak shifts from 99 cm^{-1} at 100 K down to 85 cm^{-1} at 1100 K, whereas the frequency position of the maximum of the 125-cm^{-1} line remains practically unchanged over the same temperature range. The frequency shift is maximum for the 194-cm^{-1} line, which shifts down to 160 cm^{-1} at 1200 K. This behavior of the low-frequency modes certainly indicates that they are formed differently from phonon modes at the BZ boundary of the initial cubic structure, as shown in Fig. 3. The $\nu^2(T)$ dependences for these soft modes are plotted in Fig. 8b. The almost linear dependence of the square of the natural phonon frequency (ν_i^2) on $T - T_j$ typically indicates the occurrence of a second-order phase transition. Here, T_j is the temperature at which the phase transition occurs. Extrapolating the $\nu^2(T)$ dependences to high temperatures shows that there are three such temperatures (hypothetical high-temperature phase transitions). These temperatures are very high; they exceed the melting point of crystal $CdTiO_3$, so the corresponding phase transitions cannot be observed experimentally under conventional conditions.

In the centrosymmetric $CdTiO_3$ crystal with *Pnma* symmetry, the involvement of phonon modes in infrared absorption and Raman scattering is determined by the mutual exclusion selection rule. Therefore, the phonon modes differing in parity with respect to space inversion (*g*, *u*) cannot manifest themselves simultaneously in the experiments discussed above. The selection rules are broken if the crystal ceases to be centrosymmetric as a result of a phase transition to a lower symmetry phase belonging to a polar crystal class. In such ferroelectric phases, all modes are both infrared- and Raman-active. Therefore, we may expect that additional lines will appear in the first-order Raman spectra as a result of a ferroelectric phase transition. In the bottom panel in Fig. 3, two types of correlation between the irreducible representations for the D_{2h} and C_{2v} crystal classes are shown. The choice of the two space groups for the C_{2v} crystal class is based on the results of analyzing the available dielectric measurements [8, 10]. This issue will be discussed in greater detail in a later paper.

In recent infrared spectroscopic studies on calcium titanate $CaTiO_3$ [30], it was determined that the lowest frequency spectral lines correspond to three phonon modes (B_{1u}, B_{2u}, B_{3u}) that originate from the polar, threefold degenerate F_{1u} phonon mode at the BZ center of the cubic phase. The threefold degeneracy of this mode is lifted due to orthorhombic lattice distortions caused by a sequence of high-temperature phase transitions. Since $CaTiO_3$ and $CdTiO_3$ are similar in struc-

ture, it is natural to assume that the situation for $CdTiO_3$ is the same.

If cadmium titanate undergoes phase transitions to a polar state, then infrared-active B_{1u}, B_{2u}, and B_{3u} phonon modes must become Raman-active. This situation does indeed take place and is demonstrated in Fig. 9, where the lowest frequency range of the Raman spectrum is shown. In this range, no fist-order Raman lines were observed above 80 K. At lower temperatures, three new lines appeared and their frequencies reached fixed values of 50, 30, and 70 cm^{-1} at 20 K in the *yy*, *yz*, and *zz* spectra, respectively. The temperature dependences of the parameters of these lines are shown in Fig. 10. It is seen that, as the temperature decreases, the line intensities gradually increase almost from zero and their frequencies also increase, but from nonzero values. This behavior is typical of soft modes in the ferroelectric phase after a first-order phase transition. It is worth noting that the extrapolated temperature dependences of the integrated intensities intersect the temperature axis at different points corresponding to approximately 71 and 62 K. This fact indicates that at least two ferroelectric phase transitions in which the spontaneous polarization changes its direction occur over this narrow range (this issue is discussed in detail in [32]).

5. CONCLUSIONS

The polarized phonon Raman spectra of crystal $CdTiO_3$ have been taken and studied for the first time over the temperature range 10–1200 K. Full information on the Raman tensor components α_{ij} has been given, and symmetry identification of Raman lines has been performed.

The experimental Raman spectra have been shown to correlate well with the predictions from factor-group analysis, which allows us to conclude that $CdTiO_3$ does indeed belong to the *Pnma* (D_{2h}^{16}) space group over the temperature range 78–1200 K.

Studies of the Raman spectra at high temperatures have revealed the presence of fully symmetric modes (associated with a rotation of octahedra) whose behavior is typical of soft modes. The high-temperature extrapolation of their frequencies suggests that there is a sequence of three hypothetical phase transitions. The temperatures of these hypothetical phase transitions were found to exceed the melting temperature of cadmium titanate. Therefore, $CdTiO_3$ with $GdFeO_3$-type structure is stable up to the melting temperature. This conclusion agrees well with the *ab initio* calculations performed in [33].

Studies of the low-temperature Raman spectra have revealed new lines that appear below ~78 K. It was concluded that the symmetry of the crystal lattice reduces to the C_{2v} symmetry. Analysis of the Raman spectra and their comparison with infrared reflection spectra and dielectric measurements [32] have revealed multistage structural transformation of $CdTiO_3$ into different polar states.

ACKNOWLEDGMENTS

This study was supported by the Russian Foundation for Basic Research (project nos. 04-02-16228, 03-02-16720) and, in part, by grants of the President of the Russian Federation (projects NSh-2168.2003.2, NSh-1415.2003.2).

REFERENCES

1. M. E. Lines and A. M. Glass, *Principles and Applications of Ferroelectrics and Related Materials* (Clarendon, Oxford, 1977; Mir, Moscow, 1981).
2. G. A. Smolenskiĭ, Dokl. Akad. Nauk SSSR **70**, 405 (1950).
3. G. A. Smolenskiĭ, Zh. Tekh. Fiz. **20**, 137 (1950).
4. G. A. Smolenskiĭ, Dokl. Akad. Nauk SSSR **85**, 985 (1952).
5. E. Hegenbarth, Monatsber. Dtsch. Acad. Wiss. Berlin **1**, 411 (1959).
6. G. Martin and E. Hegenbarth, Phys. Status Solidi A **18**, K151 (1973).
7. P.-H. Sun, T. Nakamura, Y. J. Shan, Y. Inaguma, and M. Itoh, Ferroelectrics **217**, 137 (1998).
8. Y. J. Shan, H. Mori, H. Imoto, and M. Itoh, Ferroelectrics **270**, 381 (2002).
9. M. E. Guzhva, V. V. Lemanov, P. A. Markovin, and T. A. Shuplygina, Ferroelectrics **218**, 93 (1998).
10. M. E. Guzhva, V. V. Lemanov, and P. A. Markovin, Fiz. Tverd. Tela (St. Petersburg) **43**, 2058 (2001) [Phys. Solid State **43**, 2146 (2001)].
11. T. Sugai and M. Wada, Jpn. J. Appl. Phys. **18**, 1709 (1979).
12. H. El-Mallah, B. E. Watts, and B. Wanklyn, Phase Transit. **9**, 235 (1987).
13. Yu. V. Kabirov, M. F. Kupriyanov, Ya. Dets, and P. Wawzala, Fiz. Tverd. Tela (St. Petersburg) **42** (7), 1291 (2000) [Phys. Solid State **42**, 1329 (2000)].
14. H. F. Kay and J. L. Miles, Acta Crystallogr. **10**, 213 (1957).
15. S. Sasaki, C. T. Prewitt, J. D. Bass, and W. A. Schulze, Acta Crystallogr. C **43**, 1668 (1987).
16. H. D. Megaw, Proc. Phys. Soc. London **58**, 133 (1946).
17. B. J. Kennedy, C. J. Howard, and B. C. Chakoumakos, J. Phys.: Condens. Matter **11**, 1479 (1999).
18. V. M. Lebedev, Yu. N. Venevtsev, and G. S. Zhdanov, Kristallografiya **15**, 377 (1970) [Sov. Phys. Crystallogr. **15**, 318 (1970)].
19. V. V. Shvartsman, S. G. Prutchenko, E. D. Politova, and S. Yu. Stefanovich, Neorg. Mater. **36**, 875 (2000).
20. B. Koulboujev, M. Kupriyanov, and Yu. Kabirov, Ferroelectrics **269**, 261 (2002).
21. W. Cochran and A. Zia, Phys. Status Solidi **25**, 273 (1968).
22. K. S. Aleksandrov and J. Bartolome, Phase Transit. **74**, 255 (2001).

23. A. S. Knyazev, Yu. M. Poplavko, and V. P. Zakharov, Fiz. Tverd. Tela (Leningrad) **16**, 2215 (1974) [Sov. Phys. Solid State **16**, 1446 (1974)].

24. E. J. Baran and I. L. Botto, Z. Anorg. Allg. Chem. **448**, 188 (1979).

25. N. V. Porotnikov, O. I. Kondratov, and L. N. Margolin, Zh. Neorg. Khim. **33**, 1377 (1988).

26. A. V. Ulinzheev, V. G. Smotrakov, O. E. Fesenko, and V. V. Eremkin, Kristallografiya **30**, 1036 (1985) [Sov. Phys. Crystallogr. **30**, 604 (1985)].

27. B. E. Watts, H. Dabkowska, and B. M. Wanklyn, J. Cryst. Growth **94**, 125 (1989).

28. R. A. Cowley, Phys. Rev. A **134**, 981 (1964).

29. O. V. Kovalev, *Irreducible Representations of Space Groups* (Akad. Nauk Ukr. SSR, Kiev, 1961) [in Russian].

30. V. Zelezny, E. Cockayne, J. Petzelt, M. F. Limonov, D. E. Usvyat, V. V. Lemanov, and A. A. Volkov, Phys. Rev. B **66**, 224303 (2002).

31. E. Cockayne and B. P. Burton, Phys. Rev. B **62**, 3735 (2000).

32. B. P. Gorshunov, A. V. Pronin, I. Kutskov, A. A. Volkov, V. V. Lemanov, and V. I. Torgashev, Fiz. Tverd. Tela (St. Petersburg) **47** (3) (2005) (in press).

33. G. Fabricius and A. López Garcýa, Phys. Rev. B **66**, 233106 (2002).

Translated by Yu. Epifanov

Physics of the Solid State, Vol. 47, No. 2, 2005, pp. 347–351. Translated from Fizika Tverdogo Tela, Vol. 47, No. 2, 2005, pp. 334–338.

LOW-DIMENSIONAL SYSTEMS AND SURFACE PHYSICS

The Intrinsic Structure of Spherical Particles of Opal

I. A. Karpov, É. N. Samarov, V. M. Masalov, S. I. Bozhko, and G. A. Emel'chenko

Institute of Solid State Physics, Russian Academy of Sciences, Chernogolovka, Moscow oblast, 142432 Russia

e-mail: emelch@issp.ac.ru

Received April 27, 2004

Abstract—The intrinsic structure of spherical SiO_2 particles synthesized by hydrolysis of tetraethyl orthosilicate in an alcohol–water–ammonia medium was studied using transmission electron microscopy. It was established that the relatively large spherical silica particles were "tertiary" structures made up of smaller spherical particles ("secondary" particles), which in turn consisted of even smaller primary spherical particles 5–10 nm in diameter. It was shown that, under the experimental conditions, the large SiO_2 particles can contain a central core comprising primary particles surrounded by several layers of secondary particles smaller than the core diameter. © *2005 Pleiades Publishing, Inc.*

INTRODUCTION

In recent years, studies of nanostructures obtained by filling the regular arrays of voids in synthetic opals with a material have attracted more and more interest due to the prospects for using such materials in optoelectronics [1 – 3]. Monodisperse spherical particles of amorphous silica (SiO_2), from which the ordered packing in opal is formed, are themselves objects with a complicated fractal intrinsic structure [4–6]. Two methods of producing suspensions of silica nanoparticles are currently widely used, namely, growth from a water solution of sodium silicate (similar to the natural mechanism of opal particle growth [7]) and hydrolysis of tetraethyl orthosilicate (TEOS) in an alcohol–water–ammonia medium [8]. The latter method is more often applied in laboratories, because it enables one to obtain a more homogeneous size distribution of SiO_2 particles. The sizes and polydispersity of silica particles depend on the synthesis conditions, which include the concentrations of the components (TEOS, C_2H_5OH, H_2O, NH_4OH) and the order in which they are mixed, as well as the solution pH, the temperature at which the reaction proceeds, etc. The synthesis reaction itself includes the following stages: hydrolysis of TEOS, polymerization of molecular silicon dioxide, condensation of polymer clusters, and aggregation of primary SiO_2 nanoparticles into monodisperse colloidal particles of amorphous silica [9–16]. Because the number of parameters determining the conditions of synthesis of colloidal particles is large, the results obtained are widely scattered.

The majority of published results relate to the synthesis of SiO_2 colloidal particles at low (1- to 2-M) water concentrations. High water concentration in a solution causes primary seed particles to decrease in size, which results in narrow size distributions of particles provided they grow stepwise [9]. The water concentration not only influences the kinetics of the particle growth [17] but can also cause changes in the intrinsic structure of these particles. Several publications concerned with the structure of natural opal specimens [4, 18] have shown that spherical SiO_2 particles about 250 nm in diameter consist of smaller structures 10 to 20 nm in size. In a number of studies [5, 19–21], both the intrinsic structure of particles and the processes that take place during their production through the chemical reaction of TEOS hydrolysis are modeled. In [22, 23], the sizes of the structural units comprising a spherical opal particle are calculated and substantiated following from thermodynamic considerations. However, almost no experimental results of transmission electron microscopic observations of the intrinsic structure of opal particles have been presented to confirm those calculations. As regards particles greater than 300 nm in size, there are no experimental results relating to their structure in the literature.

The objective of the present work is to study, by means of transmission electron microscopy (TEM), the intrinsic structure of opal particles synthesized at high water concentrations (16–24 M).

EXPERIMENTAL

SiO_2 particles were synthesized by TEOS hydrolysis in water solutions of ethyl alcohol (the concentration of water was 16–24 M, the concentration of ammonia was 1–5 M, and the concentration of TEOS was 0.14 M) at 22°C.

The structure of the particles obtained was studied with a JEM-100CX transmission electron microscope. A suspension of silica particles was spread on a copper grid and then, after drying at room temperature, was introduced into the microscope column. In order to observe the intrinsic structure of large SiO_2 particles (about 1000 nm in diameter), specimens were prepared

1063-7834/05/4702-0347$26.00 © 2005 Pleiades Publishing, Inc.

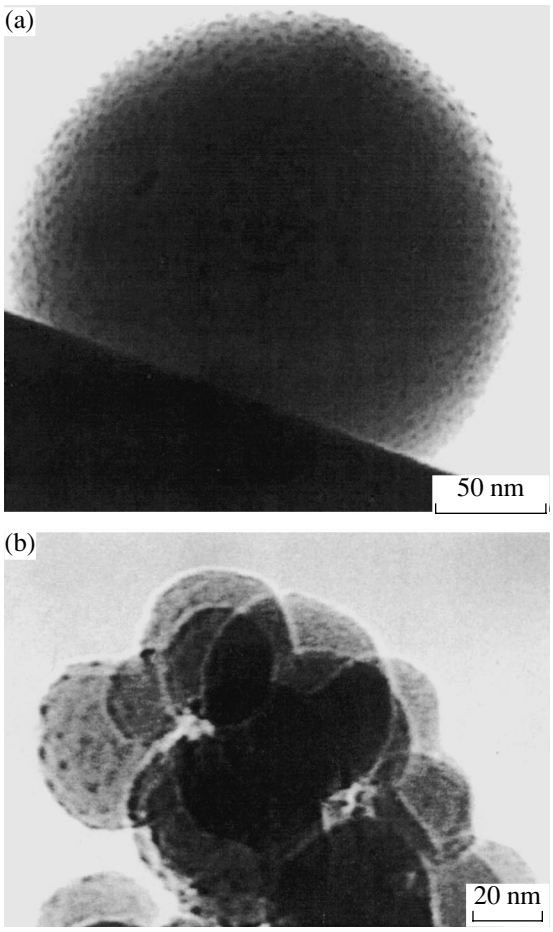

Fig. 1. TEM images of (a) an individual spherical SiO_2 particle 225 nm in diameter and (b) a druse of particles 20–40 nm in size.

by etching opal nanospheres in a 1% hydrofluoric acid solution for 20–30 s, followed by neutralization of the solution by 3% caustic potash and repeated washing off of the deposit in distilled water.

RESULTS AND DISCUSSION

Figure 1 shows images of SiO_2 particles spread from suspension on a copper grid and then introduced into the column of a transmission electron microscope without additional treatment. Images of a separate spherical particle 225 nm in diameter (Fig. 1a) and of a druse of particles 20–40 nm in diameter (Fig. 1b) show an intrinsic substructure of these particles with a period of 7–10 nm, which agrees well with the model of an aggregated (secondary) particle composed of smaller, primary SiO_2 particles suggested by researchers in studies on natural opals [4, 18]. Similar results were also obtained on specimens of synthetic opal [5]. The size of the primary particles depends on the synthesis conditions and changes in the range 5–20 nm [4, 21, 24].

From the thermodynamic point of view, as mentioned in [23], primary particles of silicon dioxide cannot have a diameter of larger than 20 nm; therefore, spherical silica particles larger than 20 nm in diameter are aggregated and consist of particles 5 to 20 nm in diameter, depending on the synthesis conditions. The same authors pointed out in [25] that secondary particles composed of primary particles also have an upper size limit (their maximum diameter was about 350 nm). This result suggests that the spherical particles of silicon dioxide of a larger diameter obtained by us (from 500 to 1500 nm) are "tertiary" and comprise smaller secondary particles whose diameter is less than 350 nm, and these structures, in turn, consists of even smaller, primary particles less than 20 nm in diameter.

TEM microphotographs of larger particles about 1000 nm in diameter show quite distinctly that the surface of these particles is composed of spherical particles ten times smaller in diameter than the particle they make up. The form of the large particles vaguely resembles a raspberry. Similar results were published in [5, 20, 26]. In those papers, however, only secondary particles consisting of primary particles were seen in the electron microphotographs. We managed to observe "tertiary" particles consisting of secondary particles, each of which looked like a raspberry, as it was composed of primary particles (Fig. 2), with the sizes of the primary and secondary particles falling in the range of sizes based on the thermodynamic considerations from [22, 23].

It should be noted that the intrinsic structure of spherical silica particles is not always revealed during electron microscopic examination. Sometimes, the surface of a large particle looks almost smooth and uniform (Fig. 3). Apparently, this could be possible for two reasons. First, when large particles are synthesized, in the solution there may be free ends of polymer siloxane chains whose aggregation generates a gel-like mass, which we often observed by electron microscopy along with SiO_2 spherical particles. This mass, as deposited on the surface of a growing large spherical particle, lutes all roughnesses of the surface, thus disguising the real structure of the large particle. This mechanism of particle formation with a smooth surface was suggested in [27]. Next, one can assume that, under certain synthesis conditions, large particles do not have a complicated intrinsic structure and are monolithic, gigantic primary particles. However, such a state of things does not seem very likely. It is more likely that large spherical silica particles have a smooth surface due to the silicic acid gel stuck to them.

In order to check this assumption, spherical particles 1000 nm in diameter prepared for TEM studies were briefly treated in dilute hydrofluoric acid in order to remove the upper layer of silica hydrogel stuck to them. Owing to this treatment, the actual surface structure of a large particle was disclosed, as can be seen from the electron microphotograph of a spherical particle of sil-

icon dioxide primarily etched in hydrofluoric acid given in Fig. 2. Therefore, particles 1000 nm in diameter, at least as regards the conditions of synthesis used in our study, had a smooth surface due to the silicic acid gel sticking to them rather than to their monolithic character.

The question arises as to whether a large tertiary particle that is about 1000 nm in diameter is composed of secondary spheres about 100 nm in diameter throughout its entire volume or if it contains a core of primary particles about 350 nm in diameter with which secondary spheres about 100 nm in diameter have aggregated. The possibility of silica particles having the latter structure also follows from an analysis of the electron microscopy images shown in [4], though the authors of that work did not pay attention to this fact. Sometimes, when large spherical particles of silicon dioxide etched in dilute hydrofluoric acid were studied by electron microscopy, the following picture was observed: under a thin spherical shell made of secondary particles about 100 nm in diameter, there was a hollow about 500 nm in diameter that was partly filled with a gel-like mass (Fig. 4). It should be noted that particles larger than 200 nm in diameter that are not treated in a hydrofluoric acid solution are not transparent to electrons accelerated by a voltage of 100 kV. However, when treated in hydrofluoric acid, even large particles 1100 nm in diameter become transparent to some extent (Fig. 4). We observed this effect many times.

It can be suggested that particles about 1000 nm in diameter (or at least some of them) have a core consisting of primary particles and that the core diameter is equal to that of the observed spherical hollow (about 500 nm). As a result of the treatment of tertiary particles in a hydrofluoric acid solution, the etchant penetrated into narrow pores of the core between the primary particles. After etching for 30 s, the etchant was neutralized and the spheres were repeatedly rinsed in distilled water. However, it is rather difficult to wash the etchant away from the narrow channels between the primary particles of a large core. Therefore, the etching process continues, with the result that the core turns into a gel-like mass, which partly fills the formed hollow. At the same time, in wide channels between secondary particles, which form the exterior spherical shell of the hollow, the etchant rapidly neutralizes. This is the reason why the structure is not etched as dramatically here.

It should be noted that not all tertiary particles had spherical hollows. The reason for this can be spatial inhomogeneity of the etching, as well as differences in the particle structures resulting from the synthesis conditions. One can assume that the presence or the absence of a core in large tertiary particles is dictated by the probability of secondary particles aggregating with each other and thus forming a tertiary particle. If this probability is high, there is almost no chance that secondary particles 100–150 nm in diameter will grow into large cores 500–600 nm in diameter with subsequent agglomeration of ordinary secondary particles on them as on the nucleus of growth. In the opposite case, the percentage of particles with a large core inside would

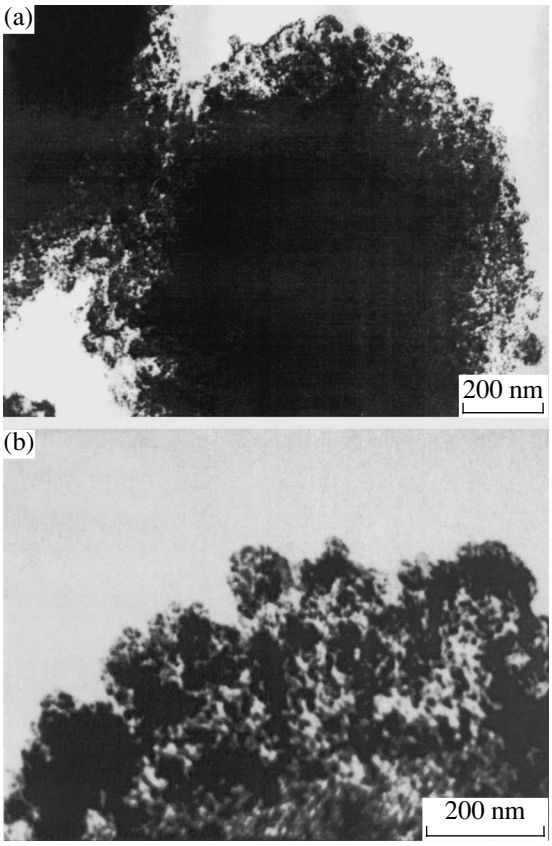

Fig. 2. (a) TEM image of a large SiO_2 particle about 1000 nm in diameter etched in a HF solution, and (b) a section of the same particle under a higher magnification, where the intrinsic structure of both tertiary and secondary particles is seen. The sizes of primary particles are 7–10 nm, and secondary particles are about 100 nm in size.

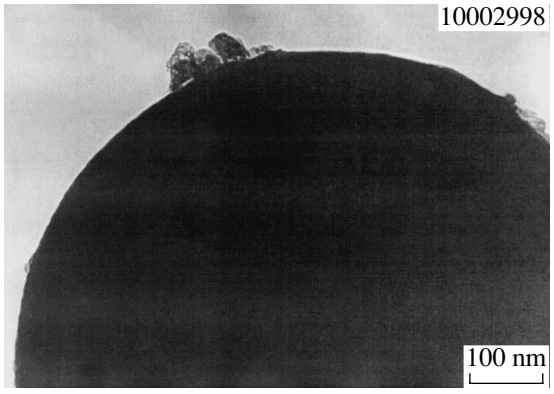

Fig. 3. Spherical opal particle with a smooth surface; its intrinsic structure is disguised by an amorphous mass of silica hydrogel.

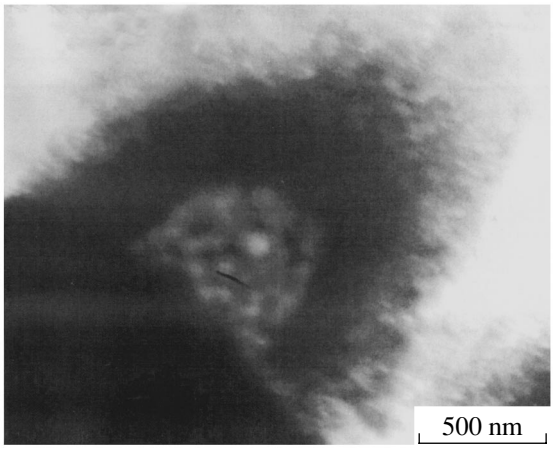

Fig. 4. TEM image of the inner hollow of a SiO_2 particle treated in a hydrofluoric acid solution.

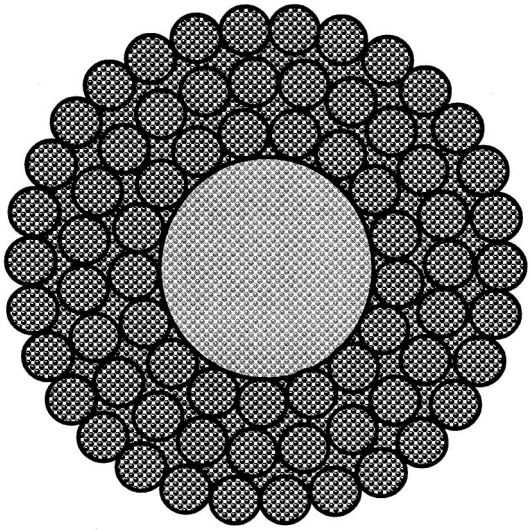

Fig. 5. Schematic structure of a large particle with a core. In the center, there is a large core composed of primary particles; the core is covered with several layers of secondary particles smaller than the core.

increase among tertiary particles. The probability of this agglomeration probably depends on the conditions of synthesis of the particles.

In summary, the experimental results suggest that large spherical SiO_2 particles contain a central core that is composed of primary particles and surrounded by several layers of secondary particles smaller than the core in size. The schematic structure of such a particle is shown in Fig. 5.

The existence of secondary particles 1000 nm in diameter seems unlikely. The existence of monolithic primary particles of such diameter seems even less probable, though, perhaps, one should not rule out this possibility. We have never observed such particles in our experiments.

4. CONCLUSIONS

By means of transmission electron microscopy, it has been shown for the first time that relatively large spherical silica particles (about 1000 nm in diameter) are composed of smaller spherical particles about 100 nm in diameter (secondary particles), which, in turn, are composed of even smaller, primary spherical particles 5–10 nm in diameter.

It has also been established that large SiO_2 particles can contain a central core that is composed of primary particles and surrounded by several layers of secondary particles smaller than the core in size.

It seems unlikely that secondary or primary particles about 1000 nm in diameter can exist, though the generation of such particles cannot be regarded as absolutely impossible if synthesis conditions different from those studied in this work are used.

ACKNOWLEDGMENTS

This work was supported by INTAS (project no. 2002-796), the Russian Foundation for Basic Research (project no. 04-02-97263), and the Ministry of Industry, Science, and Technology of the Russian Federation (contract no. 40.012.1.1.11.54).

REFERENCES

1. V. N. Bogomolov, Usp. Fiz. Nauk **124** (1), 171 (1978) [Sov. Phys. Usp. **21**, 77 (1978)].
2. V. N. Astratov, V. N. Bogomolov, A. A. Kaplyanskii, A. V. Prokofiev, L. A. Samoilovich, S. M. Samoilovich, and Yu. A. Vlasov, Nuovo Cimento D **17**, 1349 (1995).
3. T. F. Kraus and R. M. De La Rue, Prog. Quantum Electron. **23**, 51 (1999).
4. P. J. Darragh, A. J. Gaskin, B. C. Terrell, and J. V. Sanders, Nature **209** (5018), 13 (1966).
5. N. D. Deniskina, D. V. Kalinin, and E. I. Sysoeva, Geol. Geofiz. **28** (7), 87 (1987).
6. V. N. Bogomolov, L. S. Parfen'eva, A. V. Prokof'ev, I. A. Smirnov, S. M. Samoĭlovich, A. Jezowski, J. Mucha, and H. Miserek, Fiz. Tverd. Tela (St. Petersburg) **37** (11), 3411 (1995) [Phys. Solid State **37**, 1874 (1995)].
7. A. J. Gaskin and P. J. Darragh, U.S. Patent No. 3,497,367 (1970).
8. W. Stober, A. Fink, and E. Bohn, J. Colloid Interface Sci. **26**, 62 (1968).
9. G. H. Bogush, M. A. Tracy, and C. F. Zukoski, J. Non-Cryst. Solids **104**, 95 (1988).
10. G. H. Bogush and C. F. Zukoski, J. Colloid Interface Sci. **142**, 19 (1991).
11. J. K. Bailey and M. L. Mecartney, Colloids Surf. **63**, 151 (1992).

12. K. Lee, J. L. Look, M. T. Harris, and A. V. McCormick, J. Colloid Interface Sci. **194**, 78 (1997).
13. A. K. Van Helden, J. W. Jansen, and A. Vrij, J. Colloid Interface Sci. **81**, 354 (1981).
14. T. Shimohira and N. Tomuro, J. Jpn. Soc. Powder Powder Metall. **23** (4), 137 (1976).
15. H. Boukari, J. S. Lin, and M. T. Harris, J. Colloid Interface Sci. **194**, 311 (1997).
16. D. Pontoni, T. Naranyanan, and A. R. Rennie, Langmuir **18** (1), 56 (2002).
17. V. M. Masalov, E. N. Samarov, I. A. Karpov, and G. A. Emelchenko, in *Proceedings of ICSMC-2002* (Chishineu, 2002), Vol. 1, p. 50.
18. J. B. Jones and E. R. Segnit, Miner. Mag. **37** (287), 357 (1969).
19. L. K. Kazantseva, N. D. Deniskina, D. V. Kalinin, and N. G. Vasil'eva, Izv. Sib. Otd. Akad. Nauk SSSR, Ser. Khim. Nauk **6** (14), 104 (1983).
20. L. K. Kazantseva, D. V. Kalinin, and G. P. Panasyuk, Izv. Sib. Otd. Akad. Nauk SSSR, Ser. Khim. Nauk **6** (19), 124 (1987).
21. V. V. Serdobintseva, D. V. Kalinin, and S. V. Vosel', Geol. Geofiz. **39** (8), 1116 (1998).
22. S. V. Vosel' and D. V. Kalinin, Geol. Geofiz. **40** (4), 606 (1999).
23. S. V. Vosel', D. V. Kalinin, N. A. Rudina, and P. A. Purtov, Geol. Geofiz. **40** (6), 926 (1999).
24. R. K. Iler, *Chemistry of Silica: Solubility, Polymerization, Colloid and Surface Properties, and Biochemistry* (Wiley, New York, 1979; Mir, Moscow, 1982), Vol. 1.
25. D. V. Kalinin, S. V. Vosel', and V. V. Serdobintseva, in *Proceedings of X National Conference on Crystal Growth (NCCG-2002)* (Moscow, 2002), p. 571.
26. S. Reculusa, C. Poncet-Legrand, S. Ravaine, C. Mingotaud, E. Duguet, and E. Bourgeat-Lami, Chem. Mater. **14** (5), 2354 (2002).
27. M. T. Harris, R. R. Brunson, and C. H. Byers, J. Non-Cryst. Solids **121**, 397 (1990).

Translated by E. Borisenko

Physics of the Solid State, Vol. 47, No. 2, 2005, pp. 352–356. Translated from Fizika Tverdogo Tela, Vol. 47, No. 2, 2005, pp. 339–344.

LOW-DIMENSIONAL SYSTEMS AND SURFACE PHYSICS

Pentagonal Copper Crystals: Various Growth Shapes and Specific Features of Their Internal Structure

A. A. Vikarchuk and A. P. Volenko

Tol'yatti State University, Tol'yatti, 445667 Russia

e-mail: fti@tltsu.ru

Received January 29, 2004; in final form, May 19, 2004

Abstract—It is shown that at least eight types of copper crystals having one or six fivefold symmetry axes can form during electrodeposition. Their structures and the possible mechanisms of their formation and growth are considered. Different-type pentagonal crystals that form during electrodeposition are assumed to have the same disclination nature. © *2005 Pleiades Publishing, Inc.*

1. INTRODUCTION

Particles with pentagonal symmetry, which is forbidden by classic crystallography, have been extensively studied over the past several decades. The results of studies into the structure and properties of small particles with pentagonal symmetry that have been performed in the past fifty years are most completely presented and generalized in [1, 2]. Numerous investigations referred to in those reviews clearly indicate that there is great interest in these unique physical objects. Microcrystals with pentagonal symmetry forming in copper were detected in 1957 [3]. Pentagonal symmetry has been currently detected in almost all fcc metals during different-type crystallization. However, such crystals have maximum sizes upon electrolytic deposition [4, 5]. For example, we have succeeded in growing pentagonal crystals as large as 200–300 μm [5].

There are two substantially different approaches to explaining the formation of pentagonal crystals in electrodeposited fcc metals: in one approach, crystal growth is assumed to begin from two-dimensional nucleation centers, and in the other, from three-dimensional nucleation centers [6, 7]. There are also models proposed for pentagonal crystals that are produced by sputtering and consist of irregular decahedrons [8]. All these models conflict one another and cannot explain a number of new experimental findings [4, 5], in particular, the presence of rather large crystals with fivefold symmetry. These models were created without regard for the concepts of disclination. In [2, 9, 10], the disclination approach was used to analyze nonuniform elastic strains in small pentagonal particles and to describe their structure-sensitive properties. Disclinations were shown to be an intrinsic feature of pentagonal symmetry in small particles. However, as follows from energy considerations (i.e., irrespective of the formation mechanism), pentagonal small particles (PSPs) are stable only if their dimensions are less than a certain critical value (~100 nm) [9, 10]. In larger pentagonal crystals, which form upon electrolytic deposition and are sometimes three orders of magnitude larger than this critical size, the presence of disclinations is debatable.

In this work, we study the origin and the internal structure of relatively large pentagonal crystals that form during copper electrocrystallization and have different shapes with the aim of substantiating or refuting the disclination nature of such objects.

2. EXPERIMENTAL

To produce pentagonal crystals, as well as copper coatings and copper films from them, we used a standard addition-free sulfuric acid electrolyte for copper plating; the electrolyte was produced from twice-distilled products made of chemically pure components and contained 250 g/l $CuSO_4 \cdot 5H_2O$ and 90 g/l H_2SO_4. Copper was deposited at an electrolyte temperature of 20 to 50°C in the galvanostatic mode at i_c = 0.01–10 A/m^2 and in the current-reversal mode (the current density in the cathode pulses was i_c = 1–3 A/m^2, and that in the anode pulses was i_a = 0.4–1.0 A/m^2). As a substrate, we used polished stainless steel with a predeposited 10-μm-thick coating made from polycrystalline copper with ⟨110⟩ axial texture or from titanium nitride deposited by ion-plasma deposition. We assumed that the layer-by-layer mechanism of growth from two-dimensional nuclei would be realized on a substrate of the first type. Indifferent substrates of the second type should favor the formation of three-dimensional clusters. To this end, we also electrodeposited copper onto the (110) face of a copper single crystal and onto a platinum substrate.

To examine the structure and the surface morphology of the crystals and coatings produced, we applied transmission electron microscopy (PRÉM-200, UMV 100K), scanning electron microscopy (JSM-6500FE, Hitachi S-3500H), electron diffraction (ÉR-100), and metallography (MIM-7 and Axiotech optical micro-

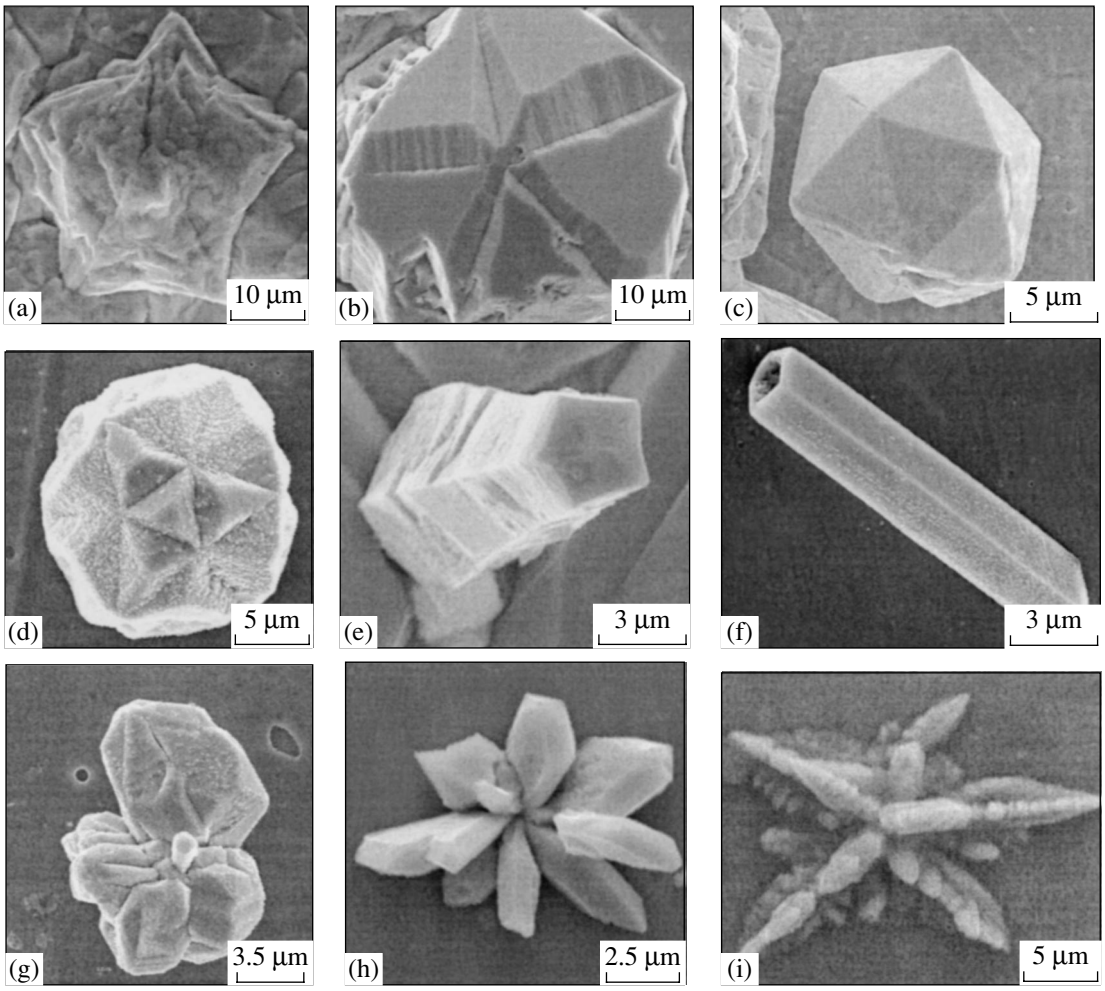

Fig. 1. Various shapes of copper crystals with pentagonal symmetry formed during electrodeposition.

scopes). Polished sections of coatings were made in the transverse direction from the electrolyte side and from the substrate side.

3. RESULTS AND DISCUSSION

By varying the conditions of electrodeposition and the substrate type, we grew pentagonal copper crystals having cross-sectional dimensions from 1 to 300 μm and different habit planes. At least eight types of crystals were grown differing in shape, size, and internal structure, with each type forming on a certain substrate in a rather narrow current-density range. Most of the relatively large pentagonal crystals were produced by electrodeposition for the first time.

In terms of their growth shape and size, the pentagonal crystals can be characterized as follows (d and l are the dimensions in the tangential and normal directions relative to the substrate, respectively):

(1) conelike crystals ($l/d \approx 2$–5) grown from two-dimensional nuclei formed on the (110) copper atomic planes (Fig. 1a);

(2) disklike crystals ($l/d \approx 0.2$–0.5) grown on an indifferent substrate presumably from three-dimensional decahedron clusters having one fivefold symmetry axis (Fig. 1b);

(3) crystals formed from two-dimensional icosahedral cluster nuclei ($l/d \approx 1$) that have six fivefold symmetry axes and are shaped like a buckyball (Fig. 1c) or a starlike polyhedron (Fig. 1d);

(4) filament crystals in the form of pentahedral prisms or whiskers ($l/d \approx 20$–100), which often form at substrate defects (Fig. 1e);

(5) crystals in the form of pentagonal tubes ($l/d \approx$ 20–100) (Fig. 1f) or pentagonal hollow screw-nuts ($l/d \approx 1$);

(6) five-leafed configurations ($l/d \approx 1$) (Fig. 1g), which are formed around a pentagonal prism and are likely to form from decahedron particles;

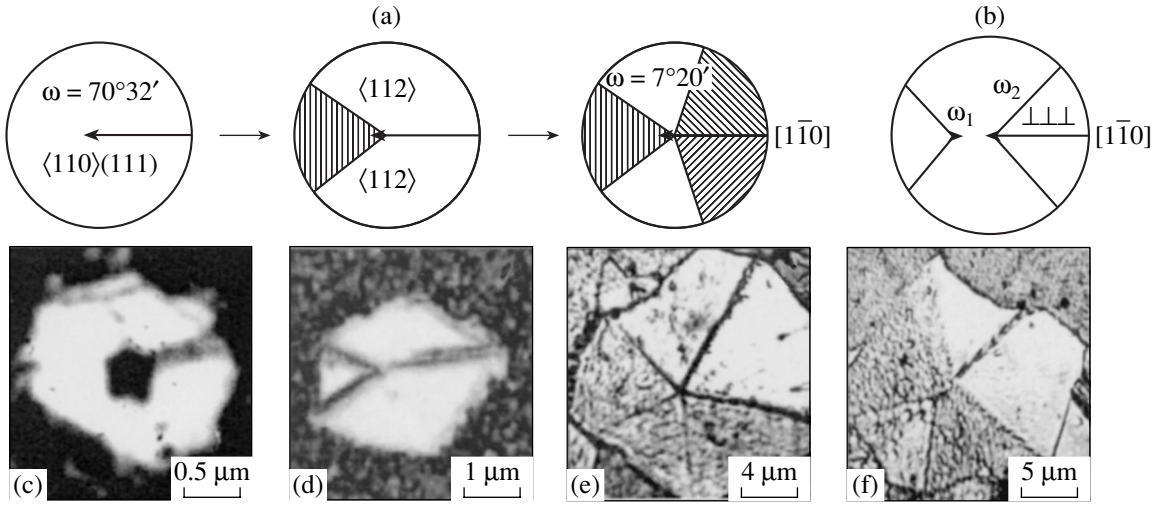

Fig. 2. (a) Schematic diagram and (c–e) the disclination mechanism of formation of pentagonal crystals from two-dimensional nucleation centers. (b) Schematic diagram and (f) a micrograph in which a node with five twin boundaries converging to it is seen to split into two nodes and emit dislocations.

(7) "hedgehog" crystals ($l/d \approx 1$), which are likely to form from icosahedral cluster nuclei (multileafed configurations) (Fig. 1h); and

(8) dendrites with pentagonal symmetry ($l/d \approx 0.2$–0.5), which are formed at a relatively high current density (high growth rate) (Fig. 1i).

We assume that all the crystals formed from one nucleation center and have one or six fivefold symmetry axes. The crystals are characterized by twin subboundaries and the tendency toward self-organization during growth. Let us consider the structure and possible mechanisms of formation of the first five types of pentagonal crystals.

Conelike fivefold crystals (Fig. 1a) grow from two-dimensional crystalline nuclei formed on the {110} atomic planes of a copper single crystal or on a polycrystalline copper coating with ⟨110⟩ texture. These crystals are extended along the ⟨110⟩ direction. Electron diffraction patterns indicate that sector boundaries in the crystals are twinned; four of them are normal to the (110) plane, and one is tilted at an angle of 35°16′ to this plane [4, 11]. The model of formation of such crystals is described in detail in [4]. According to this model, a microcrystal is formed on the {110} atomic plane of a copper crystal from two-dimensional nuclei. The crystal contains a broken <110>(111) twin boundary tilted with respect to the substrate, which has a growth origin and is equivalent to a partial disclination of strength ω = 70°32′ with regard to its elastic stress field (Fig. 2a). The growth of the crystal with a partial disclination creates energy and kinetic prerequisites [4, 11] for twinning on two {111} planes normal to the (110) plane; during twinning, part of the elastic energy relaxes. Twinning results in reorientation of the unhatched part of the crystal in Fig. 2a and creates conditions for further twinning along two more {111} planes. The crystal becomes divided into five sectors separated by twin boundaries that converge to a 7° partial disclination. One of the boundaries originated from growth and is tilted to the substrate plane. The other four boundaries form due to deformation during the subsequent crystal growth (they are normal to the substrate). Under these conditions, the energetically favorable transformation of a 70° partial disclination into a 7° disclination with five outgoing twin boundaries ($E_{70} \longrightarrow E_7 + 5\gamma_{111}$) occurs [12]. This mechanism is confirmed by micrographs (Figs. 2c–2e) taken from different crystals and demonstrating the transformation stages.

Convincing experimental evidence supporting the disclination origin of the pentagonal crystal during its growth in the course of electrocrystallization is the observation that the node where the five twin boundaries converge splits into two nodes (Fig. 2f). The disclination energy in the crystal depends on its size R and the Frank vector ω ($E \sim \omega^2 R^2$); therefore, it is energetically favorable for the 7° partial disclination (ω = 7°20′) to split into two disclinations ($\omega^2 > \omega_1^2 + \omega_2^2$) and emit dislocations along one of the {111}⟨110⟩ interfaces (Fig. 2b). When the initial disclination splits, the products of splitting become closer to the free crystal surface. The displacement of the partial-disclination axis requires the emission of a dislocation, which decreases the twin-boundary length and, eventually, the elastic energy of the system. The appearance of a pentagonal etching pit at the periphery of a broken twin boundary and the stage character of twinning in the microcrystal also indicate the presence of a high-energy defect—7° partial disclination (Figs. 2c, 2d).

All other types of pentagonal crystals (Figs. 1b–1i) were produced on structureless, indifferent substrates

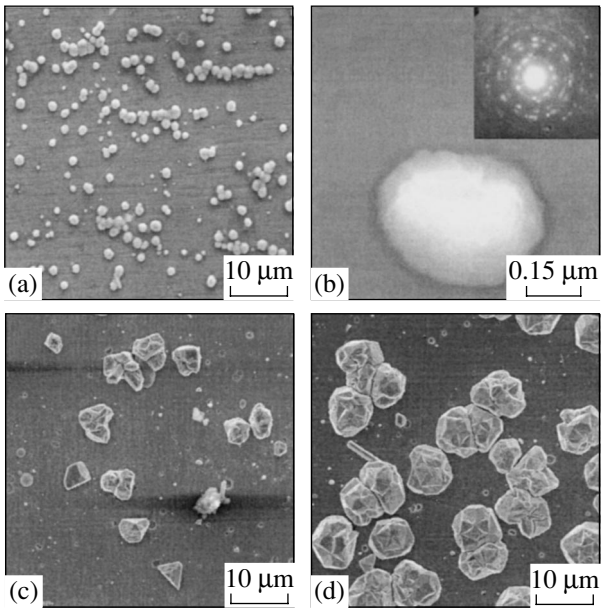

Fig. 3. Kinetics of growth of pentagonal crystals from noncrystalline islands on an indifferent substrate.

by varying the cathode overvoltage η, which characterizes the deviation of the cathode potential φ from its equilibrium value φ_0 ($\eta = \varphi - \varphi_0$) during electrocrystallization. Electron-microscopic studies (Fig. 3) show that crystal growth on such substrates always starts from spherical or semispherical noncrystalline islands, which are clearly visible in micrographs when the islands are larger than 100 nm (Fig. 3b) [5]. When the islands reach a certain critical size (0.5–1.5 μm), they acquire facets and transform into microcrystals that differ in shape (habitus) (Fig. 3c). During growth to 3–5 μm, only microcrystals that have an icosahedral, decahedral, or star-polyhedron shape and contain twin boundaries inside develop predominantly (Fig. 3d). As a result, the spherical islands grow into microcrystals with different shapes and, then, into two-type pentagonal crystals with one or six fivefold symmetry axes (Figs. 1b–1d).

Let us consider a possible mechanism of formation of pentagonal crystals with one fivefold symmetry axis (Fig. 1b). We assume that, at low overvoltages ($\eta = 10^{-3}$ V), three-dimensional clusters with a decahedral atomic arrangement first form on the indifferent substrate (Fig. 4a). It has been proved that small decahedral or icosahedral particles are more stable than ordinary crystalline nucleation centers and that the spherical shape is energetically favorable for small particles [2]. In our case, spherical growing islands that have noncrystalline atomic arrangements form from three-dimensional decahedral clusters (Figs. 4a, 4b). In the next growth stage, atoms in the islands are regrouped from a noncrystalline decahedral structure into a crystalline structure with a defect in the form of a $\pi/3$ disclination (Fig. 4c). This transformation is facilitated by a relatively low disclination energy in crystals that are smaller than 0.1 μm, by a high internal pressure due to surface tension and a small island radius, and by a decrease in the surface energy caused by island faceting.

When the microcrystal size increases to 1–3 μm, the elastic energy related to the defect relaxes via step-by-step twinning. The disclination with a strength $\omega = \pi/3$ transforms into a 7°20′ partial disclination and five similar twin boundaries converging to this disclination (this is energetically favorable, since $E_{60} > E_7 + 5\gamma_{111}$) (Fig. 4d). Figures 4a–4d show the scheme of formation and growth of a perfect pentagonal crystal with one fivefold symmetry axis (Fig. 1b) from a decahedral cluster at low overvoltages. The presence of dihedral grooves at the twin boundaries (Fig. 1b) favors more intense growth of the pentagonal crystals than any other crystals and the formation of regular decahedral disks from them.

If the cathode overvoltage increases to 5×10^{-3} V, the decahedral shape of the growing copper crystals is distorted. Under these conditions, the crystals grow predominantly along twin boundaries and fivefold axes. Thus, a 1-μm dodecahedral microcrystal grows into a five-leafed 10–15 μm configuration (Fig. 4e). Each leaf contains a twin boundary, and all the leaves are arranged around one common crystallization center in the form of a pentagonal prism (Fig. 1g). As the overvoltage is increased still further ($\eta \approx 10^{-2}$ V), dendrites with pentagonal symmetry can also form (Fig. 1i).

We sometimes detected individual pentagonal filament crystals in the form of pentahedral whiskers or prisms extended along the ⟨110⟩ direction. As a rule, they are faceted from above by five octahedral planes converging to the symmetry axis (Fig. 1e). The crystal length can be as long as several tens of microns at a cross-sectional dimension of 1–10 μm, and the crystals

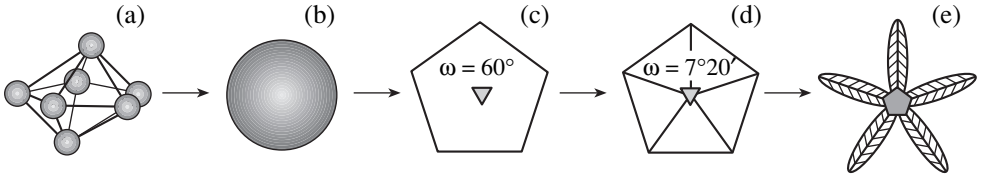

Fig. 4. Schematic diagram of the transformation of a noncrystalline island into a pentagonal crystal having one fivefold symmetry axis.

grow via discrete sequential attachment to a crystal of pentagonal layers ("terraces") growing parallel to the substrate. This process is most pronounced for prisms (Fig. 1e). The coordinated terrace growth and the retained growth direction indicate that the layer attachment is coordinated and that there is a structural relation between the attached layers and the genetic origin of this growth. The origin is likely also the partial disclination of strength $\omega = 7°20'$ and five twin boundaries converging to it.

Apart from the whiskers and prisms, we also detected copper pentagonal tubes ($l/d \approx 20$–100), formed during copper deposition (Fig. 1f), and their modifications, namely, pentagonal hollow screw-nuts ($l/d \approx 1$). The appearance of a cavity inside a filament crystal was predicted earlier in [13] from disclination concepts regarding its structure.

Therefore, the transformation shown schematically in Fig. 4 can be used to explain the fact that pentagonal crystals of types *2, 4, 5, 6,* and *8* with one fivefold axis form during copper electrocrystallization (Figs. 1b, 1e–1g, 1i).

Energetically, an even more favorable event is the formation of three-dimensional nucleation centers in the form of icosahedral clusters on an indifferent substrate during electrocrystallization [2, 9]. They are likely to serve as centers for the formation of pentagonal crystals with six fivefold symmetry axes shaped like buckyballs (Fig. 1c), starlike polyhedrons (Fig. 1d), or (at higher overvoltages) hedgehogs (Fig. 1h). A polished cross section of a buckyball or a starlike polyhedron contains ten twin boundaries converging to one node (Figs. 1c, 1d). When a polished section is etched, a pentagonal pit appears at the center of such crystals, which indicates the presence of a possible disclination [5].

According to [9], growing icosahedral buckyballs or starlike polyhedrons (Figs. 1c, 1d) should contain six partial disclinations or the so-called Marx–Ioffe disclination with strength $k = 0.12$ in order to conserve the integrity of the material and to remove the angular deficit [14]. Due to the six fivefold symmetry axes, there are twelve disclination exits on the surface of a pentagonal crystal (Figs. 1c, 1d) that are active growing zones. Since the crystal is on a substrate, not all of the growth directions are realized in practice, especially at high overvoltages; for this reason, hedgehogs are observed that consist of seven to ten radial fragments arranged around one growth center (Fig. 1h). Each fragment contains a twin boundary and is extended along the <112> twinning direction, which is the direction of predominant growth in fcc metals.

Thus, the disclination origin of all eight types of pentagonal crystals is beyond question and the models of their growth from two-dimensional nucleation centers and decahedral clusters are reasonable. However, the growth mechanism of crystals with six fivefold symmetry axes during electrocrystallization is still unclear.

Further investigation of crystals with fivefold symmetry axes will allow one to solve some problems in the theory of strength and plasticity, such as the effect of single disclinations on the properties of solids; to check theoretical models of the relaxation of the elastic energy related to disclinations; to reveal the mechanisms of formation and growth of such crystals; to design processes of their growth; and to produce coatings made from these crystals.

Fivefold symmetry crystals have unique properties, since they have no long-range order. They contain disclinations and twin boundaries. In such crystals, translational dislocation glide is prohibited and the crystals exhibit a texture and, hence, highly anisotropic properties. It is natural to assume that coatings, films, and foils made up of such crystals should also have unique properties due to the specific features of their structure. Therefore, studying exotic pentagonal crystals and quasicrystalline structures is of current importance and is of interest from both the scientific and practical standpoint, since it opens up fresh opportunities for the creation of new materials with unique properties. In particular, pentagonal crystals in the form of tubes, hedgehogs, or dendrites (Figs. 1f, 1h, 1i) have a developed free surface and, hence, can be applied for the production of blood purification filters, vessels for liquefied gases, catalysts, etc.

REFERENCES

1. H. Hofmeister, Cryst. Res. Technol. **33** (1), 3 (1998).
2. V. G. Gryaznov, I. Heidenreich, A. M. Kaprelov, S. A. Nepijko, A. E. Romanov, and I. Urban, Cryst. Res. Technol. **34** (9), 1091 (1991).
3. J. Segall, J. Met. **9**, 50 (1957).
4. A. A. Vikarchuk and A. Yu. Krylov, in *Proceedings of the XXXVI International Conference on Actual Problems of Strength* (Vitebsk, 2000), Vol. 2, p. 458.
5. A. A. Vikarchuk, A. P. Volenko, and I. S. Yasnikov, Tekh. Mashinostr., No. 3, 29 (2003).
6. N. A. Pangarov, in *Crystal Growth* (1974), Vol. 10, p. 71.
7. M. Froment and C. Mourin, J. Microsc. **7**, 39 (1968).
8. S. Ino and S. Ogawa, J. Phys. Soc. Jpn. **22**, 1365 (1967).
9. V. G. Gryaznov, A. M. Kaprelov, and A. E. Romanov, in *Disclination and Rotational Deformation of Solids* (Fiz.–Tekh. Inst., Leningrad, 1986), p. 47 [in Russian].
10. V. A. Likhachev, A. E. Volkov, and V. E. Shudegov, *Continual Theory of Defects* (Leningr. Gos. Univ., Leningrad, 1986) [in Russian].
11. A. A. Vikarchuk, Tekh. Mashinostr., No. 1, 42 (2002).
12. R. de Wit, J. Phys. C: Solid State Phys. **5**, 529 (1972).
13. A. E. Romanov, L. A. Polonsky, V. G. Gryaznov, S. A. Nepijko, T. Junghaus, and N. I. Vitrykhovski, J. Cryst. Growth **129** (3), 691 (1993).
14. V. G. Gryaznov, A. M. Kaprelov, A. E. Romanov, and L. A. Polonskii, Phys. Status Solidi B **167** (2), 441 (1991).

Translated by K. Shakhlevich

Physics of the Solid State, Vol. 47, No. 2, 2005, pp. 357–361. Translated from Fizika Tverdogo Tela, Vol. 47, No. 2, 2005, pp. 345–349.

LOW-DIMENSIONAL SYSTEMS AND SURFACE PHYSICS

Spin–Orbit Interaction and Two-Dimensional Weak Localization in a Carbon Matrix with Cobalt Nanoclusters

Yu. A. Bumaĭ*, I. A. Bashmakov, S. M. Lukashevich**, T. F. Tikhonova**, and M. G. Lukashevich****

** Belarussian National Technical University, Minsk, 220027 Belarus*

*** Belarussian State University, pr. F. Skoriny 4, Minsk, 220050 Belarus*

e-mail: Lukashevich@bsu.by

Received May 20, 2004

Abstract—The magnetic-field dependence of the magnetoresistive effect in carbon fibers that contain cobalt nanoclusters and exhibit effects of weak localization at low temperatures ($T < 45$ K) is investigated on the metal side of the dielectric–metal transition. The carbon fibers are prepared by heat treatment of carboxylated cellulose after the substitution of cobalt cations for protons of COOH groups. It is found that, under conditions of two-dimensional weak localization at temperatures below 10 K, the carbon fibers possess an alternating magnetoresistance due to spin–orbit scattering of electrons by cobalt nanoclusters. The time of phase breaking of the wave function and the time of spin–orbit scattering are determined from a comparison of the experimental and theoretical magnetic-field dependences of the electrical resistance. © *2005 Pleiades Publishing, Inc.*

1. INTRODUCTION

Over the two past decades, the mechanisms of conduction in low-dimensional electronic systems have been extensively studied by experimental and theoretical methods. Two aspects of this problem are especially important for the case of electron transfer in weakly disordered systems: (i) inclusion of the processes of weak localization that depend on the dimensionality of the system and are caused by the quantum interference of electron waves [1, 2] and (ii) inclusion of the electron–electron interactions occurring in the system [3, 4]. These effects have been investigated in sufficient detail for two-dimensional systems, such as thin metallic films [5], inversion layers, and heterostructures based on semiconductors [6, 7]. One of the decisive factors responsible for the processes of weak localization in these systems is associated with strong spin–orbit interactions upon scattering of free charge carriers [5–7].

In our opinion, the quasi-two-dimensional nature of electron conduction can also manifest itself in carbon compounds with a turbostratum graphite-like structure. As a rule, these materials have been prepared by heat treatment at temperatures above 2000°C. It is worth noting that, in carbon materials with a turbostratum graphite-like structure, the electrical conductivities measured parallel and perpendicular to graphite layers can differ significantly (by a factor of 10^4 or greater) [8]. This anisotropic conduction is favorable for the formation of planar self-intersecting trajectories of conduction electrons, which, in turn, gives rise to interference phenomena.

In our previous work [9], we established that the cobalt nanoclusters formed through heat treatment of carboxylated cellulose fibers under vacuum after the substitution of cobalt cations for protons of COOH groups have a catalytic effect on the structuring of the carbon matrix with the formation of graphite planes. In this case, the cobalt salt of carboxylated cellulose is subjected to final heat treatment at a temperature T_F ranging from 700 to 900°C, which is considerably lower than the graphitization temperature of cellulose fibers [10]. By varying the cobalt concentration in initial fibers and performing heat treatment under specific conditions with preliminary annealing in air at a temperature T_P lying in the range from 250 to 300°C, it is possible to prepare carbon fibers that contain inclusions of cobalt nanoclusters, correspond to both sides of the dielectric–metal transition [11], and are characterized by low-dimensional effects of electron transfer.

The main objective of the present work was to investigate the spin–orbit interaction in cobalt-containing carbon fibers that form a disordered electronic system on the metal side of the dielectric–metal transition with an anomalous temperature dependence of the electrical resistance in the low-temperature range. Moreover, we determined the most important characteristic times of quantum interference of electron waves, namely, the time of phase breaking of the wave function upon inelastic scattering and the time of spin flip due to elastic spin–orbit scattering, which are responsible for the weak localization effects.

2. EXPERIMENTAL TECHNIQUE

The temperature dependences of the electrical resistance were measured in the temperature range $T = 2$–

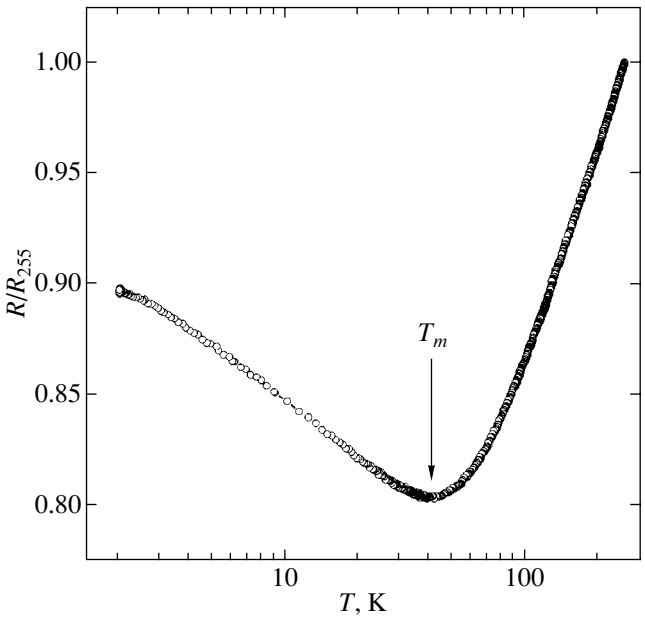

Fig. 1. Temperature dependence of the electrical resistance normalized to the resistance at $T = 255$ K for the Co_xC_{1-x} ($x = 0.19$) carbon fiber annealed at $T = 900$°C.

300 K. The magnetoresistive effect was investigated in the range corresponding to a linear portion of the current–voltage characteristic in the magnetic field of a superconducting solenoid with an induction of up to 1.2 T under conditions of an increase and decrease in the magnetic field strength. The synthesis of cobalt-containing carbon fibers; the sample preparation; the experimental technique; and the structural, transport, and magnetic characteristics of samples on the dielectric and metal sides of the dielectric–metal transition were described earlier in [9, 11].

3. RESULTS AND DISCUSSION

Figure 1 shows the temperature dependence of the electrical resistance of Co_xC_{1-x} ($x = 0.19$) carbon fibers prepared upon preliminary annealing in air at T_P = 300°C for 1 h with subsequent annealing under vacuum at T_F = 900°C. It can be seen from Fig. 1 that the electrical resistance of these fibers corresponds to the metal side of the dielectric–metal transition, because their temperature coefficient of resistance remains positive down to temperatures at which the temperature dependence of the electrical resistance exhibits a minimum ($T_m \cong 45$ K). At lower temperatures, the temperature coefficient of resistance reverses sign. The minimum in the temperature dependences of the electrical resistance appears after preliminary annealing in air for a time t = 0.5–1.0 h. The temperature corresponding to the minimum resistance only slightly depends on the time of annealing in air and lies in the range T_m = 45–50 K. It should be noted that, upon annealing in air for a time longer than 1 h, the minimum in the temperature dependence of the electrical resistance disappears and the resistance reaches saturation at low temperatures. As the temperature of annealing under vacuum decreases, the temperature coefficient of resistance becomes positive in sign over the entire temperature range under investigation. This corresponds to the dielectric side of the dielectric–metal transition.

According to modern concepts, the change in the sign of the temperature coefficient of resistance on the metal side of the dielectric–metal transition at low temperatures is caused by the processes of weak localization and (or) electron–electron interactions. It should be noted that the type of temperature dependence of the electrical resistance is governed by the dimensionality of the system. As can be seen from Fig. 1, the temperature dependence of the electrical resistance in the low-temperature range ($T < T_m$) is virtually linear on a logarithmic scale. This indicates that the charge transfer has a two-dimensional character (with respect to the aforementioned processes) [1–5]. By choosing the type of temperature dependence of the electrical conductivity from the known theoretical dependences for quantum corrections to the conductivity [1–4] and fitting them to the experimental data, we obtained an equation that adequately describes the experimental temperature dependence of the conductivity at $T < T_m$:

$$\sigma(T) = \sigma_D + A_0 T^{1/2} + A_1 \ln(T/T_0). \qquad (1)$$

Here, σ_D is the classical Drude conductivity and A_0, A_1, and T_0 are constants ($A_0 = 0.018$, $A_1 = 0.049$). It can be seen that the logarithmic term is dominant in relationship (1). Such a temperature dependence of the quantum corrections to the classical conductivity suggests that the localized processes with the participation of electron–electron interactions have a three-dimensional character [the second term in relationship (1)], whereas the processes of weak localization for noninteracting electrons show a two-dimensional character [the third term in relationship (1)]. It can also be seen from Fig. 1 that the temperature dependence of the electrical resistance at the lowest temperatures deviates from the logarithmic law (toward lower resistances). In our opinion, this behavior is associated with the manifestation of spin–orbit scattering, which results in the suppression of interference effects, i.e., in the phenomenon of antilocalization [5].

It should be noted that the two-dimensional processes of weak localization are not typical of large-sized carbon samples (three-dimensional systems), including our fibers that were approximately 0.5 mm in diameter and 5–6 mm in length. However, Carl *et al.* [12] and Peng *et al.* [13] observed similar temperature dependences of the electrical resistance for other heterogeneous carbon systems containing metal nanoclusters.

According to our earlier results [9] obtained with the use of transmission electron microscopy, the size of cobalt clusters at the heat treatment temperatures used in the experiments varies from ~30 to 200 nm or

greater. It was established that the cobalt nanoclusters are separated by carbon interlayers and that the most pronounced structuring of the carbon matrix in the form of graphite planes with an interplanar distance d = 0.37 nm is observed in the immediate vicinity of the nanocluster. However, the interplanar distances that are somewhat larger than the interplanar distance of pyrolytic carbon are characteristic of strongly disordered carbon fibers. Since the cobalt nanoclusters are separated by carbon interlayers, the two-dimensional nature of conduction in these fibers under conditions of weak localization can be associated with a carbon component in the form of a layer composed of turbostratum graphite planes between the cobalt nanoclusters. The conductivity of this layer is only slightly dependent on the temperature. For lower cobalt contents in the initial fibers and for fibers containing no cobalt nanoclusters, the electrical resistance increases by several orders of magnitude upon cooling from room temperature to liquid-helium temperature and is described by an exponential dependence characteristic of the tunneling and hopping mechanisms of charge transfer.

The magnetic-field dependences of the transverse magnetoresistance at different temperatures for opposite directions of the magnetic field are plotted in Fig. 2. Despite the presence of magnetic nanoclusters in the cobalt-containing carbon fiber, the magnetic-field dependences of the transverse magnetoresistance do not exhibit hysteresis phenomena typical of giant magnetoresistive effects. This also indicates that conduction over the graphite-like matrix is dominant. As the magnetic field increases, the resistance of the cobalt-containing carbon fiber at the lowest temperature (Fig. 2, curve *1*) initially increases and reaches a maximum at a magnetic-field induction $B \approx 0.08$ T. With a further increase in the magnetic field, the positive magnetoresistance component decreases and becomes negative at $B > 0.3$ T. As can be seen from Fig. 2, the positive magnetoresistance component decreases with an increase in the temperature and the magnetoresistive effect becomes negative at temperatures $T > 4$–5 K. Furthermore, the magnitude of this effect decreases rapidly with an increase in the temperature at $T > 10$ K (Fig. 2, curves *2*–*4*). It should be noted that, at these temperatures, the carbon fibers with a substantially higher cobalt content, for which the temperature dependence of the electrical resistance does not have a minimum (i.e., no processes of weak localization occur), and the samples with a resistance corresponding to the dielectric side of the dielectric–metal transition exhibit hysteresis phenomena in the magnetoresistance with coercive forces $B_c \cong 0.08$ and $B_c \cong 0.125$ T, respectively. According to the magnetic measurements performed earlier in [9], the carbon fibers annealed at T_F = 900°C are characterized by a coercive force $B_c \cong 0.043$ T at room temperature.

This alternating magnetoresistive effect, which is observed under conditions of weak localization at low

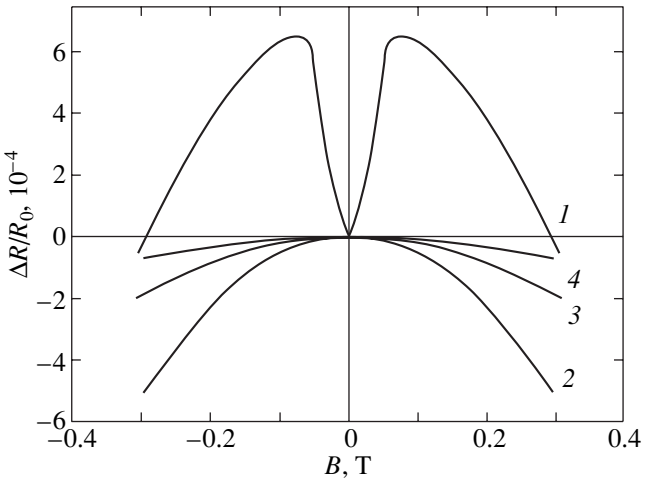

Fig. 2. Magnetic-field dependences of the magnetoresistance measured at temperatures T = (*1*) 2, (*2*) 10, (*3*) 50, and (*4*) 100 K for the Co_xC_{1-x} (x = 0.19) carbon fiber annealed at T = 900°C.

temperatures, can be caused by strong spin–orbit interactions [5, 14]. Actually, spin–orbit scattering results in a decrease in the quantum localization correction to the conductivity (i.e., it leads to the phenomenon of antilocalization), whereas the external magnetic field suppressing spin–orbit scattering brings about the removal of antilocalization (i.e., an increase in the resistance or a positive magnetoresistive effect). A further increase in the magnetic field is accompanied by the suppression of quantum interference and gives rise to a negative magnetoresistive effect. As can be seen from the temperature and magnetic-field dependences of the resistance, the spin–orbit interaction manifests itself only at the lowest temperatures (T = 2–4 K).

For the two-dimensional mechanism of charge transfer, the change in the localization correction to the conductivity in a magnetic field can be determined from the relationship [14]

$$\Delta\sigma(B) = \frac{\Delta R_s}{R_s^2} = \left(\frac{e^2}{2\pi^2\hbar}\right)\left[\Psi\left(\frac{1}{2}+\frac{B_1}{B}\right) - \frac{3}{2}\Psi\left(\frac{1}{2}+\frac{B_2}{B}\right) + \frac{1}{2}\Psi\left(\frac{1}{2}+\frac{B_3}{B}\right)\right], \quad (2)$$

where $\Psi(x)$ is the digamma function, B is the induction of the magnetic field, R_s is the sheet resistance, e is the elementary charge, and $\hbar$ is the Planck constant. The inductions of characteristic magnetic fields B_i (i = 0, 1, 2, 3) and the characteristic relaxation times τ_i of electrons are related by the expression

$$B_i\tau_i = \frac{\hbar}{4eD}, \quad (3)$$

where D is the diffusion coefficient of electrons.

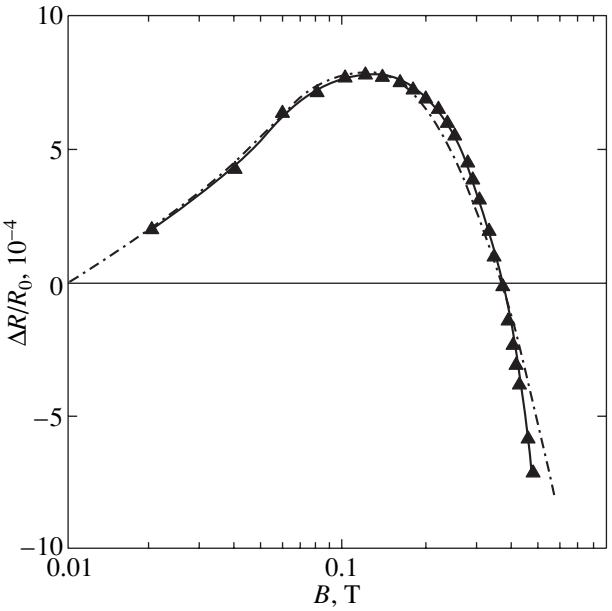

Fig. 3. Comparison of the magnetoresistance measured at $T = 2$ K (triangles) and the magnetoresistance calculated from expression (2) (dot-dashed line) for characteristic times $\tau_\varphi = 3.7 \times 10^{-10}$ s and $\tau_{so} = 1.15 \times 10^{-10}$ s.

In turn, the quantities B_i (or τ_i) are related to the characteristic magnetic fields B_o, B_{so}, B_s, and B_{in} by the following expressions:

$$B_1 = B_o + B_{so} + B_s, \quad (4)$$

$$B_2 = \frac{4}{3}B_{so} + \frac{2}{3}B_s + B_{in}, \quad (5)$$

$$B_3 = 2B_s + B_{in}. \quad (6)$$

The quantities B_o, B_{so}, B_s, and B_{in} are related through expression (3) to the elastic scattering time τ_o, the spin–orbit scattering time τ_{so} (the time of spin flip due to elastic spin–orbit scattering), the time of scattering by magnetic impurities τ_s (the time of spin flip due to the exchange interaction between magnetic impurities and electrons), and the time τ_{in} of inelastic scattering (due to electron–phonon and electron–electron interactions under conditions of weak localization).

The characteristic time τ_3 involved in expression (6) through relationship (3) is the phase-breaking time τ_φ of the wave function (the time during which the coherence of interfering electron waves is retained). This time can be expressed in terms of the inelastic scattering time τ_{in} and the magnetic impurity scattering time τ_s:

$$\frac{1}{\tau_3} = \frac{2}{\tau_s} + \frac{1}{\tau_{in}}. \quad (7)$$

Since the elastic scattering time τ_o of electrons is considerably shorter than the times τ_{in}, τ_{so}, and τ_s, we can assume that $B_1 \approx B_0$. Considering this circumstance, it is difficult to determine uniquely the characteristic times τ_{in}, τ_{so}, and τ_s and to separate the contributions from particular mechanisms to the inelastic scattering time τ_{in} on the basis of expressions (2)–(6) without introducing simplifying assumptions. Note that, according to relationship (7), the high content of magnetic cobalt impurities in carbon fibers should result in a dominant contribution of the magnetic impurity scattering time τ_s to the phase-breaking time τ_φ of the wave function and, hence, in a weak temperature dependence of the magnetoresistive effect, because, to a first approximation, the times τ_s and τ_{so} are independent of temperature. Therefore, the observed temperature dependence of the magnetoresistance (Fig. 2) allows us to make the inference that the inelastic scattering time τ_{in}, which is dependent on the temperature, predominantly contributes to the phase-breaking time τ_φ. Furthermore, the fact that the magnetic impurity scattering dominates over the other processes should lead only to a decrease in the resistance in an external magnetic field [15]. However, we experimentally observed the alternating magnetoresistive effect. Hence, in order to determine the times τ_φ and τ_{so} from the nonmonotonic magnetic-field dependence of the magnetoresistance for cobalt-containing carbon fibers, we disregard magnetic impurity scattering; in other words, we assume that $\tau_s \gg \tau_\varphi$.

The maximum diffusion coefficient of electrons in carbon materials with the electrical conductivity under consideration is determined to be $D = 0.5$ cm^2/s [16]. Figure 3 depicts the experimental magnetic-field dependence of the magnetoresistance (shown by triangles) and the dependence calculated from relationship (2) (dot-dashed line) for the above diffusion coefficient. The best agreement between the experimental and calculated data is observed at characteristic times $\tau_\varphi = 3.5 \times 10^{-10}$ s and $\tau_{so} = 1.19 \times 10^{-10}$ s.

The dependences depicted in Figs. 1 and 2 are observed for cobalt-containing carbon fibers prepared through heat treatment in air for different times and characterized by different resistances at room temperature (in samples of identical size, these resistances vary from one to several tens of ohms). Despite the difference in the electrical resistances, the magnetic-field dependences of the magnetoresistive effect are adequately described by relationship (2) and the characteristic times τ_φ and τ_{so} differ from the above values by no more than 10%. According to the theoretical predictions made by Hikami *et al.* [14], the inequality $\tau_\varphi > \tau_{so}$ which is a necessary condition for observation of an alternating magnetoresistance, is satisfied in all cases.

Since the atomic number of carbon is small, it is unlikely that the spin–orbit interaction can be strong in turbostratum carbon layers. It should be noted that, in thin films based on a considerably heavier element (manganese), the alternating magnetoresistive effect was observed only after the films were covered with a gold layer [5], which provided the necessary spin–orbit

interaction in the system. In our opinion, sufficiently strong spin–orbit scattering in the samples studied is associated with the presence of both nanoclusters and individual atoms of heavier cobalt in a graphite-like carbon matrix. According to Abrikosov and Gor'kov [17], the ratio between the characteristic times τ_0 and τ_{so} is defined by the expression $\tau_0/\tau_{so} = (\alpha Z)^4$, where α is the fine structure constant and Z is the atomic number of impurity ions. For cobalt ($Z = 27$), this ratio is equal to 1.5×10^{-3}, which is close to the ratio of 3×10^{-3} determined for the best agreement between the experimental and theoretical magnetic-field dependences of the magnetoresistance for the cobalt-containing carbon fibers (Fig. 3).

Knowing the phase-breaking time of the wave function, it is easy to calculate the characteristic length along which the electron wave phase is retained: $l_\varphi = (D\tau_\varphi)^{1/2} \cong 130$ nm. The sheet resistance $R_s = 2724 \pm 122\ \Omega/\square$, which was determined by fitting the magnetic-field dependence of the magnetoresistance, permits us to estimate the thickness of conducting layers for the known electrical resistance, length, and cross sectional area of the sample. This thickness for the samples studied varies from 15 to 70 nm and, as should be expected, appears to be smaller than the phase-breaking length l_φ of the wave function.

It is of interest to compare the calculated characteristic times τ_φ and τ_{so} for cobalt-containing carbon fibers with the corresponding times for metal and semiconductor systems at the same temperatures. In particular, Bergman [5] obtained the characteristic times $\tau_\varphi = 2.5 \times 10^{-11}$ s and $\tau_{so} = 4.5 \times 10^{-12}$ s for films based on a heavier metal (copper). These times turned out to be slightly longer for indium phosphate inversion layers and heterojunctions based on them: $\tau_\varphi = 6 \times 10^{-11}$ s, $\tau_{so} = 8 \times 10^{-12}$ s [6] and $\tau_\varphi = 3 \times 10^{-10}$ s, $\tau_{so} = 2 \times 10^{-10}$ s [7], respectively. It can be seen that the characteristic times for Co_xC_{1-x} fibers appeared to be closer to those of the two-dimensional electron gas of the heterojunction, even though the atomic numbers of cobalt and copper are close to each other. This can be associated with the fact that the processes of weak localization are governed, to a large extent, not only by the degree of disordering of the electronic system but also by the presence or the absence of quantization of the electron energy spectrum in the system.

4. CONCLUSIONS

Thus, it has been established that the two-dimensional processes of weak electron localization and spin–orbit scattering occur in carbon fibers with inclusions of cobalt nanoclusters on the metal side of the dielectric–metal transition at low temperatures. The inference was made that the two-dimensional nature of electron conduction is associated with the turbostratum graphite-like structure formed upon incorporation of cobalt nanoclusters. It was found that, in these fibers, the positive magnetoresistive effect in weak magnetic fields is caused by the spin–orbit scattering, whereas the negative magnetoresistive effect in stronger magnetic fields is associated with the suppression of the processes of weak localization by the magnetic field.

ACKNOWLEDGMENTS

We would like to thank H. Micklitz (Köln University, Germany) for his participation in discussions of the results and for providing an opportunity to perform low-temperature measurements.

This work was supported by the Belarussian State Committee of Science and Engineering, Belarussian State University (project no. 961/06), and the Bundesministerium für Forschung und Technologie (project no. WEI-99-002).

REFERENCES

1. E. Abrahams, P. W. Anderson, D. C. Licciardello, and T. V. Ramakrishnan, Phys. Rev. Lett. **42**, 673 (1979).
2. P. A. Lee and T. V. Ramakrishnan, Rev. Mod. Phys. **57**, 287 (1985).
3. B. L. Al'tshuler and A. G. Aronov, Zh. Éksp. Teor. Fiz. **77**, 2028 (1979) [Sov. Phys. JETP **50**, 968 (1979)].
4. B. L. Altshuler, A. G. Aronov, and P. A. Lee, Phys. Rev. Lett. **44**, 1288 (1980).
5. G. Bergman, Phys. Rep. **107**, 1 (1984).
6. D. A. Poole, M. Pepper, and A. Hughes, J. Phys. C **15**, L1137 (1982).
7. T. A. Polyanskaya and Yu. V. Shmartsev, Fiz. Tekh. Poluprovodn. (Leningrad) **23** (1), 3 (1989) [Sov. Phys. Semicond. **23**, 1 (1989)].
8. V. Boyot, L. Piraux, and J. P. Issi, Phys. Rev. B **41**, 11770 (1990).
9. I. A. Bashmakov, V. A. Dorosinez, M. G. Lukashevich, A. A. Mazanik, and T. F. Tihonova, J. Mater. Res. **16**, 2832 (2001).
10. I. N. Ermolenko, I. P. Lyubliner, and N. V. Gul'ko, *Element-Containing Coal Fibrous Materials* (Nauka i Tekhnika, Minsk, 1982) [in Russian].
11. I. A. Bashmakov, V. A. Dorosinets, M. G. Lukashevich, A. A. Mazanik, T. F. Tikhonova, and D. A. Skripka, Fiz. Tverd. Tela (St. Petersburg) **44**, 1614 (2002) [Phys. Solid State **44**, 1689 (2002)].
12. A. Carl, G. Dumpich, and E. F. Wassermann, Phys. Rev. B **50**, 4802 (1994).
13. D. L. Peng, K. Sumiyama, T. J. Konno, T. Hihara, and S. Yamamuro, Phys. Rev. B **60**, 2093 (1999).
14. S. Hikami, A. L. Larkin, and J. Nagajka, Prog. Theor. Phys. **63**, 707 (1980).
15. J. Kondo, Prog. Theor. Phys. **32**, 37 (1964).
16. G. Du, V. N. Prigodin, A. Burns, J. Joo, C. S. Wang, and A. J. Epstein, Phys. Rev. B **58**, 4485 (1998).
17. A. A. Abrikosov and L. P. Gor'kov, Zh. Éksp. Teor. Fiz. **42**, 1088 (1962) [Sov. Phys. JETP **15**, 752 (1962)].

Translated by O. Borovik-Romanova

Physics of the Solid State, Vol. 47, No. 2, 2005, pp. 362–365. Translated from Fizika Tverdogo Tela, Vol. 47, No. 2, 2005, pp. 350–353.

LOW-DIMENSIONAL SYSTEMS AND SURFACE PHYSICS

Vibrational and Electronic Properties of a $Cu_{90}Nb_{10}$ Nanocrystalline Composite

M. G. Zemlyanov, G. Kh. Panova, G. F. Syrykh, and A. A. Shikov

Russian Research Center Kurchatov Institute, pl. Kurchatova 1, Moscow, 123182 Russia

e-mail: shikov@isssph.kiae.ru

Received May 20, 2004

Abstract—The vibrational, electronic, and superconducting properties of a $Cu_{90}Nb_{10}$ nanocrystalline composite undergoing a transition from a coarse-grained state to a nanocrystalline state are investigated using neutron scattering and low-temperature heat capacity measurements. It is found that, compared to a coarse-grained sample, the nanocomposite is characterized by a higher density of low-frequency excitations and a decrease both in the density of states and in the superconducting transition temperature due to the size effect. © *2005 Pleiades Publishing, Inc.*

1. INTRODUCTION

The particular interest expressed by researchers in nanocrystalline systems is associated with their unique physical properties. Investigation into the influence of size effects on the vibrational and thermodynamic properties of nanocrystals is an important problem. Undeniably, deeper insight into the structural features of nanomaterials and the mechanisms of the influence of surface atoms and grain boundaries on their vibrational and thermodynamic properties could lead to considerable progress in the field of applications of nanostructured systems.

Compact nanosystems as objects of investigation have some advantages over powdered nanosystems for a number of reasons. For example, compact nanosystems are characterized by a higher degree of dispersion (of the order of 10 nm) in combination with a narrower size distribution of particles and are devoid of porosity. This excludes specific contacts between grains and corresponding interactions.

Similar systems have been prepared and studied in a number of works [1–3]. In particular, Cline *et al.* [1] prepared a composite consisting of niobium thin wires embedded in a copper matrix by using wire drawing. The diameter of the wires thus fabricated was smaller than 100 nm. Oleksienko *et al.* [2] prepared Cu–Nb composites by two methods: (i) crystallization with subsequent deformation of copper–niobium alloys and (ii) mechanical assembly with drawing of a copper–niobium bimetallic wire. The transverse size of wires varied from 2.5 to 20 nm. Tsai *et al.* [3] synthesized a nanocrystalline system containing 20 wt % Pb dispersed in a matrix of the $Al_{75}Cu_{15}V_{10}$ metallic glass through rapid quenching of a liquid melt on a cold surface. The size of the particles varied from 5 to 100 nm. However, all the aforementioned works dealt only with the influence of size effects on the superconducting properties (superconducting transition temperature, critical current, critical magnetic field). It has been revealed that a decrease in the particle size leads to a decrease in all the superconducting parameters under investigation. The problem concerning the influence of size effects on the electronic and phononic properties of both the composites themselves and a system of nanoparticles has not been adequately investigated. This information can be obtained only from combined investigations performed by different methods.

In this work, the vibrational, electronic, and superconducting properties of a $Cu_{90}Nb_{10}$ composite undergoing a transition from a coarse-grained state to a nanocrystalline state were investigated using neutron scattering and low-temperature heat capacity measurements. Moreover, the superconducting transition temperature was measured by the inductive method. Such experiments provide valuable information on the energy spectrum of a vibrational system and on the changes in the density of states at the Fermi surface. These data are essential to the understanding of the nature of the changes observed upon transition from a coarse-grained state to a nanocrystalline state.

2. SAMPLE PREPARATION AND EXPERIMENTAL TECHNIQUE

A $Cu_{90}Nb_{10}$ nanocrystalline sample was prepared by quenching of a melt on the outer surface of a spinning copper wheel in a purified argon atmosphere. The initial elements were placed in a boron nitride cell. The cell was heated by the inductive method with a VChG6-60/0.44 high-frequency generator. The melt was expelled under positive pressure of argon through a hole 1 mm in diameter on the wheel surface. The linear velocity of the wheel was equal to 40 m/s. The quenching rate was estimated at ~10^6 K/s.

1063-7834/05/4702-0362$26.00 © 2005 Pleiades Publishing, Inc.

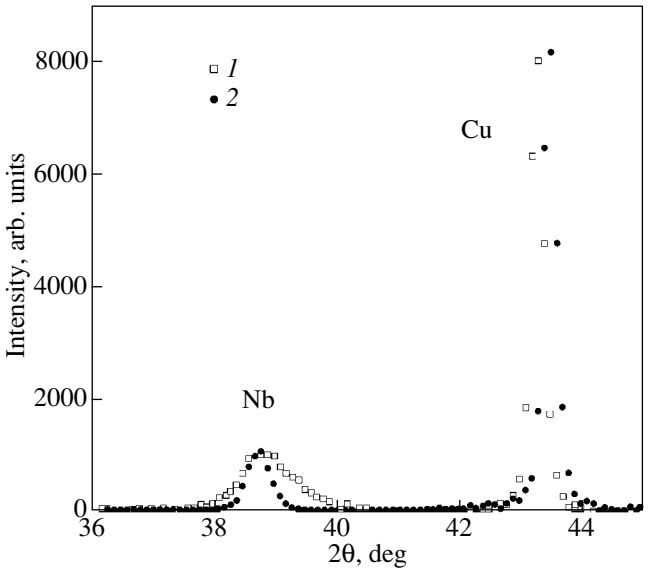

Fig. 1. X-ray diffraction patterns of the $Cu_{90}Nb_{10}$ composite after (*1*) quenching and (*2*) subsequent annealing at temperature $T = 477°C$ for 3 h.

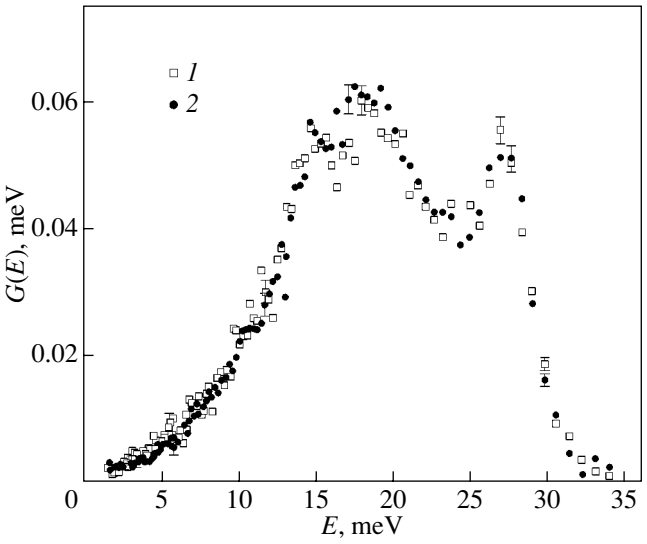

Fig. 2. Generalized densities of vibrational states $G(E)$ for the $Cu_{90}Nb_{10}$ composite in (*1*) nanocrystalline and (*2*) coarse-grained states.

The sample prepared was annealed in a helium gas stream through a quartz tube placed in a muffle furnace. The first and second annealing stages were performed at a temperature of 477°C for 3 h and at 770°C for 4 h, respectively.

The structure of the sample thus prepared and the influence of annealing on its properties were investigated on a DRON-2 diffractometer (CoK_α radiation). The x-ray diffraction patterns are shown in Fig. 1. It can be seen from this figure that the x-ray diffraction patterns contain reflections attributed to copper and niobium. The narrow lines associated with copper indicate that copper is in a coarse-grained state. The lines assigned to niobium are considerably broadened. The mean size of niobium crystallites was determined by the Selyakov–Scherrer method [4]. In the quenched sample, the mean size of niobium crystallites was approximately equal to 20 nm. After annealing at a temperature of 477°C for 3 h, the width of the line attributed to copper remained virtually unchanged, whereas the lines of niobium were substantially narrowed. According to the observed linewidth, the mean size of niobium crystallites is approximately equal to 30 nm. Further annealing at a temperature of 770°C for 4 h under the same conditions did not result in a noticeable change in the width of the lines attributed to niobium. Therefore, it can be assumed that the annealing temperature will have a profound effect on the growth of niobium nanocrystals in the temperature range corresponding to premelting of the copper matrix.

3. RESULTS AND DISCUSSION

Inelastic neutron scattering in the nanocrystalline and coarse-grained samples of the $Cu_{90}Nb_{10}$ compound was studied on a KDSOG-M spectrometer [5] installed on an IBR-2 reactor (Dubna, Moscow oblast). The measurements were performed at room temperature for scattering angles of 80°, 100°, 120°, and 140°. The results were processed within the incoherent approximation. The generalized densities of vibrational states [6] obtained for the initial and quenched $Cu_{90}Nb_{10}$ samples are presented in Fig. 2. Figure 3 shows the relative change in these densities of vibrational states. It can be seen that the density of low-energy vibrational states for the nanocrystalline sample is higher than the density of low-energy vibrational states for the coarse-grained sample.

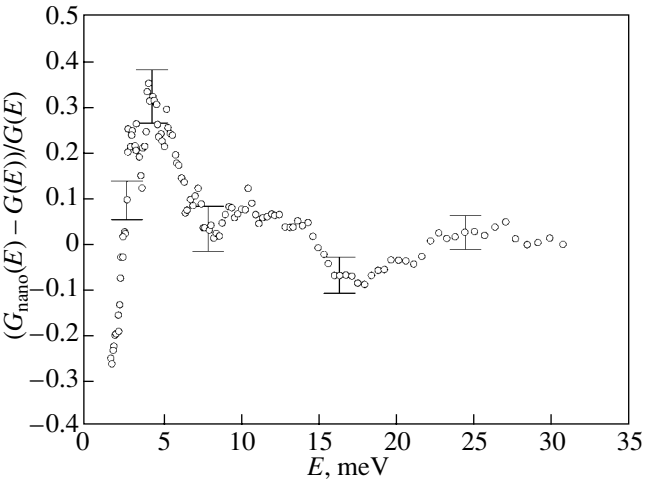

Fig. 3. Relative change in the generalized density of vibrational states for the $Cu_{90}Nb_{10}$ composite upon transition from a nanocrystalline state to a coarse-grained state.

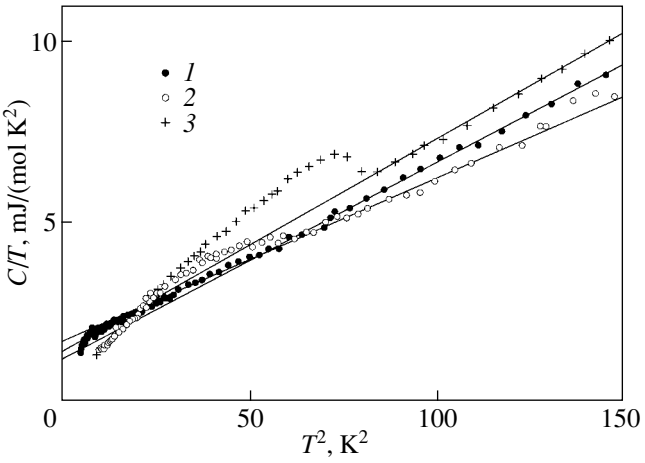

Fig. 4. Temperature dependences of the low-temperature heat capacity for the $Cu_{90}Nb_{10}$ nanocrystalline sample (*1*) before and (*2*) after annealing and for (*3*) the coarse-grained sample in the range 1.5–12 K.

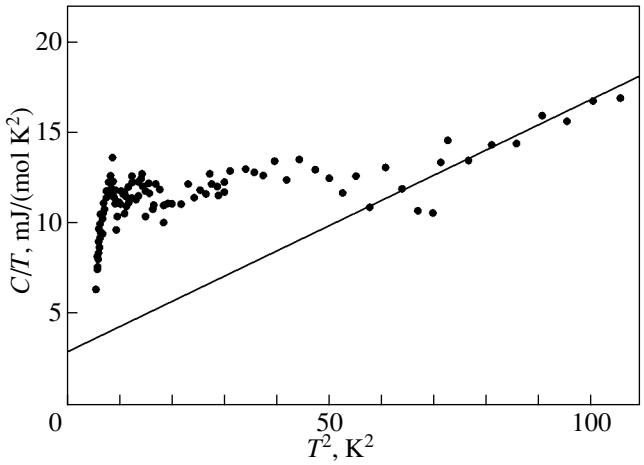

Fig. 5. Temperature dependence of the heat capacity of nanocrystalline niobium (determined from the heat capacity of the $Cu_{90}Nb_{10}$ nanocomposite) in the range 1.5–12 K.

The heat capacity of the samples was measured using an adiabatic calorimeter with pulsed heating [7] in the temperature range 1.5–35.0 K. The experimental error in determining the heat capacity was equal to 2.0% in the temperature range 1.5–4.0 K, 1.0% in the range 4–10 K, and 0.2–0.5% in the range 10–35 K. The superconducting transition temperature was determined from the jumps in the heat capacity, the inductance, and the electrical resistance.

Figure 4 shows the temperature dependences of the heat capacity for the studied samples in the T^2–C/T coordinates in the temperature range 1.5–12.0 K. It can be seen that the $Cu_{90}Nb_{10}$ nanocomposite undergoes a smeared superconducting transition in the temperature range from 3 to 7 K. After annealing at T = 477°C for 3 h, the superconducting transition is shifted toward the high-temperature range with a transition temperature $T_c \sim 7.0$ K. For the coarse-grained sample, the superconducting transition temperature was estimated as $T_c \sim$ 8.8 K.

The difference between the temperature dependences of the heat capacity for the $Cu_{90}Nb_{10}$ nanocrystalline composite and metallic copper [8] is shown in Fig. 5. Since the interaction of copper and niobium atoms in the $Cu_{90}Nb_{10}$ composite is relatively weak, this difference is predominantly determined by the contribution from niobium nanoparticles. The temperature dependence of the heat capacity obtained for niobium nanoparticles allowed us to determine the Debye temperature $\Theta(0)$ and the coefficient of the electronic heat capacity $\gamma(0)$, which are the vibrational and electronic parameters of niobium nanoparticles in the $Cu_{90}Nb_{10}$ composite, and to compare these quantities with those of the massive niobium sample [9]. The experimental results are presented in the table. It can be seen from these data that the coefficient of the electronic heat capacity $\gamma(0)$, the Debye temperature $\Theta(0)$, and the superconducting transition temperature T_c for the nanocrystalline niobium sample are less than those for the massive niobium sample.

The observed changes in the superconducting transition temperature T_c, the Debye temperature, and the density of electronic states upon heat treatment indicate that these characteristics of the nanocrystalline composite depend on the nanocrystal size. A decrease in the nanocrystal size leads to a decrease in the aforementioned characteristics. It is obvious that the appearance

Vibrational and electronic parameters of the $Cu_{90}Nb_{10}$ coarse-grained sample, $Cu_{90}Nb_{10}$ nanocrystalline composite before and after annealing, nanocrystalline niobium, and niobium and copper massive samples

Sample	T_c, K	$\gamma(0)$, mJ/(mol K^2)	$\Theta(0)$, K
$Cu_{90}Nb_{10}$ (coarse-grained sample)	8.8	1.4	319
$Cu_{90}Nb_{10}$ (nanocomposite before annealing)	3–7	1.2	328
$Cu_{90}Nb_{10}$ (nanocomposite after annealing)	7.0	1.68	348
Cu	–	0.73	334
Nb (massive sample)	9.2	8.5	252
Nb (nanocrystalline sample)	3–7	3.0	240

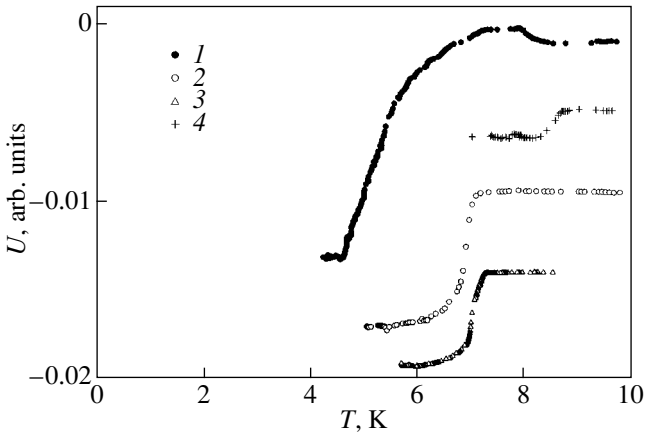

Fig. 6. Temperature dependences of the ac magnetic susceptibility for the $Cu_{90}Nb_{10}$ nanocrystalline sample (*1*) before and (*2*) after annealing at $T = 477°C$, (*3*) after subsequent annealing at $T = 770°C$, and for (*4*) the coarse-grained sample.

of additional low-energy modes of the nanocrystalline composite is associated both with the strong effect of surface atoms and grain boundaries and with the mutual orientation of adjacent crystals.

The experimental data on the superconducting transition temperatures measured by the inductive method for the samples under investigation are presented in Fig. 6. These results confirm the inference made from the heat capacity data that the nanocomposite undergoes a smeared superconducting transition at $T_c = 3$–7 K. The annealing of the sample at $T = 447°C$ results in a considerable narrowing of the temperature range of the superconducting transition observed at ~7 K. As the annealing temperature increases to 770°C, the temperature and the range of the superconducting transition remain unchanged. These findings are in agreement with the x-ray diffraction data, according to which the width of the x-ray diffraction lines does not decrease upon subsequent annealing. For comparison, the experimental data on the superconducting transition temperature for the coarse-grained composite are also presented in Fig. 6.

4. CONCLUSIONS

Thus, the results of the above investigation have demonstrated that the size of nanoparticles has an effect both on the vibrational and electronic spectra and on the superconducting properties of niobium nanocrystals in a $Cu_{90}Nb_{10}$ composite. The comparison of the data obtained for the nanocrystalline and massive niobium samples showed that the superconducting transition temperature, the Debye temperature, and the density of states at the Fermi level for the former sample are lower than those for the latter sample. The decrease in the Debye temperature agrees with the neutron scattering data, which indicate an increase in the density of low-energy states. The above changes in the characteristics under investigation allowed us to make the inference that the observed size effects are the decisive factors responsible for the weakening of interatomic interactions, primarily, at grain boundaries [10].

ACKNOWLEDGMENTS

This work was supported by the Russian Foundation for Basic Research, project no. 03-02-16803a.

REFERENCES

1. H. E. Cline, B. P. Strauss, R. M. Rose, and J. Wulff, J. Appl. Phys. **37** (1), 5 (1966).
2. M. M. Oleksienko, V. T. Petrenko, M. A. Tikhonovskiĭ, and A. P. Berdnik, in *Problems in Atomic Science and Engineering* (Kharkov, 1980), No. 3 (13), p. 29 [in Russian].
3. A. R. Tsai, N. Chandrasekhar, and K. Chattopadhyay, Appl. Phys. Lett. **75** (11), 1527 (1999).
4. S. S. Gorelik, L. N. Rastorguev, and Ya. A. Skakov, *X-ray Diffraction and Electron Optical Analysis* (Metallurgiya, Moscow, 1970) [in Russian].
5. G. Baluka, A. V. Belushkin, S. I. Bragin, T. Zaleski, M. Z. Ishmukhametov, I. Natkanets, V. Oleyarchik, and Ya. Pavelchik, Preprint No. R13-84-242, OIYaI (Joint Inst. for Nuclear Research, Dubna, 1984).
6. N. A. Chernoplekov, M. G. Zemlyanov, E. G. Brovman, and A. G. Checherin, Fiz. Tverd. Tela (Leningrad) **5**, 112 (1963) [Sov. Phys. Solid State **5**, 78 (1963)].
7. M. N. Khlopkin, N. A. Chernoplekov, and P. A. Cheremnykh, Preprint No. 3549/10, IAÉ (Inst. of Atomic Energy, Moscow, 1982).
8. J. A. Kok and W. H. Keesom, Physica (Amsterdam) **3**, 1035 (1936).
9. A. Brown, M. W. Zemansky, and H. A. Boorse, Phys. Rev. **86**, 134 (1952).
10. P. M. Derlet, R. Meyer, L. J. Lewis, U. Stuhr, and H. Van Swygenhoven, Phys. Rev. Lett. **87** (20), 205501 (2001).

Translated by O. Borovik-Romanova

Physics of the Solid State, Vol. 47, No. 2, 2005, pp. 366–369. Translated from Fizika Tverdogo Tela, Vol. 47, No. 2, 2005, pp. 354–356.

LOW-DIMENSIONAL SYSTEMS AND SURFACE PHYSICS

Dichroism in Transmission of Light by an Array of Self-Assembled GaAs Quantum Wires on a Nanofaceted A(311) Surface

V. A. Volodin*, M. D. Efremov*, R. S. Matvienko, V. V. Preobrazhenskiĭ*, B. R. Semyagin**, N. N. Ledentsov***, I. R. Soshnikov***, D. Litvinov****, A. Rosenauer****, and D. Gerthsen******

** Institute of Semiconductor Physics, Siberian Division, Russian Academy of Sciences, pr. Akademika Lavrent'eva 13, Novosibirsk, 630090 Russia*

e-mail: volodin@isp.nsc.ru

*** Novosibirsk State University, ul. Pirogova 2, Novosibirsk, 630090 Russia*

**** Ioffe Physicotechnical Institute, Russian Academy of Sciences, Politekhnicheskaya ul. 26, St. Petersburg, 194021 Russia*

***** Laboratory of Electron Microscopy, University of Karlsruhe, Karlsruhe, 76128 Germany*

Received June 9, 2004

Abstract—Dichroism in the transmission of light (the dependence of the transmittance on the direction of polarization of light) is revealed in corrugated GaAs/AlAs superlattices grown on a nanofaceted A(311) surface. It is assumed that the observed effect is associated with the structural anisotropy, i.e., with the formation of an array of GaAs quantum wires. This inference is confirmed by high-resolution electron microscopy. The GaAs/AlAs superlattices containing quantum wires also exhibit polarization anisotropy of the photoluminescence observed in the yellow–red spectral range. © *2005 Pleiades Publishing, Inc.*

1. INTRODUCTION

Research on GaAs/AlAs superlattices grown on periodically nanofaceted surfaces is of interest for the design of lateral superlattices containing arrays of quantum wires with unique optical and transport properties [1–3]. These structures offer promise for use in fabricating both lasers (including cascade lasers) with a vertical cavity and intersubband infrared photodetectors for recording light incident at angles close to 90° [1, 3–5]. The possibility of forming an array of quantum wires in GaAs/AlAs superlattices grown on a nanofaceted A(311) surface was first demonstrated by Nötzel *et al.* [6]. It was shown that the heteroepitaxial growth of GaAs/AlAs superlattices on a nanofaceted A(311) surface occurs with the formation of a vertically correlated array of quantum wires that are separated by a distance equal to the period of facets (3.2 nm) along the $[01\bar{1}]$ direction. The quantum wires are aligned along the $[\bar{2}33]$ direction, and the modulation of their thickness is determined by the height of the facets (1 nm).

2. SAMPLE PREPARATION AND EXPERIMENTAL TECHNIQUE

Samples were prepared by molecular-beam epitaxy at a growth temperature of 550°C. The growth conditions were described in detail in [7]. The GaAs/AlAs superlattices were grown on A(311) substrates with a 0.1-μm-thick GaAs buffer layer and a 0.2-μm-thick AlAs layer (the misorientation angle between the substrate surface and the [311] direction was less than 15′). Nanofaceting of the surface, i.e., the development of an (8×1) surface reconstruction, was confirmed by *in situ* high-energy electron diffraction measurements. The effective thickness of AlAs layers was equal to 1.7 nm (10 monolayers along the [311] direction). The effective thickness of GaAs layers was equal to 1 nm (sample *1*) or 1.7 nm (sample *2*). The number of periods in samples *1* and *2* was 150 and 100, respectively. The transmission spectra were measured with the use of membranes prepared by selective etching of the substrate to a transparent AlAs buffer layer. A solution of ammonia and hydrogen peroxide in a 1 : 10 ratio was used as a selective etching agent. The transmission spectra in polarized light were recorded on an SF-30 double-beam spectrometer with polarizers in the channel with the sample and in the reference channel. Photoluminescence was excited by light from an Ar^+ laser (λ = 448 nm). The photoluminescence spectra were recorded on an SDL-1 spectrometer (polarization resolution, Glan prism as a polarizer) with a FÉU-79 photomultiplier as a detector. Moreover, the samples were examined using high-resolution electron microscopy

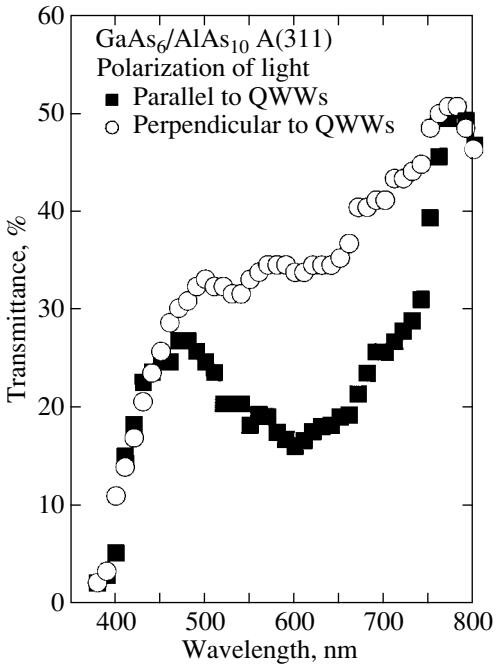

Fig. 1. Transmission spectra of the $GaAs_6/AlAs_{10}$ A(311) superlattice containing quantum wires.

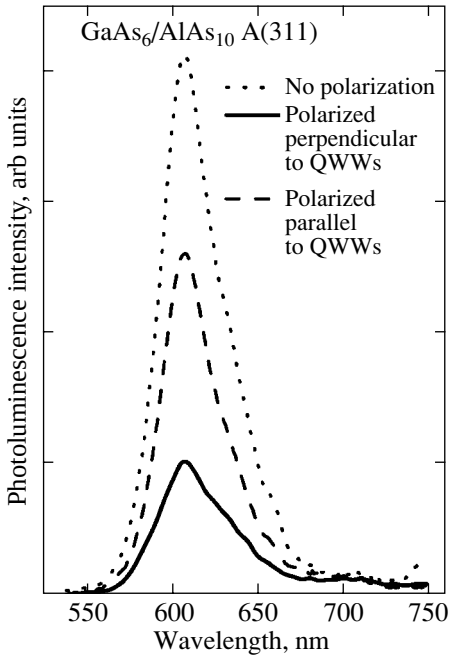

Fig. 2. Photoluminescence spectra of the $GaAs_6/AlAs_{10}$ A(311) superlattice containing quantum wires. The dotted line corresponds to the photoluminescence signal without analysis of the polarization, the solid line shows the spectrum measured in light polarized along the $[01\bar{1}]$ direction, and the dashed line represents the spectrum measured in light polarized along the $[\bar{2}33]$ direction.

(HREM) on a Philips CM200 FEG/ST instrument according to the technique described in detail in [8].

3. RESULTS AND DISCUSSION

Figure 1 shows the transmission spectra of the $GaAs_6/AlAs_{10}$ A(311) superlattice (sample *1*) measured in light polarized parallel and perpendicular to the direction of the quantum-well wires (QWWs). The transmission spectra were recorded at room temperature. It can be seen from this figure that there is a considerable difference in the transmission (and, correspondingly, in the absorption) of light with different polarizations, i.e., dichroism. The difference is most pronounced in the range of fundamental absorption of light in the superlattice. The data on the polarization dependence of the absorption correlate well with the data on the polarization anisotropy of the photoluminescence (Fig. 2). The minimum observed in the transmittance for the light polarized along the growth direction of quantum wires (along the $[\bar{2}33]$ direction) coincides in wavelength with the maximum in the intensity of the photoluminescence signal (Figs. 1, 2). The intensity of the photoluminescence signal in this polarization is approximately 2.5 times higher than that of the photoluminescence signal polarized along the $[01\bar{1}]$ direction, i.e., in the direction perpendicular to the quantum wires. The dichroism revealed in the transmission of light and the observed polarization of the photoluminescence signal can be associated with the fact that the probability of fundamental optical transitions occurring depends on the polarization of the electromagnetic wave. It should be noted that the photoluminescence spectra were recorded at room temperature, the exciting light from the argon laser was polarized along the $[\bar{2}33]$ direction, and the pumping power was approximately equal to 100 W/cm^2. Under these conditions, an intense photoluminescence signal (visible to the eye) is observed in the yellow–red spectral range. The maximum photoluminescence intensity corresponds to orange radiation.

In each growth experiment, reference samples with the (100) and B(311) orientations were grown side-by-side (i.e., under the same conditions) in addition to the superlattices with the A(311) orientation. In polar semiconductors, the A(311) and B(311) orientations are not equivalent; hence, the orientation of the substrate (side A or B) was determined by the anisotropy of chemical etching. For the reference samples, either no photoluminescence signal was observed altogether or its intensity was two orders of magnitude lower, with the maximum shifted to the long-wavelength range of the spectrum [9].

It is known that GaAs/AlAs superlattices with approximately equal thicknesses of the GaAs and AlAs layers and a GaAs layer thickness of less than 3.5 nm are type-II superlattices [10]. However, in our case, the

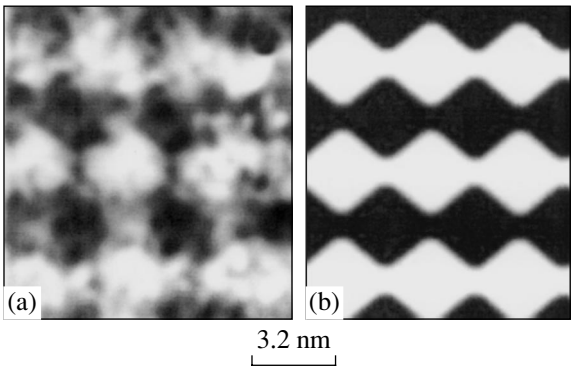

Fig. 3. (a) Cross-sectional HRTEM image (along the $[\bar{2}33]$ direction) of the $GaAs_{10}/AlAs_{10}$ A(311) superlattice grown under conditions of nanofaceting of the surface and (b) the model HRTEM image in the case of formation of a strictly periodic array of quantum wires. Dark regions are enriched with gallium.

period of the superlattice and the layer thickness are very small; consequently, the tunneling barriers for both electrons and holes are relatively narrow and they are not strictly localized in layers of GaAs or AlAs. Therefore, it can be assumed that the quantum wires are not isolated and form a tunnel-coupled array. In this case, an additional lateral symmetry that leads to folding of the Brillouin zone appears not only along the [311] direction of the growth but also along the direction perpendicular to the nanofacets, i.e., along the $[01\bar{1}]$ direction. The lateral period (the period of facets) along this direction is equal to 3.2 nm. The high periodicity of facets with a period of 3.2 nm was repeatedly confirmed by different methods, for example, by scanning electron microscopy [11]. It seems likely that the folding of the Brillouin zone in two directions brings about a mixing of electronic states from the Γ, *X*, and *L* valleys, which, in turn, leads to a more enhanced radiative recombination in this structure as compared to the superlattices grown along the [100] direction with a higher symmetry. It can also be assumed that the less intense photoluminescence (or the complete absence of a photoluminescence signal) from the GaAs/AlAs superlattice grown on the B(311) surface is associated with the less pronounced corrugation (nanofaceting) of this surface as compared to the A(311) surface. On the other hand, the background impurities, which are incorporated into the layers from the residual atmosphere of the growth chamber, can interact with surfaces in different ways. However, the superlattices with thicker AlAs and GaAs layers (~10 nm), which are grown on the A(311), B(311), and (100) surfaces, are characterized by photoluminescence intensities that are comparable in magnitude.

Belousov *et al.* [12] revealed that the reflectance depends on the polarization of light in a GaAs/AlAs A(311) superlattice with a relatively large period (6.5 nm or greater). The existence of a pronounced structural anisotropy in GaAs/AlAs A(311) short-period superlattices was confirmed by Raman scattering in these structures [13, 14]. The results obtained from direct HRTEM measurements also indicate the presence of quantum wires in the superlattices grown under the conditions of nanofaceting of the A(311) surface (Fig. 3). These data were obtained for sample *2* grown under the same conditions as those used for sample *1*. This superlattice with quantum wires is also characterized by polarization anisotropy of the photoluminescence signal [9]. According to high-resolution plan-view transmission electron microscopy, the GaAs–AlAs quantum wires in multilayer structures are aligned parallel to the $[\bar{2}33]$ direction of facets [8]. Moreover, the good lateral periodicity of 3.2 nm suggests a strict vertical correlation of AlAs and GaAs quantum wires.

4. CONCLUSIONS

Thus, it can be assumed that the anisotropy of the optical properties (dichroism in the transmission of light and polarized photoluminescence signals) of the GaAs/AlAs short-period superlattices grown on a nanofaceted A(311) surface is associated with their structural anisotropy, i.e., with the formation of an array of quantum wires in the superlattices.

ACKNOWLEDGMENTS

We would like to thank R.A. Soots for assistance in performing chemical treatment in the preparation of the membranes used in the measurements.

REFERENCES

1. N. N. Ledentsov, D. Litvinov, A. Rosenauer, D. Gerthsen, I. P. Soshnikov, V. A. Shchukin, V. M. Ustinov, A. Yu. Egorov, A. E. Zukov, V. A. Volodin, M. D. Efremov, V. V. Preobrazhenskii, B. R. Semyagin, D. Bimberg, and Zh. I. Alferov, J. Electron. Mater. **30**, 464 (2001).
2. M. Henini, P. A. Crump, and P. J. Rodgers, J. Cryst. Growth **150**, 446 (1995).
3. P. O. Vaccaro, M. Hirai, K. Fujita, and T. Watanabe, J. Phys. D: Appl. Phys. **29**, 2221 (1996).
4. R. Nötzel, N. N. Ledentsov, L. A. Däweritz, and K. Ploog, U.S. Patent No. 5,714,765 (January 29, 1991).
5. N. N. Ledentsov, D. Litvinov, D. Gerthsen, G. A. Ljubas, V. V. Bolotov, B. R. Semyagin, V. A. Shchukin, I. P. Soshnikov, V. M. Ustinov, and D. Bimberg, Proc. SPIE **4656**, 33 (2002).
6. R. Nötzel, N. N. Ledentsov, L. A. Däweritz, H. Hohenstein, and K. Ploog, Phys. Rev. Lett. **67**, 3812 (1991).
7. M. D. Efremov, V. A. Volodin, V. V. Preobrazhenskii, B. R. Semyagin, D. V. Marin, R. S. Matvienko, N. N. Ledentsov, I. P. Soshnikov, D. Litvinov, A. Rosenauer, and D. Gerthsen, Physica E (Amsterdam) **23** (3–4), 461 (2004).

8. D. Litvinov, A. Rosenauer, D. Gerthsen, N. N. Ledentsov, D. Bimberg, G. A. Ljubas, V. V. Bolotov, V. A. Volodin, M. D. Efremov, V. V. Preobrazhenskii, B. R. Semyagin, and I. P. Soshnikov, Appl. Phys. Lett. **81**, 1080 (2002).
9. M. D. Efremov, V. A. Volodin, V. V. Bolotov, V. A. Sachkov, G. A. Lubas, V. V. Preobrazhenski, and B. R. Semyagin, Solid State Phenom. **60–70**, 507 (1999).
10. M. Nakayama, I. Tanaka, and I. Kimura, Jpn. J. Appl. Phys. **29**, 41 (1990).
11. L. Geelhaar, J. Marquez, and K. Jacobi, Phys. Rev. B **60**, 15890 (1999).
12. M. V. Belousov, V. L. Berkovich, A. O. Gusev, E. L. Ivchenko, P. S. Kop'ev, N. N. Ledentsov, and A. I. Nesvizhskiĭ, Fiz. Tverd. Tela (St. Petersburg) **36**, 1098 (1994) [Phys. Solid State **36**, 596 (1994)].
13. V. A. Volodin, M. D. Efremov, V. Ya. Prints, V. V. Preobrazhenskiĭ, B. R. Semyagin, and A. O. Govorov, Pis'ma Zh. Éksp. Teor. Fiz. **66**, 45 (1997) [JETP Lett. **66**, 47 (1997)].
14. V. A. Volodin, M. D. Efremov, V. V. Preobrazhenskiĭ, B. R. Semyagin, V. V. Bolotov, and V. A. Sachkov, Fiz. Tekh. Poluprovodn. (St. Petersburg) **34**, 62 (2000) [Semiconductors **34**, 61 (2000)].

Translated by O. Moskalev

Physics of the Solid State, Vol. 47, No. 2, 2005, pp. 370–373. Translated from Fizika Tverdogo Tela, Vol. 47, No. 2, 2005, pp. 357–360.

LOW-DIMENSIONAL SYSTEMS AND SURFACE PHYSICS

Thermal and Acoustic Properties of Chrysotile Asbestos

Yu. A. Kumzerov*, L. S. Parfen'eva*, I. A. Smirnov*, A. I. Krivchikov, G. A. Zvyagina**, V. D. Fil'**, H. Misiorek***, J. Mucha***, and A. Jezowski*****

**Ioffe Physicotechnical Institute, Russian Academy of Sciences, Politekhnicheskaya ul. 26, St. Petersburg, 194021 Russia*
e-mail: igor.smirnov@pop.ioffe.rssi.ru

***Physico-Technical Institute of Low-Temperature Research, National Academy of Sciences of Ukraine, Kharkov, 61103 Ukraine*

****Institute of Low-Temperature and Structural Research, Polish Academy of Sciences, Wroclaw, 50-950 Poland*

Received June 24, 2004

Abstract—The thermal conductivity, specific heat, and sound velocity of crystalline chrysotile asbestos made up of hollow tubular fibrils of composition $Mg_3Si_2O_5(OH)_4$ have been measured at temperatures of 5–300, 3–65, and 77 K, respectively. An analysis is made of the experimental data obtained. © *2005 Pleiades Publishing, Inc.*

The present communication reports on a continuation of earlier investigations into the thermal properties of chrysotile asbestos [1], which is used as a nanochannel dielectric matrix in studies of the physical properties of clusters and ultrathin quantum wires of metals and semiconductors embedded in nanochannels of this matrix [2, 3].

Chrysotile asbestos, hydrous magnesium silicate $Mg_3Si_2O_5(OH)_4$, is a fibrillar material of the serpentine group. Its chemical composition may vary (in the ratio of SiO_2 to MgO and bound water H_2O) from one deposit to another. It may contain Al, Fe, Ca, Ni, Mn, K, and Na as impurities [4].

Chrysotile asbestos has an unusual crystalline structure made up of structural layers, which are bounded on the inner side by a silicon–oxygen framework and on the outside by a framework corresponding to magnesium hydroxide [2–5]. Because the inner framework is smaller in size than the outer one, the layers of chrysotile asbestos tend to roll up into cylinders (tubes) with the silicon–oxygen layer on the inner side. Such tubes have an outer diameter $d_1 \sim 300$–500 Å and an inner diameter $d_2 \sim 20$–150 Å (Fig. 1b). The space between the tubes is usually filled with an amorphous mass of the tube material.

The fibrils of chrysotile asbestos are alternating chains of Si tetrahedra, Mg octahedra (extended along the fibril axis), and hydroxyl groups.

On the whole, the crystalline lattice of the asbestos layers belongs to the monoclinic system, and the lattice parameters are $a = 5.30$ Å, $b = 9.1$ Å, $c = 7.32$ Å, and $\beta = 93°$ [8]. The a axis is directed along the tube channels. The tubes are packed in a close to hexagonal arrangement. The porosity of chrysotile asbestos (percentage of channel voids in the total sample volume) is ~5–6%.

A large number of studies of the physical properties of thin filaments (quantum wires) of metals and semiconductors confined in channels of a chrysotile asbestos matrix have been carried out in recent years [3]. Unfortunately, the available literature lacks data on the acoustic and thermal properties of such a nanochannel matrix (except for our thermal conductivity measurements [1]). This information, however, frequently turns out to be indispensable for thermophysical calculations, as well as sometimes for extracting data on mate-

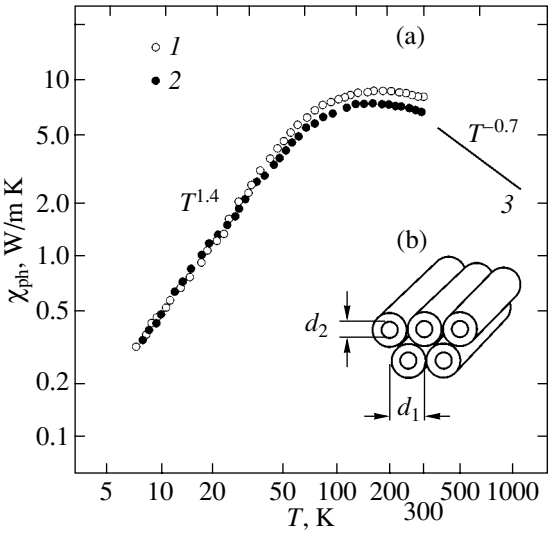

Fig. 1. (a) Temperature dependence of the thermal conductivity of crystalline chrysotile asbestos samples from (*1*) the first and (*2*) second lots and (*3*) of the forsterite mineral with zero porosity [6, 7]; (b) close-packed array of tubular chrysotile asbestos fibrils.

1063-7834/05/4702-0370$26.00 © 2005 Pleiades Publishing, Inc.

rials of fibrils in the nanocomposite asbestos matrix + channel filling.

We report here on our measurements of the thermal conductivity (κ), specific heat (C), and sound velocity (v) performed on a number of chrysotile asbestos samples.

In the experiments, we used samples of natural "brittle" chrysotile asbestos obtained from two deposits. The samples differed in coloring; namely, those of lot 1 were yellowish and those of lot 2, greenish. The tube diameters of the samples studied were $d_1 \sim 300$ Å and $d_2 \sim 50$ Å (Fig. 1b).

The thermal conductivity of the sample from lot 1 was studied in the range 5–300 K on a setup similar to that employed in [9]. The procedure of κ measurement did not differ from the one described in [1].

To remove water from the tube channels, the sample was preliminarily annealed in air at ~150°C. This procedure did not entail any loss of bound water from the sample [10]. After the annealing, a thin layer of varnish was applied to the sample end faces to prevent atmospheric moisture from penetrating into the asbestos tube channels while the sample was being fixed in the setup. The thermal conductivity κ was measured in vacuum. The heat flux was directed along the asbestos fibrils. The sample dimensions were $3 \times 4 \times 12$ mm. Since chrysotile asbestos is an insulator, the experimentally measured κ is actually the thermal conductivity of the crystal lattice, κ_{ph}.

Figure 1a presents experimental data on $\kappa_{ph}(T)$ for chrysotile asbestos. The data obtained in this work (symbols *1*) are complemented by $\kappa_{ph}(T)$ measurements from [1] made by us on a sample from lot 2 (symbols *2*). Also shown for comparison are the results reported on $\kappa_{ph}(T)$ for forsterite (symbols *3*) [6, 7]. Forsterite $2MgO \cdot SiO_2$, a mineral of the olivine group, is close in chemical composition to chrysotile asbestos.

As follows from Fig. 1, the thermal conductivities of samples of chrysotile asbestos taken from two different deposits are fairly similar. There is only a slight deviation for $T > 50$ K, which can probably be assigned to the presence of different kinds (or concentrations) of residual impurities in them. For $T < 50$ K, their thermal conductivities turned out to be practically identical (for the temperature region 5–50 K, $\kappa_{ph} \sim T^{1.4}$).

Ultrasonic measurements were conducted in a compensation arrangement operating in a pulsed regime, thus permitting reliable isolation of different sonic modes [11]. The measurements were done on two samples of chrysotile asbestos from lots 1 and 2.

The samples were cut along the fibrils. To prevent foliation from occurring in the mechanically weak samples, they were clamped rigidly and the end faces were ground with micron-grit abrasive paper without the use of any wetting fluid. The plane-parallel adjustment of the operating faces was monitored with an optimeter to within ~1 μm. To improve sonic mode separation, germanium delay lines were used, which sandwiched the sample. GKZh-94 silicone oil was used to provide acoustic contact between the sample, the delay lines, and lithium-niobate piezoelectric transducers. The absolute values of the sound velocities were measured at 77 K. The technique employed ensured a sufficiently high measurement accuracy (~1%) in strongly scattering samples. We measured the phase–frequency characteristic (PFC) of the acoustic train, which consisted of two delay lines within a fixed frequency interval. Next, the PFC of the sample sandwiched between these same delay lines was determined at the same temperature. The difference between the two PFCs, i.e., the PFC of the sample, was given in the form of a straight line; its slope yielded the phase velocity of sound, $v = 360L/S$, where v is the sound velocity (cm/s), L is the sample thickness (cm), and S is the slope of the sample PFC (deg/Hz).

We obtained the following values for the sound velocities: $v_l \approx 8.4 \times 10^5$ cm/s and $v_t \approx 2.6 \times 10^5$ cm/s (longitudinal and transverse velocities, respectively) for the asbestos sample from lot 1 with an acoustic path length $L = 4.13$ mm and $v_l \approx 8.3 \times 10^5$ cm/s and $v_t \approx 2.7 \times 10^5$ cm/s for the asbestos sample from lot 2 with an acoustic path length $L = 7.24$ mm.

We calculated the elastic moduli to be $c_{33} \approx 19.1 \times 10^{11}$ dyn/cm^2 and $c_{44} \approx 1.83 \times 10^{11}$ dyn/cm^2 for the sample from lot 1 and $c_{33} \approx 18.6 \times 10^{11}$ dyn/cm^2 and $c_{44} \approx 1.96 \times 10^{11}$ dyn/cm^2 for the sample from lot 2.

The density of chrysotile asbestos used in the calculations (2.7 g/cm^3) was determined from x-ray diffraction data. As was the case with thermal conductivity, the acoustic characteristics of the samples of chrysotile asbestos taken from different deposits turned out to be almost identical.

Figure 2a displays experimental data on the specific heat C_p of the sample of chrysotile asbestos from lot 2. The heat capacity was measured in the temperature interval 3–65 K by the pulsed quasi-adiabatic method [12]. Below 6 K, $C_p(T)$ can be written as the sum of two terms:

$$C_p = 4.26373 \times 10^{-5} T + 1.04994 \times 10^{-6} T^3. \quad (1)$$

For $T > 6$ K, the specific heat scales as $C_p \sim T^{2.4}$.

Figure 2b presents data on the specific heat C for the forsterite mineral [6]. It was found that its specific heat is close to the specific heat we measured for chrysotile asbestos.

As already mentioned [1], the behavior of $\kappa_{ph}(T)$ of chrysotile asbestos is distinguished by the presence of a maximum at a fairly high temperature (~150–170 K). The actual behavior of $\kappa_{ph}(T)$ in the vicinity of the maximum and at the maximum itself depends on many factors [13–15]. One could put forward at least two possible explanations for the observed effect.

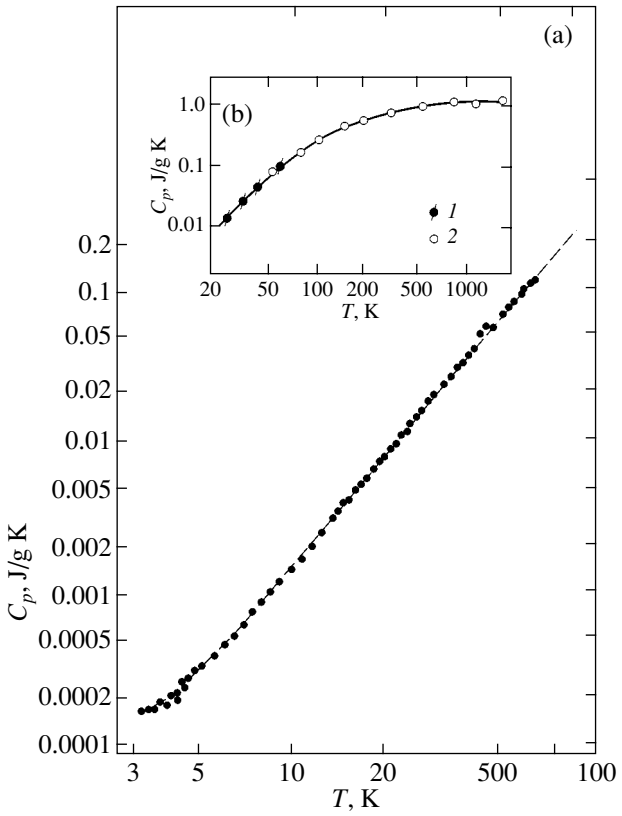

Fig. 2. Specific heats (a) of crystalline chrysotile asbestos and (b) of (*1*) chrysotile asbestos and (*2*) the forsterite mineral [6].

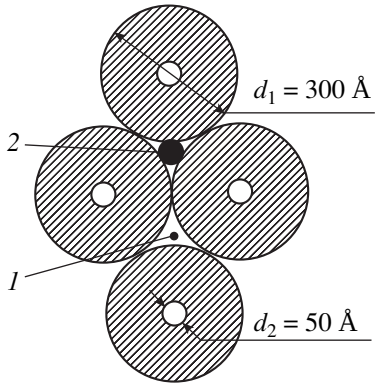

Fig. 3. Chrysotile asbestos lattice (schematic). The dimensions of the tubes (d_1), channels (d_2), and (*1*) gaps between tubes are drawn in the same scale corresponding to d_1 = 50 Å and d_2 = 300 Å; (*2*) filled channels.

(1) Samples of the chrysotile asbestos contain large amounts of impurities and, possibly, of defects, and this is what accounts for the shift in T_{max} of the thermal conductivity toward higher temperatures. It is assumed that T_{max} for a more perfect sample of chrysotile asbestos lies at low temperatures. This effect has been reported in the literature for a number of materials with defects and impurities. However, the values of T_{max} for them may or may not exhibit a shift toward higher temperatures as compared to the pure material, depending on the nature of the material and the actual types of impurities and defects. For instance, the T_{max} of thermal conductivity is displaced toward higher temperatures in KCl and LiF with KNO_2 and Mg impurities, respectively; in KCl, LiF, and CaF_2 under deformation; and in InSb with an increased carrier concentration or under electron irradiation. No shift has been observed in KCl having an iodine impurity or in samples of crystalline quartz irradiated by fast neutrons, although a substantial decrease in κ_{ph} was detected in this case [13].

Regrettably, there is no way to check this assumption experimentally for chrysotile asbestos, because this material is not a synthetic crystal, whose purity can be varied at will and monitored, but rather a natural mineral, with impurities and defects and their concentrations set by nature.

Our $\kappa_{ph}(T)$ measurements conducted on samples from two different deposits (samples *1* and *2*, Fig. 1a) argue against the above explanation of the effect observed in chrysotile asbestos. T_{max} of κ_{ph} for them lies in the range 150–170 K, although they should, most likely, contain impurities in different amounts (and, possibly, of different types).

(2) $\kappa_{ph}(T)$ may pass through a maximum when the phonon mean free path length l in the classical case becomes comparable to the dimensions of the sample (or of part of it if the sample has a complex geometric configuration). Such "critical" dimensions in the chrysotile asbestos samples studied in this work could be cross-sectional dimensions: 3 × 4 mm for sample *1*, 5.5 × 6.5 mm for sample *2* [1] (Fig. 1a), $(d_1 - d_2)/2$ = 125 Å for tube walls, or ~40–50 Å for the space between tubes filled with an amorphous (or fine-grained) mass of the tube material [3] (void *1* in Fig. 3) and extended along the asbestos fibrils.

Using the experimental values of κ_{ph} and $\bar{v} = (2v_t + v_l)/3$ and the data on C_p from Fig. 2b, we can estimate the value of l corresponding to the maximum in κ_{ph} at $T \approx$ 150–170 K from the formula

$$l = (3\kappa_{ph}/C\bar{v}). \quad (2)$$

For T = 170 K, l was found to be ~40 Å, which corresponds to the dimensions of filled channels between the tubular fibrils (channel *2* in Fig. 3). The results obtained require comprehensive theoretical analysis.

In the table, we list the averaged values of $C_p(T)$ and $\kappa_{ph}(T)$ relating to samples from lots 2 and 1 (points in Fig. 1a), respectively, which may prove useful in thermophysical calculations for systems based on chrysotile asbestos.

Averaged experimental values of $C_p(T)$ and $\kappa_{ph}(T)$ for chrysotile asbestos

T, K	κ, W/m K	C_p, J/g K
5	0.207	0.00034
10	0.48	0.0015
20	1.25	0.0086
30	2.50	0.0240
40	3.55	0.045
50	4.75	0.070
60	5.75	0.108
80	7.00	
100	7.75	
120	8.20	
140	8.40	
160	8.55	
180	8.60	
200	8.55	
220	8.42	
240	8.27	
260	8.18	
280	8.07	
300	8.00	

ACKNOWLEDGMENTS

This work was conducted within a bilateral agreement between the Russian and Polish Academies of Sciences and was supported by the Russian Foundation for Basic Research (project nos. 02-02-17657, 04-02-16550) and the Polish State Committee for Scientific Research (KBN, project no. 3T08A05426).

REFERENCES

1. Yu. A. Kumzerov, L. S. Parfen'eva, I. A. Smirnov, H. Misiorek, J. Mucha, and A. Jezowski, Fiz. Tverd. Tela (St. Petersburg) **45** (1), 56 (2003) [Phys. Solid State **45**, 57 (2003)].
2. V. N. Bogomolov and Yu. A. Kumzerov, Preprint No. 971, FTI (Physicotechnical Inst., USSR Academy of Sciences, Leningrad, 1985).
3. Yu. A. Kumzerov, in *Nanostructured Films and Coatings*, Ed. by Gan-Moog Chow, I. A. Ovid'ko, and T. Tsakalakos (Kluwer Academic, Dordrecht, 2000), NATO Science, Ser. 3: High Technology, Vol. 78, p. 63.
4. V. V. Bakhterev and V. I. Solomonov, Neorg. Mater. **31** (4), 567 (1995).
5. W. L. Bragg and G. F. Claringbull, *Crystal Structure of Minerals* (Bell, London, 1965; Mir, Moscow, 1967).
6. R. E. Krzhizhanovskiĭ and Z. Yu. Shtern, *Thermal Properties of Nonmetallic Materials* (Énergiya, Leningrad, 1973) [in Russian].
7. W. D. Kingery and J. Franel, J. Am. Ceram. Soc. **37** (2), 107 (1954).
8. K. Yada, Acta Crystallogr. **23**, 704 (1967).
9. A. Jezowski, J. Mucha, and G. Pompe, J. Phys. D: Appl. Phys. **7**, 1247 (1974).
10. L. A. Drobyshev and Ya. Ya. Govorova, Kristallografiya **16** (3), 544 (1971) [Sov. Phys. Crystallogr. **16**, 460 (1971)].
11. E. A. Masalitin, V. D. Fil', K. R. Zhekov, A. N. Zholobenko, and T. Ignatova, Fiz. Nizk. Temp. **29** (1), 93 (2003) [Low Temp. Phys. **29**, 72 (2003)].
12. A. I. Krivchikov, B. Ya. Gorodilov, and A. Czopnik, in *Proceedings of Conference on Low Temperature Thermometry and Dynamic Temperature Measurement* (ILTandSR, Wroclaw, 1997), p. V7.
13. V. S. Oskotskiĭ and I. A. Smirnov, *Defects in Crystals and Thermal Conductivity* (Nauka, Leningrad, 1972) [in Russian].
14. I. A. Smirnov and V. S. Oskotski, in *Handbook on the Physics and Chemistry of Rare Earths*, Ed. by K. A. Gschneidner, Jr. and L. Eyring (Elsever, Amsterdam, 1993), Vol. 16, p. 107.
15. R. Berman, *Thermal Conduction* (Oxford Univ. Press, Oxford, 1976; Mir, Moscow, 1979).

Translated by G. Skrebtsov

Physics of the Solid State, Vol. 47, No. 2, 2005, pp. 374–377. Translated from Fizika Tverdogo Tela, Vol. 47, No. 2, 2005, pp. 361–364.

POLYMERS AND LIQUID CRYSTALS

Specific Features of Structural Defects in Twisted Nematic Liquid Crystals under Conditions of Electrohydrodynamic Instability

O. A. Skaldin*, G. R. Yakupova*, V. A. Delev*, Yu. A. Lebedev*, and A. A. Nazarov**

** Institute of Molecular and Crystal Physics, Ufa Scientific Center, Russian Academy of Sciences, Ufa, 450075 Bashkortostan, Russia*

e-mail: scala@anrb.ru

*** Ufa State Technical University of Aviation, Ufa, 450000 Bashkortostan, Russia*

e-mail: nazarov@anrb.ru

Received March 17, 2004

Abstract—The influence of inhomogeneous boundary conditions (director orientation) on the specific features of the formation and evolution of structural defects in 90·-twisted nematic liquid crystals (twisted structures) is investigated in the regime of electrohydrodynamic instability. It is found that, unlike the domain structure of nematic liquid crystals with a planar orientation, in which defects with topological indices of ±1 are formed under conditions of electrohydrodynamic instability, the domain structure of twisted nematic liquid crystals contains both the above defects and defects with a topological index of 0. It is shown that structural defects with a topological index of 0 are stable and that the existence of these defects is associated with the axial velocity $\mathbf{u}_a$ of nematic liquid-crystal flow in the domains. © *2005 Pleiades Publishing, Inc.*

1. INTRODUCTION

In recent years, considerable advances have been made in the study of nonlinear phenomena in nonequilibrium media, specifically in liquid crystals; however, the mechanisms of the formation and evolution of spatially modulated structures in these systems are poorly understood [1]. Nematic liquid crystals undergo nonequilibrium structural phase transformations, such as transitions to a dynamic disorder under conditions of electrohydrodynamic instability, the formation of stable domain structures with different symmetries, and the nucleation and evolution of structural defects.

It is well known that the crossover to a spatiotemporal turbulence or a "weak" turbulence [2, 3], as a rule, is accompanied by the nucleation of defects of different types. This is characteristic of both isotropic liquids (Rayleigh–Benard convection) and anisotropic liquids (electrohydrodynamic instability in a nematic liquid crystal) [2–4]. Eventually, the interaction of these defects determines the specific properties of one or another state of the system. In particular, the nucleation and annihilation of defects in different structures are the most general mechanisms responsible for the selection of wave vectors of the domain lattice. Therefore, in order to understand the complex dynamics of structural phase transitions or a weakly turbulent state of the system, it is necessary first of all to investigate the properties and behavior of defects in the domain structures. From this point of view, liquid crystals are excellent model objects for use in analyzing the mechanisms of the nucleation and evolution of structural defects [4, 5].

The mechanisms of the nucleation and evolution of structural defects have been most thoroughly investigated under conditions of electrohydrodynamic instability in a nematic liquid crystal with a planar orientation of the field of the director **n**. The sequence of structural transitions up to the dynamic scattering mode, the statistical properties of defects, and their dynamic behavior were described in sufficient detail in [4, 6]. However, there are only a few works concerned with the properties of defects and the structural transformations occurring in nematic liquid crystals with inhomogeneous (twisted and homeoplanar) orientations of the director. In particular, Delev *et al.* [7] analyzed the linear threshold characteristics of the electrohydrodynamic instability in twisted nematic liquid crystals and the evolution of domain structures for different angles of twist. In regard to determining the role played by defects in structural transitions in twisted nematic liquid crystals above the instability threshold, there are only fragmentary data in the literature [8].

In this respect, the purpose of the present work was to study and classify defects inherent in the domain structure in a 90°-twisted nematic liquid crystal in the conducting regime of electrohydrodynamic instability and their behavior in an ac electric field.

1063-7834/05/4702-0374$26.00 © 2005 Pleiades Publishing, Inc.

2. SAMPLE PREPARATION AND EXPERIMENTAL TECHNIQUE

A nematic liquid crystal, namely, 4-*n*-methoxybenzylidene-*n*-butylaniline, was chosen as the object of our investigation. The liquid crystal was sandwiched between two glass substrates with SnO_2 conducting coatings. The substrates were separated by mica spacers of thickness $d = 20$ μm. In order to provide appropriate orientation by the substrates, the conducting coatings were rubbed in one direction and were then rotated through 90° with respect to each other. Since the adhesion of nematic liquid-crystal molecules at the boundary was sufficiently strong, the voltage used in the experiment had no effect on the orientation of the nematic liquid crystal at the boundary. An alternating voltage U at a frequency of 20 Hz was applied across the nematic liquid-crystal layer.

3. RESULTS AND DISCUSSION

In an electric field with a voltage $U = U_{cr} \approx 6$ V (i.e., at $\varepsilon = 0$, where $\varepsilon = \left[\frac{U^2}{U_{cr}^2} - 1\right]$ is the supercriticality parameter) across the nematic layer, there arises a periodic structure of stripe domains (rolls) arranged perpendicularly to the nematic liquid-crystal orientation at the center of an undisturbed layer [9]. The elementary defect formed in this structure is an additional pair of broken rolls (dislocation). Unlike the domain structure of nematic liquid crystals with a planar orientation, the domain structure of twisted nematic liquid crystals contains both dislocations with topological indices of ±1 (Fig. 1a) and new defects with a topological index of 0 (Fig. 1b). The existence of the latter defects is associated with the axial velocity $\mathbf{u}_a$ of nematic liquid-crystal flow in domains. The direction of the axial velocity is shown by arrows in Fig. 1. The schemes illustrating the nematic liquid-crystal flows in domains with defects of two types are depicted in Figs. 1c and 1d. It should be noted that defects of the first type are singular. This becomes evident from the following reasoning. Let us consider a homogeneous periodic structure of the domains oriented along the Y axis. This structure is characterized by the wave vector $\mathbf{q}_0 = \mathbf{grad}\Phi(q_0/X)$, where $\Phi = q_0x + \varphi$ is the spatial phase of the change, for example, in the vertical component of the convective velocity $\mathbf{u}_c$ of the rolls, and φ is a phase constant (in the general case, it is a function of x and y). For φ = const, the integral taken along the line of the defect (Fig. 1a)

$$\oint_C \mathbf{grad}\,\Phi\, ds \neq 0 \qquad (1)$$

is equal to 2π for defects of the first type. This is consistent with the assumption that such a defect with topological indices of ±1 is an additional pair of domains in the structure; i.e., this determines the singularity of defects of the first type. By contrast, defects of the second type (Fig. 1b) should be nonsingular, because the contour integral (1) is found to be equal to zero. However, in the latter case, there exist specific features that require explanation. In actual fact, when the contour integral (1) in the general case is less than 2π, spatial distortions of the nonsingular domain structure can be associated with the local dependence φ(x, y). Such defects (which, in essence, are large-scale spatial fluctuations of the field of velocities and the director) are usually referred to as localized phase modulations [10]. In general, these defects are homotopic to a point. This property is responsible for their instability and, consequently, for their relaxation with time to an equilibrium homogeneous state of the one-dimensional domain lattice. Such a situation is typical of the planar case. In our case, the defect has a stable configuration due to the specific features of hydrodynamic flows in the domain structure of the twisted nematic liquid crystal. As was noted above, apart from the conventional convective component of the velocity $\mathbf{u}_c$, which is characteristic of spatially modulated structures with a planar homogeneous orientation of liquid-crystal molecules, the velocity of flows in domains of twisted structures has an axial component $\mathbf{u}_a$. The continuity of this component ensures the existence of a local potential wall (Fig. 1b) that prevents annihilation of the defects.

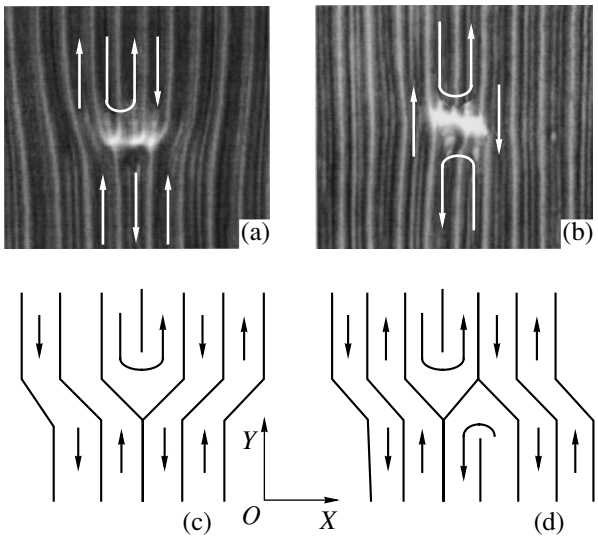

Fig. 1. Micrographs of defects with topological indices of (a) ±1 and (b) 0 in a twisted nematic liquid crystal and (c, d) the schemes of hydrodynamic flows in these defects.

In the core of dislocations with topological indices of ±1, there exists a region in which the domain structure is distorted significantly (see inset to Fig. 2). This region is located perpendicularly to the domain axes. Beginning from the instant of nucleation of a defect, the effective size L_{eff} of this core initially increases with an increase in the voltage (a similar effect was observed by

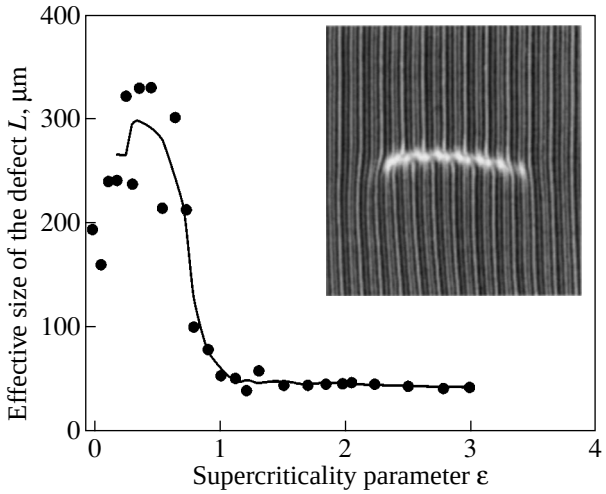

Fig. 2. Dependence of the size of the dissociated core of a dislocation with topological indices of ±1 on the parameter ε. The inset shows the micrograph of a dislocation with $L > 2d$.

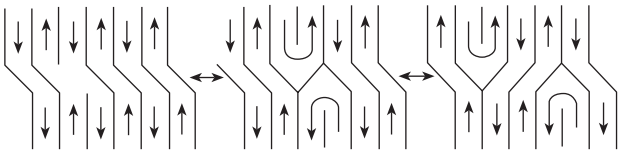

Fig. 3. Schematic diagram illustrating the periodic redistribution of convective flows in the course of oscillations of a defect with topological indices of ±0 at ac voltages higher than 7.4 eV (ε = 0.52).

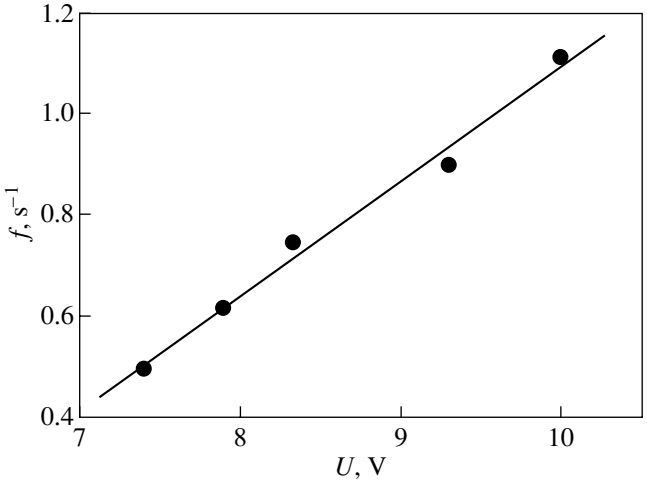

Fig. 4. Dependence of the oscillation frequency of a defect on the applied voltage U.

Joets and Ribotta [10] for liquid-crystal layers with a homogeneous planar orientation) but only in the vicinity of $\varepsilon \geq 0$. A further increase in the voltage leads to a decrease in the core size to the size of the core of an elementary defect with $L = 2\lambda$ at $\varepsilon = 1.3$ (where λ is the size of a single domain) (Fig. 2). In our opinion, this behavior is specific to twisted structures.

Now, we consider a defect of size L in a one-dimensional homogeneous lattice at a voltage U applied across the layer (see inset to Fig. 2). According to Friedel [11], the dissociated cores of these defects are arranged in a line and the entire structure is isomorphic to two partial dislocations separated by a distance L. The distance L depends on the effective force and energy parameters of the domain lattice and on the dynamics of nematic liquid-crystal flows. In this case, a partial dislocation is associated with either the presence or the absence of one stripe domain that cannot exist individually by virtue of the symmetry of the twisted structure. The partial dislocations are separated by a fault defect, i.e., a line separating regions displaced with respect to each other by one domain. This line indicates a discontinuity in the monotonic distribution of the axial velocity $\mathbf{u}_a$ of nematic liquid-crystal flows along the domains. Therefore, the equilibrium state of this system of dislocations can be described by the following equation [11, 12]:

$$\frac{b^2 G}{r} = \gamma_0 + \gamma_a. \qquad (2)$$

Here, b is the Burgers vector of the partial dislocation (which is equal to the spacing of the one-dimensional lattice $\lambda \sim d$), G is the effective modulus of elasticity (rigidity) of the one-dimensional lattice of the rolls (this modulus depends on the character of convective flows of the nematic liquid crystal and, to a first approximation, is proportional to the square of the velocity of convection $|\mathbf{u}_c|^2$, which itself is quadratic in the field E or in the voltage U) [13], and r is the dislocation spacing. To a first approximation, the quantities γ_0 and γ_a are the constants related to the linear energy density of the fault defect. In this case, γ_0 and γ_a are determined by the convective and axial components of the nematic liquid-crystal flows in the twisted structures, respectively. As a result, the effective modulus of elasticity G for small supercriticality parameters ε can be written in the form

$$G \sim \alpha |u_c|^2 \sim \beta U^4 \sim \beta \varepsilon^2, \qquad (3)$$

where α and β are coefficients of proportionality.

According to relationship (3), the mean distance between the partial dislocations (the mean size of the defect) at voltages that are slightly above the threshold U_{cr} increases quadratically with an increase in the supercriticality parameter ε: $L_{eff} \simeq b\beta\varepsilon^2/(\gamma_0 + \gamma_a)$. This is confirmed by the results obtained by Joets and Ribotta [10]. As was noted above, with a further increase in the supercriticality parameter ε, the effec-

tive size L_{eff} tends to a minimum value equal to twice the spacing of the domain lattice. The deformation field (or the core of the defect with a topological index of 0) is characterized by the size $L = 2\lambda$, which does not change with increasing voltage.

At voltages below $U = 7.4$ V ($\varepsilon = 0.52$), the convective flow in the cores of defects of both types becomes steady. As the alternating voltage applied across the cell increases, the velocity of the flow in the defect core begins to vary periodically with time. In essence, this behavior corresponds to domain oscillations. The redistribution of convective flows in the defect with a topological index of 0 is schematically depicted in Fig. 3. The oscillation of this defect is associated with the periodic nucleation and annihilation of a pair of topological defects with indices of ±1. It is found that the oscillation frequency is directly proportional to the applied voltage (Fig. 4). This finding correlates with the linear dependence of the axial velocity of nematic liquid-crystal flow in the domain on the applied voltage [9].

4. CONCLUSIONS

Thus, in the present work, we studied defects of the domain structure in a 90°-twisted nematic liquid crystal under conditions of electrical convection. A new type of defects with a topological index of 0 was revealed in the nematic liquid crystals under investigation. The stability of these defects is provided by a specific feature of hydrodynamic flows, namely, the axial c velocity $\mathbf{u}_a$ of the hydrodynamic flow along the domain axis. The dependences of the effective size of the deformation field and the frequency of oscillations of these defects on the applied voltage were determined. It was shown that an increase in the voltage leads to a decrease in the size of the deformation field to the size of an elementary defect ($2\lambda = 40$ μm).

ACKNOWLEDGMENTS

This work was supported by the Russian Foundation for Basic Research (project no. 02-02-17435) and the Russian federal program "Integration" (project no. B0065).

REFERENCES

1. W. Pesch and U. Behn, in *Evolution of Spontaneous Structures in Dissipative Continuous Systems*, Ed. by F. H. Busse and S. C. Muller (Springer-Verlag, Berlin, 1999).
2. E. Bodenschatz, A. Weber, and L. Kramer, J. Stat. Phys. **64**, 1007 (1991).
3. F. H. Busse, in *Hydrodynamic Instabilities and the Transition to Turbulence*, Ed. by H. L. Swinney and J. P. Gollub (Springer-Verlag, Berlin, 1985).
4. S. Rasenat, V. Steinberg, and I. Rehberg, Phys. Rev. A **42**, 5998 (1990).
5. A. Joets and R. Ribotta, J. Phys. (Paris) **47**, 595 (1986).
6. S. Kai, N. Chizumi, and M. Kohno, J. Phys. Soc. Jpn. **58**, 3541 (1989).
7. V. A. Delev, P. Toth, and A. P. Krekhov, Mol. Cryst. Liq. Cryst. **351**, 179 (2000).
8. G. R. Yakupova and O. A. Skaldin, Pis'ma Zh. Tekh. Fiz. **29** (21), 27 (2003) [Tech. Phys. Lett. **29**, 892 (2003)].
9. A. Hertrich, A. P. Krekhov, and O. A. Scaldin, J. Phys. II **4**, 239 (1994).
10. A. Joets and R. Ribotta, J. Stat. Phys. **64** (5/6), 981 (1991).
11. J. Friedel, *Dislocations* (Pergamon, Oxford, 1964; Mir, Moscow, 1967).
12. J. P. Hirth and J. Lothe, *Theory of Dislocations* (McGraw-Hill, New York, 1967; Atomizdat, Moscow, 1972).
13. O. S. Tarasov, A. P. Krekhov, and L. Kramer, Phys. Rev. E **68**, 031708 (2003).

Translated by O. Borovik-Romanova

Physics of the Solid State, Vol. 47, No. 2, 2005, pp. 378–389. Translated from Fizika Tverdogo Tela, Vol. 47, No. 2, 2005, pp. 365–375.

FULLERENES AND ATOMIC CLUSTERS

Dimension of Mesogenic Molecules as Atomic Clusters

E. M. Aver'yanov

Kirensky Institute of Physics, Siberian Division, Russian Academy of Sciences, Akademgorodok, Krasnoyarsk, 660036 Russia

e-mail: aver@iph.krasn.ru

Received February 24, 2004

Abstract—The problem regarding the mass dimension D of mesogenic molecules as atomic clusters is formulated and solved using computer simulation and analytical calculations. For a large number of compounds belonging to different chemical classes, it is shown that the cores of discotic lacunar (rodlike, lathlike) molecules forming nematic or columnar discotic (calamitic) phases have a fractional dimension $1 < D_c < 2$ ($D_c \approx 1$). The dependences of the dimension D_c on the symmetry, the conformation, and the structural–chemical features of the molecular core are determined. It is demonstrated that, in the region of side flexible chains in molecules of both types, the dimension D_{ch} can be either smaller or larger than unity, depending on the chain conformation. An analytical expression accounting for the results of numerical experiments is obtained for the dimension D_{ch}. *© 2005 Pleiades Publishing, Inc.*

1. INTRODUCTION

In recent years, considerable attention has been focused on the physical and chemical properties of nanoparticles and their clusters with a fractional mass dimension $D < 3$ [1, 2]. In this respect, investigation into the dimension of the molecules treated as atomic clusters is an important problem. This problem is of special interest for mesogenic molecules that consist of tens or hundreds of atoms and are characterized by a wide variety of chemical structures and shapes [3–9]. These factors are primarily responsible for the character of molecular packing in the condensed state, the anisotropy of the local coordination environment of molecules, and the type of liquid crystals (calamitic, discotic) and their mesophases (nematic, smectic, columnar).

The shape of the molecules reflects the distribution of force centers throughout the molecular volume and affects the anisotropy of intermolecular interactions, the intermolecular correlations, the degree of orientational ordering of the molecules in a liquid crystal, the interrelation between the orientational and conformational degrees of freedom of the molecules, and the character of phase transitions. For example, discotic molecules, as a rule, have a planar central aromatic core with radial, relatively long, flexible aliphatic chains [5, 10]. The loose (lacunar [1]) structure of discotic molecules with the statistical symmetry axis C_k ($k \geq 2$) is characterized by large-sized lacunas (holes, cavities) between the core fragments or side chains and a large free volume per chain. It should be noted that the free volume increases with an increase in the chain length. This structure enhances the high conformational mobility of the chains. In turn, the high conformational mobility manifests itself both in the temperature dependence of the orientational order parameter of molecules $S(T)$ for discotic nematic liquid crystals N_D [11, 12] and in a decrease in the orientational order parameter S in the phases N_D and N_{Dre} with an increase in the chain length [13, 14].

The difference between the mass dimensions D of discotic lacunar molecules in the regions of the molecular core and side chains can account for the large differences between the orientational order parameters S, which are observed experimentally [11–14] and predicted by modern variants of the molecular-statistical theory and computer simulation for discotic nematic liquid crystals N_D (see [14] and references therein). In a recent paper [14], I analyzed these data, formulated a problem regarding the dimension of real discotic molecules, and made the assumption that the mass dimension D of these molecules is less than 2.

The purpose of this paper is to investigate both numerically and analytically the mass dimension for a representative set of known lathlike and lacunar mesogenic molecules of different chemical classes and to elucidate how the dimension of these molecules D_c (in the core region) and D_{ch} (in the region of side chains) depends on the symmetry, the size, the structural–chemical features, the conformation of molecular core fragments, and the length and conformation of the chains. The specific features of the objects under investigation and the technique of their computer simulation are considered in Section 2. The results of numerical treatment of the dimension D_c are presented and analyzed in Section 3. The results of numerical and analytical investigations of the dimension D_{ch} are discussed in Section 4. The main results obtained in this work and the conclusions drawn are briefly summarized in Section 5.

1063-7834/05/4702-0378$26.00

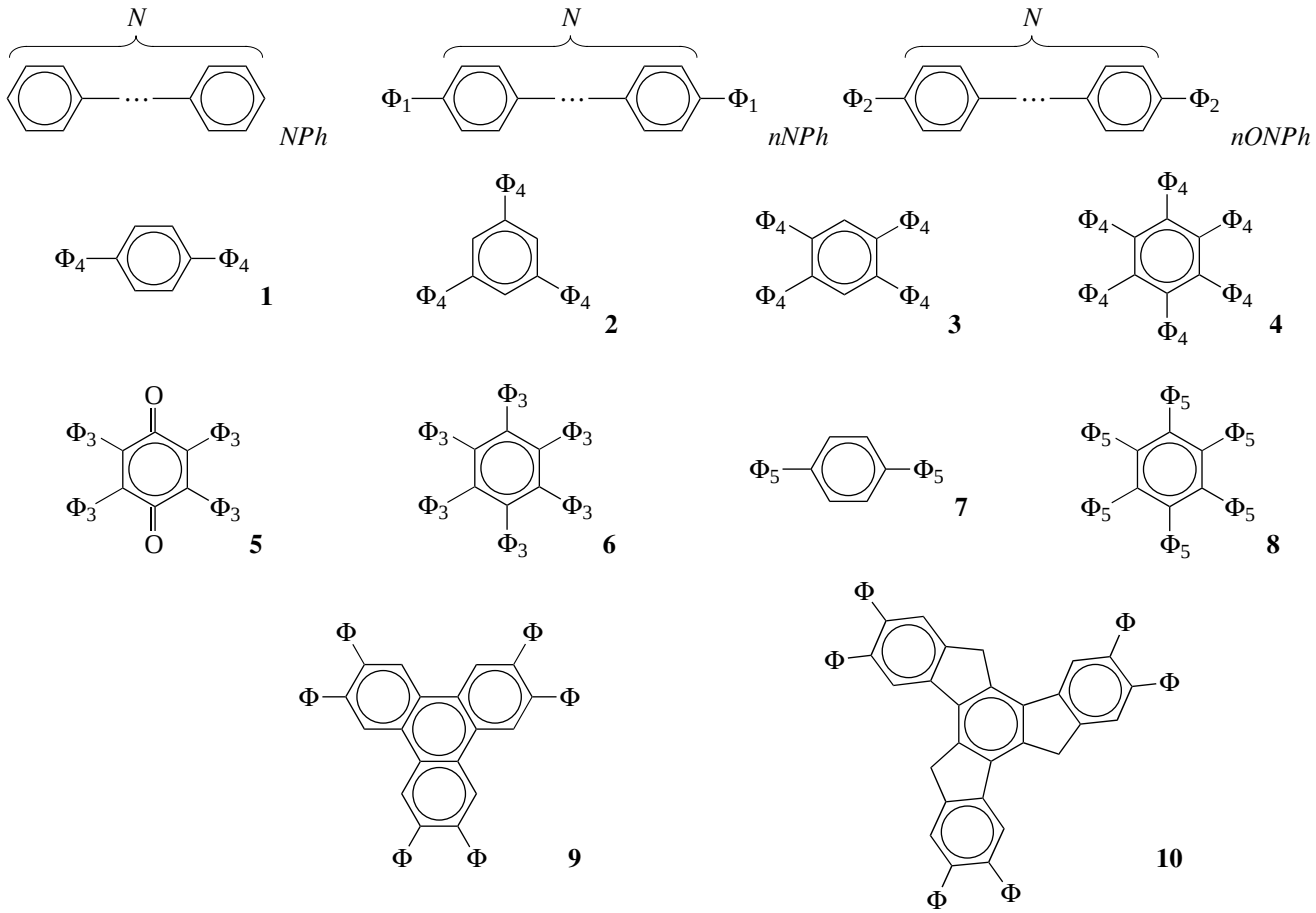

Fig. 1. Objects of investigation.

2. OBJECTS OF INVESTIGATION AND THEIR MODELS

The structural formulas of the studied compounds are presented in Fig. 1. These are the symmetrical molecules *NPh* [4, 7], *nNPh* [4, 15], and *nONPh*; molecules **1** and **7** [15] with rodlike or lathlike cores, which are abundant among calamitic liquid crystals; discotic molecules **2** [3, 16] and **3** [3, 4, 6]; model molecule **4** (for comparison with molecules **1**–**3**); and well-known molecules **5**, **6**, **8**, **9***a*–**9***d*, and **10***a*–**10***c* [3–7, 10], which form nematic and (or) columnar liquid-crystal phases. The orientational ordering of the usual, reentrant, or inverse nematic liquid-crystal phases was investigated for a number of homologs of compounds **8** [11, 12], **9***c* [14], and **10***b* [12, 13]. The chosen set include compounds with discotic molecules that have twofold (**3**, **5**), threefold (**2**, **9**, **10**), and sixfold (**4**, **6**, **8**) statistical symmetry axes C_k. It should be noted that, in each of the three core fragments related by the symmetry axis C_3 in molecules **10***a*–**10***c*, two Φ fragments occupy symmetrically nonequivalent positions. The discotic molecules under consideration differ both in the structure, size, and lacunarity of the central core fragment and in the structure of the Φ_1–Φ_5 fragments whose attachment differently increases the transverse size of the core and the degree of its lacunarity.

In order to avoid details that are immaterial for the qualitative and quantitative results of the analysis, each molecule is simulated by a cluster consisting of identical spherical atoms of radius *r* whose centers coincide with the centers of carbon and oxygen atoms in the core and alkyl (alkyloxy) chains of the molecule without regard for the differences between the van der Waals radii of the carbon and oxygen atoms and the CH, CH_2,

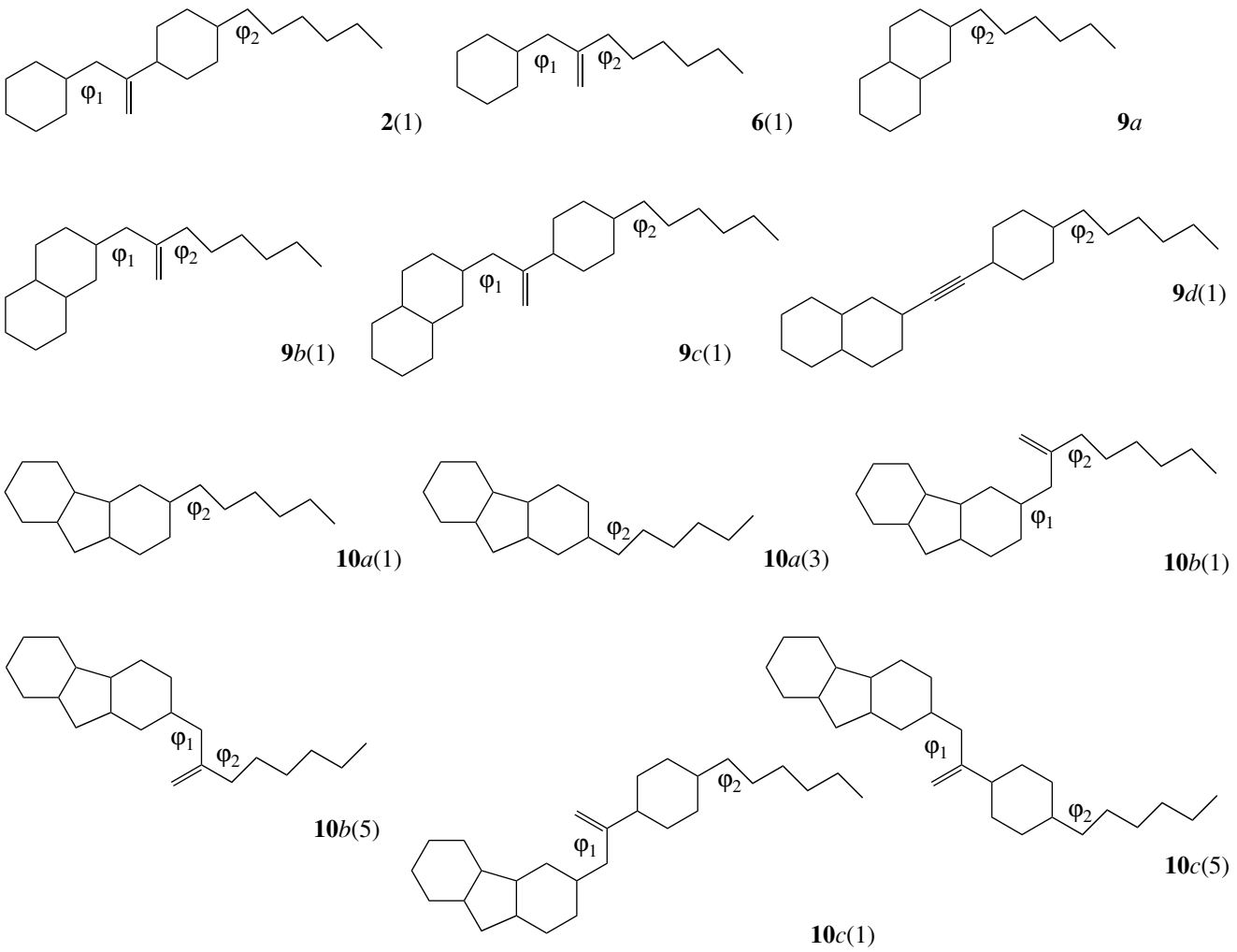

Fig. 2. Conformers of the side molecular fragments in the studied compounds.

and CH_3 groups. The lengths of all the bonds C–C, C≡C, C–O, and C=O are assumed to be $l = 2r$. All bond angles in the molecular cores and in the Φ_k fragments are taken to be equal to 120° (except for molecules **10***a*–**10***c* with regular pentagons and hexagons in the core), and the C–C–C bond angles in the alkyl chains are assumed to be equal to a tetrahedral angle of 109.47°. Hereafter, all the linear sizes will be given in conventional units that correspond to $r = 3.5$.

The main conformations of the Φ_k fragments with six (five) carbon atoms in the alkyl (alkyloxy) chains are shown in Fig. 2. The other conformations obtained from the main conformations by varying either the angle φ_1 between the planes of the C(O)O group and the O-phenyl ring of the core or the angle φ_2 between the plane of the carbon backbone of the side alkyl (alkyloxy) chain in the *trans* conformation and the plane of the phenyl ring or the C(O)O group bonded to this chain are listed in Table 1. For all the conformers containing the Φ_4 fragment, the plane of the C(O)O group coincides with the plane of the C-phenyl ring bound to this group. In what follows, we will use designations of the type **9***b*(1/3). This designation means that, in each of the three core fragments in molecule **9***b*, one Φ_3 fragment has conformation **9***b*(1) and another Φ_3 fragment has conformation **9***b*(3); in this case, identical conformers in each core fragment are related by the molecular symmetry axis C_3. It should be noted that the results given below do not depend on the angle $\varphi_1(\varphi_2)$ for molecules **1**–**6** [*nNPh*, *nOPh*, **7**, **8**, conformers **9***b*(1), **9***b*(2), **9***c*(1), **9***c*(2)] or on the dihedral angles between the phenyl rings for molecules *NPh*, *nNPh*, and *nOPh*.

The number $N(R)$ of spherical atoms inside the sphere of radius R whose center coincides with the center of the molecular core is counted in the numerical experiment. Since the atoms have identical mass, the mass $M(R)$ of the part of the molecule within the sphere varies as $M(R) \sim N(R)$. For the Φ_3 (Φ_4, Φ_5) fragments, it is assumed that the C(O)O group (phenyl ring) enters into the composition of the molecular core. The core

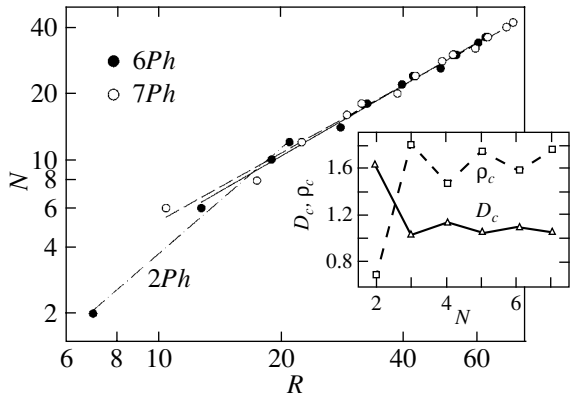

Fig. 3. Dependence $N(R)$ for *NPh* molecules. The inset shows the dependences of the parameters ρ_c and D_c on the number N of phenyl rings in the same molecules.

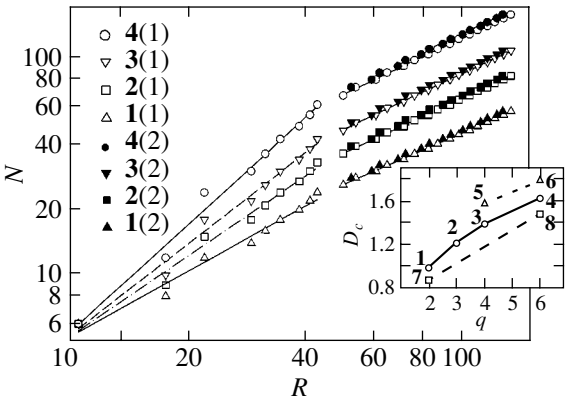

Fig. 4. Dependences $N(R)$ for compounds **1**–**8**. The inset shows the dependences of the parameter D_c on the number q of radial core fragments for molecules **1**–**8**.

radii R_c and the numbers of atoms in the cores $N_c = N(R_c)$ for the conformers of the compounds under consideration are presented in Table 2.

3. DIMENSION OF MOLECULES IN THE CORE REGION

The dependences of $\log N(R)$ on $\log R$ are characterized by the derivative

$$D(R) = \frac{d\ln N(R)}{d\ln R}. \quad (1)$$

For all the compounds and their conformers under investigation, the dependences of $\log N(R)$ on $\log R$ exhibit two linear portions with different derivatives $D(R) \approx$ const in the core region ($R \le R_c$) and the region of side chains ($R > R_c$). In the core region, these dependences in all the cases are described well by the relationship

$$\log N(R) = a_c + D_c \log R \quad (2)$$

with constant coefficients a_c and D_c. The observed deviations of a number of points from this dependence are primarily caused by the inclusion of the values of R for which the quantity $N(R)$ changes by an integral number of atoms. The use of a continuous function $M(R)$ leads to a smoothing of these deviations. In the range $R \le R_c$,

Table 1. Dihedral angles of the conformers under investigation

Conformer	**2**(1)	**2**(2)	**6**(1)	**6**(2)	**9***a*	**9***b*(1)	**9***b*(2)
φ_1	0–2π		0–2π		–	0	
φ_2	0	±π	0	±π	0	0	±π
Conformer	**9***b*(3)	**9***b*(4)	**9***c*(1)	**9***c*(2)	**9***c*(3)	**9***c*(4)	**9***d*(1)
φ_1	±π		0		±π		–
φ_2	0	±π	0	±π	0	±π	0
Conformer	**9***d*(2)	**10***a*(1)	**10***a*(2)	**10***a*(3)	**10***a*(4)	**10***b*(1)	**10***b*(2)
φ_1	–	–				0	
φ_2	±π	0	±π	0	±π	0	±π
Conformer	**10***b*(3)	**10***b*(4)	**10***b*(5)	**10***b*(6)	**10***b*(7)	**10***b*(8)	**10***c*(1)
φ_1	±π		0		±π		0
φ_2	±π	0	0	±π	±π	0	0
Conformer	**10***c*(2)	**10***c*(3)	**10***c*(4)	**10***c*(5)	**10***c*(6)	**10***c*(7)	**10***c*(8)
φ_1	0	±π		0		±π	
φ_2	±π	±π	0	0	±π	±π	0

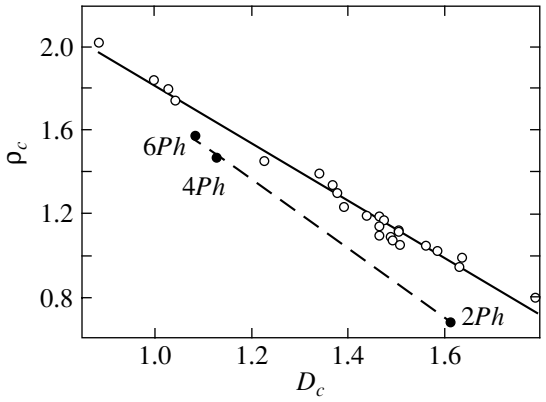

Fig. 5. Correlation between the parameters ρ_c and D_c in expression (3) for the studied compounds.

the dependence $N(R)$ can be approximated by the expression

$$N(R) = \rho_c(R/r)^{D_c} \quad (3)$$

with the fractional dimension $D = D_c$. The prefactor ρ_c characterizes the density of infill of the molecular core with atoms and depends on the shape and chemical structure of the core. The coefficients of relationship (2) were determined using the option of the Statistics (Linear Regression) of the Sigma Plot 8.0 software package. The parameters ρ_c and D_c for the compounds under investigation are given in Table 2. The parameters D_c for molecules *NPh*, *nNPh*, and *nONPh* with $N \geq 3$ are obtained by ignoring the data at $R = 7$ and $N = 2$.

It can be seen from Fig. 3 and the data presented in Table 2 that the values of D_c for molecules *NPh*, *nNPh*, *nONPh* ($N \geq 3$), and **1** are close to unity. This is consistent with the linear shape of these molecules. A decrease in the width of molecule **7** (the appearance of lacunas) between the central and terminal phenyl rings of the core results in a decrease in the parameter D_c to 0.885, whereas the presence of two adjacent planar phenyl rings in the cores of molecules 2*Ph*, *n*2*Ph*, and *nO*2*Ph* leads to a considerable increase in the parameter D_c. As a result, the cores of these molecules become similar to the cores of discotic molecules. The even–odd alternation of the parameters $\rho_c(N)$ and $D_c(N)$ for molecules *NPh* with a variation in the number N of phenyl rings (see inset to Fig. 3) indicates a difference between the properties of the first compounds with even and odd values of N in this series and also a high sensitivity of the parameters ρ_c and D_c to similar structural features of the core.

Judging from the parameters $1 < D_c < 2$ obtained for the discotic compounds, the disklike shape acceptable in the literature for their molecules does not correspond to the actual shape, because the disklike (disk-shaped) molecules should be described by expression (3) at $D_c = 2$. It seems likely that the loose structure of discotic molecules can be more precisely defined as a lacunar structure.

Let us consider the dependence of the parameter D_c on the number q of radial core fragments and the parameters R_c and N_c. At R_c = const, an increase in the parameter N_c and the number q of Φ_4 fragments in the series of compounds **1**–**2**–**3**–**4** leads to an almost linear increase in the parameter $D_c(q)$ and an irregular change in the index k of the symmetry axis C_k of the molecule. A similar increase in the parameter D_c is observed with an increase in the number of Φ_5 (Φ_3) fragments from two (four) to six upon transition **7** ⟶ **8** (**5** ⟶ **6**). Note that the slopes of the curves $D_c(q)$ in the above three cases are close to each other (see inset to Fig. 4). Owing to the denser infill of the circle of radius R with core fragments due to an increase in their number q, the parameter D_c tends to 2.

For q = const, an increase in the parameter R_c in the series **6**–**4**–**8** (**5**–**3**) is accompanied by an increase in the size of lacunas between the core fragments and a decrease in the parameter D_c. A similar situation is observed in the series **9***b*(1, 2)–**9***c*(1, 2)–**9***d*(1, 2). An increase in the lacuna size and the corresponding decrease in the parameter D_c also occur upon transition **9***a* ⟶ **10***a* (**9***b* ⟶ **10***b*, **9***c* ⟶ **10***c*) for molecules containing identical substituting fragments Φ due to the larger parameters R_c and the greater looseness of the unsubstituted core of molecule **10** as compared to the core of unsubstituted molecule **9**. However, the transition from conformer **10***b* to conformer **10***c* or **9***c* leads to an increase in the parameter D_c, because the relative increase in N_c is larger than that in R_c.

For N_c = const and q = const, the parameters R_c and D_c can depend on the conformation of the substituting side fragments Φ. The transitions **9***b*(1, 2) ⟶ **9***b*(3, 4), **9***c*(1, 2) ⟶ **9***c*(1/3, 2/3, 1/4, 2/4), **10***b*(1/5, 2/6) ⟶ **10***b*(1/8, 2/7), and **10***c*(1/5, 2/6) ⟶ **10***c*(1/8, 2/7) are accompanied by an increase in the parameter R_c and a decrease in the quantity D_c. On the other hand, the transitions **9***b*(3, 4) ⟶ **9***b*(1/3, 2/3, 1/4, 2/4) and **10***b*(1/8, 2/7) ⟶ **10***b*(3/6, 4/5) result in an increase in the parameter D_c for the former transitions and in a decrease in this parameter for the latter transitions at the same values of R_c. In these cases, when the parameter R_c varies insignificantly, the quantity D_c is predominantly determined by the density of infill of the core area with atoms of the substituting fragments Φ.

The correlation between the parameters ρ_c and D_c in expression (3) for all the studied compounds and their conformers is illustrated in Fig. 5. Without regard for the molecules *NPh* (N = 2, 4, 6), the dependence shown in Fig. 5 can be approximated by the relationship

$$\rho_c = b - fD_c \quad (4)$$

with parameters b = 3.186 and f = 1.378 and a correlation coefficient of 0.985. At D_c = 1, the density ρ_c =

1.808 exceeds $\rho_c = 1$ for a linear chain of spheres and reflects the specific features of the chemical structure of the cores in lathlike mesogenic molecules of types **1** and **7** with planar bridging fragments and (or) phenyl rings, which are responsible for the increase in the parameter ρ_c. At $D_c = 2$, the atomic packing density in the cores of the model molecules under consideration $\rho_c = 0.430$ is half as high as the density $\rho_c = \pi/(12)^{1/2} \approx 0.907$ for a close hexagonal packing of spheres in the plane at $R \gg r$ [2]. For molecules *NPh* ($N = 2, 4, 6$), the dependence shown in Fig. 5 can be approximated by relationship (4) with parameters $b = 3.349$ and $f = 1.657$ and a correlation coefficient of 0.999. According to this dependence, the density $\rho_c(D_c = 1) = 1.692$ appears to be close to that for the other compounds.

4. DIMENSION OF MOLECULES IN THE REGION OF SIDE CHAINS

It can be seen from Figs. 4 and 6 that, for all the studied compounds and their conformers, the dependence of $\log N(R)$ on $\log R$ in the range $R > R_c$ exhibits an almost linear behavior and, to a first approximation, can be represented in the form

$$\log N(R) = a_{ch} + D_{ch} \log R \qquad (5)$$

with constant parameters a_{ch} and D_{ch}. The effective mass dimensions D_{ch} of molecules in the chain region were obtained by averaging over the length of the chain containing 16 atoms (Table 2). As can be seen from Table 2, the dimensions $D_{ch} < 1$ and $D_{ch} > 1$ are observed for different compounds.

At $R_c = \text{const}$, an increase in the parameter N_c and the number q of chains per molecule in the series of compounds **1**–**2**–**3**–**4** leads to a monotonic increase in the dimension $D_{ch} < 1$. A similar increase in the parameter D_{ch} is observed with an increase in the number of chains from two (four) to six upon transition **7** ⟶ **8** (**5** ⟶ **6**). Therefore, owing to the denser infill of the spherical layer between the spheres of radii R_c and R with chains due to an increase in their number, the dimension D_{ch} tends to 1.

For molecules *nNPh*, an increase in the parameters N, N_c, and R_c results in a monotonic decrease in the dimension $D_{ch} < 1$. A similar regularity is observed upon transitions **6** ⟶ **4** (**5** ⟶ **3**) and **9***b*(1, 2) ⟶ **9***c*(1, 2). Upon transitions **9***b*(1/3, 2/3) ⟶ **9***c*(1/3, 2/3), **9***b*(1/4, 2/4) ⟶ **9***c*(1/4, 2/4), and **10***b*(3/6, 4/5) ⟶ **10***c*(3/6, 4/5), the inequality $D_{ch} > 1$ is reversed. This indicates that the dimension D_{ch} depends strongly on the parameters N_c and R_c. For effective dimensions $D_{ch} < 1$ ($D_{ch} > 1$), the derivative $D(R)$ [relationship (1)] increases (decreases) insignificantly with an increase in R and tends to unity.

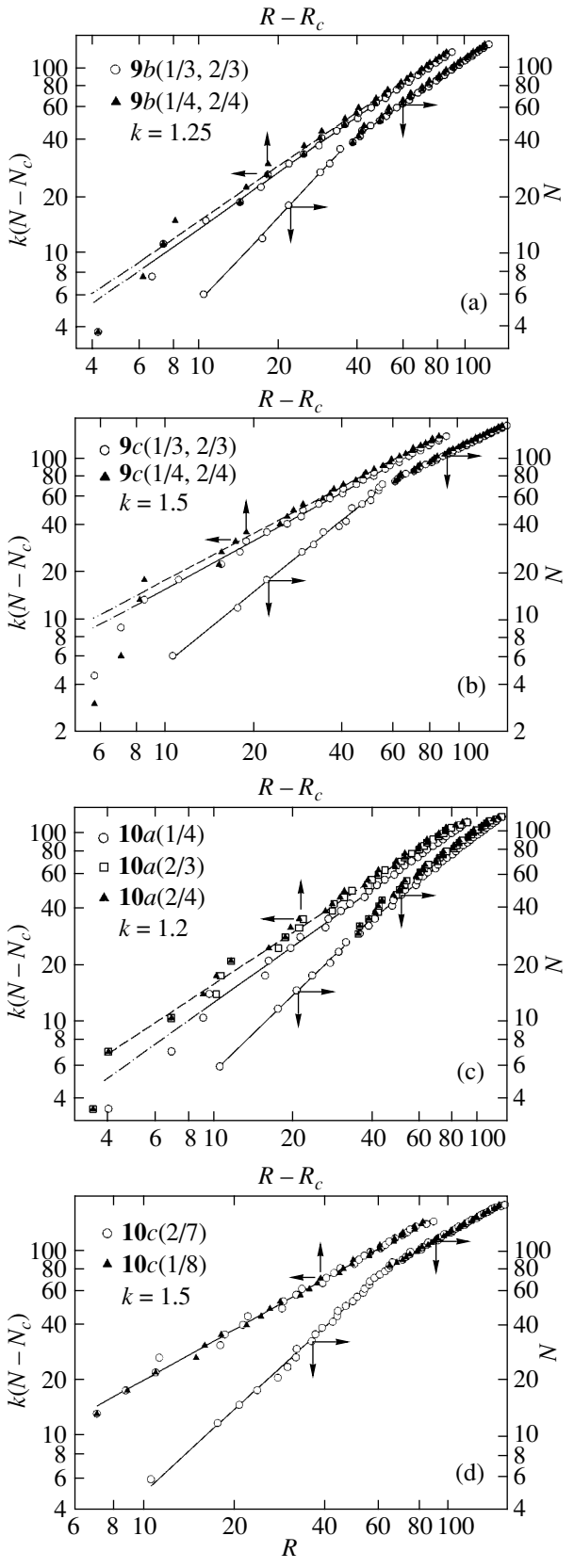

Fig. 6. Dependences of the parameters $N(R)$ and $k(N - N_c)$ on $(R - R_c)$ for the studied compounds.

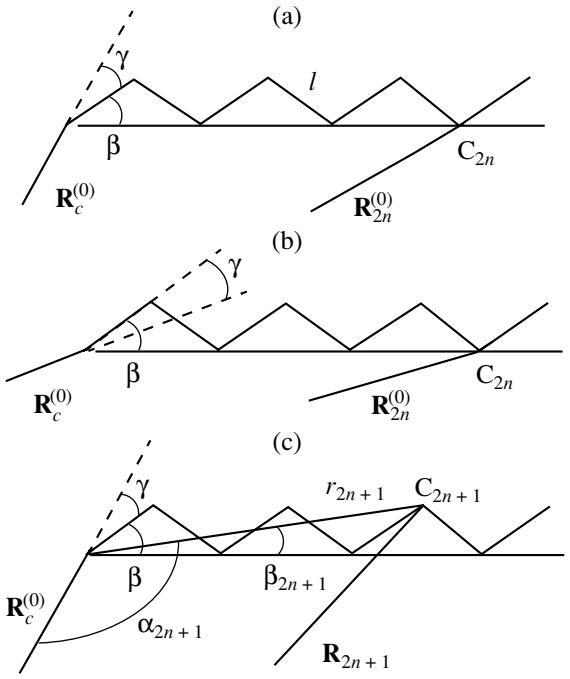

Fig. 7. Relative positions of the vectors $\mathbf{R}_c^{(0)}$ and $\mathbf{R}_p^{(0)}$ and the carbon backbone of the chain.

In the range $R > R_c$, we introduce the derivative

$$b_{ch}(R) = \frac{d\ln[N(R) - N_c]}{d\ln(R - R_c)}. \quad (6)$$

The dependences of $\log[N(R) - N_c]$ on $\log(R - R_c)$ for a number of compounds are plotted in Fig. 6. These dependences for the homologs with $n > 2$ exhibit a nearly linear behavior and are approximated well by the expression

$$\log[N(R) - N_c] = C_{ch} + b_{ch}\log(R - R_c) \quad (7)$$

with constant parameters C_{ch} and b_{ch}. The effective values of b_{ch} are presented in Table 2. For the majority of compounds, the inequality $b_{ch} \le 1$ is satisfied and the differences between the values of $b_{ch} > 1$ and unity are within the error in determining b_{ch}. It is seen that the studied compounds satisfy both inequalities $D_{ch} < b_{ch}$ and $D_{ch} > b_{ch}$ and the equality $D_{ch} = b_{ch}$ [for molecules **9***b*(1), **9***b*(2)]. Using compounds *n*2*Ph*–*n*4*Ph* as an example, it can be shown that the sensitivity of the quantity b_{ch} to variations in the parameters N_c and R_c is less than the sensitivity of the quantity D_{ch}. At R_c = const, an increase in the parameter N_c and in the number q of chains per molecule in the series of compounds **1**–**2**–**3**–**4** has no effect on the quantity b_{ch}, as is the case with the transition **7** ⟶ **8** (**5** ⟶ **6**). For all the compounds and their conformers, the dependence of the quantity b_{ch} on the conformation of the side core fragments and chains is substantially more pronounced than the corresponding dependence of the quantity D_{ch}.

Now, we turn to the explanation of the features revealed in the dependences of $D(R)$, D_{ch}, $b_{ch}(R)$, and b_{ch}. Let us consider a lacunar (lathlike) molecule with a statistical symmetry axis C_k ($k \ge 2$) that passes through the center of the molecular core perpendicularly to the core plane (i.e., normally to the longitudinal axis of the core). We assume that each of q core fragments related by the symmetry axis C_k has m side chains and each chain adopts a specific conformation. Then, within the cluster model for the molecule whose chains are located in the region $R > R_c$, we can write the relationship

$$N(R) = N_c + \frac{q}{2r}(R - R_c)\sigma(R). \quad (8)$$

The function $\sigma(r)$ is defined by the expression

$$\sigma(R) = \sum_{i=1}^{m} \kappa_p^{(i)}(R), \quad (9)$$

where the index i numbers the chains in a particular core fragment and p is the parity index of the C atoms in the chain. The function $\kappa_p^{(i)}(R)$, whose properties will be considered below, depends on the chain conformation and the angle between the axis of the chain in a *trans* conformation and the radius vector $\mathbf{R}_c^{(0)}$ that connects the center of the core to the center of the C_0 atom to which the chain is bonded. From expression (8), we obtain the relationship

$$\sigma(R) = \frac{2r[N(R) - N_c]}{q(R - R_c)}, \quad (10)$$

which can be conveniently used for determining the function $\sigma(R)$ from the results of the computer simulation.

From formula (6) with due regard for expression (8), we find

$$b_{ch}(R) = 1 + (R - R_c)\frac{d\ln\sigma(R)}{dR}. \quad (11)$$

As will be shown below, for chains that adopt a *trans* conformation and do not make very large angles with the radius vector $\mathbf{R}_c^{(0)}$, the decreasing function $\sigma(R)$ is weakly pronounced and tends to a limiting value with an increase in the parameter R. Therefore, we have the inequality $b_{ch}(R) \le 1$ and find that the quantity $b_{ch}(R)$ tends to unity with an increase in R. For the homologs with n in the range $2 \le n \le 16$, the increase in the difference $(R - R_c)$ with an increase in n in formula (11) compensates for the decrease in the quantity $\sigma(R)$. This explains the approximate equality $b_{ch}(R) \approx b_{ch}$ and the observed dependence described by relationship (7).

Table 2. Parameters N_c, R_c, ρ_c, D_c, D_{ch}, and b_{ch} determined from computer simulation of molecules of the compounds under consideration for different conformations of side fragments

Compound	*n*2*Ph*	*n*3*Ph*	*n*4*Ph*	**1**(1)	**1**(2)	**2**(1)	**2**(2)	**3**(1)
$N_c(R_c)$	12(21)	18(31.5)	24(42)	24(42.8)		33(42.8)		42(42.8)
ρ_c	0.679	1.793	1.463	1.833		1.452		1.233
D_c	1.612	1.025	1.128	0.998		1.224		1.391
D_{ch}	0.814	0.786	0.769	0.770	0.780	0.813	0.821	0.837
b_{ch}	0.973	0.973	0.977	0.993	0.959	0.993	0.959	0.993

Compound	**3**(2)	**4**(1)	**4**(2)	**5**(1)	**5**(2)	**6**(1)	**6**(2)	8
$N_c(R_c)$	42(42.8)	60(42.8)		20(22)		24(22)		54(45.5)
ρ_c	1.233	0.989		1.026		0.799		1.090
D_c	1.391	1.634		1.582		1.788		1.489
D_{ch}	0.844	0.862	0.868	0.904	0.879	0.995	0.959	0.933
b_{ch}	0.959	0.993	0.959	1.011	0.923	1.011	0.923	0.967

Compound	**9***a*	**9***b*(1) **9***b*(2)	**9***b*(3)	**9***b*(4)	**9***b*(1/3) **9***b*(2/3)	**9***b*(1/4) **9***b*(2/4)	**9***c*(1) **9***c*(2)	**9***c*(1/3) **9***c*(2/3)
$N_c(R_c)$	18(22)	36(31.5)	36(34.3)		36(34.3)		72(53.2)	72(54.5)
ρ_c	1.186	0.944	1.166		1.122		1.050	1.116
D_c	1.464	1.630	1.472		1.503		1.561	1.503
D_{ch}	1.109	0.973	1.005	1.018	1.009	1.017	0.890	0.899
b_{ch}	1.011	0.973	0.983	0.914	0.999	0.971	0.970	1.010

Compound	**9***c*(1/4) **9***c*(2/4)	**9***d*(1)	**9***d*(2)	**10***a*(1/4, 2/3, 2/4)	**10***b*(1/5)	**10***b*(2/6)	**10***b*(2/7)	**10***b*(1/8)
$N_c(R_c)$	72.(54.5)	66(56.7)		27(31.5)	45(41.6)		45(43.1)	
ρ_c	1.116	1.334		1.389	1.133		1.188	
D_c	1.503	1.367		1.339	1.466		1.438	
D_{ch}	0.922	0.966	0.984	$1 < D_{ch} \le D_c$	0.988	0.984	0.973	1.009
b_{ch}	0.975	0.983	0.949	0.993*	0.930	0.874	0.892	0.931

Compound	**10***b*(3/6)	**10***b*(4/5)	**10***c*(1/5)	**10***c*(2/6)	**10***c*(2/7)	**10***c*(1/8)	**10***c*(3/6)	**10***c*(4/5)
$N_c(R_c)$	45(43.1)		81(62.8)		81(63.7)		81(62.8)	
ρ_c	1.299		1.052		1.077		1.098	
D_c	1.377		1.506		1.491		1.466	
D_{ch}	1.016	$1 < D_{ch} \le D_c$	0.891	0.895	0.881	0.906	0.901	0.931
b_{ch}	0.995	0.913	0.955	0.853	0.908	0.932	1.011	0.956

* For molecules **10***a*(2/3) and **10***a*(2/4), $b_{ch} = 0.914$.

Substituting expression (8) into formula (1) gives the relationship

$$D(R) = \frac{R[N(R) - N_c]}{N(R)(R - R_c)} b_{ch}(R) \equiv D_0(R) b_{ch}(R). \quad (12)$$

At $R \gg R_c$ and $N(R) \gg N_c$, we have $D_0(R) \approx 1$ and $D(R) \approx b_{ch}(R)$. By disregarding the dependence $\sigma(R)$, from formula (10), we obtain the relationship $[N(R) - N_c] \sim (R - R_c)$ and the equality $D(R) = D_0(R)$. Setting $[N(R) - N_c]/(R - R_c) \equiv \tan\alpha$ and $N(R)/R \equiv \tan\theta(R)$, we can write the expression for $D_0(R)$ in the form

$$D_0(R) = \tan\alpha/\tan\theta(R). \quad (13)$$

At $\alpha < \theta(R)$, the inequality $D_0(R) < 1$ is satisfied for the majority of the studied compounds. At $\alpha > \theta(R)$, we have the inequality $D_0(R) > 1$ for molecules **9***a*, **9***b*(3, 4, 1/3, 2/4), **10***a*(1/4, 2/3, 2/4), and **10***b*(1/8, 3/6, 4/5). At $\alpha < \theta(R)$ [$\alpha > \theta(R)$], an increase in R leads to a slow decrease (increase) in the angle $\theta(R)$ tending to the

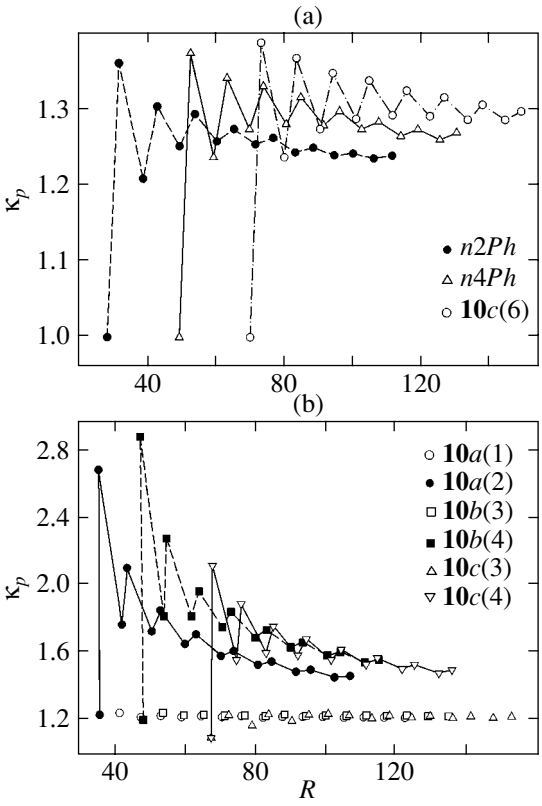

Fig. 8. Dependences $\kappa_p(R)$ for the studied compounds with (a) $\gamma = 0$ and (b) different values of $\beta - \gamma$. For explanation, see the text.

angle α and an increase (decrease) in the quantity $D_0(R)$ tending to unity. The dependence $D_0(R)$ can be well pronounced for molecules with small values of N_c and R_c. This is actually observed for compounds *n*2*Ph*, **5**(1, 2), **9***a*, and **10***a*(1/4, 2/3, 2/4).

At $D_0(R) < 1$, the insignificant decrease in the function $\ln\sigma(R)$ with an increase in R in relationships (11) and (12) partially compensates for the increase in $D_0(R)$ with an increase in the chain length and is responsible for the observed approximate equality $D(R) \approx D_{ch} < 1$. By contrast, at $D_0(R) > 1$, the decrease in the function $\ln\sigma(R)$ with an increase in R in relationships (11) and (12) enhances the decrease in $D(R)$ with an increase in the chain length. This is characteristic of molecules **9***a* and **10***b*(4/5) and can be seen in Fig. 6c for molecules **10***a*(1/4, 2/3, 2/4).

The same limiting value $D_{ch}(n \longrightarrow \infty) = 1$ obtained for lathlike and lacunar nematic molecules with long side chains suggests that, in the limit, these molecules are isomorphic with respect to the quantity D_{ch}. This explains the close limiting temperatures $T_l = T_c(n \longrightarrow \infty)$ of the N_D–I phase transition with an increase in the length of only one chain in molecule **8** or all chains in molecule **9***c* [17].

Let us analyze the basic properties of the function $\kappa_p^{(i)}(R)$ for even and odd homologs with the chains in the *trans* conformation. For simplicity, we assume that the carbon backbone of the chain, the vector $\mathbf{R}_c^{(0)}$, and the vector $\mathbf{R}_{2n}^{(0)}$ ($\mathbf{R}_{2n+1}^{(0)}$) connecting the core center to the center of the even (odd) atom in the chain lie in the same plane. The arrangement of these vectors is schematically depicted in Fig. 7. For the even atoms in the chain, we have the exact expression

$$R_{2n}^{(0)} = [R_c^{(0)} + r_{2n}]\left\{1 - \frac{2r_{2n}R_c^{(0)}[1 - \cos(\beta \pm \gamma)]}{[R_c^{(0)} + r_{2n}]^2}\right\}^{1/2}, \quad (14)$$

where $r_{2n} = 2nl\cos\beta$ is the distance between the centers of the C_0 and C_{2n} atoms. The signs "+" and "–" ahead of γ corresponds to the schemes shown in Figs. 7a and 7b, which differ from each other by the rotation of the chain around the C_0–C_1 bond through an angle of 180°. With due regard for the inequality $2r_{2n}R_c^{(0)}/[R_c^{(0)} + r_{2n}]^2 \le 1/2$ at $\gamma = 0$, we have $\cos\beta = (2/3)^{1/2}$ and $(1 - \cos\beta) \approx 0.184$. Then, expression (14) can be reduced to the approximate relationship

$$R_{2n}^{(0)} = R_c^{(0)} + r_{2n}\frac{2nl\cos\beta + R_c^{(0)}\cos(\beta \pm \gamma)}{2nl\cos\beta + R_c^{(0)}}, \quad (15)$$

which is better satisfied at large differences between r_{2n} and $R_c^{(0)}$ and also at $[1 - \cos(\beta - \gamma)] \ll 1$. Making allowance for the expressions $R_{2n} = r + R_{2n}^{(0)}$, $R_c = r + R_c^{(0)}$, and $2r = l$ and formula (15), from the relationship

$$2n = \kappa_{2n}(R_{2n} - R_c)/l \quad (16)$$

we obtain

$$\kappa_{2n} = \frac{2nl\cos\beta + R_c^{(0)}}{\cos\beta[2nl\cos\beta + R_c^{(0)}\cos(\beta \pm \gamma)]} \quad (n \ge 1). \quad (17)$$

From relationship (17) for $\cos\beta = (2/3)^{1/2}$, we find that the inequalities $\kappa_{2n} \ge (3/2)^{1/2} \approx 1.225$ and $\kappa_{2n} < 3/2$ at $\gamma = 0$ are satisfied, κ_{2n} monotonically decreases and tends to $(3/2)^{1/2}$ with an increase in n or a decrease in the difference $(\beta - \gamma)$ at fixed n, and κ_{2n} increases with an increase in the sum $(\beta + \gamma)$ or the ratio $R_c^{(0)}/l$. At $\beta - \gamma = 0$, all the even atoms in the chain lie in the extension of the vector $\mathbf{R}_c^{(0)}$ and $\kappa_{2n} = (3/2)^{1/2}$. Therefore, at $0 \le (\beta - \gamma) \le \beta$, the function $\kappa_{2n}(R)$ is a decreasing function and the values of $\kappa_{2n}(R)$ fall in a narrow

range; hence, the dependence $\kappa_{2n}(R)$ in expression (9) can be ignored.

For odd atoms in the chain, we first consider the case where $\gamma = 0$. In the same approximation as for formula (15), we can write the relationship

$$R_{2n+1}^{(0)} = R_c^{(0)} + l + r_{2n}\cos\beta\frac{(2n+1)l + R_c^{(0)}}{2nl\cos\beta + R_c^{(0)} + l}, \quad (18)$$

which differs from formula (15) at $\gamma = 0$ in the substitution of $R_c^{(0)} + l = R_1^{(0)}$ for $R_c^{(0)}$. With allowance made for the equality $R_{2n+1} = r + R_{2n+1}^{(0)}$ and expression (18), from relationship

$$\begin{aligned} 2n+1 &= \kappa_{2n+1}(R_{2n+1} - R_c)/l \\ &= \kappa_{2n+1}[(R_{2n+1} - R_1)/l + 1] \end{aligned} \quad (19)$$

we obtain

$$\kappa_{2n+1} = (2n+1)\left[1 + (2n\cos^2\beta)\frac{(2n+1)l + R_c^{(0)}}{2nl\cos\beta + l + R_c^{(0)}}\right]^{-1}. \quad (20)$$

For $n = 0$, we have $\kappa_1 = 1$. This explains the deviation of $\log[N(R) - N_c]$ from the linear dependence [described by formula (7)] in Figs. 6a–6c for the first homologs of compounds having conformers with $\gamma = 0$. In relationship (20), the fractional expression in brackets varies in the range from 1 to $(3/2)^{1/2}$ and, at $n \gg 1$, relationship (20) is reduced to the following formula:

$$\kappa_{2n+1} = (3/2)\frac{[2n(2/3)^{1/2} + 1]l + R_c^{(0)}}{(2n+1)l + R_c^{(0)}}. \quad (21)$$

For $2n(2/3)^{1/2} \gg [1 + R_c^{(0)}/l]$, the function κ_{2n+1} tends to $(3/2)^{1/2}$. In the case of the reverse inequality $[1 + R_c^{(0)}/l] \gg 2n$, according to relationship (20), the function $\kappa_{2n+1} = 3(2n+1)/(4n+3)$ monotonically increases with an increase in n. In particular, we have $\kappa_3 = 9/7 \approx 1.286 > (3/2)^{1/2}$. This indicates that the function κ_{2n+1} [relationship (20)] varies nonmonotonically with an increase in n (i.e., it has a maximum).

For $\gamma \neq 0$, it can be seen from the scheme shown in Fig. 7c that $\alpha_{2n+1} = \pi - (\beta \pm \gamma) + \beta_{2n+1}$. As a result, at $[1 - \cos(\beta \pm \gamma - \beta_{2n+1})] \ll 1$, we obtain

$$R_{2n+1}^{(0)} = R_c^{(0)} + r_{2n+1}\frac{r_{2n+1} + R_c^{(0)}\cos(\beta \pm \gamma - \beta_{2n+1})}{r_{2n+1} + R_c^{(0)}}. \quad (22)$$

Substituting this expression into formula (19) gives the relationship

$$\kappa_{2n+1} = \frac{l(2n+1)}{r_{2n+1}}\left[\frac{r_{2n+1} + R_c^{(0)}}{r_{2n+1} + R_c^{(0)}\cos(\beta \pm \gamma - \beta_{2n+1})}\right]. \quad (23)$$

For $n = \gamma = 0$, we have $r_1 = l$, $\beta_1 = \beta$, and $\kappa_1 = 1$. At $n = \beta - \gamma = 0$ and $R_c^{(0)} \gg l$, we obtain $\kappa_1 = (3/2)^{1/2}$. In the case of $n > 1$, the following relationships are satisfied to a high accuracy:

$$\begin{aligned} r_{2n+1} &= l(2n+1)\cos\beta[1 + \tan^2\beta/(2n+1)^2]^{1/2} \\ &\approx l(2n+1)(2/3)^{1/2}[1 + (1/4)/(2n+1)^2], \\ \cos(\beta \pm \gamma - \beta_{2n+1}) &= \frac{l(2n+1)\cos\beta}{r_{2n+1}}[\cos(\beta \pm \gamma) \\ &+ \frac{\tan\beta}{(2n+1)}\sin(\beta \pm \gamma)\Big] \approx [1 + (1/4)/(2n+1)^2]^{-1} \\ &\times\left[\cos(\beta \pm \gamma) + \frac{1}{(2n+1)\sqrt{2}}\sin(\beta \pm \gamma)\right]. \end{aligned} \quad (24)$$

With allowance made for relationships (24) at $4(2n+1)^2 \gg 1$ (this inequality is valid even at $n = 1$), formula (23) takes the form

$$\kappa_{2n+1} = \frac{(2n+1)l\cos\beta + R_c^{(0)}}{\cos\beta\{(2n+1)l\cos\beta + R_c^{(0)}[\cos(\beta \pm \gamma) + \sin(\beta \pm \gamma)/\sqrt{2}(2n+1)]\}}. \quad (25)$$

For larger values of n satisfying the inequality $(2n + 1) \gg 1$, formula (25) differs from formula (17) in the substitution of $(2n + 1)$ for $2n$ and all the results obtained for formula (17) are valid for formula (25). In particular, for these values of n and $\cos\beta = (2/3)^{1/2}$, the inequality $\kappa_{2n+1} \geq (3/2)^{1/2}$ is satisfied, while at $(\beta - \gamma) = 0$, we have $\kappa_{2n+1} = (3/2)^{1/2}$. By ignoring the term $\sim\sin(\beta \pm \gamma)$ in the denominator of formula (25), i.e., by using the overestimated value of κ_{2n+1} and comparing it with formula (17), it can be shown that $\kappa_{2n+1} < \kappa_{2n}$. The branch of the κ_{2n+1} values lies below the branch of the κ_{2n} values at all n. Therefore, at $n \geq 1$ and $0 \leq (\beta - \gamma) \leq \beta$, the nonmonotonic function $\kappa_{2n+1}(R)$ varies in a narrow range and the dependence $\kappa_{2n+1}(R)$ in expression (9) can be ignored with a high accuracy.

Figure 8 depicts the exact dependences $\kappa_p(R)$ calculated from relationships (16) and (19) for a number of molecules and their conformers at different values of

($\beta \pm \gamma$). It can be seen from Fig. 8 that all the aforementioned qualitative and quantitative results obtained from expressions (17), (20), (21), (23), and (25) are valid for molecules *n*2*Ph*, *n*4*Ph*, and **10***c*(6) with $\gamma = 0$ and the parameters $\lambda = R_c^{(0)}/l = 2.5$, 5.5, and 8.5, respectively; conformers **10***a*(1) and **10***b*(3) with $\beta - \gamma \approx 0$ and $\lambda = 3.7$ and 5.5, respectively; and conformer **10***c*(3) with $\beta - \gamma > 0$ and $\lambda = 8.2$. Note that we have $i = 1$ and $\kappa_p(R) = \sigma(R)$ in formula (9) for molecules *nNPh*.

In the above case where $0 \le (\beta - \gamma) \le \beta$, the dependence $\sigma(R)$ described by relationship (9) is also weak and can be disregarded. This explains the good agreement between the effective parameters D_{ch} obtained from relationship (5) and the values of $\langle D_0(R) \rangle$ calculated from expression (12) and averaged over all homologs of the studied molecules and conformers satisfying the condition $0 \le (\beta - \gamma) \le \beta$.

The quantitative results of the analytical treatment performed are not applicable to conformers **10***a*(2) and **10***b*(4) with $\beta + \gamma \approx 2\beta$. It can be seen from Fig. 8b that, for these conformers, the values of $\kappa_p(R)$ considerably increase for the first homologs and the values of $\kappa_{2n}(R)$ [$\kappa_{2n+1}(R)$] decrease monotonically [nonmonotonically, with passing through a maximum] more rapidly than those in Fig. 8a with an increase in *n* and *R*. The presence of such conformers in molecules favors a leading increase in the values of $N(R)$ represented by expression (8) for the first homologs and results in an increase in the parameters $D_0(R)$ and $D(R)$ described by formula (12). This explains the results of the numerical experiment for molecules **10***a*(2/3, 2/4) (Fig. 6c) and **10***b*(4/5) involving these conformers, for which the dependence of $\log N(R)$ on $\log R$ is hump-shaped with $D(R) \approx D_c$ for the first chain homologs and exhibits a rapid decrease in the parameters $D(R)$ with an increase in the chain length. For molecule **10***c*(4/5) including conformer **10***c*(4) with smaller values of γ and $(\beta + \gamma) < 2\beta$, the dependence of $\log N(R)$ on $\log R$ is also hump-shaped, but it is less pronounced.

The ignored thermal conformational mobility of chains should lead to an increase in the values of $\sigma(R)$, $b_{ch}(R)$, and $D(R)$ due to the smearing of the region of location of chain atoms in the directions perpendicular to the vectors $\mathbf{R}_p^{(0)}$ and the leading increase in $N(R)$ as compared to R in formula (10). This situation is qualitatively similar to the above situation associated with the increase in the sum $(\beta + \gamma)$ for the chain in the *trans* conformation. For molecules of type **1** and **7**, the presence of the chains in the *ortho* positions of the terminal phenyl rings [with respect to the –C(O)O– and –C≡C– bridging fragments] should assist the filing of lacunas of the core and the increase in the dimension D_c. This is important from the standpoint of the design of biaxial molecules capable of forming a biaxial thermotropic nematic phase N_b.

Now, we consider the mean density of atoms $\bar{\rho}(R) = N(R)/V(R)$ in the volume of a sphere $V(R) = 4\pi R^3/3$ and the differential (local) density of atoms $\rho(R) = dN(R)/dV(R)$ in the volume of a spherical layer $dV(R) = 4\pi R^2 dR$. These densities are related by the expression

$$\rho(R) = D(R)\bar{\rho}(R)/3 \qquad (26)$$

and coincide with each other at $D(R) = \text{const} = 3$. In the region of molecular cores, when relationship (3) is satisfied and at $1 < D_c < 2$, the densities $\rho(R) \sim \bar{\rho}(R) \sim R^{D_c - 3}$ decrease with an increase in R ($R \le R_c$). In the region of side chains, with due regard for formula (8), we have

$$\bar{\rho}(R) = \frac{3}{4\pi}\left\{\frac{q\sigma(R)}{2rR^2} + \frac{1}{R^3}[N_c - qR_c\sigma(R)/2r]\right\}. \qquad (27)$$

According to expression (27), the densities $\bar{\rho}(R)$ and $\rho(R)$ decrease even more rapidly with an increase in R due the weak dependence $\sigma(R)$. Therefore, the mass density of an isolated lacunar molecule $\rho_M \sim M(R_M)/V(R_M) \sim \bar{\rho}(R_M)$ rapidly decreases with an increase in the radius R_M of the sphere containing the molecule. However, the density $\rho = m/v$ (m is the molecular weight, v is the molar volume) of discotic nematic phases N_D is identical to the density of calamitic nematic liquid crystals with a relatively close packing of lathlike molecules. This implies that, in the N_D phase, molecules should mutually penetrate into each other and lacunas of a particular molecule should be filled with side chains of neighboring molecules (similar to engaged gears). As a consequence, discotic nematic liquid crystals should possess a high viscosity which is actually one or two orders of magnitude higher than the viscosity of calamitic nematic liquid crystals [18, 19].

5. CONCLUSIONS

Thus, the results obtained in this work have demonstrated that, for a large number of lathlike and lacunar mesogenic molecules (and their conformers) with different chemical structures, the dependence of $\log N(R)$ on $\log R$ exhibits two linear portions that correspond to the core region ($R \le R_c$) and the region of side chains ($R_c < R \le R_M$). Moreover, these portions correspond to the mass dimensions $1 < D_c < 2$ and $D_{ch} \le 1$ or $D_{ch} \ge 1$, depending on the chain conformation. The difference between the dimensions D_c and D_{ch} accounts for the fact that, at $R \le R_M$, the molecules under consideration are not self-similar objects and the topological dimension $D_T = 3$ for these molecules as physical bodies (rather than molecular graphs, i.e., systems of valence bonds connecting the points of atomic positions) is larger than the dimensions D_c and D_{ch}. Therefore, the molecules studied are not fractals for which $D > D_T$ by

definition [1] but belong to a particular class of lacunar objects with a nonuniform (on their size scale) fractional mass dimension $D < D_T$. On the other hand, it can be expected that mesogenic molecules of the monodendron and dendrimer types [6, 7] (not discussed in this work), as well as amphiphilic starlike and dendritic molecules [8, 9] with a branching structure of side fragments, which are characterized by a rather close packing in the three-dimensional space, should have by dimensions $D \leq 3$.

It was established how the main molecular characteristics (molecular symmetry, the number and size of core fragments, their structural–chemical features and conformation, the length and conformation of side chains) affect the values of D_c and ρ_c and the dependence $b_{ch}(R)$. The proposed analytical approach to the analysis of the dependences $D(R)$ and $b_{ch}(R)$ made it possible to explain all the main results of the numerical simulation of the compounds under investigation. The high sensitivity of the parameters D_c and ρ_c to variations in the fine features of the molecular structure indicates that the use of these parameters as descriptors for identifying and predicting the mesogenic properties of molecules in addition to the descriptors already serving for these purposes [16] holds considerable promise.

REFERENCES

1. B. B. Mandelbrot, *The Fractal Geometry of Nature* (Freeman, New York, 1983; Inst. Komp. Issled., Moscow, 2002).
2. J. Feder, *Fractals* (Plenum, New York, 1988; Mir, Moscow, 1991).
3. D. Demus, Liq. Cryst. **5** (1), 75 (1989).
4. D. Demus, in *Handbook of Liquid Crystals*, Ed. by D. Demus, J. Goodby, H.-W. Spiess, and V. Vill (VCH, London, 1998), Vol. 1, Chap. 6, p. 133.
5. K. Praefcke, EMIS Datarev. Ser. **25**, 17 (2000).
6. C. T. Imrie, EMIS Datarev. Ser. **25**, 36 (2000).
7. D. Demus, Mol. Cryst. Liq. Cryst. **364**, 25 (2001).
8. C. Tschierske, Annu. Rep. Prog. Chem., Sect. C: Phys. Chem. **97** (1), 191 (2001).
9. C. Tschierske, J. Mater. Chem. **11**, 2647 (2001).
10. C. Destrade, P. Foucher, H. Gasparoux, N. H. Tinh, A. M. Levelut, and I. Malthete, Mol. Cryst. Liq. Cryst. **106**, 121 (1984).
11. E. M. Aver'yanov, Pis'ma Zh. Éksp. Teor. Fiz. **61** (10), 796 (1995) [JETP Lett. **61**, 815 (1995)].
12. E. M. Aver'yanov, Zh. Éksp. Teor. Fiz. **110** (5), 1820 (1996) [JETP **83**, 1000 (1996)].
13. E. M. Aver'yanov, Zh. Strukt. Khim. **38** (1), 89 (1997).
14. E. M. Aver'yanov, Fiz. Tverd. Tela (St. Petersburg) **46** (8), 1509 (2004) [Phys. Solid State **46**, 1554 (2004)].
15. D. Demus, H. Demus, and H. Zaschke, *Flussige Kristalle in Tabellen* (VEB Deutscher Verlag für Grundstoffindustrie, Leipzig, 1974 and 1984), Vols. 1 and 2.
16. O. B. Akopova, O. V. Zemtsova, and N. V. Usol'tseva, Zhidk. Krist. Ikh Prakt. Ispol., No. 1, 25 (2002).
17. E. M. Aver'yanov, Zhidk. Krist. Ikh Prakt. Ispol., No. 1, 25 (2003).
18. T. W. Warmerdam, D. Frenkel, and R. J. J. Zijlstra, Liq. Cryst. **3** (8), 1105 (1988).
19. M. Ebert, D. A. Jungbauer, R. Kleppinger, T. H. Wendorff, B. Kohne, and K. Praefcke, Liq. Cryst. **4** (1), 53 (1989).

Translated by O. Borovik-Romanova

Physics of the Solid State, Vol. 47, No. 2, 2005, pp. 390–396. Translated from Fizika Tverdogo Tela, Vol. 47, No. 2, 2005, pp. 376–382.

FULLERENES AND ATOMIC CLUSTERS

Rotation of the Inner Shell in a $C_{20}@C_{80}$ Nanoparticle

O. E. Glukhova, A. I. Zhbanov, and A. G. Rezkov

Chernyshevsky State University, ul. Bol'shaya Kazach'ya 112a, Saratov, 410601 Russia

e-mail: GlukhovaOE@info.sgu.ru; ZhbanovAI@info.sgu.ru

Received in final form June 21, 2004

Abstract—The stability of a $C_{20}@C_{80}$ nanoparticle and the rotation of its inner shell are studied theoretically within the tight-binding approximation. It is found that the C_{20} skeleton in the free state is described by space group D_{3d}; in the case where C_{20} is placed into the C_{80} (I_h) fullerene field, the space group of C_{20} is raised to I_h due to isomerization. The total energy surface of the $C_{20}@C_{80}$ compound is scanned over two rotation angles. Based on an analysis of the surface relief and energy isoline map, orientational melting of the nanoparticle is predicted. A nanoparticle gyroscope—C_{20} rotating in the field of C_{80} at a certain relative orientation and energy supply—is also predicted to exist. © *2005 Pleiades Publishing, Inc.*

1. INTRODUCTION

Multilayer carbon nanoparticles consisting of closed curved graphite surfaces inserted into each other have been attracting increased attention [1–3]. These particles are distinguished by a variety of shapes and are referred to as Russian matreshkas, onionlike fullerenes, multilayer fullerenes, etc. Depending on their envelope, these particles can be classified as spherical particles, elongated or tubular fullerenes, or conical fullerenes. Strongly elongated tubular fullerenes with a radius of the cylindrical part from several angstroms to tens of nanometers [2] are usually referred to as carbon nanotubes. Spherical particles [4–7] several nanometers in size with a diamond or hollow core are formed during diamond annealing in vacuum in certain synthesis technologies [4, 5]. Multilayer carbon nanoparticles became a subject of study due to their predicted unique nanomechanical, thermodynamic, and optical properties. They are of nanomechanical interest due to possible relative and directed rotation of the nanoparticle shells [8]. From the thermodynamic viewpoint, clusters could prove to be a new material whose melting would be accompanied by a variety of phase transitions with changes in the relative orientation of the shells [8, 9]. Nanoparticles with a diamond or hollow core are also of astrophysical interest. Being presumably incorporated into cosmic dust, they are characterized by absorptivity at 217.5 nm in the ultraviolet region. Therefore, the optical properties of nanoparticles have become an object of study [10, 11].

The spherical particles known to date, which have been synthesized by various methods, can be conventionally classified into three groups according to their shell shape: spherical, spheroidal, and icosahedral. Icosahedral particles are in a separate group, since it is difficult to attribute them to the first two groups in terms of their appearance. Icosahedral fullerenes, whose topology is controlled only by penta- and hexagons with more than two hundred atoms, appear in the form of spherical and polyhedral fullerenes along the twofold and fivefold axes, respectively [12]. The surface shape of these particles differs strongly from spherical. Fullerene C_{60}, which is the smallest of these particles, can be considered spherical or icosahedral [13]. Spherical shells are isomers of the icosahedral fullerene, and their topology is enriched by seven- and eight-membered cycles, which makes their surface very close to spherical [9, 12–15]. Such spherical shells are characterized by space groups D_{2h} and O_h; groups C_1 and D_{2h} are inherent to nanoparticles [15]. Thus, high-symmetry multilayer fullerenes, whose shape is very close to a sphere, are considered spherical particles. Low-symmetry fullerenes, whose surface substantially differs from spherical, can be attributed to spheroidal fullerenes.

Multilayer tubular fullerenes and conical nanoparticles (similar to an ice-cream cone) are the least studied [16]. There are experimental findings which show that they are metastable and transform into spherical fullerenes as a result of annealing [6]. Among these particles, conical ones are least stable [16].

Spherical and icosahedral nanoparticles have been studied theoretically using various models. Among theses models are models of spherical nanoparticles, corresponding to a global or local minimum of the bond length of an isomer of the outer icosahedral shell [9, 15]; models of nanoparticles whose shells were subjected to preliminary Stone–Wales isomerization [15]; and models of nanoparticles simulated using parallel alignment of their fivefold axes to magnetic field lines [17]. The first two models are most commonly used. Within these models, multilayer fullerenes are considered whose outer shells are described by groups I_h, D_{2h}, and O_h [9, 12–15]. Fullerenes with groups D_{2h} and O_h whose skeletons contain not only pentagons and hexagons but also hepta- and octagons can be produced

from icosahedral fullerenes by Stone–Wales isomerization. As a rule, the energy of a nanoparticle formed by such fullerenes corresponds to a global maximum or to one of the local maxima of the potential energy surface of the particle [15]. It should be noted that the authors of all the papers cited above did not study the potential surface itself and the nanoparticle conformations and did not consider the metric parameters and many energy parameters (e.g., the formation enthalpy and electronic structure). Those authors mainly studied the stability of nanoparticles belonging to various symmetry groups. A few papers devoted to studying the orientational order of nanoparticle shells demonstrate the possibility of changing the relative orientations and even of rotating the shells through energy transfer to a particle. However, changes in the symmetry of the system and transformations in the molecule skeleton were not traced [8].

We study the $C_{20}@C_{80}$ nanoparticle and the configuration and electronic structure of fullerene C_{20} in the ground state in the absence and in the presence of the attracting potential of fullerene $C_{80}(I_h)$. The total energy surface of $C_{20}@C_{80}$, nanoparticle conformers, and relative rotation of C_{20} in the C_{80} field are analyzed. The electronic structure; the conformer topology; the C_{20} position, for which gyroscope-like rotation is possible; and the rotation frequency are determined. The study is carried out using the tight-binding approximation with original parametrization of the Hamiltonian matrix elements.

2. CALCULATION OF THE ELECTRONIC STRUCTURE OF CARBON NANOCLUSTERS

The tight-binding approximation has been efficiently used to calculate electron and phonon spectra of micro- and macroscopic carbon systems [18], including clusters (fullerenes, nanotubes, nanotori, etc.) [19–21]. This method does not require high computing power and yields results that agree well with experimental data. The scheme first proposed in [18] for calculating the diamond and graphite band structure makes it possible to construct the Hamiltonian in real space, in terms of *s* and *p* orbitals of the outer electron shells of carbon atoms. This makes it possible to calculate geometrical parameters and electronic levels under various local changes in the structure of carbon compounds. An approximation is used in which the wave functions of the valence electrons of various atoms are considered nonoverlapping.

According to the scheme mentioned above, the total energy

$$E = E_{\text{bond}} + E_{\text{rep}} \tag{1}$$

(where E_{bond} is the energy of occupied electronic levels and E_{rep} is the phenomenological energy) is minimized with respect to characteristic linear parameters of the cluster skeleton to calculate the configuration and energy characteristics corresponding to the ground state.

The phenomenological energy accounting for the electron–electron and internuclear interactions is written as a sum of pair repulsive potentials:

$$E_{\text{rep}} = \sum_{i<j} V_{\text{rep}}(|r_i - r_j|), \tag{2}$$

where i and j are indices of interacting atoms and r_i and r_j are Cartesian coordinates. The function V_{rep} is given by [18]

$$V_{\text{rep}}(r) = V^0_{\text{rep}}\left(\frac{1.54}{r}\right)^{4.455} \times \exp\left\{4.455\left[-\left(\frac{r}{2.32}\right)^{22} + \left(\frac{1.54}{2.32}\right)^{22}\right]\right\}, \tag{3}$$

where $V^0_{\text{rep}} = 10.92$ eV.

The energy of the occupied levels is

$$E_{\text{bond}} = 2\sum_n \varepsilon_n, \tag{4}$$

where ε_n is the energy of the occupied state with index n (the Hamiltonian eigenvalue) and the factor of 2 accounts for the electron spin.

The interatomic matrix elements of the Hamiltonian are written as [18]

$$V_{ij\alpha}(r) = V^0_{ij\alpha}\left(\frac{1.54}{r}\right)^{2.796} \times \exp\left\{2.796\left[-\left(\frac{r}{2.32}\right)^{22} + \left(\frac{1.54}{2.32}\right)^{22}\right]\right\}, \tag{5}$$

where r is the interatomic distance, i and j are the orbital quantum numbers of wave functions, and α is the index indicating the bond type (σ or π).

To calculate the electronic structure of carbon nanoclusters, original parametrization of the atomic terms ε_s and ε_p and equilibrium overlap integrals $V^0_{ss\sigma}$, $V^0_{sp\sigma}$, $V^0_{pp\sigma}$, and $V^0_{pp\pi}$ was carried out [21]. This parametrization proved effective in calculating the bond lengths and energy spectra of fullerenes and single-layer nanotubes [21]. It is largely advantageous to analogous schemes [18–20] because of the possibility of calculating the ionization potential, whereas the initial parametrization version [18] allowed determination of only the energy gap (this quantity is applied to solids; here, it implies the gap spacing between the highest occupied and lowest vacant levels, rather than the energy interval between bands). In this case, the highest occupied level was coincident with the ground level, which made it

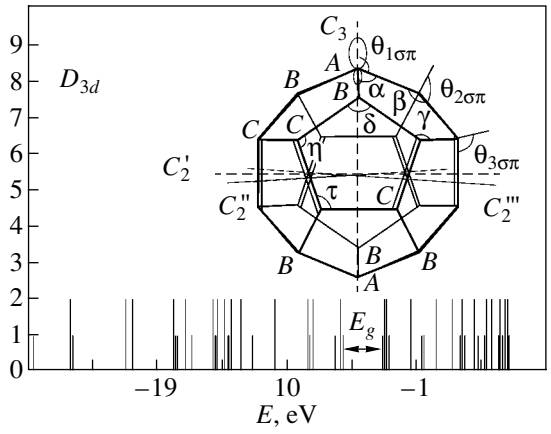

Fig. 1. Electronic spectrum of fullerene C_{20} with space group D_{3d}.

impossible to apply Koopmans' theorem to calculate the ionization potential by using the electronic spectrum. The ionization potential calculated for fullerene $C_{20}@C_{80}$ agrees well with that determined experimentally, as well as with other characteristics (the bond length and energy gap).

3. SYMMETRY AND ELECTRONIC PROPERTIES OF FREE FULLERENE C_{20}

Fullerene C_{20} is the smallest synthesized stable carbon cluster with a three-dimensional structure. The study of its chemical and physical properties, as well as those of nanoparticles with C_{20}, is complicated by the fact that there is no common opinion about the symmetry of the C_{20} cage. Many papers [22–28] are devoted to the study of the geometric and electronic structure of this smallest fullerene. It is commonly accepted that the symmetry of both neutral C_{20} and ionized C_{20}^- is not icosahedral due to the Jahn–Teller effect. However, calculations of the geometric and electronic structure of the fullerene using various quantum-chemical methods yield different point groups for its skeleton: C_2 or C_i [24], C_s [25], D_{3d} [26, 28], and C_{2h} [27]. Even studies that use the same method (the density-functional method, but with various modifications) yield different point groups [24, 26].

The disagreements in the optimized configurations and in the space group found for the skeleton formed by σ electrons of C_{20} can be explained by the specific features of the quantum-chemical methods used to calculate the electron density distribution. The latter, in turn, depends on the correct inclusion of rehybridization, due to which the hybridization in σ bonds becomes $sp^{2+\Delta}$ instead of sp^2 [27].

The optimum geometric and electronic structure of C_{20} was calculated by minimizing the total energy of the cluster over 54 coordinates (six coordinates specified the position of the molecule in space). The tight-binding approximation does not allow determination of the ground state multiplicity; however, rehybridization is included automatically in calculating the interaction energy between electron clouds.

The initial atomic coordinates correspond to a dodecahedral lattice. By optimizing over the coordinates, the total energy is found to have a minimum for space group D_{3d}, which agrees with the results of [26, 28]. Figure 1 shows the electron spectrum and C_{20} (D_{3d}) fullerene, whose threefold and twofold symmetry axes; valence angles α, β, γ, δ, η, and τ; angles $\theta_{1\sigma\pi}$, $\theta_{2\sigma\pi}$, and $\theta_{3\sigma\pi}$ between the π and σ electron lobe axes; and shortest bond length (double line) are indicated. Independent atomic bases *A*, *B*, and *C* of the molecule are also indicated. Symmetry operations applied to the coordinates of a single atom can reconstruct the coordinates of the other atoms relative to the basis under consideration. The energy and metric characteristics of C_{20} (D_{3d}) are listed in Table 1. It contains ionization potential *I*, energy gap E_g, molecule energy E_1, atomization energy E_a (per atom), enthalpy ΔH_f, electron populations in atomic bases *A*, *B*, *C* (taking into account only valence electrons), bond lengths *r* (r_{A-B}, r_{B-C}, r_{C-C} are distances between atoms of various bases), distances *d* between atoms that are opposite with respect to the inversion center (indices *A*, *B*, *C* characterize various bases), valence angles, and pyramidalization angles θ_{1p}, θ_{2p}, and θ_{3p} ($\theta_p = \theta_{\sigma\pi} - 90°$). The angle designations correspond to Fig. 1. The data from Table 1 show that rehybridization takes place in C_{20} and that atoms are in the $sp^{2+\Delta}$ rather than the sp^2 state [27], which makes it promising for polymerization [23]. The degree of rehybridization for atoms of various bases varies depending on the pyramidalization and valence angles. As the pyramidalization angle decreases (positions *A* and *B* in Fig. 1), the electron populations in atoms decrease due to weaker hybridization of *s* and p_π clouds and to an increase in the energy of hybrid orbitals. An increase in the electron density allows us to expect a higher chemical activity of basis *C* atoms, as well as directionality in the bond formation.

4. STRUCTURE AND ENERGY CHARACTERISTICS OF THE $C_{20}@C_{80}$ COMPOUND

To study $C_{20}@C_{80}$, we consider the icosahedral isomer C_{80}, which has a larger binding energy than the other isomers [29]. The bond lengths are calculated by minimizing the total energy of the molecule and are found to be 1.425 and 1.458 Å, respectively. These values are in good agreement with *ab initio* calculations performed in [29], where the interval 1.43–1.47 Å is given for the bond lengths of the I_h isomer. The icosahedral C_{80} shape is closest to spherical (atoms are spaced from the center at 4.11–4.15 Å), which con-

forms to the geoid shape of C_{20}. The C_{80} (I_h) enthalpy is 13.66 kcal/mol atom^{-1}.

The C_{80} cage sizes exceed those of C_{20} only slightly; therefore, it can be expected that no more than one stable position will be observed for C_{20} in the outer-shell field and that the fullerene centers will coincide. However, relative rotation of the shells and C_{20} isomerization are possible in the outer-shell field. The goal of this study is to detect the C_{20} structure in the outer-shell field, to calculate the energy characteristics of the ground state of the C_{100} nanoparticle, and to study possible C_{20} reorientation and rotation when a certain energy is transferred to the compound.

In the zeroth approximation, the C_{20} and outer-shell centers are set at the same point taken as the coordinate origin of the system. The C_{80} and C_{20} symmetries are defined by groups I_h and D_{3d}, respectively. The fivefold axis of the outer fullerene and the threefold axis coincide with the Z axis. The $C_{20}@C_{80}$ symmetry and ground-state parameters are determined by minimizing the total energy, which takes into account the band-structure energy, internuclear and electron–electron interactions inside each shell [21], and the interaction energy between atoms from different shells, calculated using the Lennard–Jones formula [30]

$$U_i = \frac{A}{\sigma^6}\left(\frac{1}{2}y_0^6\frac{1}{(r_i/\sigma)^{12}} - \frac{1}{(r_i/\sigma)^6}\right). \quad (6)$$

Expression (6) allows calculation of the interaction potential of a pair of atoms from different shells. Here, r_i is the distance between the atoms of the ith pair, σ = 1.42 Å is the C–C bond length, and y_0 = 2.7 and A = 24.3×10^{-79} J m^6 are empirically fitted parameters. The shell interaction energy is determined by summing the pair interaction potentials U_i between each atom of one shell and all atoms of the other shell over all atoms of the first shell.

Energy minimization over the coordinates of all atoms is used to determine the C_{100} nanoparticle ground state. This state is described by space group C_5 ($I_h@I_h$). The C_{100} enthalpy is 29.04 kcal/mol atom^{-1}. In this case, the C_{20} fullerene restored high symmetry from D_{3d} to I_h in the attracting potential as a result of isomerization with a change in the orientation with respect to the outer shell (the fivefold axes of C_{20} and outer shell now coincide). Figure 2a shows the C_{20} orientation inside C_{80} and the nanoparticle electron spectrum and demonstrates the overlap of the spectra of shells with the formation of an energy gap E_g in the nanoparticle spectrum, which is smaller than E_g for fullerenes in the free state. Table 2 lists metric and energy characteristics of the compound, including the shell sphere radii R and the enthalpy ΔH of the reaction C_{20} (D_{3d}) + C_{80} (I_h) $\longrightarrow$ C_{100}. Other designations are the same as in Table 1.

Table 1. Metric and energy characteristics of C_{20} isomers

Bond lengths, Å	C_{20}, D_{3d}	C_{20}, I_h ($C_{20}@C_{80}$)
$r_{A–B}$	1.461	1.425
$r_{B–C}$	1.469	–
$r_{C–C}$	1.514	–
$r_{C–C}$ (double line in Fig. 1)	1.436	–
Internuclear distances, Å		
$d_{A–A}$	4.047	3.997
$d_{B–B}$	4.085	–
$d_{C–C}$	4.147	–
Valence angles, deg		
α	108.60	108.00
β	108.80	–
γ	107.00	–
δ	108.00	–
η	109.50	–
τ	108.50	–
Pyramidalization angles, deg		
θ_{1p}	20.36	20.89
θ_{2p}	20.43	–
θ_{3p}	21.23	–
Energy parameters		
E_1, eV/atom	−42.36	−42.23
E_a, eV/atom	6.15	6.03
ΔH_f, kcal/mol atom^{-1}	29.42	32.32
I, eV	6.69	6.39
E_g, eV	2.88	3.52
Atomic electron density		
Basis A	3.912	4.00
B	3.904	
C	4.062	

The surface of the total energy E_{tot} of the nanoparticle is calculated for rotations of C_{20}(I_h) inside C_{80} (I_h). The initial configuration of the nanoparticle corresponds to the ground state (global energy minimum). Rotation of C_{20} is carried out by sequential rotations of the C_{20} fivefold axis through the angle φ_z about the Z axis and through φ_y about the Y axis (Fig. 2a). The E_{tot} surface is calculated by minimizing the nanoparticle energy with respect to three parameters: the bond length of icosahedral C_{20} and two bond lengths of the outer fullerene. During C_{20} rotations and shell optimization in the two-layer cluster, the space group changes from C_5 (C_{100}) to D_{5d}, T, C_2, C_{2h}, and C_i. In this case, the energy exhibits many local minima (Fig. 3a). In [31], where $C_{20}@C_{60}$ stability was studied, C_{20} was rotated with retention of the D_{5d} space group in the system.

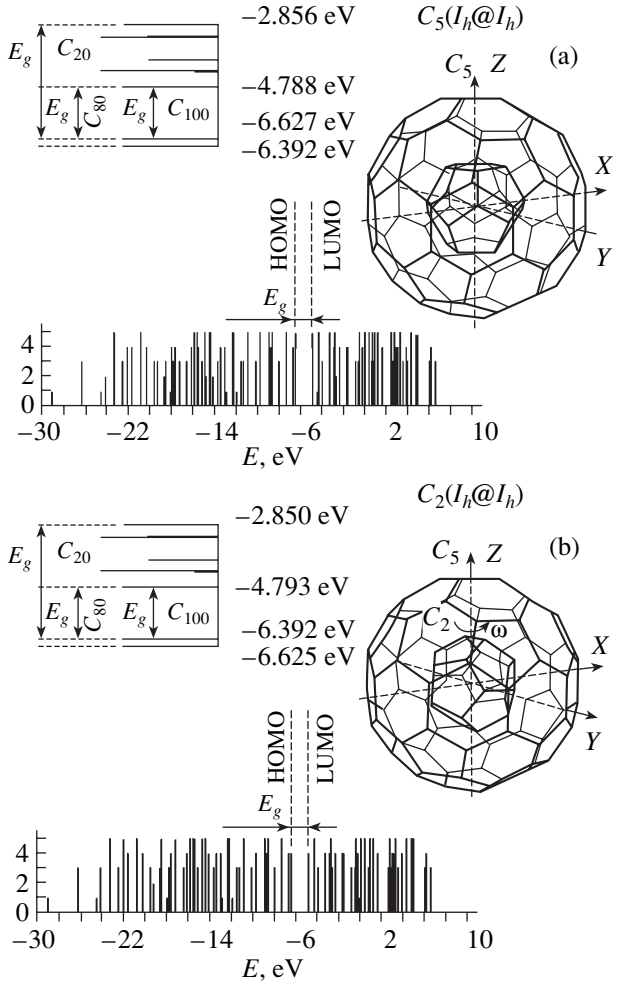

Fig. 2. Electron spectrum of the $C_{20}@C_{80}$ nanoparticle with (a) space group C_5 corresponding to the ground state and (b) space group C_2 controlling the nanogyroscope.

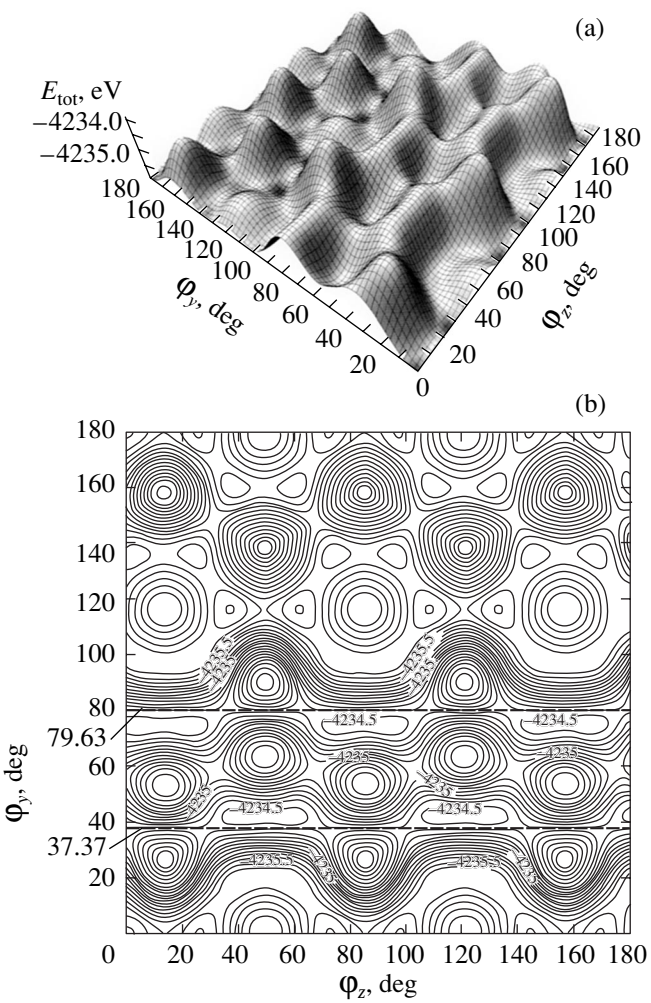

Fig. 3. Total-energy surface of the $C_{20}@C_{80}$ nanoparticle at sequential rotations about the *Z* and *Y* axes: (a) general view and (b) the map of isolines of the total energy surface (top view).

An analysis of the multiwell surface and the energy isoline map (Fig. 3b) shows periodicity of the energy variations along the *Z* and *Y* axes in steps of 72° and 180°, respectively. Table 2 lists the nanoparticle energies E_{tot} and the geometrical and energy characteristics of conformations corresponding to the local minima (with high symmetry), the global maximum, and an intermediate energy (the distinguishing feature of this conformation is explained below). The coordinates (φ_y, φ_z) of the surface points corresponding to conformations are shown taking into account the periodicity along the axes.

An analysis of the results obtained shows that all the nanoparticle conformations are stable. The distance between the shells is 2.344–2.4 Å (C_{100}), which is 1 Å smaller than the graphite interlayer distance. There are no chemical bonds between shell atoms.

Several features in the nanoparticle energy parameters were found.

The ionization potential is identical for all the C_{100} conformations, since the highest occupied level in the spectra of two-layer clusters is controlled by the corresponding fourfold degenerate level of C_{20}, whose value remains unchanged. The energy gap of all the nanoparticle conformations is narrower than those of the fullerenes comprising them. This effect is explained by the overlapping spectra of the inner and outer shells, which is shown in Fig. 2.

5. C_{20} NANOGYROSCOPE IN COMPOUND $C_{20}@C_{80}$

Scanning of the total energy surface of the nanoparticle showed that the surface is characterized by "specific" isolines arranged between a ridge of local maxima and minima, which can be reached by rotating C_{20} about the *Z* axis at a fixed φ_y angle. The *Z* axis coincides with the twofold axis of C_{20}.

Table 2. Characteristics of $C_{20}@C_{80}$ conformations of the potential energy surface E_{tot}

Parameters	E_{tot} minima		E_{tot} maximum	Gyroscope conformation
Total energy values	global −4237.262 eV	local −4235.696 eV	global −4233.943 eV	−4234.592 eV
Space groups and angular coordinates	$C_5(\varphi_y; \varphi_z)$ (0°; 0°), (0°; 26°) (116°; 34°)	D_{5d} (63.5°; 49°) (53.5°; 13°)	T (90°; 49°) (26.5°; 13°)	C_2 (37.38°; 0°) (79.19°; 0°)
$r_1(C_{80})$, Å	1.551	1.528	1.533	1.533
$r_2(C_{80})$, Å	1.500	1.532	1.532	1.531
$r(C_{20})$, Å	1.426	1.425	1.424	1.424
R_{80}, Å	4.342	4.391	4.395	4.393
R_{20}, Å	1.998	1.997	1.995	1.996
$I(C_{80})$, eV	6.627	6.629	6.623	6.625
$I(C_{20})$, eV	6.392	6.392	6.392	6.392
$I(C_{20}@C_{80})$, eV	6.392	6.392	6.392	6.392
$E_g(C_{80})$	1.839	1.839	1.828	1.832
$E_g(C_{20})$	3.536	3.537	3.545	3.542
$E_g(C_{20}@C_{80})$	1.604	1.603	1.587	1.599
E_1, eV/atom	−42.373	−42.357	−42.339	−42.346
E_a, eV/atom	6.167	6.152	6.134	6.143
ΔH, kcal/mol atom^{-1} $C_{80} + C_{20}(D_{3d}) \longrightarrow C_{100}$	29.049	29.394	29.808	29.647

The isoline energies and positions are shown in Fig. 3b. The configuration and energy parameters of this conformation are shown in Table 2. The enthalpy of the C_{100} (C_5) $\longrightarrow$ C_{100} (C_2) transition is 59.8 kcal/mol. If an energy exceeding 59.8 kcal/mol is transferred to the system, it is possible that relative rotational vibration of the shells, initiated in the global minimum, will not be completed by the transition to the $C_{100}(C_2)$ state and will continue by rotating C_{20} about the Z axis (its twofold symmetry axis, Fig. 2b); i.e., we have a gyroscope. In this case, energy transfer to the particle is possible through various processes, including orientational melting [9], quasi-elastic collisions, and inelastic collisions of fullerenes accompanied by a 1.5–21.5-eV energy transfer to the fullerenes with an increase in their temperature and potential energy by 5–10 eV [32]. Given the rotation energy, the nanogyroscope frequency can be calculated as

$$\frac{kT}{2} = \frac{J\omega^2}{2}, \qquad (7)$$

where k is the Boltzmann constant, J is the moment of inertia, T is the temperature, and ω is the angular rotation rate. For C_{20}, we have $J = 8.332 \times 10^{-38}$ g cm^2. For example, if an excess enthalpy corresponds to a temperature increase of only 0.01 K (during a quasi-elastic central collision of fullerenes [32]), then $\omega = 4.07 \times 10^9$ rad/s (6.48×10^8 s^{-1}). The molecular weight of the nanogyroscope is 240. For comparison, the frequency ω at $T = 300$ K is 3.8×10^8 rad/s for a desoxyribonucleic acid molecule with a molecular weight of 1.2×10^8 containing 1.2×10^4 turns with a turn radius of 6.7 Å [33].

6. CONCLUSIONS

By optimizing the neutral C_{20} configuration, it has been found that the ground state has D_{3d} symmetry. At the same time, if the symmetry of the C_{20} icosahedral fullerene in the free state reduces, isometrization takes place in the (C_{80}) field, which restores the pentagonal dodecahedron cage.

The study of the $C_{20}@C_{80}$ model makes it possible (i) to conclude that the nanoparticle retains stability at all points of the total energy surface, (ii) to assume that orientational melting of the particle takes place with the transition to nearby global and local minima as a result of relative rotational vibration of the shells [9], and to predict the existence of the C_{20} nanoparticle gyroscope inside C_{80} when a certain energy is transferred. It can also be assumed that a similar rotation of the inner shell will also take place for a variety of nanoparticles. If this phenomenon is confirmed experimentally, a new direction will arise in the nanomechanics of carbon clusters.

ACKNOWLEDGMENTS

This study was supported by the Russian Foundation for Basic Research (project no. 04-02-17484-a) and the International Scientific and Engineering Center (project no. 1024.2).

REFERENCES

1. S. Iijima, J. Cryst. Growth **50**, 675 (1980).
2. S. Iijima, Nature **354**, 56 (1991).
3. D. Ugarte, Chem. Phys. Lett. **198** (6), 596 (1992).
4. V. L. Kuznetsov, A. L. Chuvilin, Y. V. Butenko, I. Y. Mal'kov, and V. M. Titov, Chem. Phys. Lett. **222**, 343 (1994).
5. S. Tomita, M. Fujii, S. Hayashi, and K. Yamamoto, J. Chem. Phys. **114**, 7477 (2001).
6. D. Ugarte, Nature **359**, 707 (1992).
7. F. Banhart, T. Fuller, P. Redlich, and P. M. Ajayan, Chem. Phys. Lett. **269**, 349 (1997).
8. M. Porto, M. Urbakh, and J. Klafter, Phys. Rev. Lett. **84** (26), 6058 (2000).
9. Yu. E. Lozovik and A. M. Popov, Fiz. Tverd. Tela (St. Petersburg) **44** (1), 180 (2002) [Phys. Solid State **44**, 186 (2002)].
10. W. A. de Heer and D. Ugarte, Chem. Phys. Lett. **207**, 480 (1993).
11. S. Tomita, S. Hayashi, Y. Tsukuda, and M. Fujii, Fiz. Tverd. Tela (St. Petersburg) **44** (3), 433 (2002) [Phys. Solid State **44**, 450 (2002)].
12. A. Maiti, C. J. Brabec, and J. Bernholc, Phys. Rev. Lett. **70** (20), 3023 (1993).
13. Jian Ping Lu and W. Yang, Phys. Rev. B **49** (16), 11421 (1994).
14. Y.-L. Lin and F. Nori, Phys. Rev. B **49** (7), 5020 (1994).
15. M. I. Heggie, M. Terrones, B. R. Eggen, G. Jungnickel, R. Jones, C. D. Latham, P. R. Briddon, and H. Terrones, Phys. Rev. B **57** (21), 13339 (1998).
16. D. Toma'nek, W. Zhong, and E. Krastev, Phys. Rev. B **48** (20), 15461 (1993).
17. Q. Ru, M. Okamoto, Y. Kondo, and K. Takayanagi, Chem. Phys. Lett. **259**, 425 (1996).
18. L. Goodwin, J. Phys.: Condens. Matter **3**, 3869 (1991).
19. N. V. Khokhryakov and S. S. Savinskiĭ, Fiz. Tverd. Tela (St. Petersburg) **36** (12), 3524 (1994) [Phys. Solid State **36**, 1872 (1994)].
20. N. V. Khokhryakov, S. S. Savinskiĭ, and J. M. Molina, Pis'ma Zh. Éksp. Teor. Fiz. **62** (7), 595 (1995) [JETP Lett. **62**, 617 (1995)].
21. O. E. Glukhova and A. I. Zhbanov, Fiz. Tverd. Tela (St. Petersburg) **45** (1), 180 (2003) [Phys. Solid State **45**, 189 (2003)].
22. K. Tanaka, H. Ago, T. Yamabe, K. Okahara, and M. Okada, Int. J. Quantum Chem. **63**, 637 (1997).
23. S. Okada, Y. Miyamoto, and M. Saito, Phys. Rev. B **64**, 245405 (2001).
24. Z. Wang, P. Day, and R. Pachter, Chem. Phys. Lett. **248**, 121 (1996).
25. M. Sawtarie, M. Menon, and K. R. Subbaswamy, Phys. Rev. B **49** (11), 7739 (1994).
26. G. Galli, F. Gygi, and J.-C. Golaz, Phys. Rev. B **57** (3), 1860 (1998).
27. M. Saito and Y. Miyamoto, Phys. Rev. Lett. **87**, 035503 (2001).
28. A. L. Chistyakov and I. V. Stankevich, Fiz. Tverd. Tela (St. Petersburg) **44** (3), 565 (2002) [Phys. Solid State **44**, 593 (2002)].
29. K. Nakao, N. Kurita, and M. Fujita, Phys. Rev. B **49** (16), 11 415 (1994).
30. D. Qian, W. K. Liu, and R. S. Ruoff, J. Phys. Chem. B **105**, 10 753 (2001).
31. I. V. Stankevich, A. L. Chistyakov, and M. I. Skvortsova, Izv. Ross. Akad. Nauk, Ser. Khim. **3**, 436 (1999).
32. Y. Xia, Y. Xing, C. Tan, and L. Mei, Phys. Rev. B **53**, 13871 (1996).
33. C. Kittel, W. D. Knight, and M. A. Ruderman, in *Mechanics* (McGraw-Hill, New York, 1973; Nauka, Moscow, 1978).

Translated by A. Kazantsev